AEROSERVOELASTIC ANALYSIS AND ROBUST CONTROLLER
SYNTHESIS FOR FLUTTER SUPPRESSION OF AIR VEHICLE
CONTROL ACTUATION SYSTEMS

A THESIS SUBMITTED TO
THE GRADUATE SCHOOL OF NATURAL AND APPLIED SCIENCES
OF
THE MIDDLE EAST TECHNICAL UNIVERSITY

BY

ALPER AKMEŞE

IN PARTIAL FULFILLMENT OF THE REQUIREMENTS
FOR
THE DEGREE OF DOCTOR OF PHILOSOPHY
IN
THE DEPARTMENT OF MECHANICAL ENGINEERING

JUNE 2006

Approval of the Graduate School of Natural and Applied Sciences

_____

Prof. Dr. Canan ÖZGEN

Director

I certify that this thesis satisfies all the requirements as a thesis for the degree of Doctor of Philosophy.

_____

Prof. Dr. S. Kemal İDER

Head of Department

This is to certify that we have read this thesis and that in our opinion it is fully adequate, in scope and quality, as a thesis for the degree of Doctor of Philosophy.

_____   _____

Dr. Mutlu D. CÖMERT   Prof. Dr. Bülent E. PLATİN

Co-Supervisor   Supervisor

Examining Committee Members

Prof. Dr. Tuna BALKAN   (METU, ME)   _____

Prof. Dr. Bülent E. PLATİN (METU, ME)   _____

Prof. Dr. Yavuz YAMAN   (METU, AEE)   _____

Assoc. Prof. Dr. Mehmet Ö. EFE (TOBB ETU, EE)   _____

Dr. Mutlu D. CÖMERT   (TÜBİTAK-SAGE)   _____

I hereby declare that all information in this document has been obtained and presented in accordance with academic rules and ethical conduct. I also declare that, as required by these rules and conduct, I have fully cited and referenced all material and results that are not original to this work.

Name, Last Name   :   Alper AKMEŞE

Signature   :

ABSTRACT

AEROSERVOELASTIC ANALYSIS AND ROBUST CONTROLLER
SYNTHESIS FOR FLUTTER SUPPRESSION OF AIR VEHICLE
CONTROL ACTUATION SYSTEMS

AKMEŞE, Alper

Ph.D., Department of Mechanical Engineering

Supervisor: Prof. Dr. Bülent E. PLATİN

Co-Supervisor: Dr. Mutlu D. CÖMERT

June 2006, 411 pages

Flutter is one of the most important phenomena in which aerodynamic
surfaces become unstable in certain flight conditions. Since the 1930's
many studies were conducted in the areas of flutter prediction in design
stage, research of design methods for flutter prevention, derivation and
confirmation of flutter flight envelopes via tests, and in similar subjects for
aircraft wings. With the use of controllers in 1960's, studies on the active
flutter suppression began. First the classical controllers were used. Then,
with the improvement of the controller synthesis methods, optimal
controllers and later robust controllers started to be used. However, there
are not many studies in the literature about fully movable control surfaces,
commonly referred to as fins. Fins are used as missile control surfaces,
and they can also be used as a horizontal stabilizer or as a canard in

aircraft. In the scope of this thesis, controllers satisfying the performance and flutter suppression requirements of a fin are synthesized and compared. For this purpose, H2, H∞, and μ controllers are used. A new flutter suppression method is proposed and used. In order to assess the performance of this method, results obtained are compared with the results of another flutter suppression method given in the literature. For the purpose of implementation of the controllers developed, aeroelastic model equations are derived by using the typical section wing model with thin airfoil assumption. The controller synthesis method is tested for aeroelastic models that are developed for various flow regimes; namely, steady incompressible subsonic, unsteady incompressible subsonic, unsteady compressible subsonic, and unsteady compressible supersonic.

Keywords: Aeroservoelasticity, Aeroelasticity, Robust Controller Synthesis, Flutter Suppression, μ-method Flutter Analysis.

ÖZ

HAVA ARACI KONTROL TAHRİK SİSTEMLERİNİN AEROSERVOELASTİK AÇIDAN İNCELENMESİ VE ÇIRPINTI BASTIRMA İÇİN DAYANIKLI KONTROLCÜ SENTEZİ

AKMEŞE, Alper

Doktora, Makina Mühendisliği Bölümü

Tez Yöneticisi: Prof. Dr. Bülent E. PLATİN

Ortak Tez Yöneticisi: Dr. Mutlu D. CÖMERT

Haziran 2006, 411 sayfa

Çırpıntı aerodinamik yüzeylerde bazı uçuş koşullarında oluşan kararsızlıkların en önemlilerinden biridir. Uçak kanatlarındaki çırpıntının tasarım aşamasında öngörülmesi, çırpıntının önlenmesi için gerekli tasarım yöntemlerinin araştırılması, çırpıntı uçuş zarfının testlerle belirlenmesi ve doğrulanması ve benzeri konularda 1930'lardan beri bir çok çalışma yapılmıştır. Kontrolcülerin 1960'lardan itibaren kullanılmasıyla çırpıntının aktif olarak bastırılması ile ilgili çalışmalara başlanılmıştır. Başlarda klasik kontrolcüler kullanılırken, kontrolcü tasarım yöntemlerinin ilerlemesi ile birlikte optimal kontrol yöntemleri ve daha sonra gürbüz kontrol yöntemlerinin kullanılmasına başlanılmıştır. Ancak literatürde tamamı hareketli kontrol kanatları ile ilgili fazla çalışma bulunmamaktadır.

Tamamı hareketli kontrol kanatları, füze kontrol yüzeylerinde kullanıldığı gibi, uçakların yatay dümenlerinde ya da bağımsız ön kontrol kanatçıklarında da kullanılabilmektedir. Bu tez kapsamında hareketli kontrol kanatlarının başarım ve çırpıntı bastırma gereksinimlerini sağlayan kontrolcüler tasarlanmış ve karşılaştırılmıştır. Bu amaçla H_2, H_∞ ve μ kontrolcüleri kullanılmıştır. Çırpıntının bastırılması için yeni bir yöntem önerilerek denenmiştir. Yöntemin başarısının değerlendirilmesi için bu yöntemle elde edilen sonuçlar literatürde bulunan başka bir yöntem kullanılarak elde edilen sonuçlar ile karşılaştırılmıştır. Geliştirilen kontrolcülerin uygulamada kullanımı amacıyla, aeroelastik model denklemleri tipik kanat kesit modeli için ince kanat kabulü ile türetilmiştir. Kontrolcü tasarım yöntemi, durağan sıkıştırılamaz ses altı akış, durağan olmayan sıkıştırılamaz ses altı akış, durağan olmayan sıkıştırılabilir ses altı akış ve durağan olmayan sıkıştırılabilir ses üstü akış gibi çeşitli akış koşullarında geliştirilmiş aeroelastik modeller için denenmiştir.

Anahtar Kelimeler: Aeroservoelastisite, Aeroelastisite, Gürbüz Kontrolcü Tasarımı, Çırpıntı Bastırma, μ-yöntemiyle Çırpıntı Analizi.

Anneme, Babama, Ağabeyime

ve

Biricik Eşim Gülsün'e

ACKNOWLEDGMENTS

TABLE OF CONTENTS

LIST OF TABLES

xvii

LIST OF FIGURES

NOMENCLATURE

Latin Script:

a	:	Parameter for the position of elastic axis from the mid chord, positively defined in backwards direction
$[A_{AE}]$	:	System matrix of the aeroelastic system
$[A_i]$	:	Aerodynamic coefficient matrices (i=1,..,4)
b	:	Half chord
b_i	:	Coefficients of Küssner and indicial functions
bv	:	Backlash value
c_h	:	Plunge damping coefficient of a typical section wing
c_α	:	Torsion damping coefficient of a typical section wing
c_θ	:	Equivalent damping coefficient of motor and transmission calculated at the wing shaft
$c_{l\alpha}$	:	Aerodynamic lift coefficient
c_m	:	Motor and transmission damping
$c_{m\alpha}$	:	Aerodynamic moment coefficient
c_i	:	Coefficients of Theodorsen's function
c_{ir}	:	Coefficients of indicial function (*i:1..n, r: c, cM, cq, cMq*)
$[C]$	:	Damping matrix of a typical section structural model
$[C_o]$	:	Nominal damping matrix of a typical section structural model
$[C_{eq}]$	:	Equivalent damping matrix
$C(k)$	:	Theodorsen's function
$\{d\}_r$	:	Disturbance input vectors (*r*: disturbance identifier)

$[D]$	:	Scaling matrix for μ calculations
$[D_A]$, $[D_{Ar}]$	:	Aerodynamic coefficient matrices (r: c, cM, cq, cMq)
$\{e\}_r$	:	Error/performance output vectors (r: error/performance identifier)
e_{ss}	:	steady state error
$[E_1]$, $[E_{1r}]$	:	Aerodynamic coefficient matrices (r: c, cM, cq, cMq)
$[E_2]$, $[E_{2r}]$	:	Aerodynamic coefficient matrices (r: c, cM, cq, cMq)
$[F_A]$, $[F_{Ar}]$	:	Aerodynamic coefficient matrices (r: c, cM, cq, cMq)
F_{ext}	:	External force
$F_l\big([P],[K]\big)$	:	Lower linear fractional transformation
$F_u\big([P],[K]\big)$	:	Upper linear fractional transformation
I_α	:	Mass moment of inertia of a wing about its elastic axis
I_m	:	Mass moment of inertia of motor and transmission calculated at the wing shaft
k	:	Reduced frequency
k_h	:	Plunge spring constant of a typical section wing
k_α	:	Torsion spring constant of a typical section wing
k_θ	:	Equivalent spring constant of motor and transmission calculated at the wing shaft
$k_{\theta\alpha}$	:	Equivalent spring constant obtained from serial connection of plunge spring and equivalent spring constant of motor and transmission calculated at the wing shaft.
kT	:	Motor torque constant
$[K]$	:	Stiffness matrix of a typical section structural model
$[K_c]$	:	Transfer matrix of the controller
$[K_o]$	:	Nominal stiffness matrix of a typical section structural model
$[K_{eq}]$	:	Equivalent stiffness matrix
l	:	Wing span, distance from the root chord to the tip of wing

m	:	Mass of the wing
m_p	:	Total plunging mass
$[M]$	:	Mass matrix of a typical section structural model
M	:	Mach number
Mp	:	Percentage of overshoot
M_{ext}	:	External moment
n	:	Relaxation constant
N	:	Transmission ratio
$[N]$	:	System transfer function matrix of the aeroservoelastic system
p	:	Laplace variable
$[P]$	:	System transfer function matrix of the aeroservoelastic system without a controller
$[P_{ae}]$	:	System transfer function matrix of the aeroelastic plant
$[\bar{P}_{ae}]$	:	Scaled system transfer function matrix of the aeroelastic plant
q_i	:	Generalized coordinates
q_α	:	Pitch motion of a typical section wing (angle of attack)
q_h	:	Plunge motion of the elastic axis of a typical section wing from undeflected position
q_θ	:	Angle of the motor shaft kinematically amplified to the wing shaft
$\bar{q}$	:	Dynamic pressure
$\bar{q}_0$	:	Nominal dynamic pressure
$\bar{q}_{nom}$	:	Nominal flutter pressure
$\bar{q}_{rob}$	:	Robust flutter pressure
$\{q\}$	:	Structural state vector
$\{q\}_a$	:	Aerodynamic state vector

Q_{AL}	:	Aerodynamic lift force
Q_{AM}	:	Aerodynamic moment
Q_c	:	Control force
$\{Q_A\}$	:	Aerodynamic force vector
$\{Q_{ext}\}$	:	External force vector
$[Q]$	:	Scaling matrix for μ calculations
S	:	Wing area
S_α	:	Static mass moment of a typical section wing about its elastic axis
t	:	Time
$tr_{5\%}$	:	rise time from 5% to 95% of command
ts	:	settling time for 5% error
T_{cs}	:	Motor continuous stall torque
T_p	:	Allowable peak torque
U	:	Free stream speed
V_0	:	Initial speed
V_f	:	Final speed
$\{w\}_{\bar{q}}$	:	Perturbation vector to dynamic pressure
$\{w\}_k$	:	Perturbation vector to stiffness
$\{w\}_c$	:	Perturbation vector to damping
$\{w\}_{clm\alpha}$	:	Perturbation vector to aerodynamic coefficients
$[W_r]$	:	Weighting matrix for uncertainty/performance (r: identifier of weighting function)
$[\,W_k\,]$	:	Weighting matrix for uncertainty of stiffness
$[\,W_c\,]$	:	Weighting matrix for uncertainty of damping
$[\,W_{clm\alpha}\,]$	:	Weighting matrix for uncertainty of aerodynamic coefficients

x_{cg}	:	Position of the center of mass from elastic axis, defined positively in backwards direction
$\{x\}_{Ar}$	:	Aerodynamic state vector (*r: c, cM, cq, cMq*)
$\{z\}_{\bar{q}}$	:	Vector of additional states due to perturbation to dynamic pressure
$\{z\}_k$	:	Vector of additional states due to perturbation to stiffness
$\{z\}_c$	:	Vector of additional states due to perturbation to damping
$\{z\}_{clm\alpha}$	:	Vector of additional states due to perturbation to aerodynamic coefficients

Greek Script:

β_i	:	Coefficients of Küsner and indicial functions
$\delta_{\bar{q}}$	:	Norm bounded perturbation multiplier of dynamic pressure
$\delta_{\alpha\theta}$	:	Deflection due to torsional stiffness
$[\Delta]$	:	Norm bounded perturbation multiplier matrix excluding $\delta_{\bar{q}}$
$[\Delta]$	:	Norm bounded perturbation multiplier matrix including $\delta_{\bar{q}}$
$\left[\ddots \delta_k \ddots\right]$	:	Norm bounded perturbation multiplier matrix of stiffness
$\left[\ddots \delta_c \ddots\right]$	:	Norm bounded perturbation multiplier matrix of damping
$\left[\ddots \delta_{clm\alpha} \ddots\right]$	:	Norm bounded perturbation multiplier matrix of aerodynamic coefficients
$\phi(s)$	:	Aerodynamic indicial function
Γ_{nom}	:	Nominal flutter margin
Γ_{rob}	:	Robust flutter margin
ε	:	Coefficient of restitution
ρ	:	Density of air

κ_i	:	Magnitude scaling constant of weighting functions (*i*: identifier of weighting function)
ζ	:	Damping ratio
ω_d	:	Damped natural frequency
ω_n	:	Natural frequency
υ	:	Equivalent stiffness
$\{\xi\}$	:	State vector of aeroelastic/aeroservoelastic system

Miscellaneous notation:

$\dot{a}$	:	First time derivative of *a*
$\ddot{a}$	:	Second time derivative of *a*
$[0_{n \times n}]$	:	n by n null matrix
$[I_{n \times n}]$	:	n by n identity matrix
$[\ddots A \ddots]$	:	Diagonal matrix
$\inf$	:	infinity norm

Abbreviations:

AE	:	Aeroelastic
ASE	:	Aeroservoelastic
ATD	:	Aeroservoelastic test setup of TÜBİTAK-SAGE
CCV	:	Control configured vehicles
CFD	:	Computational fluid dynamics
FAA	:	Federal aviation agency
LCO	:	Limit cycle osscillation
LFT	:	Linear fractional transformation
USA	:	United States of America

CHAPTER 1

INTRODUCTION

1.1. General Information on Aeroservoelasticity

1.1.1. Definition of Aeroservoelasticity

Some people traveling on the window side in an airplane might have wondered: Is the motion of the wing normal? How much is it bending? How far could it bend? If the people who asked these questions are alive, the answer of the first question is yes. The answer of the second question is in the field of *aeroelasticity*.

"Aeroelasticity is the study of the effect of aerodynamic forces on elastic bodies" [1]. In Figure 1, the aeroelastic triangle of forces introduced by Collar is given [2]. This figure also describes the classification of aeroelasticity problems. In Figure 1, A, E, and I represent the Aerodynamic, Elastic, and Inertial forces, respectively. The phenomena involving only aerodynamic and elastic forces are named as the *static aeroelastic phenomena* and the others that involve all three forces are named as the *dynamic aeroelastic phenomena*. The dashed lines given in the figure define the related fields to given forces other than aeroelasticity.

A: Aerodynamic forces
E: Elastic forces
I: Inertia forces

Related Fields
V: Mechanical vibrations
DS: Dynamic stability

Static Aeroelastic Phenomena
SSA: Aeroelastic effects on static stability
L: Load distribution
C: Control effectiveness
D: Divergence
R: Control system reversal

Dynamic Aeroelastic Phenomena
F: Flutter
B: Buffeting
Z: Dynamic response
DSA: Aeroelastic effects on dynamic stability

Figure 1. The aeroelastic triangle of forces [2]

In the following paragraphs, some short definitions of the aeroelastic phenomena given in Figure 1 are presented [2]:

Flutter, F. Flutter is a dynamic instability; physically it is an unstable oscillation of the airframe with the following characteristics:

- Flutter is a self excited oscillation; no external excitation is required to sustain it once the structure is set in motion. The system absorbs the required energy from the flow by itself.
- This instability occurs at a specific airspeed called flutter speed.
- Above the flutter speed, the amplitude of oscillations increases until a structural failure occurs. On the other hand, in a nonlinear system the oscillations may converge to a limit amplitude at a fixed

frequency. This phenomenon is named as the limit cycle oscillation instead of flutter and it is a stable condition. However, the limit cycle oscillation is still an undesired phenomenon, since it decreases the remaining fatigue life of the structure.

- The flutter speed is a function of:
  - o Airplane structural parameters such as
    - ▪ Geometry, mass distribution, stiffness distribution, and structural damping
  - o Flight parameters such as
    - ▪ Airspeed, altitude, Mach number, and angle-of-attack

Buffeting, B. "Buffeting is transient vibrations of aircraft structural components due to aerodynamic impulses produced by the wake behind wings, nacelles, fuselage pods, or other components of the airplane."

Dynamic response, Z. "Transient response of aircraft structural components produced by rapidly applied loads due to gusts, landing, gun reactions, abrupt control motions, moving shock waves, or other dynamic loads."

Aeroelastic effects on stability, (S/D)SA. "Influence of elastic deformation of the structure on dynamic and static airplane stability."

Load distribution, L. "Influence of elastic deformations of the structure on the distribution of aerodynamic pressure over the structure."

Divergence, D. "A static instability of a lifting surface of an aircraft in flight, at a specific speed called the *divergence speed*, where the elasticity of the lifting surface plays an essential role in the instability." Divergence is also named as *zero frequency flutter*.

Control effectiveness, C. "Influence of elastic deformation of the structure on the controllability of an airplane." For example; in a typical wing with flap configuration, changing the flap angle with control purposes causes deformation of the wing which results in a decrease of control. Rotating the flap down to increase lift deforms the wing nose down, which results in a decrease in lift.

Control system reversal, R. "A condition occurring in flight, at a speed called the control reversal speed, at which the intended effects of displacing a given component of the control system are completely nullified by elastic deformations of the structure."

For many years, people were faced with aeroelastic problems and solved them by passive solutions. These passive solutions are generally still used as a first step. On the other side, with the improving technology and mankind's passion of obtaining the better, the control technology has been introduced to the field of aeroelasticity. The new field that is emerged as an intersection of the aeroelasticity and controlled structures technology is named as the *aeroservoelasticity*. Its main objective is to modify the aeroelastic behavior of a system by introducing calculated control forces. Common research areas of aeroservoelasticity are:

Flutter suppression: Its objective is to increase the flutter-free operational envelope of the system. From the control point of view, its objective is to stabilize an unstable aeroelastic system and to increase the stability region of a system.

Gust alleviation: The objective is to smooth the ride by minimizing the response due to unsteady dynamic air loads. This objective is developed to increase the ride comfort and/or structural load alleviation.

The controller's objective is to keep the aeroelastic system well regulated and to improve its disturbance rejection properties.

Maneuver enhancement: This objective is applied to improve the ability of the aircraft to produce sudden changes in lift and moment required for maneuver. The objective of the controller is to make the control surface a good servo-command tracking system.

1.1.2. History of Aeroelasticity and Aeroservoelasticity

In this Section, the history of the aeroelasticity and the aeroservoelasticity is presented based on the studies of Fung [1], Bisplinghoff et al. [2, 3], Garic [4, 5, 6], and Felt et al. [7] .

The history of aeroelasticity is older than human history. Because, the aeroelasticity is not confined to manmade structures. Aeroelastic phenomena are also observed in biomechanics, on the wing of birds, in plants, etc. Human race must have been faced with aeroelastic problems as they improved their tools and goods, and they may have solved the problems empirically. However, the first evidence of manmade aeroelastic improvement was found in the 16th century, where the aeroelastic problems of windmills were solved empirically in the Netherlands, by moving the spars of the blades from the mid-chord to quarter-chord position.

In civil engineering, aeroelastic problems were encountered in bridges in the 20th century. On November 7, 1940, Tacoma Narrows Bridge in the U.S.A. collapsed at a wind speed of 42 mph (68 km/h), which is well below the static design speed of 100 mph (161 km/h). This bridge failure is generally believed to be due to stall flutter.

In the aviation field, aeroelastic problems arose with the beginning of powered flight trials of airplanes. Professor S. P. Langley of the Smithsonian Institute flew a ½ scale of his aerodromes up to 300 meters. But the full scale model failed twice, last on December 8, 1903. Second failure was generally believed to be due to wing torsional divergence. In 1914, Curtis flew the Langley aerodrome with slight modifications, well before the wing torsional divergence problem was solved theoretically.

Nine days after Langley's second failure, in December 17, 1903, Wright brothers made their historical flight. The torsional stiffness of wings of Wright brothers' biplane was greater than Langley's mono-wing aerodrome. Since the divergence speed is directly related to the torsional stiffness, the Wright biplane did not suffer divergence problem. Wright brothers also made beneficial use of aeroelastic effects for roll control of their biplane by the use of wing warping in place of ailerons. Furthermore, they were aware of the adverse effect of torsional deformations on the thrust of propellers.

Through the success of Wright brothers, early aircrafts were almost exclusively biplanes. The most widespread early aeroelastic problem in those days was the tail flutter problem. One of the first documented cases of flutter occurred in the horizontal tail of the twin engined Handley Page 0/400 bomber, at the beginning of World War I. The symptoms were violent oscillations of the fuselage and tail surfaces. After investigations it was discovered that the fuselage and tail had two principal low-frequency modes of vibration. In one mode, the left and right elevators oscillated about their hinges with a phase difference of 180 degrees. The elevators were connected to the control stick with separate long control cables which had low stiffnesses. The second mode was the torsional oscillation of the fuselage. It was concluded that the vibrations were due to self-excited oscillations involving coupling between these modes. This problem was

solved by connecting the two elevators by a torque tube. Similar problems were experienced in DH-9 airplanes.

In World War One (WW1), Germans also experienced aeroelastic problems. Fokker D-8, a monoplane, had a great performance but suffered from wing failures in steep dives. Early monoplanes had insufficient torsional stiffness resulting in wing flutter, divergence, wing-aileron flutter, and loss of aileron effectiveness. These problems were usually solved by increasing the torsional stiffness and by mass balancing. However the problem in Fokker D-8's was slightly different. After many losses of aircraft and their best pilots, the Luftwaffe conducted static strength tests. Through these tests of the airplane, it was found that the wings had enough strength with an ultimate safety factor of 6. Fokker Company stated that the prototype wing showed no structural deficiencies. The only difference between the prototype wings and the production wing was the strengthening of the rear spar. This was ordered by the Luftwaffe, due to regulations for wire braced wings. Ironically, strengthening the rear spars moved the elastic axis backwards which resulted in a decrease of the divergence speed, which eventually caused the loss of Fokker D-8 aircrafts.

After WW1 many flutter phenomena were seen; in 1923 wing-aileron flutter was seen in von Berkel Seaplane (monoplane), which was solved by Baumhauer and Koning by mass-balancing the aileron. In 1924-1925 a wing-aileron flutter was seen in Gloster Grebe and Gloster Gamecock. The problem was solved by increasing the stiffness and reducing the unbalanced area near the tip.

In early days, aeroelastic problems were solved by trial and error methods. In 1926, Reissner published papers about the theory of wing-load distribution and wing torsional divergence. In 1929, Frazer and

Duncan published their works about wing flutter. Robert Cox and Pugsley published a theory of loss of lateral control and aileron reversal. Between 1923 and 1929 many works about unsteady aerodynamics were published by Brimbaum, Glauert, Wagner, Frazer, Duncan, and Küssner. The mechanism of potential flow flutter was understood by 1935, with the help of previous studies (1923-1929) and Theodorsen's studies.

During this period, many flutter phenomena occurred all over the world on different types of airplanes; air racers, transporters, observer airplanes, passenger airplanes, bombers, and attack airplanes. Different types of flutter were observed; wing-aileron, rudder-fuselage, tail, rudder-fin, elevator- fuselage, and elevator-tab.

With the increase incidences of flutter phenomenon, flight flutter tests became important. Early tests were to dive the airplane to its maximum speed and hope the best. In 1935 in Germany, von Schippe employed resonance testing techniques during the flight. Schipple's method was to obtain the frequency response as the speed increases. In this method, the flutter is expected to occur as the resonant amplitude tends to increase asymptotically against increasing airspeed. However, the flutter was a sudden phenomenon and in those days the technology required the test engineers to be in the plane to check the data. Successful tests ended in 1938, in the test of a Junker JU90 an unexpected flutter of the wing encountered. The plane crashed with the engineers on board.

Manufacturers became reluctant to flight flutter tests, due to their hazards. However, it would be more dangerous to use an airplane, which had not been tested. With the improvement of testing methods, test and communication apparatus, flight flutter tests began to gain acceptance by late 1940's.

In the theoretical standpoint, in 1938 Frazer, Duncan, and Collar published a unique textbook, which gave examples for the use of matrices for flutter. In 1941, S. J. Loring published a paper that gave systematic solution for flutter problem with the use of matrices.

Prandtl in 1936 published a paper, in which he used the acceleration potential, instead of the velocity potential. Using the acceleration potential he included the compressibility effect. The compressibility effect had to be formulated because the speed of the airplanes in those years approached to the speed of sound. However Prandtl's method was useful for small disturbances, which made it applicable for subsonic and supersonic speed ranges, but not for transonic and hypersonic speed ranges. In 1938, Camille Possio applied the acceleration potential to the two-dimensional non-stationary problem.

Prandtl's equation was useful for drag and span-load calculations for steady flow about a finite wing. In 1937, Cicalla introduced a method to generalize Prandtl's approach for unsteady flows, still using the two-dimensional exact theory as a limit for the infinite aspect ratio wing. W.P. Jones in 1940, Küssner in 1943, and Reissner in 1944 made related works, which had important applications until computational methods applicable to true lifting surfaces were developed some years later. R.T. Jones' contribution was the approximation to Wagner's function in a form useful for transfer functions as given in Equation (1.1)

$$ k_1\left(s\right) = 1 - b_1\, e^{\beta_1 s} - b_2\, e^{\beta_2 s}\ldots $$

(1.1)

The general lifting surface theory for finite wings was published by Küssner.

In 1942, Smig and Wasserman gave comprehensive table of unsteady aerodynamic coefficients based on the theory of Theodorsen. In the United States, these tables and the suggested computation methods were used for flutter analysis for several years. This method was named as the *K method*. Since then, several flutter search methods were developed such as *P-K method* by Hassing in 1971, *p-method* by Abel in 1979, and *μ-method* by Lind and Brenner in 1998.

In 1960's, control concepts were introduced into analytical models, followed by active control aeroelastic wind tunnel models that were used to verify analytical models. At the last half of this decade, flight tests of B-52 and XB-70 aircraft were successfully conducted, which demonstrated the concept of using flight control to modify the dynamic characteristics of the aircraft structure. On August 2, 1973, a CCV B-52 test aircraft was flown 10 knots faster than its flutter speed.

1.2. Projectile Control Methods

Control actuation system (CAS) is an important part in every guided projectile. It controls the direction and/or magnitude of forces maneuvering the projectile. This control is accomplished by various means. Some control types and their schematic illustrations are given in Figure 2.

This study focuses on aerodynamic surface controllers. Although the aerodynamic surfaces have a general meaning, in this study it is used for airplane wings and missile control surfaces. Specifically, the current study applies to those in which the entire control surface is actuated in order to obtain the desired aerodynamic forces while there is no adjacent lifting surface. Such control surfaces are commonly referred as *fins* as opposed to flaps, ailerons, rudders, etc. Although the requirements of this study is based on the missile control surfaces, it is applicable to all fins,

which could be for instance the horizontal stabilizers of an airplane such as the F-4 Phantom.

THRUST CONTROLLERS:

Reaction Jet Control

Gimbaled Control

Thrust Vector Control

Jet Vane Control

AERODYNAMIC SURFACE CONTROLLERS:

Wing Control

Canard Control

Tail Control

Wingless Tail Control

Tail-less Wing Control
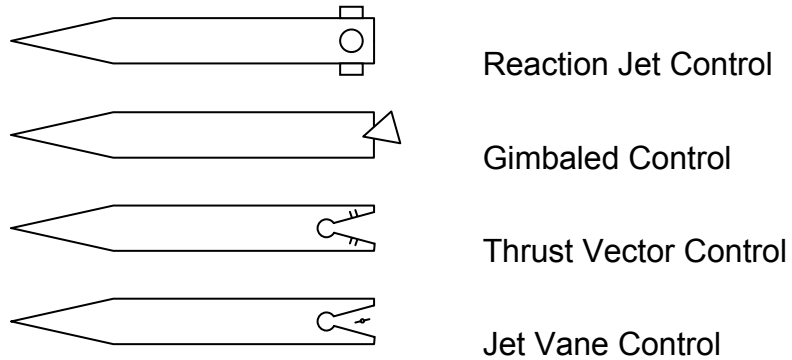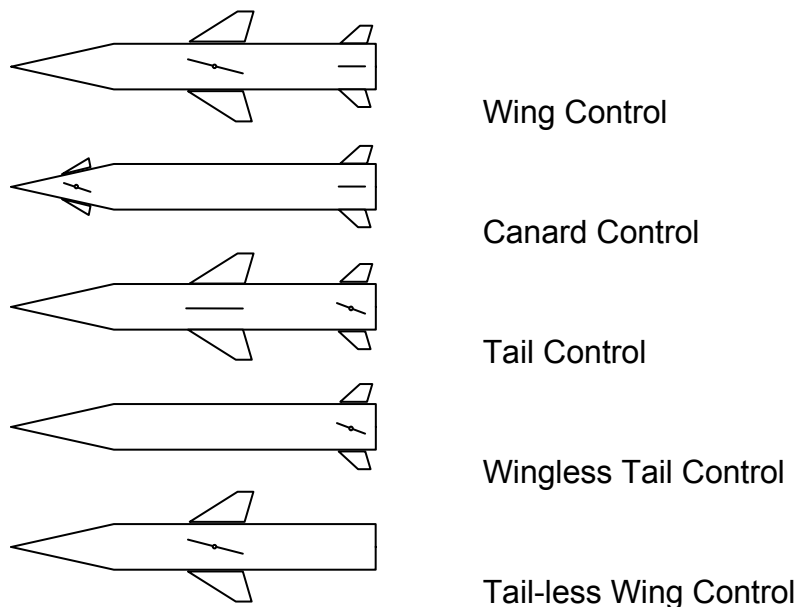
Figure 2. Projectile control types

A CAS can be pneumatic, electromechanical, or hydraulic. Although there are several secondary influences, the type of CAS actuation is primarily selected according to its power requirements. From low power to high power capabilities, CAS types are classified as pneumatic, electromechanical, and hydraulic. This study is directly applicable to electromechanically driven control surfaces, since in those cases the

actuator can be modeled as linear without any gross simplification. Additional works are required for pneumatic and hydraulic actuators, which incorporate nonlinearities.

1.3. Rationale and Objectives of the Thesis

Aeroelasticity is an old subject in which the studies were started before 1930's. Aeroservoelastic studies were performed since 1960's. However, most of these studies were concentrated on aircraft wings. There exist few studies about the flutter suppression of missile control surfaces (fins). Aircraft wings are mainly composed of a fixed lifting surface and a trailing control surface (flap). Flutter suppression of the aircraft wing can be achieved by controlling the motion of the flap. On the other hand, fins are fully movable control surfaces without any adjacent lifting surface. The flutter suppression of the fin can be achieved via controlling the angular position of the fin shaft. This fact differentiates the aircraft wings and the fin.

In TÜBİTAK-SAGE, a leading research and development institute in the defense industry of Turkey, various studies were performed about aeroelasticity since the beginning of the 1990s. Among these studies, Tanrıkulu [8, 9], Kuran et al. [10, 11], Durak [12], Yıldız [13], Sever [14] Pehlivanoğlu et al. [15], Akmeşe et al. [16], and Ünal [17] performed aeroelastic analysis of rocket and missile fins including linear and nonlinear structural models. In early 1990s, an introductory study was also conducted by Tanrıkulu [18] about aeroservoelasticity without performing a detailed investigation. The practical research needs at TÜBİTAK-SAGE require some in-depth studies to be conducted on the control actuation systems of missiles. Therefore, the need for aeroservoelastic analysis of control surfaces and controller synthesis for elastic control surfaces is eminent.

In controller synthesis studies for flutter suppression of airplane wings, first classical controllers were used in a study of Horikawa [19]. Then, optimal controllers similar to LQG/LQR type were used in the studies of Roger et al. [20], Poyneer et al. [21], Edwards et al. [22], Mahesh et al. [23], Ohta et al. [24], and Block et al. [25]. Although these controllers did suppress the flutter, due to their synthesis method the uncertainties of the system were not considered. In some recent studies, robust controller methods that consider the uncertainties of the system were used, as in the studies of Vipperman et al. [26], Waszak [27], Gade [28], and Kim et al. [29]. However, these studies were applied to aircraft wings. Although aeroservoelastic analyses of fully movable control surfaces were performed in some studies by Yehezkely et al. [30], and Laurenson et al. [31], controller synthesis for control actuation systems of fully movable elastic control surfaces was rare.

While H_∞ and μ are robust controller methods, H_2 is basically a LQG/LQR controller using similar definitions with robust controller methods for the construction of the synthesis problem. Controllers synthesized by means of these three methods have different advantages over each other. The H_2 controller stands out with current consumption performance and tracking performance at the design conditions. It takes into account the plant noise but it does not guarantee the stability of the controlled system. The H_∞ controller guarantees the stability while taking into account the uncertainties as well; but as a result of this, it is a conservative controller. The μ controller synthesis method yields a less conservative controller than the H_∞ method, still guarantees the stability, and takes into account the uncertainties. However, the degree of conservatism decreases as the order of the μ controller is increased.

Simply, aeroelastic or aeroservoelastic instabilities happen with changes in aerodynamic loads, which change with the flight parameters. The result can be explained on a root locus plot; changes in aerodynamic loads moves the poles of the system from the left hand plane to the right hand plane. Hence, in the robust controller synthesis two different approaches can be used. The shift in the poles can be modeled as an uncertainty and a robust controller can be synthesized considering this uncertainty. This method was applied by Vipperman et al. [26] in 1999 to an airplane wing model. On the other hand, it is also possible to define uncertainties for flight parameters and a robust controller can be synthesized considering these uncertainties. Waszak [27] performed a similar study. In that study, the uncertainty of the aeroelastic system was derived by applying a disturbance to the dynamic pressure. At the controller synthesis step, the aeroelastic system uncertainty was included, hence the disturbance to dynamic pressure was included indirectly. However, a controller synthesis procedure that directly includes the dynamic pressure disturbance at the controller synthesis step was not come across during the survey of the open literature.

In their studies, Kim et al. [29], Yehezkely et al. [30], Laurenson et al. [31], Ko et al. [32], Tang et al. [33, 34], Lee et al. [35], Price et al. [36], Brase et al. [37], and Yıldız [13] performed a flutter analysis of airplane wings or missile fins with several types of structural nonlinearities. In addition to the nonlinearities studied in literature, it is known by experience through the studies performed in TÜBİTAK-SAGE that the backlash type nonlinearity usually exists in the missile fins.

In line with the research needs of TÜBİTAK-SAGE, aeroservoelastic analysis and controller synthesis for flutter suppression of missile control surfaces are defined as the research subject of this study with the following primary objectives.

- Establish a method for the synthesis of various types of controllers for a CAS, considering some performance specifications and also taking the flutter suppression into account,
- Investigate and apply appropriate approaches for the analysis of the aeroservoelastic system synthesized.

In reaching the objectives mentioned above, the following studies are aimed as original contributions to the literature:
- Development of a controller synthesis procedure that directly uses the disturbance to dynamic pressure for flutter suppression,
- Synthesis and comparison of H2, H_∞, and μ controllers for control actuation systems with fully movable control surfaces by using the controller design procedure developed,
- Analysis of the effect of a backlash type of nonlinearity on the performance of the aeroservoelastic system with controllers mentioned above.

In addition to the contributions listed above, the following studies are also aimed in this thesis:
- Employment of the flutter suppression method used in the controller synthesis procedure of Vipperman et al. [26] for airplane wings for a control actuation system with fully movable control surfaces.
- Comparison of two different flutter suppression methods.
- Aeroelastic and aeroservoelastic analysis with p and μ-methods.
- Performance analyses of the aeroservoelastic systems.
- Analysis of the effect of the backlash type of nonlinearity on the the aeroelastic.
- Investigation of the effect of the backlash type of nonlinearity on the performance of the aeroservoelastic system with the controller mentioned above.

In order to develop the study in the control domain rather than the aerodynamics or structures domains the following limitations are applied in this study:

- The structural part of the control actuation surface is modeled as a typical section model.
- The torsional mode of the typical section model is assumed to be dominated by the low stiffness of fin shaft and the actuation mechanism rather then by the torsional stiffness of the fin itself.
- In the calculation of the aerodynamics, the fin geometry is assumed as a thin airfoil which has no thickness.
- The aerodynamic forces are calculated using potential flow approach that is basically an irrotational and inviscid linear aerodynamic theory.

1.4. Scope of the Thesis

Chapter 2 includes the development of an aeroelastic model of a fin which is used throughout the thesis to reach its objectives. A literature survey on aeroelastic modeling is given. In two consecutive parts, brief introductory information about the aerodynamics and the finite dimensional aeroelastic modeling are given. An aeroelastic modeling via typical section wing with thin airfoil assumption is given. The derivations of the state space equations of the aeroelastic model for various flow conditions are also presented.

In Chapter 3, flutter search methods are presented. A brief information is given about the widely used flutter search methods. The μ flutter search method on the aeroelastic fin model is applied. Methods for determining the flutter flight envelope are given.

In Chapter 4, controller synthesis methods for the flutter suppression are given. The aeroservoelastic model of the fin is constructed by using the aeroelastic model defined in Chapter 2. The μ flutter search method is implemented on this model. The proposed controller synthesis method for flutter suppression is presented. In order to compare the performance of this method, an alternative method is given. The implementation of this alternative method is based on the study of Vipperman J.S. [26] which was originally applied to an airplane wing model.

In Chapter 5, the analysis tools that are developed for the purpose of performance and LCO analyses of the aeroservoelastic system are presented. A Simulink$^{®}$ model constructed for the performance analyses of the ASE system with linear AE sub-system is given. The selected time and frequency domain methods are provided for the modeling of the backlash, which is assumed to exist in the pitch freedom of the fin. A frequency domain analysis method is given for limit cycle search.

In Chapter 6, implementations of controller synthesis and analysis methods that are presented in Chapters 2 to 5 are performed on numerical models. An aeroelastic model for unsteady subsonic incompressible flow, Model 1, is constructed. The flutter analysis is performed for Model 1 via different methods given in Chapter 3 and the results are compared. H_2, H_∞, and μ controllers are synthesized for Model 1, with each of the flutter suppression method given in Chapter 4. The analysis and the comparison of the derived aeroservoelastic systems are performed by using the methods given in Chapters 4 and 5. In order to analyze the effect of compressibility, the implementations are also performed for unsteady compressible subsonic and unsteady compressible supersonic region. In the compressible domain only the flutter suppression methods are compared, hence only one type controller synthesis method, the H_∞

method is used. In the implementation part of H_∞ controller synthesis, a method is devised for simplification of the tuning procedure of weightings. In this Chapter, a method suggested by Lind et al. [38], which is a robust controller synthesis approach that considers system nonlinearities, is also implemented.

In Chapter 7, the summary of the study is given by stating the contributions. Discussions and conclusions regarding the study in general are presented. Recommendations for future work are given.

CHAPTER 2

AEROELASTIC MODELING

2.1. Preview

Aeroelasticity deals with the interaction of structural and aerodynamic forces in airborne elastic bodies or elastic bodies subject to airflow. Hence, the aeroelastic modeling of such systems is composed of the aerodynamic and the structural parts. In this chapter, a literature survey on structural and aerodynamic modeling of aerodynamic control surfaces is conducted. An introductory survey is performed on aerodynamic modeling. A general method of using finite element structural model for constructing the aeroelastic system is presented. Aerodynamic modeling of the control surfaces under various aerodynamic conditions with thin airfoil and typical section airfoil assumptions are achieved.

2.2. Literature Survey

The typical section modeling is a method that can be used with simple aerodynamic models by which closed form solutions or easily solvable equations can be obtained. The typical section model is a simplified 2-D modeling method for 3-D elastic aerodynamic surfaces [1, 3], which is applicable to airplane wings and control surfaces. A schematic of the typical section is given in Figure 3. In their aeroelasticity studies, Horikawa et al. [19], Edwards et al. [22], Ohta et al. [24], Liebst et al. [39],

and Leishman et al. [40] was used the typical section model for linear modeling of aerodynamic surfaces. This method was also used for structurally nonlinear aeroelastic systems by Block et al. [25], Ko et al. [32], Tang et al. [33, 34], and Conner et al. [41] in their studies. The typical section model was also used with some modifications, such that the rigidly defined chord in standard typical section model was replaced with an elastic (beam model) chord. This modified model was used by Lee for analyzing free-play type nonlinearity in pitch motion [35]. The typical section structural modeling was also used in modern control studies by Vipperman et al. [26], Lind et al. [38], and Özbay et al. [42].
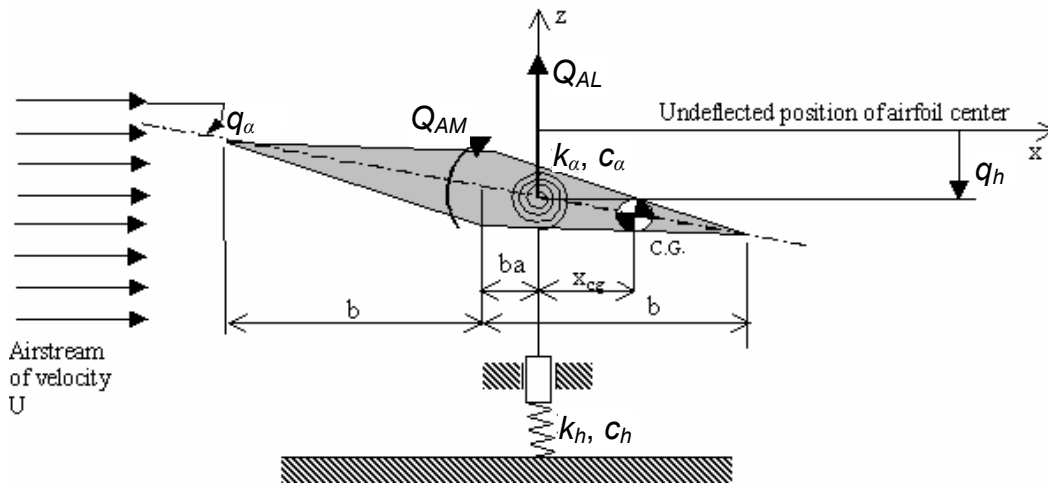
Figure 3. Typical Section

An alternative approach to the typical section is the elastic modeling of airplane wings and missile control surfaces. This approach is more realistic but complicated than typical section applications. Hence, it was used when the typical section model was not valid or more realistic solutions were required. Roger et al. [20], Nissim [43], and Hoadley et al. [44] used linear elastic models in their studies. The elastic modeling was also used for models with structural nonlinearities by Yehezkely et al. [30],

in modern control studies by Mahesh et al. [23], and in robust flutter analysis by Lind et al. [45].

However, in aeroservoelastic research studies, elastic models were not widely used. The reason is the introduction of large number of states due to elastic modeling, which increase the model complexity and computation time. From the papers surveyed, it is seen that elastic models were used for linear aeroservoelastic analysis problems but not in synthesis problems. Moreover, it is seen that, in the robust controller synthesis studies, only typical section models were used.

On the aerodynamics side, through the literature survey it is seen that the thin airfoil modeling was used with steady incompressible aerodynamics by Horikawa et al. [19] and Liebst et al. [39] and with unsteady incompressible aerodynamics by Edwards et al. [22] in their introductory studies. In the study of Ohta et al. [24], the differences between steady, quasisteady, and unsteady aerodynamic models were reported. On the other hand, Roger et al. [20], Mahesh et al [23], and Nissim [43] used the doublet lattice method in order to calculate the aerodynamic forces on the elastic structure model for an unsteady compressible subsonic flow. In these studies, the unsteady aerodynamic forces were approximated by various techniques such as Padé method.

In most of the studies using a structural nonlinearity, some 2-D aerodynamic models were employed. Ko et al. [32] used a thin airfoil model with incompressible quasisteady aerodynamics. On the other hand, Conner et al. [41], Block et al. [25], Tang et al. [34], and Kim et al. [29] used a thin airfoil model with the unsteady incompressible aerodynamics.

In the literature, there are also some studies reported about aeroelastic analysis of missile control surfaces with structural

nonlinearities. Laurenson et al. [31] used a rigid airfoil with the steady subsonic aerodynamics, Yehezkely et al. [30] used an elastic airfoil with the unsteady supersonic aerodynamics via piston theory.

Özbay [42] used the thin airfoil assumption with the unsteady incompressible aerodynamics in his study on the robust controller synthesis for flutter suppression of an airplane wing. On the other hand, Lind and Brenner [45, 46, 47] used doublet lattice and other panel methods, with the unsteady subsonic and supersonic aerodynamics in their robust control studies.

2.3. Aerodynamic Modeling

In aerodynamic modeling, various theories can be used, as listed from more realistic to simpler below:

Nonlinear, viscous, compressible
- Navier–Stokes
- Turbulence Models

Nonlinear, inviscid, compressible
- Euler

Irrotational, inviscid, compressible
- Potential Theory: Panel methods
- Slender body theory

Irrotational, inviscid, incompressible
- Piston theory

The aerodynamics can be modeled more accurately with nonlinear aerodynamic theories. Using computational fluid dynamics (CFD) the generalized aerodynamic forces can be calculated using nonlinear aerodynamic theories as in the study of Newsom [48]. The generalized

aerodynamic forces are calculated in a matrix form, named as the generalized aerodynamic force matrix. In this matrix, each element defines the effect of the aerodynamic force from the corresponding aerodynamic generalized coordinate to the corresponding structural generalized coordinate. Once the generalized aerodynamic force matrix is obtained, it can be transformed into to state space and then be used in standard linear aeroelastic analyses.

Using full and simplified versions of potential theory, the generalized aerodynamic force matrix of an aerodynamic surface can be calculated. There are package programs such as MSC/NASTRAN™ Flight Loads and Dynamics [49] that can calculate the generalized aerodynamic coefficient matrices of an aerodynamic surface using a thin airfoil assumption.

In terms of flow regime, aeroelastic and aeroservoelastic problems can be grouped in five categories according to the Mach number (Table 1) [50].

Table 1. Flow regimes

Incompressible subsonic flow	0<M<0.3
Compressible subsonic flow	0.3<M<0.8
Transonic flow	0.8<M<1.2
Supersonic flow	M>1.2
Hypersonic flow	M>5

The potential flow theory and its simplified versions are used in incompressible subsonic flow, compressible subsonic flow, and supersonic flow. It is also applicable in some part of transonic flow with some modifications; however it is not applicable between 0.9 to 1.1 Mach.

On the other hand, the thin airfoil has a special place in aeroelasticity research. The thin airfoil, performing lateral oscillations in a uniform air stream, has a closed form solution in incompressible flow. The solution was first derived by Theodorsen [51] and it can be also found in the references [2, 52]. Using these references, the rational approximation of aerodynamic forces can be found. For compressible flow, the rational approximations of aerodynamic forces for the thin airfoil were derived for specific Mach numbers by Mazelsky and Drischler [53, 54]. For supersonic flow, the piecewise closed form solutions are available [2].

The abovementioned unsteady thin airfoil solutions can be further simplified by neglecting the memory effect of the airfoil, thereby obtaining what is called as the steady aerodynamics. On the other hand, there exists a third method, the quasisteady aerodynamics which includes the memory effect as static characteristics.

2.4. Finite Element Modeling

A frequently used method for dealing with elastic models is the finite element method. This Section is prepared by using the study of Dowell et al. [55]. In the finite element method, the wing is meshed with sufficient amount of elements, such that the required minimum number of elastic modes can be represented. For the modeling of the wing, a small number of lowest modes of the structural system should be kept for the purpose of performance as well as some additional number of modes in the crossover frequency range of the system should be kept to ensure the close loop stability. For the modeling of the control surface, less number of modes can be kept since its structure is simpler than a wing structure.

The general form of equation for the finite element structural modeling is given by Equation (2.1). As an alternative to finite element

modeling, one can use Ritz or other formulation to derive the discrete equation.

$$[M]\{\ddot{q}\} + [K]\{q\} = \{Q\}_A + \{Q\}_{ext}$$ (2.1)

where

$\{q\}$: Vector of generalized coordinates

$[M]$: Mass matrix of the structure, structural actuator, any store or attachments, and control surface

$[K]$: Stiffness matrix of the structure, structural actuator, and any stores or attachments

$\{Q\}_A$: Vector of aerodynamic forces

$\{Q\}_{ext}$: Vector of external forces

Decoupling the system into normal modes can be achieved by the following modal transformation

$$\{q\} = [\Phi]\{\xi\}$$ (2.2)

where

$[\Phi]$: Eigenvector matrix composed of eigenvectors $\{\phi\}_j$, which include rigid body motions

$\{\xi\}$: Vector of normalized coordinates

Inserting Equation (2.2) into Equation (2.1), and premultiplying by $[\Phi]^T$ the open loop modal equation in vacuum is obtained. This equation with linear viscous damping, [C], is expressed as

$$\left[\,\ddots M'_{i}\,\ddots\,\right]\{\ddot{\xi}\} + \left[\,\ddots C'_{i}\,\ddots\,\right]\{\dot{\xi}\} + \left[\,\ddots K'_{i}\,\ddots\,\right]\{\xi\} = \{\Xi\}_A + \{\Xi\}_{ext}$$ (2.3)

where modal mass, modal damping, modal stiffness and forces are

$$
\left.
\begin{aligned}
M_i' &= \{\phi\}_i^{T} [M] \{\phi\}_i \\
C_i' &= \{\phi\}_i^{T} [C] \{\phi\}_i \\
K_i' &= \{\phi\}_i^{T} [K] \{\phi\}_i \\
\left(\{\Xi\}_A\right)_i &= \{\phi\}_i^{T} \{Q\}_A \\
\left(\{\Xi\}_{ext}\right)_i &= \{\phi\}_i^{T} \{Q\}_{ext}
\end{aligned}
\right\}
\tag{2.4}
$$

Equation (2.3) includes the full structural model, which is in general too large to use in subsequent modeling steps. Thus the dynamics which are beyond the bandwidth of interest and which are not physically important are truncated, and a reduced equation of motion given in Equation (2.5) is obtained. Note that the system size, n_s, is greater than the modal size, n_m, $n_s \geq n_m$.

$$
[M_m'] \{\ddot{\xi}\}_m + [C_m'] \{\dot{\xi}\}_m + [K_m'] \{\xi\}_m = [\Phi_m]^{T} \{Q\}_A + [\Phi_m]^{T} \{Q\}_{ext}
\tag{2.5}
$$

where, $[M_m']$, $[C_m']$, and $[K_m']$ are of the order $n_m \times n_m$, and $[\Phi_m]$ is $n_s \times n_m$.

While modeling wings, aerodynamic control surfaces are appended to the model as shape functions in the following form

$$
\{\psi\} = [\Phi_m \ \Phi_\delta] \begin{Bmatrix} \{\xi\}_m \\ \{\delta\} \end{Bmatrix}
\tag{2.6}
$$

where

$\{\psi\}$: Generalized coordinates including the generalized coordinates of control surface and reduced generalized coordinates of the structural modes

$[\Phi_\delta]$: n_sxn_δ matrix of vectors corresponding to the n_δ deflections of the control surface δ, defined relative to the adjacent lifting surface. Since the control surface is a separate structure, $[\Phi_\delta]$ may not be orthogonal to the $[\Phi_\xi]$

δ : Generalized coordinates for control surface deflection

Neglecting the damping and the stiffness effects of the actuator, the equation of motion for the wing with aerodynamic control surfaces can be written by using the generalized coordinates given in Equation (2.6) and the equation of motion of the wing given in Equation (2.5) as

$$
\begin{bmatrix} M'_m & M'_{m\delta} \\ M'_{m\delta} & M'_{\delta\delta} \end{bmatrix} \begin{Bmatrix} \{\ddot{\xi}\}_m \\ \{\ddot{\delta}\} \end{Bmatrix} + \begin{bmatrix} C'_m & 0 \\ 0 & 0 \end{bmatrix} \begin{Bmatrix} \{\dot{\xi}\}_m \\ \{\dot{\delta}\} \end{Bmatrix} + \begin{bmatrix} K'_m & 0 \\ 0 & 0 \end{bmatrix} \begin{Bmatrix} \{\xi\}_m \\ \{\delta\} \end{Bmatrix} = \begin{bmatrix} \Phi_m^{\ T} \\ \Phi_\delta^{\ T} \end{bmatrix} \{Q\}_A + \begin{bmatrix} 0 \\ Q_\delta \end{bmatrix}
$$

(2.7)

where

$[Q_\delta]$: Actuators hinge moment

2.4.1. Generalized Aerodynamic Force Matrices

The aerodynamic forces can be derived by using panel methods and its simplified form slender body theory. The derived aerodynamic forces will contain an implicit or explicit irrational dependence on reduced frequency. To be compatible with most control design approaches, the aerodynamic forces are fit by explicit rational functions of the states of the system by the following two-step process:

a) Identify the structural motions for which the aerodynamic effects will be calculated. Then calculate the unsteady aerodynamic forces for these modal motions, control surface motions, or gust inputs. Use an aerodynamic model for the appropriate Mach number of interest at distinct values of reduced frequency k, which is defined as

$$k = \frac{\omega b}{U} \tag{2.8}$$

where

ω : frequency

b : semichord length of the wing

U : airspeed

and over the frequency range of interest.

b) Fit the aerodynamic forces with a rational function approximation in the frequency domain.

Aerodynamic influences will be calculated for $n_A=n_m+n_\delta$ modes, for which states are defined as

$$\{\xi\}_A = \begin{Bmatrix} \{\xi\}_m \\ \{\delta\} \end{Bmatrix} \tag{2.9}$$

Then the modal forces due to aerodynamics in Equation (2.7) are written as

$$\begin{bmatrix} \Phi_m{}^T \\ \Phi_\delta{}^T \end{bmatrix} \{Q\}_A = \begin{bmatrix} \Phi_{mA}{}^T \end{bmatrix} \{Q\}_A = \bar{q} [Q_{mA}(p)] \{\xi\}_A \tag{2.10}$$

where

$\bar{q}$: Dynamic pressure

$[Q_{mA}(p)]$: Matrix of modal aerodynamic force coefficients due to ξ
and δ

p : Laplace variable

The elements $(Q_{mA}(p))_{jl}$ of influence matrices are calculated by using a proper method for a number of discrete reduced frequencies $p = ik$. For subsonic flow doublet lattice or kernel function methods can be used to calculate these influence matrices. Note that the aerodynamic forces calculated at aerodynamic control points should be transformed to the structural nodes. This transformation can be performed by using a splining method, [56].

The second step is to fit the exact values of $(Q_{mA}(ik))_{jl}$ using a rational function approximation. Four different rational function approximation methods that are widely used in aeroelastic studies are given below.

Most common form (Roger's Method) [55]:

In this method, the approximated values $\left(\hat{Q}_{mA}(ik) \right)_{jl}$ of $\left(Q_{mA}(ik) \right)_{jl}$ are as

$$\left(\hat{Q}_{mA}(ik) \right)_{jl} = \left(A_0 \right)_{jl} + \left(A_1 \right)_{jl}(ik) + \left(A_2 \right)_{jl}(ik)^2 + \sum_{r=1}^{\left(n_R \right)_{jl}} \left(A_{r+2} \right)_{jl} \frac{(ik)}{(ik) + \left(\overline{a}_r \right)_{jl}} \qquad (2.11)$$

where

$\left(\hat{Q}_{mA}(ik) \right)_{jl}$: Estimate of exact calculated values

i : $\sqrt{-1}$

n_R : Order of the denominator polynomial used to fit the lag terms.

[A_0], [A_1], [A_2] are the equivalent displacement, velocity, and acceleration matrices of the aerodynamics, respectively. The partial fraction sum captures the dependence on the aerodynamic lag, which is referenced to velocity due to (ik) term in nominator. The following equation can be obtained by multiplying both sides of the Equation (2.8) with i and substituting p for $i\omega$.

$$ik = \frac{pb}{U} \tag{2.12}$$

In order to transform Equation (2.11) to time domain, first it is transformed from frequency to Laplace domain, by substituting the Equation (2.12) into Equation (2.11) as

$$\left(\widehat{Q}_{mA}(p)\right)_{jl} = (A_0)_{jl} + (A_1)_{jl}(\frac{pb}{U}) + (A_2)_{jl}(\frac{pb}{U})^2 + \sum_{r=1}^{(n_R)_{jl}} (A_{r+2})_{jl} \frac{(\frac{pb}{U})}{(\frac{pb}{U}) + (\bar{a}_r)_{jl}} \tag{2.13}$$

Roger's method has the advantage of defining different number of aerodynamic lag terms for each modal aerodynamic force coefficient. With this property, Roger's method can define the aerodynamic forces with the best approximation among the four rational function approximation methods.

Least-Squares-Method [55]:

Least-Squares-Method uses an equation similar to the equation of the Rogers Method as given in Equation (2.14) for rational function approximation.

$$\left[\widehat{Q}_{mA}(p)\right] = [A_0] + [A_1]p + [A_2]p^2 + \sum_{r=1}^{n_R} [A_{r+2}] \frac{p}{p + \bar{a}_r} \tag{2.14}$$

However, in the Least-Squares-Method, same aerodynamic lag terms, which are the terms given in summation operator in Equation (2.14), were assigned for each term of modal aerodynamic force coefficient matrix. This assignment reduces the order of the equations of motion. On the other hand, it also reduces the success of the rational function approximation.

Modified Matrix Padé Method [55]:

In the modified matrix Padé method, different number of aerodynamic lag terms and values can be defined for each column of the modal aerodynamic force coefficient matrix as

$$\left(\widehat{Q}_{mA}(p)\right)_{jl} = \left(A_0\right)_{jl} + \left(A_1\right)_{jl} p + \left(A_2\right)_{jl} p^2 + \sum_{r=1}^{(n_R)_l} \left(A_{r+2}\right)_{jl} \frac{p}{p + \left(\bar{a}_r\right)_l} \quad (2.15)$$

Karpel's (Minimum State) Method [55]:

Karpel's method is a modified form of the Least-Squares-Method in which the lag terms are represented as

$$\left[\widehat{Q}_{mA}(p)\right] = \left[A_0\right] + \left[A_1\right]p + \left[A_2\right]p^2 + \left[D\right]\left(p\left[I\right] - \left[R\right]\right)^{-1}\left[E\right]p \quad (2.16)$$

This method has an equivalent accuracy with that of the Least Square Method, possibly with fewer states. The number of aerodynamic lag states is equal to the dimension of $[R]$.

2.4.2. Linear Aeroelastic Model

The generalized equation of motion of the aeroelastic structure can be written from Equations (2.5) and (2.10) as

$$[M'_A]\{\ddot{\xi}\}_A + [C'_A]\{\dot{\xi}\}_A + [K'_A]\{\xi\}_A = \bar{q}\left[\widehat{Q}_{mA}(p)\right]\{\xi\}_A + \{Q'\}_{ext} \quad (2.17)$$

Equation (2.17) is valid for a particular Mach number with different $\left[\widehat{Q}_{mA}(p)\right]$. Hence, for each Mach number of interest, a re-derivation of the corresponding $\left[\widehat{Q}_{mA}(p)\right]$ is required. The unsteady aerodynamic forces, $\left[\widehat{Q}_{mA}(p)\right]$, can be derived using one of the suggested methods given in Section 2.4.1 or any other appropriate aerodynamic method. The unsteady aerodynamic forces are fit by a rational function approximation given in Section 2.4.1. Note that the rational function approximations given are in a common format as

$$\left[\widehat{Q}_{mA}(p)\right] = [A_0] + [A_1]p + [A_2]p^2 + \left[\widehat{Q}''_{mA}(p)\right] \quad (2.18)$$

where $\left[\widehat{Q}''_{mA}(p)\right]$ represents the lag terms.

Substituting Equation (2.18) into Equation (2.17), the generalized equation of motion is obtained as follows

$$[M''_A]\{\ddot{\xi}\}_A + [C''_A]\{\dot{\xi}\}_A + [K''_A]\{\xi\}_A = \bar{q}\left[\widehat{Q}''_{mA}(p)\right]\{\xi\}_A + \{Q'\}_{ext} \quad (2.19)$$

where

$$\left.\begin{aligned}
[M''_A] &= [M'_A] - \bar{q}[A_2] \\
[C''_A] &= [C'_A] - \bar{q}[A_1] \\
[K''_A] &= [K'_A] - \bar{q}[A_0]
\end{aligned}\right\} \quad (2.20)$$

For the lag terms of these rational function approximations, a standard state space system can be derived in order to apply standard control techniques as

$$\left[\hat{Q}''_{mA}(p)\right] = \begin{bmatrix} \begin{bmatrix} A_Q \end{bmatrix} & \begin{bmatrix} B_Q \end{bmatrix} \\ \begin{bmatrix} C_Q \end{bmatrix} & \begin{bmatrix} D_Q \end{bmatrix} \end{bmatrix} = \begin{bmatrix} D_Q \end{bmatrix} + \begin{bmatrix} C_Q \end{bmatrix}(p[I] - \begin{bmatrix} A_Q \end{bmatrix})^{-1}\begin{bmatrix} B_Q \end{bmatrix} \quad (2.21)$$

With n_Q aerodynamic states, define $A_Q \in \mathbb{R}^{n_Q \times n_Q}$, $B_Q \in \mathbb{R}^{n_Q \times n}$, $C_Q \in \mathbb{R}^{n \times n_Q}$, $D_Q \in \mathbb{R}^{n \times n}$ as the state space elements of $\left[\hat{Q}''_{mA}(p)\right]$. Hence, a new state space system can be formed for the aeroelastic system by using generalized states, ξ, $\dot{\xi}$ and aerodynamic states x as

$$\begin{Bmatrix} \{\dot{\xi}\}_A \\ \{\ddot{\xi}\}_A \\ \{\dot{x}\} \end{Bmatrix} = \begin{bmatrix} 0 & I & 0 \\ -[M''_A]^{-1}([K''_A] + \bar{q}[D_Q]) & -[M''_A]^{-1}[C''_A] & -\bar{q}[M''_A]^{-1}[C_Q] \\ [B_Q] & 0 & [A_Q] \end{bmatrix} \begin{Bmatrix} \{\xi\}_A \\ \{\dot{\xi}\}_A \\ \{x\} \end{Bmatrix} + \begin{Bmatrix} 0 \\ [M''_A]^{-1}\{Q'\}_{ext} \\ 0 \end{Bmatrix}$$

$$(2.22)$$

2.5. Typical Section

The typical section is a simplified model of a flexible wing that is suitable for an aeroelastic analysis. It is developed in early studies of aeroelasticity and used by aeroelastic pioneers as Theodorsen [51] and Garric. The typical section is used to model the three-dimensional elastic lifting surface by a two-dimensional model as shown in Figure 3. This model has the properties of the lifting surface section at the 70%-75% of the span from root. However, the typical section model is applicable to lifting surfaces which has large aspect ratios, small sweeps, and smoothly varying cross sectional characteristics across span.

The typical section models can also be used for modeling of the aerodynamic control surfaces. Control surfaces are connected to the main body via torsionally less stiff shafts. This assures that the first elastic mode of the aerodynamic control surface is the torsional mode which is the pitch mode of the typical section. However, it is required to check if the second elastic mode of the aerodynamic control surface is the bending mode, which is the plunge mode of the typical section. In addition, the aerodynamic control surface must satisfy the requirement of the typical section given in previous paragraph.

The equation of motion of the unconservative system given in Figure 3 can be written as

$$[M]\{\ddot{q}\} + [C]\{\dot{q}\} + [K]\{q\} = \{Q\}_A + \{Q\}_{ext} \tag{2.23}$$

where

$$[M] = \begin{bmatrix} m & S_\alpha \\ S_\alpha & I_\alpha \end{bmatrix} \tag{2.24}$$

$$[C] = \begin{bmatrix} c_h & 0 \\ 0 & c_\alpha \end{bmatrix} \tag{2.25}$$

$$[K] = \begin{bmatrix} k_h & 0 \\ 0 & k_\alpha \end{bmatrix} \tag{2.26}$$

$$\{q\} = \begin{Bmatrix} q_h \\ q_\alpha \end{Bmatrix} \tag{2.27}$$

$$\{Q\}_A = \begin{Bmatrix} -Q_{AL} \\ Q_{AM} \end{Bmatrix} \tag{2.28}$$

$$\{Q\}_{ext} = \begin{Bmatrix} F_{ext} \\ M_{ext} \end{Bmatrix} \tag{2.29}$$

$$S_\alpha = m.x_{cg} \tag{2.30}$$

and

m : Mass of the wing

I_α : Mass moment of inertia of a wing about its elastic axis

S_α : Static mass moment of a typical section wing about its elastic axis

c_h : Plunge damping coefficient of a typical section wing

c_α : Torsion damping coefficient of a typical section wing

k_h : Plunge spring constant of a typical section wing

k_α : Torsion spring constant of a typical section wing

q_h : Plunge motion of the elastic axis of a typical section wing from undeflected position

q_α : Pitch motion of a typical section wing (angle of attack)

Q_{AL} : Aerodynamic lift force

Q_{AM} : Aerodynamic moment

F_{ext} : External force

M_{ext} : External moment

x_{cg} : Position of the center of mass from elastic axis, defined positively in backwards direction

Disregarding the damping matrix $[C]$, it can be seen that Equation (2.23) is same as the general form of the equation for finite element structure defined in Equation (2.1).

In Equation (2.23), the term $\{Q\}_A$ represents the aerodynamic force vector. In this study, the aerodynamic forces are calculated using the thin airfoil assumption. In this thin airfoil assumption, the modeling of $\{Q\}_A$ differs according to aerodynamic regimes. In the following sections, the equations of motions are derived for subsonic incompressible, subsonic compressible, and supersonic flow regimes.

2.5.1. Incompressible Subsonic Flow

2.5.1.1. Steady Flow

The aerodynamic forces for thin airfoil in steady subsonic incompressible flow are [2]

$$\{Q\}_A = \begin{Bmatrix} -Q_{AL} \\ Q_{AM} \end{Bmatrix} = \begin{Bmatrix} \bar{q}.S.c_{l\alpha}(q_\alpha + \dfrac{\dot{q}_h}{U}) \\ \bar{q}.S.b.c_{m\alpha}(q_\alpha + \dfrac{\dot{q}_h}{U}) \end{Bmatrix} \qquad (2.31)$$

where S is the wing area defined as

$$S = 2bl \qquad (2.32)$$

The parameters $c_{l\alpha}$ and $c_{m\alpha}$ in Equation (2.31) are the aerodynamic coefficients which are defined in this study slightly different than Theodorsen [51] for simplifications in equations as

$$\begin{aligned} c_{l\alpha} &= 2.\pi \\ c_{m\alpha} &= 2.\pi.\left(a + \dfrac{1}{2}\right) \end{aligned} \qquad (2.33)$$

where *a* is the parameter used to represent the position of elastic axis from mid chord in backwards direction.

The aerodynamic forces for thin airfoil in steady subsonic flow can be written as

$$\{Q\}_A = [A_1]\bar{q}\{q\} + [A_2]\bar{q}\{\dot{q}\} \tag{2.34}$$

where $[A_1]$ and $[A_2]$ are the aerodynamic coefficient matrices are defined in this study as

$$[A_1] = \begin{bmatrix} 0 & -S.c_{l\alpha} \\ 0 & S.b.c_{m\alpha} \end{bmatrix} \tag{2.35}$$

$$[A_2] = \begin{bmatrix} -S.c_{l\alpha}\dfrac{1}{U} & 0 \\ S.b.c_{m\alpha}\dfrac{1}{U} & 0 \end{bmatrix} \tag{2.36}$$

Note that in steady aerodynamics, the aerodynamic forces are linear function of generalized coordinates and their derivatives. Actually examining Equation (2.31), it can be seen that the aerodynamic forces are linear functions of $(q_\alpha + \dfrac{\dot{q}_h}{U})$, where $\dfrac{\dot{q}_h}{U}$ is a virtual angle of attack. Substituting the aerodynamic forces for thin airfoil in steady incompressible flow given in Equation (2.34) into Equation (2.23), the equation of motion becomes a set of homogenous differential equation that depends on structural parameters, free stream speed, and dynamic pressure as

$$[M]\{\ddot{q}\} + [C]\{\dot{q}\} + [K]\{q\} = [A_1]\overline{q}\{q\} + [A_2]\overline{q}\{\dot{q}\} + \{Q\}_{ext} \quad (2.37)$$

In order to apply standard control techniques, Equation (2.37) can be easily formulated in state space as

$$\{\dot{\xi}\} = \left[A_{AEsys} \right]\{\xi\} + \left[B_{AEsys} \right]\{v\} \quad (2.38)$$

where

$$\{\xi\} = \left\{ \begin{matrix} \{q\} \\ \{\dot{q}\} \end{matrix} \right\} \quad (2.39)$$

$$\{v\} = \{Q\}_{ext} \quad (2.40)$$

$$\left[A_{AEsys} \right] = \begin{bmatrix} [0_{2x2}] & [I_{2x2}] \\ [M]^{-1}([A_1]\overline{q} - [K]) & [M]^{-1}([A_2]\overline{q} - [C]) \end{bmatrix} \quad (2.41)$$

$$\left[B_{AEsys} \right] = \begin{bmatrix} [0_{2x2}] \\ [M]^{-1} \end{bmatrix} \quad (2.42)$$

2.5.1.2. Unsteady Flow

In order to calculate the unsteady aerodynamic forces, the complete motion of the airfoil must be known. On the other side, for an harmonic analysis, which is used for the flutter analysis, the previous motion of model is well defined. This simplifies the problem and the unsteady forces for oscillatory thin airfoil can be found by solving potential flow equations as [2]

$$Q_{AL} = \frac{\pi}{2}\rho bS\left[\ddot{q}_h + U\dot{q}_\alpha - ba\ddot{q}_\alpha\right] + \pi\rho USC(k)\left[\dot{q}_h + Uq_\alpha + b\left(\frac{1}{2} - a\right)\dot{q}_\alpha\right]$$

$$Q_{AM} = \frac{\pi}{2}\rho bS\left[ba\ddot{q}_h - Ub\left(\frac{1}{2} - a\right)\dot{q}_\alpha - b^2\left(\frac{1}{8} + a^2\right)\ddot{q}_\alpha\right]$$

$$+ \pi\rho UbSC(k)\left(\frac{1}{2} + a\right)\left[\dot{q}_h + Uq_\alpha + b\left(\frac{1}{2} - a\right)\dot{q}_\alpha\right]$$

(2.43)

where

ρ : Density of air

$C(k)$: Theodorsen's function

Arranging Equation (2.43) into matrix form, the aerodynamic force vector becomes

$$\{Q\}_A = \bar{q}[A_1]\{\ddot{q}\} + \bar{q}[A_2]\{\dot{q}\} + \frac{\bar{q}S}{U}C(k)\{R'\}[S_2]\{\dot{q}\} + \bar{q}SC(k)\{R'\}[S_1]\{q\} \quad (2.44)$$

where

$$[A_1] = \frac{bS}{U^2}\begin{pmatrix} -\pi & \pi ba \\ \pi ba & -\pi b^2\left(\frac{1}{8} + a^2\right) \end{pmatrix} \quad (2.45)$$

$$[A_2] = \frac{S}{U}\begin{pmatrix} 0 & -\pi b \\ 0 & -\pi b^2\left(\frac{1}{2} - a\right) \end{pmatrix} \quad (2.46)$$

$$\{R'\} = \begin{Bmatrix} -2\pi \\ 2\pi b\left(\frac{1}{2} + a\right) \end{Bmatrix} \quad (2.47)$$

$$[S_1] = [0 \quad 1] \tag{2.48}$$

$$[S_2] = \left[1 \quad b\left(\frac{1}{2} - a\right) \right] \tag{2.49}$$

$$\bar{q} = \frac{1}{2}\rho U^2 \tag{2.50}$$

and $\{R'\}$, $\{S1\}$, and $\{S2\}$ are vectors defined similarly in the study of Edwards [57] for ease of matrix formulation, [A1] and [A2] are aerodynamic coefficient matrices.

The Theodorsen's function, $C(k)$, is complex by itself. The exact expression of this function is defined by using Hänkel function as [2]

$$C(k) = F(k) + iG(k) = \frac{H_1^{(2)}(k)}{H_1^{(2)}(k) + iH_0^{(2)}(k)} \tag{2.51}$$

Usually approximations for Theodorsen's functions are used for thin airfoil, such as [2]

$$\left. \begin{aligned} C(k) &= \frac{1}{2} + \frac{c_1 \, ik + c_2}{(ik)^2 + c_3 \, ik + c_4} \\ \Rightarrow C(k) &= \frac{1}{2} + C'(k) \end{aligned} \right\} \tag{2.52}$$

where $c_1 = 0.10805$, $c_2 = 0.006825$, $c_3 = 0.3455$, and $c_4 = 0.01365$.

In unsteady subsonic incompressible flow, the aerodynamic flow is composed of two parts; namely, circulatory and noncirculatory parts. The circulatory part of the aerodynamic force given in Equation (2.44) is

$$
\begin{aligned}
\{Q\}_{Ac} &= \frac{\bar{q}S}{U}C(k)\{R'\}[S_2]\{\dot{q}\} + \bar{q}SC(k)\{R'\}[S_1]\{q\} \\
&\Rightarrow \bar{q}SC(k)\{R'\}\left(\frac{1}{U}[S_2]\{\dot{q}\} + [S_1]\{q\}\right) \\
&\Rightarrow \bar{q}S\left(\frac{1}{2} + C'(k)\right)\{R'\}\left(\frac{1}{U}[S_2]\{\dot{q}\} + [S_1]\{q\}\right) \\
&\Rightarrow \bar{q}[A_3]\{\dot{q}\} + \bar{q}[A_4]\{q\} + \bar{q}SC'(k)\{R'\}\left(\frac{1}{U}[S_2]\{\dot{q}\} + [S_1]\{q\}\right)
\end{aligned}
$$

(2.53)

where $[A_3]$ and $[A_4]$ are aerodynamic coefficient matrices defined as

$$
\left.\begin{aligned}
[A_3] &= \{R'\}\frac{S}{2U}[S_2] \\
[A_4] &= \{R'\}\frac{S}{2}[S_1]
\end{aligned}\right\}
$$

(2.54)

Theodorsen's function can be transferred to Laplace domain as follows

$$
\left.\begin{aligned}
C(k) &= \frac{1}{2} + \frac{c_1 ik + c_2}{(ik)^2 + c_3 ik + c_4} \\
&\Rightarrow C(p') = \frac{1}{2} + \frac{c_1 p' + c_2}{(p')^2 + c_3 p' + c_4} \quad, \quad p' = \frac{b}{U}p \\
&\Rightarrow C(p) = \frac{1}{2} + \frac{c_1 p + \frac{U}{b}c_2}{p^2 + \frac{U}{b}c_3 p + \frac{U^2}{b^2}c_4}\frac{U}{b}
\end{aligned}\right\}
$$

(2.55)

where $c_1 = 0.10805$, $c_2 = 0.006825$, $c_3 = 0.3455$, and $c_4 = 0.01365$.

The second part of the circulatory aerodynamic force in Equation (2.53) can be further evaluated as follows

$$\bar{q}SC'(k)\{R'\}\left(\frac{1}{U}[S_2]\{\dot{q}\}+[S_1]\{q\}\right)$$

$$\Rightarrow \bar{q}S\frac{c_1 p+\frac{U}{b}c_2}{p^2+\frac{U}{b}c_3 p+\frac{U^2}{b^2}c_4}\frac{U}{b}\{R'\}\left(\frac{1}{U}[S_2]\{Q(p)p\}+[S_1]\{Q(p)\}\right)$$

$$\Rightarrow \bar{q}\frac{S}{b}\{R'\}\left(c_1 p+\frac{U}{b}c_2\right)\left(\frac{[S_2]\{Q(p)p\}+U[S_1]\{Q(p)\}}{p^2+\frac{U}{b}c_3 p+\frac{U^2}{b^2}c_4}\right)$$

(2.56)

Defining

$$Q_{as}(p)=\left(\frac{[S_2]\{Q(p)p\}+U[S_1]\{Q(p)\}}{p^2+\frac{U}{b}c_3 p+\frac{U^2}{b^2}c_4}\right)$$

(2.57)

and substituting Equation (2.57) into Equation (2.56), the second part of the circulatory aerodynamic force in Equation (2.53) becomes

$$\Rightarrow \bar{q}\frac{S}{b}\{R'\}\left(c_1 p+\frac{U}{b}c_2\right)Q_{as}(p)$$

$$\Rightarrow \bar{q}\frac{S}{b}\{R'\}\left(c_1\dot{q}_{as}+\frac{U}{b}c_2 q_{as}\right)$$

$$\Rightarrow \bar{q}\frac{S}{b}\{R'\}\begin{bmatrix}\frac{U}{b}c_2 & c_1\end{bmatrix}\begin{Bmatrix}q_{as}\\\dot{q}_{as}\end{Bmatrix}$$

$$\Rightarrow \bar{q}[D_A]\{q\}_a$$

(2.58)

where $[D_A]$ is the aerodynamic coefficient matrix and $\{q\}_a$ is the aerodynamic state vector defined as

$$[D_A]=\frac{S}{b}\{R'\}\begin{bmatrix}\frac{U}{b}c_2 & c_1\end{bmatrix}$$

(2.59)

$$\{q\}_a = \begin{Bmatrix} q_{as} \\ \dot{q}_{as} \end{Bmatrix} \tag{2.60}$$

Consequently, substituting the Equation (2.58) into Equation (2.53) and substituting the resultant equation into Equation (2.44), the equation of aerodynamic forces become as

$$\{Q\}_A = \bar{q}[A_1]\{\ddot{q}\} + \bar{q}[A_2]\{\dot{q}\} + \bar{q}[A_3]\{\dot{q}\} + \bar{q}[A_4]\{q\} + \bar{q}[D_A]\{q\}_a \tag{2.61}$$

From Equation (2.57) the equations for the generalized coordinates of aerodynamics can be derived as follows

$$
\begin{aligned}
Q_{as}(p) &= \left(\frac{[S_2]\{Q(p)p\} + U[S_1]\{Q(p)\}}{p^2 + \frac{U}{b}c_3 p + \frac{U^2}{b^2}c_4} \right) \\
\Rightarrow \left(p^2 + \tfrac{U}{b}c_3 p + \tfrac{U^2}{b^2}c_4 \right) Q_{as}(p) &= [S_2]\{Q(p)p\} + U[S_1]\{Q(p)\} \\
\Rightarrow \ddot{q}_{as} + \tfrac{U}{b}c_3 \dot{q}_{as} + \tfrac{U^2}{b^2}c_4 q_{as} &= [S_2]\{\dot{q}\} + U[S_1]\{q\} \\
\Rightarrow \ddot{q}_{as} &= -\tfrac{U}{b}c_3 \dot{q}_{as} - \tfrac{U^2}{b^2}c_4 q_{as} + [S_2]\{\dot{q}\} + U[S_1]\{q\}
\end{aligned}
\tag{2.62}
$$

Defining

$$
\left.
\begin{aligned}
q_{a1} &= q_{as} \\
q_{a2} &= \dot{q}_{as} \\
\dot{q}_{a2} &= \ddot{q}_{as} \\
\{q\}_a &= \begin{Bmatrix} q_{a1} \\ q_{a2} \end{Bmatrix}
\end{aligned}
\right\}
\tag{2.63}
$$

and substituting Equation (2.63) into Equation (2.62), the equation of aerodynamics becomes as

$$\{\dot{q}\}_a = [F_A]\{q\}_a + [E_2]\{\dot{q}\} + [E_1]\{q\} \tag{2.64}$$

where $[F_A]$, $[E_1]$, and $[E_2]$ are aerodynamic coefficient matrices defined as

$$\begin{aligned}
[F_A] &= \begin{bmatrix} 0 & 1 \\ -\dfrac{U^2}{b^2}c_4 & -\dfrac{U}{b}c_3 \end{bmatrix} \\[2mm]
[E_1] &= \begin{bmatrix} 0 & 0 \\ 0 & U \end{bmatrix} \\[2mm]
[E_2] &= \begin{bmatrix} 0 & 0 \\ 1 & b\left(\dfrac{1}{2}-a\right) \end{bmatrix}
\end{aligned} \right\} \qquad (2.65)$$

Using Equations (2.23), (2.61), and (2.64), the equation of motions of the thin airfoil for the subsonic incompressible unsteady flow can be arranged in state space form as follows

$$\{\dot{\xi}\} = \left[A_{AEsys}\right]\{\xi\} + \left[B_{AEsys}\right]\{v\} \qquad (2.66)$$

where

$$\{\xi\} = \begin{Bmatrix} \{q\} \\ \{\dot{q}\} \\ \{q\}_a \end{Bmatrix} \qquad (2.67)$$

$$\{v\} = \{Q\}_{ext} \qquad (2.68)$$

$$\left[A_{AEsys}\right] = \begin{bmatrix} [0_{2x2}] & [I_{2x2}] & [0_{2x2}] \\ \left[[M]-[A_1]\bar{q}\right]^{-1}([A_4]\bar{q}-[K]) & \left[[M]-[A_1]\bar{q}\right]^{-1}\left(([A_3]+[A_4])\bar{q}-[C]\right) & \left[[M]-[A_1]\bar{q}\right]^{-1}\bar{q}[D_A] \\ [E_1] & [E_2] & [F_A] \end{bmatrix}$$

$$(2.69)$$

$$\left[B_{AEsys} \right] = \begin{bmatrix} \left[0_{2x2} \right] \\ \left[M \right]^{-1} \\ \left[0_{2x2} \right] \end{bmatrix} \qquad (2.70)$$

2.5.1.3. Quasisteady Flow

The quasisteady model is a simplified version of the unsteady aerodynamic model. For the thin airfoil, the generalized aerodynamic forces for the quasisteady flow are obtained by replacing Theodorsen's function, $C(k)$, in Equation (2.44) with 1 (one). It is suggested to use quasisteady model for divergence analysis by Ohta et al. [24].

2.5.2. Unsteady Compressible Subsonic Flow

In this Section, a procedure for creating aeroelastic model for unsteady compressible flow is given. The unsteady compressible aerodynamic forces are defined, [2]. For numerical solutions, the output of Mazelsky and Drischler's studies [53, 54] for Mach numbers of 0.5, 0.6, and 0.7 are selected. A procedure that converts the indicial functions of Mazelsky and Drischler to Theodorsen's notation used in this thesis is given. The state space equations for the aeroelastic part of the system are constructed.

Edwards et al. [57], Leisman et al. [40], and Nam et al. [52] presented methods for aerodynamic modeling in state space. These studies contained methods for unsteady incompressible flow. Furthermore, the presented methods were originally derived for the general case in which the aerodynamic force matrix was available as an output of a program (NASTRAN). In this Section, these methods are tailored to derive equations for the thin airfoil unsteady compressible flow.

In order to derive the unsteady aerodynamic loads in compressible flow, unsteady aerodynamic loads for arbitrary small motions were used, [2]. This was performed by means of Fourier integral superposition of theoretical results of simple harmonic oscillations.

In unsteady incompressible flow, the flow patterns can be divided into circulatory and non circulatory parts. Furthermore, the aerodynamic loads are functions of displacement, speed, and acceleration of the wing. Hence, concepts of virtual mass, virtual damping, and virtual stiffness can be used in incompressible flow. However, this is not applicable for compressible flow. Because in compressible flow, in addition to the instantaneous values of 'states and their derivatives', the aerodynamic loads depend on the time histories of the 'states and their derivatives'.

Furthermore, in incompressible flow the circulation around a chord wise rigid airfoil can be determined just by the vertical velocity of the fluid particle at the three-quarter-chord or any other specific point. However, in compressible flow, this is not sufficient due to the complexity of flow. Two indicial motions are required to define it. In Figure 4 and Figure 5 the two distinct motions, the indicial motions, of an airfoil are given. These two indicial motions generate their own lift and moment forces. The aerodynamic forces on the airfoil are derived by superposing these separate lift and moment terms. Hence, four indicial functions are generated. In compressible flow, these four indicial functions replace the Wagner function of incompressible flow.
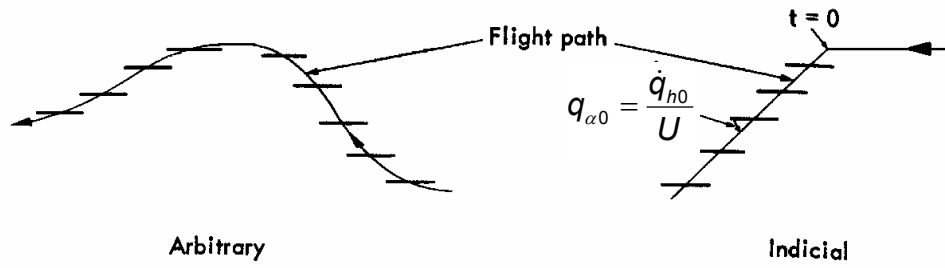
Figure 4. Vertical motion of an airfoil [13].
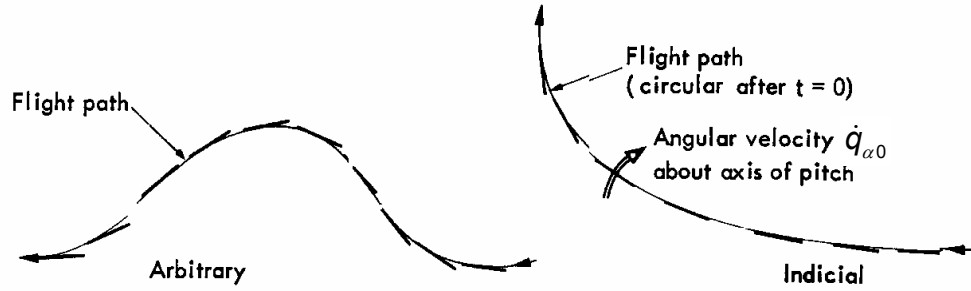
Figure 5. Pitch motion of an airfoil with zero angle of attack [13].

The aerodynamic lift and moment due to the translational motion of the airfoil are [2]

$$L_T{}'(s) = 2\pi \frac{\rho}{2} U^2 S \left(\frac{\dot{q}_{h0}}{U} + q_\alpha \right) \phi_c(s) \qquad (2.71)$$

$$M_{yT}{}'(s) = 2\pi \frac{\rho}{2} U^2 S (2b) \left(\frac{\dot{q}_{h0}}{U} + q_\alpha \right) \phi_{Mc}(s) \qquad (2.72)$$

In Equations (2.71) and (2.72), the parameter $\dot{q}_{h0}$ is the constant speed for which the indicial function of vertical motion is defined. However, as it is seen from these equations, the angular displacement is also introduced in the lift and moment of translational motion. Analyzing Figure 4, one can see that the plunge motion with the airfoil speed is actually generating an artificial angle of attack, $\dot{q}_{h0}/U$. In Equation (2.72), the variable s is the

47

distance traveled by the wing after the start of plunging, measured in semichords, which is defined as [2]

$$s = \frac{Ut}{b} \tag{2.73}$$

where t is the time.

Similarly, the lift and moment for an indicial angular speed of $\dot{q}_{\alpha 0}$ about the leading-edge axis can be written as [2]

$$L_q{'}(s) = 4\pi \frac{\rho}{2} U^2 S \left(\frac{\dot{q}_{\alpha 0} b}{U} \right) \phi_{cq}(s) \tag{2.74}$$

$$M_{yq}{'}(s) = 4\pi \frac{\rho}{2} U^2 S (2b) \left(\frac{\dot{q}_{\alpha 0} b}{U} \right) \phi_{cMq}(s) \tag{2.75}$$

The total lift and moment can be obtained by superposing the lifts and moments of the two indicial motions. The total lift and moment for an arbitrarily moving airfoil, for zero initial conditions, can be derived by taking the convolution integral of Equations (2.74) and (2.75) for impulsive motions as [2]

$$\begin{aligned} L'(s) = 2\pi \frac{\rho}{2} U^2 S \int_0^s \frac{d}{d\sigma} \left[q_\alpha (\sigma) + \frac{\dot{q}_h(\sigma)}{U} \right] \phi_c(s - \sigma) d\sigma \\ + 4\pi \frac{\rho}{2} U^2 S \int_0^s \frac{b}{U} \frac{d\dot{q}_\alpha(\sigma)}{d\sigma} \phi_{cq}(s - \sigma) d\sigma \end{aligned} \tag{2.76}$$

$$M_y'(s) = 2\pi \frac{\rho}{2} U^2 S(2b) \int_0^s \frac{d}{d\sigma} \left[q_\alpha(\sigma) + \frac{\dot{q}_h(\sigma)}{U} \right] \phi_{cM}(s-\sigma) d\sigma$$

$$+ 4\pi \frac{\rho}{2} U^2 S(2b) \int_0^s \frac{b}{U} \frac{d\dot{q}_\alpha(\sigma)}{d\sigma} \phi_{cMq}(s-\sigma) d\sigma$$

(2.77)

Equations (2.76) and (2.77) are general equations. Thus, they can be used for any flow regime if proper indicial functions are known.

The Equations (2.71), (2.72), and (2.74) through (2.77) are derived for the pitch about the leading edge. However, in the study of Bisplinghoff et al. [2], an aeroelastic model was constructed according to Theodorsen's notations. Thus the pitch axis is placed *b(a+1)* behind the leading edge. The lift and moment equations, which are compatible with Theodorsen's notation, are given as

$$L(s) = 2\pi \frac{\rho}{2} U^2 S \int_0^s \frac{d}{d\sigma} \left[q_\alpha(\sigma) + \frac{\dot{q}_h(\sigma)}{U} \right] \phi_c^T(s-\sigma) d\sigma$$

$$+ 4\pi \frac{\rho}{2} U^2 S \int_0^s \frac{b}{U} \frac{d\dot{q}_\alpha(\sigma)}{d\sigma} \phi_{cq}^T(s-\sigma) d\sigma$$

(2.78)

$$M_y(s) = 2\pi \frac{\rho}{2} U^2 S(2b) \int_0^s \frac{d}{d\sigma} \left[q_\alpha(\sigma) + \frac{\dot{q}_h(\sigma)}{U} \right] \phi_{cM}^T(s-\sigma) d\sigma$$

$$+ 4\pi \frac{\rho}{2} U^2 S(2b) \int_0^s \frac{b}{U} \frac{d\dot{q}_\alpha(\sigma)}{d\sigma} \phi_{cMq}^T(s-\sigma) d\sigma$$

(2.79)

The closed form solutions for indicial functions are not available in subsonic flow, but the asymptotic values are available.

Mazelsky and Drischler [53, 54] numerically calculated the indicial functions for Mach numbers of 0.5, 0.6, and 0.7, and then curve fitted to the results in the form of Equation (2.80) which is Laplace transformable.

$$\phi(s) = b_0 + b_1 e^{-\beta_1 s} + b_2 e^{-\beta_2 s} + b_3 e^{-\beta_3 s} \tag{2.80}$$

The solutions of Mazelsky and Drischler are given in Table 2 through Table 5 [54]. These tables contain the results for each indicial function for Mach numbers of 0.5, 0.6, and 0.7. The sign of $b_{3c'}$ term at 0.7 Mach for ϕ_c in Mazelsky and Drichler's study [54] is changed from negative (-) to positive (+) in order to match the corresponding plot given in the same study.

Table 2. Curve fit results for ϕ_c at compressible subsonic speeds.

$\phi_{c'}(s) = b_{0c'} + b_{1c'} e^{-\beta_{1c'}s} + b_{2c'} e^{-\beta_{2c'}s} + b_{3c'} e^{-\beta_{3c'}s}$						
M	$b_{0c'}$	$b_{1c'}$	$\beta_{1c'}$	$b_{2c'}$	$\beta_{2c'}$	$b_{3c'}$	$\beta_{3c'}$
0.5	1.155	-0.406	0.0754	-0.249	0.372	0.773	1.890
0.6	1.250	-0.452	0.0646	-0.630	0.481	0.893	0.958
0.7	1.400	-0.5096	0.0536	-0.567	0.357	0.5866	0.902

Table 3. Curve fit results for ϕ_{cM} at compressible subsonic speeds.

$\phi_{cM'}(s) = b_{0cM'} + b_{1cM'} e^{-\beta_{1cM'}s} + b_{2cM'} e^{-\beta_{2cM'}s} + b_{3cM'} e^{-\beta_{3cM'}s}$						
M	$b_{0cM'}$	$b_{1cM'}$	$\beta_{1cM'}$	$b_{2cM'}$	$\beta_{2cM'}$	$b_{3cM'}$	$\beta_{3cM'}$
0.5	0	0.0557	2.555	-1.000	3.308	0.6263	6.09
0.6	0	-0.100	1.035	-1.502	4.040	1.336	5.022
0.7	0	-0.2425	0.974	0.084	0.668	-0.069	0.438

Table 4. Curve fit results for ϕ_{cq} at compressible subsonic speeds.

$\phi_{cq'}(s) = b_{0cq'} + b_{1cq'}e^{-\beta_{1cq'}s} + b_{2cq'}e^{-\beta_{2cq'}s} + b_{3cq'}e^{-\beta_{3cq'}s}$						
M	$b_{0cq'}$	$b_{1cq'}$	$\beta_{1cq'}$	$b_{2cq'}$	$\beta_{2cq'}$	$b_{3cq'}$	$\beta_{3cq'}$
0.5	0	-2.68	4.08	2.362	4.90	0	0
0.6	0	-0.2653	1.345	0	0	0	0
0.7	0	-0.083	0.800	-0.293	1.565	0.149	2.44

Table 5. Curve fit results for ϕ_{cMq} at compressible subsonic speeds.

$\phi_{cMq'}(s) = b_{0cMq'} + b_{1cMq'}e^{-\beta_{1cMq'}s} + b_{2cMq'}e^{-\beta_{2cMq'}s} + b_{3cMq'}e^{-\beta_{3cMq'}s}$						
M	$b_{0cMq'}$	$b_{1cMq'}$	$\beta_{1cMq'}$	$b_{2cMq'}$	$\beta_{2cMq'}$	$b_{3cMq'}$	$\beta_{3cMq'}$
0.5	-0.0721	-0.248	1.562	0.522	2.348	-0.2879	6.605
0.6	-0.0781	-0.077	0.551	0.380	2.117	-0.2469	4.138
0.7	-0.0875	-0.00998	0.1865	0.1079	1.141	-0.0292	4.04

However, Mazelsky and Drischler tabulated the coefficients for airfoils rotating about three-quarter-chord point with moments taken about quarter-chord point. Using the following relations, the pitch indicial functions for a rotating point that is '*x*' distance behind the three-quarter-chord point, can be calculated. In these equations, prime superscript is used to denote the indicial functions of Mazelsky and Drischler.

$$\left(\phi_{cq}\right)_x = \phi_{cq'} - \frac{x}{c}\phi_{c'}$$
(2.81)

$$\left(\phi_{cMq}\right)_x = \phi_{cMq'} - \frac{x}{c}\phi_{cM'}$$
(2.82)

The following equations can be used to calculate the new indicial function if the axis that the moment is taken about is changed. Here '*y*' is

51

the distance of the new point from quarter-chord point, positively defined in backwards direction.

$$\left(\phi_{cM}\right)_y = \phi''_{cM'} + \frac{y}{c}\phi_{c'} \tag{2.83}$$

$$\left(\phi_{cMq}\right)_y = \phi_{cMq'} + \frac{y}{c}\phi_{cq'} \tag{2.84}$$

The indicial functions of Mazelsky and Drischler can be converted to Theodorsen's notation, if x and y values set as in Equation (2.85). The indicial functions in Theodorsen's notations can be calculated with the help of Equations (2.86) through (2.89).

$$x = c\left(\frac{a}{2} - \frac{1}{4}\right), \ y = c\left(\frac{a}{2} + \frac{1}{4}\right) \tag{2.85}$$

$$\phi^T{}_c = \phi_{c'} \tag{2.86}$$

$$\phi^T{}_{cM} = \phi_{cM'} + \left[\frac{a}{2} + \frac{1}{4}\right]\phi_{c'} \tag{2.87}$$

$$\phi^T{}_{cq} = \phi_{cq'} - \left[\frac{a}{2} - \frac{1}{4}\right]\phi_{c'} \tag{2.88}$$

$$\phi^T{}_{cMq} = \phi_{cMq'} + \left[\frac{a}{2} + \frac{1}{4}\right]\phi_{cq'} - \left[\frac{a}{2} - \frac{1}{4}\right]\phi_{cM'} - \left[\frac{a}{2} + \frac{1}{4}\right]\left[\frac{a}{2} - \frac{1}{4}\right]\phi_{c'} \tag{2.89}$$

The aerodynamic forces can be calculated using these indicial functions. However, with the transformations, the orders of the indicial functions may increase up to 12. This order increase in the indicial functions will directly increase the order of the controller. Hence, the

results are curve fitted to the expression given in Equation (2.80), which results in a third order indicial model after Laplace transformation. In order to satisfy the value of $\phi(s)$ as $s \to \infty$, the steady value, b_0 term is excluded from the curve fitting operation and it is directly obtained by adding the constant terms of the equation which will be curve fitted. The curve fit function is selected as $b_1 e^{-\beta_1 s} + b_2 e^{-\beta_2 s} + b_3 e^{-\beta_3 s}$

The curve fitting is applied to the indicial functions $\phi^T{}_{cM}$, $\phi^T{}_{cq}$, and $\phi^T{}_{cMq}$, whereas the indicial function $\phi^T{}_c$ is directly used without any curve fitting since $\phi^T{}_c = \phi_{c'}$. In order to measure the quality of the curve fit, the squared 2-norms of the residuals of the curve fits are used. Since Equations (2.87) through (2.89) contain a system dependent parameter a, the indicial functions for Theodorsen's notation change from model to model. Hence the indicial functions $\phi^T{}_c$, $\phi^T{}_{cM}$, $\phi^T{}_{cq}$, and $\phi^T{}_{cMq}$ are calculated during the numerical implementation.

Since the full order indicial functions given in Equations (2.86) through (2.89) are not used in rest of this study, the ϕ^T notation is used for the curve fitted indicial functions. The curve fitted indicial functions are in the following form

$$\phi^T{}_c(s) = b_{0c} + b_{1c} e^{-\beta_{1c} s} + b_{2c} e^{-\beta_{2c} s} + b_{3c} e^{-\beta_{3c} s} \qquad (2.90)$$

$$\phi^T{}_{cM}(s) = b_{0cM} + b_{1cM} e^{-\beta_{1cM} s} + b_{2cM} e^{-\beta_{2cM} s} + b_{3cM} e^{-\beta_{3cM} s} \qquad (2.91)$$

$$\phi^T{}_{cq}(s) = b_{0cq} + b_{1cq} e^{-\beta_{1cq} s} + b_{2cq} e^{-\beta_{2cq} s} + b_{3cq} e^{-\beta_{3cq} s} \qquad (2.92)$$

$$\phi^T{}_{cMq}(s) = b_{0cMq} + b_{1cMq} e^{-\beta_{1cMq} s} + b_{2cMq} e^{-\beta_{2cMq} s} + b_{3cMq} e^{-\beta_{3cMq} s} \qquad (2.93)$$

The equations above can be converted to time based equations with the help of Equation (2.73). Hence, the equation of motion of the aeroelastic system can be written with the help of Equations (2.78) and (2.79) as follows

$$m\ddot{q}_h + m\,x_{cg}\ddot{q}_\alpha + c_h\dot{q}_h + k_h q_h = -2\pi\frac{\rho}{2}U^2 S\int_0^t \frac{d}{d\sigma}\left[q_\alpha(\sigma) + \frac{\dot{q}_h(\sigma)}{U}\right]\phi_c^T(t-\sigma)d\sigma$$

$$+4\pi\frac{\rho}{2}U^2 S\int_0^t \frac{b}{U}\frac{d\dot{q}_\alpha(\sigma)}{d\sigma}\phi_{cq}^T(t-\sigma)d\sigma$$

(2.94)

$$m\,x_{cg}\ddot{q}_h + I_\alpha\ddot{q}_\alpha + c_\alpha\dot{q}_\alpha + k_\alpha q_\alpha = 2\pi\frac{\rho}{2}U^2 S(2b)\int_0^t \frac{d}{d\sigma}\left[q_\alpha(\sigma) + \frac{\dot{q}_h(\sigma)}{U}\right]\phi_{cM}^T(t-\sigma)d\sigma$$

$$+4\pi\frac{\rho}{2}U^2 S(2b)\int_0^t \frac{b}{U}\frac{d\dot{q}_\alpha(\sigma)}{d\sigma}\phi_{cMq}^T(t-\sigma)d\sigma$$

(2.95)

Taking the Laplace transform of Equations (2.94) and (2.95), with zero initial conditions, one gets

$$mH(p)p^2 + m\,x_{cg}A(p)p^2 + c_h H(p)p + k_h H(p) =$$

$$-2\pi\frac{\rho}{2}U^2 S\left[A(p) + \frac{H(p)p}{U}\right]p\Phi_c^T(p) + 4\pi\frac{\rho}{2}U^2 S\frac{b}{U}(A(p)p)p\Phi_{cq}^T(p)$$

(2.96)

$$m\,x_{cg}H(p)p^2 + I_\alpha A(p)p^2 + c_\alpha A(p)p + k_\alpha A(p) =$$

$$2\pi\frac{\rho}{2}U^2 S(2b)\left[A(p) + \frac{H(p)p}{U}\right]p\Phi_{cM}^T(p) + 4\pi\frac{\rho}{2}U^2 S(2b)\frac{b}{U}(A(p)p)p\Phi_{cMq}^T(p)$$

(2.97)

54

where

$$\Phi_c{}^T(p) = \frac{b_{0c}}{p} + \frac{b_{1c}}{p + \frac{U}{b}\beta_{1c}} + \frac{b_{2c}}{p + \frac{U}{b}\beta_{2c}} + \frac{b_{3c}}{p + \frac{U}{b}\beta_{3c}} \qquad (2.98)$$

$$\Phi_{cM}^T(p) = \frac{b_{0cM}}{p} + \frac{b_{1cM}}{p + \frac{U}{b}\beta_{1cM}} + \frac{b_{2cM}}{p + \frac{U}{b}\beta_{2cM}} + \frac{b_{3cM}}{p + \frac{U}{b}\beta_{3cM}} \qquad (2.99)$$

$$\Phi_{cq}^T(p) = \frac{b_{0cq}}{p} + \frac{b_{1cq}}{p + \frac{U}{b}\beta_{1cq}} + \frac{b_{2cq}}{p + \frac{U}{b}\beta_{2cq}} + \frac{b_{3cq}}{p + \frac{U}{b}\beta_{3cq}} \qquad (2.100)$$

$$\Phi_{cMq}^T(p) = \frac{b_{0cMq}}{p} + \frac{b_{1cMq}}{p + \frac{U}{b}\beta_{1cMq}} + \frac{b_{2cMq}}{p + \frac{U}{b}\beta_{2cMq}} + \frac{b_{2cMq}}{p + \frac{U}{b}\beta_{2cMq}} \qquad (2.101)$$

The indicial functions can also be written in the following form

$$\Phi^T{}_i(p) = \frac{1}{p}\left(c_{0i} + \frac{c_{1i}p^2 + c_{2i}p + c_{3i}}{p^3 + c_{4i}p^2 + c_{5i}p + c_{6i}}\frac{U}{b}\right) \qquad (2.102)$$

Equation (2.103) can be applied to all indicial functions by substituting the subscript i with the concerned subscript. The terms in Equation (2.102) are explicitly given below. Note that the terms are functions of airfoil speed U, but they are free of dynamic pressure, $\bar{q}$.

$$\left.\begin{array}{l} c_{0i} = b_{0i} + b_{1i} + b_{2i} + b_{3i} \\[4pt] c_{1i} = -b_{1i}\beta_{1i} - b_{2i}\beta_{2i} - b_{3i}\beta_{3i} \\[4pt] c_{2i} = -\left(\dfrac{U}{b}\right)\Big(\left(b_{2i} + b_{3i}\right)\beta_{2i}\beta_{3i} + \left(b_{1i} + b_{3i}\right)\beta_{1i}\beta_{3i} + \left(b_{1i} + b_{2i}\right)\beta_{1i}\beta_{2i}\Big) \\[6pt] c_{3i} = -\left(\dfrac{U}{b}\right)^2 \left(b_{1i} + b_{2i} + b_{3i}\right)\left(\beta_{1i}\beta_{2i}\beta_{3i}\right) \\[6pt] c_{4i} = \left(\dfrac{U}{b}\right)\left(\beta_{1i} + \beta_{2i} + \beta_{3i}\right) \\[6pt] c_{5i} = \left(\dfrac{U}{b}\right)^2 \left(\beta_{1i}\beta_{2i} + \beta_{2i}\beta_{3i} + \beta_{1i}\beta_{3i}\right) \\[6pt] c_{6i} = \left(\dfrac{U}{b}\right)^3 \left(\beta_{1i}\beta_{2i}\beta_{3i}\right) \end{array}\right\} \quad (2.103)$$

Substituting the indicial functions given in Equations (2.98) through (2.101) in the form of Equation (2.102) into Equation (2.96) gives

$$mH(p)p^2 + m\,x_{cg}A(p)p^2 + c_h H(p)p + k_h H(p) =$$
$$-2\pi\frac{\rho}{2}U^2 S\left[A(p) + \frac{H(p)p}{U}\right]p\frac{1}{p}\left(C_{0c} + \frac{c_{1c}p^2 + c_{2c}p + c_{3c}}{p^3 + c_{4c}p^2 + c_{5c}p + c_{6c}}\frac{U}{b}\right)$$
$$+4\pi\frac{\rho}{2}U^2 S\frac{b}{U}\left(A(p)p\right)p\frac{1}{p}\left(C_{0cq} + \frac{c_{1cq}p^2 + c_{2cq}p + c_{3cq}}{p^3 + c_{4cq}p^2 + c_{5cq}p + c_{6cq}}\frac{U}{b}\right)$$

$$(2.104)$$

Equation (2.104) can be rearranged as follows

$$mH(p)p^2 + m\,x_{cg}A(p)p^2 + c_h H(p)p + k_h H(p) =$$
$$-2\pi\frac{\rho}{2}U^2 S\left[A(p) + \frac{H(p)p}{U}\right]\left(C_{0c}\right)$$
$$-2\pi\frac{\rho}{2}U^2 S\left(c_{1c}p^2 + c_{2c}p + c_{3c}\right)\left(\frac{A(p)\dfrac{U}{b} + \dfrac{H(p)p}{b}}{p^3 + c_{4c}p^2 + c_{5c}p + c_{6c}}\right)$$
$$+4\pi\frac{\rho}{2}U^2 S\frac{b}{U}\left(A(p)p\right)\left(C_{0cq}\right)$$
$$+4\pi\frac{\rho}{2}U^2 S\frac{b}{U}\left(c_{1cq}p^2 + c_{2cq}p + c_{3cq}\right)\left(\frac{A(p)p\dfrac{U}{b}}{p^3 + c_{4cq}p^2 + c_{5cq}p + c_{6cq}}\right)$$

$$(2.105)$$

56

Two new states are defined for the aerodynamic lift as

$$
\left.\begin{array}{c}
X_c(p) = \left(\dfrac{A(p)\dfrac{U}{b} + \dfrac{H(p)p}{b}}{p^3 + c_{4c}p^2 + c_{5c}p + c_{6c}} \right) \\[4mm]
X_{cq}(p) = \left(\dfrac{A(p)p\dfrac{U}{b}}{p^3 + c_{4cq}p^2 + c_{5cq}p + c_{6cq}} \right)
\end{array}\right\}
$$

(2.106)

Replacing these new states into Equation (2.105)

$$
\begin{aligned}
mH(p)p^2 + m\,x_{cg}A(p)p^2 &+ c_h H(p)p + k_h H(p) = \\
&-2\pi \frac{\rho}{2}U^2 S\left[A(p) + \frac{H(p)p}{U} \right](c_{0c}) \\
&-2\pi \frac{\rho}{2}U^2 S\left(c_{1c}p^2 + c_{2c}p + c_{3c} \right) X_c(p) \\
&+4\pi \frac{\rho}{2}U^2 S\frac{b}{U}\left(A(p)p \right)(c_{0cq}) \\
&+4\pi \frac{\rho}{2}U^2 S\frac{b}{U}\left(c_{1cq}p^2 + c_{2cq}p + c_{3cq} \right) X_{cq}(p)
\end{aligned}
$$

(2.107)

Substituting equation of dynamic pressure given by Equation (2.50) into Equation (2.107) and taking the Inverse Laplace transform of the resulting expression give

$$
\begin{aligned}
m\ddot{q}_h + m\,x_{cg}\ddot{q}_\alpha &+ c_h \dot{q}_h + k_h q_h = \\
&-2\pi\bar{q}S\left[c_{0c}\left(q_\alpha + \frac{\dot{q}_h}{U} \right) - 2\frac{b}{U}c_{0cq}(\dot{q}_\alpha) \right] \\
&-2\pi\bar{q}S\left(c_{1c}\ddot{x}_{Ac} + c_{2c}\dot{x}_{Ac} + c_{3c}x_{Ac} \right) \\
&+4\pi\bar{q}S\frac{b}{U}\left(c_{1cq}\ddot{x}_{Acq} + c_{2cq}\dot{x}_{Acq} + c_{3cq}x_{Acq} \right)
\end{aligned}
$$

(2.108)

Taking the Inverse Laplace transform of Equation (2.106), the time domain equations of the aerodynamic states are obtained as

$$\ddot{X}_c = -c_{4c}\ddot{X}_c - c_{5c}\dot{X}_c - c_{6c}X_c + q_\alpha \frac{U}{b} + \frac{\dot{q}_h}{b} \tag{2.109}$$

$$\ddot{X}_{cq} = -c_{4cq}\ddot{X}_{cq} - c_{5cq}\dot{X}_{cq} - c_{6cq}X_{cq} + \dot{q}_\alpha \frac{U}{b} \tag{2.110}$$

Defining the states for the aerodynamic lift due to translational motion as in Equation (2.111), the time domain equation of aerodynamic state given in Equation (2.109) can be transformed to the state space equation given in Equation (2.112).

$$\left.\begin{array}{l} X_{Ac1} = X_c \\[4pt] X_{Ac2} = \dot{X}_{Ac1} = \dot{X}_c \\[4pt] X_{Ac3} = \dot{X}_{Ac2} = \ddot{X}_c \\[4pt] \dot{X}_{Ac3} = \dddot{X}_c = -c_{4c}\ddot{X}_c - c_{5c}\dot{X}_c - c_{6c}X_c + q_\alpha \dfrac{U}{b} + \dfrac{\dot{q}_h}{b} \\[8pt] \{x\}_{Ac} = \begin{Bmatrix} X_{Ac1} \\ X_{Ac2} \\ X_{Ac3} \end{Bmatrix} \end{array}\right\} \tag{2.111}$$

$$\{\dot{x}\}_{Ac} = \begin{bmatrix} 0 & 1 & 0 \\ 0 & 0 & 1 \\ -c_{6c} & -c_{5c} & -c_{4c} \end{bmatrix} \{x\}_{Ac} + \begin{bmatrix} 0 & 0 \\ 0 & 0 \\ 0 & \dfrac{U}{b} \end{bmatrix} \{q\} + \begin{bmatrix} 0 & 0 \\ 0 & 0 \\ 1/b & 0 \end{bmatrix} \{\dot{q}\} \tag{2.112}$$

The state space equation derived above can be written in a compact manner as

$$\{\dot{x}\}_{Ac} = [F_{Ac}]\{x\}_{Ac} + [E_{1c}]\{q\} + [E_{2c}]\{\dot{q}\} \tag{2.113}$$

where $[F_{Ac}]$, $[E_{1Ac}]$, and $[E_{2Ac}]$ are aerodynamic coefficient matrices defined as

$$\left.\begin{aligned}
\left[F_{Ac}\right] &= \begin{bmatrix} 0 & 1 & 0 \\ 0 & 0 & 1 \\ -c_{6c} & -c_{5c} & -c_{4c} \end{bmatrix} \\[2mm]
\left[E_{1Ac}\right] &= \begin{bmatrix} 0 & 0 \\ 0 & 0 \\ 0 & \dfrac{U}{b} \end{bmatrix} \\[2mm]
\left[E_{2Ac}\right] &= \begin{bmatrix} 0 & 0 \\ 0 & 0 \\ 1/b & 0 \end{bmatrix}
\end{aligned}\right\} \tag{2.114}$$

The state space equation for the state of the aerodynamic lift due to pitch motion can be written as

$$\{\dot{x}\}_{Acq} = \left[F_{Acq}\right]\{x\}_{Acq} + \left[E_{2cq}\right]\{\dot{q}\} \tag{2.115}$$

$$\{x\}_{Acq} = \begin{Bmatrix} x_{cq} \\ \dot{x}_{cq} \\ \ddot{x}_{cq} \end{Bmatrix} \tag{2.116}$$

$$\left.\begin{aligned}
\left[F_{Acq}\right] &= \begin{bmatrix} 0 & 1 & 0 \\ 0 & 0 & 1 \\ -c_{6cq} & -c_{5cq} & -c_{4cq} \end{bmatrix} \\[2mm]
\left[E_{2Acq}\right] &= \begin{bmatrix} 0 & 0 \\ 0 & 0 \\ 0 & \dfrac{U}{b} \end{bmatrix}
\end{aligned}\right\} \tag{2.117}$$

Performing similar operations on moment equation, one gets

$$m\,x_{cg}H(p)p^2 + I_\alpha A(p)p^2 + c_\alpha A(p)p + k_\alpha A(p) =$$

$$2\pi\frac{\rho}{2}U^2 S(2b)\left[A(p) + \frac{H(p)p}{U}\right]p\frac{1}{p}\left(c_{0cM} + \frac{c_{1cM}p^2 + c_{2cM}p + c_{3cM}}{p^3 + c_{4cM}p^2 + c_{5cM}p + c_{6cM}}\frac{U}{b}\right)$$

$$+4\pi\frac{\rho}{2}U^2 S(2b)\frac{b}{U}(A(p)p)p\frac{1}{p}\left(c_{0cMq} + \frac{c_{1cMq}p^2 + c_{2cMq}p + c_{3cMq}}{p^3 + c_{4cMq}p^2 + c_{5cMq}p + c_{6cMq}}\frac{U}{b}\right) \qquad (2.118)$$

$$m\,x_{cg}\ddot{q}_h + I_\alpha\ddot{q}_\alpha + c_\alpha\dot{q}_\alpha + k_\alpha q_\alpha =$$

$$2\pi\bar{q}S(2b)\left(c_{0cM}\left(q_\alpha + \frac{\dot{q}_h}{U}\right) + 2\frac{b}{U}c_{0cMq}(\dot{q}_\alpha)\right)$$

$$+2\pi\bar{q}S(2b)(c_{1cM}\ddot{x}_{AcM} + c_{2cM}\dot{x}_{AcM} + c_{3cM}x_{AcM})$$

$$+4\pi\bar{q}S(2b)\frac{b}{U}(c_{1cMq}\ddot{x}_{AcMq} + c_{2cMq}\dot{x}_{AcMq} + c_{3cMqx}x_{AcMq}) \qquad (2.119)$$

The state space equation for the aerodynamic moment due to translational motion becomes

$$\{\dot{x}\}_{AcM} = [F_{AcM}]\{x\}_{AcM} + [E_{1cM}]\{q\} + [E_{2cM}]\{\dot{q}\} \qquad (2.120)$$

$$\{x\}_{AcM} = \begin{Bmatrix} x_{cM} \\ \dot{x}_{cM} \\ \ddot{x}_{cM} \end{Bmatrix} \qquad (2.121)$$

$$[F_{AcM}] = \begin{bmatrix} 0 & 1 & 0 \\ 0 & 0 & 1 \\ -c_{6cM} & -c_{5cM} & -c_{4cM} \end{bmatrix}$$

$$[E_{1AcM}] = \begin{bmatrix} 0 & 0 \\ 0 & 0 \\ 0 & \dfrac{U}{b} \end{bmatrix} \qquad (2.122)$$

$$[E_{2AcM}] = \begin{bmatrix} 0 & 0 \\ 0 & 0 \\ 1/b & 0 \end{bmatrix}$$

Similarly, the state space equation for aerodynamic moment due to pitch motion can be written as

$$\{\dot{x}\}_{AcMq} = \left[F_{AcMq}\right]\{x\}_{AcMq} + \left[E_{2cMq}\right]\{\dot{q}\} \qquad (2.123)$$

$$\{x\}_{AcMq} = \begin{Bmatrix} x_{cMq} \\ \dot{x}_{cMq} \\ \ddot{x}_{cMq} \end{Bmatrix} \qquad (2.124)$$

$$\left[F_{AcMq}\right] = \begin{bmatrix} 0 & 1 & 0 \\ 0 & 0 & 1 \\ -c_{6cMq} & -c_{5cMq} & -c_{4cMq} \end{bmatrix}$$

$$\left[E_{2AcMq}\right] = \begin{bmatrix} 0 & 0 \\ 0 & 0 \\ 0 & \dfrac{U}{b} \end{bmatrix} \qquad (2.125)$$

Combining the lift and moment equations given by Equations (2.108) and (2.119), the equation of motion of the aeroelastic system can be written as

$$[M]\{\ddot{q}\} + [C]\{\dot{q}\} + [K]\{q\} = [A_1]\bar{q}\{q\} + [A_2]\bar{q}\{\dot{q}\}$$
$$+ [D_{Ac}]\bar{q}\{x\}_{Ac} + [D_{Acq}]\bar{q}\{x\}_{Acq} + [D_{AcM}]\bar{q}\{x\}_{AcM} + [D_{AcMq}]\bar{q}\{x\}_{AcMq} \quad (2.126)$$

where $[A_1]$, $[A_2]$, $[D_{Ac}]$, $[D_{Acq}]$, $[D_{AcM}]$, and $[D_{AcMq}]$ are aerodynamic coefficient matrices defined as

$$[A_1] = 2\pi S \begin{bmatrix} 0 & -c_{0c} \\ 0 & (2b)c_{0cM} \end{bmatrix} \quad (2.127)$$

$$[A_2] = 2\pi S \frac{1}{U} \begin{bmatrix} -c_{0c} & 2bc_{0cq} \\ 2bc_{0cM} & 4b^2 c_{0cMq} \end{bmatrix} \quad (2.128)$$

$$[D_{Ac}] = -2\pi S \begin{bmatrix} c_{3c} & c_{2c} & c_{1c} \\ 0 & 0 & 0 \end{bmatrix} \quad (2.129)$$

$$[D_{Acq}] = 4\pi S \frac{b}{U} \begin{bmatrix} c_{3cq} & c_{2cq} & c_{1cq} \\ 0 & 0 & 0 \end{bmatrix} \quad (2.130)$$

$$[D_{AcM}] = 2\pi S (2b) \begin{bmatrix} 0 & 0 & 0 \\ c_{3cM} & c_{2cM} & c_{1cM} \end{bmatrix} \quad (2.131)$$

$$[D_{AcMq}] = 4\pi S (2b) \frac{b}{U} \begin{bmatrix} 0 & 0 & 0 \\ c_{3cMq} & c_{2cMq} & c_{1cMq} \end{bmatrix} \quad (2.132)$$

Defining the states as in Equation (2.133), and including the external forces, the state space equation of the aeroelastic model for unsteady compressible flow can be obtained as

$$\{\dot{\xi}\} = \left[A_{AEsys}\right]\{\xi\} + \left[B_{AEsys}\right]\{v\}$$ (2.133)

where

$$\{\xi\} = \begin{Bmatrix} \{q\} \\ \{\dot{q}\} \\ \{x\}_{Ac} \\ \{x\}_{Acq} \\ \{x\}_{AcM} \\ \{x\}_{AcMq} \end{Bmatrix}$$ (2.134)

$$\{v\} = \{Q\}_{ext}$$ (2.135)

$$\left[A_{AEsys}\right] = \begin{bmatrix} [0_{2x2}] & [I_{2x2}] & [0_{2x3}] & [0_{2x3}] & [0_{2x3}] & [0_{2x3}] \\ [M]^{-1}([A_1]\bar{q}-[K]) & [M]^{-1}([A_2]\bar{q}-[C]) & [M]^{-1}[D_{Ac}]\bar{q} & [M]^{-1}[D_{Acq}]\bar{q} & [M]^{-1}[D_{AcM}]\bar{q} & [M]^{-1}[D_{AcMq}]\bar{q} \\ [E_{1Ac}] & [E_{2Ac}] & [F_{Ac}] & [0_{3x3}] & [0_{3x3}] & [0_{3x3}] \\ [0_{3x2}] & [E_{2Acq}] & [0_{3x3}] & [F_{Acq}] & [0_{3x3}] & [0_{3x3}] \\ [E_{1AcM}] & [E_{2AcM}] & [0_{3x3}] & [0_{3x3}] & [F_{AcM}] & [0_{3x3}] \\ [0_{3x2}] & [E_{2AcMq}] & [0_{3x3}] & [0_{3x3}] & [0_{3x3}] & [F_{AcMq}] \end{bmatrix}$$

(2.136)

$$\left[B_{AEsys}\right] = \begin{bmatrix} [0_{2x2}] \\ [M]^{-1} \\ [0_{2x2}] \\ [0_{2x2}] \\ [0_{2x2}] \\ [0_{2x2}] \end{bmatrix}$$ (2.137)

2.5.3. Unsteady Compressible Supersonic Flow

The lift and moment equations, Equation (2.76) and Equation (2.77) given for unsteady compressible subsonic flow are also valid for supersonic flow. It is only required to derive the indicial functions to extend the formulation to supersonic flow. In contrast to the subsonic case, the derivations of indicial functions are much easier in supersonic flow. In supersonic flow it is also possible to obtain closed form solutions. The piecewise solutions of the indicial functions for unsteady compressible supersonic flow are given in Equations (2.138) through (2.141) [2].

$$\phi_c(s) = \begin{cases} \dfrac{2}{\pi M}, & 0 \le s \le \dfrac{2M}{M+1} \\[3mm] \dfrac{2}{\pi^2} \left\{ \begin{aligned} & \dfrac{1}{M}\cos^{-1}\left[M - \dfrac{2M}{s}\right] \\ & + \dfrac{1}{\sqrt{M^2-1}}\cos^{-1}\left[\dfrac{s}{2M} + M - \dfrac{sM}{2}\right] \\ & + \dfrac{1}{M}\sqrt{\dfrac{s^2}{4M^2} - \left(1 - \dfrac{s}{2}\right)^2} \end{aligned} \right\}, & \dfrac{2M}{M+1} \le s \le \dfrac{2M}{M-1} \\[3mm] \dfrac{2}{\pi\sqrt{M^2-1}}, & s \ge \dfrac{2M}{M-1} \end{cases} \tag{2.138}$$

$$\phi_{cM}(s) = \begin{cases} \dfrac{-1}{2\pi M}\left(2 - \dfrac{s^2}{4M^2}\right), & 0 \le s \le \dfrac{2M}{M+1} \\[3mm] \dfrac{-1}{\pi^2} \left\{ \begin{aligned} & \dfrac{1}{M}\left(1 - \dfrac{s^2}{8M^2}\right)\cos^{-1}\left[M - \dfrac{2M}{s}\right] \\ & + \dfrac{1}{\sqrt{M^2-1}}\cos^{-1}\left[\dfrac{s}{2M} + M - \dfrac{sM}{2}\right] \\ & + \dfrac{1}{M}(2+s)\sqrt{\dfrac{s^2}{4M^2} - \left(1 - \dfrac{s}{2}\right)^2} \end{aligned} \right\}, & \dfrac{2M}{M+1} \le s \le \dfrac{2M}{M-1} \\[3mm] \dfrac{-1}{\pi\sqrt{M^2-1}}, & s \ge \dfrac{2M}{M-1} \end{cases} \tag{2.139}$$

$$\phi_{cq}(s) = \frac{1}{\pi^2} \begin{cases} \dfrac{1}{\pi M}\left(1+\dfrac{s^2}{8M^2}\right), & 0 \le s \le \dfrac{2M}{M+1} \\[4mm] \left[\begin{array}{l} \dfrac{1}{M}\left(1+\dfrac{s^2}{8M^2}\right)\cos^{-1}\left[M-\dfrac{2M}{s}\right] \\[3mm] +\dfrac{1}{\sqrt{M^2-1}}\cos^{-1}\left[\dfrac{s}{2M}+M-\dfrac{sM}{2}\right] \\[3mm] +\dfrac{(6-s)}{4M}\sqrt{\dfrac{s^2}{4M^2}-\left(1-\dfrac{s}{2}\right)^2} \end{array}\right], & \dfrac{2M}{M+1} \le s \le \dfrac{2M}{M-1} \\[10mm] \dfrac{1}{\pi\sqrt{M^2-1}}, & s \ge \dfrac{2M}{M-1} \end{cases}$$

(2.140)

$$\phi_{cMq}(s) = \frac{-2}{3\pi^2} \begin{cases} \dfrac{-2}{3\pi M}\left(1+\dfrac{s^3}{16M^2}\right), & 0 \le s \le \dfrac{2M}{M+1} \\[4mm] \left[\begin{array}{l} \dfrac{1}{M}\left(1+\dfrac{s^3}{16M^2}\right)\cos^{-1}\left[M-\dfrac{2M}{s}\right] \\[3mm] +\dfrac{1}{\sqrt{M^2-1}}\cos^{-1}\left[\dfrac{s}{2M}+M-\dfrac{sM}{2}\right] \\[3mm] +\dfrac{\left[8-\dfrac{s}{2}-\dfrac{s^2}{2M^2}-\dfrac{s^2}{4}\right]}{4M}\sqrt{\dfrac{s^2}{4M^2}-\left(1-\dfrac{s}{2}\right)^2} \end{array}\right], & \dfrac{2M}{M+1} \le s \le \dfrac{2M}{M-1} \\[10mm] \dfrac{-2}{3\pi\sqrt{M^2-1}}, & s \ge \dfrac{2M}{M-1} \end{cases}$$

(2.141)

where M is the Mach number.

These indicial functions are derived for the pitch of the airfoil about the leading edge, and the moment is also taken about the leading edge. Hence, it is required to calculate the indicial functions at the elastic axis. For this purpose, Equations (2.81) through (2.84) are used with a shift distance of $x = y = b(a+1)$ to obtain the following equations.

$$\phi^T{}_c = \phi_{c'}$$

(2.142)

$$\phi^T{}_{cM} = \phi_{cM'} + \left[\frac{a}{2} + \frac{1}{2}\right]\phi_{c'} \tag{2.143}$$

$$\phi^T{}_{cq} = \phi_{cq'} - \left[\frac{a}{2} + \frac{1}{2}\right]\phi_{c'} \tag{2.144}$$

$$\phi^T{}_{cMq} = \phi_{cMq'} + \left[\frac{a}{2} + \frac{1}{2}\right]\left(\phi_{cq'} - \phi_{cM'}\right) - \left[\frac{a}{2} + \frac{1}{2}\right]^2\phi_{c'} \tag{2.145}$$

The equations of indicial functions Equations (2.142) through (2.145) are the substitutes for Equations (2.86) through (2.89) in subsonic flow. The rest of the procedures and equations given in Section 2.5.2 are all valid for supersonic flow.

2.6. Postscript on Chapter 2

In this section the equations of the aeroelastic system are derived in state variable form for the thin airfoil in the following flow regimes:

- Steady incompressible subsonic flow,
- Unsteady incompressible subsonic flow,
- Unsteady compressible subsonic flow,
- Unsteady compressible supersonic flow.

Note that no output equations are derived since the inputs and outputs of these systems are modified according to the requirements. For the aeroelastic analysis, these equations are directly used after some proper input/output modifications. These equations are also used in constructing the equations of the aeroservoelastic systems.

In the derivation of the aeroelastic matrices for unsteady flows, Theodorsen's function and indicial functions are used. In this Chapter,

step by step derivations of these functions to the state space are given. In literature, a derivation with a different method was presented by Chang [52] and Lind [38]. However in the presented method, every indicial function is restricted to have the same number of lag terms. A proper method that allows the selection of a different number of lag terms for each indicial function was provided by Edwards [57]. But the equations were only valid for incompressible flow and the derivations were not provided. Hence the derivation details of these equations and their extension to compressible subsonic flow equations are performed and presented in this Chapter.

CHAPTER 3

FLUTTER SEARCH METHODS

3.1. Preview

In this Chapter, the flutter search methods are examined and some well known flutter search algorithms are surveyed. Among them application of the so called p-method is briefly presented. The μ flutter search method is described in detail. Application methods of the μ-method on the nominal and robust aeroelastic models are presented. Algorithms are constructed in order to implement the μ-method for flight envelope analysis.

3.2. Flutter Search Methods

Since flutter is a frightful instability in aviation, several studies were conducted for the prediction of flutter speed using various methods. The derivations involved in these methods are out of the scope of this study. However, some of these methods are used in this study in order to derive the flutter speed of the aeroelastic and aeroservoelastic systems. Some common flutter prediction methods are given below:

K-method, (1942);

- This flutter computation procedure uses the structural damping concept such that an artificial damping is introduced to enforce an harmonic solution to the following equation,

$$[M]\{\ddot{q}\} + [C]\{\dot{q}\} + (1+ig)[K]\{q\} = \{Q\}_A + \{Q\}_{ext} \qquad (3.1)$$

- Damping factor, g, is calculated for every mode at several discrete speed values in the range of interest.
- The flutter occurs at the speed that damping factor, g, crosses zero.
- Mode switching often occurs making interpretation of the results difficult.

KE-method:

- Similar to K-method, except the viscous damping is ignored.

$$[M]\{\ddot{q}\} + (1+ig)[K]\{q\} = \{Q\}_A + \{Q\}_{ext} \qquad (3.2)$$

PK-method, (Hassing, 1971);

- Similar to K-method, but all matrices are real.

$$[M]\{\ddot{q}\} + [C]\{\dot{q}\} + [K]\{q\} = \{Q\}_A + \{Q\}_{ext} \qquad (3.3)$$

- Aerodynamic load matrices are real but non-symmetric yielding complex roots.
- Mode switching often occurs causing difficulties in the analysis.
- User is responsible for determining "match point solutions".
- Flight control system may be included in the analysis.

p-method [Abel, 1979];

- A transformation into state space is applied and the eigenvalues of state space A-matrix are computed.

- Flight control system may be included.

- Use of standard control analysis tools is possible.

μ-method [Lind and Brenner, 1998]

- State space model of the system is derived and written in LFT-form with the dynamic pressure $\bar{q}$ as a free parameter to perform μ-analysis.

- Model uncertainties fit in LFT model.

- Worst case flutter margin is computed.

- Flight control system may be included.

The μ-method search algorithm is the base of the controller synthesis method for flutter suppression, which is presented in this study. Thus, among the flutter suppression methods the μ-method is selected as the main search algorithm. A second method is used in order to crosscheck the results of the μ-method. For this purpose p-method is selected. Since both methods use the state space equations, this selection simplifies the applied procedures applied. Moreover, the usage of standard control analysis tools for the p-method analysis also simplifies its application.

In the analysis using the p-method the state space system matrix is computed for several discrete values of dynamic pressure or airspeed and the stability of the system is analyzed for each dynamic pressure or airspeed. Thus the results can be presented on a root locus plot or a plot of damping ratio and frequency versus dynamic pressure or airspeed.

3.3. *μ-method*

The *μ*-method is the implementation of robust system analysis in flutter analysis. A general information about robust system analysis is given in Appendix A. The application of this method is given in Section 3.3.1. This application involves a nominal flutter analysis which is actually a robust stability problem. In Section 3.3.2, the robust flutter analysis concept and its application are given.

3.3.1. Parameterization over Flight Conditions

The *μ* analysis searches for the minimum perturbation on a system parameter that causes instability. Thus, in order to obtain the stability margin of a nominal system via *μ* analysis, it is required to select the particular parameter to perturb. Since the state space equations of the aeroelastic model are linear functions of dynamic pressure $\bar{q}$, the model is parameterized around the dynamic pressure. Hence, the perturbation of $\bar{q}$ can be entered as a fractional transformation. This perturbation is treated as a system uncertainty, hence the resulting stability margin specifies the amount of change in dynamic pressure required to cause the flutter.

Considering an additive perturbation, $\delta_{\bar{q}} \in \mathbb{R}$, on the nominal dynamic pressure, $\bar{q}_0$, the total dynamic pressure $\bar{q}$ is defined as

$$\bar{q} = \bar{q}_0 + \delta_{\bar{q}} \tag{3.4}$$

Substituting Equation (3.4) into the generalized Equation (2.37) of steady incompressible flow, and collecting the $\delta_{\bar{q}}$ terms, the following equation is obtained.

$$[M]\{\ddot{q}\} + [C]\{\dot{q}\} + [K]\{q\} = [A_1](\bar{q}_o + \delta_{\bar{q}})\{q\} + [A_2](\bar{q}_o + \delta_{\bar{q}})\{\dot{q}\}$$

$$= [A_1](\bar{q}_o)\{q\} + [A_2](\bar{q}_o)\{\dot{q}\} + [A_1](\delta_{\bar{q}})\{q\} + [A_2](\delta_{\bar{q}})\{\dot{q}\}$$

$$= [A_1](\bar{q}_o)\{q\} + [A_2](\bar{q}_o)\{\dot{q}\} + \delta_{\bar{q}}([A_1]\{q\} + [A_2]\{\dot{q}\})$$

$$= [A_1](\bar{q}_o)\{q\} + [A_2](\bar{q}_o)\{\dot{q}\} + \delta_{\bar{q}}\{z\}_{\bar{q}}$$

$$= [A_1](\bar{q}_o)\{q\} + [A_2](\bar{q}_o)\{\dot{q}\} + \{w\}_{\bar{q}}$$

$$(3.5)$$

In Equation (3.5), the term $\{w\}_{\bar{q}}$ is the perturbation that is defined as an external operator affecting the nominal system with a feedback approach. The perturbation equation is

$$\{w\}_{\bar{q}} = \delta_{\bar{q}}\{z\}_{\bar{q}} \qquad (3.6)$$

where $\{w\}_{\bar{q}}$ and $\{z\}_{\bar{q}}$ are the input and output signals, respectively. The equation of the output $\{z\}_{\bar{q}}$ is as follows

$$\{z\}_{\bar{q}} = [A_1]\{q\} + [A_2]\{\dot{q}\} \qquad (3.7)$$

Defining the plant of the state space system as $[P_{ae}]$, such that $\{z\}_{\bar{q}} = [P_{ae}]\{w\}_{\bar{q}}$, and disregarding the rest of the external forces, the nominal aeroelastic state space model becomes

$$\begin{Bmatrix} \{\dot{q}\} \\ \{\ddot{q}\} \\ \{z\}_{\bar{q}} \end{Bmatrix} = \begin{bmatrix} [0_{2x2}] & [I_{2x2}] & [0_{2x2}] \\ [M]^{-1}([A_1]\bar{q}_o - [K]) & [M]^{-1}([A_2]\bar{q}_o - [C]) & [M]^{-1} \\ [A_1] & [A_2] & [0_{2x2}] \end{bmatrix} \begin{Bmatrix} \{q\} \\ \{\dot{q}\} \\ \{w\}_{\bar{q}} \end{Bmatrix} \qquad (3.8)$$

where the general format of these equations is

$$\left\{\begin{matrix}\{\dot{\xi}\}\\ \hline \{e\}\end{matrix}\right\} = [P]\left\{\begin{matrix}\{\xi\}\\ \hline \{d\}\end{matrix}\right\} \tag{3.9}$$

and

$$[P] = \left[\begin{array}{c:c}[A] & [B]\\ \hdashline [C] & [D]\end{array}\right] \tag{3.10}$$

The equations for the other flight regimes can be found in Appendix B.

Equations (3.9) and (3.10) are used for nominal stability analysis in the μ framework. Linear fractional transformation system for nominal stability analysis in the μ framework with parameterization around perturbation in dynamic pressure is given in Figure 6. It depicts the feedback interconnection between the perturbation in dynamic pressure and the nominal plant model parameterized around that perturbation.
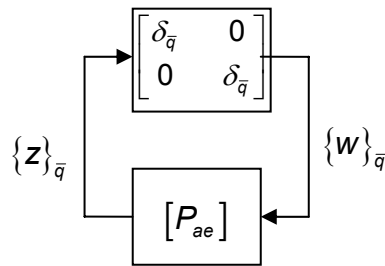
Figure 6. LFT system for nominal flutter analysis

Using the robust stability analysis tools and the small gain theorem, the largest perturbation to dynamic pressure for which the nominal aeroelastic system is still stable can be found. For a given system in Figure 6, $[P_{ae}]$ is robustly stable with respect to the perturbation set $\begin{bmatrix}\delta_{\bar{q}} & 0\\ 0 & \delta_{\bar{q}}\end{bmatrix}$, which is infinite norm bounded by real scalar α, if and only if

$\mu\left(\left[P_{ae}\right]\right) < \frac{1}{\alpha}$. Here α is the largest perturbation given to the dynamic pressure for which the nominal aeroelastic system is still stable. Since $\delta_{\bar{q}}$ is a real scalar, the solution is the maximum spectral radius of the frequency varying transfer function matrix. However the spectral radius is a discontinuous function of frequency, thus the true solution of μ can not be guaranteed via search over finite frequency points.

A simpler alternative method is to iteratively search the stability of the system for different perturbations. One of the simplest approaches used for the nominal flutter margin search is the bisection method [38], which is given below.

1. construct the $\left[P_{ae}\right]$ matrix at dynamic pressure $\bar{q}_o$,

2. select an initial value for the operator $\delta_{\bar{q}}$ that is related to $\left[P_{ae}\right]$ as in Figure 6,

3. define scalars $\delta_{upper} > \delta_{lower} \geq 0$ to bound $\delta_{\bar{q}}$,

4. define scalar $\varepsilon > 0$ for accuracy,

5. compute $\delta_{\bar{q}} = \frac{1}{2}\left(\delta_{upper} + \delta_{lower}\right)$,

6. if $F_u\left(\left[P_{ae}\right], \delta_{\bar{q}}\right)$ has an unstable pole then take $\delta_{upper} = \delta_{\bar{q}}$ otherwise take $\delta_{lower} = \delta_{\bar{q}}$,

7. if $\delta_{upper} - \delta_{lower} > \varepsilon$ then go to step 5,

8. the nominal dynamic pressure of flutter is $\bar{q}_{flut} = \bar{q}_o + \delta_{upper}$,

9. the nominal dynamic pressure of flutter margin is $\Gamma_{flut} = \delta_{upper}$.

This method can be easily applied to the aeroservoelastic problem by replacing the system transfer function matrix of the aeroelastic plant $\left[P_{ae}\right]$ with the system transfer function matrix of the aeroservoelastic

system. However, for an aeroservoelastic system the lower bound also gains importance. For the search of the lower bound the method given here is used with some small tailorings.

3.3.2. Robust Model in the Structured Singular Value Framework

One can introduce additional uncertainties in addition to the dynamic pressure such as mass, damping, stiffness, etc. in order to model the variations between the theoretical model and the physical system. In this Section, two uncertainty models are added to the nominal aeroelastic model. These uncertainties are added to stiffness and damping.

3.3.2.1. Uncertainty in Stiffness

Parametric multiplicative uncertainties are used for linear uncertainty of stiffness. For that purpose, the uncertainty is multiplied with the stiffness in diagonal matrix form and with some weighting functions as given in Equation (3.11). Weighting functions are used to consider the uncertainty of each element separately.

$$[K] = [K_o]\left([I_{2x2}] + \begin{bmatrix} \ddots & W_k & \ddots \end{bmatrix}\begin{bmatrix} \ddots & \delta_k & \ddots \end{bmatrix}\right) \tag{3.11}$$

where

$$\left.\begin{aligned} [K_o] &= \begin{bmatrix} k_{ho} & 0 \\ 0 & k_{\alpha o} \end{bmatrix} \\ \begin{bmatrix} \ddots & W_k & \ddots \end{bmatrix} &= \begin{bmatrix} W_{kh} & 0 \\ 0 & W_{k\alpha} \end{bmatrix} \\ \begin{bmatrix} \ddots & \delta_k & \ddots \end{bmatrix} &= \begin{bmatrix} \delta_{kh} & 0 \\ 0 & \delta_{k\alpha} \end{bmatrix} \end{aligned}\right\} \tag{3.12}$$

and

k_{ho} : Nominal plunge stiffness of typical section wing

$k_{\alpha o}$: Nominal pitch stiffness of typical section wing

W_{kh} : Weighting for uncertainty of plunge stiffness

$W_{k\alpha}$: Weighting for uncertainty of pitch stiffness

δ_{kh} : Norm bounded perturbation multiplier of plunge stiffness

$\delta_{k\alpha}$: Norm bounded perturbation multiplier of pitch stiffness

Inserting Equation (3.11) into the nominal aeroelastic equation of motion in Equation (3.5), and collecting $\begin{bmatrix} \ddots \delta_k \ddots \end{bmatrix}$ terms Equation (3.13) is obtained

$$[M]\{\ddot{q}\} + [C]\{\dot{q}\} + \left([K_o] + [K_o]\begin{bmatrix} \ddots W_k \ddots \end{bmatrix}\begin{bmatrix} \ddots \delta_k \ddots \end{bmatrix}\right)\{q\} = [A_1](\bar{q}_o)\{q\} + [A_2](\bar{q}_o)\{\dot{q}\} + \{w\}_{\bar{q}}$$

$$\{\ddot{q}\} = [M]^{-1}\left([A_1]\bar{q}_o - \left([K_o] + [K_o]\begin{bmatrix} \ddots W_k \ddots \end{bmatrix}\begin{bmatrix} \ddots \delta_k \ddots \end{bmatrix}\right)\right)\{q\} + [M]^{-1}\left([A_2]\bar{q}_o - [C]\right)\{\dot{q}\} + [M]^{-1}\{w\}_{\bar{q}}$$

$$\{\ddot{q}\} = [M]^{-1}\left([A_1]\bar{q}_o - [K_o]\right)\{q\} + [M]^{-1}\left([A_2]\bar{q}_o - [C]\right)\{\dot{q}\} + [M]^{-1}\{w\}_{\bar{q}} - [M]^{-1}\begin{bmatrix} \ddots \delta_k \ddots \end{bmatrix}\left([K_o]\begin{bmatrix} \ddots W_k \ddots \end{bmatrix}\{q\}\right)$$

$$\{\ddot{q}\} = [M]^{-1}\left([A_1]\bar{q}_o - [K_o]\right)\{q\} + [M]^{-1}\left([A_2]\bar{q}_o - [C]\right)\{\dot{q}\} + [M]^{-1}\{w\}_{\bar{q}} - [M]^{-1}\begin{bmatrix} \ddots \delta_k \ddots \end{bmatrix}\{z\}_k$$

$$\{\ddot{q}\} = [M]^{-1}\left([A_1]\bar{q}_o - [K_o]\right)\{q\} + [M]^{-1}\left([A_2]\bar{q}_o - [C]\right)\{\dot{q}\} + [M]^{-1}\{w\}_{\bar{q}} - [M]^{-1}\{w\}_k$$

(3.13)

In Equation (3.13), the term $\{w\}_k$ is introduced to relate the perturbation-to-stiffness to nominal dynamics with a feedback approach and it is expressed as

$$\{w\}_k = \begin{bmatrix} \ddots \delta_k \ddots \end{bmatrix}\{z\}_k$$ (3.14)

The elements of $\{z\}_k$ are added to the system as additional outputs. $\{z\}_k$ is obtained by multiplying the position states with the weighting matrix and the nominal stiffness matrix as

$$\{z\}_k = [K_o]\begin{bmatrix} \ddots W_k \ddots \end{bmatrix}\{q\}$$ (3.15)

Thus, the equation of motion of the robust aeroelastic system with multiplicative uncertainty on stiffness becomes as

$$
\begin{Bmatrix} \{\dot{q}\} \\ \{\ddot{q}\} \\ \{z\}_{\bar{q}} \\ \{z\}_k \end{Bmatrix} = \begin{bmatrix} [0_{2x2}] & [I_{2x2}] & [0_{2x2}] & [0_{2x2}] \\ [M]^{-1}([A_1]\bar{q}_o - [K_o]) & [M]^{-1}([A_2]\bar{q}_o - [C]) & [M]^{-1} & -[M]^{-1} \\ [A_1] & [A_2] & [0_{2x2}] & [0_{2x2}] \\ [K_o][W_k] & [0_{2x2}] & [0_{2x2}] & [0_{2x2}] \end{bmatrix} \begin{Bmatrix} \{q\} \\ \{\dot{q}\} \\ \{w\}_{\bar{q}} \\ \{w\}_k \end{Bmatrix} \quad (3.16)
$$

3.3.2.2. Uncertainty in Damping

The uncertainty in damping is modeled by using a parametric additive uncertainty as follows

$$
[C] = [C_o] + \left[\ddots W_c \ddots \right]\left[\ddots \delta_c \ddots \right] \quad (3.17)
$$

where

$$
\left.\begin{aligned}
[C_o] &= \begin{bmatrix} c_{ho} & 0 \\ 0 & c_{\alpha o} \end{bmatrix} \\
\left[\ddots W_c \ddots \right] &= \begin{bmatrix} W_{ch} & 0 \\ 0 & W_{c\alpha} \end{bmatrix} \\
\left[\ddots \delta_c \ddots \right] &= \begin{bmatrix} \delta_{ch} & 0 \\ 0 & \delta_{c\alpha} \end{bmatrix}
\end{aligned}\right\} \quad (3.18)
$$

and

c_{ho} : Nominal plunge damping of typical section wing

$c_{\alpha o}$: Nominal pitch damping of typical section wing

W_{ch} : Weighting for uncertainty of plunge damping

$W_{c\alpha}$: Weighting for uncertainty of pitch damping

δ_{ch} : Norm bounded perturbation multiplier of plunge damping

$\delta_{c\alpha}$: Norm bounded perturbation multiplier of pitch damping

77

Inserting Equation (3.17) into Equation (3.13), and collecting $\begin{bmatrix} \ddots & \delta_c & \ddots \end{bmatrix}$ terms, Equation (3.19) is obtained

$$[M]\{\ddot{q}\} + \left([C_o] + \begin{bmatrix} \ddots W_c \ddots \end{bmatrix}\begin{bmatrix} \ddots \delta_c \ddots \end{bmatrix}\right)\{\dot{q}\} + [K_o]\{q\} = [A_1](\bar{q}_o)\{q\} + [A_2](\bar{q}_o)\{\dot{q}\} + \{w\}_{\bar{q}} - \{w\}_k$$

$$\{\ddot{q}\} = [M]^{-1}\left([A_1]\bar{q}_o - [K_o]\right)\{q\} + [M]^{-1}\left([A_2]\bar{q}_o - \left([C_o] + \begin{bmatrix} \ddots W_c \ddots \end{bmatrix}\begin{bmatrix} \ddots \delta_c \ddots \end{bmatrix}\right)\right)\{\dot{q}\}$$

$$+ [M]^{-1}\{w\}_{\bar{q}} - [M]^{-1}\{w\}_k$$

$$\{\ddot{q}\} = [M]^{-1}\left([A_1]\bar{q}_o - [K_o]\right)\{q\} + [M]^{-1}\left([A_2]\bar{q}_o - [C]\right)\{\dot{q}\}$$

$$+ [M]^{-1}\{w\}_{\bar{q}} - [M]^{-1}\{w\}_k - [M]^{-1}\begin{bmatrix} \ddots \delta_c \ddots \end{bmatrix}\left(\begin{bmatrix} \ddots W_c \ddots \end{bmatrix}\{\dot{q}\}\right)$$

$$\{\ddot{q}\} = [M]^{-1}\left([A_1]\bar{q}_o - [K_o]\right)\{q\} + [M]^{-1}\left([A_2]\bar{q}_o - [C]\right)\{\dot{q}\}$$

$$+ [M]^{-1}\{w\}_{\bar{q}} - [M]^{-1}\{w\}_k - [M]^{-1}\begin{bmatrix} \ddots \delta_c \ddots \end{bmatrix}\{z\}_c$$

$$\{\ddot{q}\} = [M]^{-1}\left([A_1]\bar{q}_o - [K_o]\right)\{q\} + [M]^{-1}\left([A_2]\bar{q}_o - [C]\right)\{\dot{q}\} + [M]^{-1}\{w\}_{\bar{q}} - [M]^{-1}\{w\}_k - [M]^{-1}\{w\}_c$$

$$(3.19)$$

In Equation (3.19), the term $\{w\}_c$ is introduced to relate the perturbation to damping to nominal dynamics with a feedback approach and it is expressed as

$$\{w\}_c = \begin{bmatrix} \ddots \delta_c \ddots \end{bmatrix}\{z\}_c \qquad (3.20)$$

The elements of $\{z\}_c$ are added to the system as additional outputs. $\{z\}_c$ vector is obtained by multiplying velocity states with a weighting matrix as

$$\{z\}_c = \begin{bmatrix} \ddots W_c \ddots \end{bmatrix}\{\dot{q}\} \qquad (3.21)$$

Thus the equation of motion of the robust aeroelastic system with additive uncertainty in damping and multiplicative uncertainty in stiffness becomes as given below

$$
\begin{Bmatrix} \{\dot{q}\} \\ \{\ddot{q}\} \\ \hline \{z\}_{\bar{q}} \\ \{z\}_k \\ \{z\}_c \end{Bmatrix} = \left[\begin{array}{cc|ccc} [0_{2x2}] & [I_{2x2}] & [0_{2x2}] & [0_{2x2}] & [0_{2x2}] \\ [M]^{-1}([A_1]\bar{q}_o - [K_o]) & [M]^{-1}([A_2]\bar{q}_o - [C_o]) & [M]^{-1} & -[M]^{-1} & -[M]^{-1} \\ \hline [A_1] & [A_2] & [0_{2x2}] & [0_{2x2}] & [0_{2x2}] \\ [K_o][W_k] & [0_{2x2}] & [0_{2x2}] & [0_{2x2}] & [0_{2x2}] \\ [0_{2x2}] & [W_c] & [0_{2x2}] & [0_{2x2}] & [0_{2x2}] \end{array} \right] \begin{Bmatrix} \{q\} \\ \{\dot{q}\} \\ \{w\}_{\bar{q}} \\ \{w\}_k \\ \{w\}_c \end{Bmatrix}
$$

$$(3.22)$$

3.3.2.3. Robust Flutter Margin

In the equations given in the previous subsection, uncertainties are modeled as a constant parametric uncertainty. It is also possible to model the uncertainties as frequency varying uncertainties. In that case, the [W] matrices become transfer function matrices. Linear fractional transformation system for robust stability analysis in the μ framework with parameterization around perturbation in dynamic pressure and structured uncertainty is given in Figure 7.
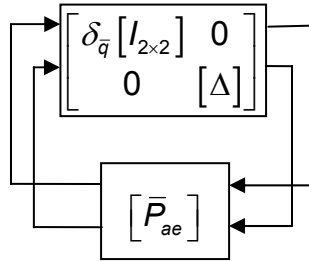
Figure 7. LFT system for robust flutter analysis

In Figure 7, $\delta_{\bar{q}}$ is the unit norm bounded uncertainty operator for dynamic pressure, $\left\| \delta_{\bar{q}} \right\|_{\infty} \leq 1$, [$\Delta$] is the unit norm bounded aeroelastic model uncertainty, $\left\| [\Delta] \right\|_{\infty} \leq 1$, and $\left[\bar{P}_{ae} \right]$ is the scaled plant,

$$\left[\bar{P}_{ae}\right] = \left[P_{ae}\right]\begin{bmatrix} \left[\ddot{W_{\bar{q}}}\right] & [0] \\ [0] & [I] \end{bmatrix}.$$ In the scaled plant, $\left[\ddot{W_{\bar{q}}}\right] = W_{\bar{q}}\left[I_{2x2}\right]$ is the weighting function that scales the perturbation of dynamic pressure from 1 Pa (or unit of dynamic pressure) to the desired search value. Thus the dynamic pressure becomes

$$\bar{q} = \bar{q}_0 + W_{\bar{q}}\delta_{\bar{q}} \tag{3.23}$$

For the ease of formulation, the uncertainty matrix in Figure 7 is defined as

$$\left[\mathbb{A}\right] = \begin{bmatrix} \delta_{\bar{q}}\left[I_{2\times2}\right] & 0 \\ 0 & [\Delta] \end{bmatrix} \tag{3.24}$$

The robustness of $\left[\bar{P}_{ae}\right]$ with respect to $\left[\mathbb{A}\right]$ can be determined via small gain theorem, as defined in the last paragraph of Section 3.3.1. The solution guaranties the stability for any value of uncertainty if $\left\|\left[\bar{P}_{ae}\right]\right\|_{\infty} < 1$. However this robustness condition is overconservative since it does not concern the structure of the uncertainty matrix. The structured singular value, μ, is the least conservative measure of robustness.

Given the complex, stable, linear, time invariant transfer function matrix $\left[\bar{P}_{ae}\right]$ defined for rational elements and associated norm bounded set of uncertainty operators $\left[\mathbb{A}\right]$, μ is defined as

$$\mu\left(\left[\bar{P}_{ae}\right]\right) = \frac{1}{\min_{[\Delta_i]\in[\mathbb{A}]}\left\{\bar{\sigma}\left([\Delta_i]\right) : \det\left([I] - \left[\bar{P}\right][\Delta_i]\right) = 0\right\}} \tag{3.25}$$

here $\left[\Delta_i\right]$ are diagonal elements or matrices of $\left[\Delta\right]$ and $\bar{\sigma}$ is the largest singular value.

Using the definitions above, the robust flutter stability is obtained at $\mu\left(\left[\bar{P}_{ae}\right]\right)=1$ for which the robust flutter pressure is $\bar{q}_{flutter}^{rob}=\bar{q}_0+W_{\bar{q}}$. Thus the least conservative robust flutter margin is

$$\Gamma_{rob}=W_{\bar{q}} \tag{3.26}$$

$\mu\left(\left[\bar{P}_{ae}\right]\right)$ can be related to familiar linear algebra quantities, when the set of Δ is at two extreme sets

    1) if $\left[\Delta\right]=\left\{\delta[I]:\delta\in\mathbb{C}\right\}$ then $\mu\left(\left[\bar{P}_{ae}\right]\right)=\rho\left(\left[\bar{P}_{ae}\right]\right)$, where ρ is spectral radius of $\bar{P}$.

    2) if $\left[\Delta\right]\in\mathbb{C}^{nxn}$ then $\mu\left(\left[\bar{P}_{ae}\right]\right)=\bar{\sigma}\left(\left[\bar{P}_{ae}\right]\right)$.

In general it can be shown that,

$$\rho\left(\left[\bar{P}_{ae}\right]\right)\le\mu\left(\left[\bar{P}_{ae}\right]\right)\le\bar{\sigma}\left(\left[\bar{P}_{ae}\right]\right) \tag{3.27}$$

However, these bounds are not sufficient to estimate a useful $\mu\left(\left[\bar{P}_{ae}\right]\right)$, because the gap between the spectral radius $\rho\left(\left[\bar{P}_{ae}\right]\right)$ and the largest singular value $\bar{\sigma}\left(\left[\bar{P}_{ae}\right]\right)$ can be arbitrarily large. But, the bounds can be refined by considering transformations on $\left[\bar{P}_{ae}\right]$ that do not affect $\mu\left(\left[\bar{P}_{ae}\right]\right)$, but do affect $\rho\left(\left[\bar{P}_{ae}\right]\right)$ and $\bar{\sigma}\left(\left[\bar{P}_{ae}\right]\right)$. This can be accomplished by defining two subsets of $\mathbb{C}^{nxn}$:

$$[Q] = \left\{ \left[\hat{Q} \right] \in [\mathcal{A}] : \left[\hat{Q} \right] \left[\hat{Q} \right]^* = \left[I_{n \times n} \right] \right\} \tag{3.28}$$

$$[D] = \left\{ \begin{array}{l} diag \left[\left[\hat{D}_1 \right], ..., \left[\hat{D}_s \right], d_1 \left[I_{m_1} \right], ..., d_{F-1} \left[I_{m_{F-1}} \right], \left[I_{m_F} \right] \right] : \\ \left[\hat{D}_i \right] \in \mathbb{C}^{r_i \times r_i}, \left[\hat{D}_i \right] = \left[\hat{D}_i \right]^* > 0, d_j \in \mathbb{R}, d_j > 0 \end{array} \right\} \tag{3.29}$$

Note that for any $[\Delta] \in [\mathcal{A}]$, $\left[\hat{Q} \right] \in [Q]$, and $\left[\hat{D} \right] \in [D]$,

$$\left. \begin{array}{ccc} \left[\hat{Q} \right]^* = [Q] & \left[\hat{Q} \right][\Delta] \in [\mathcal{A}] & [\Delta]\left[\hat{Q} \right] \in [\mathcal{A}] \\ \bar{\sigma}\left(\left[\hat{Q} \right][\Delta] \right) = \bar{\sigma}\left([\Delta]\left[\hat{Q} \right] \right) = \bar{\sigma}([\Delta]) \end{array} \right\} \tag{3.30}$$

$$\left[\hat{D} \right][\Delta] = [\Delta]\left[\hat{D} \right] \tag{3.31}$$

The theorem is; for all $\left[\hat{Q} \right] \in [Q]$, and $\left[\hat{D} \right] \in [D]$,

$$\mu_{\mathcal{A}}\left(\left[\bar{P}_{ae} \right]\left[\hat{Q} \right] \right) = \mu_{\mathcal{A}}\left(\left[\hat{Q} \right]\left[\bar{P}_{ae} \right] \right) = \mu_{\mathcal{A}}\left(\left[\bar{P}_{ae} \right] \right) = \mu_{\mathcal{A}}\left(\left[\hat{D} \right]\left[\bar{P}_{ae} \right]\left[\hat{D}^{-1} \right] \right) \tag{3.32}$$

Therefore the bounds can be tightened to

$$\max_{\left[\hat{Q} \right] \in [Q]} \rho\left(\left[\hat{Q} \right]\left[\bar{P}_{ae} \right] \right) \leq \mu_{\mathcal{A}}\left(\left[\bar{P}_{ae} \right] \right) \leq \inf_{\left[\hat{D} \right] \in [D]} \bar{\sigma}\left(\left[\hat{D} \right]\left[\bar{P}_{ae} \right]\left[\hat{D}^{-1} \right] \right) \tag{3.33}$$

A simple method to iteratively search the $\left[W_{\bar{q}} \right]$ for $\mu\left(\left[\bar{P}_{ae} \right] \right) = 1 \mp \varepsilon$, with accuracy ε, is given below [38].

1. construct the $\left[P_{ae} \right]$ matrix at dynamic pressure $\bar{q}_o$,

2. select an initial value for the operator $\delta_{\bar{q}}$ that is related to $\left[P_{ae} \right]$ as in Figure 7,

3.   select the dimensions of the unity norm bounded operator $[\Delta]$,

4.   define weighting $W_{\bar{q}1} > 1$ to scale $\bar{q}$ feedback,

5.   define scalar $\varepsilon > 0$ for accuracy,

6.   compute $\left[\bar{P}_{ae}\right] = \left[P_{ae}\right] \begin{bmatrix} \left[W_{\bar{q}} \right] & [0] \\ [0] & [I] \end{bmatrix}$,

7.   calculate $W_{\bar{q}1} = \dfrac{W_{\bar{q}1}}{\mu\left(\left[\bar{P}_{ae}\right]\right)}$,

8.   compute $\left[\bar{P}_{ae}\right] = \left[P_{ae}\right] \begin{bmatrix} \left[W_{\bar{q}} \right] & [0] \\ [0] & [I] \end{bmatrix}$,

9.   if the value of $\mu\left(\left[\bar{P}_{ae}\right]\right)$ is greater than $1+\varepsilon$ or less than $1-\varepsilon$ then go to step 7,

10.   the robust dynamic pressure of flutter is $\bar{q}_{rob} = \bar{q}_o + W_{\bar{q}1}$,

11.   the robust dynamic pressure of flutter margin is $\Gamma_{rob} = W_{\bar{q}1}$.

However, this method does not guarantee that the dynamic pressure of flutter is at the upper edge corresponding to high pressure. To ensure this, the following algorithm can be used [38].

1.   construct the $\left[P_{ae}\right]$ matrix at dynamic pressure $\bar{q}_o$,

2.   select an initial value for the operator $\delta_{\bar{q}}$ that is related to $\left[P_{ae}\right]$ as in Figure 7,

3.   select the dimensions of the unity norm bounded operator $[\Delta]$,

4.   select an initial value for the nominal dynamic pressure $\bar{q}_o$,

5.   Compute plant P at nominal dynamic pressure $\bar{q}_o$,

6.   Compute $\bar{q}_{rob}$ and associate $W_{\bar{q}1}$ from above algorithm,

7.   If the term $W_{\bar{q}1}$ is greater than $\bar{q}_o$, then compute ($\bar{q}_o = 1.1\, W_{\bar{q}1}$) and go to step 5, otherwise the calculated the robust dynamic pressure of flutter and the robust dynamic pressure of flutter margin from the above algorithm in last iteration are the guaranteed upper edge results.

Similar to the nomial flutter search case; these methods are sufficient for an aeroelastic system, and for the search of lower bound in aeroservoelastic systems the given methods are used with some small tailorings.

3.4. Determination of Flutter Flight Envelope

The flight envelope is the region in which an airplane or missile can fly without encountering any problems. Hence, the flutter flight envelope should be a flutter free region. In the airplane design, a safety margin is put between the instability limits and the limits of the flight envelope. According to FAA, this safety margin is defined as 20% of the design speed for the transportation airplane [58]. In military requirements/standarts of USA, the safety margins were set as 15% of the equivalent airspeed for military aircrafts [59] and missiles [60]. In MSC Aeroelasticity course notes [61], which is the course notes of a commercial aeroelasticy analysis program, this margin was also given as 15% of the equivalent airspeed. In this study, the flutter flight envelopes are calculated without using any safety margin.

Examining the aeroelastic equations derived in Section 2.5, it can be seen that the airspeed terms still exist in equations. Thus the perturbation to dynamic pressure does not affect all airspeed terms although it is a function of airspeed. Furthermore, the airspeed appears as a nonlinear term in these equations. This is the main reason behind

selecting the dynamic pressure as the perturbation term. However, due to the unperturbed airspeed terms in the aeroelastic equation, the perturbation to dynamic pressure actually only affects the air density, it can be seen from the equation of dynamic pressure defined as [3]

$$\bar{q} = \frac{1}{2}\rho U^2.$$

(3.34)

Hence the results of the procedures presented in the previous sections give the flutter margin in terms of air density, which may be termed as the margin of flutter air density. In incompressible flow, the equations are independent of Mach number. Hence the calculated air density of instability corresponds to an altitude. On the contrary, the equations are Mach number dependent in compressible flow. For this reason, the calculated air density of instability does not define a physical state unless the margin of flutter air density; i.e., the difference between the calculated density and the density at which the system is set up, is equal to zero. Hence the air density of instability does not directly correspond to an altitude. However, the margin of flutter air density is still a useful data and it is used to determine the flutter flight envelope in compressible flow.

3.4.1. Incompressible Flow

In incompressible flow, the Theodorsen function used to model the aerodynamics is valid for all Mach numbers below 0.3. Consequently, the aeroelastic model and the μ-method flutter search equations are valid for every Mach number below 0.3. Hence, a corresponding altitude can be calculated without any iteration. Therefore, a straightforward method to determine the flutter flight envelope is to calculate the air density of instability for a number of airspeeds. As a result, the flutter flight envelope can be given as an altitude versus airspeed plot. In these plots the

resultant altitudes may be below sea level, but it is recommended to keep these values to catch the behavior of the system.

In the second search procedure, the airspeed of instability is calculated for a given dynamic pressure. A simple method to iteratively search the airspeed of instability, with accuracy ε, is given below.

1. construct the $[P_{ae}]$ matrix at initial air density ρ_0 and initial airspeed U_0,

2. define a scalar $\varepsilon > 0$ for accuracy,

3. define a scalar j for indexing and set $j = 1$,

4. calculate the dynamic pressure of instability $\bar{q}_j$ using μ-method,

5. calculate the corresponding airspeed, $U_j = \sqrt{\dfrac{2\bar{q}_j}{\rho_0}}$. Note that this airspeed is not the actual airspeed of instability due to the unperturbed airspeed terms in the equations of μ-method,

6. calculate the percentage of the change of airspeed, $\%\delta U_j = \dfrac{U_j - U_{j-1}}{U_{j-1}}$ (Alternatively the change of airspeed $\delta U_j = U_j - U_{j-1}$ can be used),

7. setup plant $[P_{ae}]$ at initial air density ρ_0 and airspeed U_j,

8. increase the index j by one,

9. if $\%\delta U_{j-1} > \varepsilon$ go to step 4,

10. the flutter speed is $U_{flutter} = U_{j-1}$

This procedure is actually devised to determine the airspeed of instability at a specific altitude, but repeating the sequence for different initial air densities will produce a flutter flight envelope.

3.4.2. Flight Envelope Search in Compressible Flow

In contrast to incompressible flow, the aerodynamic equations of compressible flow are valid for a corresponding Mach number. The reason is the indicial functions that are separately defined for each Mach number. In the atmosphere model, a physical state can be obtained by setting two parameters, for fixed temperature. Hence, any two of three quantities, namely, Mach number, air density, and airspeed define the remaining third one. This physical state is named as a *match point*. In μ-method, the plant $[P_{ae}]$ is established for a match point. The result of μ-method gives an air density of instability. Since one of the three parameters is altered, a second parameter should be changed to make this new point a match point. However, Mach number is fixed due to indicial functions of compressible flow, and the airspeed is fixed due to undisturbed airspeeds in μ-method equations. Hence the new point is an unphysical point. But the instability margin of air density is still a valuable data. In addition to defining the stability of the initial point, it can be used to determine the actual flutter margin. A simple method to iteratively search the match point of instability, with accuracy ε, is given below.

1.   construct the $[P_{ae}]$ matrix at initial air density ρ_0, initial airspeed U_0 and initial Mach number,

2.   define a scalar ε >0 for accuracy,

3.   define a scalar *j* for indexing and set *j* = 1,

4.   calculate the air density of instability ρ_j using μ-method,

5.   calculate the corresponding airspeed U_j of the new match point, by using the initial Mach number and the calculated air density of instability ρ_j,

6.   calculate the percentage of the change of airspeed,

$$\%\delta U_j = \frac{U_j - U_{j-1}}{U_{j-1}},$$

7.   setup plant $\left[P_{ae} \right]$ for the new match point,

8.   increase the index j by one,

9.   if $\%\delta U_{j-1} > \varepsilon$ go to step 4,

10.   the parameters of match point of instability are; airspeed $U_{flut} = U_{j-1}$, air density $\rho_{flut} = \rho_{j-1}$, and initial Mach number.

This method works if the system is stable at the obtained match point in iteration, otherwise it fails. In order to solve the problem, a check procedure is introduced after the 5th step of the method given above as

1.   if the system is unstable at the jth match point;
   a. decrease the index j by one,
   b. calculate $U_j = n * \%\delta U_j + U_{j-1}$, where n is the relaxation constant.
   c. calculate corresponding air density, ρ_j, by using the initial Mach number and U_j,
   d. goto step 6.

The results of the analysis can be given as an altitude versus airspeed plot. The match points for each Mach number construct a line in this figure. On each line, the match point of flutter can be given.

3.5. Postscript on Chapter 3

In this Chapter, the analysis tools for calculating instability points are given. Among the methods presented, the μ–method is selected as the

main analysis tool in this thesis, since it has the advantage of modifying the flight conditions without reconstructing the main system matrix. This advantage decreases the calculation effort, furthermore the equations become suitable for time domain analysis. The only drawback of this method is that the airspeed is kept constant in the analysis. This drawback is overcome with additional search algorithms. In order to cross-check the results of the μ-method, p-method is selected as an alternative method.

CHAPTER 4

CONTROLLER SYNTHESIS FOR FLUTTER SUPPRESSION

4.1. Preview

This chapter deals with controller synthesis methods for flutter suppression. An aeroservoelastic model of the fin is constructed by using the aeroelastic model defined in Chapter 2. An implementation of μ flutter search method on the aeroservoelastic model is performed for both nominal and robust flutter analyses. A novel controller synthesis method for flutter suppression is proposed. The mathematical model of the aeroservoelastic system is adapted and the disturbance, uncertainty, and performance weightings are defined for a robust controller synthesis. The methodology used for flutter suppression is presented. An existing alternative flutter suppression approach is applied to the aeroservoelastic model that is developed for the robust controller synthesis in this Chapter.

4.2. Aeroservoelastic Model

The block diagram of the basic aeroservoelastic system is given in Figure 8. Note that the input and output signals are not weighted at this stage for simplicity. The state space equations of the aeroelastic part are partially defined in Section 2.5. The aeroelastic fin defined in Section 2.5 is a rigid thin airfoil, which is connected to the ground via torsional and

translational springs. While constructing the aeroservoelastic plant, the torsional spring of the aeroelastic fin is disconnected from the ground and connected to the output shaft of the transmission as depicted in Figure 9.
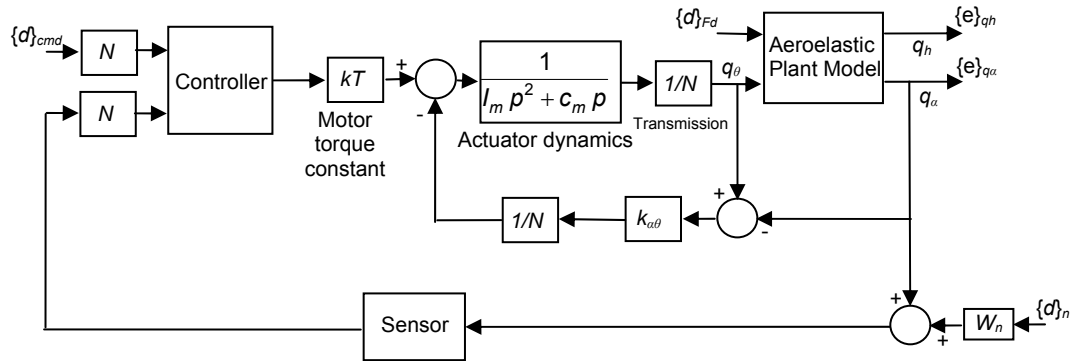
Figure 8. Block diagram of the aeroservoelastic system
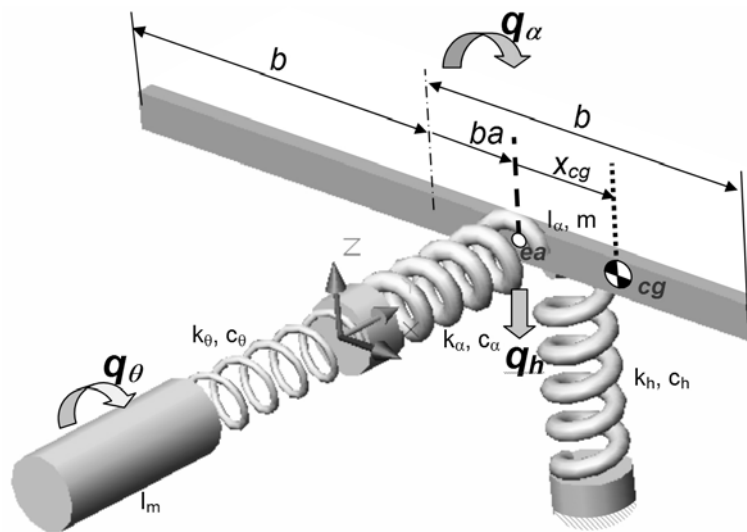
Figure 9. Modified typical section wing for the aeroservoelastic system

Hence in Figure 8, the shaft angle q_θ, which is the output of the transmission block, is fed to the aeroelastic plant model block as an input. Due to this modification of the aeroelastic plant, the state space equation of the aeroelastic plant model is also modified. States of the aeroelastic

plant are not affected from this modification. Thus the system matrices $[A_{AE}]$ derived in Section 2.5 are directly used in this Chapter. The modification is conducted to the input of the aeroelastic system. Hence, in order to interconnect the aeroelastic plant with the rest of the aeroservoelastic plant, the input matrix $[B_{AE}]$ and input terms $\{v\}$ are modified as given in Equations (4.1) and (4.2), respectively.

$$[B_{AE}] = \begin{bmatrix} [0_{2x2}] & [0_{2x2}] \\ [M]^{-1} & [M]^{-1} \begin{Bmatrix} 0 \\ k_\alpha \end{Bmatrix} \end{bmatrix} \tag{4.1}$$

$$\{v\} = \begin{Bmatrix} \{Q\}_{ext} \\ q_\theta \end{Bmatrix} \tag{4.2}$$

According to the interconnection requirements, the output equation is defined as given in Equations (4.3) through (4.5).

$$\{e\} = [C_{AE}]\{\xi\} + [D_{AE}]\{v\} \tag{4.3}$$

$$[C_{AE}] = \begin{bmatrix} [I_{2x2}] & [0_{2x2}] \end{bmatrix} \tag{4.4}$$

$$[D_{AE}] = \begin{bmatrix} [0_{2x2}] & [0_{2x2}] \end{bmatrix} \tag{4.5}$$

In previous paragraphs, the modification of the aeroelastic plant is presented on the equations of the steady incompressible subsonic flow. Similar modifications can be easily introduced to the equations of other flow regimes. Once the blocks in Figure 8 are defined, the system transfer

matrix $[P]$ of the aeroservoelastic system without any controller, can be constructed in state space as

$$[P] = \begin{bmatrix} [A_{ASE'}] & [B_{ASE'}] \\ [C_{ASE'}] & [D_{ASE'}] \end{bmatrix} \tag{4.6}$$

where $[P]$ can be obtained by using *sysic* command of MATLAB® [62]. The block diagram of aeroservoelastic system in linear fractional transformation (LFT) form is given in Figure 10.
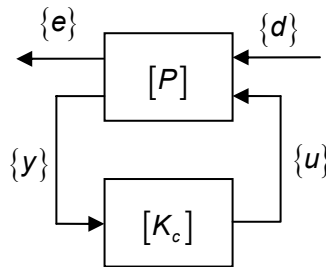
Figure 10. LFT model of the aeroservoelastic system

In Figure 10, the variable $\{d\}$ is the disturbance input vector, $\{e\}$ is the error/performance output vector, $\{u\}$ is the controller command vector, and $\{y\}$ is the observed output vector of the plant.

For a nominal flutter analysis, the inputs and outputs of the aeroservoelastic system are configured as given in Figure 11. The equations of the aeroelastic part are obtained as in Equation (4.7) by modifying Equation (3.8) according to the input and output requirements. In Figure 12, a general LFT model of the aeroservoelastic system for flutter analysis is given, where $[P]$ is the system transfer function matrix of the aeroservoelastic system without any controller.
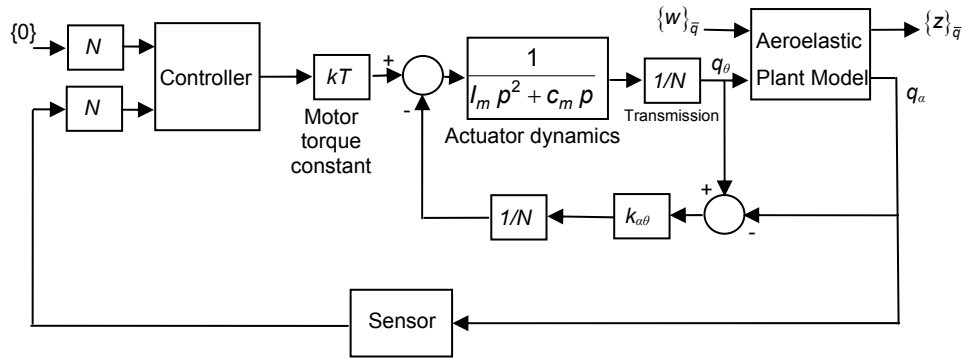
Figure 11. Block diagram of the aeroservoelastic system for nominal flutter analysis

$$\begin{Bmatrix} \{\dot{q}\} \\ \{\ddot{q}\} \\ \{z\}_{\bar{q}} \\ q_{\alpha} \end{Bmatrix} = \begin{bmatrix} [0_{2x2}] & [I_{2x2}] & \vdots & [0_{2x2}] & \{0_{2x1}\} \\ [M]^{-1}([A_1]\bar{q}_o - [K]) & [M]^{-1}([A_2]\bar{q}_o - [C]) & \vdots & [M]^{-1} & [M]^{-1}\begin{Bmatrix} 0 \\ k_{\alpha} \end{Bmatrix} \\ \hdashline [A_1] & [A_2] & \vdots & [0_{2x2}] & \{0_{2x1}\} \\ \{0 \ \ 1\} & \{0_{1x2}\} & \vdots & \{0_{1x2}\} & 0 \end{bmatrix} \begin{Bmatrix} \{q\} \\ \{\dot{q}\} \\ \{w\}_{\bar{q}} \\ q_{\theta} \end{Bmatrix}$$

(4.7)
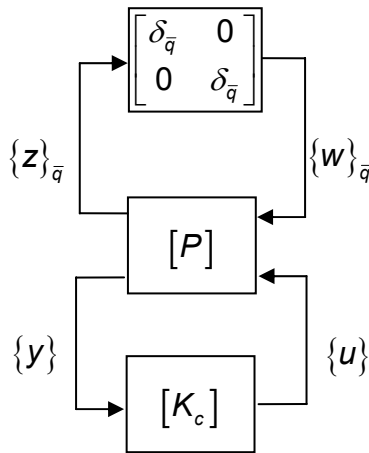
Figure 12. General LFT model of aeroservoelastic system for nominal flutter analysis

94

If a lower LFT is applied on the plant $[P]$ and the controller $[K_c]$ the transfer function matrix of the aeroservoelastic plant $[N]$ is obtained as

$$[N] = F_l([P],[K_c]) = \left[[P_{11}] + [P_{12}][K_c]([I] - [P_{22}][K_c])^{-1}[P_{21}]\right] \quad (4.8)$$

Hence, the general LFT model becomes as given in Figure 13. This form is same as the nominal μ-method flutter analysis form given in Figure 6. Thus, the methods given in Section 3.3 are applicable to this model.
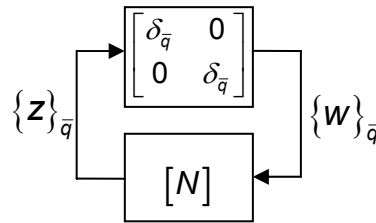
Figure 13. LFT model of aeroservoelastic system for nominal flutter analysis

The robust flutter analysis searches for the stability limits of a system with uncertainties. The uncertainty included in this model is the uncertainty of the sensor. For the robust flutter analysis, the inputs and outputs of the aeroservoelastic system are configured as given in Figure 14. As it can be seen from the figure, weightings of the sensor are introduced to the input and output channels of the Aeroservoelastic plant, which is different than the nominal flutter search model given in Figure 11. However, the input and output channels of the dynamic pressure disturbance are not weighted for the compatibility with the flutter analysis method. The equation of the aeroelastic plant given in Equation (4.7) is used in the robust flutter analysis, since no uncertainty is introduced to the aeroelastic plant.
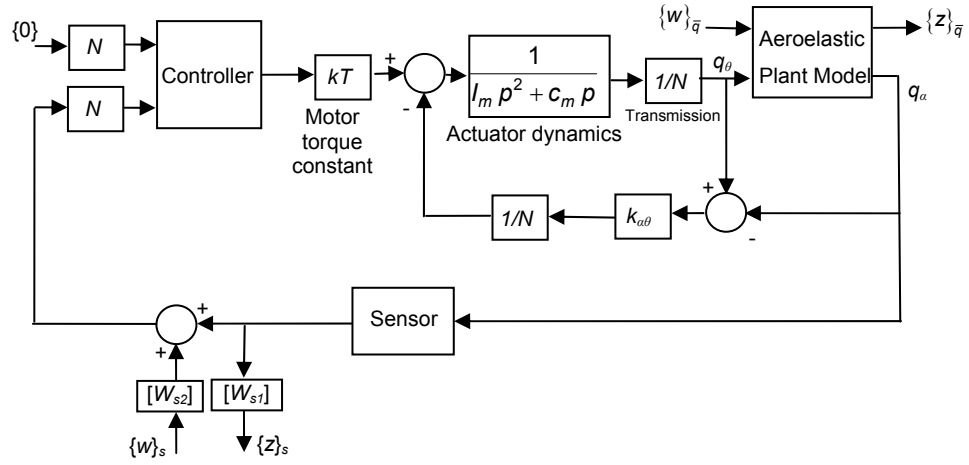
Figure 14. Block diagram of aeroservoelastic system for robust flutter analysis

The sensor uncertainty is actually introduced to decrease control commands at higher frequencies. An output multiplicative uncertainty is used for the sensor uncertainty. $[W_{s1}]$ and $[W_{s2}]$ are the input and output weightings respectively. In the robust analysis and μ controller synthesis these two blocks are coupled and analyzed as an output multiplicative uncertainty. However in H_2 and H_∞ controller syntheses this coupling information cannot be used, but these weightings are not omitted.

The block $[W_{s1}]$ is the normalization weighting function of measured pitch angle, that normalizes the sensor output to one. This function is taken as a constant, as given in Equation (4.9), where g_{s1} is the inverse of the maximum value of the expected/permitted pitch angle measurement.

$$W_{s1} = g_{s1} \qquad (4.9)$$

The block $[W_{s2}]$ is the weighting function for the uncertainty of the measured pitch angle. This function scales the unit disturbance signal into the expected value of uncertainty. With this function it is aimed to decrease the control efforts at high frequencies. At low frequencies the uncertainty is taken equal to noise level at measurement, g_{noise}, and a highpass type function is used as

$$W_{s2} = g_{s2} \, \kappa_{s2} \, \frac{p + \omega_{s2}}{p + \kappa_{s2}\omega_{s2}} \tag{4.10}$$

where

g_{s2} : g_{noise},

ω_{s2} : first corner frequency,

w_{s2_H} : maximum sensor noise at high frequencies,

W_{s2_L} : maximum sensor noise at low frequencies,

κ_{s2} : scaling factor, $\kappa_{s2} = \left| \dfrac{w_{s2_H}}{w_{s2_L}} \right| > 1$

In the robust flutter analysis, the system transfer function matrix $[P]$ of the aeroservoelastic system without any controller includes the uncertainty weightings. Through the similar steps given in the nominal flutter paragraphs of this Section, the LFT model of the aeroservoelastic system for a robust flutter analysis can be obtained as given in Figure 15, which is similar to Figure 7. Here, the block $[\bar{N}]$ is the scaled form of $[N]$, which is the transfer function matrix of the aeroservoelastic plant. The scaling is performed for the flutter analysis as described in Section 3.3.2.3. Once the aeroservoelastic plant is put in the LFT form given in Figure 15, the μ-method given in Section 3.3.2.3 can be applied to this problem.
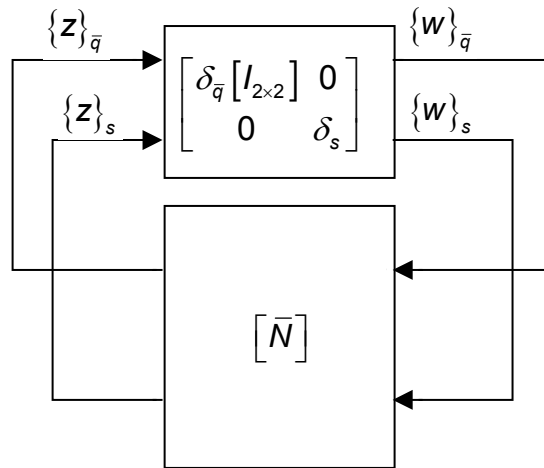
Figure 15. LFT model of aeroservoelastic system for robust flutter analysis

4.3. Flutter Suppression Controller Synthesis by Using Uncertainty on Dynamic Pressure (q-Method)

Flutter is an aeroelastic instability which occurs when the flow keeps transferring energy to the structure exposed to the flow. Flutter analysis methods given in Chapter 3, search for the aerodynamic parameters at which this instability occurs. The aim of flutter suppression is to enlarge the flight flutter margin. However, the aeroservoelastic system that is used in this study is physically a Control Actuation System, thus there are also performance requirements on the aeroservoelastic system such as bandwidth, steady state error, and overshoot. Thus, any synthesized controller should satisfy the performance requirements as well as yielding a flutter-free system.

In a robust controller synthesis and analysis problem, the weightings play a central role. All performance requirements, limitations, disturbances, and uncertainties are described by these weightings. Thus the result of the analysis or the controller synthesis depends on these weightings. The placement of the weighting blocks in the corresponding

block diagram, the types of the weighting functions, and their numerical values are very important.

In the following paragraphs these weightings are described. It is a fact that, due to the procedure of the robust controller synthesis, the orders of controllers synthesized are of the same as the order of the plant $[P]$ for H_2 or H_∞ controllers and greater than the order of the plant $[P]$ for a μ controller. The important point here is that the plant $[P]$ includes the weightings. Hence, each additional order of weighting increases the order of the controller, which is not desirable. On the other hand, constant weightings lead to conservative controllers, or sometimes a satisfactory controller may not even be obtained. The interconnection structure of the aeroservoelastic plant except the controller, $[P]$, is given in Figure 16.
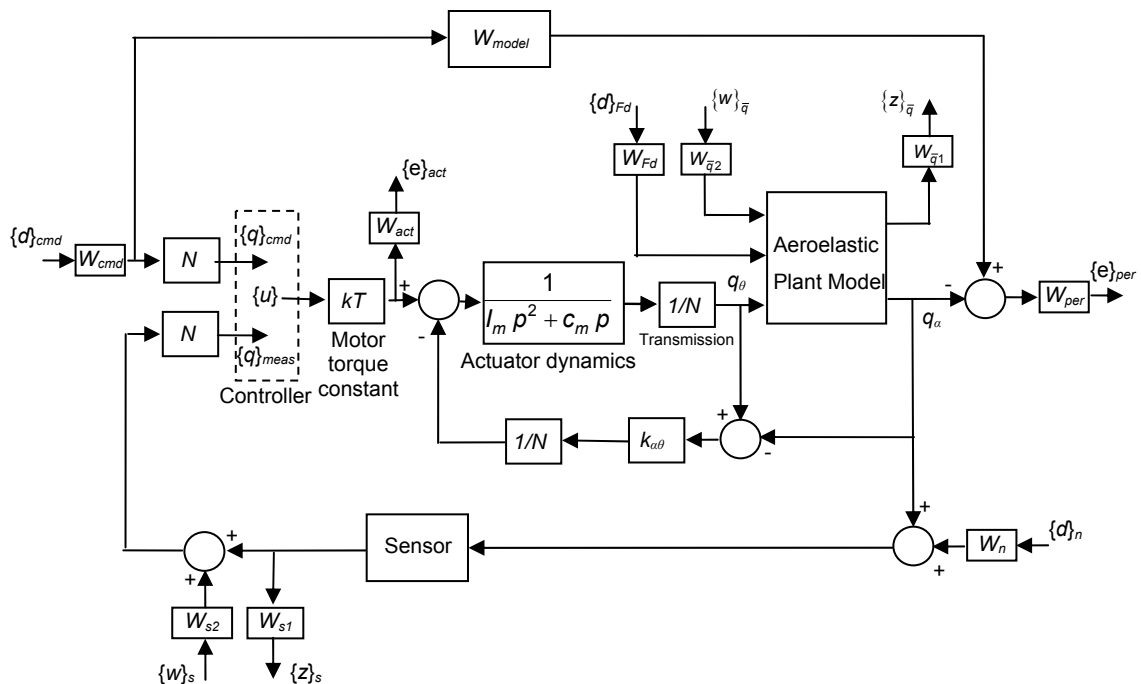
Figure 16. Interconnection structure of aeroservoelastic plant for g-method

The block $[W_{model}]$ defines the required reference CAS model. The performance of the main system is compared with the output of this block. It is defined as a second order system with a natural frequency of ω_{nref} and damping ratio of ζ_{ref} as

$$W_{model} = \frac{\omega_{nref}^2}{p^2 + 2\zeta_{ref}\,\omega_{nref}\,p + \omega_{nref}^2} \qquad (4.11)$$

The block $[W_{cmd}]$ defines the expected input commands. It is used to convert the unit disturbance input $\{d\}_{cmd}$ into the physical value of expected commands in radians. This weighting function is defined as a lowpass type as given in Equation (4.12), in which the command is expected to be high at low frequencies and low at high frequencies.

$$W_{cmd} = g_{cmd}\,\kappa_{cmd}\,\frac{p + {\omega_{cmd}}/{\kappa_{cmd}}}{p + \omega_{cmd}} \qquad (4.12)$$

where

g_{cmd} : magnitude of the expected command at low frequencies,

ω_{cmd} : first corner frequency,

w_{cH} : maximum expected command at high frequencies,

w_{cL} : maximum expected command at low frequencies,

κ_{cmd} : scaling factor, $\kappa_{cmd} = \left| \dfrac{w_{cH}}{w_{cL}} \right| < 1$

The block $[W_n]$ is the weighting function of sensor noise. This weighting function converts the unit disturbance input $\{d\}_n$ into sensor

noise. The sensor noise is taken as a constant error as given in Equation (4.13), with the magnitude of the smallest increment of the measurement, g_{noise} .

$$W_n = g_{noise} \tag{4.13}$$

The block $[W_{Fd}]$ is used to minimize the steady state error. Furthermore, it is also used to define the aerodynamic disturbance forces, which include the unmodeled aerodynamics. This weighting function scales the unit disturbance signal $\{d\}_F$ into the actual aerodynamic disturbance forces that are expected to exist. A lowpass filter type weighting function is used for aerodynamic disturbance as

$$W_{Fd} = g_{Fd} \, \kappa_{Fd} \, \frac{p + {\omega_{Fd}}/{\kappa_{Fd}}}{p + \omega_{Fd}} \tag{4.14}$$

where

g_{Fd} : magnitude of the expected aerodynamic disturbance at low frequencies,

ω_{Fd} : first corner frequency,

w_{FdH} : maximum expected disturbance at high frequencies,

w_{FdL} : maximum expected disturbance at low frequencies,

κ_{Fd} : scaling factor, $\kappa_{Fd} = \left| \dfrac{w_{FdH}}{w_{FdL}} \right| < 1$

The block $[W_{act}]$ is used to define the actuator limits. This block normalizes the torque output of the motor torque constant block into unit output $\{e\}_{act}$. Hence, it acts as a penalty function, and it is proportional to

the inverse of the actuator limits. On the other hand, there exists only a "motor torque constant" block between the block $[W_{act}]$ and the controller output. Hence, this weighting function also limits the controller output. Due to the characteristics of the actuators, a highpass type function is used for the normalization function $[W_{act}]$ as

$$W_{act} = g_{act} \, \kappa_{act} \, \frac{p + \omega_{act}}{p + \kappa_{act} \omega_{act}} \tag{4.15}$$

where

g_{act} : inverse of motor peak torque T_p limit at low frequencies,

ω_{act} : first corner frequency,

w_{aH} : T_p limit at high frequencies,

w_{aL} : T_p limit at low frequencies,

κ_{act} : scaling factor, $\kappa_{act} = \left| \dfrac{w_{aH}}{w_{aL}} \right| > 1$

The block $[W_{per}]$ is used to penalize the tracking error of the system. This function scales the tracking error of pitch motion to one. In general, it is required from the aeroservoelastic system to track better in low frequencies and the system is permitted to be worse at high frequencies. Due to the inverting characteristic of the normalization blocks, this block is modeled with a lowpass type function as

$$W_{per} = g_{per} \, \kappa_{per} \, \frac{p + \omega_{per}/\kappa_{per}}{p + \omega_{per}} \tag{4.16}$$

where

g_{per} :   inverse of magnitude of permitted error in low frequencies,

ω_{per} :   first corner frequency,

w_{pH} :   maximum permitted error at high frequency,

w_{pL} :   maximum permitted error at low frequency,

κ_{per} :   scaling factor, $\kappa_{per} = \left| \dfrac{w_{pH}}{w_{pL}} \right| < 1$

The important point in a robust controller synthesis for flutter supression is how to describe the flutter to the robust controller synthesis problem. As written in the first paragraph of this Section, the change of aerodynamics triggers the phenomenon. Hence, introducing the variation of aerodynamics into the robust controller synthesis problem may be a solution. For this purpose, the μ-method flutter analysis given in Section 3.3 is taken as a model. The dynamic pressure (actually the air density) is taken as the changing aerodynamic parameter. μ-method searches for the maximum perturbation for which the system is still stable. The synthesis procedure differs at this stage. In flutter suppression controller synthesis by using uncertainty on dynamic pressure, the minimum perturbation requirement that the system is required to be stable is defined in the problem. This is performed by introducing weightings $\left[W_{\bar{q}1} \right]$ and $\left[W_{\bar{q}2} \right]$ on the disturbance to dynamic pressure channels $\{z\}_{\bar{q}}$ and $\{w\}_{\bar{q}}$ respectively. This method is named as *q-Method* in this study.

The block $\left[W_{\bar{q}1} \right]$ is the normalization function that scales both channels of the output $\{z\}_{\bar{q}}$ to unity. This function is taken as a constant, as given in Equation (4.17), where $g_{\bar{q}1}$ is the inverse of the maximum of

the expected $\{z\}_{\bar{q}}$ value for each channel. The units of $\{z\}_{\bar{q}}$ is N/Pa for plunge channel and N.m/Pa for pitch channel.

$$W_{\bar{q}1} = g_{\bar{q}1} \qquad (4.17)$$

The block $\left[W_{\bar{q}2} \right]$ is the weighting function that defines the required change of aerodynamics for which the aeroservoelastic system should be robust. The units of the output of the $\left[W_{\bar{q}2} \right]$ block is Newton for plunge motion and Newton-meters for pitch motion. The block $\left[W_{\bar{q}2} \right]$ is obtained by multiplying the inverse of $\left[W_{\bar{q}1} \right]$ with the expected dynamic pressure change. Due to the physics of the problem, the dynamic pressure change is effective up to a frequency level. Hence, the weighting function $\left[W_{\bar{q}2} \right]$ can be modeled with a lowpass type function as

$$W_{\bar{q}2} = g_{\bar{q}2} \, \kappa_{\bar{q}2} \, \frac{p + {}^{\omega_{\bar{q}2}} \big/ {}_{\kappa_{\bar{q}2}}}{p + \omega_{\bar{q}2}} \qquad (4.18)$$

where

$g_{\bar{q}2}$: magnitude of the required dynamic pressure change at low frequencies divided by the $g_{\bar{q}1}$ term,

$\omega_{\bar{q}2}$: first corner frequency,

$w_{\bar{q}2_H}$: maximum effect of dynamic pressure at high frequencies,

$w_{\bar{q}2_L}$: maximum effect of dynamic pressure at low frequencies,

$\kappa_{\bar{q}2}$: scaling factor, $\kappa_{\bar{q}2} = \left| \dfrac{w_{\bar{q}2_L}}{w_{\bar{q}2_H}} \right| < 1$

Note that this weighting is similar to $\left[W_{Fd}\right]$, however their effects are separated with the selected corner frequencies, in which $\left[W_{\bar{q}2}\right]$ have higher gains at higher frequencies.

The LFT model of the aeroservoelastic system for the controller synthesis is given in Figure 17. The block $\left[P\right]$ has three uncertainty input/outputs, four disturbance inputs, two performance outputs, two signal outputs to controller, and one signal input from controller. The input/output signals and their meanings are given in Table 6.
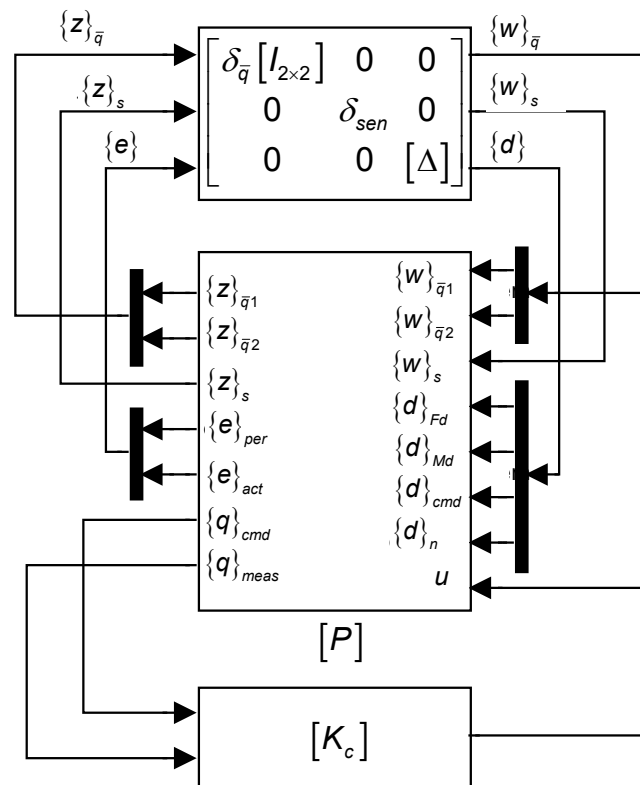
Figure 17. Generalized LFT view of aeroservoelastic plant for controller synthesis

For the controller synthesis, the Robust Control toolbox and μ-Analysis and Synthesis toolbox of MATLAB® is used. The synthesis procedures are briefly given in Appendix A.

Table 6. Input/output signals of plant

Signal	Meaning
$\{w\}_{\bar{q}1}$	Weighted uncertainty input for plunge motion
$\{w\}_{\bar{q}2}$	Weighted uncertainty input for pitch motion
$\{w\}_{s}$	Weighted uncertainty input for measurement
$\{d\}_{Fd}$	Weighted aerodynamic disturbance force
$\{d\}_{Md}$	Weighted aerodynamic disturbance moment
$\{d\}_{n}$	Weighted sensor noise
$\{d\}_{cmd}$	Weighted input command
u	Controller command
$\{z\}_{\bar{q}1}$	Normalized uncertainty output for plunge motion
$\{z\}_{\bar{q}2}$	Normalized uncertainty output for pitch motion
$\{z\}_{s}$	Normalized uncertainty output for measurement
$\{e\}_{per}$	Normalized tracking error of pitch motion
$\{e\}_{act}$	Normalized output torque of actuator
$\{q\}_{cmd}$	Input command sent to controller
$\{q\}_{meas}$	Measured value of pitch position

4.4. Flutter Suppression Controller Synthesis by Using Uncertainty on Damping (g-Method)

In Section 4.3, it is mentioned that the aerodynamic changes trigger the flutter, hence the flutter suppression mechanism is based on the source of the flutter. On the other side, if the mechanism of flutter is analyzed, it can be seen that the damping becomes zero in flutter speed and becomes negative if the speed is increased. Hence a second method may be devised by defining this damping change to the robust controller synthesis problem. This method is used by Vipperman J.S. [26] which was

106

originally applied to an airplane wing model. In his study, Vipperman J.S. introduced an uncertainty to the real part of the eigenvalue corresponding to the plunge motion of the wing. In this study the uncertainty is defined on the damping value and the related robust controller synthesis method is named as *g-method*.

In order to develope this second method, a damping uncertainty is defined in the aeroelastic plant. Hence, a procedure similar to the one defined in Section 3.3.2.2 is used. However, in contrast to the procedure given, the weighting term $[W_c]$ of the damping is taken outside the aeroelastic plant equation. This modification enables the application of frequency dependent weighting functions. The terms related to the uncertainty of the dynamic pressure are taken out from the aeroelastic plant equation. Thus, the equation of the aeroelastic plant is obtained as

$$
\left\{ \begin{matrix} \{\dot{q}\} \\ \{\ddot{q}\} \\ \{z\}_c \\ q_\alpha \end{matrix} \right\} = \left[\begin{array}{cc:ccc} [0_{2x2}] & [I_{2x2}] & [0_{2x2}] & [0_{2x2}] & \{0_{2x1}\} \\ [M]^{-1}([A_1]\bar{q}-[K]) & [M]^{-1}([A_2]\bar{q}-[C_0]) & -[M]^{-1} & [M]^{-1} & [M]^{-1}\begin{Bmatrix} 0 \\ k_\alpha \end{Bmatrix} \\ \hdashline [0_{2x2}] & [I_{2x2}] & [0_{2x2}] & [0_{2x2}] & \{0_{2x1}\} \\ \{0 \quad 1\} & \{0_{1x2}\} & \{0_{1x2}\} & \{0_{1x2}\} & 0 \end{array} \right] \left\{ \begin{matrix} \{q\} \\ \{\dot{q}\} \\ \{w\}_c \\ \{d\}_F \\ q_\theta \end{matrix} \right\}
$$

(4.19)

The additional channels $\{z\}_c$ and $\{w\}_c$ are weighted using the weightings $[W_{c1}]$ and $[W_{c2}]$, respectively.

The block $[W_{c1}]$ is the normalization function that scales both channels of the output $\{z\}_c$ to unity. This function is taken as a constant, as given in Equation (4.20), where g_{c1} is the inverse of the maximum of the expected $\{z\}_c$ value. It can be seen from Equation (4.19) that $\{z\}_c$ is

equal to the velocity state vector $\{\dot{q}\}$, hence the units of $\{z\}_c$ are m/s for plunge channel and rad/s for pitch channel.

$$W_{c1} = g_{c1} \tag{4.20}$$

The block $[W_{c2}]$ is the weighting function that defines the required change of damping for which the aeroservoelastic system should be robust. Similar to the $[W_{\bar{q}2}]$ block in q-method, the units of the output of the $[W_{c2}]$ block is Newton for the plunge motion and Newton-meter for the pitch motion. The block $[W_{c2}]$ is obtained by multiplying the inverse of $[W_{c1}]$ with the expected damping change. Due to the physics of flutter problem, the damping change is effective up to a frequency level. Hence the weighting function $[W_{c2}]$ can be modeled with a lowpass type function as

$$W_{c2} = g_{c2}\, \kappa_{c2}\, \frac{p + {\omega_{c2}}/{\kappa_{c2}}}{p + \omega_{c2}} \tag{4.21}$$

where

$\quad g_{c2}$: expected damping change at low frequencies divided by g_{c1} term,

$\quad \omega_{c2}$: first corner frequency,

$\quad w_{c2_H}$: maximum effect of damping at high frequencies,

$\quad w_{c2_L}$: maximum effect of damping at low frequencies,

$\quad \kappa_{c2}$: scaling factor, $\kappa_{c2} = \left| \dfrac{w_{c2_L}}{w_{c2_H}} \right| < 1$

The interconnection structure of the aeroservoelastic plant except the controller $[P]$ is given in Figure 18. The LFT model of the aeroservoelastic system for the controller synthesis is given in Figure 19. The block $[P]$ has three uncertainty input/outputs, four disturbance inputs, two performance outputs, two signal outputs to controller and one signal input from controller. The input/output signals and their meanings are given in Table 7.
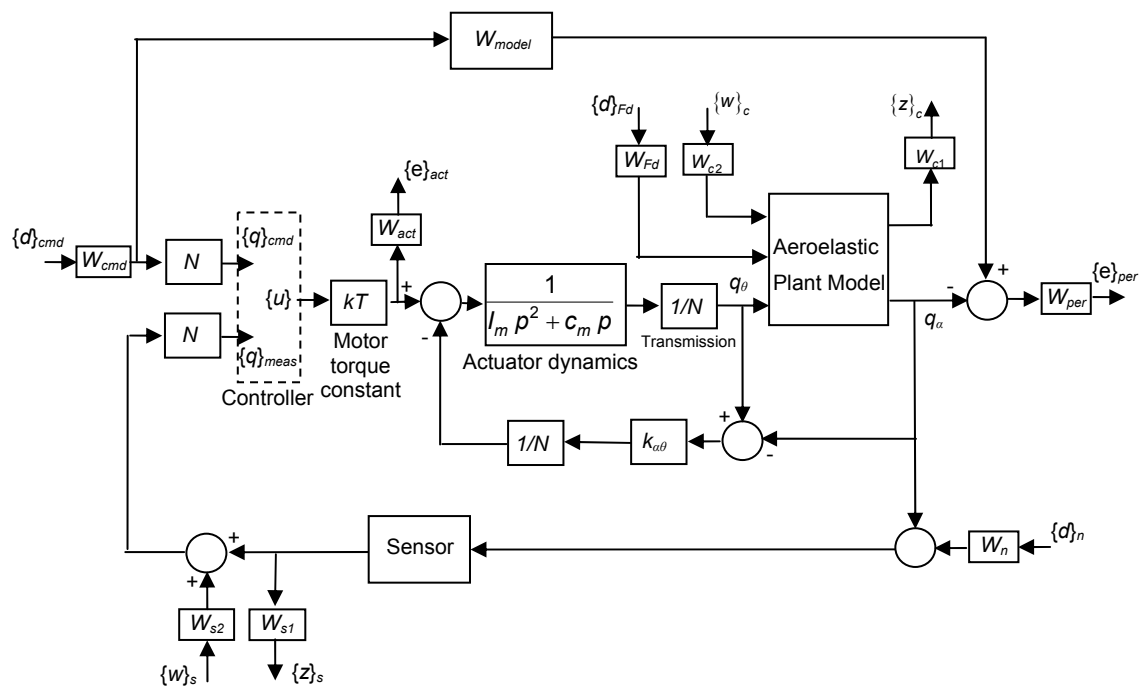

Figure 18. Interconnection structure of aeroservoelastic plant for g-method

$\begin{bmatrix} \delta_c [I_{2\times2}] & 0 & 0 \\ 0 & \delta_s & 0 \\ 0 & 0 & [\Delta] \end{bmatrix}$

$\{z\}_c$ $\{w\}_c$
$\{z\}_s$ $\{w\}_s$
$\{e\}$ $\{d\}$

$\{z\}_{c1}$ $\{w\}_{c1}$
$\{z\}_{c2}$ $\{w\}_{c2}$
$\{z\}_s$ $\{w\}_s$
$\{e\}_{per}$ $\{d\}_{Fd}$
$\{e\}_{act}$ $\{d\}_{Md}$
$\{q\}_{cmd}$ $\{d\}_{cmd}$
$\{q\}_{meas}$ $\{d\}_n$
u

$[P]$

$[K_c]$
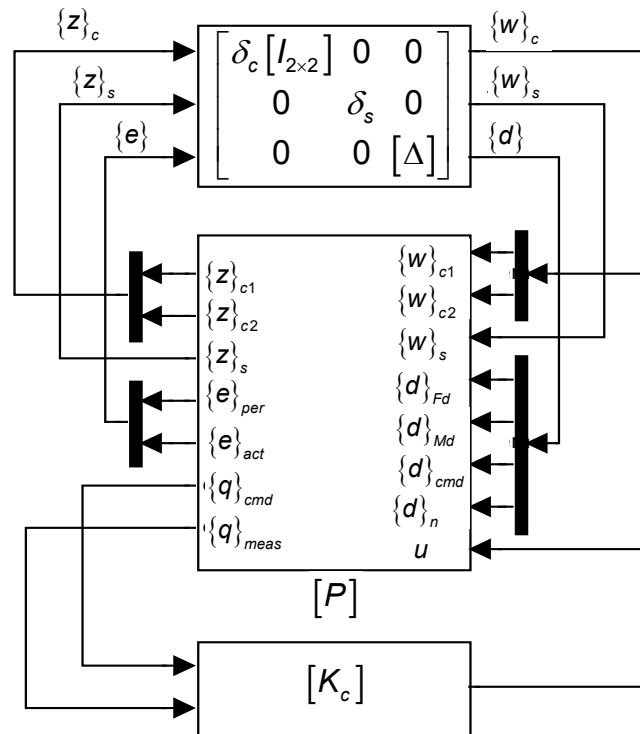
Figure 19. Generalized LFT view of aeroservoelastic plant for controller synthesis

Table 7. Input/output signals of plant

Signal	Meaning
$\{w\}_{c1}$	Weighted uncertainty input for damping in plunge motion
$\{w\}_{c2}$	Weighted uncertainty input for damping in pitch motion
$\{w\}_s$	Weighted uncertainty input for measurement
$\{d\}_{Fd}$	Weighted aerodynamic disturbance force
$\{d\}_{Md}$	Weighted aerodynamic disturbance moment
$\{d\}_n$	Weighted sensor noise
$\{d\}_{cmd}$	Weighted input command
u	Controller command
$\{z\}_{c1}$	Normalized uncertainty output for damping in plunge motion
$\{z\}_{c2}$	Normalized uncertainty output for damping in pitch motion
$\{z\}_s$	Normalized uncertainty output for measurement
$\{e\}_{per}$	Normalized tracking error of pitch motion
$\{e\}_{act}$	Normalized output torque of actuator
$\{q\}_{cmd}$	Input command sent to controller
$\{q\}_{meas}$	Measured value of pitch position

For the controller synthesis, the Robust Control toolbox and μ-Analysis and Synthesis toolbox of MATLAB® are used. The synthesis procedures are briefly given in Appendix A.

4.5. Postscript on Chapter 4

In this section the aeroservoelastic plant is derived for the μ-method analysis and the controller synthesis. The disturbance, uncertainty, and performance weightings that are used in this study for the robust controller synthesis are introduced. The purpose of these weightings, how they are modeled, and their placement in the interconnection structure are given. Two different controller synthesis methods for flutter suppression are presented. These are the g-method adapted from the study of Vipperman J.S. [26] and the proposed q-method. Flutter suppression methodologies of these two methods are given.

CHAPTER 5

MODELING

5.1. Preview

In this Chapter, the models that are used in the analyses of the aeroservoelastic system are presented. A time domain model is constructed in Simulink® with a linear aeroelastic model for the aeroservoelastic system. However, some uncertainties are introduced to this model in order to simulate a more realistic system. A second Simulink® model is constructed considering a backlash type of nonlinearity between the transmission and the fin in the aeroservoelastic system. A time domain mathematical modeling of the backlash is also presented. Alternatively, a frequency domain model for backlash is provided. For this purpose a quasi-linearization method is used. The backlash is modeled by using the sinusoidal input describing functions. A solution method is also provided for this frequency domain model.

5.2. Simulink® Model for the Time Domain Analysis

The Simulink® model of the time domain analysis is given in Figure 20. This model is constructed by using the linear aeroelastic model. In this Simulink® model, the aeroelastic models that are derived in Chapter 4 are used. The inputs of the aeroelastic plant are perturbation vector $\{w\}_{\bar{q}}$ to dynamic pressure, perturbation vector to aerodynamic forces $\{w\}_F$, and

angle q_θ of the motor shaft kinematically amplified to the wing shaft, and the outputs are vector $\{z\}_{\bar{q}}$ of additional states due to perturbation to dynamic pressure and structural states $\{q\}$ of the fin. As it is given in Equation (3.6) $\{w\}_{\bar{q}}$ is obtained by multiplying the $\{z\}_{\bar{q}}$ with the disturbance to dynamic pressure $\bar{q}_{dist}$. In the Simulink® model, the value of $\bar{q}_{dist}$ is introduced with the q_dist block. Especially in the incompressible flow, the analyses at different dynamic pressures can be easily performed by varying the value of q_dist block. In the compressible flow, due to the match point calculation requirement, varying the value of q_dist block will carry the model out of physical states considering the atmospheric properties of the world. The analyses can still give the behavior of the effect of dynamic pressure change; however, analyses should be performed at the match points for solid results. It is also possible to apply external aerodynamic disturbance forces with the help of the dL and dM signal generator blocks.

The deformation of the torsional spring $\delta_{\alpha\theta}$ is calculated by subtracting the angular position q_α of fin from the angular position q_θ of transmission that is the output of "Transmission Ratio 1" block. The feedback force applied to the motor due to the deflection of the torsional spring is calculated by multiplying the $\delta_{\alpha\theta}$ with the total torsional stiffness $k_{\alpha\theta}$ and the inverse of the transmission ratio.

Figure 20. SIMULINK® model of the ASE system for time domain analysis

114

In general, the bandwidths of the motor drivers are well over 1,000 Hz. Thus the dynamics of the motor driver is neglected in this Simulink® model and the controller block output, the current command, is directly fed to the motor torque constant block. The output of the motor torque constant block is the generated torque due to magnetic field between the permanent magnets and the current flowing through the winding of the motor. A saturation block is inserted to the output of the motor torque constant block. Thus, the generated torque is limited to a peak torque value by using this saturation block. Subtracting the feedback torque from this limited generated torque, the net torque applying on the rotor of the motor is obtained. The Motor Dynamics block includes the dynamic model of the rotor and the transmission, except the transmission ratio. This sub-system is modeled by a second order transfer function, consisting of the inertia and damping properties of the rotor and the transmission. The output of this transfer function is the angular position of the rotor. By dividing the angular position of the rotor to the transmission ratio, by means of "Transmission Ratio 1" block, the output of the transmission is calculated.

The existence of noise in the feedback signal forces the controller to suppress an artificial motion. Generally, this gives rise to small amplitude oscillations in the system and an increase the root mean square (rms) value of the current consumed. The analog signals are more vulnerable to noise than the discrete systems. Thus, a discrete sensor model is used in the time domain Simulink® model. The linear dynamics of the sensor is assumed as unity as given in Sensor block. The linear output of the Sensor block is quantized by using the "Quantizer 2" block. However, a discrete noise is added to the feedback signal q_α, before the Sensor block. The amplitude of this noise is selected as equal to the value of the least significant bit of the discrete sensor, which is the smallest incremental output of the sensor.

In Chapter 4, the controller synthesis methods are given. The synthesized controllers of these methods have one output and two inputs. These two inputs are the command signal and the feedback signal in terms of the angular position of the rotor. Thus, the feedback signal is multiplied with the transmission ratio by using "Transmission Ratio 4" block before it is fed to the controller.

The command signal is the angular position q_α of the fin. In Chapter 4, a command input is defined and used in the controller synthesis methods. Hence, the controllers are synthesized considering the defined command input limits, and the robustness of the controllers are dependent to the command input. In order to preserve the robustness of the system, the command and its maximum variation, which corresponds to the angular position and angular speed of the fin, is limited. This limitation is implemented in the Simulink® model by using the Limiter block shown in Figure 20. In order to implement a simple model and prevent phase lag, some logic operators are used in the Limiter block instead of a low-pass type filter. Similar to the feedback signal, the command signal is also multiplied with the transmission ratio N before it is fed to the controller.

The controller of the model can be selected as continuous or discrete. For the discrete case, the controller is discretized by using Tustin method at 2500 Hz. This discretization frequency of the controller is limited with the hardware in the upper limit and with the dynamics of the system in the lower limit. The frequency of the controller should be much larger than the highest frequency of interest or the bandwidth of the controlled system. A sinusoidal signal at the highest frequency of interest should be figured by the discretized controller, such that the controller can also be able to manipulate the system at this frequency. The discretization frequency of the controller can be computed by multiplying the highest frequency of

interest with a typical value of 40. Thus, a period of sine wave at the highest frequency of interest is composed of 40 points, which is sufficient to identify the signal and manipulate the system. The bandwidths of the aeroservoelastic systems used in this study varies between 6 to 10 Hz, however the frequencies of the instabilities are increased up to 50 Hz. Moreover, a backlash nonlinearity is introduced to the aeroservoelastic systems, which introduces dynamics with higher frequencies. Thus the discretization frequency is selected as 2,500 Hz. 2,500 Hz is a possible working frequency for this model in xPC-Target. xPC-target is a The MathWorks Inc. product that enables a personal computer compatible hardware for real time execution of Simulink$^{®}$ models for hardware in the loop simulations by connecting physical systems. The simulation is solved with the variable step Rosenbrock stiff solver and the maximum step size is set to 1/2500 seconds. Although the ode45 solver is sufficient in this model, the system becomes stiff when the nonlinearities are introduced, and the ode45 solver cannot solve the problems in most of the cases that are constructed in this study. By solving the equations of an aeroservoelastic system constructed in this study, alternative solvers are compared. It is seen that the Rosenbrock stiff solver method successfully solves the problems in all cases. Furthermore, it is also seen that the Rosenbrock stiff solver gives the closest results to the results of the ode45 solver for the Simulink$^{®}$ model presented in this section. Thus, the Rosenbrock stiff solver is selected as the solver of the time domain analyses executed in Simulink$^{®}$. Further details of these solvers can be found in the study of Shampine et al. [63].

5.3. Backlash Modeling

In missile fins, due to the gaps between the contacting elements of transmission, backlash usually exists in the pitch degree of freedom of the fin. In general, backlash decreases the command tracking performance,

stability envelope and increases the energy consumption of the aeroservoelastic system. Although the backlash value varies from system to system, 0.05° to 0.1°backlash values are typical, and it may increase up to 0.2°. Although the backlash in precise positioning systems is undesirable; it is expensive to remove it. Hence, instead of removing it, its effect can be analyzed and considered in the selection of the synthesized controller. Moreover, the controller can also be synthesized considering the backlash.

In this study, analyses of aeroservoelastic systems with backlash are performed both in the time domain and in the frequency domain. An analytical model of the backlash is presented for the time domain analyses. Using this backlash model, a Simulink® model is constructed for the time domain analyses of the aeroservoelastic system. For the frequency domain analyses, the aeroservoelastic system with backlash is quasi-linearized by using the sinusoidal input describing function method. An analyses method for the quasi-linearized aeroservoelastic system is also presented.

5.3.1. Time Domain Backlash Model

In this Section, a time domain backlash model is introduced. For this purpose, an inertia controlled backlash model is used. In this backlash model, both driving forces from the actuator and from the wing are included. A complete backlash model is obtained by using both restoring and dissipative behaviors of impact. In Figure 21, a schematic drawing of this backlash model is given for a translational system. This physical model for backlash can be easily adapted to rotational systems as well. In Figure 21, k is the effective contact stiffness, c is the effective damping that represents inelastic collision, m_1 and m_2 are the masses of bodies, F_1 and F_2 are the external forces acting on bodies, x_1 and x_2 are the positions

of bodies, and *bv* is the backlash value specified as the half of the total backlash. The contact stiffness and damping are active only when the bodies are in contact. In the given backlash model, m_2 is analogous to the driving part of the aeroservoelastic system, which consists of a motor and transmission mechanism, and m_1 is analogous to the typical section wing. The stiffness of the torsional spring connecting the transmission output to the typical section wing can be used as an effective contact stiffness, since the local stiffness at the contact point is much higher. The effective contact damping can be calculated from the coefficient of restitution. However, contact damping is only active when the relative speeds of the bodies are different during contact. On the other hand, a viscous damping is modeled in the pitch degree of freedom of the typical section wing, which is more significant. Thus, the contact damping can be excluded from the model to reduce the complexity. However, in order to present a complete backlash model, both contact stiffness and contact damping are used in the analogous system, Figure 21.
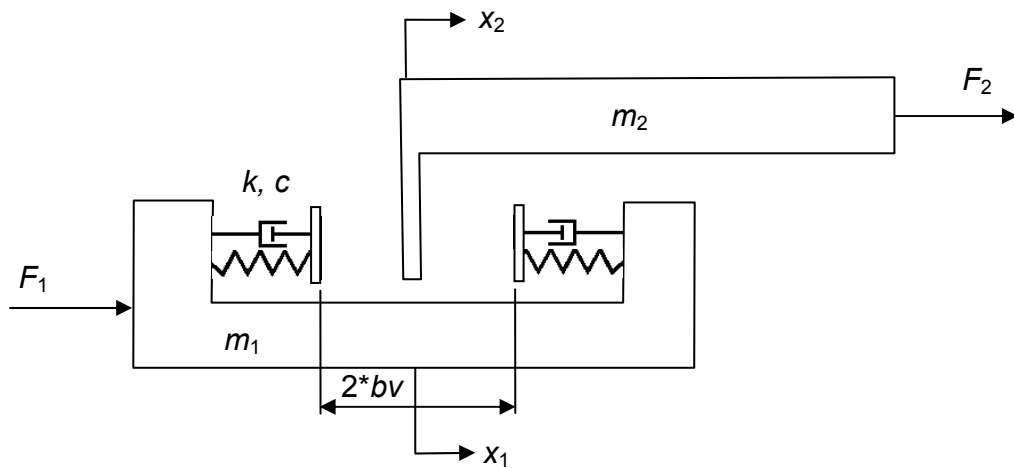
Figure 21. Physical model of backlash between two translational bodies

In Figure 22, the free body diagrams of the translational backlash model are given, where F_k and F_c are the reaction forces due to the contact stiffness and damping, respectively.
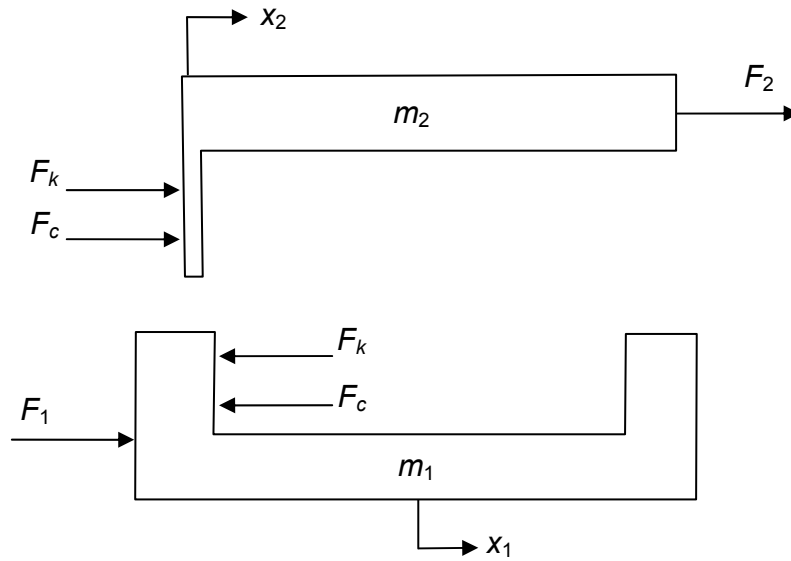
Figure 22. Free body diagram

Equations of motion of the system are

$$m_1\ddot{x}_1 = F_1 - F_k - F_c,$$
$$m_2\ddot{x}_2 = F_2 + F_k + F_c.$$

(5.1)

Examining the model given in Figure 21, it can be seen that the two bodies do not contact unless the relative displacement of the two bodies are greater than the backlash value. Thus, both F_k and F_c are zero when the relative displacement is smaller that the backlash. When contact occurs, the spring that represents the contact stiffness deforms and produces a contact force proportional to the penetration distance. Moreover, a damping force develops proportional to the relative velocity between the bodies. Therefore, F_k and F_c can be calculated as follows

$$F_k = \begin{cases} 0, & |x_1 - x_2| \le bv \\ k(x_1 - x_2 - sign(x_1 - x_2) * bv), & |x_1 - x_2| > bv \end{cases},$$

(5.2)

$$F_c = \begin{cases} 0, & |x_1 - x_2| \le bv \\ c(\dot{x}_1 - \dot{x}_2), & |x_1 - x_2| > bv \end{cases}. \qquad (5.3)$$

In vibrational systems, the viscous damping of the system can be calculated from

$$c = 2\zeta\sqrt{km}. \qquad (5.4)$$

If the damping ratio, ζ, is unknown, it can be calculated by using the coefficient of restitution, ε. In order to demonstrate this calculation, a spring-mass-damper system is used, where stiffness is the contact stiffness, damping is the contact damping, and mass is the colliding body. Equations of an underdamped single degree of freedom spring-mass-damper system with an initial speed are

$$x = \frac{V_0}{\omega_d} e^{-\zeta\omega_n t} \sin(\omega_d t), \qquad \zeta < 1,$$

$$\dot{x} = -\frac{V_0 \zeta \omega_n}{\omega_d} e^{-\zeta\omega_n t} \sin(\omega_d t) + V_0 e^{-\zeta\omega_n t} \cos(\omega_d t). \qquad (5.5)$$

In Equation (5.5), x is the distance traveled, V_0 is the initial speed, t is the time, ω_n and ω_d are the natural and damped natural frequencies of the system respectively. Since damping is related to the speed, only the response to initial speed is considered. Assume that contact initiates at $t=0$, where $x=0$, with a collision speed V_0. Starting with the initial speed, the system first slows down and the speed becomes zero. Then the system speeds up in the reverse direction and contact is lost when x becomes zero again at $t=\pi/\omega_d$. The separation speed, V_f, can be calculated by substituting the final time into Equation (5.5) as

$$V_f = -\frac{V_0 \zeta \omega_n}{\omega_d} e^{-\zeta \omega_n \pi/\omega_d} \sin(\omega_d \, \pi/\omega_d) + V_0 e^{-\zeta \omega_n \pi/\omega_d} \cos(\omega_d \, \pi/\omega_d),$$

$$V_f = -V_0 e^{-\zeta \omega_n \pi/\omega_d}.$$

(5.6)

Note that the separation speed is related to the coefficient of restitution. Substituting $\omega_d = \omega_n \sqrt{1-\zeta^2}$ into Equation (5.6), and using the definition of the coefficient of restitution damping ratio can be calculated as

$$\varepsilon = \frac{V_f}{V_0} = -e^{-\frac{\pi\zeta}{\sqrt{1-\zeta^2}}},$$

$$\Rightarrow \zeta = -\frac{\ln(\varepsilon)}{\sqrt{\pi^2 + \ln(\varepsilon)^2}}.$$

(5.7)

5.3.2. Simulink® Model for the Time Domain Analysis with Backlash

The second Simulink® model is used for the time domain simulations of the aeroservoelastic system with backlash. This model is derived from the first model given in Figure 20. The Simulink® model is given in Figure 23, and the Motor and Transmission sub-block is given in Figure 24. For this system a MATLAB® function block named as Backlash is inserted, which calculates the reaction forces between the transmission output shaft and the fin shaft according to the backlash model using Equations (5.2) and (5.3). It can be seen from the figure that the last input to the aeroelastic model is the calculated reaction force between the fin and the transmission, rather than the transmission shaft position. Thus the driving force of the aeroelastic system is a reaction force. The aeroelastic model is modified according to force input. A further modification of the aeroelastic system is also conducted, in order to receive the speed of the

structural states. The speed of the transmission is also calculated by modifying the Motor Dynamics block. The transfer function of the Motor Dynamics block is separated in two parts such that the rotor speed is obtained from the output of the first part. The second part is simply the integrator that calculates the rotor position. The speed of the transmission is obtained by multiplying the speed of the rotor by inverse of transmission ratio. The angular positions and the angular speeds of the fin and transmission are fed to the Backlash block.
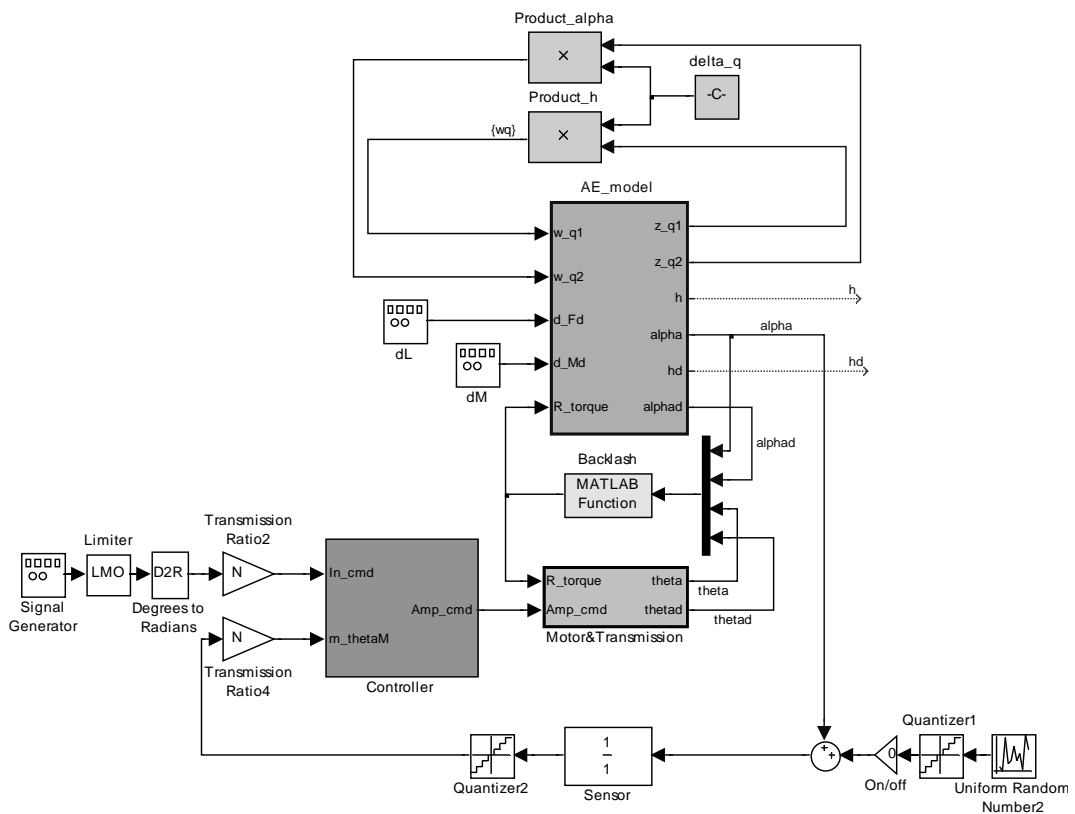
Figure 23. Simulink® model of the ASE system with backlash
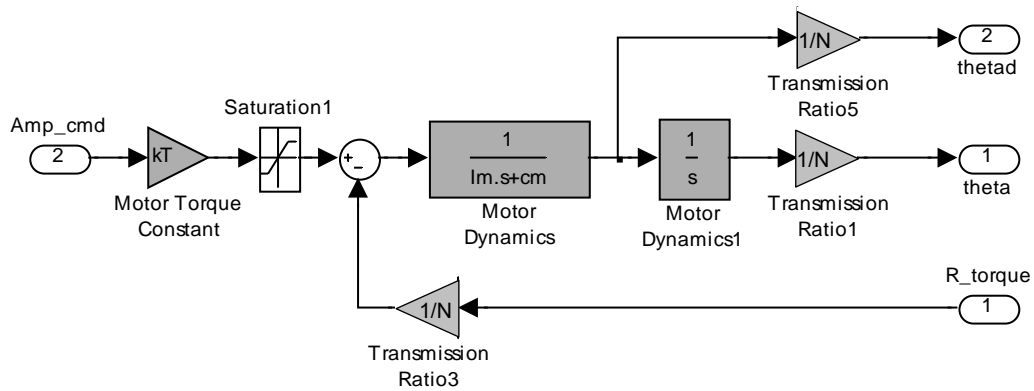
Figure 24. Motor and Transmission block

5.3.3. Frequency Domain Analysis for LCO Detection

Modeling of any type of nonlinearity is straightforward in time domain modeling. Numerical solution of this nonlinear time domain models is also straightforward. However, many simulations are required in order to understand the behavior of the system under various conditions. On the other hand, a frequency response function summarizes the behavior of the system in the frequency range of interest. Thus, the frequency domain analysis usually provides more physical insight regarding the problem, especially for linear systems. Unfortunately, frequency domain analyses are not directly applicable to nonlinear problems. A common way to analyze nonlinear systems is to linearize the equation around working conditions. However, this technique precludes the observation of nonlinear phenomena such as LCO, chaos, and frequency jump.

LCO is one of the most important nonlinear phenomena, seen in aeroservoelastic systems. LCO is a self sustained oscillation that is independent of the initial conditions. Because of nonlinearity, there may exist stable outer and unstable inner regions for a system, resulting in a sustained oscillation on the boundary. In contrast to the oscillations of linear undamped systems, the amplitude/pattern of the limit cycle

124

oscillation only depends on the system parameters. Although the initial conditions do not affect the dynamic characteristics of the LCO, there may exist more than one LCO or other stable/instable points, and which one of these will be reached depends on the initial conditions. The initial conditions of each equilibrium type forms a region in state space. The borders of these regions are called separatrices. An LCO can be stable, unstable, or semistable. All trajectories in the vicinity of a stable LCO converge to its pattern. On the other hand, all trajectories in the vicinity of an unstable LCO diverge from its pattern. Van der Pol oscillator is a well-known example for the stable limit cycle, Figure 25. As seen from the figure, response to initial conditions both in inner and outer region converges to LCO.
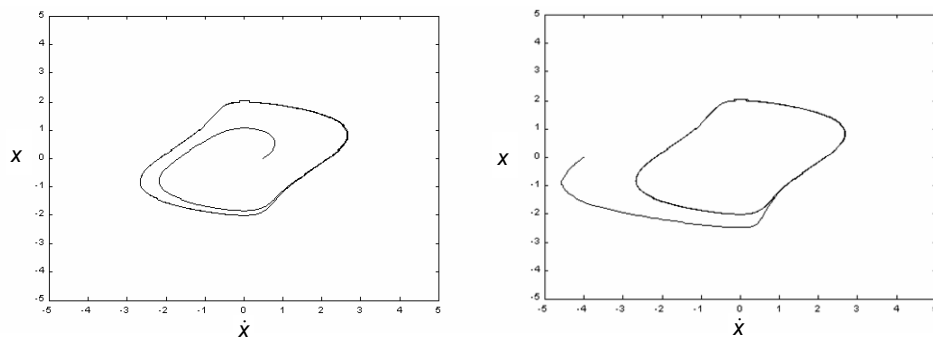
Figure 25. Van der Pol oscillator [13]

Although the LCO is a stable phenomenon in the sense of Lyapunov, it can be as dangerous as flutter. If LCO's are not considered during design, they can degrade the performance of missiles such as decrease in hit accuracy, decrease in maneuver capability, undesired coupling with autopilot, and increase in energy consumption. In aircrafts, LCO's cause discomfort, decrease in targeting accuracy, and decrease in fatigue life.

The exact pattern of LCO's can be determined by time domain simulations. To identify the LCO's in time domain, the simulations must be performed with numerous initial conditions. Despite the computational

cost, this brute search approach does not guarantee that all LCO's are identified. The describing function method, which is a quasi-linearization technique, can be used to analyze LCO phenomenon in frequency domain [64, 66]. However, the quasi-linearization brings some shortcomings, too;

- the predicted LCO amplitude and frequency are not accurate,
- the predicted LCO may not be actual,
- an actual LCO may not be predicted,

The LCO's usually involve significant higher harmonics. However, describing function method assumes that an LCO can be represented by a single fundamental frequency. This is because amplitude and frequency of the LCO predicted by the describing functions are approximate and giving the fundamental behavior. However, as the airspeed approaches to the critical flutter speed, a single frequency dominates the LCO as in flutter. Thus, the predictions become more accurate. Well below the critical flutter speed, there might exist some other LCO's with many sub and higher harmonics, and even chaos. In these cases an artificial LCO may be predicted, which actually does not exist, or even an existing LCO may be missed. A brief explanation of the describing function method is given in Appendix C.

The describing function given in Equation (5.8) defines the equivalent stiffness, υ, for sinusoidal input with backlash [66].

$$\upsilon(A) = \begin{cases} 0 & , A \le bv \\ \left[1 - \dfrac{2}{\pi}\left(\arcsin\left(\dfrac{bv}{A}\right) + \dfrac{bv}{A}\sqrt{1 - \left(\dfrac{bv}{A}\right)^2} \right) \right]k & , A \ge bv \end{cases} \qquad (5.8)$$

126

As described in Appendix C, backlash is a single valued nonlinearity. This means that its describing function is memoryless and depends only on the amplitude of the input oscillation. In Figure 26, equivalent stiffness for the backlash describing function obtained from Equation (5.8) is given. From the figure it can be seen that, for the oscillations in the free zone; i.e., below bv, the equivalent stiffness is zero. As the oscillation amplitude increases, the equivalent stiffness approaches to its asymptote, which is the linear stiffness value.
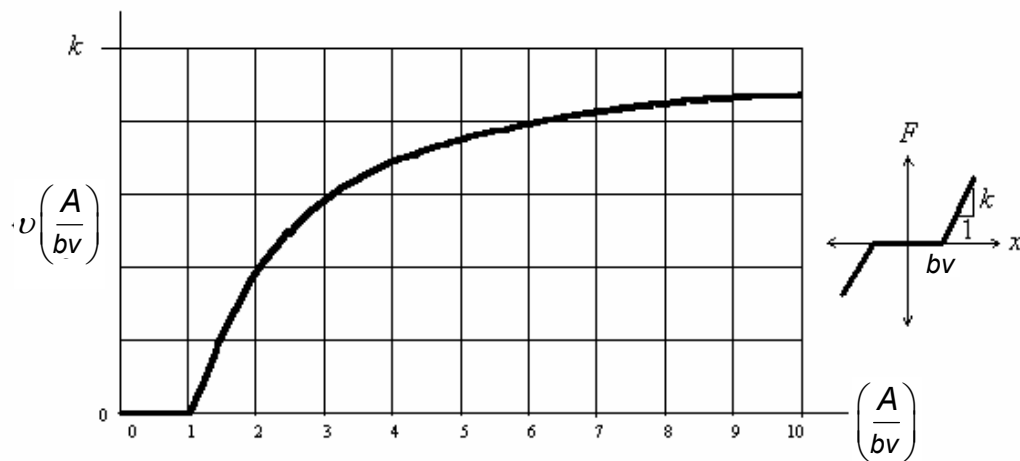
Figure 26. Equivalent stiffness for backlash describing function [13].

5.3.4. Frequency Domain Limit Cycle Oscillation Search Method

As discussed in Section 5.3.3, LCO's are self sustained oscillations. Thus, examining the eigenvalues of the quasi-linearized system, some conclusions can be drawn. Note that the quasi-linearization of the system is achieved for an assumed oscillation amplitude and a backlash value, which corresponds to an equivalent stiffness value.

If the poles of the closed loop system are all in left hand plane (LHP), implying a stable system at this search point, means the system

has positive damping and energy dissipates from the system. Thus, the oscillation amplitude decreases, which results in a decrease in the equivalent stiffness, Figure 26.

If there exists a pole in the right hand plane (RHP), implying that the system has negative damping, then the system is unstable at this search point. Therefore, the oscillation amplitudes will increase, resulting in an increase in the equivalent stiffness.

If there exists no poles in the RHP, and a pair of poles exists on the jω axis, implying that the system has zero damping, then the system is marginally stable. This means that the system sustains the oscillation at this search point without using any external input. Note that the poles moves from jω axis if the amplitude of the oscillation is varied, which shows that the result is not an ordinary linear system oscillation. Thus the oscillation at this search point is an LCO. However, the LCO can be a stable or an unstable LCO. This can be recognized by analyzing the stability of the smaller and larger oscillation amplitudes respectively.

- If the system is stable for the larger oscillation amplitudes and unstable for the smaller oscillation amplitudes, then the LCO is a stable LCO. Note that, at this point, the oscillation amplitude of the larger amplitude oscillations decreases and the smaller amplitude oscillations increases; thus, both converges to the LCO.

- If the system is unstable for the larger oscillation amplitudes and stable for the smaller oscillation amplitudes, then the LCO is an unstable LCO. An unstable LCO is the opposite of stable one, oscillation amplitude of the larger amplitude oscillations increases and smaller amplitude oscillations decreases; thus, both diverges from the LCO.

In order to search the LCO's and identify the behavior of the system, the eigenvalues of the system can be derived by varying the value of the equivalent stiffness from zero to the linear stiffness value. The geometrical locations of system poles can be drawn on a root locus plot or the changes in damping ratio and frequencies of the system by varying the equivalent stiffness value. Variation of the damping ratio and frequency values of an example system with the change of equivalent stiffness value is given in Figure 27. The example system is an aeroelastic system in incompressible flow, which is similar to the models used in this study. It has two structural (pitch and plunge) and two aerodynamic states. Note that the damping ratio crosses the zero line twice for the equivalent stiffness values of k_{uL} and k_{sL}, at which the LCO's occurs. The oscillation amplitudes of LCO can be calculated form Equation (5.8). Above the k_{sL} the damping ratios are all positive, thus the system is stable. Below the k_{sL} there is negative damping ratio, thus the system is unstable. Hence, the LCO for the equivalent stiffness value of k_{sL} is a stable LCO. On the contrary, the LCO for the equivalent stiffness value of k_{uL} an unstable LCO since the system is unstable for a greater equivalent stiffness value and stable for a smaller equivalent stiffness value. Below the equivalent stiffness value of k_{uL} the system is stable, hence the amplitude of the oscillations decrease below the backlash value.
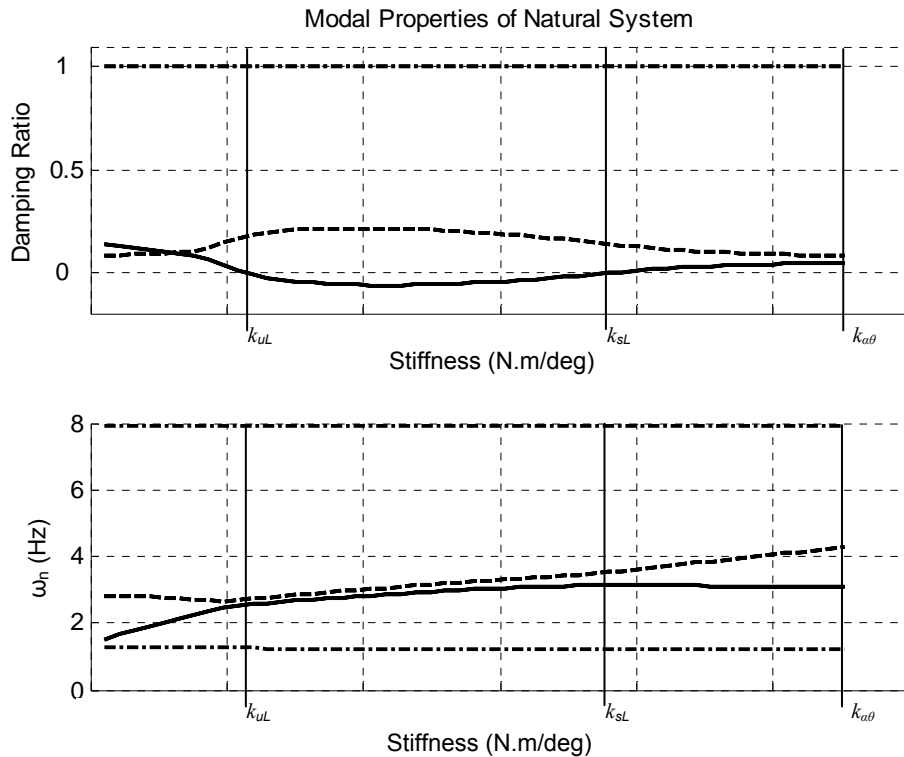
Figure 27. Frequency domain LCO search method plot example

The following procedure can be used to determine the possible stable LCO point of the aeroelastic/aeroservoelastic system. However, note that this search algorithm may fail due to unstable LCO's. As an example, for the system given in Figure 27, if the initial stiffness value is taken less than k_{uL} then the algorithm converges to the zero stiffness value, which is probably the stable focus, instead of the stable LCO at the k_{sL}. Thus it is advised to conduct a coarse search for a few stiffness values and prepare a frequency domain LCO search plot similar to Figure 27 in order to predict the existence and the stiffness values of the stable and unstable LCO's. Initial value of k_{upper} and k_{lower} can be modified in order to define the search interval.

1. construct system matrix of AE/ASE system, $[A_{AE}]/[A_{ASE}]$, at fixed aerodynamic parameters,

2. define scalars $k_{upper} = k_{\alpha\theta}$, $k_{lower} = 0$ to bound k_{eq},

3. define scalar $\varepsilon > 0$ for accuracy,

4. compute $k_{eq} = \dfrac{1}{2}(k_{upper} + k_{lower})$,

5. re-construct $[A_{AE}]/[A_{ASE}]$ by using k_{eq} instead of $k_{\alpha\theta}$,

6. if ($[A_{AE}(k_{eq})]$ / $[A_{ASE}(k_{eq})]$) has an unstable pole, then $k_{upper} = k_{eq}$, otherwise $k_{lower} = k_{eq}$,

7. if $(k_{upper} - k_{lower}) > \varepsilon$ goto step 4,

8. the equivalent stiffness at LCO is $k_{LCO} = k_{eq}$,

9. calculate the oscillation frequency from the eigenvalue of $[A_{AE}]/[A_{ASE}]$ constructed at step 5 at last iteration,

10. calculate oscillation amplitude by using Equation (5.8).

5.4. Postscript on Chapter 5

This chapter focuses on the modeling of the aeroservoelastic system. Both time domain and frequency domain models are conducted in order to analyze the performance and stability of the aeroservoelastic systems. In addition, backlash models are introduced in both models in order to conduct some LCO analyses. An LCO search method is also presented for the frequency domain analyses.

CHAPTER 6

CONTROLLER SYNTHESIS AND CASE STUDIES

6.1. Preview

In this Chapter, the methods given in previous chapters are applied to the robust flutter suppression of a typical section and the results of MATLAB® simulations are reported as case studies. These case studies are presented under three main sections according to their flow regimes. Under sections for different flow regimes, three subsections are formed according to the flutter suppression method, and different controllers are synthesized under these subsections. Table 8 summarizes these case studies. gq-method given in the table is an improved g-method, which uses the flutter suppression approach of both the q- and the g-methods.

Table 8. Case Studies

Flow Regime	Flutter Suppression Method	Controller		
		H_∞	H_2	μ
Unsteady Incompressible Subsonic Flow	q-method	Case 1	Case 2	Case 3
	g-method	Case 4	Case 5	Case 6
	gq-method	Case 7	Case 8	Case 9
Unsteady Compressible Subsonic Flow	q-method	Case 10		
	g-method	Case 11		
Unsteady Compressible Supersonic Flow	q-method	Case 12		
	g-method	Case 13		

In Case 1, the synthesis and analysis methods that are presented in previous chapters of this study are given in full detail. Additionally, the parameters tuning for the controller synthesis and parameter effects are presented. However, no optimization procedure is developed in tuning the controller parameters optimally, which is beyond the scope of this study. In rest of the case studies, only some additional information specific to each case are given in detail. The discussions of the studies performed and the results for the selected controller after tuning operations are presented for each case. At the end of each section of flow regimes, a subsection is given, in which the synthesized controllers are compared with each other.

6.2. *Unsteady Incompressible Subsonic Flow*

6.2.1. Construction and Analyses of Aeroelastic Model

In order to apply the synthesis methods in MATLAB® environment, the parameters of the Aeroservoelastic Test Setup (Aeroservoelastik Test Düzeneği - ATD) are used. The ATD is developed in TÜBİTAK-SAGE in the scope of a M.Sc. thesis conducted by Utku ÜNAL in the Mechanical Engineering Department of METU [17]. However, instead of using the actual damping values of the ATD, a set of lower damping values are used in the model of this study. By this approach, lower flutter speeds are obtained which in turn increase the requirements on the controllers designed. As a result, better comparison conditions are created for rating the performances of the controllers. On the other hand, some modifications are required on the aeroelastic system matrices that are defined in Section 2.5 due to the physical characteristics of the ATD. In contrast to the typical section model given in Figure 3, the ATD has an additional mass on the plunging degree of freedom. Thus the mass matrix given in Equation (2.24) is modified as

$$[M] = \begin{bmatrix} m_p & S_\alpha \\ S_\alpha & I_\alpha \end{bmatrix},$$ (6.1)

where m_p term is the total plunging mass. This model used in the analysis is named as Model 1, whose parameters are given in Table 9.

Table 9. Properties of the Model 1

Parameter		unit	Model 1
Elastic axis location	a	-	-0.6
Half chord	b	m	0.15
Span	l	m	0.6
Mass of the wing	m	kg	9.83
Total plunging mass	m_p	kg	28.7
Mass moment of inertia of the wing	I_α	kg.m^2	0.098
Plunge stiffness	k_h	kN/m	10
Total torsional stiffness	$k_{\theta\alpha}$	N.m/rad	55.2
Plunge damping	c_h	N.s/m	53.6
Pitch damping	c_α	N.m.s/rad	0.093
Position of center of mass from elastic axis	x_{cg}	m	0.075
Motor torque constant	kT	N.m/A	2.22
Motor continuous stall torque	T_{cs}	N.m	3.53
Allowable peak torque	T_p	N.m	17.65
Mass moment of inertia of motor and transmission calculated at the wing shaft	I_m	kg.m^2	0.000297
Motor and transmission damping	c_m	N.m.s/rad	0.000124
Transmission ratio	N	-	29

Table 10. Initial flow parameters

Altitude	h	m	800
Mach number	M	-	0.05
Airspeed	U_0	m/s	16.86
Air density	ρ	kg/m^3	1.134
Dynamic pressure	$\bar{q}_0$	Pa	161.1

Two independent flow parameters required to define the flow are selected as the altitude and Mach number. The initial values selected for the altitude and Mach number, and the calculated values of the rest of the dependent aerodynamic parameters are given in Table 10.

Using the parameters given in Table 9 and Table 9, the aeroelastic model is constructed according to the equations given in Section 2.5.1.2. Various analyses are performed on the constructed model in order to derive the aeroelastic properties of the Model 1.

The stability analyses of the aeroelastic system are conducted by using the μ and the p-methods. Furthermore, as discussed in Chapter 3, the analyses are performed both varying the dynamic pressure and the airspeed. Also it is presented in Chapter 3 that the μ-method equations are compatible with the dynamic pressure variations, but they are not compatible with airspeed variations. The required additional algorithms for the μ-method analysis by varying the airspeed are also presented in Section 3.4.

6.2.1.1. Stability analyses by varying dynamic pressure

For the μ-method analysis of the aeroelastic system, the algorithm presented in Section 3.3.1 is used. The initial values of the parameters that are used in the algorithm are defined as; the lower search limit δ_{lower} of the dynamic pressure of disturbance which is set to 0 Pa, the upper search limit δ_{upper} of the dynamic pressure of disturbance set to 2,000 Pa, and the accuracy ε set to 0.01 Pa. Thus, the stability search is conducted between 0 Pa and 2,000 Pa above the initial dynamic pressure, and the iteration is ended when the difference between the upper and lower dynamic pressure of disturbance drop below 0.01 Pa. The dynamic pressure of disturbance $\delta_{\bar{q}}$, the difference $\delta_{upper} - \delta_{lower}$ between the upper and lower

dynamic pressure of disturbance, and the pole of the aeroelastic system which has the maximum real part are recorded at each iteration, (Figure 28). At the 18th iteration, the difference between the upper and lower dynamic pressure of disturbance becomes 0.0076 Pa. At the exit step; the maximum real value of the poles of the aeroelastic system is calculated as -5.32 x 10^{-6} 1/s, and $\delta_{\bar{q}}$ is calculated as 504 Pa. Thus, $\bar{q}_{flut}$ the nominal dynamic pressure of flutter and Γ_{flut} the nominal dynamic pressure of flutter margin are computed as 665 Pa and 504 Pa, respectively. The frequency ω_{flut} of the flutter is calculated 3.5 Hz by using the pole of the aeroelastic system that has the maximum real part.

* real part of the pole of the aeroelastic system that has the maximum real part
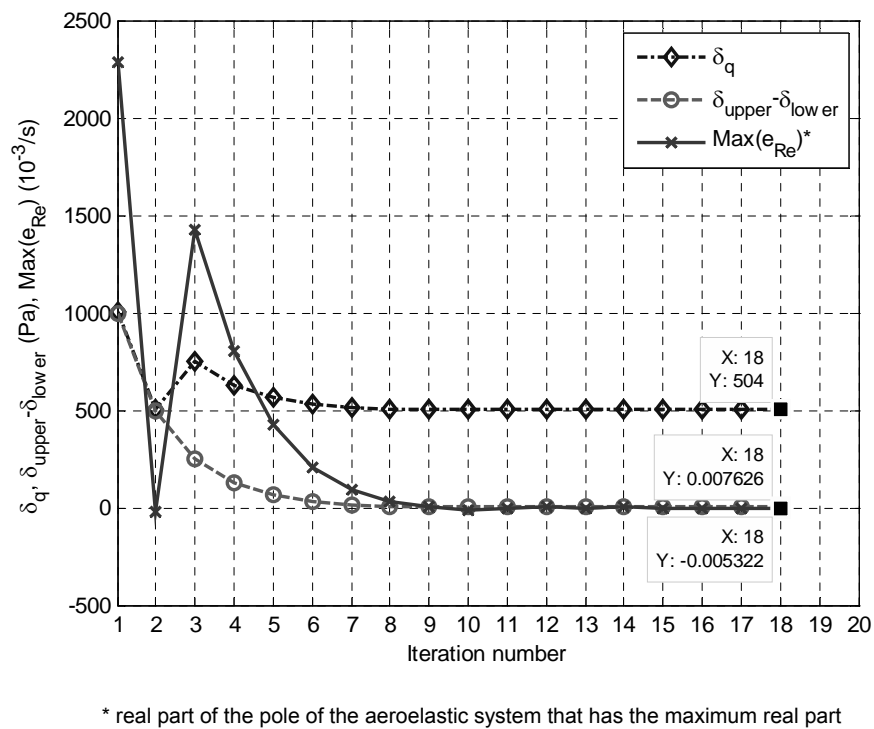
Figure 28. Iteration data of μ-method analysis for the aeroelastic system

In order to crosscheck the results, p-method analysis is used. In order to decrease the computation time of the p-method analysis, instead of reconstructing the whole aeroelastic matrix, the perturbation equations

of μ-method are used. The result of this modified method is also crosschecked with the result of the original method, and it is verified that both solutions of the p-method give the identical results. In the p-method analysis, the calculations are performed at 1,001 points by varying the dynamic pressure parameter from -1,000 Pa to 1,000 Pa with 2 Pa increments. At each point, the damping ratio and the modal frequencies of the system are calculated from the eigenvalues of the state space equations. The results are given in Figure 29. In the upper figure, the variations of damping ratio and modal frequencies with respect to dynamic pressure are given. In the lower figure, root locus plot of the aeroelastic system is given. In the figures, the results of the pitch, plunge, and the aerodynamic modes are presented. It can be seen from the figure that, the aeroelastic system is stable in vacuum and becomes unstable below -300 Pa, which is physically impossible. On the other hand, as the dynamic pressure increases, it can be seen from Figure 29 that the frequencies of the pitch and the plunge modes approach each other, the damping ratio of one of them increases, and the damping ratio of the other decreases and becomes zero. This is a typical behavior of a system that is going into flutter; two modes, a plunge and a pitch, couples with each other and the damping ratio of one of them becomes zero. It can be seen that, namely the plunge mode goes into flutter. However, note that the eigenvectors of the system is also changes with the dynamic pressure. The modes that can be named as a plunge and a pitch in vacuum, couples with each other as the dynamic pressure of the system reaches to the dynamic pressure of flutter. Hence, the motion of the aeroelastic system in flutter is not a pure plunge motion. It can be seen from the Figure 29 that the damping of the system becomes zero slightly below dynamic pressure of 666 Pa, which verifies the dynamic pressure of flutter obtained by μ-method.
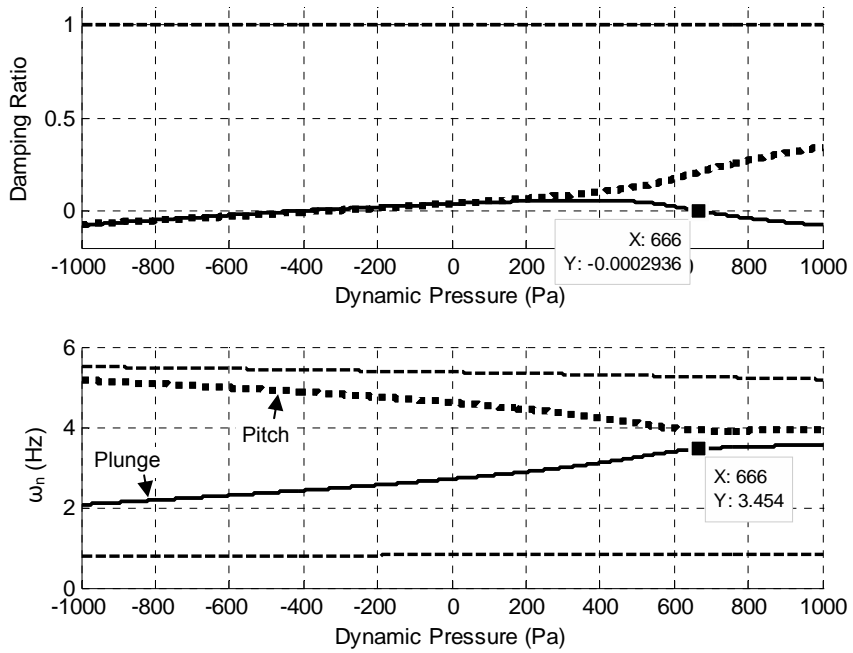
(a) modal properties of aeroelastic system
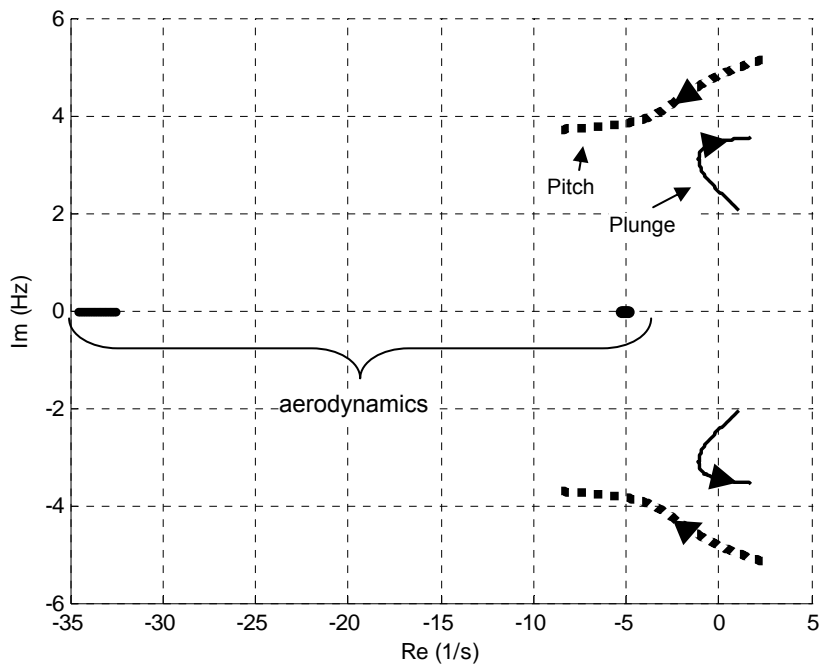
(b) root locus plot

Figure 29. Flutter search results of p-method by changing air density

6.2.1.2. Stability analyses by varying airspeed

Up to this point the dynamic pressure of instability is investigated for the aeroelastic system via μ-method and p-method. The airspeed of instability can also be calculated by using μ-method with the iterative search algorithm presented in Section 3.4.1. In Table 11, the results of this method applied on Model 1 are presented. In the 2nd and 4th iterations the μ-method failed, because the analyses are performed at an unstable point. Hence, an 80% relaxation is applied in the calculations of new airspeeds. It can be seen from the table that, at the 5th iteration, the error between the calculated airspeed of instability drops below one percent. Using the search algorithm, the airspeed of instability is obtained as 31.56 m/s.

Table 11. Results of flutter airspeed search

	iteration #		1	2	3	4	5
Input	U_0	m/s	16.86	34.25	30.77	31.63	31.46
Parameters	$\bar{q}_0$	Pa	161.2	665.2	537.0	567.2	561.1
Output	$\bar{q}_{flut}$	Pa	665.2	-	567.2	-	564.8
Parameters	U_{flut}	m/s	34.25	-	31.63	-	31.56
	%error of U_{flut}	%	-	-	7.6	-	0.2

For the verification of the result of μ-method analysis, the p-method is used again by changing the airspeed but keeping the air density fixed. In the p-method analysis by dynamic pressure variations, the μ-method equations are used. However, in the p-method analysis by airspeed variations the μ-method equations are not used since the equations derived for the μ-method are not suitable for any airspeed modification. Hence, the whole aeroelastic matrix is reconstructed at each step of the p-method analysis by changing the airspeed. This shortcoming increased the computation time of the p-method analysis. For the p-method analysis,

calculations are performed at 100 points, by changing the airspeed from 0 to 42 m/s. Hence, the results are calculated with 0.42 m/s intervals. In Figure 30, the results of the p-method analysis are presented. In the first plot, the damping ratio and modal frequency variation of the aeroelastic system with the change of airspeed are given. As it can be seen from the figure, the airspeed of instability is found slightly above 31.5 m/s, which is in agreement with the result of μ-method. In the second figure, the damping ratio and modal frequency variation are plotted against the dynamic pressure, which is calculated by using the airspeed of the corresponding step and the fixed air density. Comparing Figure 29 and Figure 30, it can be seen that the variations of the structural modes, namely the pitch and the plunge modes, look similar when the airspeed or the air density is varied. On the other hand, it is seen that the variations of aerodynamic modes are different as a response to variation in airspeed and in air density. The airspeed variation causes much more change in the aerodynamic modes than the air density variation.
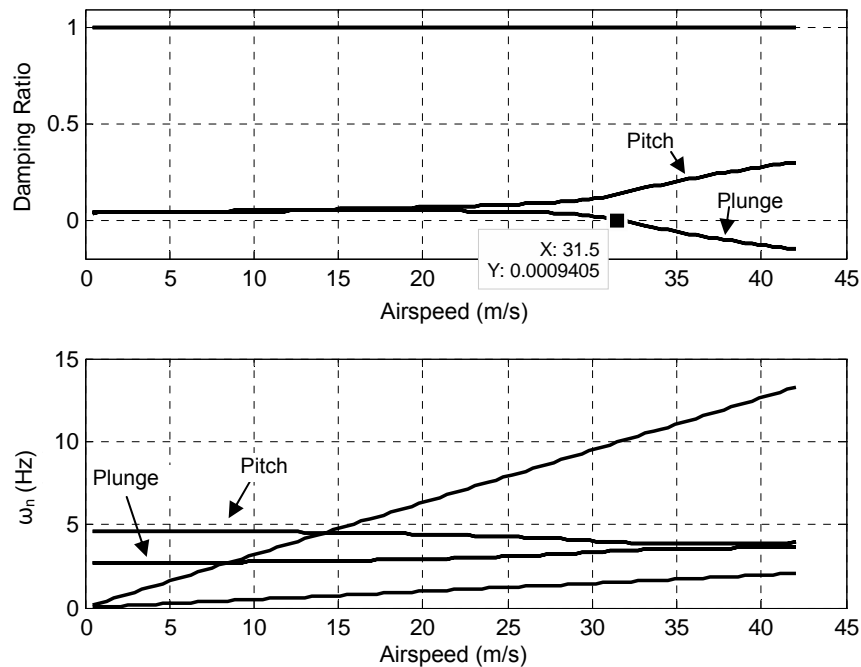
(a) airspeed graph
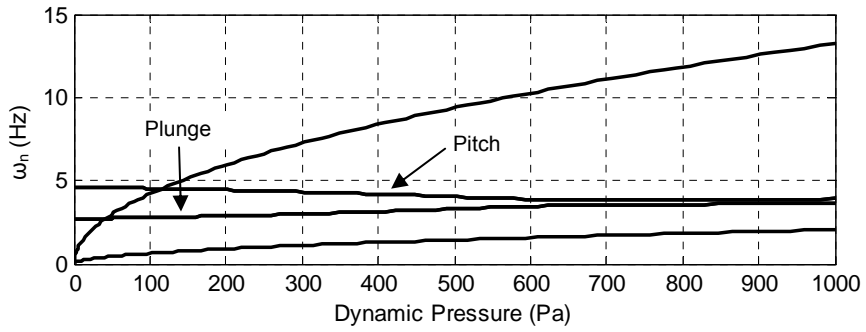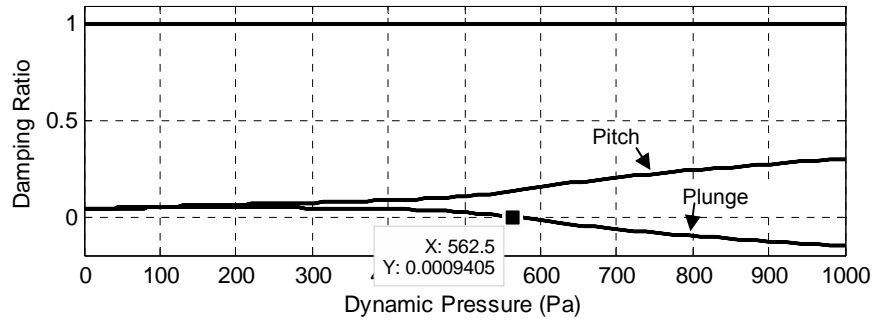
(b) dynamic pressure graph
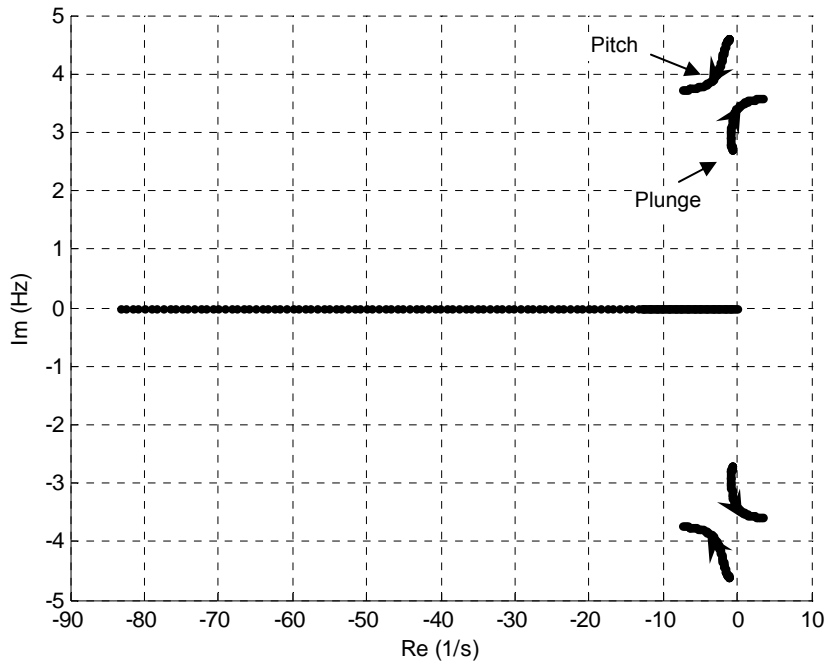
(c) root locus

Figure 30. Flutter search results of p-method by changing airspeed

6.2.1.3. Backlash analyses

The effect of backlash is analyzed for the aeroelastic system constructed. For this purpose, some frequency domain analyses are performed and possible stable LCO's are searched for by using the method presented in Section 5.3.4. Using this search algorithm, a stable LCO of the aeroelastic system at the dynamic pressure of 500 Pa is observed for k_{eq}=45.86 N.m/rad. In order to crosscheck the result the brute force approach given in Section 5.3.4 is applied. The aim of this operation is to predict the presence of the LCO rather than its numerical accuracy. The damping ratios and the frequencies of the aeroelastic system are calculated for a few number of equivalent stiffness values. The results are given in Figure 31. From the figure, it can be seen that the aeroelastic system has a stable LCO for k_{eq}=45.46 N.m/rad and an unstable LCO for k_{eq}=3.25 N.m/rad. Hence the brute force approach method also confirms that a stable LCO may exist for k_{eq}=45.86 N.m/rad. From the eigenvalues of the aeroelastic system the oscillation frequency is calculated as 3.32 Hz. The oscillation amplitude A is calculated by using Equation (5.8), as 1.5° for the backlash value of 0.2°.

Some time domain analyses are also performed for the aeroelastic system by using the Simulink® model. The results of these analyses at a dynamic pressure of 500 Pa are given in Figure 32. The analyses are performed for aerodynamic moment pulses with three different values of 10 ms durations applied to the q_α degree of freedom as initial conditions. In the first case, a 0.1 N.m amplitude moment is applied and the system converges to the 0° stable point due to the aerodynamics (Figure 32 (a)). In the second case, a 1 N.m amplitude moment is applied and the aeroelastic system converges to an LCO from lower amplitude oscillations (Figure 32 (b)). In the third and last case, a 10 N.m amplitude moment is applied and the system converges to the same LCO from higher amplitude oscillations (Figure 32

(c)). Performing a fast Fourier transformation to the time domain results of the aeroelastic system, the frequency contents of the output is obtained (Figure 33). It can be seen from this figure that the time domain results and the frequency domain results are in agreement. From Figure 33, the odd higher harmonics of the LCO can also be seen.

Repeating the searches at various dynamic pressure values, the corresponding LCO amplitudes are obtained and given in Figure 34. At a dynamic pressure of 300 Pa and below, no LCO is obtained. From the figure it can be seen that the frequency domain results and the time domain results are in accordance with each other. Although it is not presented here, the brute force analysis graphics are derived for the aeroelastic system at various dynamic pressures. From those graphics it is seen that, for the aeroelastic system;

- In lower dynamic pressures the system is always stable at 0°,
- In mid dynamic pressures, there exists both an LCO and a stable point at 0° (Figure 31),
- In mid-high dynamic pressures there exists only an LCO,
- In high dynamic pressures first the LCO amplitude increases to unacceptable values, after a value of dynamic pressure the system becomes unstable.

However, these are the characteristic of the particular aeroelastic system analyzed, and the given characteristics may not always be the same for any other system.

From Figure 34 it can be seen that the describing function and time domain solutions are in good accordance. On the other hand, it can be seen that for this model an increase in the backlash increases the amplitude of the LCO, hence decreasing the flight margin of the

aeroelastic system. For example; for an acceptable oscillation of 0.4°, the linear flight margin of 665 Pa decreases to 500 Pa for a backlash value of 0.05°, and to 400 Pa for a backlash value of 0.1°. An LCO first occurs between 300 Pa and 400 Pa; hence the lines between the results for 300 Pa and 400 Pa should not be used for interpolation.
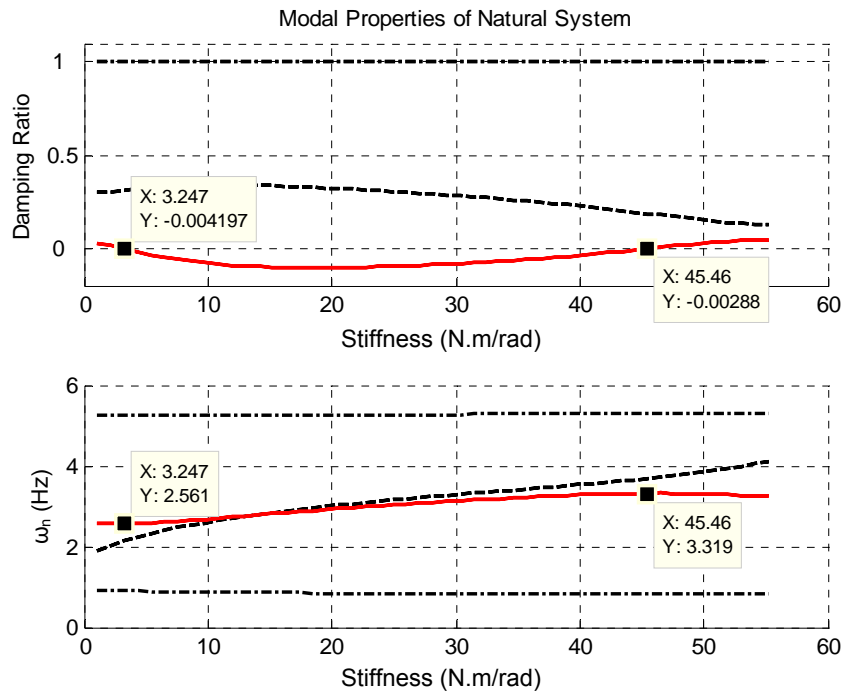
Figure 31. Modal properties of the aeroelastic system at 500 Pa
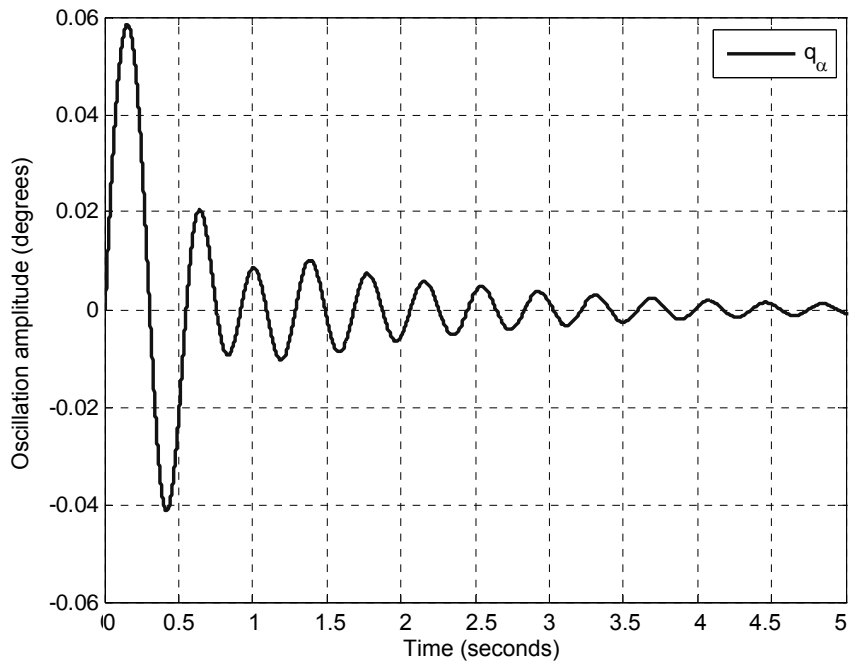
(a) q_α plot for 0.1 N.m torque initial condition
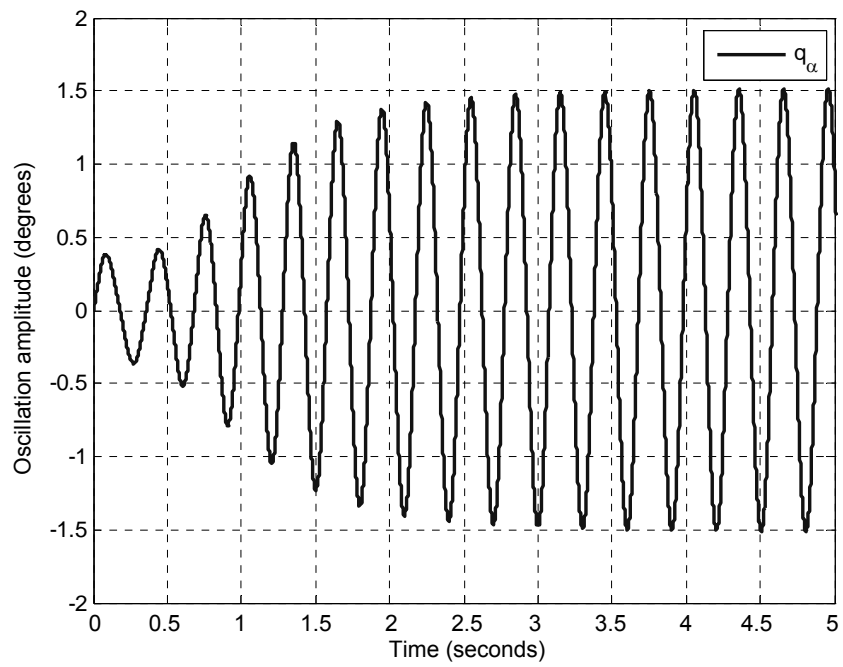
(b) q_α plot for 1 N.m torque initial condition
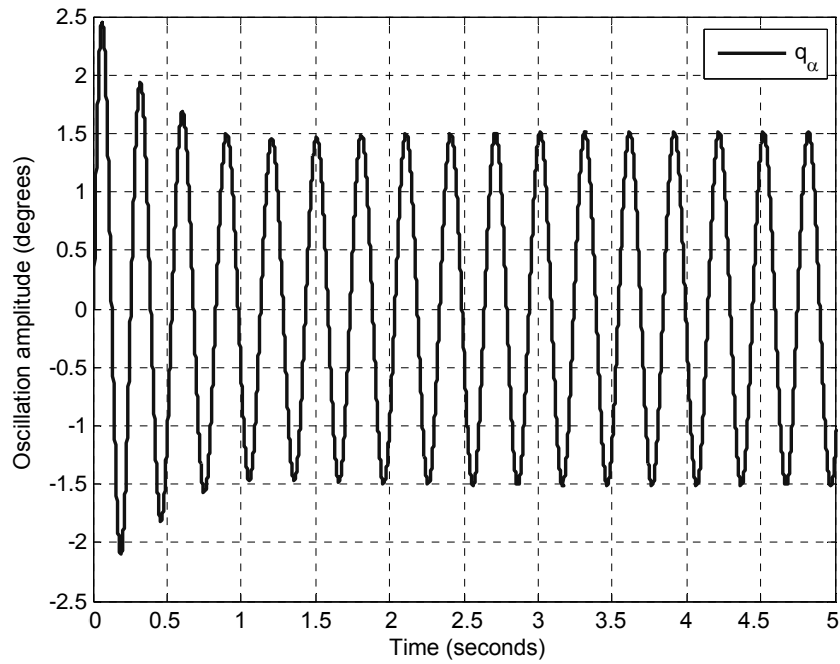
(c) q_α plot for 10 N.m torque initial condition

Figure 32. Time domain results of the aeroelastic system at 500 Pa
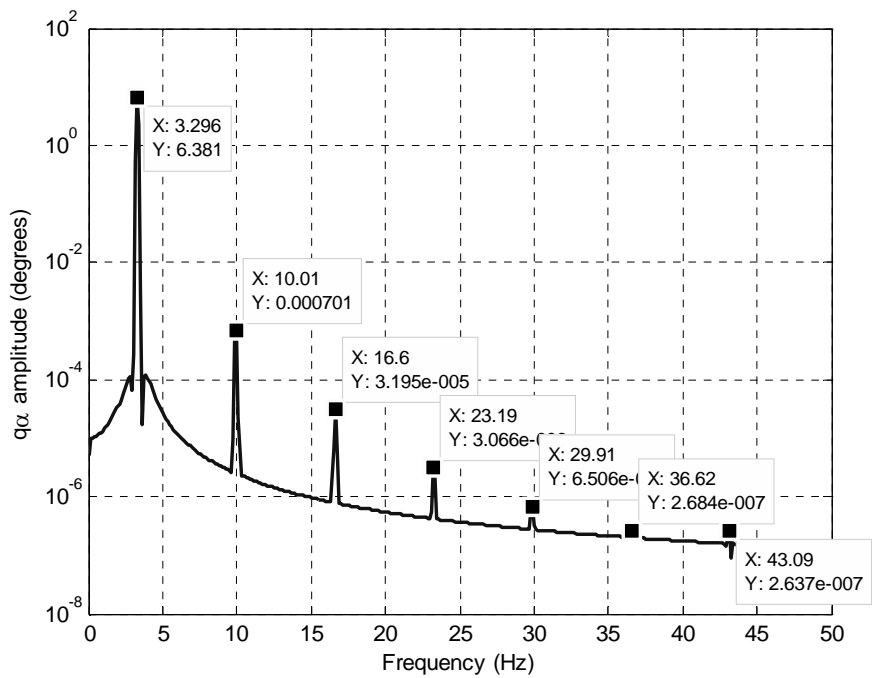
Figure 33. FFT of the time domain results of q_α degree of freedom of the aeroelastic system
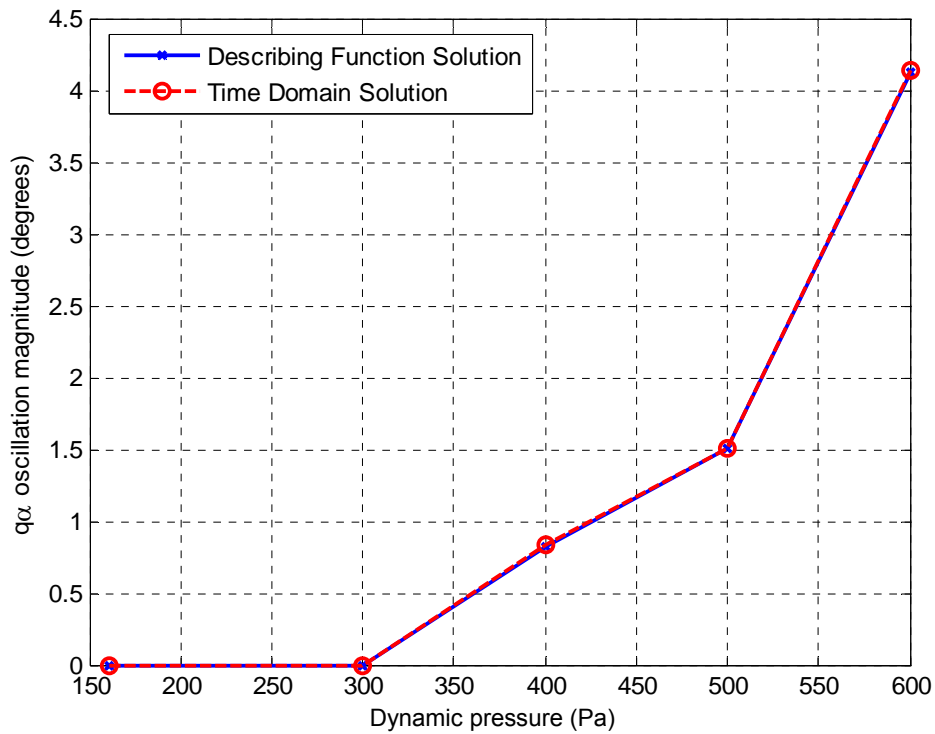
Figure 34. LCO amplitudes of the aeroelastic system with respect to dynamic pressure and for various backlash values

6.2.2. Controller Synthesis by Using q-Method

In order to start a controller synthesis using q-method, it is required to decide upon the numerical values of the parameters of the reference plant as well as upon the uncertainty/performance weightings. It should be noted that the aeroelastic Model 1 is a fictitious model whose parameters should be tuned such that the model goes in to flutter in incompressible subsonic flow. These tunings result in low stiffness and low damping values in pitch and plunge degrees of freedom of the aeroelastic system. Thus, it is meaningless to define the performance requirements of an actual control actuation system as the requirements of the controller of the Model 1 in this study.

The reference plant of the aeroservoelastic system is defined with the bandwidth and the damping ratio. The bandwidth of the reference plant ω_{nref} is set as 6 Hz, which is below a bandwidth requirement of a typical CAS requirement but it is a still demanding value. The damping ratio of a second order system is generally set between 0.4 and 0.8, in order to obtain a system with a desirable transient response. Moreover, for a better settling time performance a damping ratio around 0.76 for %2 criterion and around 0.68 for %5 criterion should be selected. Between the damping ratio of 0.7 and 1, the oscillations exist for the step response, but the oscillations are well damped. Furthermore, above the damping ratio of 0.707 no resonant peaks exist [65]. Through these data the damping ratio of the reference plant ζ_{ref} is set as 0.707.

The derivation procedures of the uncertainty/performance weightings that are used in the controller synthesis are presented in Section 4.2 and 4.3. These uncertainty/performance weightings are listed in the first column of Table 12. Selections of most of these parameters are straightforward through the explanations given in Section 4.3.

- The amplitude of the expected input command of the aeroservoelastic system is defined as 3° up to 2 Hz, and one tenth of it at higher frequencies. Thus, the parameters of the $[W_{cmd}]$ block are set as given in Table 12.
- In Section 4.3, the value of noise level g_{noise} is defined as the smallest increment of measurement. For the aeroservoelastic system, it is assumed that the angular measurement of the fin is conducted by a 14 bit encoder. Thus, the noise level is calculated by evaluating $360°/2^{14}$ as $0.022°$.
- The gain g_{act} of the actuator performance weighting is set as the inverse of the peak motor torque as discussed in Section 4.3. On

148

the other hand, it is assumed that the actuator satisfies the peak torque up to 100 Hz.

- The tracking error of the aeroservoelastic system is set as 0.4° up to 6 Hz. Thus, the gain of $\left[W_{per}\right]$ function is calculated as 2.5 deg^{-1}.

- The expected maximum pitch motion of the aeroservoelastic system is selected as ±10°. Hence, the gain g_{s1} of sensor uncertainty output weighting is calculated as 0.1 deg^{-1}.

- As defined in Section 4.3, the gain g_{s2} of sensor uncertainty input weighting is equal to the value of noise level gnoise. It is assumed that the sensor noise is effective up to 10 Hz.

Table 12. Numerical values of uncertainty/performance weightings

Uncertainty Name	Gain		Corner Frequency		Scale Parameter	
$\left[W_{cmd}\right]$	g_{cmd}	3°	ω_{cmd}	2 Hz	κ_{cmd}	0.1
$\left[W_{n}\right]$	g_{noise}	0.022°				
$\left[W_{Fd}\right]$	g_{Fd_F}	1,400 N	ω_{Fd_F}	0.03 Hz	κ_{Fd_F}	0.001
	g_{Fd_M}	25 N.m	ω_{Fd_M}	0.03 Hz	κ_{Fd_M}	0.001
$\left[W_{act}\right]$	g_{act}	0.057 (N.m)$^{-1}$	ω_{act}	100 Hz	κ_{act}	100
$\left[W_{per}\right]$	g_{per}	2.5 deg^{-1}	ω_{per}	6 Hz	κ_{per}	0.01
$\left[W_{s1}\right]$	g_{s1}	0.1 deg^{-1}				
$\left[W_{s2}\right]$	g_{s2}	0.022°	ω_{s2}	10 Hz	κ_{s2}	10,000
$\left[W_{\bar{q}1}\right]$	$g_{\bar{q}_F 1}$	9.13 N^{-1}				
	$g_{\bar{q}_M 1}$	520.8 (N.m)$^{-1}$				
$\left[W_{\bar{q}2}\right]$	$g_{\bar{q}_F 2}$	54.75 N	$\omega_{\bar{q}_F 2}$	10 Hz	$\kappa_{\bar{q}_F 2}$	0.001
	$g_{\bar{q}_M 2}$	0.96 N.m	$\omega_{\bar{q}_M 2}$	10 Hz	$\kappa_{\bar{q}_M 2}$	0.001

The selection of the parameters of the output weighting $\left[W_{\bar{q}1}\right]$ of the disturbance to dynamic pressure, the input weighting $\left[W_{\bar{q}2}\right]$ of the disturbance to dynamic pressure, and the uncertainty weighting $\left[W_{Fd}\right]$ of the aerodynamic forces requires some pre-calculations. It is required to calculate the maximum possible value of the vector $\{z\}_{\bar{q}}$ of additional states due to perturbation to dynamic pressure. This value is calculated by solving Equation (4.7), which is the equation of the aeroelastic part of the aeroservoelastic system having q_{θ} as the input parameter. This equation is solved by applying the expected command defined by the weighting function of the expected input $\left[W_{cmd}\right]$ in Table 12 as an input, and varying the dynamic pressure within the stable limits of the aeroelastic system. It is seen that the values of elements of $\{z\}_{\bar{q}}$ decrease as the dynamic pressure increases. Hence their limit values are taken when the dynamic pressure is zero and a safety factor of 1.5 is applied as

$$\{z\}_{\bar{q}} = 1.5 \left\{ \begin{array}{c} 0.073 \ \text{N/Pa} \\ 0.00128 \ \text{N.m/Pa} \end{array} \right\} \tag{6.2}$$

If Equations (4.17) and (4.18) are analyzed, it can be seen that this safety factor relaxes the $\left[W_{\bar{q}1}\right]$ weighting, but tightens the $\left[W_{\bar{q}2}\right]$ weighting. Since the common aim of these two weightings is to model the changes in aerodynamics rather than to penalize these changes, this modification is acceptable. The value of each element of the diagonal weighting matrix $\left[W_{\bar{q}1}\right]$ is calculated by taking the inverse of each element of $\{z\}_{\bar{q}}$, as given in Section 4.3.

In order to define the weighting matrix $[W_{\bar{q}2}]$, it is needed to set one more parameter. This parameter is the disturbance to dynamic pressure, $\bar{q}_{dist}$. The synthesized controller will be robust to this disturbance to dynamic pressure. This parameter is one of the mostly used parameters for controller tuning in this study. However as a start, it is selected as $\bar{q}_{dist} = 500\,\text{Pa}$.

$$\bar{q}_{dist} = 500\,\text{Pa} \qquad\qquad (6.3)$$

For the selection of the weighting $[W_{Fd}]$, again Equation (4.7) is used. Similar to the calculation of the weighting $[W_{\bar{q}1}]$, the maximum force and moment are calculated in the stable region of the aeroelastic system. In order to minimize the steady state error, 50 times the obtained maximum force and moment values are selected as the gain g_{Fd}, which is the gain of the weighting $[W_{Fd}]$ in low frequencies; i.e., 0.1 Hz. On the other hand, in order to model the aerodynamic uncertainties it is decided that the value of the weighting $[W_{Fd}]$ at 10 Hz should be one fifth of the obtained maximum force and moment values. The corner frequency of the weighting $[W_{Fd}]$ is calculated from this requirement. These parameters are further tuned during the controller synthesis. The plots of weightings for the reference model and for the uncertainty/performance are given in Figure 35 through Figure 43.
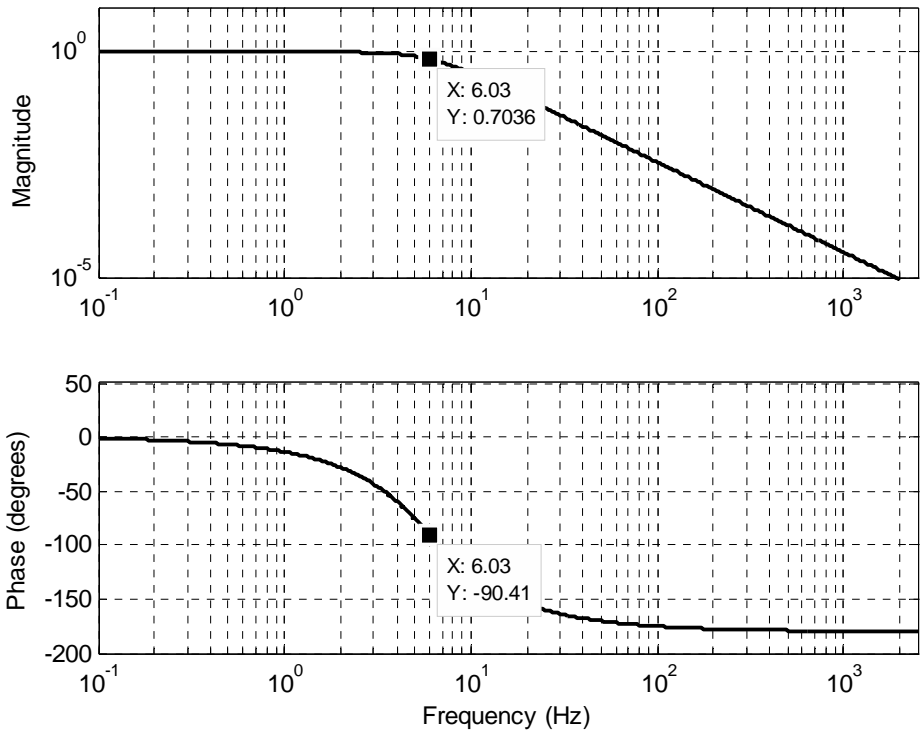
Figure 35. Bode plot of reference model
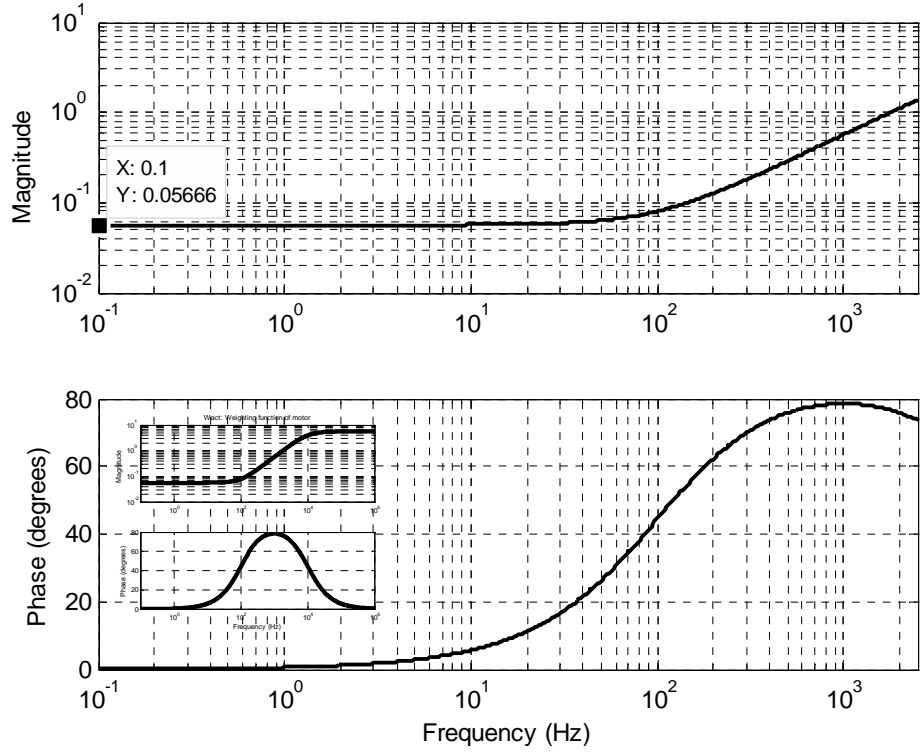
Figure 36. Bode plot of weighting function of motor
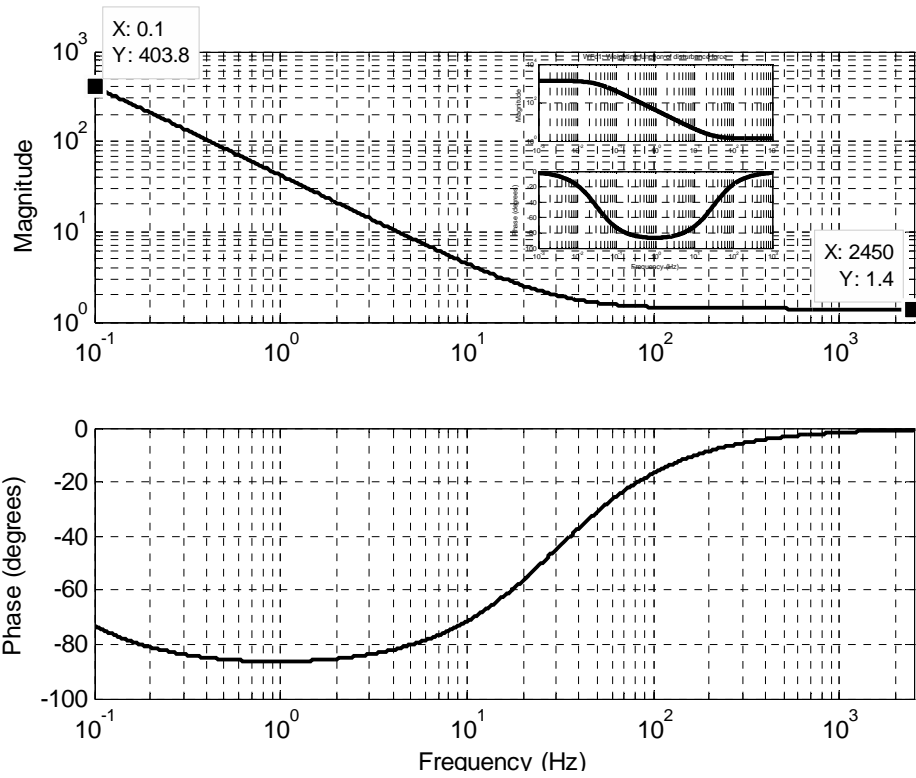
Figure 37. Bode plot of weighting function of disturbance force
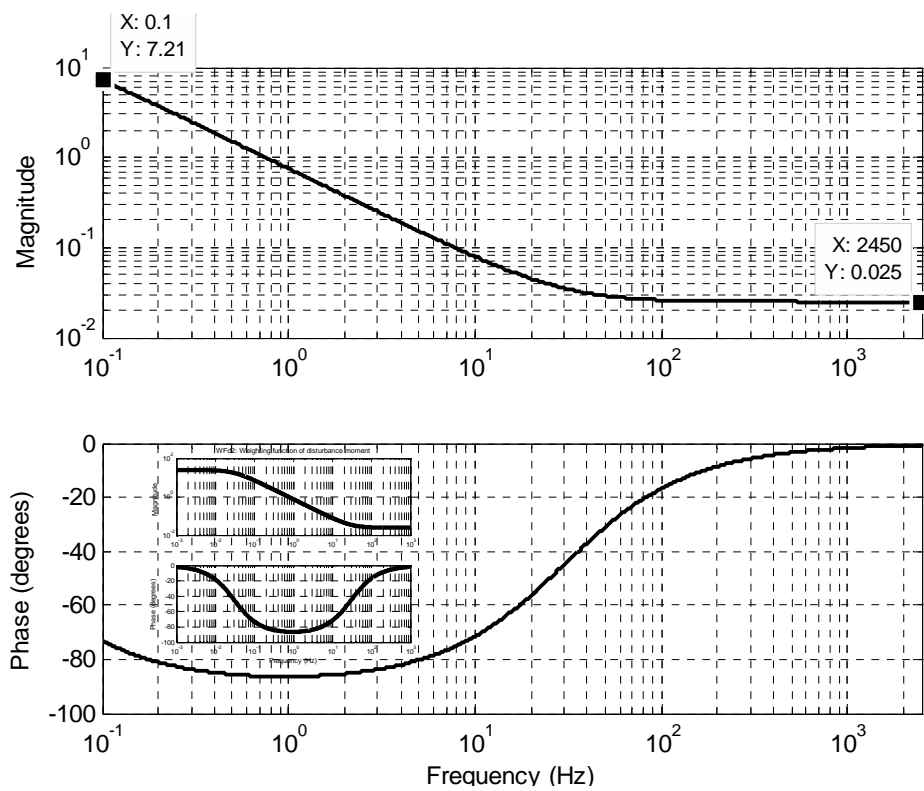
Figure 38. Bode plot of weighting function of disturbance moment

153
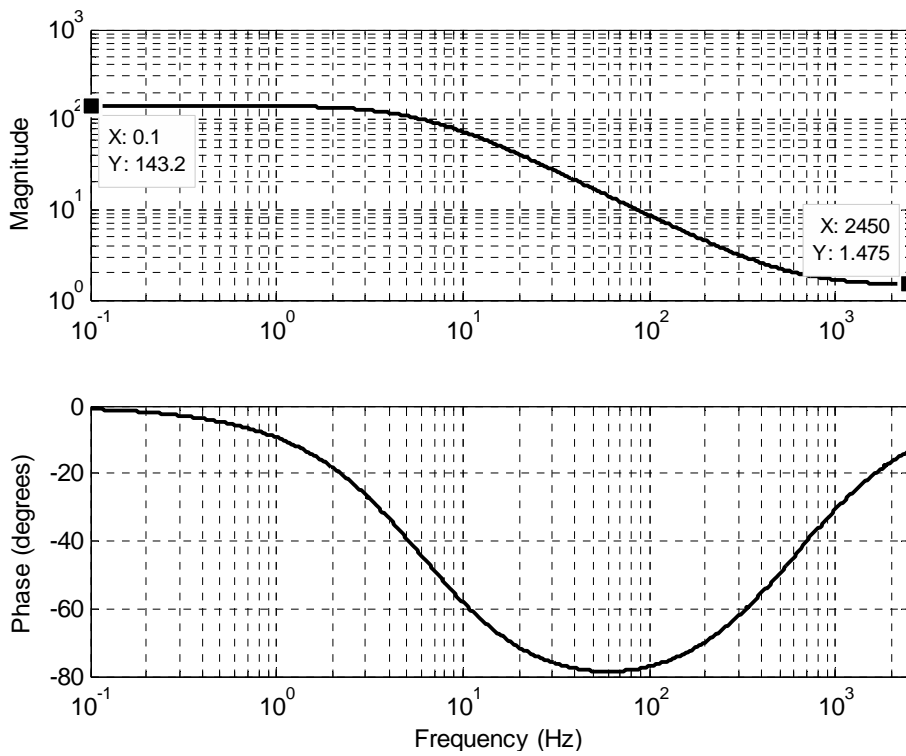
Figure 39. Bode plot of weighting function of performance
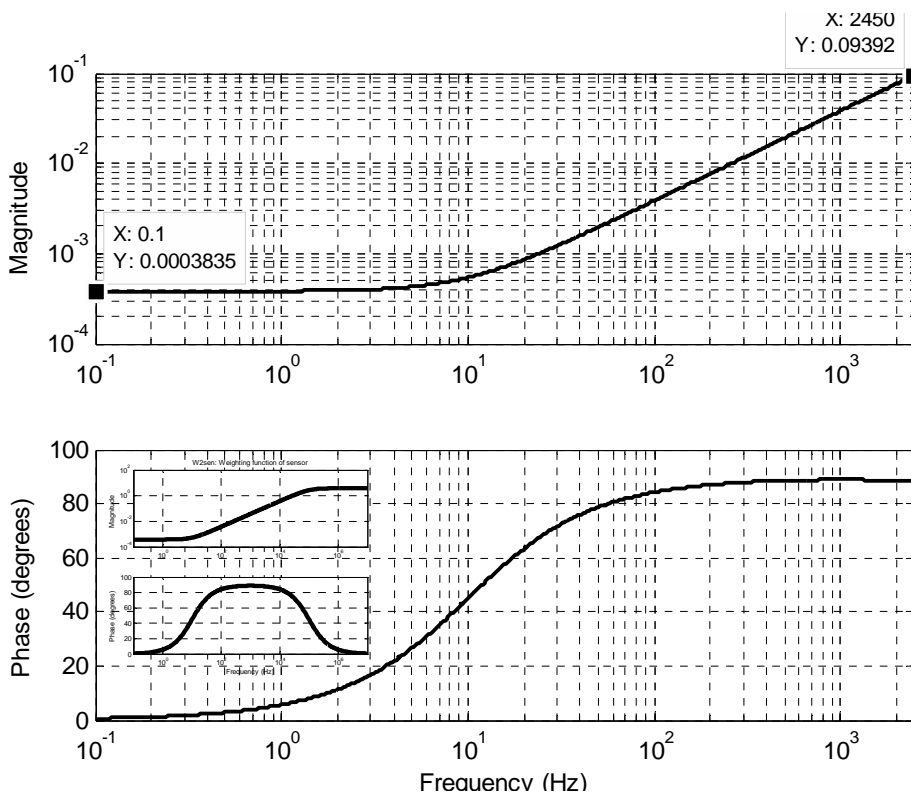
Figure 40. Bode plot of weighting function of sensor

154
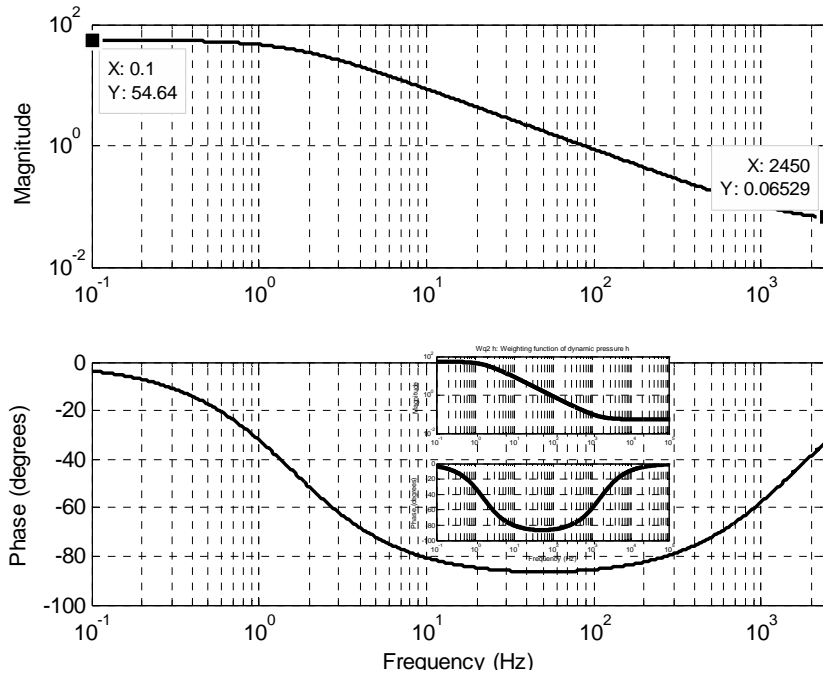
Figure 41. Bode plot of weighting function of dynamic pressure in plunge motion
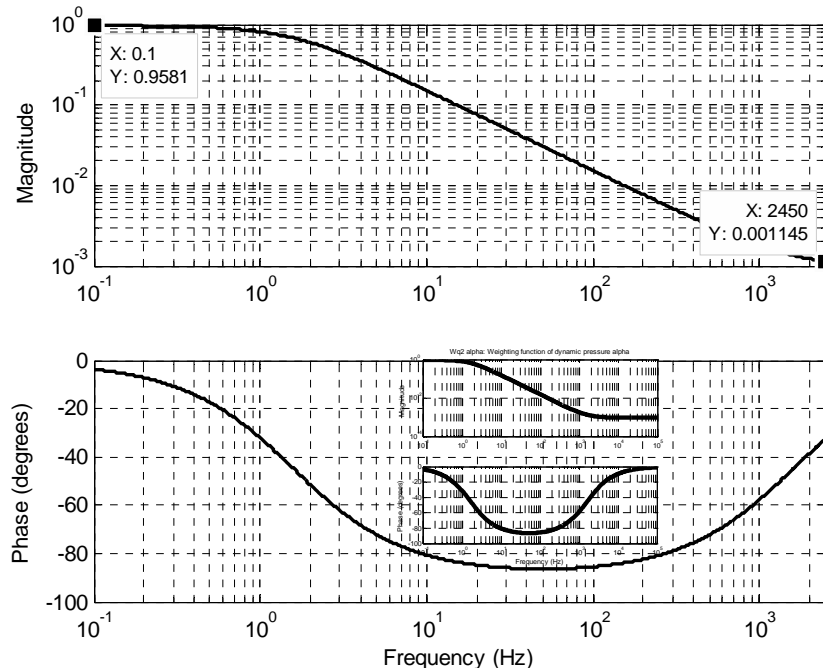
Figure 42. Bode plot of weighting function of dynamic pressure in pitch motion

155
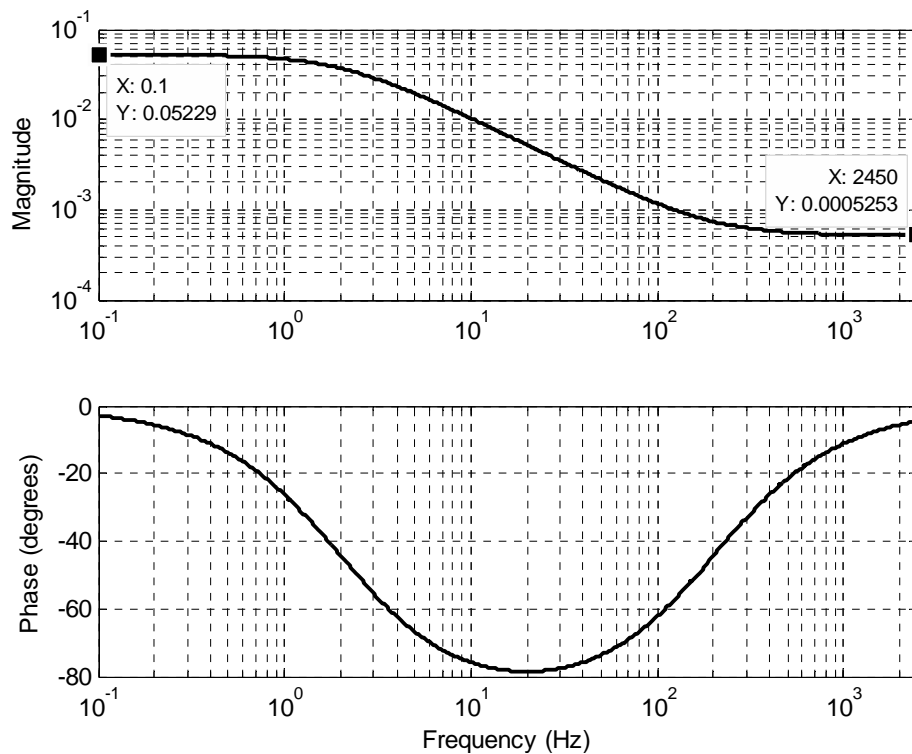
Figure 43. Bode plot of weighting function of command

After the definition of the reference model and the weighting functions, the interconnection structure of the system shown in Figure 16 is constructed by using MATLAB®. The constructed system has 18 states, seven outputs, and eight inputs. The eight of 18 states are physical states of the aeroservoelastic system; four of them are the states of the aeroelastic system, two of them belong to the aerodynamics, two of them are the states of motor dynamics. The rest of the states are the additional fictitious states due to the reference model and uncertainty/performance weightings.

6.2.2.1. H∞ controller synthesis

The controller is synthesized using MATLAB®'s *hinfsyn* command. The synthesized controller has 18 states, same as the number of states of

the interconnection structure system, $[P]$. The frequency plots of the controller are given in Figure 44. The value of the H_∞ norm of the controlled system is obtained between 0.768 and 0.769.
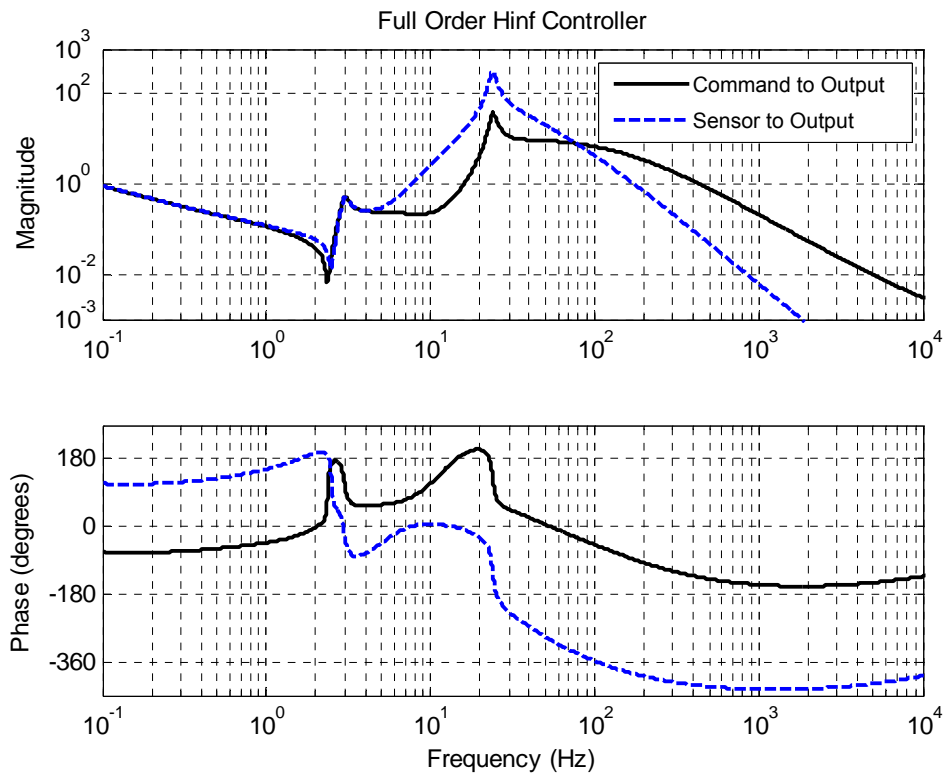
Figure 44. Bode plot of the synthesized H_∞ controller

For a strictly defined system, an H_∞ controller is synthesized in one step. The designer just checks if the norm is less than one or not, which implies whether the controller is a valid robust controller or not. If the norm is greater than one, it means that the obtained controller is not robust to the defined uncertainty/performance weightings. In this case, if the defined system has some freedom, the reference model and/or the weightings are modified in order to reduce the norm. However the result of *hinfsyn* controller synthesis command gives just one number, the H_∞ norm of the closed loop system. This is not sufficient to decide on the system

parameter to be altered. For this reason a simple method, which is not encountered during literature survey, is devised.

In this novel method, the controller is synthesized as usual. During the synthesis, the weighted closed loop system is obtained by using the *hinfsyn* command or constructed later by the *starp* command. As the main step of the method, the infinity norms of each input to output port of the weighted closed loop system are calculated. The results are written in a table as given in Table 13. In this table, the inputs are written in the first column, and the outputs are written in the first row. The infinity norm of an input to an output can be found at the intersection of the corresponding row and column.

Table 13. H∞ norms of input to outputs of $\left[\overline{N} \right]$

	$\{z_1\}_{\bar{q}}$	$\{z_2\}_{\bar{q}}$	$\{z\}_s$	$\{e\}_{per}$	$\{e\}_{act}$
$\{w_1\}_{\bar{q}}$	0.210	0.205	0.028	**0.502**	0.078
$\{w_2\}_{\bar{q}}$	0.029	0.087	0.018	**0.451**	0.051
$\{w\}_s$	0.039	0.190	0.026	0.275	0.312
$\{d_F\}_{Fd}$	0.116	0.113	0.014	0.284	0.042
$\{d_M\}_{Fd}$	0.044	0.046	0.024	**0.606**	0.049
$\{d\}_{cmd}$	**0.535**	**0.458**	0.297	0.124	0.167

Note that the highest value of the table is not equal to but less than the H∞ norm of the system. This is an expected result since the cross effects of the rest of the inputs and outputs are neglected in this method. Another drawback is that the effect of the ideal model cannot be calculated since it has no direct input or output to the system. Nonetheless, the method gives some useful information about the system. This information may be used for more than one purpose:

- Table 13 can be used to alter the system in order to decrease the H_∞ norm of the system below one. Finding the greatest norm from the table, one can decrease the corresponding input value or increase the corresponding output value. These tunings can be performed by changing the parameters of the corresponding weighting function. It can be seen from the table that the most critical input-output relation is between $\{d\}_{Md}$ and $\{e\}_{per}$ which has an infinity norm of 0.606. To decrease the norm of the system, one can increase the weighting $\left[W_{per}\right]$. This means decreasing the performance requirement. Alternatively, the weighting $\left[W_{Fd}\right]$ can be decreased. This means to loosen the steady state error requirement and/or to decrease the robustness requirement for unmodeled aerodynamics. During this modification, one should check the effect of the modified input or output on the others. For example; to decrease the norm from $\{d_M\}_{Fd}$ to $\{e\}_{per}$, one should check both the effect of decreasing $\{d_M\}_{Fd}$ and increasing $\{e\}_{per}$. The decrease of $\{d_M\}_{Fd}$ will decrease all norms in its row, and the increase of $\{e\}_{per}$ will decrease all norms in its column. Since the norms in the column of $\{e\}_{per}$ are greater than the norms in the row of $\{d_M\}_{Fd}$, one should prefer to decrease $\{e\}_{per}$ if it is possible.

- Table 13 can also be used to alter the system in order to increase the H_∞ norm of the system to one. This is the inverse of the first operation. One can select the smallest or the necessary input/output and modify the input/output constraints. During this modification, one should check the effect of the modified input or output to the other parameters as well.

159

- Table 13 may also be used for the model reduction. The least effective inputs and outputs can be selected from the table and removed from the model. It can be seen that $\{w\}_{sen}$ to $\{z\}_{sen}$ input/output cells have all small numbers in the related row and column, which may be a good candidate for a model reduction.

In this thesis the method is used only to decrease the H∞ norm of the system below one.

Once the controller is synthesized, three different reduction methods (Balanced, Hankel, and Residual) are used to decrease the order of the controller. In order to decide on the reduction size, singular values of the balanced system are analyzed, and their ratios to the next singular values are calculated (Table 14 and Figure 45). From Table 14, it can be seen that such ratios of the 10th and 13th singular values are greater than the ratios of their next singular values. Thus, 10th and 13th orders seem to be good starting points for the order of the reduced controller. The first ten states are selected as the initial reduced states. However, it is seen that 10th order reduced controller can not satisfy the robustness requirement whereas the 13th order reduced controller does. It is worthwhile to note that 11th and 12th order reduced controllers could not satisfy the robustness, either. The frequency response plots of controllers obtained with 10, 12, and 13 states are given in Figure 46, Figure 47, and Figure 48, respectively. The infinity norms of the close loop systems for each controller are given in Table 15. It can be seen from the table that norms of the thirteen state Balanced and Hankel controllers are good candidates; however, for the thirteen state Hankel controller some performance relaxation is required to decrease the norm of the closed loop system below one. In this section, the reduced (Balanced) controller with thirteen states is used. Through this study, it is seen by experience that the Hankel

singular value of the full order controller at the number equal to the proper reduction order are in general less than 0.01, mostly between 0.01 and 0.001 for the Balanced method. It can be seen from Table 14 that 13th singular value is less than 0.01, hence it satisfies the generalization.

Table 14. Singular values of controller

#	Hankel Singular Value (SV)	SV ratio $\frac{SV(i)}{SV(i+1)}$	#	Hankel Singular Value (SV)	SV ratio $\frac{SV(i)}{SV(i+1)}$
1	178	1.05	10	0.328	13.12
2	170	8.96	11	0.0250	1.53
3	18.9	1.81	12	0.0163	4.03
4	10.5	4.26	13	0.00405	17.54
5	2.46	1.15	14	$2.31 \ast 10^{-4}$	2.82
6	2.13	1.72	15	$8.19 \ast 10^{-5}$	8.07
7	1.24	1.91	16	$1.01 \ast 10^{-5}$	140.77
8	0.650	1.87	17	$7.21 \ast 10^{-8}$	991.75
9	0.348	1.06	18	$7.27 \ast 10^{-11}$	-

Note that, the norm of the system with reduced controller is still about 0.77; hence, if desired, a further improvement can be achieved via increasing the value of $\bar{q}_{dist}$. However, at this stage the analysis are performed with this controller.
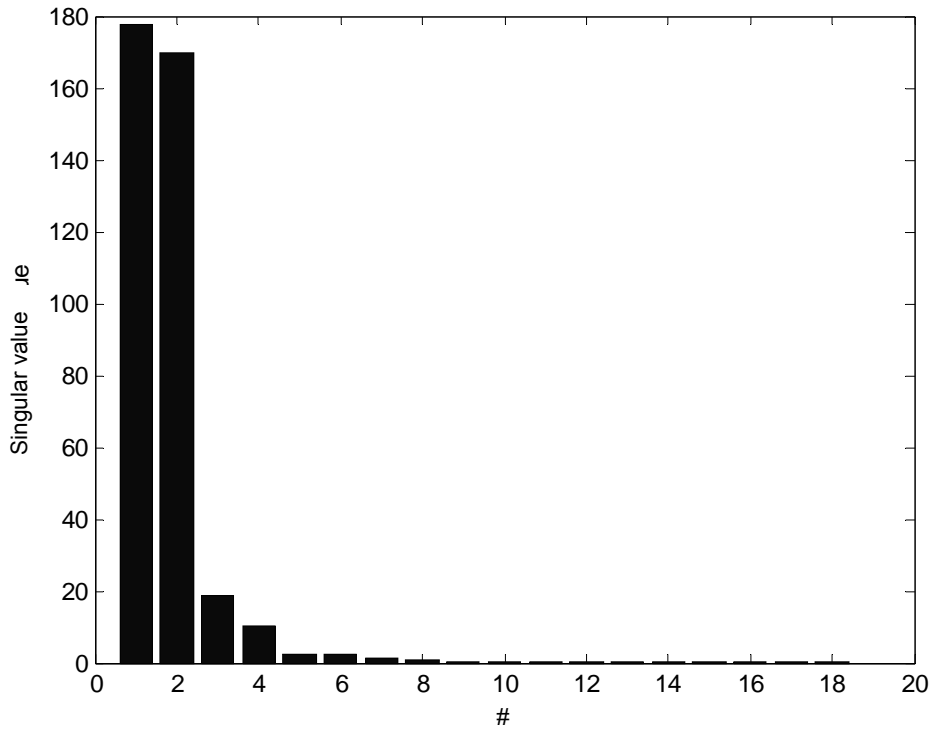
Figure 45. Singular values of the controller
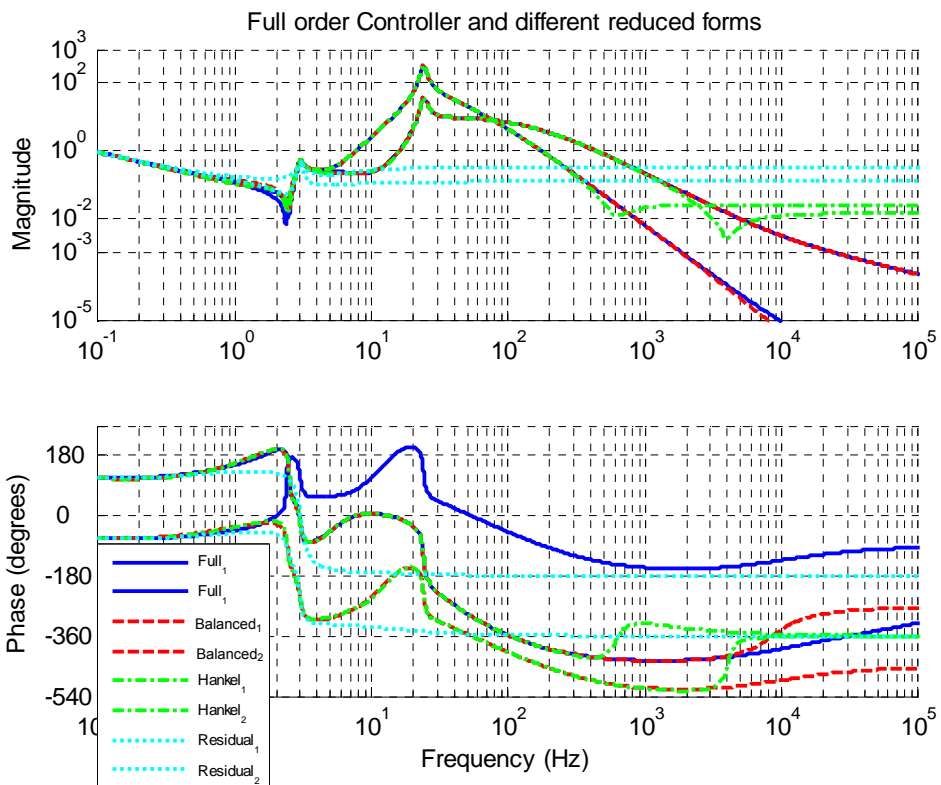
Figure 46. 10th order reduced controllers

162
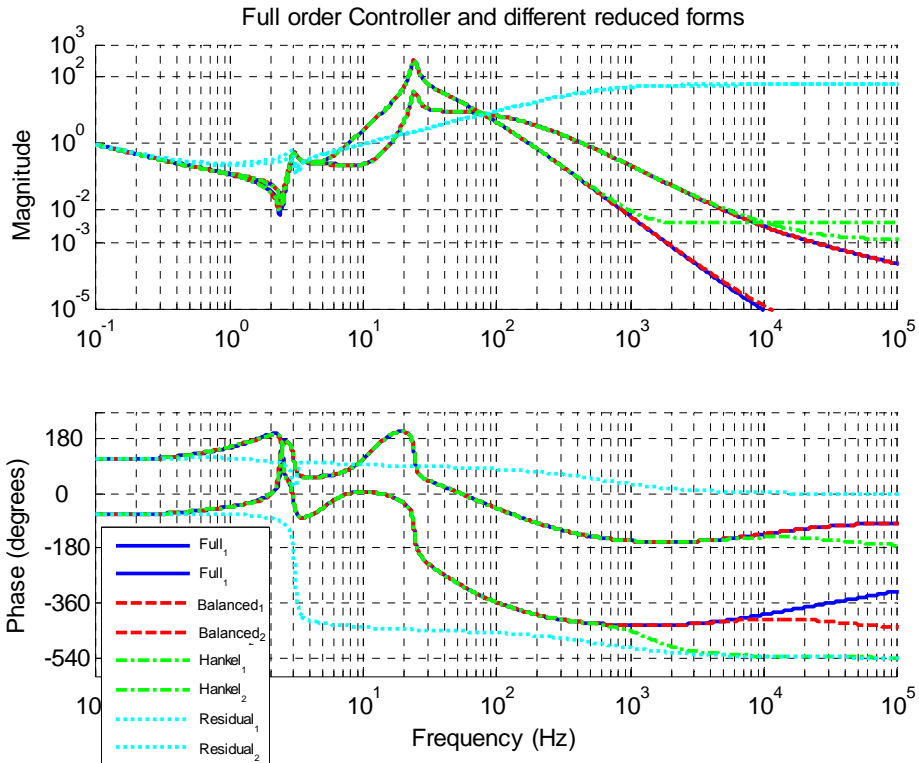
Figure 47. 12th order reduced controllers
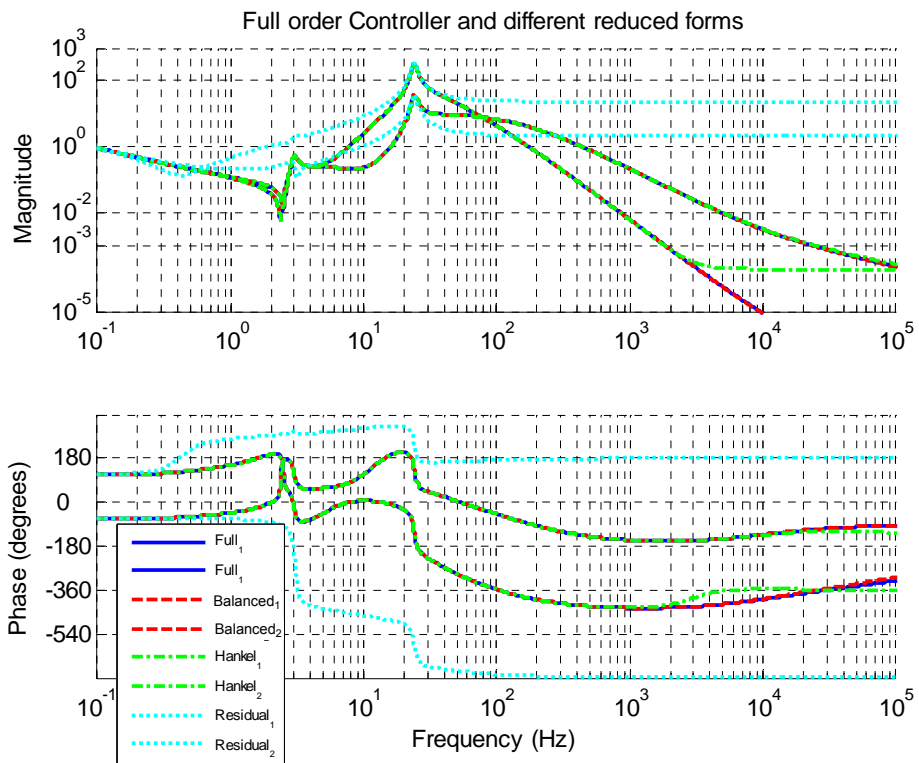
Figure 48. 13th order reduced controllers

163

Table 15. Infinity norm of weighted close loop systems

Controller		Infinity norm of closed loop system is between		Frequency (Hz)
Reduction Method	Order			
-	Full	0.768	0.769	0
Balanced	10th	315.15	315.46	4.76
Hankel	10th	338.46	338.80	Inf
Residual	10th	-	-	-
Balanced	12th	6.518	6.525	4.68
Hankel	12th	54.071	54.126	Inf
Residual	12th	-	-	-
Balanced	**13th**	**0.768**	**0.769**	**0**
Hankel	13th	2.555	2.558	Inf
Residual	13th	-	-	-

6.2.2.1.1. Analysis

Once the reduced controller is synthesized, the aeroservoelastic system is constructed with a similar procedure as explained in Chapter 4. In this Section, the analyses that are presented in previous Chapters are performed for the aeroservoelastic system constructed. Initially a step response analysis is performed by using the constructed aeroelastic and aeroservoelastic state space equations. After confirming that the controller works properly and suppresses the oscillations, the frequency domain analyses are performed. In order to compute the stability limits, μ-method and p-method analyses are conducted by varying the dynamic pressure. Time domain analyses are performed in order to verify the dynamic pressure of instability of the aeroservoelastic system computed by flutter search methods. Both μ-method and p-method are also used to calculate the airspeed of instability, and flutter free flight envelopes are computed. Then the step response and backlash analyses are performed for the aeroservoelastic system.

6.2.2.1.1.1.   The initial time domain analysis

A time domain analysis is performed as a response to a non-zero initial conditions. The non-zero initail condition is the pitch angle of the fin, which is set as 10°. The response of the natural and the controlled system are given in Figure 49. As it can be seen from the figure, the controlled system has a faster response in the controlled pitch motion than the natural system, but with some higher deflections. This is due to the fact that an initial condition release is not modeled in the controller synthesis. An initial condition release is analogous to a step command, which is well above the expected command defined in Table 12. In the Simulink® model, a limiter is added to the command input for this purpose, as defined in Section 5.2. Furthermore, the aeroelastic equations are derived for zero initial conditions of the plunge and pitch positions; which is also disregarded in this analysis. However, this analysis gives a quick opinion about the system. In the plunge motion, higher deflections occur in the controlled system, but the motion dies out faster than the natural system. The plunge response is damped out much later than the pitch response, because the plunge motion is the uncontrolled degree of freedom; i.e., the controller does not have a direct mission to suppress the plunge mode.

6.2.2.1.1.2.   Frequency domain analyses

The aeroservoelastic system is also analyzed in the frequency domain. Solutions of these analyses at the nominal dynamic pressure are given in Figure 50 through Figure 57.
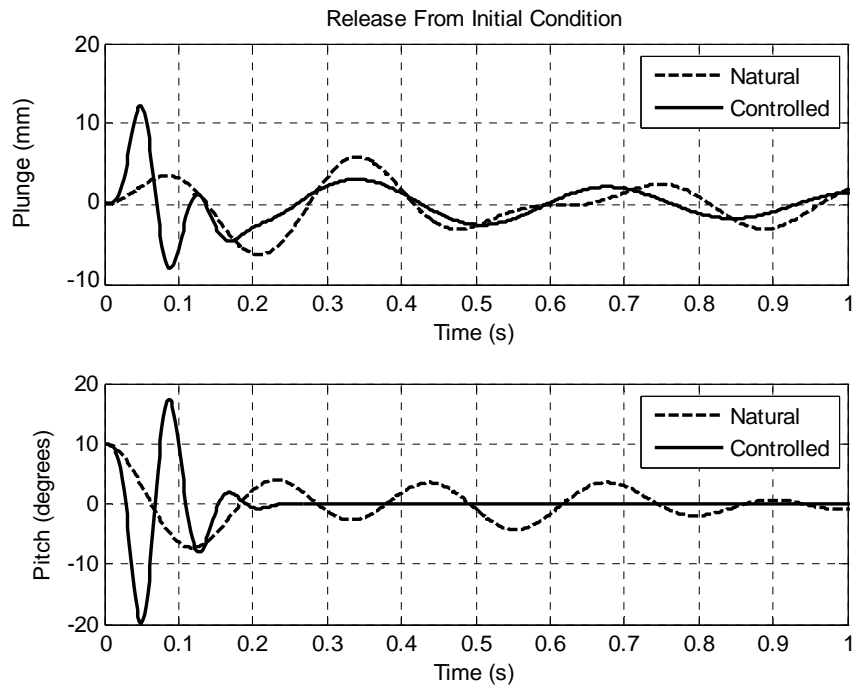
(a) first one second
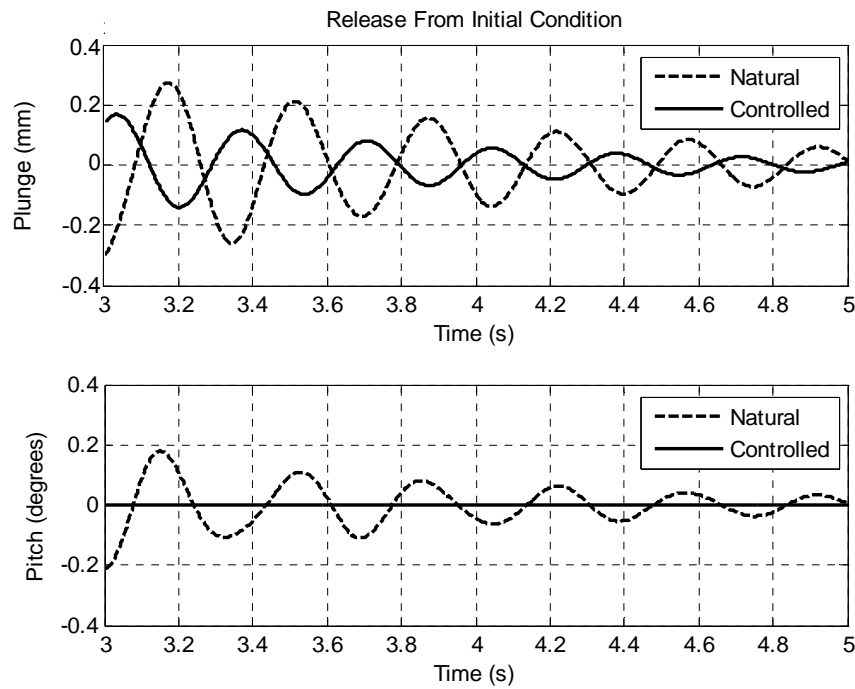
(b) plots between third and fifth seconds

Figure 49. Time response of the natural and the controlled Model 1 with H_∞ controller (release from 10° initial pitch position)

In Figure 50, the transfer function of the aeroservoelastic system from command input to pitch motion is given. It can be seen from the figure that the magnitude satisfies the 6 Hz bandwidth requirement. However, the 90° phase shift occurs at ~5.87 Hz, which is slightly below the requirement. At this point, the slight decrease of bandwidth is accepted. The bandwidth is also crosschecked with the full order controller but the same problem is observed. Thus, it is concluded that the order reduction is not the cause of the decrease of bandwidth. In Figure 51, the effect of the command input of pitch motion on the plunge motion output is given. This plot is mainly given in order to check if the amplitude of the plunge motion is in acceptable limits. Note that there exists a dip slightly above 2 Hz and a peak in 3 Hz. This dip and peak also exist in Figure 53, the frequency response from 'disturbance to dynamic pressure affected on aerodynamic moment' to plunge motion of the nominal aeroelastic system. Remembering that the system has aeroelastic poles, too, it is concluded that these are the anti-resonance and the resonance of the aeroelastic system.

In Figure 52 through Figure 55 the effect of 'disturbance to dynamic pressure' on the pitch and plunge motions are plotted. From the figures it can be seen that the disturbance to dynamic pressure causes greater motions in the aeroelastic system than the aeroservoelastic system. Motions of the systems are comparable only in the plunge motion, if the disturbance to dynamic pressure is affected on aerodynamic lift (Figure 55). Hence, it can be concluded that the controlled system performs a good suppression to the disturbance to dynamic pressure. The effects of the aerodynamic disturbance on the pitch and plunge motions are not given, since the plots are identical to their plots given in Figure 52 through Figure 55. Both inputs are kept in the system in order to define the 'disturbance to dynamic pressure' and 'aerodynamic disturbance forces'

separately. Note that 'aerodynamic disturbance force' uncertainties are also used to decrease the steady state error in this study.

In Figure 56 and Figure 57, the effects of the sensor noise to the pitch and plunge inputs are given. It is seen that the noise results in a small peak in pitch motion between 2 Hz and 2.5 Hz, which is close to the frequency of motor obtained by using the torsional stiffness of the fin.

In Figure 58, the frequency responses of the aeroservoelastic system from the command input to the pitch output are given for various values of dynamic pressure. It can be seen from the plots that the magnitude increases around 5.5 Hz as the dynamic pressure approaches to 5,582 Pa, and a 180° phase jump occurs at 5,582 Pa. Thus, it can be concluded that the damping ratio of the aeroservoelastic system becomes zero at 5,582 Pa, and the system becomes marginally stable at this point. From subplot (b) it can be seen that above 4,000 Pa a 30% decrease occurs at ~1.8 Hz, which is below 6 Hz. From subplot (c), the frequency at which a 90° phase lag occurs is calculated for the graphics of 1,000 Pa dynamic pressure via interpolation as ~5.6 Hz. Although the bandwidth value is degraded, an acceptable bandwidth is obtained at 1,000 Pa. Note that, at the start of the synthesis a 6 Hz bandwidth and a disturbance to dynamic pressure of 500 Pa is required. Note that, at the start of the synthesis a 6 Hz bandwidth and a disturbance to dynamic pressure $\bar{q}_{dist}$ of 500 Pa is required. The upper limit of the dynamic pressure can be obtained by adding the $\bar{q}_{dist}$ on the nominal dynamic pressure as

$$\bar{q}_0 + \bar{q}_{dist} =\sim 621\,\text{Pa} \tag{6.4}$$

168
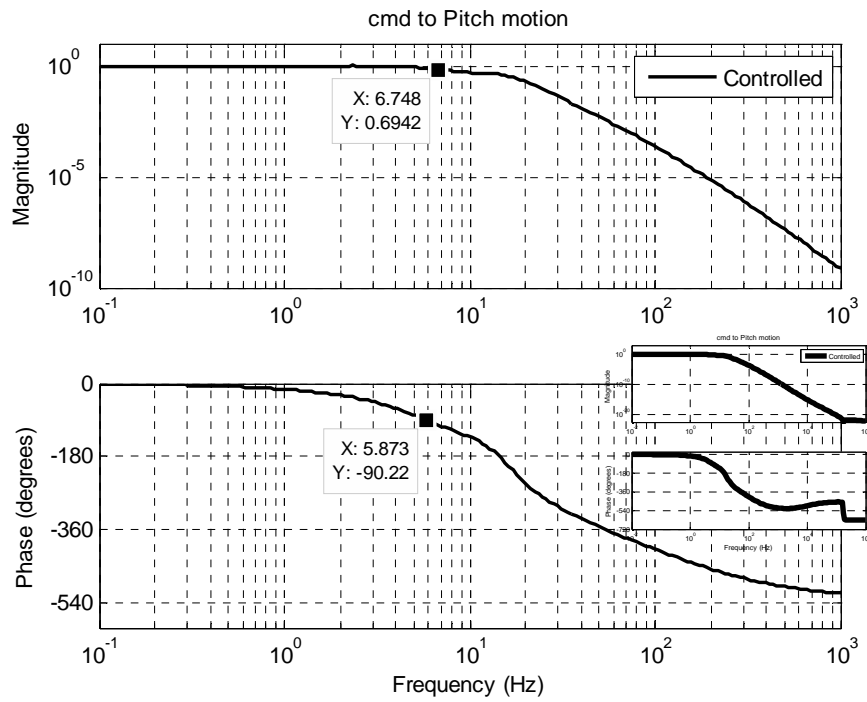
Figure 50. Frequency response from command input to pitch motion
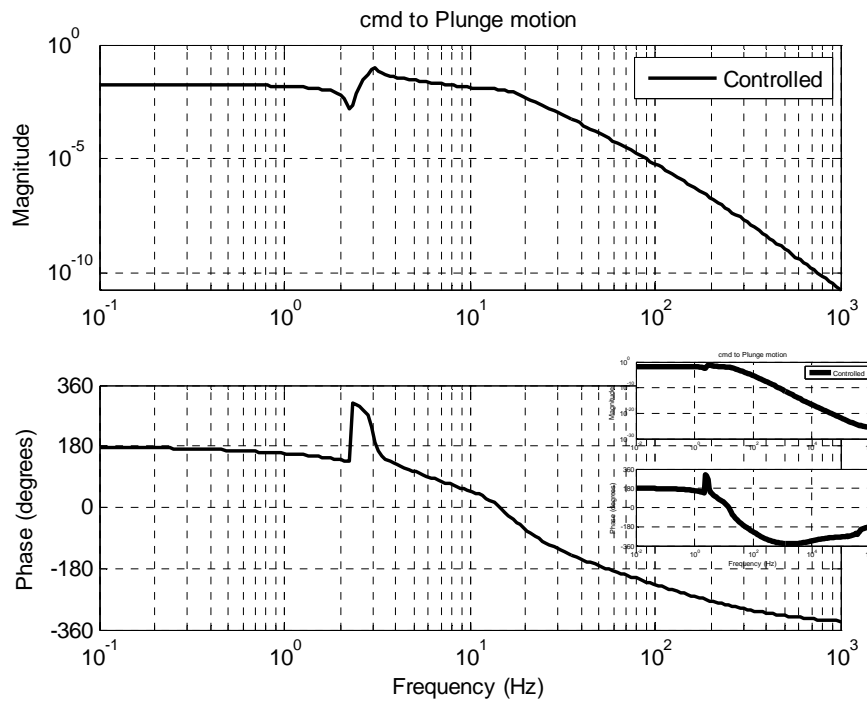
Figure 51. Frequency response from command input to plunge motion

169
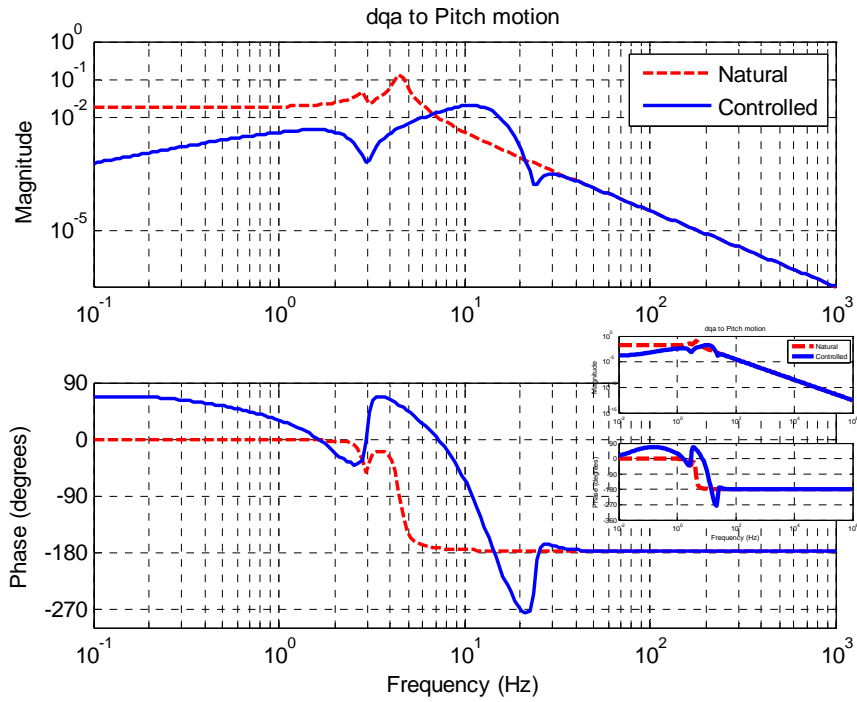
Figure 52. Frequency response from disturbance to dynamic pressure affected on aerodynamic moment to pitch motion
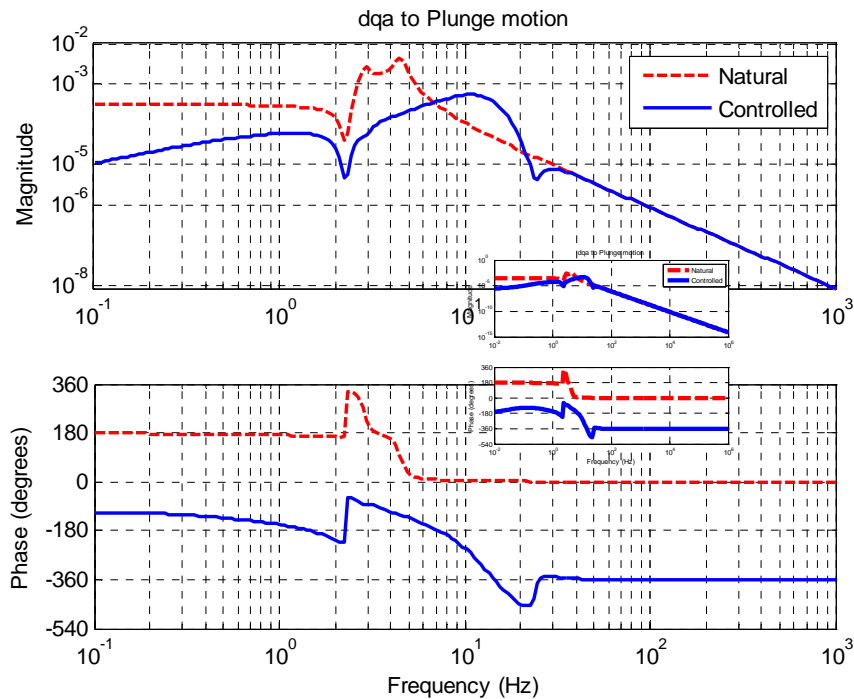
Figure 53. Frequency response from disturbance to dynamic pressure affected on aerodynamic moment to plunge motion
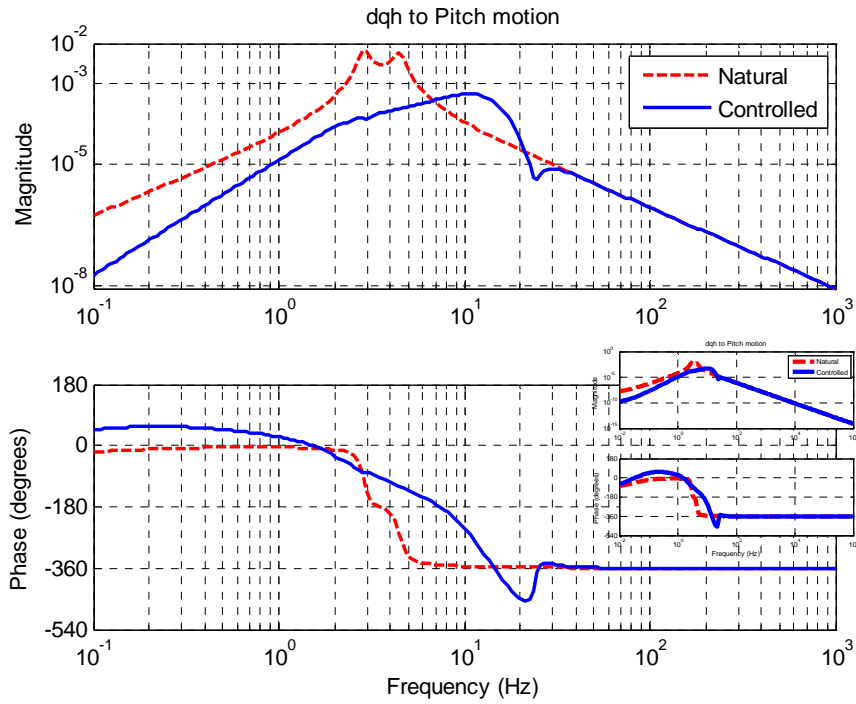
Figure 54. Frequency response from disturbance to dynamic pressure
affected on aerodynamic lift to pitch motion
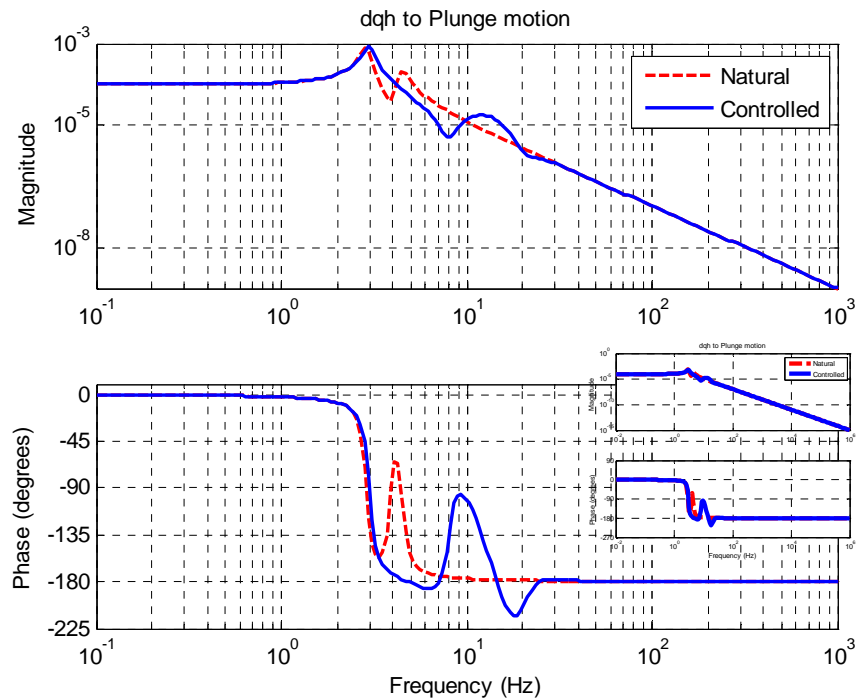
Figure 55. Frequency response from disturbance to dynamic pressure
affected on aerodynamic lift to plunge motion

171
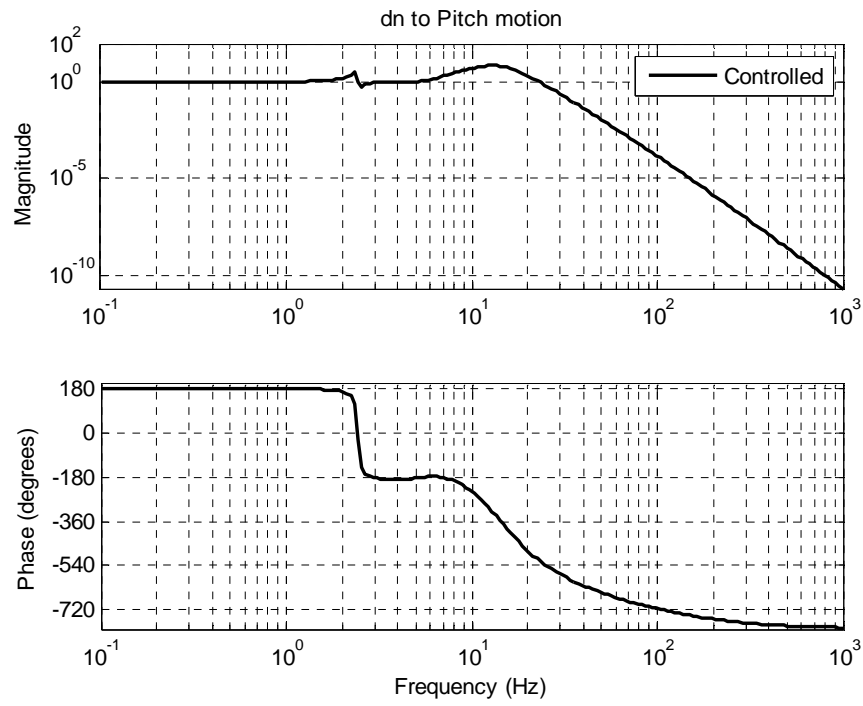
Figure 56. Frequency response from sensor noise input to pitch motion
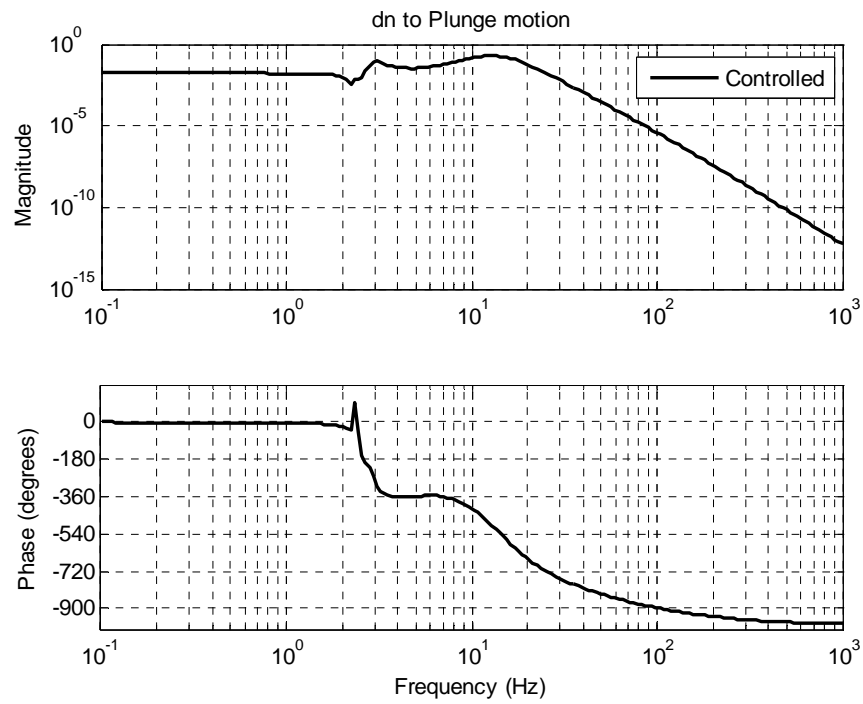
Figure 57. Frequency response from sensor noise input to plunge motion

172
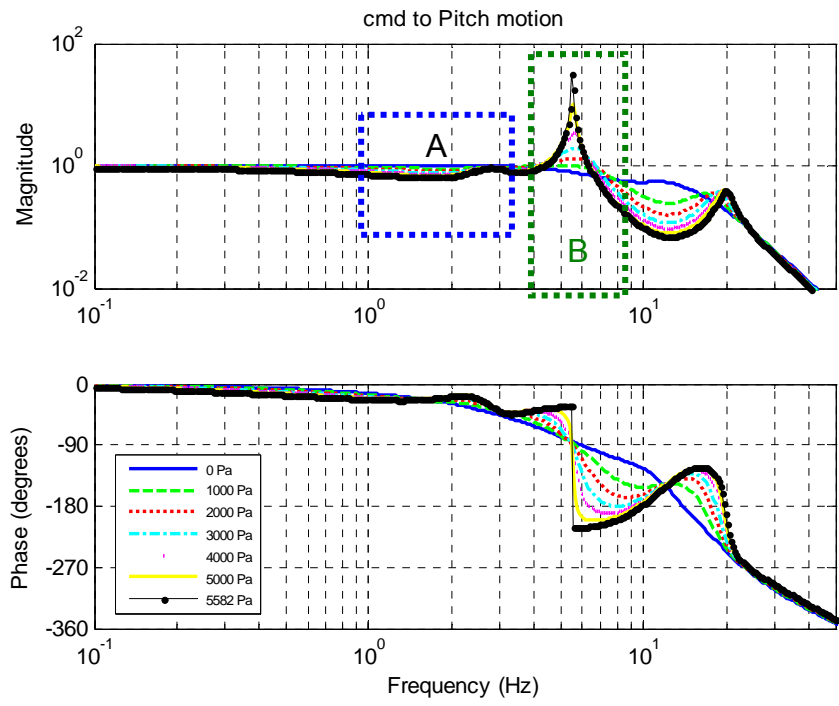
(a) main graphics
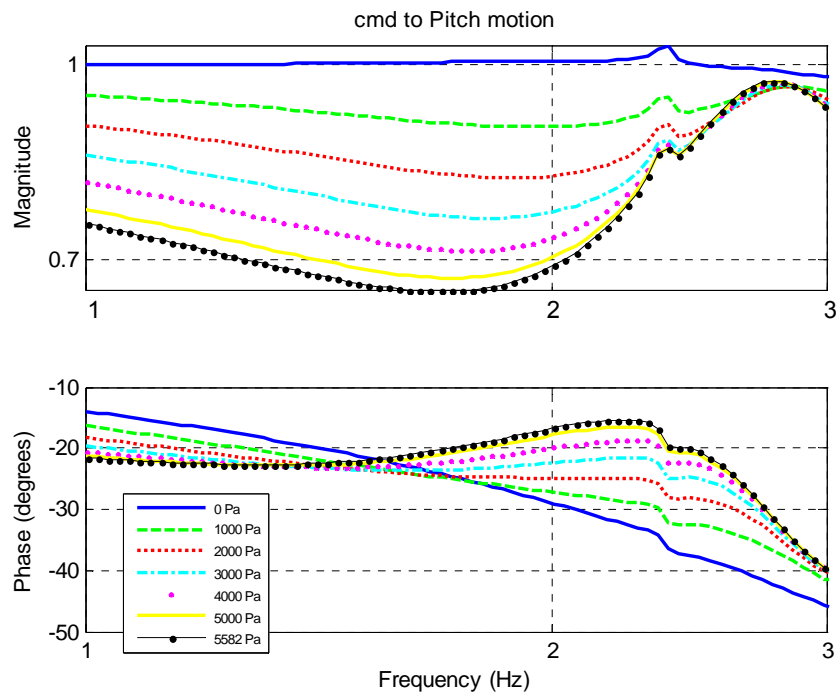
(b) detailed graphics of section A
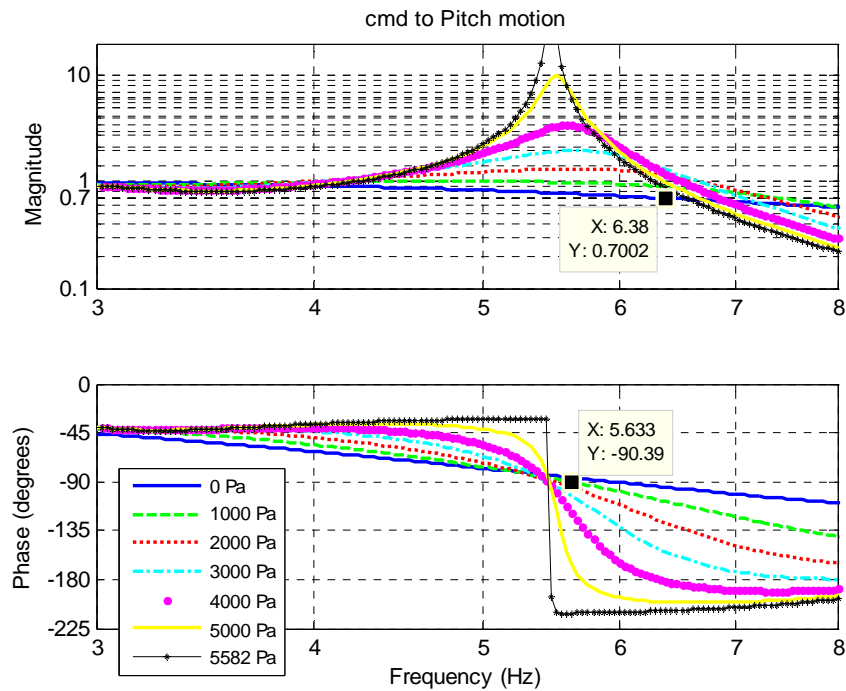
(c) detailed graphics of section B

Figure 58. Frequency response from command input to pitch motion for various values of dynamic pressure

6.2.2.1.1.3. Stability analysis by varying dynamic pressure

Similar to the nominal aeroelastic system, stability analyses are performed for the nominal aeroservoelastic systems in order to compute the dynamic pressure of instability of the system. The μ-method analyses are performed for the upper and lower dynamic pressure of instabilities as defined in Section 3.3.1. Results of iterations of the μ-method analyses are presented in Figure 59. The upper limit search is performed between 0 Pa and 50,000 Pa above the initial dynamic pressure. The disturbance value of dynamic pressure that destabilizes the system is computed as 5,423 Pa. Similarly, a lower search is performed below 0 and 10,000 Pa of initial dynamic pressure, and the disturbance value of the dynamic pressure for the lower limit is computed as 979 Pa. The frequency of the instability is

calculated from the corresponding pole of the system at each case. The *μ*-method analyses results for both the aeroelastic and the aeroservoelastic systems are given in Table 16. From the results it is seen that the synthesized H∞ controller can successfully suppress the flutter of the nominal aeroservoelastic system for the initial airspeed at sea level. Note that the dynamic pressure of nominal ASE instability is 5,423 Pa greater than the $\bar{q}_0$, the dynamic pressure at which the controller is synthesized, which is 161 Pa. This difference, which is taken as the stability margin, is larger than the design requirement of 500 Pa. The difference between the design value and the result of the nominal analysis is an expected result. Since, the additional robustness and performance requirements that are used in the controller synthesis are neglected in nominal stability analysis.

Table 16. Instability points of Model 1 with H∞ controller

Dynamic pressure of flutter of the AE system	$\bar{q}_{flut}$	Pa	665
Frequency of flutter of the AE system	ω_{flut}	Hz	3.5
Lower dynamic pressure of instability of the ASE system	$\bar{q}_{ins_{low}}$	Pa	-818
Frequency of lower instability point of the ASE system	$\omega_{ins_{low}}$	Hz	11.8
Upper dynamic pressure of instability of the ASE system	$\bar{q}_{ins}$	Pa	5,582
Frequency of upper instability point of the ASE system	ω_{ins}	Hz	5.5
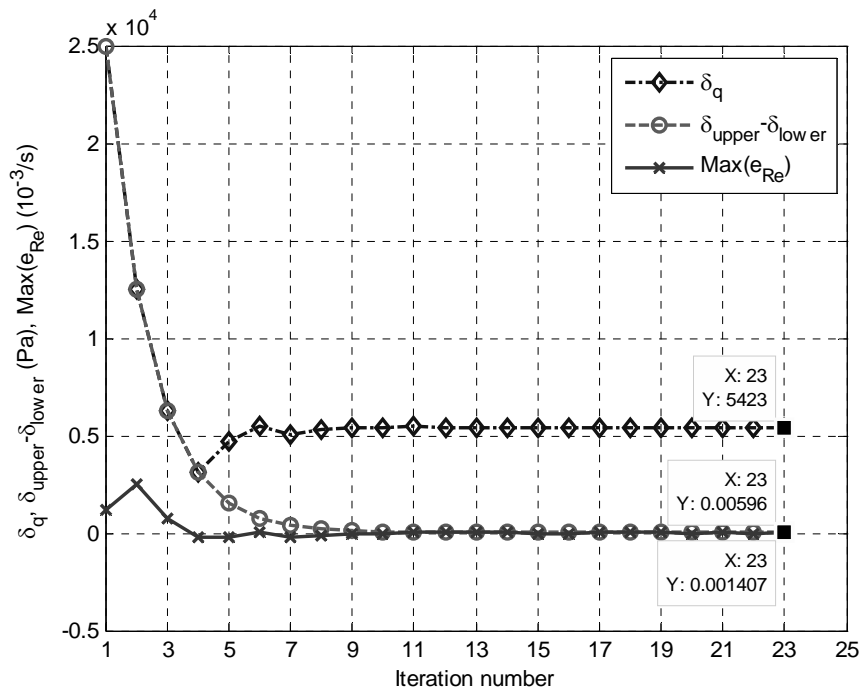
(a) upper limit search results
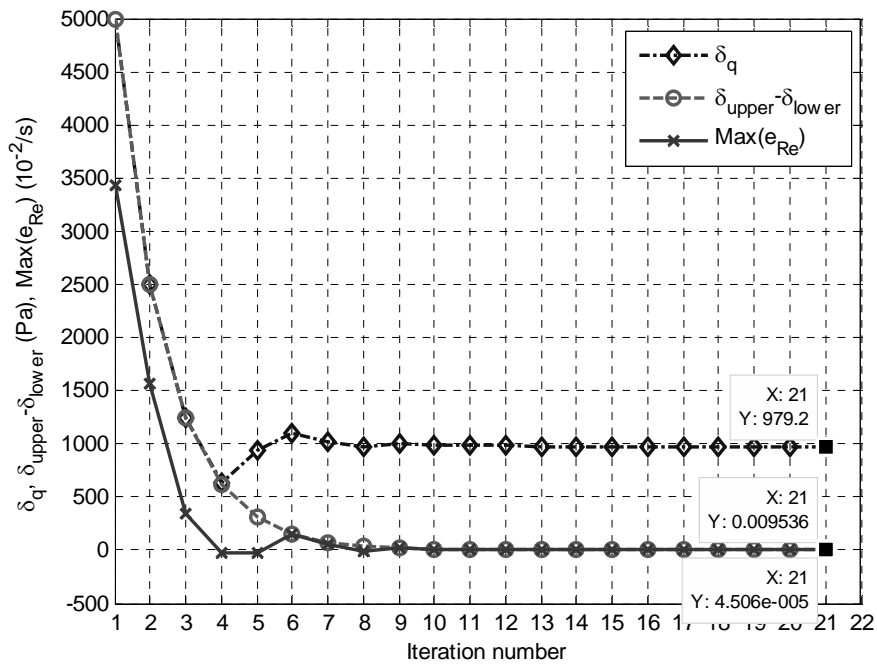
(a) lower limit search results

Figure 59. Flutter search results of μ-method

176
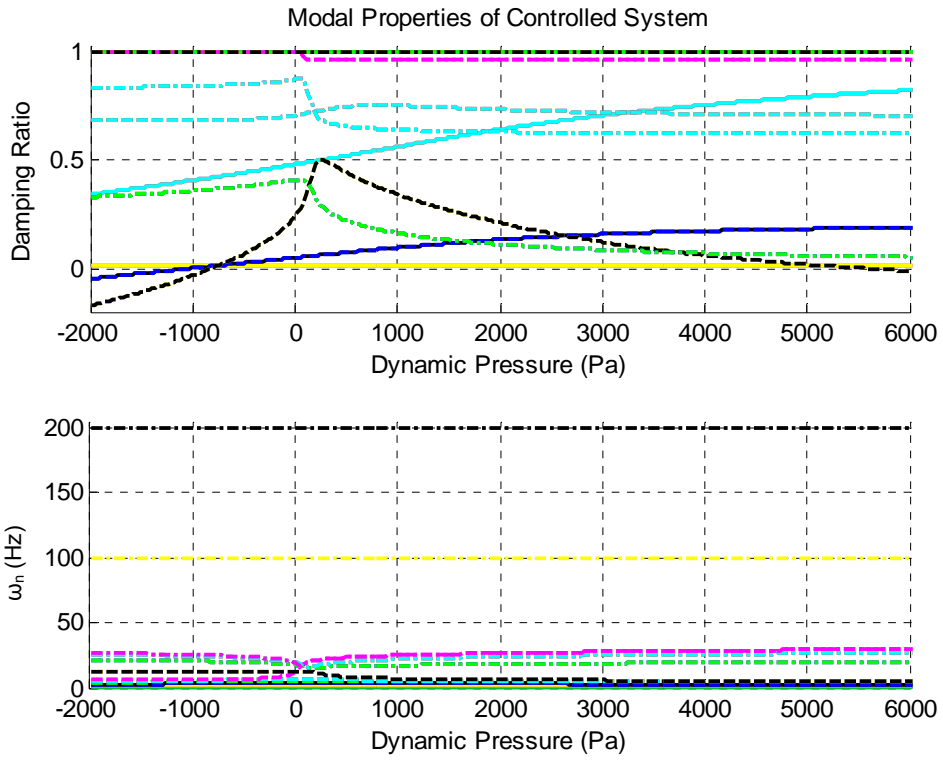
(a) damping and frequency versus dynamic pressure
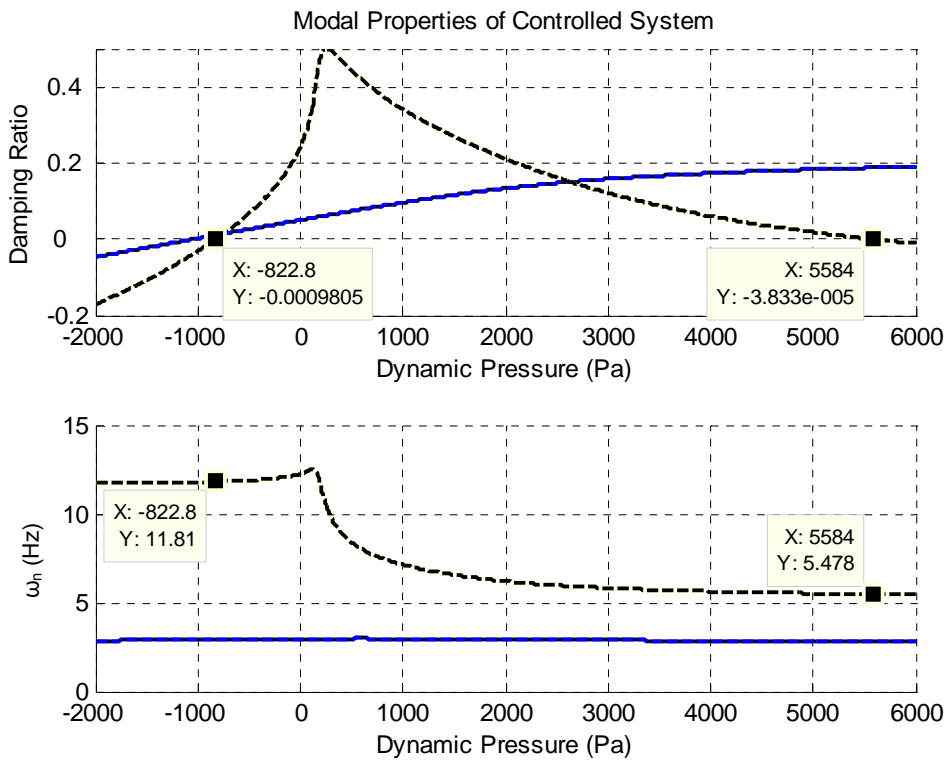
(b) damping and frequency versus dynamic pressure for instable modes
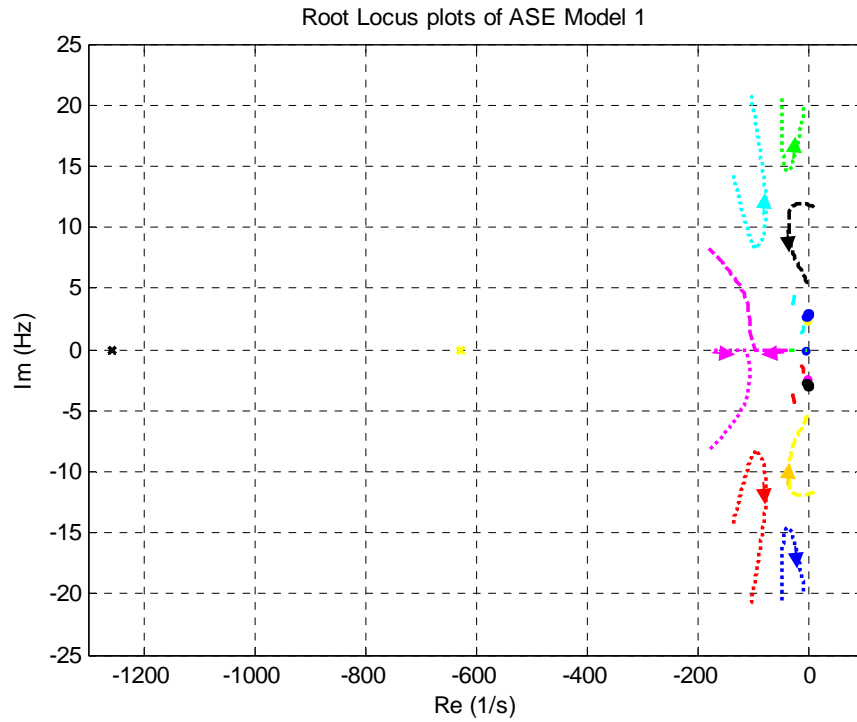
(c) root locus
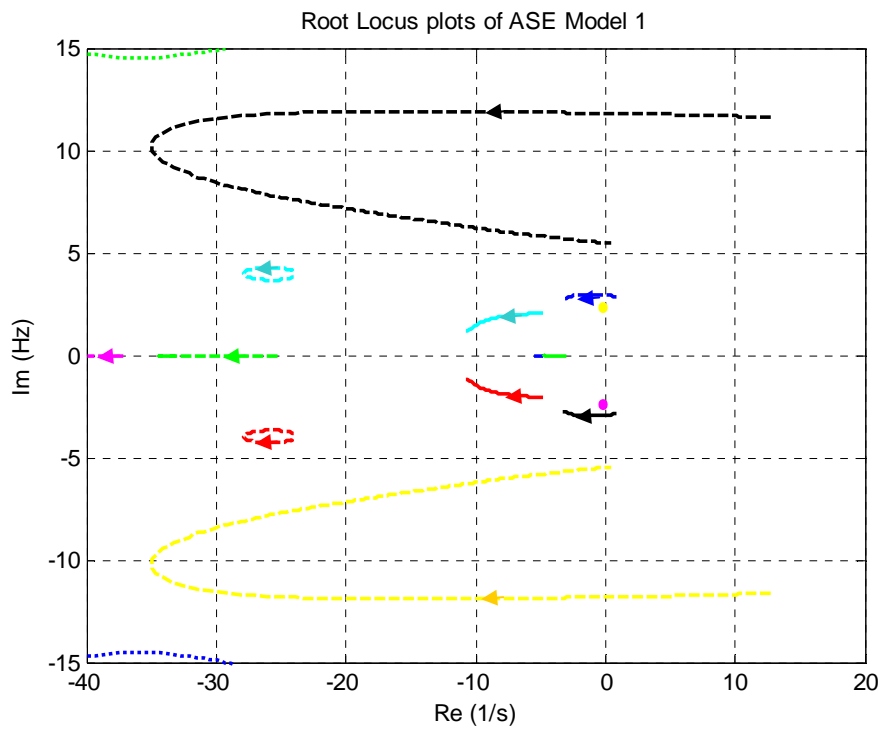
(d) root locus detail

Figure 60. Flutter search results of p-method by changing air density

In order to crosscheck the results of the μ-method analyses, a p-method analysis is performed similar to the aeroelastic case. The results of the p-method analysis are given in Figure 29. It can be seen that the damping value becomes negative slightly above -822 Pa and slightly below 5,584 Pa. The damping value of the aeroservoelastic system is positive between these values, thus the system is stable. Comparing the results of the two methods it can be seen that their results are consist.

In order to cross-check the dynamic pressure of instability results obtained by using the μ-method and the p-method, the time domain model is used. For the time domain analysis the Simulink® model presented in Section 5.2 is used with the synthesized H_∞ controller. In order to simulate the real environment, the H_∞ controller is converted to discrete form. In the conversion, the sampling time is chosen as 1/2500 s, which is a possible execution interval of code on the xPC-target. The frequency response of the discrete H_∞ controller is given in Figure 61.
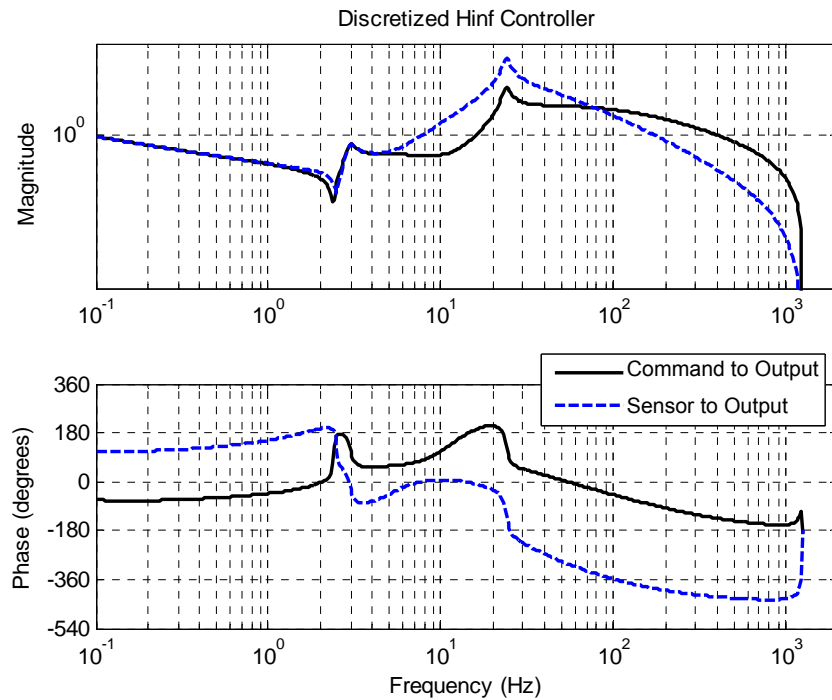
Figure 61. Frequency response of discrete controller

The time domain simulations of the aeroservoelastic system are performed at, slightly over, and well over the dynamic pressure of instability. The analyses are performed without any uncertainty or disturbance. In order to see the effect of sensor quantization, two different sets of analyses are performed. The results are given in Figure 62. In figure (a), (c), and (e) the results for a linear sensor are given. It is seen that the time domain results are in accordance with the previous results. Introducing the sensor quantization, it is seen that for small disturbances the instability is not initiated, rather small amplitude oscillations occur at the dynamic pressures that are slightly over the dynamic pressure of instability. However, a large amount of disturbance can still cause the instability.
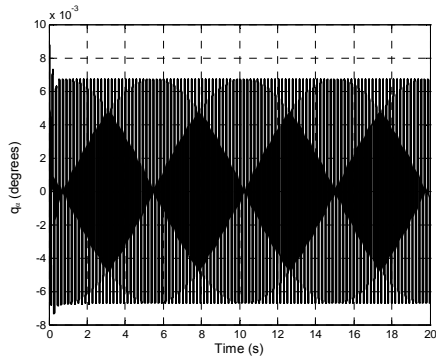
(a) $\bar{q}$ =5,582 Pa, δ_{dist} =0.1 N.m
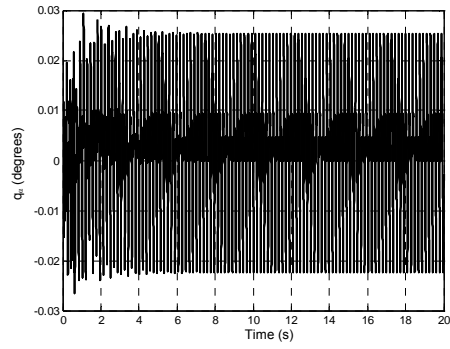
(b) $\bar{q}$ =5,582 Pa, δ_{dist} =0.1 N.m, quantized feedback
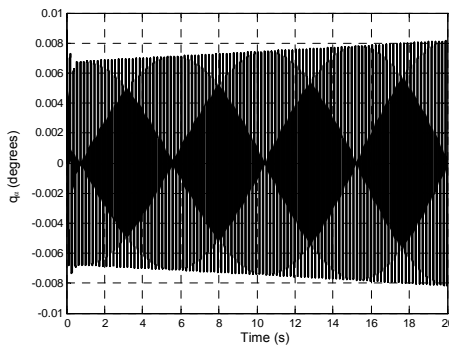
(c) $\bar{q}$ =5,592 Pa, δ_{dist} =0.1 N.m
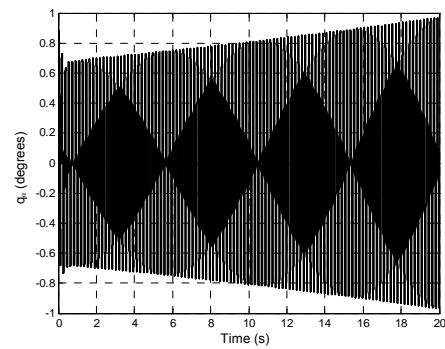
(d) $\bar{q}$ =5,592 Pa, δ_{dist} =10 N.m, quantized feedback
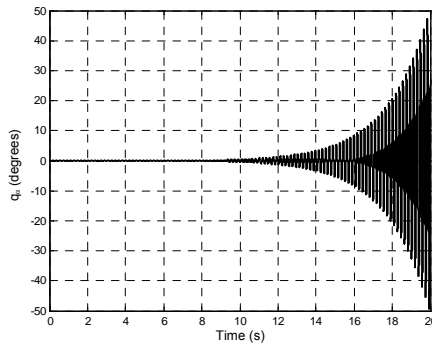
(e) $\bar{q}$ =6,082 Pa, δ_{dist} =0.1 N.m
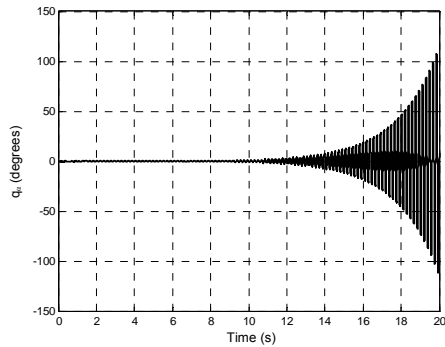
(f) $\bar{q}$ =6,082 Pa, δ_{dist} =0.1 N.m, quantized feedback

Figure 62. Time domain simulation results at and above the dynamic pressure of instability

6.2.2.1.1.4. Stability analysis by varying airspeed

Similar to the analysis of aeroelastic system, the airspeed of instability is calculated for the aeroservoelastic Model 1 by using the iterative procedure given in Section 3.4.1. Results are given in Table 17. It can be seen from the table that the error between the calculated airspeeds of instability drops below one percent at the 5th iteration. The airspeed of instability is obtained as 95 m/s. For the verification of the result, the p-method is used again. The calculations of the p-method are performed at 100 points, by changing the airspeed from 1 to 100 m/s. Hence the results are calculated with 1 m/s intervals. The results are given in Figure 63. In the frequency versus airspeed plot, two modes, those have the frequencies around 100 Hz and 200 Hz, are not plotted for ease of analyzing the figure. As it can be seen from the figure, the airspeed of instability is found slightly below 95 m/s, which is in agreement with the result of μ-method.

Table 17. Results of flutter airspeed search

	iteration #		1	2	3	4	5
Input Parameters	U_0	m/s	16.86	99.24	82.76	95.50	92.95
	$\bar{q}_0$	Pa	161.2	5,582.3	3,883.8	5,172.1	4,899.1
Output Parameters	$\bar{q}_{flut}$	Pa	5,582.3	-	5,172.1	-	5,115.9
	U_{flut}	m/s	99.24	-	95.50	-	94.98
	%error of U_{flut}	%	-	-	-3.77	-	-0.54
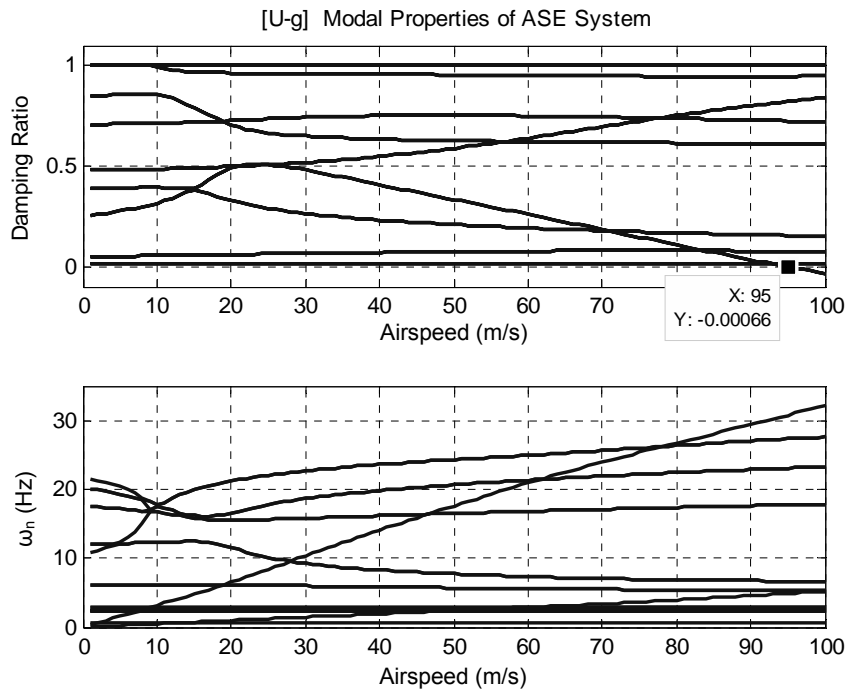
Figure 63. Flutter search results of p-method by changing airspeed
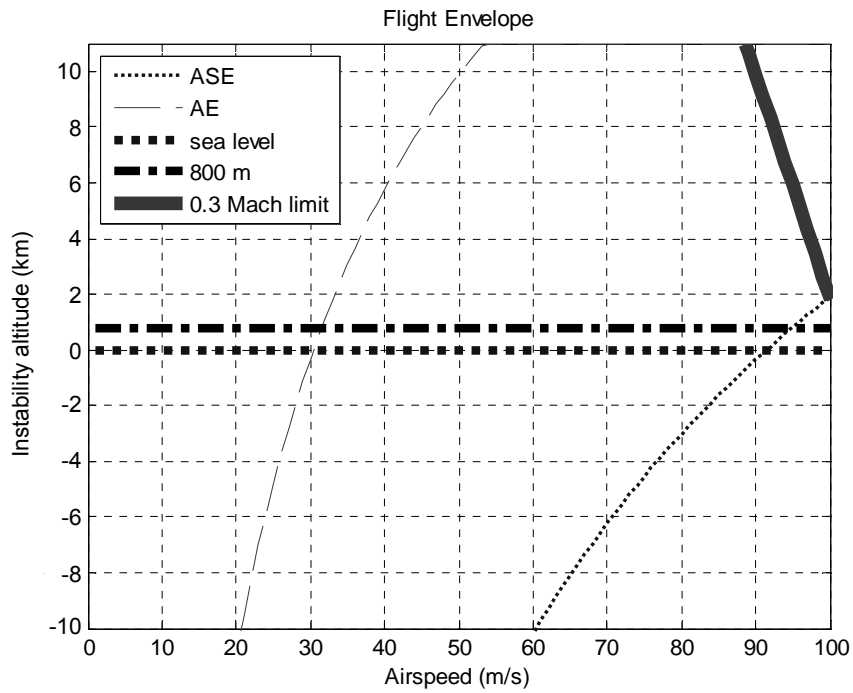
Figure 64. Flutter flight envelope

The flutter free flight envelopes of the aeroelastic and aeroservoelastic systems are derived by using the method given in Section 3.4.1. The results are presented in Figure 64. The plot contains the sea and ground level lines, as well as the 0.3 Mach line, which is the limit of the incompressible flow. The systems are stable on the left and upper part of the corresponding stability lines. It can be seen that the synthesized H$_\infty$ controller enlarges the stability envelope of the aeroelastic system.

6.2.2.1.1.5.   Time domain step response analyses

The results of the time domain solutions at dynamic pressure of 0 Pa and 4,000 Pa to a 1° step command are depicted in Figure 65 through Figure 68. In these simulations, noise and disturbances are not introduced. The results are summarized in Table 18. Note that the minimum sensor increment is 0.022°; hence the steady state oscillations obtained are reasonable. This can also be concluded from Figure 66. It can also be seen from the results that the damping of the aeroservoelastic system decreases as the dynamic pressure increases, and shows an underdamped behavior. Thus, with the increasing dynamic pressure, both the overshoot value and settling time of the aeroservoelastic system increase.

The simulation is repeated by introducing a sensor noise. The results are given in Figure 69 through Figure 72. From the figures it can be seen that the sensor noise increases the oscillation amplitude, current consumption, and torsional spring deformation amplitude as expected.
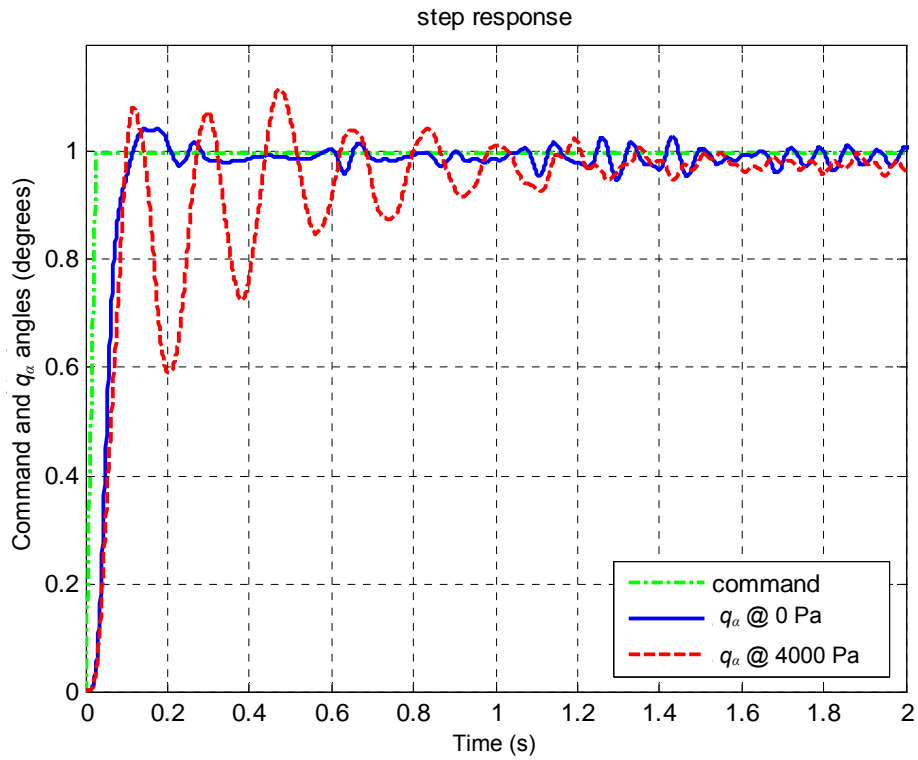
Figure 65. Step response of the aeroservoelastic system
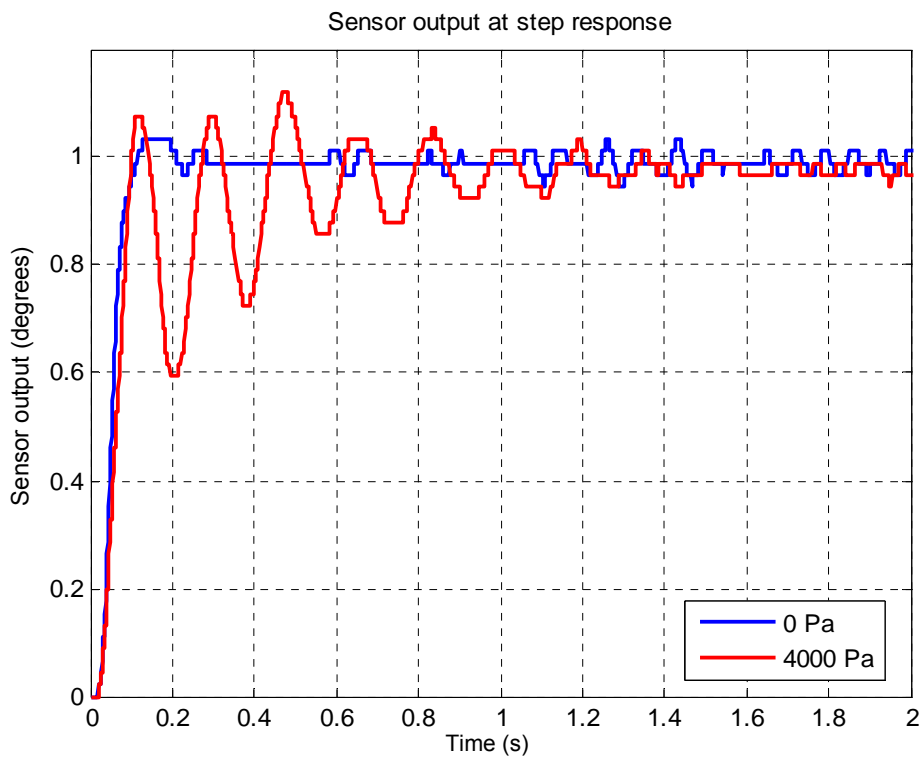
Figure 66. Sensor output history

185
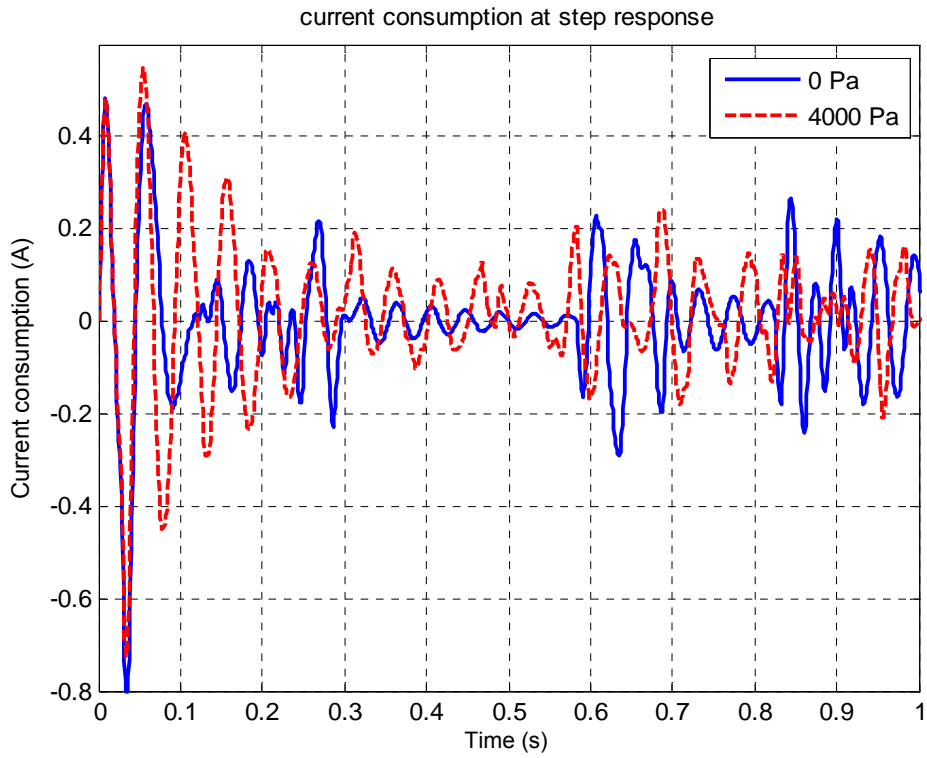
Figure 67. Current consumption history
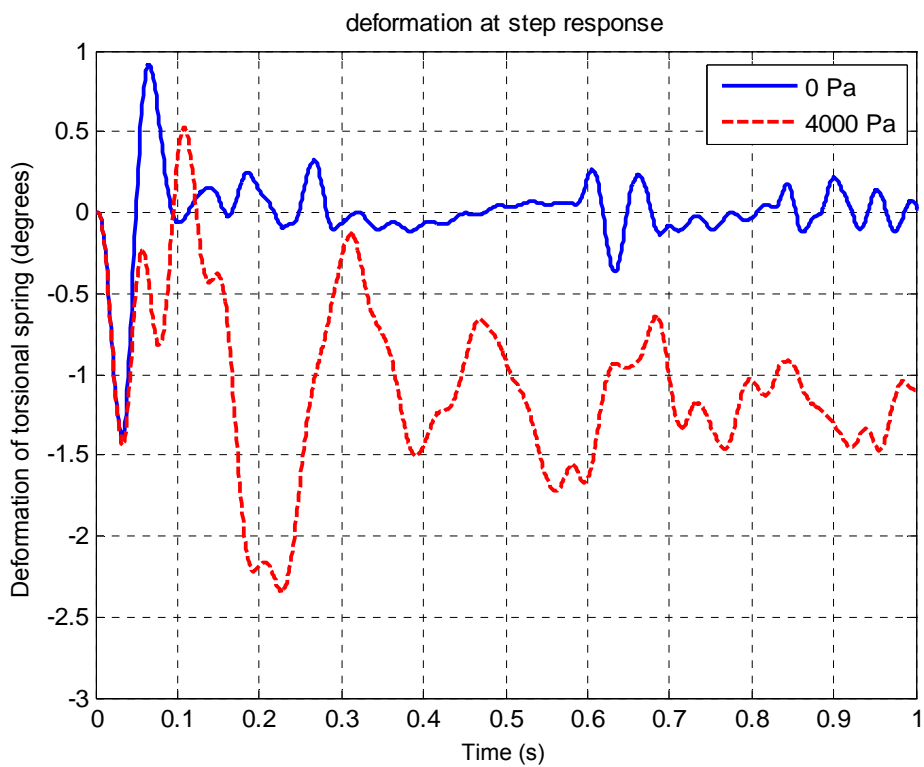
Figure 68. Deformation history of torsional spring

186
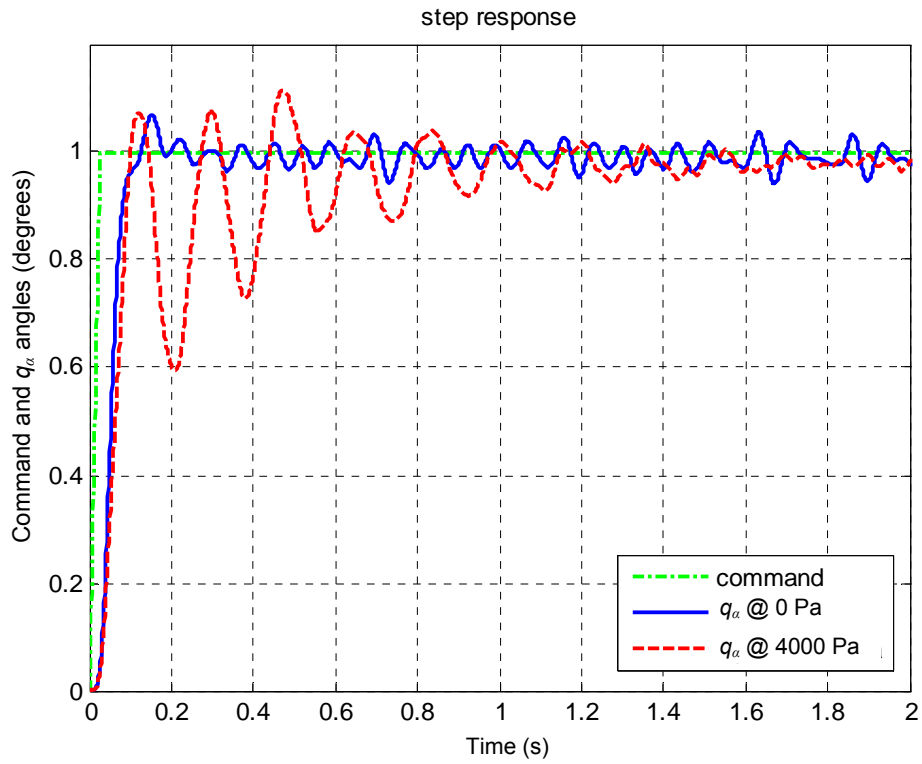
Figure 69. Step response of the aeroservoelastic system (with noise)
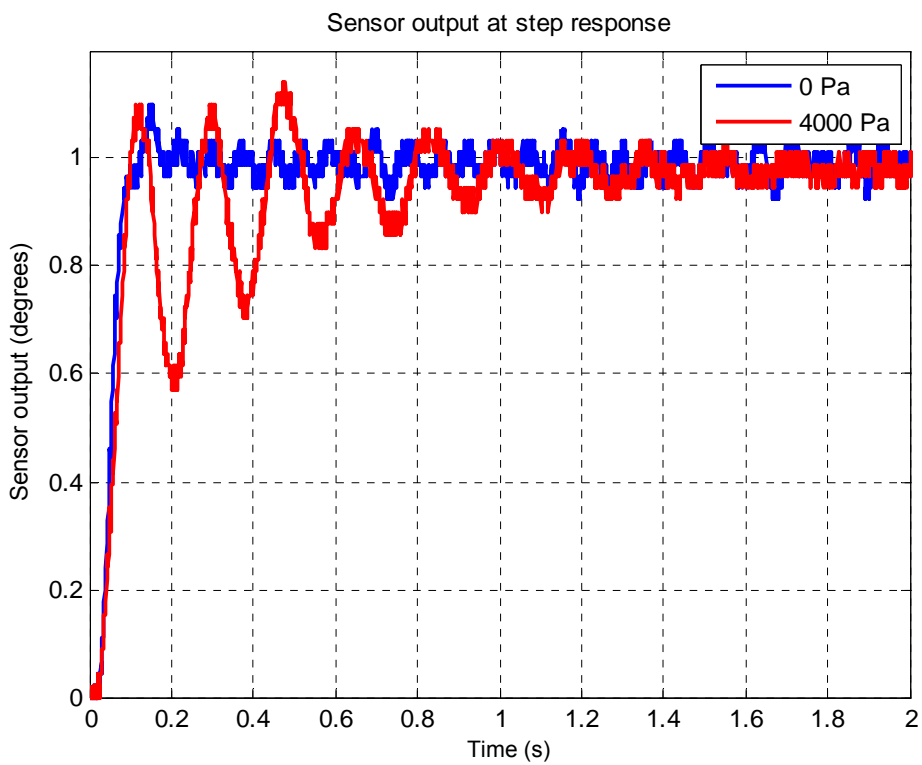
Figure 70. Sensor output history (with noise)
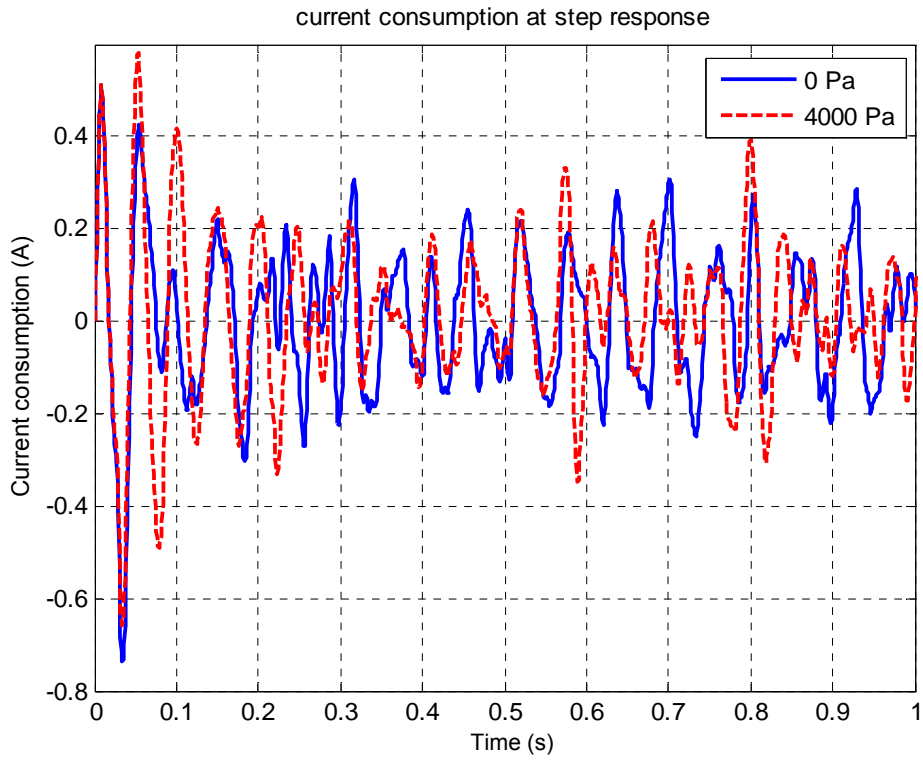
Figure 71. Current consumption history (with noise)
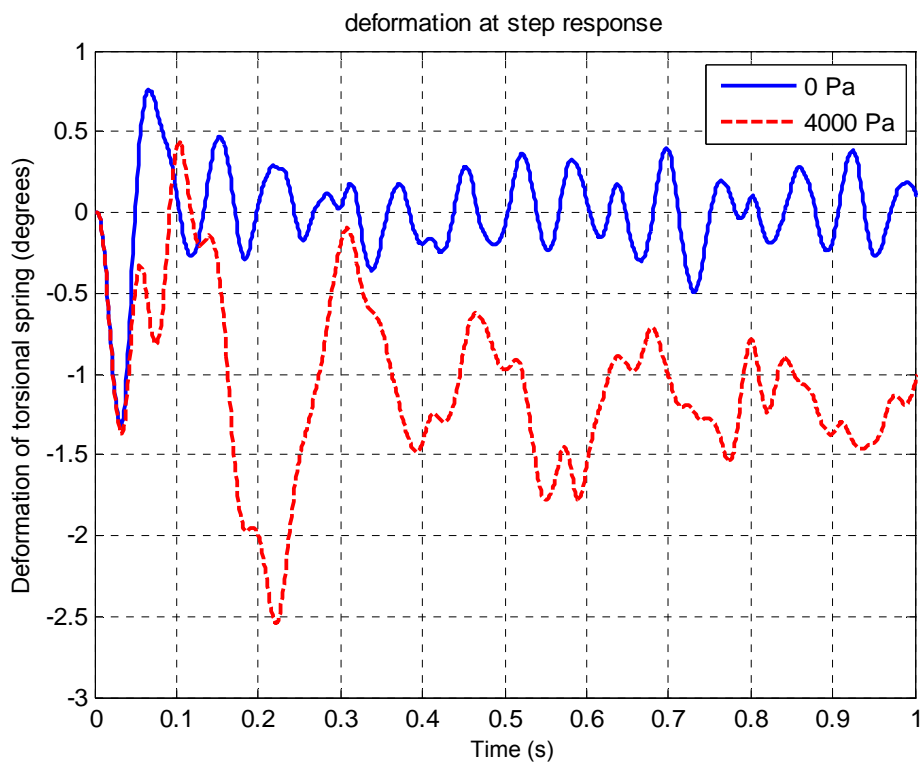
Figure 72. Deformation history of torsional spring (with noise)

Table 18. Properties of ASE system with H∞ controller

$\bar{q}$ simulation		0 Pa	4,000 Pa
$tr_{5\%}$	s	0.072	0.070
ts	s	0.098	1.3
Mp	%	4.5	11.7
e_{ss}	deg	-0.01±0.02	-0.02±0.02
$\delta_{\alpha\theta}$	deg	1.4	2.3
current	A	0.8	0.8

6.2.2.1.1.6.   Backlash analyses

The same steps that are performed for the aeroelastic system are followed for the backlash analysis of the aeroservoelastic system. The graphics obtained by the brute force approach as presented in Section 5.3.4, for the aeroservoelastic system at the dynamic pressure of 500 Pa are given in Figure 73. From the graphics it is seen that the aeroservoelastic system has only a stable LCO at the dynamic pressure of 500 Pa. Using the LCO search algorithm presented in Section 5.3.4, this stable LCO for the aeroservoelastic system at a dynamic pressure of 500 Pa is obtained for k_{eq}=36.31 N.m/rad. From the eigenvalues of the aeroservoelastic system the oscillation frequency is calculated as 6.60 Hz. The oscillation amplitude A is calculated by using Equation (5.8), as 0.73° for the backlash value of 0.2°.

Time domain analyses for the backlash analyses of the aeroservoelastic system are conducted by using the Simulink® model presented in Section 5.3.2. In order to separate the effects of backlash and the other nonlinearities included in the Simulink® model; the discrete controller, quantization blocks and disturbances are omitted from the Simulink® model. The results of the time domain analysis of the aeroservoelastic system at the dynamic pressure of 500 Pa are given in

Figure 74. The time domain analyses are performed for two different initial disturbances; namely, 0.1 N.m and 10 N.m amplitude moments. It is observed that the aeroservoelastic system converges to a stable LCO, from both lower and upper amplitude oscillations correspondingly. In Figure 74, two plots are given for each case, the pitch oscillation of the fin and the deformation of the torsional spring ($\delta_{\alpha\theta}$ = q_θ-q_α). Both have an importance for the system; the fin oscillation q_α affects the performance of the system; on the other hand, the deformation of the torsional spring affects the resulting stress and the fatigue life. Performing a fast Fourier transformation on the time domain response of the aeroservoelastic system, the frequency content of the output is obtained as given in Figure 75. It can be seen from the figure that the time domain results and the frequency domain results are not as consistent as in the aeroelastic case. The LCO is obtained, however the frequency domain method predicts the amplitude and the frequency of the LCO at some lower values. This is due to the effect of the higher harmonics, which is neglected in describing function method. These higher harmonics of the LCO, which are at the odd multiples of the LCO frequency, can also be seen in Figure 75. Comparing Figure 33 and Figure 75, it can be seen that the amplitude ratio of the first and the second peaks of the aeroelastic is 10,000, but for the aeroservoelastic systems the ratio is 65. Thus, the contribution of the higher harmonics is negligible in the aeroelastic system. However, in aeroservoelastic system the higher harmonics have a larger contribution, which causes a difference in the results of the describing function and time domain results. In the figure (a), there exists a peak at 2.2 Hz, which is nearly one third of the LCO frequency. By applying an FFT on the initial and final portions of the signal, it is seen that the amplitude of this peak decreases with time. Hence, this peak is not a lower harmonic of the LCO, but it is a damped oscillation.

A set of search are performed at various dynamic pressures. Different than the aeroelastic system, a stable point at 0°, or an unstable LCO are not found for this particular aeroservoelastic system. In the aeroelastic system, if the disturbance is not sufficient to deflect the fin above the unstable LCO which corresponds to a pitch angle slightly above backlash, the aerodynamics damps and stabilizes the fin to 0°. However in aeroservoelastic system, although a small disturbance is applied such that the pitch motion is less than the backlash, the motor moves and the relative motion between the fin and the transmission shaft exceeds the backlash value due to the feedback. Hence, any motion of the fin that the sensor detects causes the motion of the motor, and a subsequent LCO.

The analyses are also performed for various backlash values. The pitch motion of the fin and the deflection of the torsional spring values that is calculated via describing function method and time domain solutions are given in Figure 76. From the figure it can be seen that, the difference between the results of the two solution methods, which is seen for the backlash value of 0.2°, is also exist for other backlash values. The percentage of the error between the predicted LCO amplitude from the describing function method and time domain solutions are similar for different backlash values. On the other hand, it can be seen that for this model, an increase in backlash increases the amplitude of the LCO, hence decreases the flight margin of the aeroservoelastic system. For example; just consider the oscillation amplitude of the pitch motion of the fin. For a 0.4° acceptable oscillation, the linear flight margin of 4,000 Pa decreases to 3,300 Pa for 0.2° backlash value. However the stability is not the only requirement of the aeroservoelastic system. In order to investigate the performance of the aeroservoelastic system with backlash, time domain simulations are performed. The solutions of the time domain simulations are given in Table 19. These simulations are performed at two different dynamic pressures and for two different backlash values. The simulations

reveals that the backlash increases the overshoot and elastic deformation of torsional spring. Moreover, the LCO occurs after 1° command for the analysis at 0 Pa. The LCO occur about 1° pitch position. On the other side, it is seen that, the preload and the damping effect of the aerodynamics suppresses the oscillations after this 1° pitch position step command at 4,000 Pa.

As it is mentioned in the beginning of the backlash analysis, the quantization block of the sensor is taken out of the time domain simulation block. Finally, the time domain analyses are rerun with the sensor quantization block. It is seen that, the LCO do not occur for very small perturbations if the feedback does not detect any fin motion. However, the LCO still occurs with slightly greater amplitudes for large perturbations.
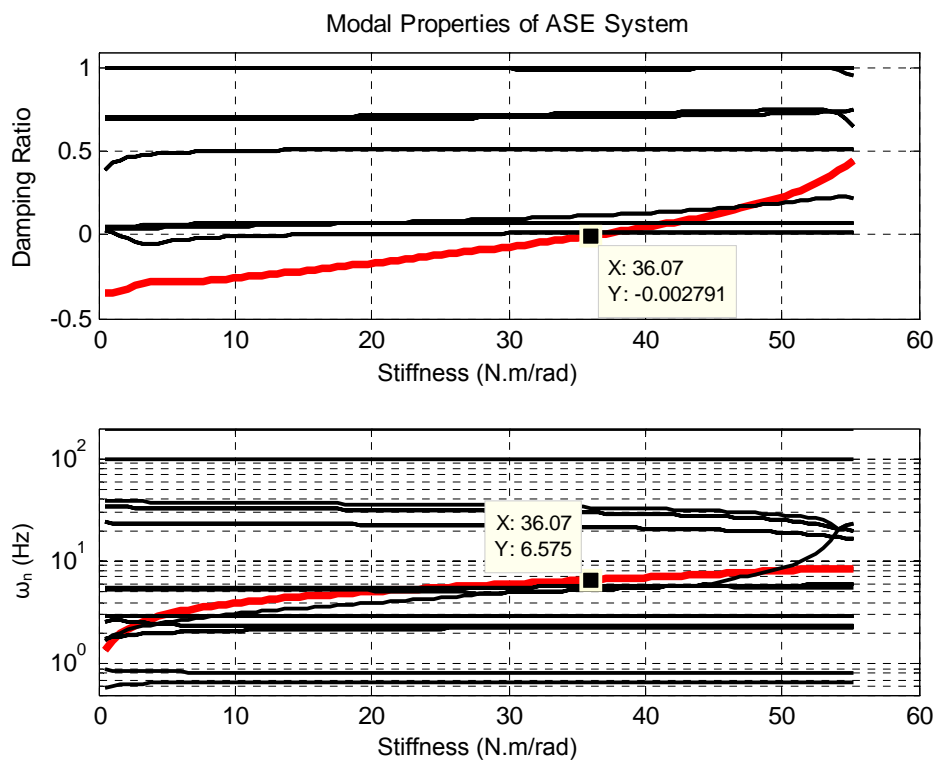
Figure 73. Modal properties of the aeroservoelastic system at 500 Pa
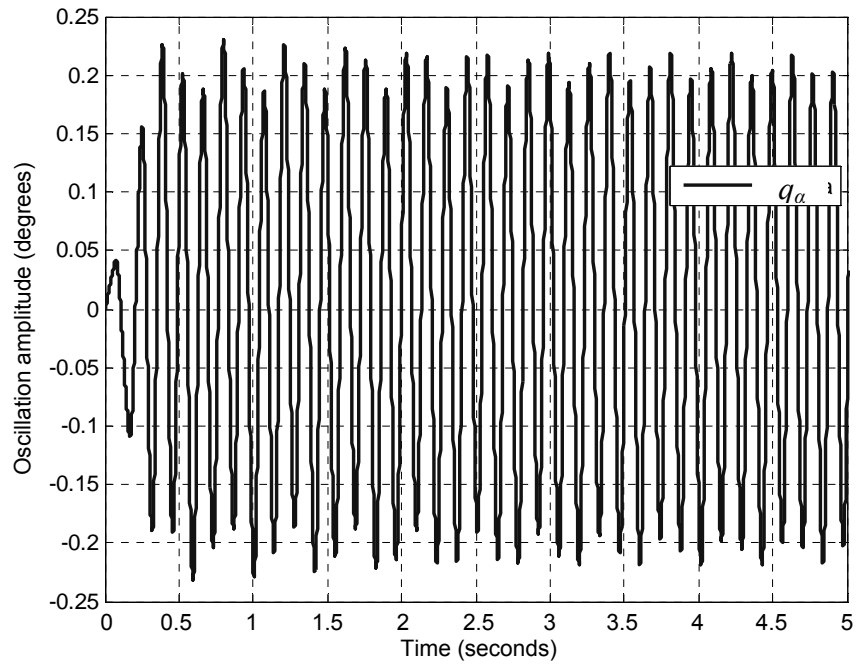
(a) q_α plot for 0.1 N.m torque initial condition
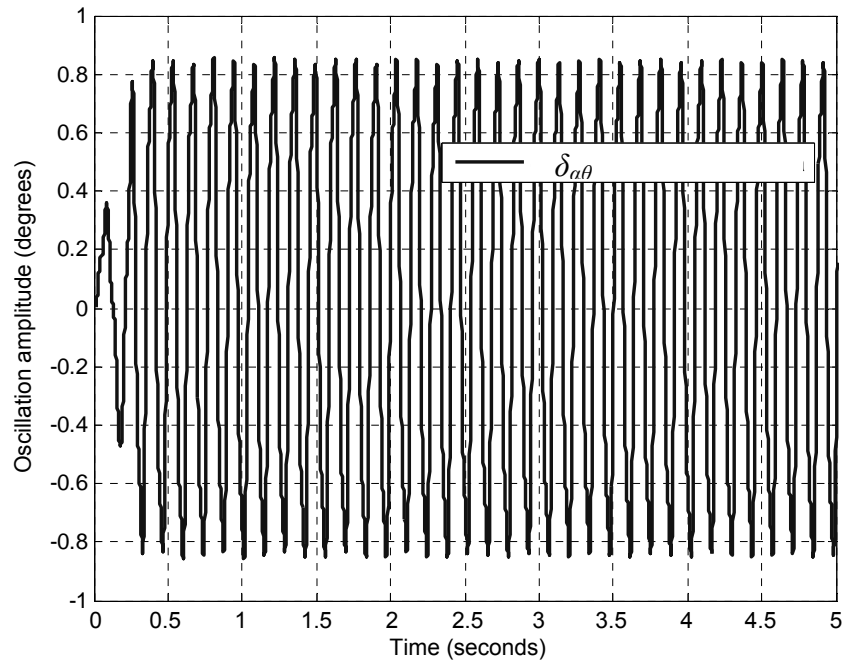
(b) deflection of torsional spring plot for 0.1 N.m torque initial condition
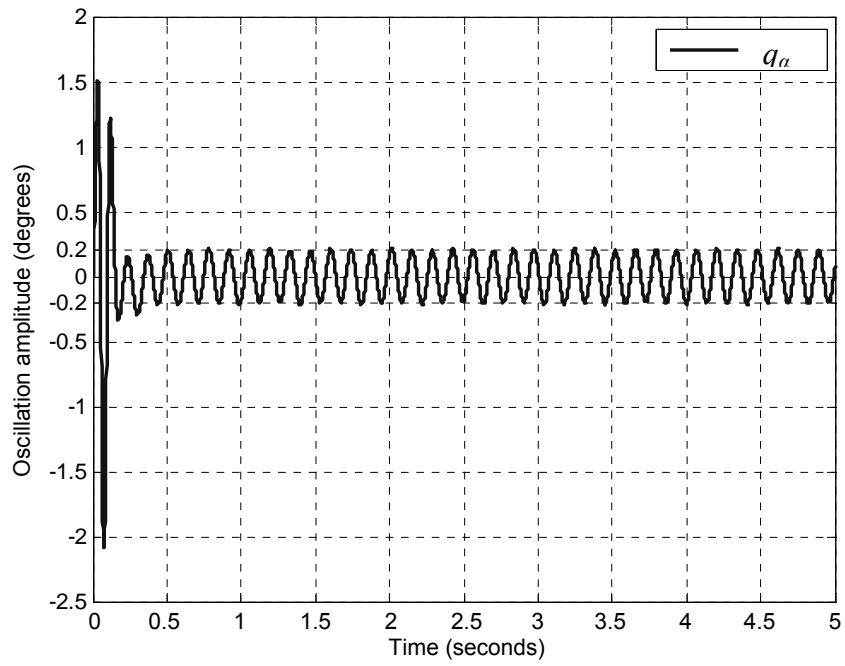
(c) q_α plot for 10 N.m torque initial condition
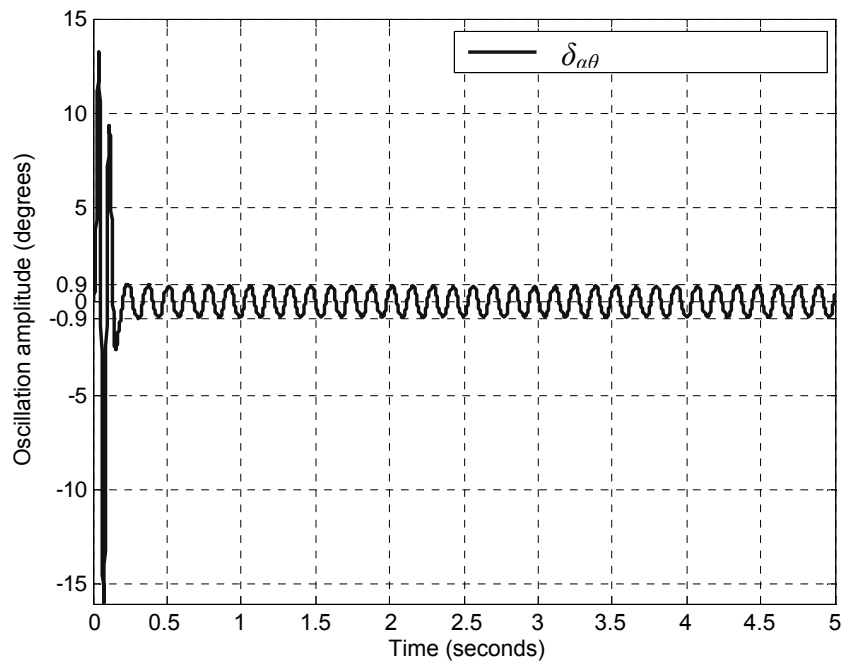
(d) deflection of torsional spring plot for 10 N.m torque initial condition

Figure 74. Time domain results of the aeroservoelastic system at 500 Pa
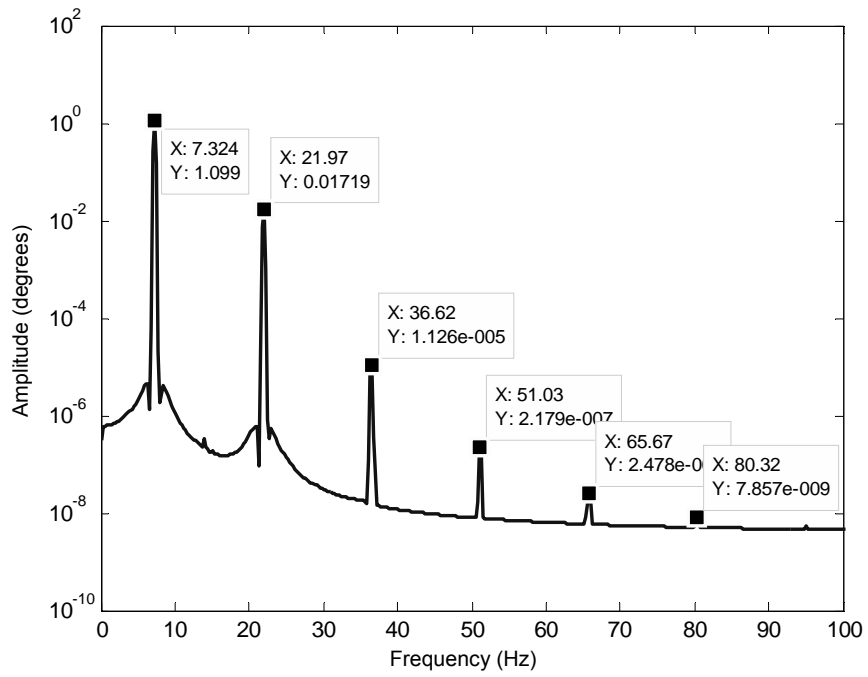
(a) FFT of ($\delta_{\alpha\theta}$)
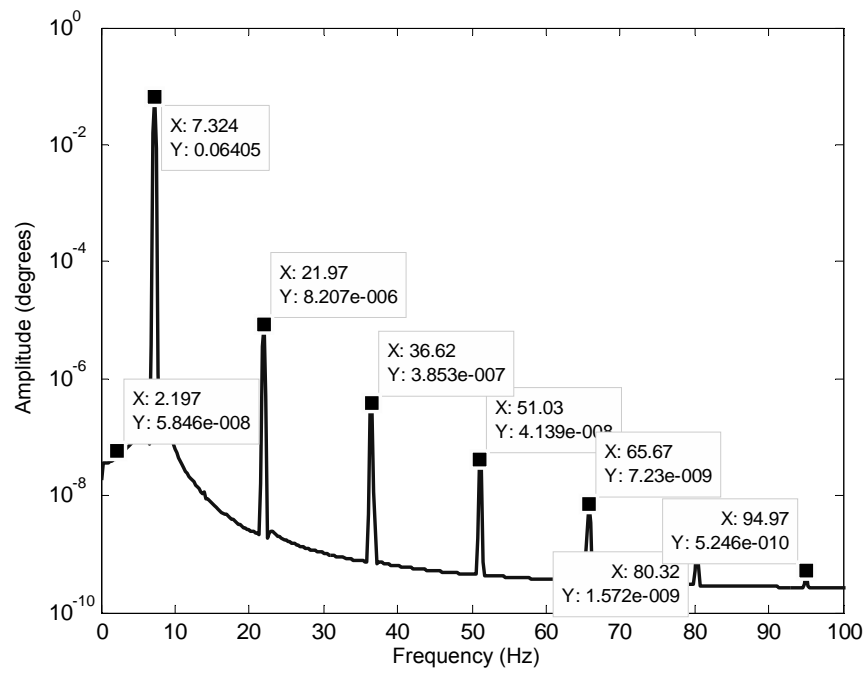
(b) FFT of q_α

Figure 75. FFT of the time domain results of the aeroservoelastic system

TDS : Time domain solution results
DF : Describing function solution results
bv : Backlash value in degrees

(a) deflection of torsional spring ($\delta_{\alpha\theta}$)

(b) q_α
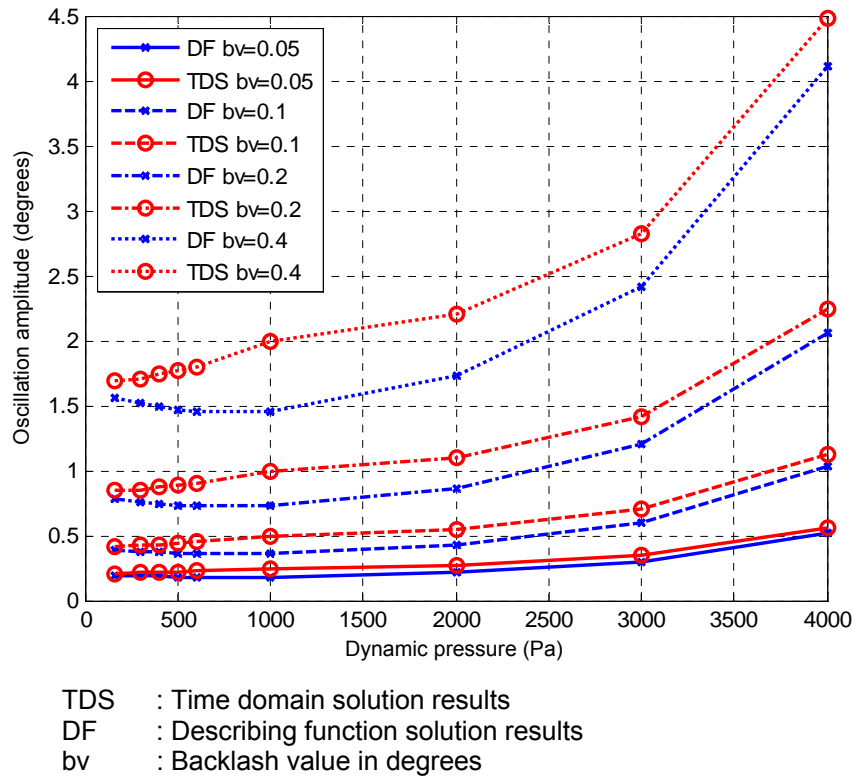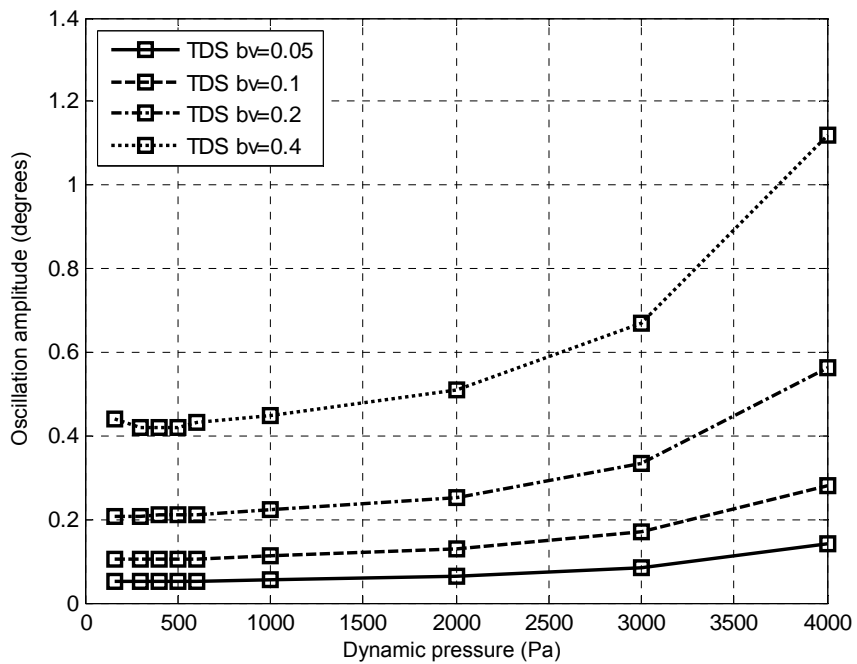
Figure 76. LCO amplitudes of the aeroservoelastic system with respect to dynamic pressure for various backlash values

196

Table 19. Step response properties of aeroservoelastic system for various backlash values

	Backlash	deg	0	0.05	0.2
q simulation 0 Pa	$tr_{5\%}$	s	0.072	0.058	0.050
	Mp	%	4.5	7.3	21.0
	e_{ss}	deg	-0.01 ±0	-0.002 ±0.048	-0.010 ±0.208
	$\delta_{\alpha\theta}$	deg	1.37	1.41	1.50
	cr_1^*	A	0.77	0.75	0.68
	cr_2^*	A	0	0	0
	cr_3^*	A	0	0.028	0.035
	cr_4^*	A	0	0.31	0.26
q simulation 4,000 Pa	$tr_{5\%}$	s	0.068	0.067	0.065
	Mp	%	11.8	13.6	33.0
	e_{ss}	deg	-0.022 ±0	-0.022 ±0.001	-0.022 ±0.009
	$\delta_{\alpha\theta}$	deg	2.29	2.50	3.20
	cr_1^*	A	0.68	0.67	62
	cr_2^*	A	0.018	0.018	0.020
	cr_3^*	A	0	0	0
	cr_4^*	A	0.019	0.019	0.019

cr_1^* : maximum current consumed at step motion
cr_2^* : mean current consumed at steady part
cr_3^* : standard deviation of current consumption at steady part
cr_4^* : maximum current consumed at steady part

6.2.2.1.2. Effect of Initial dynamic pressure and dynamic pressure disturbance to the controller performance

The controller synthesis method given in Section 4.3 defines the disturbance to dynamic pressure as an uncertainty and uses this disturbance to define the required margin of stability. The aeroservoelastic system has both upper and lower margins and the dynamic pressure uncertainty is used for both margins. Hence, the dynamic pressure $\bar{q}_{cont}$ at

which the controller is synthesized affects the margins of the aeroservoelastic system. In order to analyze this, six different aerodynamic points (AP) are selected as shown in Table 20. In all these aerodynamic points, the airspeed is kept as the same.

Table 20. Aerodynamic points for controller synthesis

AP #	h (m)	Mach	$\bar{q}_{cont}$ (Pa)
1	800	0.0500	161.1
2	-5,000	0.0470	274.5
3	-10,000	0.0448	414.7
4	-15,000	0.0428	601.1
5	-20,000	0.0411	849.4
6	-30,000	0.0383	1,571.0

For each case, a controller is synthesized by keeping the rest of the parameters fixed. After the syntheses of these controllers, analyses are performed for the aeroservoelastic system with each controller. The upper and lower limit variations of the dynamic pressure of instabilities with the variation of $\bar{q}_{cont}$ are given in Figure 77. The aeroservoelastic system is stable between the upper and the lower limits. From the figure it can be seen that the upper limit increases with the increase of $\bar{q}_{cont}$. However, the lower limit also increases with the increase of $\bar{q}_{cont}$ and crosses 0 Pa, which means that the aeroservoelastic system becomes unstable in vacuum.

In addition to the stability analysis, the performance analyses are also performed for the aeroservoelastic system with the synthesized controllers. The step response properties of these systems at two different aerodynamic environments (0 Pa and 4,000 Pa) are achieved by time domain simulations. The results are given in Table 21. From the table it

can be seen that the performance at 0 Pa decreases, but the performance at 4,000 Pa increases with the increase of $\bar{q}_{cont}$. This is in accordance with the results of the instability analyses. Moreover, some frequency response analyses are performed, which are similar to the Figure 58, and it is seen that the system can satisfy the bandwidth requirement at higher dynamic pressures, when $\bar{q}_{cont}$ is increased.
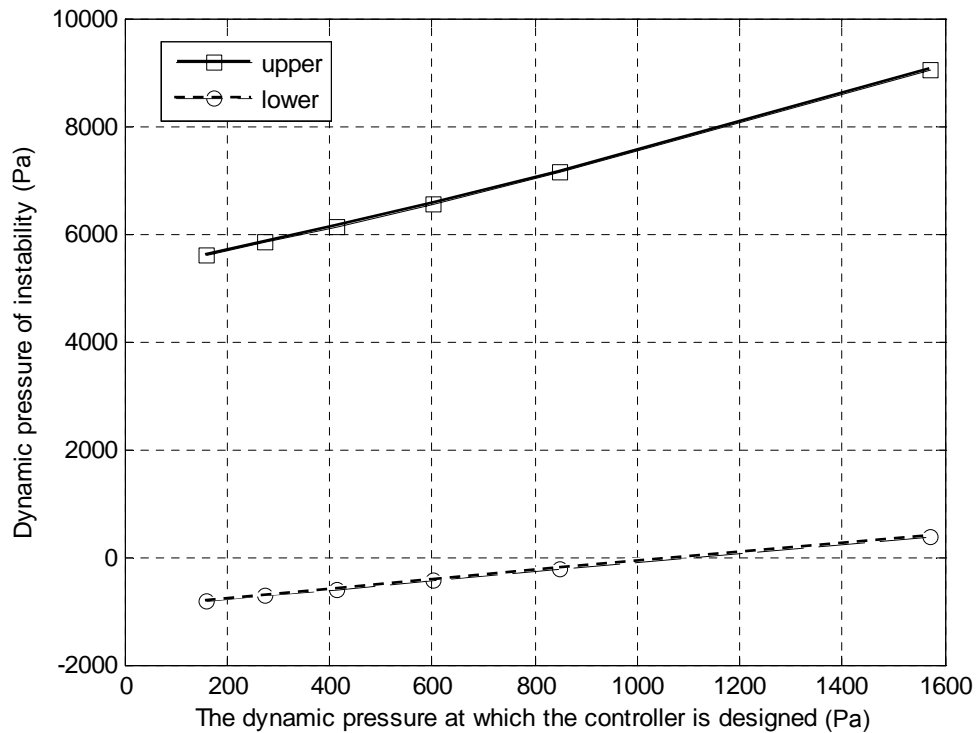
Figure 77. Change of dynamic pressure of instability with $\bar{q}_{cont}$

As a result, it is required to tune the $\bar{q}_{cont}$ in order to increase the performance and the stability margins of the system. The analyses are performed for 0 Pa and 4,000 Pa, however the tuning of the $\bar{q}_{cont}$ should be performed according to the working range of the aeroservoelastic system. For example, for an air to air missile with an operating range between 2,000-3,000 Pa, the tuning may be performed accordingly.

Table 21. Step response properties of aeroservoelastic system with various controllers

	AP #		1	2	3	4	5	6
q simulation 0 Pa	$tr_{5\%}$	s	0.072	0.075	0.081	0.087	0.092	-
	ts	s	0.098	0.44	0.48	0.24	0.26	-
	Mp	%	4.5	6.0	8.5	11.8	17.8	-
	e_{ss}	deg	-0.009 ±0.023	-0.009 ±0.023	-0.009 ±0.022	-0.010 ±0.025	-0.010 ±0.026	-
	$\delta_{\alpha\theta}$	deg	1.38	1.40	1.42	1.45	1.50	-
	cr_1^*	A	0.8	0.81	0.81	0.81	0.82	-
	cr_2^*	A	0	0	0	0	0	-
	cr_3^*	A	0.099	0.090	0.090	0.096	0.083	-
	cr_4^*	A	0.27	0.18	0.18	0.30	0.27	-
q simulation 4,000 Pa	$tr_{5\%}$	s	0.068	0.067	0.067	0.067	0.067	0.067
	ts	s	1.275	1.107	1.103	0.76	0.76	0.41
	Mp	%	11.9	10.3	8.4	8.5	8.4	7.8
	e_{ss}	deg	-0.022 ±0.025	-0.022 ±0.024	-0.022 ±0.021	-0.021 ±0.021	-0.019 ±0.012	-0.018 ±0.018
	$\delta_{\alpha\theta}$	deg	2.34	2.33	2.27	2.28	2.29	2.23
	cr_1^*	A	0.71	0.73	0.73	0.74	0.74	0.77
	cr_2^*	A	0.018	0.018	0.018	0.018	0.018	0.018
	cr_3^*	A	0.182	0.169	0.158	0.156	0.130	0.139
	cr_4^*	A	0.42	0.42	0.39	0.37	0.28	0.31

cr_1^* : maximum current consumed at step motion
cr_2^* : mean current consumed at steady part
cr_3^* : standard deviation of current consumption at steady part
cr_4^* : maximum current consumed at steady part

$\bar{q}_{dist}$ is another parameter for the tuning of the system performance. In order to analyze this, controllers are synthesized at the aerodynamic point number 1 and 3 for various values of $\bar{q}_{dist}$. The resultant controllers are compared for the stability limits of the aeroservoelastic system, and the results are given in the Table 22. From the table it can be seen that, in

contrary to $\bar{q}_{cont}$, an increase in $\bar{q}_{dist}$ enlarges the flight envelope from both upper and lower limits.

Table 22. Effect of aerodynamic disturbance on stability margin

	$\bar{q}_{dist}$	Pa	500	1,000	1,290	1,500
AP #1	$\bar{q}_{ins_{low}}$	Pa	-818	-872	-	-
	$\omega_{ins_{low}}$	Hz	5.51	13.3	-	-
	$\bar{q}_{ins}$	Pa	5,582	7,306	-	-
	ω_{ins}	Hz	11.8	5.90	-	-
AP #3	$\bar{q}_{ins_{low}}$	Pa	-603	-649	-729	-815
	$\omega_{ins_{low}}$	Hz	11.8	13.2	13.9	14.4
	$\bar{q}_{ins}$	Pa	6,132	7,986	8,859	9,359
	ω_{ins}	Hz	5.49	5.88	6.12	6.30

The analyses are continued with the controller synthesized at AP #3 for $\bar{q}_{dist}$ =1,500 Pa. From Figure 78, it can be seen that, by tuning the controller, the bandwidth of the aeroservoelastic system is also altered and becomes ~6 Hz at least for a dynamic pressure range between 0-5,582 Pa. The enlarged flutter flight envelop can be seen by comparing Figure 79 and Figure 64. Results of the performance analysis are given in Figure 80 and Table 23. Comparing the results of the Controller synthesized at AP #1 given in Table 21 and the results of the tuned controller given in Table 23; it can be seen that a slight performance decrease in 0 Pa and a considerable performance increase in 4,000 Pa are obtained with the new controller. The new controller also decreases the amplitudes of the LCO as given in Figure 81.
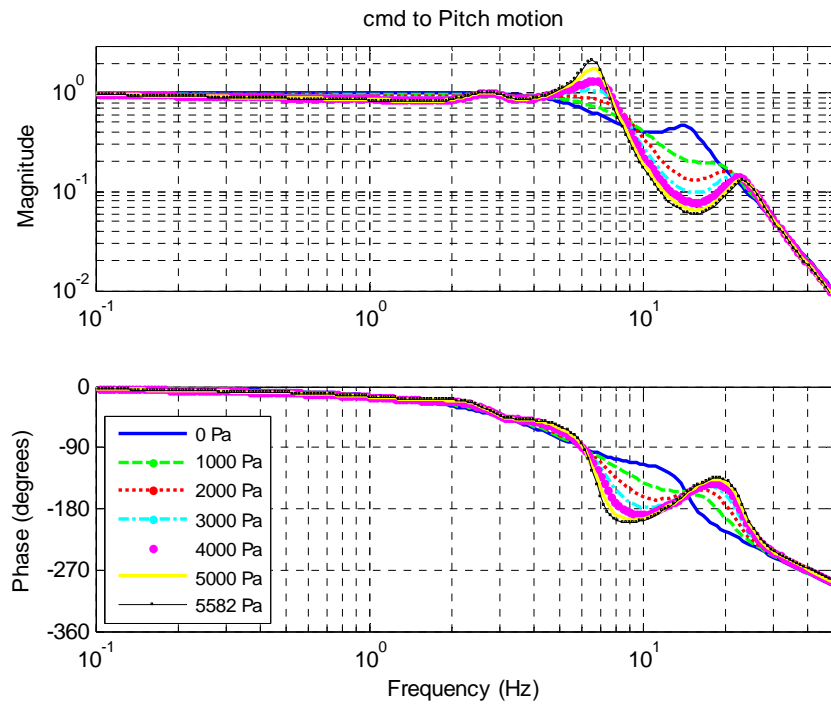
(a) main graphics
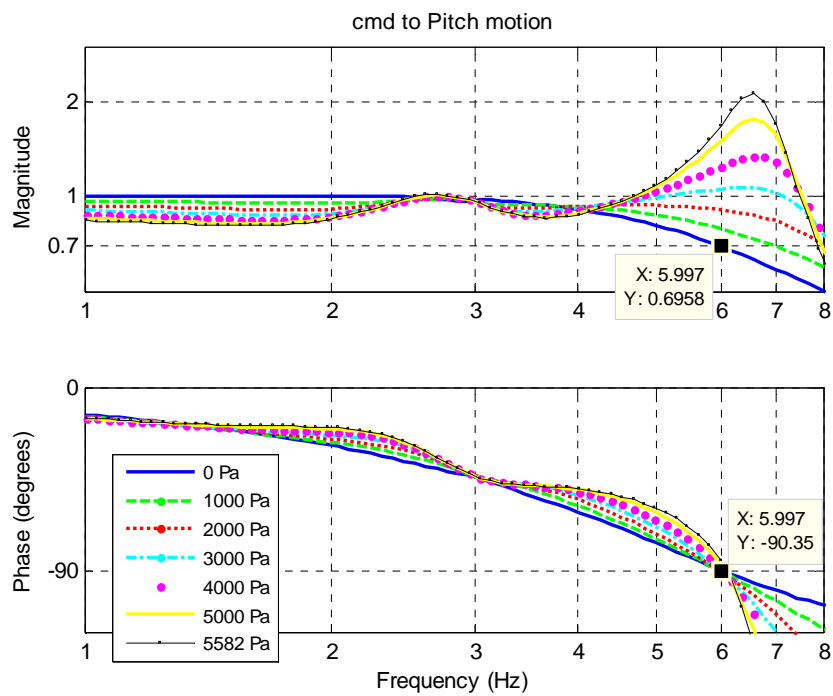
(b) detailed graphics

Figure 78. Frequency response from command input to pitch motion for various values of dynamic pressure

Figure 79. Flutter flight envelope
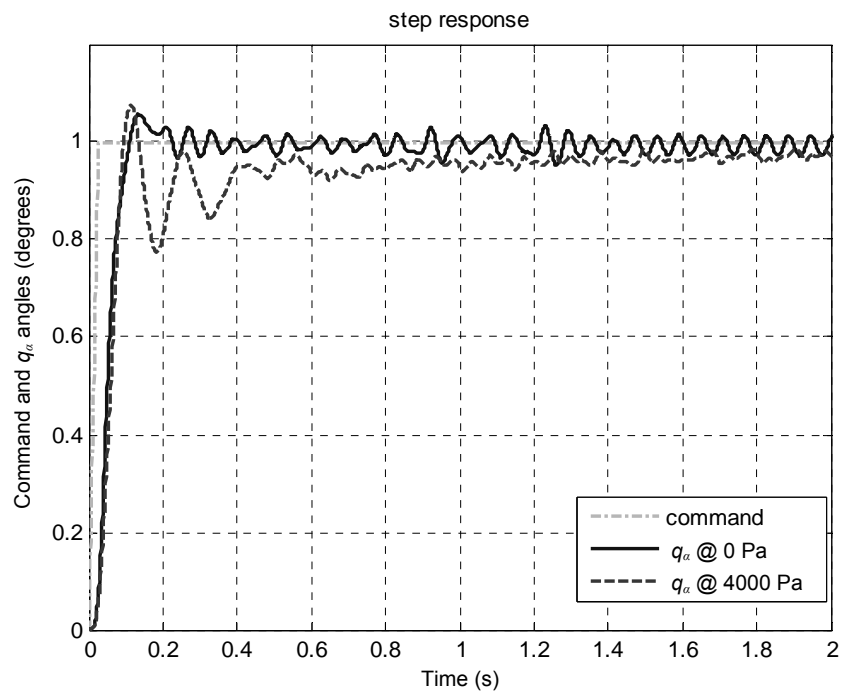
Figure 80. Step response of the aeroservoelastic system

203

(a) deflection of torsional spring, $\delta_{\alpha\theta}$

(b) q_α

Figure 81. LCO amplitudes of the aeroservoelastic system with respect to dynamic pressure for various backlash values

Table 23. Step response properties of aeroservoelastic system with quantized sensor for AP #3, $\bar{q}_{dist}$ =1,500 Pa

$\bar{q}$ simulation		0 Pa	4,000 Pa
ω_n	Hz	6.00	6.03
$tr_{5\%}$	s	0.076	0.065
ts	s	0.145	1.130
Mp	%	5.7	6.5
e_{ss}	deg	-0.008 ±0.022	-0.024 ±0.019
$\delta_{\alpha\theta}$	deg	1.29	2.32
cr_1^*	A	0.98	0.80
cr_2^*	A	0	0.019
cr_3^*	A	0.233	0.323
cr_4^*	A	0.50	0.73

cr_1^* : maximum current consumed at step motion
cr_2^* : mean current consumed at steady part
cr_3^* : standard deviation of current consumption at steady part
cr_4^* : maximum current consumed at steady part

6.2.2.1.3. Aeroservoelastic Test Setup

As it is mentioned in Section 6.2, an Aeroservoelastic Test Setup (ATD) is developed in TÜBİTAK-SAGE (Figure 82). ATD is tested in the Ankara Wind Tunnel. From the tests it is seen that, ATD encounters some LCO at 48 m/s airspeed and flutter occurs at 60.5 m/s airspeed. The details of the ATD can be found in reference [17]. After these tests a small demonstration is performed for flutter suppression. For this purpose an H_∞ controller is synthesized using the proposed controller synthesis method, q-Method, which uses the perturbation to dynamic pressure for the purpose of flutter suppression. However, the synthesis is performed with a limited knowledge about the ATD. The detailed system identification is not performed before demonstration. Furthermore, during the tests it is observed that the ATD has more friction and damping than the expected

values. However, the synthesis is performed according to design specifications of the ATD.

In order to implement the controller, a MATLAB$^®$ xPC-target computer is used. The xPC-target computer sends the command to the SERVOSTAR 6020 motor driver: the motor and the fin angles are collected from encoder channels and the plunge motion is collected from an analog to digital card. Additionally, four accelerometer measurements are collected from the fin for further studies.

The setup is started and the airspeed of the wind tunnel is increased up to 48 m/s. Then some plunge disturbances are applied to the mechanism in order to initiate an LCO or flutter. After some oscillations are developed, the disturbances are stopped in order to monitor the effect of the controller. It is observed that the controller suppresses the oscillations successfully. This demonstration is repeated at 50, 55, 60, 65, and 70 m/s airspeeds - which is the practical limit of the wind tunnel – and it is seen that the controller suppresses the oscillations. From the analysis of the aeroservoelastic model that is constructed with the limited knowledge, the airspeed of instability is obtained above 100 m/s.

(a) fin   (b) wind tunnel view

(a) 2 d.o.f. structural part   (b) upper view

Figure 82. Aeroservoelastic Test Setup

In Figure 83 and Figure 84, the q_h and q_α graphics of the aeroelastic system are given at 48 m/s airspeed in the LCO and at 60.5 m/s airspeed in the flutter. From Figure 83(a), the initiator disturbances applied in the pitch degree of freedom can be seen. It is observed that an LCO starts if the pitch disturbance is greater than the amplitude of 6º. From the graphics it is observed that up to 5º of disturbance amplitude the pitch motion could not initiate a motion in plunge degree of freedom. In 5º of pitch disturbance motion, only a small motion can be started in plunge and it is damped. It is understood that at 6º of pitch disturbance motion the system could transferred an enough amount of energy to the plunge degree of freedom to initiate the LCO. Hence, it is concluded that introducing a plunge disturbance will easily introduced an LCO or flutter, and it is confirmed by some demonstrations performed at 48, 50, and 55 m/s airspeed. In Figure 84, the oscillatory divergence, the flutter phenomena can be seen. Between 137.5-138 seconds the system reaches the pitch limits. In the Figure 85 and Figure 86 the q_α, q_θ, and q_h graphics of the aeroservoelastic system are given at 48 m/s and 70 m/s airspeed correspondingly. From the figures it can be seen that the controller suppresses the LCO and flutter observed in the aeroelastic tests.
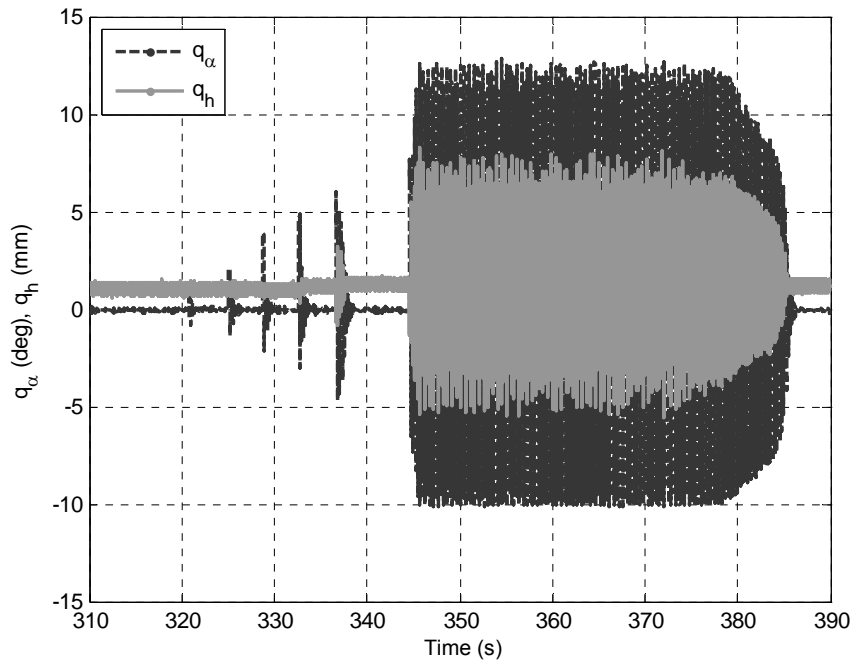
(a) initiator disturbances and LCO
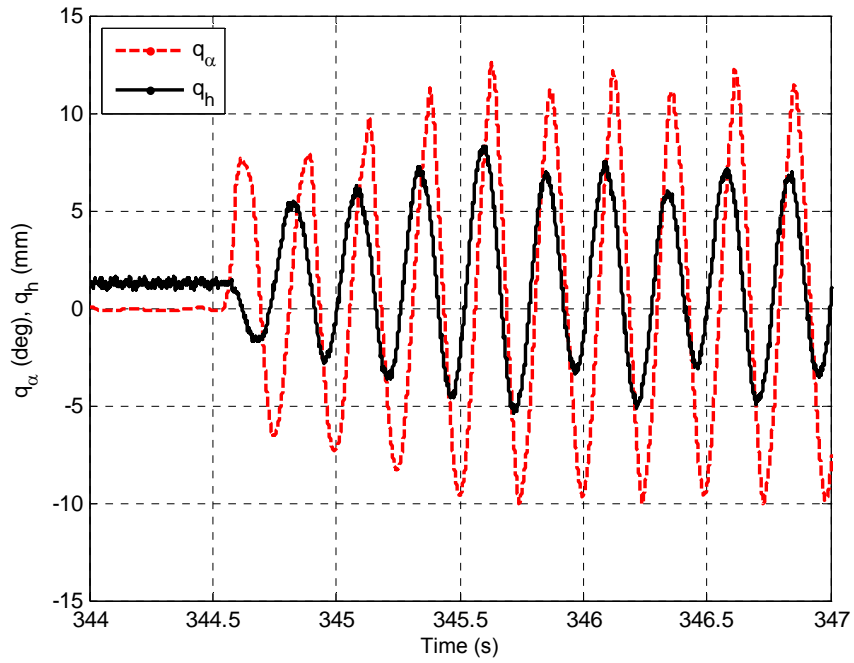
(b) detailed view

Figure 83. LCO of aeroelastic system at 48 m/s airspeed
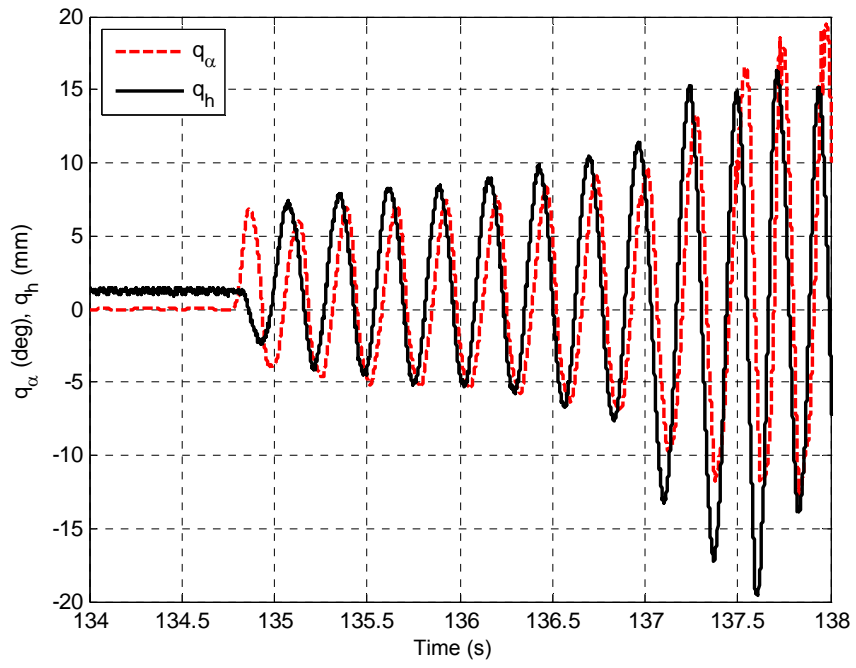
Figure 84. Flutter of aeroelastic system at 60.5 m/s airspeed
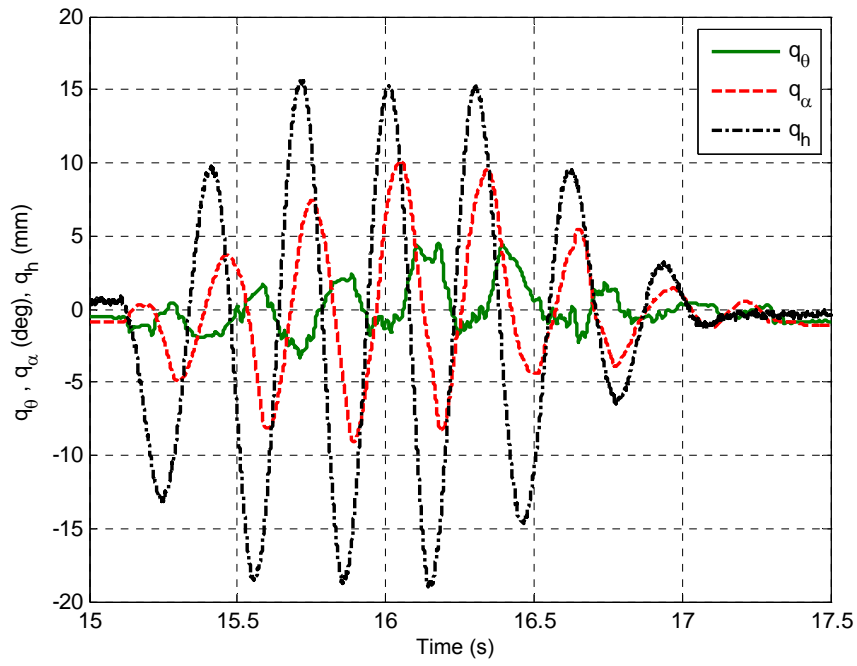
Figure 85. Aeroservoelastic system response at 48 m/s airspeed
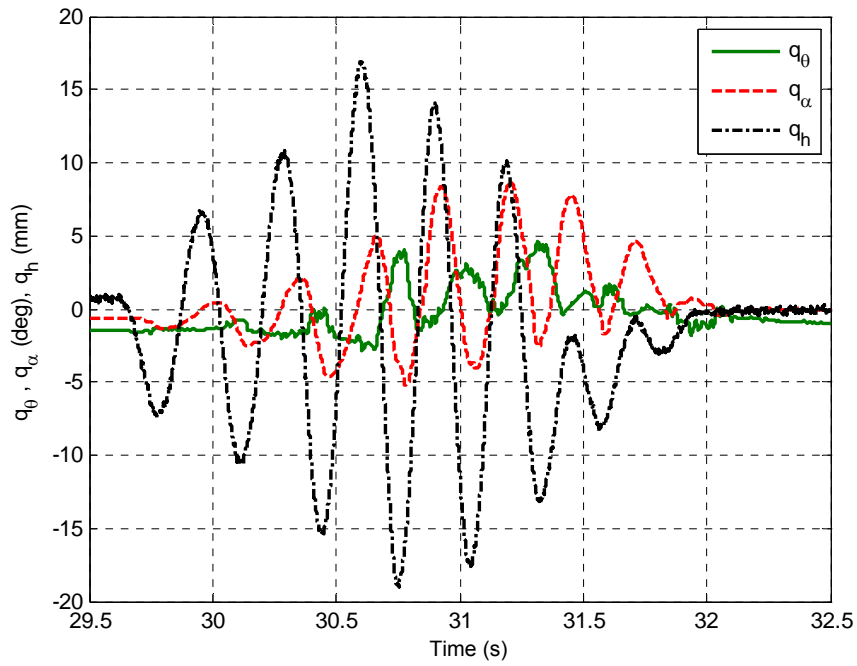
Figure 86. Aeroservoelastic system response at 70 m/s airspeed

6.2.2.2. H$_2$ controller synthesis

In this section an H$_2$ controller is synthesized. In order to perform the H$_2$ synthesis the uncertainty, noise, and performances given in Table 12 are defined as the respective noise and performances. Similar to the H$_\infty$ controller synthesis, various controllers are synthesized considering the disturbance to dynamic pressure $\bar{q}_{dist}$, disturbance to aerodynamic force, and the dynamic pressure $\bar{q}_{cont}$ at which the controller is synthesized. The results are presented in Appendix D.

From the results it is seen that, as the $\bar{q}_{cont}$ value increases the dynamic pressure of upper and lower instability values also increase as in the case of H$_\infty$ controller synthesis (Figure 77). In addition to the decrease in lower stability margin, the overshoot values also increase with an increase in $\bar{q}_{cont}$. Hence, considering the $\bar{q}_{cont}$, controller synthesized at AP #3 is selected.

Considering the disturbance to the dynamic pressure $\bar{q}_{dist}$ and the corner frequency $\omega_{\bar{q}2}$ of the output weighting function $\left[W_{\bar{q}2} \right]$ of the dynamic pressure disturbance are disturbed and it is seen that increases in these terms increase the stability envelope; however they also increase the current consumption value. Among those trial values, $\bar{q}_{dist}$ and $\omega_{\bar{q}2}$ are selected as 1,500 Pa and 10 Hz, respectively.

In order to see the effect of the disturbance on the aerodynamic force, two different syntheses are performed. In these syntheses, two different set of gains are used for the disturbance to aerodynamic force weighting functions $\left[W_{Fd} \right]$. Comparing the aeroservoelastic system with these two controllers, it is seen that increasing the disturbance value

increases the bandwidth at 4,000 Pa. However, it also increases the overshoot at 4,000 Pa, increases the current consumption, and reduces the stability envelope. Thus, as the scale factors of the disturbance to aerodynamic force weighting functions, the smaller values are selected among the two cases. The selected values are 50 at 0 Hz and 0.2 at 10 Hz. The tuned and selected parameters in this synthesis are given in Table 24.

Table 24. Tuned parameters of H_2 controller

Parameter			Value
$[W_{Fd}]$	g_{Fd_F}	@ 0 Hz	1,400 N
		@ 10 Hz	25 N.m
	g_{Fd_M}	@ 0 Hz	5.6 N
		@ 10 Hz	0.1 N.m
$[W_{\bar{q}2}]$	$\bar{q}_{dist}$		1,500 Pa
	$\omega_{\bar{q}2}$		10 Hz
$\bar{q}_{cont}$			AP #3
Order of the reduced controller			13

For the aeroservoelastic system with the synthesized H_2 controller; a stability analysis via μ-method, a flutter free flight envelope analysis, a frequency domain analysis, time domain step response analyses and backlash analyses are performed. These analyses are applied to all cases of incompressible flow, and named as standard analyses in incompressible flow cases. The results of these analyses are given in Table 25, Table 26, and in Figure 87 through Figure 90.

Table 25. Nominal stability limits

$\bar{q}_{ins_{low}}$	Pa	-612
$\omega_{ins_{low}}$	Hz	12.7
$\bar{q}_{ins}$	Pa	8,036
ω_{ins}	Hz	5.61
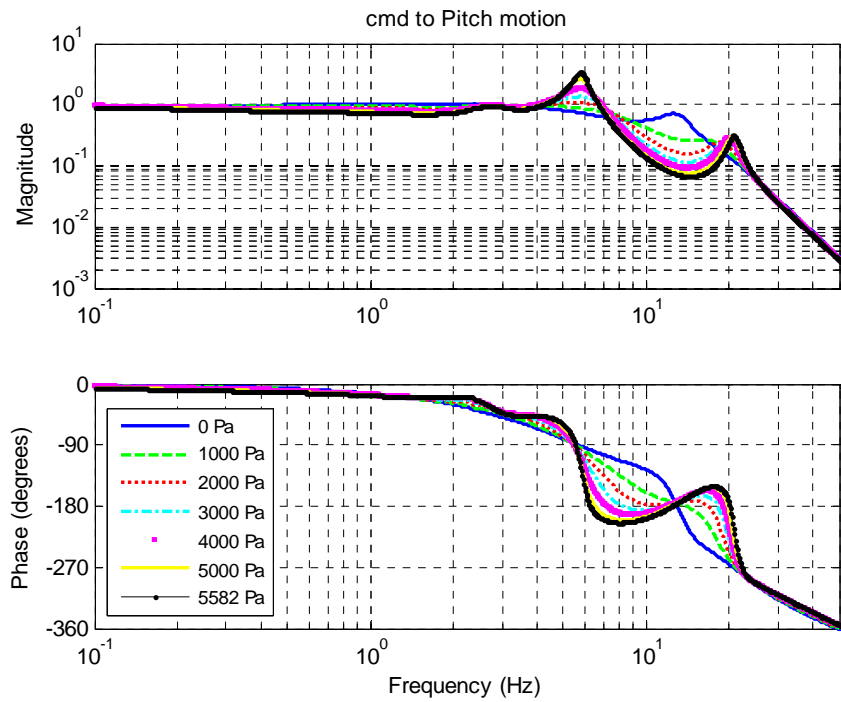
(a) main graphics
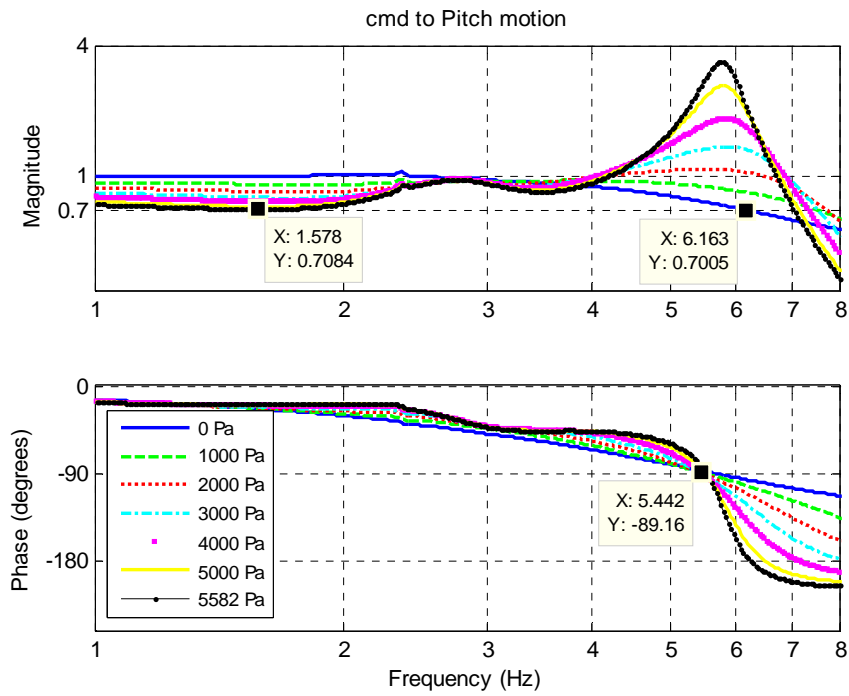
(b) detailed graphics

Figure 87. Frequency response from command input to pitch motion for various values of dynamic pressure
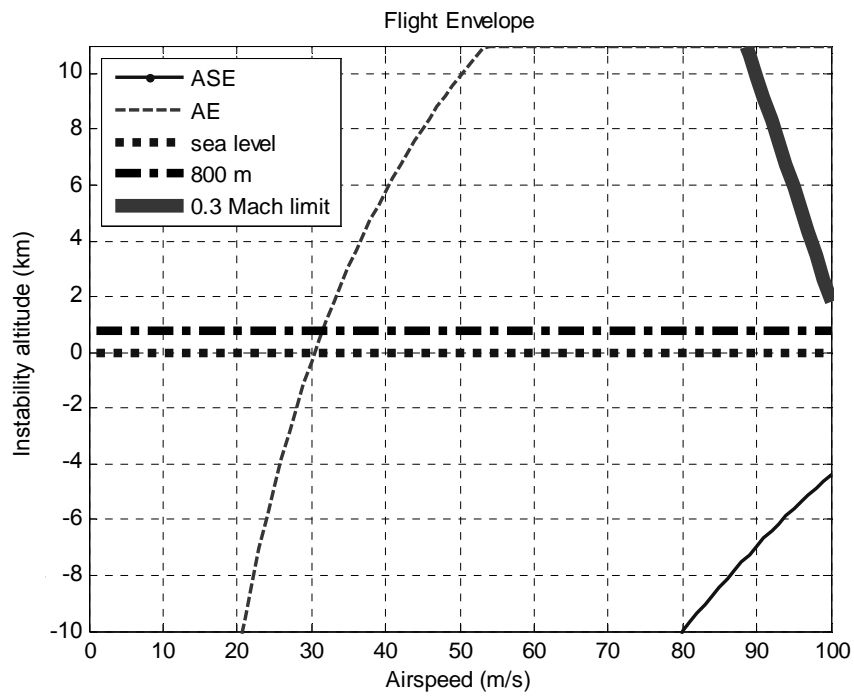
214
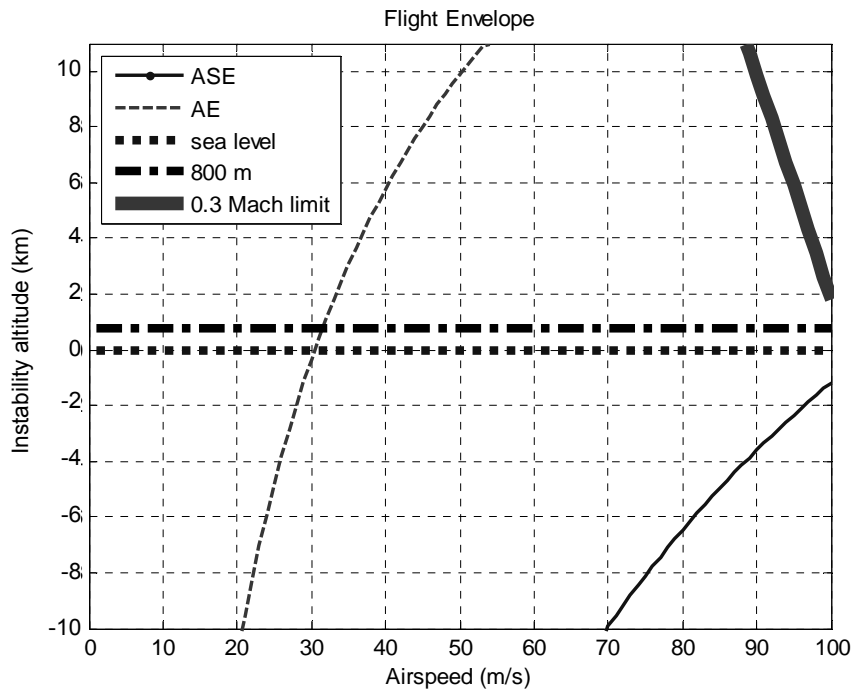
Figure 88. Flutter flight envelope
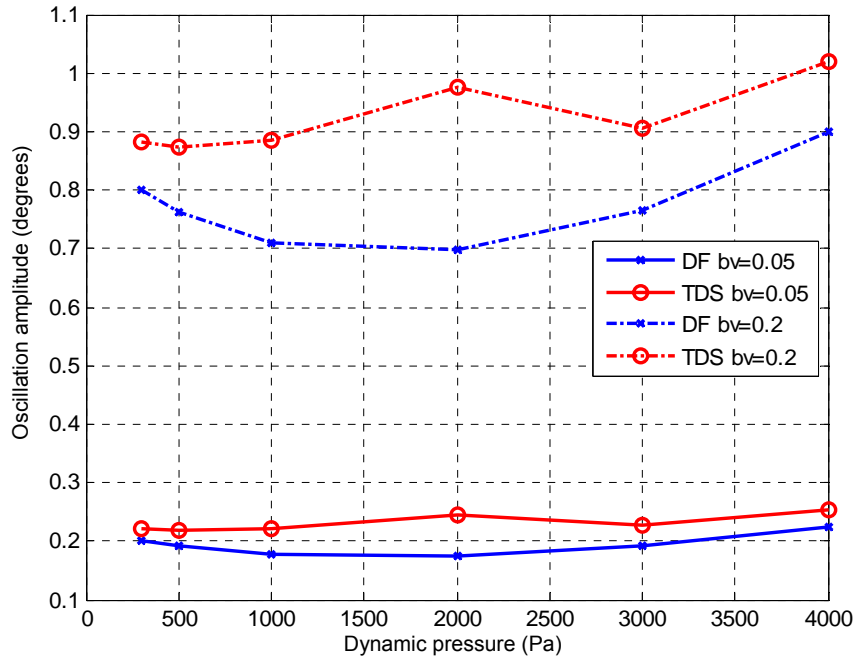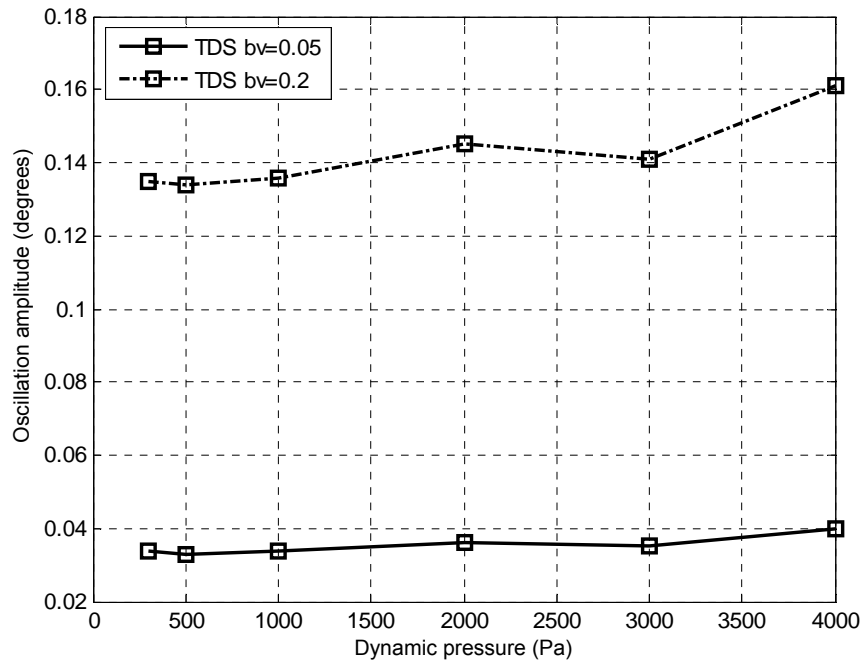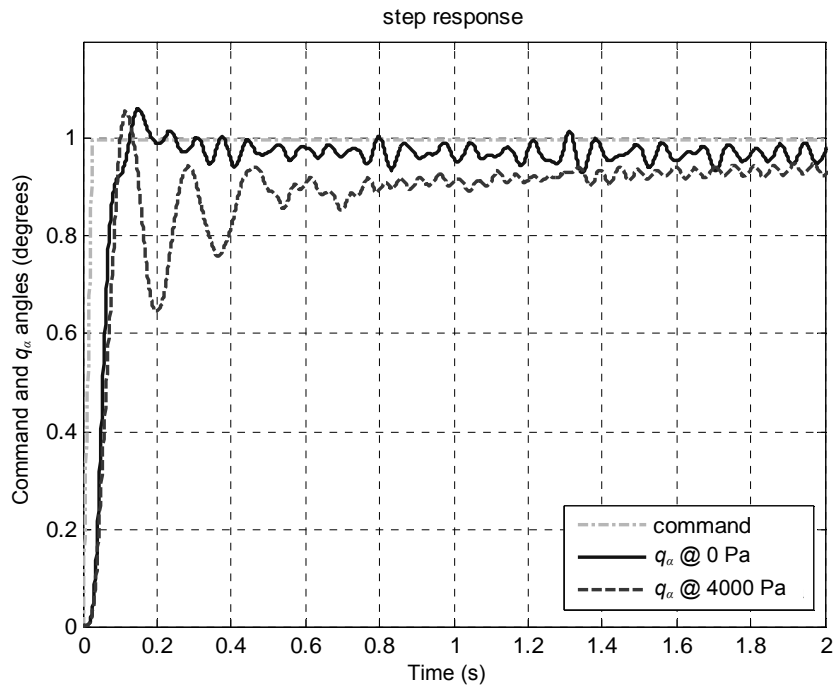

Figure 89. Step response of the aeroservoelastic system

215

(a) deflection of torsional spring, $\delta_{\alpha\theta}$

(b) q_α
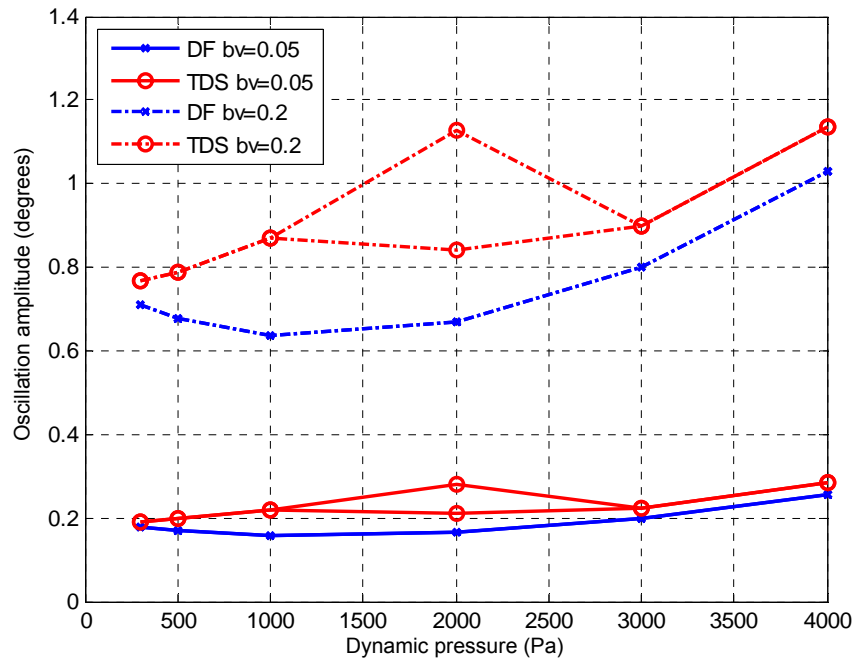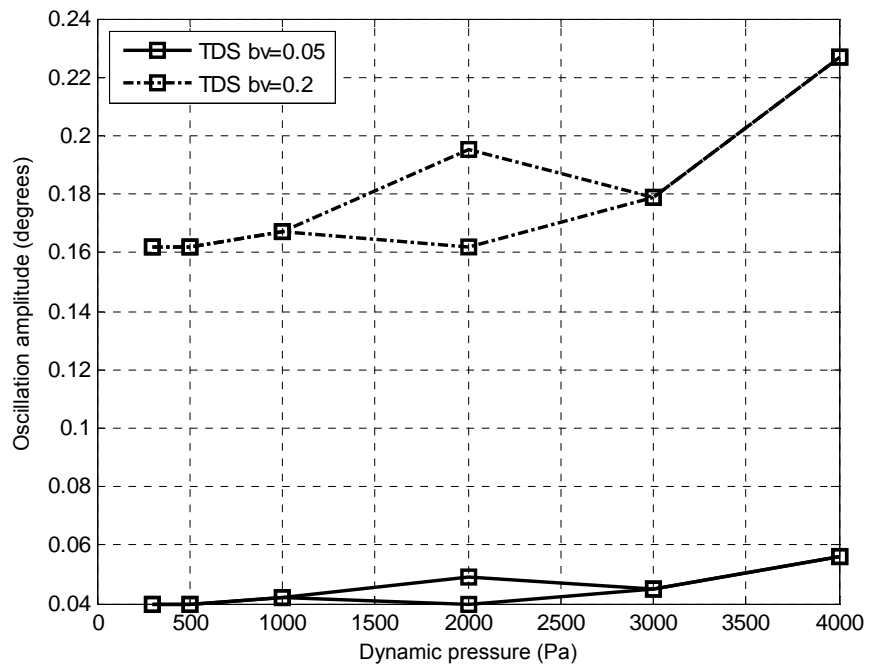
Figure 90. LCO amplitudes of the aeroservoelastic system with respect to
dynamic pressure for various backlash values

Table 26. Step response properties of aeroservoelastic system with
quantized sensor at two different dynamic pressure conditions

$\bar{q}$ simulation		0 Pa	4,000 Pa
ω_n	Hz	5.63	5.47
$tr_{5\%}$	s	0.085	0.068
ts	s	-	-
Mp	%	6.3	5.9
e_{ss}	deg	-0.032 ±0.023	-0.055 ±0.019
$\delta_{\alpha\theta}$	deg	1.33	2.21
cr_1	A	0.66	0.58
cr_2	A	0	0.017
cr_3	A	0.111	0.246
cr_4	A	0.25	0.45

It can be seen from the Figure 88 that the synthesized H_2 controller enhances the flutter free flight envelope out of incompressible region above sea level. However, as it can be seen from Figure 87, over the dynamic pressure of 4,000 Pa the bandwidth of the aeroservoelastic system drops below 2 Hz. The controller suppresses the oscillations the fin in pitch degree of freedom to a comparable level with the backlash value. During the time domain analysis of LCO at 2,000 Pa the aeroservoelastic system encountered two different LCO, Figure 90.

6.2.2.3. *μ* controller synthesis

For the μ synthesis, various controllers are synthesized by tuning the $\bar{q}_{dist}$, $\bar{q}_{cont}$, and $\left[W_{Fd} \right]$ values, the results are presented in Appendix D. It is seen from these results that, similar to previous cases, the increase of the $\bar{q}_{cont}$; enhances the performance of the system at 4,000 Pa, but decreases the performance at 0 Pa. The increase of $\bar{q}_{dist}$, increases the flutter margin in lower and upper limits. However, the increase of $\bar{q}_{dist}$, also

increases the μ norm, thus it cannot be increased after a certain value. The increase of the amplitude of $[W_{Fd}]$ at 0 Hz and 10 Hz, slightly decreases the steady state error and increases the flutter margin, however it also increases the current consumption and the μ norm of the system. The tuned parameters and their final values are presented in Table 27. The standatd analyses which are conducted to the aeroservoelastic system with H_2 controller are conducted for aeroservoelastic system with μ controller. The results of the analyses of the aeroservoelastic system with the selected controller are given in Table 28, Table 29, and in Figure 95 through Figure 94. Analyzing the results it can be seen that the synthesized controller enlarged the flutter free flight envelope of the aeroservoelastic system out of incompressible flow limits. Furthermore, the controller also satisfies the design value of the bandwidth in an acceptable tolerance.

Table 27. Tuned parameters of μ controller

Parameter			Value
$[W_{Fd}]$	g_{Fd_F}	@ 0 Hz	2,800 N
		@ 10 Hz	50 N.m
	g_{Fd_M}	@ 0 Hz	56 N
		@ 10 Hz	1 N.m
$[W_{\bar{q}2}]$	$\bar{q}_{dist}$		2,500 Pa
$\bar{q}_{cont}$			AP #3
Order of the reduced controller			20
μ norm of the weighted ASE system			0.979

Table 28. Nominal stability limits

$\bar{q}_{ins_{low}}$	Pa	-1,036
$\omega_{ins_{low}}$	Hz	2.95
$\bar{q}_{ins}$	Pa	9,754
ω_{Ins}	Hz	7.57
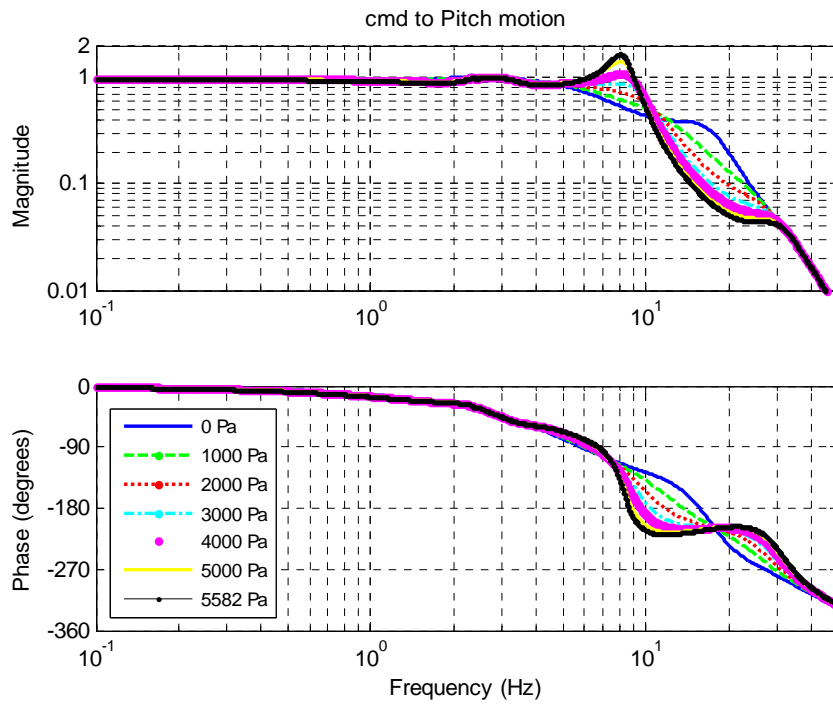
(a) main graphics
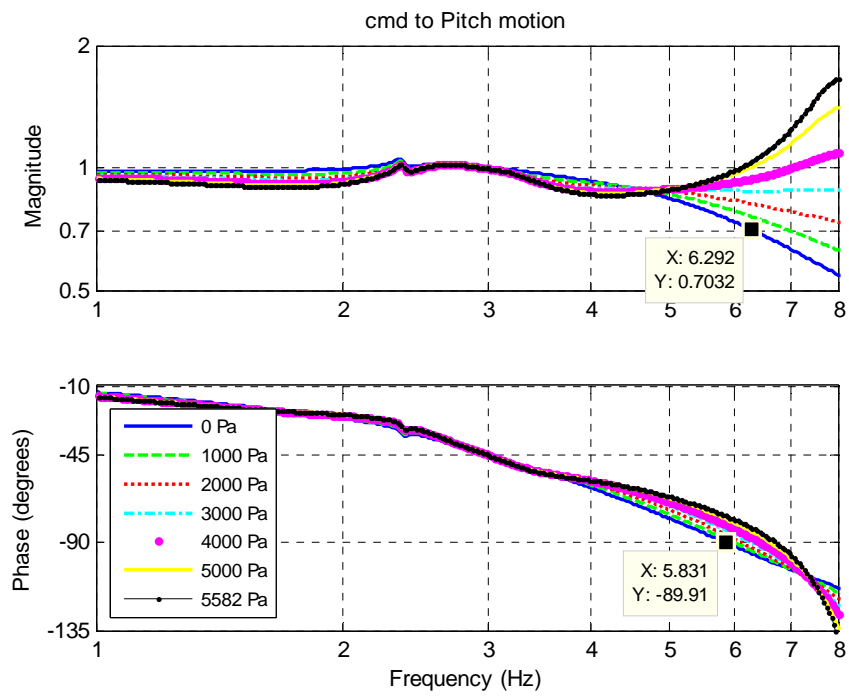
(a) detailed graphics

Figure 91. Frequency response from command input to pitch motion for various values of dynamic pressure

219
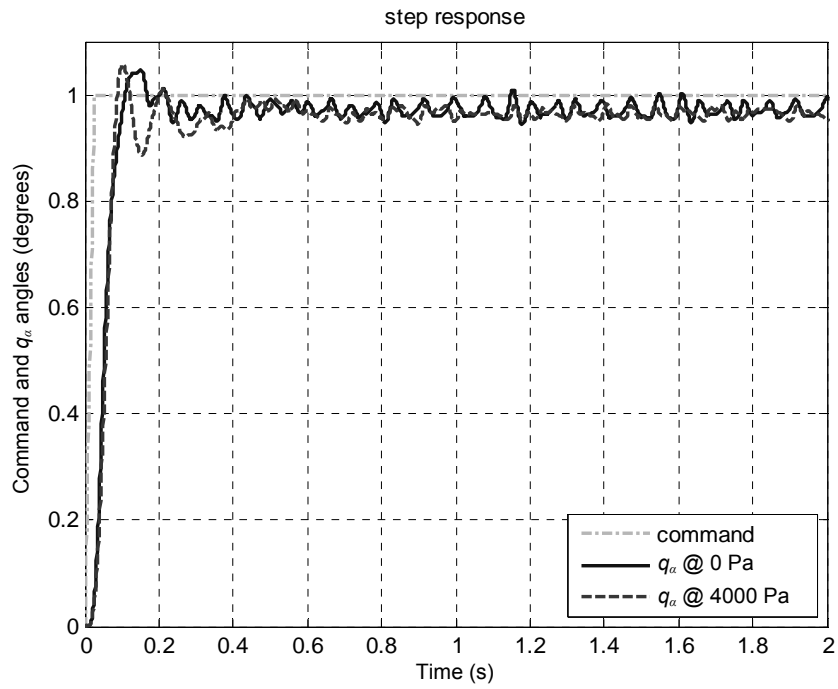
Figure 92. Step response of the aeroservoelastic system
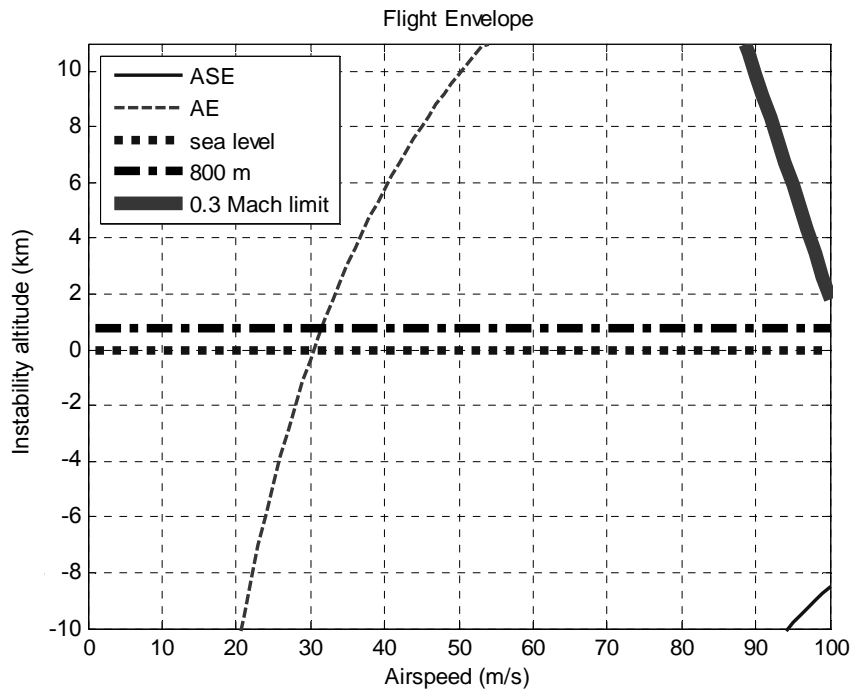
Figure 93. Flutter flight envelope

220

(a) deflection of torsional spring, $\delta_{\alpha\theta}$

(b) q_α
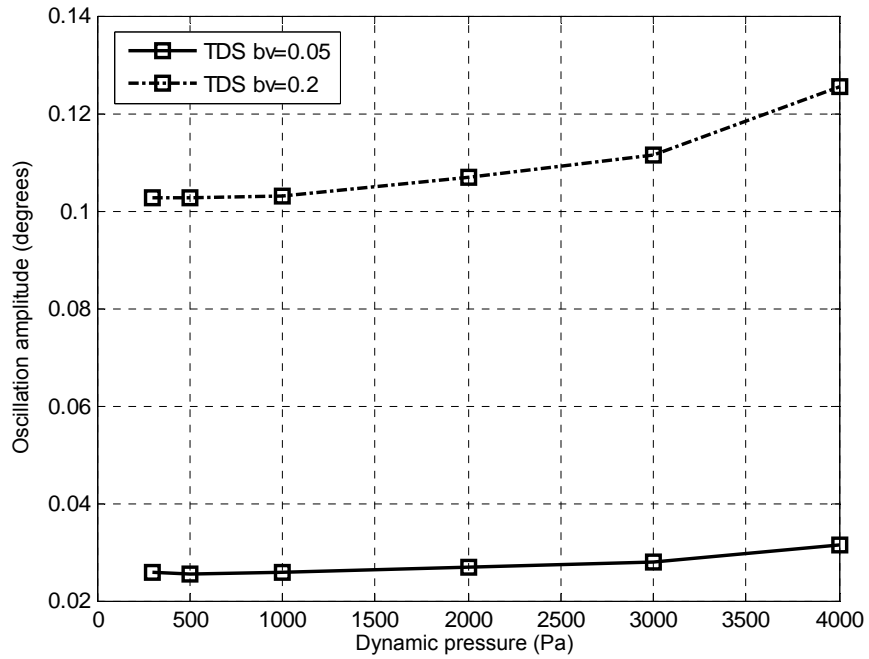
Figure 94. LCO amplitudes of the aeroservoelastic system with respect to dynamic pressure for various backlash values

Table 29. Step response properties of aeroservoelastic system with quantized sensor at two different dynamic pressure conditions

$\bar{q}$ simulation		0 Pa	4,000 Pa
ω_n	Hz	5.84	6.43
$tr_{5\%}$	s	0.072	0.056
ts	s	0.371	-
Mp	%	4.8	5.6
e_{ss}	deg	-0.028 ±0.021	-0.039 ±0.014
$\delta_{\alpha\theta}$	deg	1.23	2.11
cr_1	A	2.65	2.93
cr_2	A	0	0.018
cr_3	A	0.774	0.896
cr_4	A	2.19	2.93

6.2.3. Controller Synthesis by Using g-Method

As explained in Section 4.4, g-method uses the damping as the uncertainty parameter in order to suppress the flutter. The interconnection block diagram of the aeroservoelastic plant is given in Figure 18. As it can be seen from the figure, the additional elements are the output weighting function $[W_{c1}]$ of damping uncertainty and input weighting function $[W_{c2}]$ of damping uncertainty blocks. All parameters of the other blocks are taken same as in q-Method, which are given in Table 12. The damping uncertainty is only introduced to the pitch degree of freedom of the typical section wing. The uncertainty blocks and their parameters that are used to define the uncertainty of damping are given in Table 30. The δ_c term is the damping uncertainty in N.m.s/rad, which is a free parameter for tuning. The g_{c1} and g_{c2} terms, as the gains of the weighting functions, are obtained by solving the Equation (4.19). As the value of the q_θ input of Equation (4.19), the expected command input defined in Table 12 is used.

Table 30. Numerical values of uncertainty/performance weightings

Uncertainty Name	Gain		Corner Frequency		Scale Parameter	
$[W_{c1}]$	g_{c1}	1.141 s/rad				
$[W_{c2}]$	g_{c2}	δ_c*0.876 rad/s	ω_{c2}	6 Hz	κ_{c2}	0.01

Other tuning parameters of g-method are the dynamic pressure $\bar{q}_{cont}$ at which the controller is synthesized and the weighting functions $[W_{Fd}]$ of the disturbance to aerodynamic force. In the $[W_{Fd}]$ block, the gains at 0 Hz and 10 Hz can be tuned. However, as stated in Section 4.3, the $[W_{Fd}]$ function has similar effects to the system as the input weighting function $[W_{\bar{q}2}]$ of the disturbance to dynamic pressure of q-method has. The difference is separated as the function $[W_{Fd}]$ affects the lower frequencies in order to consider the steady state error, and the function $[W_{\bar{q}2}]$ considers the frequencies of which the instability occurs. Hence an increase in the gain of the function $[W_{Fd}]$ at 10 Hz affects the system as the function $[W_{\bar{q}2}]$, especially in H$_2$ and H$_\infty$ type controller syntheses. Hence, if the gain of the function $[W_{Fd}]$ at 10 Hz is increased, the resulting system can be considered as a mixture of q and g-methods. Thus for the g-method, the gain of function $[W_{Fd}]$ at 10 Hz is kept fixed and the gain of the function $[W_{Fd}]$ at 0 Hz is altered only.

6.2.3.1. H$_\infty$ controller synthesis

Similar to the q-method cases, various controllers are synthesized by altering the tuning parameters. Results of these analyses are presented in Appendix D. The main tuning parameter in g-method is the δ_c term. Three different controllers are synthesized by selecting the δ_c term as 1, 2,

and 3 N.m.s/rad. It is seen that for the δ_c =1, the bandwidth of the ASE system at 4,000 Pa becomes 1.8 Hz, which is unacceptable. On the other side, it is seen that the increase of the δ_c term;

- increases the infinity norm of the weighted ASE system, which limits the increase of the δ_c at a certain value,
- decreases the margin of stability at the lower bound, but the change is not unacceptable,
- deteriorate the mean and the oscillation amplitude of the steady state error at 4,000 Pa,
- increases the overshoot at 0 Pa,
- increases the current consumption,
- improves the rise time at 0 Pa,
- decreases the deformation of the torsional spring.

Considering the upper statements, δ_c is selected as 2 N.m.s/rad.

The second tuning parameter is the dynamic pressure $\bar{q}_{cont}$ at which the controller is synthesized. The previous syntheses performed in this Section are synthesized for $\bar{q}_{cont}$ =161.1 Pa, which is named as AP #1 in Table 20. In order to see the effect of the $\bar{q}_{cont}$, two more controllers are synthesized for δ_c=2 N.m.s/rad. The new controllers are synthesized for AP #3 and #5, as defined in Table 20. It is seen that the increase of $\bar{q}_{cont}$;

- decreases the infinity norm of the weighted ASE system,
- slightly increases the margin of stability at the lower bound,
- slightly decreases the mean value of the steady state error at 4,000 Pa,
- slightly increases the bandwidth of the system at 4,000 Pa, from 4.97 to 5.12,
- decreases the bandwidth of the system at 0 Pa, from 5.83 to 5.43,
- slightly increases the rise time at 0 Pa,
- increases the overshoot at 0 Pa,

- increases the deformation of the torsional stiffness at 0 Pa.

Considering statements given above, controller synthesized at AP #1 is selected.

By increasing the gain of the $[W_{Fd}]$ function at 0 Hz, and analyzing the magnitude of frequency response of the ASE system at 4,000 Pa it is seen that the decrease in the amplitude of the frequency response at 1.8 Hz increases to 2.92 dB. Furthermore, it is seen that the improvements obtained are not considerable. The selected values of the tuning parameters and the properties of the synthesized controller are given in Table 31.

Table 31. Tuned parameters of H∞ controller

Parameter			Value
$[W_{Fd}]$	g_{Fd_F}	@ 0 Hz	1,400 N
		@ 10 Hz	25 N.m
	g_{Fd_M}	@ 0 Hz	5.6 N
		@ 10 Hz	0.1 N.m
$[W_{c2}]$	δ_c		2 N.m.s/rad
	ω_{c2}		6 Hz
$\bar{q}_{cont}$			AP #1
Order of the reduced controller			13
Infinity norm of the weighted ASE system			0.810

The results of the standard analyses for the ASE system with the selected controller are given in Table 32, Table 33, and Figure 95 through Figure 98. From the flutter flight envelopes it can be seen that the controller suppresses the instability well above the incompressible limits. From the step response graphics and Table 33, it can be seen that the system has very small or no overshoot, and has about 3%-5% steady state error. As it can be seen from the Figure 98, the amplitude of the LCO

at 4,000 Pa for 0.2° backlash value is about 0.65°. The fin motion for the same condition is ~0.13° which is less than the backlash value.

Table 32. Nominal stability limits

$\bar{q}_{ins_{low}}$	Pa	-995
$\omega_{ins_{low}}$	Hz	2.88
$\bar{q}_{ins}$	Pa	-*
ω_{ins}	Hz	-*

* There is no instability up to 100,000 Pa

Table 33. Step response properties of aeroservoelastic system with quantized sensor at two different dynamic pressure conditions

$\bar{q}$ simulation		0 Pa	4,000 Pa
ω_n	Hz	5.83	4.97
$tr_{5\%}$	s	0.079	0.076
ts	s	-	-
Mp	%	1.1	-
e_{ss}	deg	-0.033 ±0.022	-0.044 ±0.010
$\delta_{\alpha\theta}$	deg	1.21	1.99
cr_1	A	0.81	0.77
cr_2	A	0	0.019
cr_3	A	0.248	0.263
cr_4	A	0.80	0.58
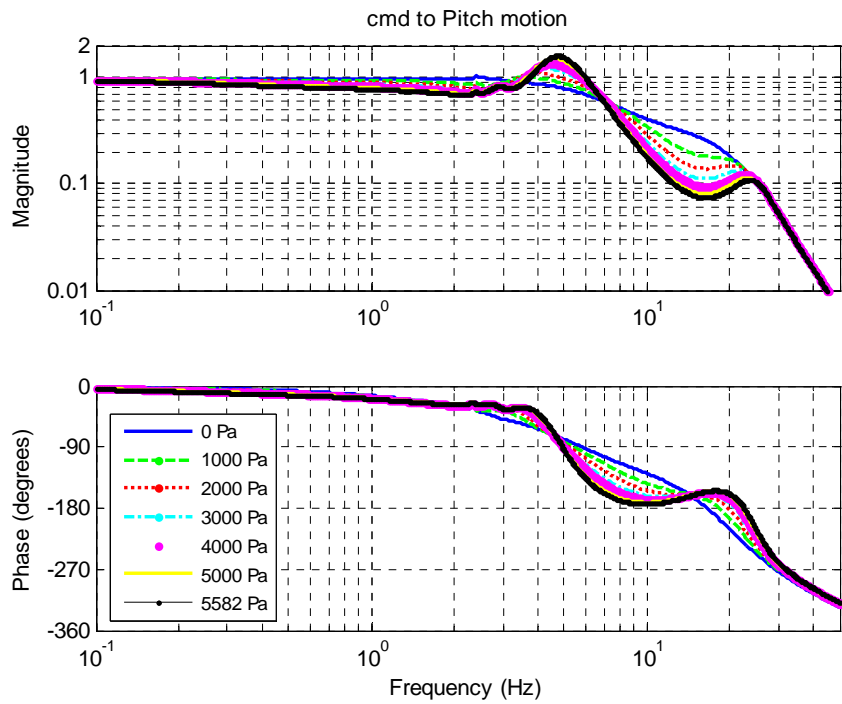
(a) main graphics
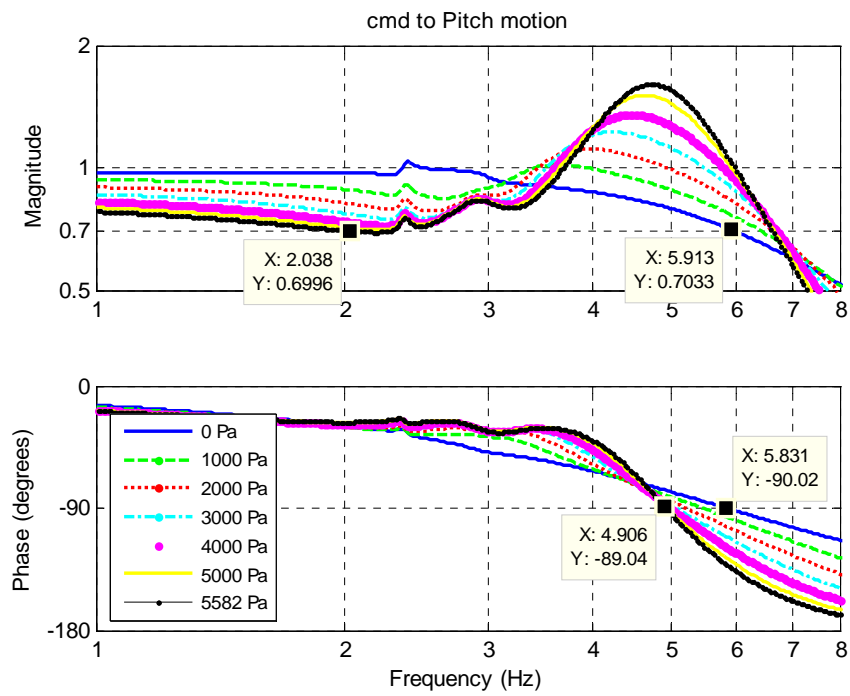
(b) detailed graphics

Figure 95. Frequency response from command input to pitch motion for various values of dynamic pressure

Figure 96. Step response of the aeroservoelastic system

Figure 97. Flutter flight envelope

(a) deflection of torsional spring, $\delta_{\alpha\theta}$

(b) q_α

Figure 98. LCO amplitudes of the aeroservoelastic system with respect to dynamic pressure for various backlash values

6.2.3.2. H₂ controller synthesis

For the H₂ synthesis, a set of controllers are synthesized by tuning the $[W_{c2}]$ function, $\bar{q}_{cont}$, and gain of $[W_{Fd}]$ function at 0 Hz. The results are presented in Appendix D. It is seen that the obtained ASE systems have 30% decrease in magnitude around 1-2 Hz at 4,000 Pa dynamic pressure. This value is well below the design specification of 6 Hz. Hence, although the synthesized controllers adequately enhanced the stability limit, due the violation of performance requirements a proper controller can not be obtained.

6.2.3.3. μ controller synthesis

For the selection of μ controller, less number of syntheses are performed and most parameters are kept the same as the selected g-method H∞ controller. Results of these analyses are presented in Appendix D. In these syntheses only the δ_c term, the main tuning parameter in g-method, is altered. From the analyses, it is seen that the increase of the δ_c term;

- slightly enlarges the margin of stability at the lower bound,
- slightly decreases the bandwidth,
- increases the steady state error,
- increases the rise time,
- decreases the overshoot,
- increases the current consumption,

of the aeroservoelastic system. Considering these statements, δ_c is selected as 1 N.m.s/rad. The selected values of the tuning parameters and the properties of the synthesized controller are given in Table 34.

Table 34. Tuned parameters of μ controller

Parameter			Value
$[W_{Fd}]$	g_{Fd_F}	@ 0 Hz	1,400 N
		@ 10 Hz	25 N.m
	g_{Fd_M}	@ 0 Hz	5.6 N
		@ 10 Hz	0.1 N.m
$[W_{c2}]$	δ_c		1 N.m.s/rad
	ω_{c2}		6 Hz
$\bar{q}_{cont}$			AP #1
Order of the reduced controller			18
μ norm of the weighted ASE system			0.428

The results of the standard analyses for the ASE system with the selected controller are given in Table 35, Table 36, and Figure 99 through Figure 102. From the flutter flight envelopes it can be seen that the controller suppresses the instability well above the incompressible limits. Analyzing the Figure 102 it can be seen that the amplitude of the LCO at 4,000 Pa for 0.2° backlash value is less than 0.50°. The fin motion for the same condition is less than 0.07° which is less than half of the backlash value.

Table 35. Nominal stability limits

$\bar{q}_{ins_{low}}$	Pa	-1,004
$\omega_{ins_{low}}$	Hz	2.92
$\bar{q}_{ins}$	Pa	-*
ω_{ins}	Hz	-*

* There is no instability up to 100,000 Pa
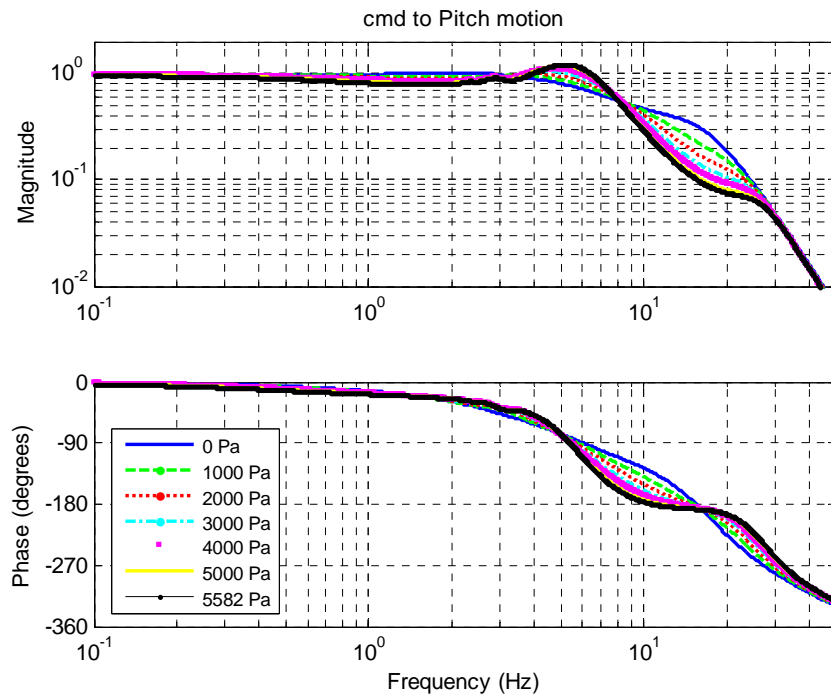
(a) main graphics
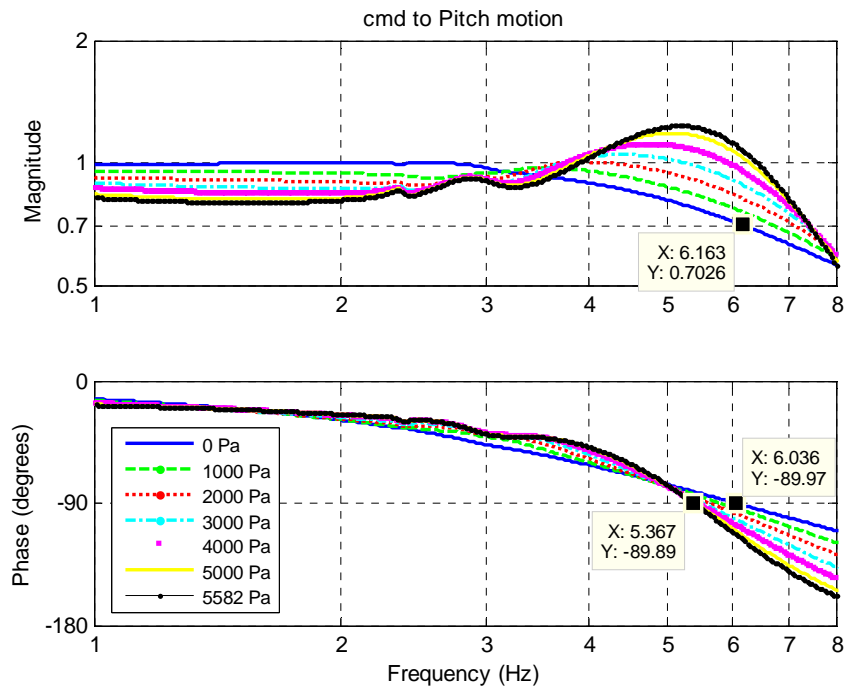
(b) detailed graphics

Figure 99. Frequency response from command input to pitch motion for various values of dynamic pressure
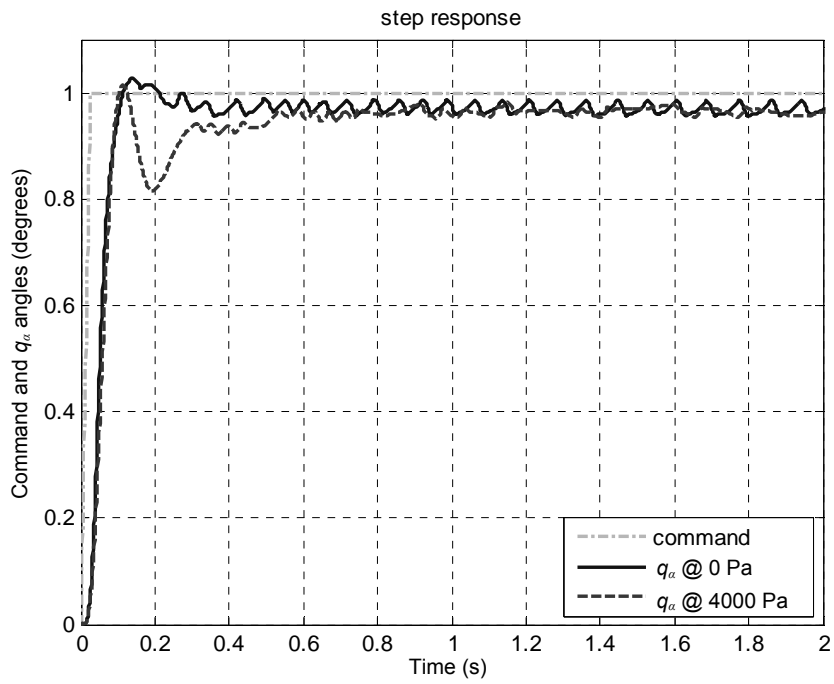
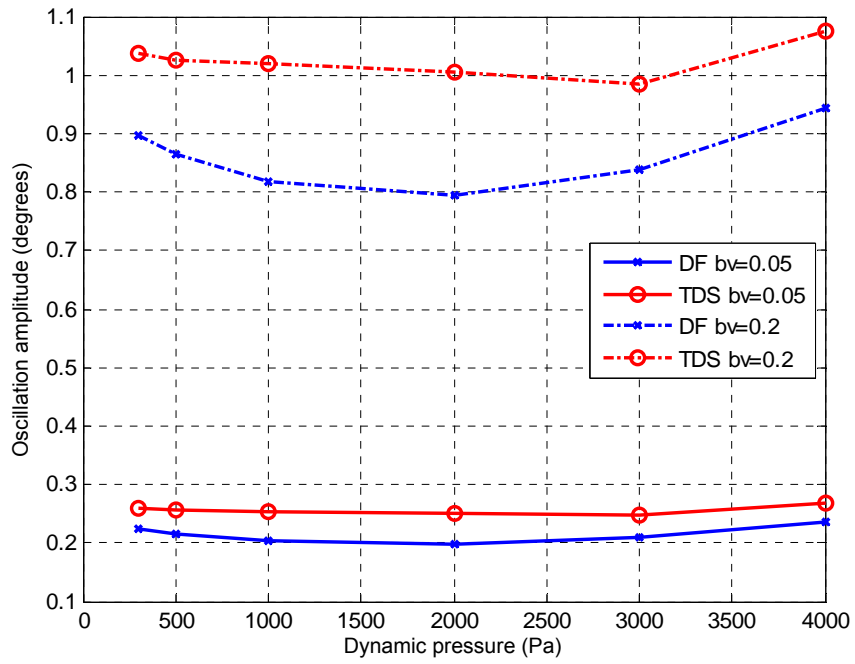**Figure 100.** Step response of the aeroservoelastic system
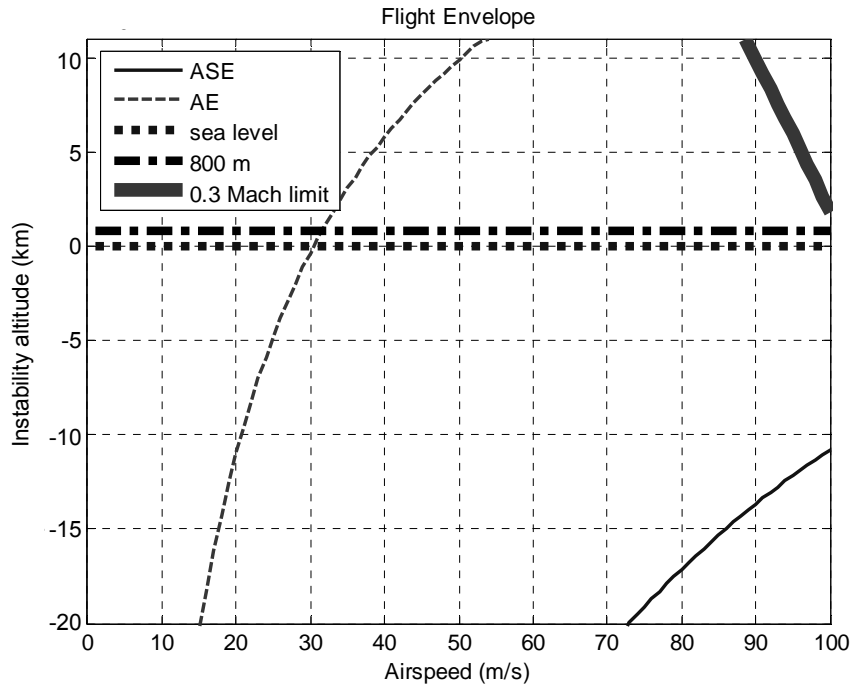

Figure 101. Flutter flight envelope

(a) deflection of torsional spring, $\delta_{\alpha\theta}$

(b) q_α
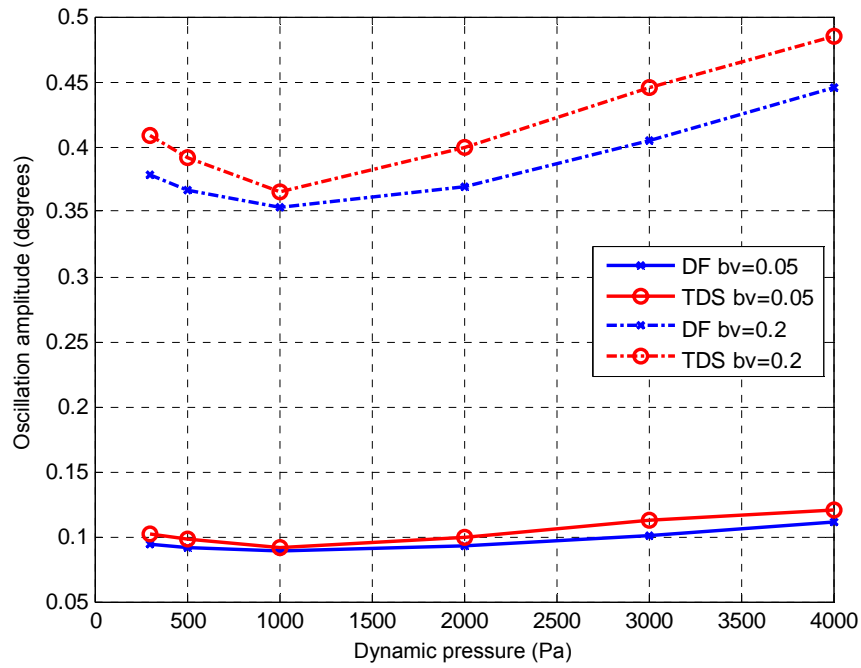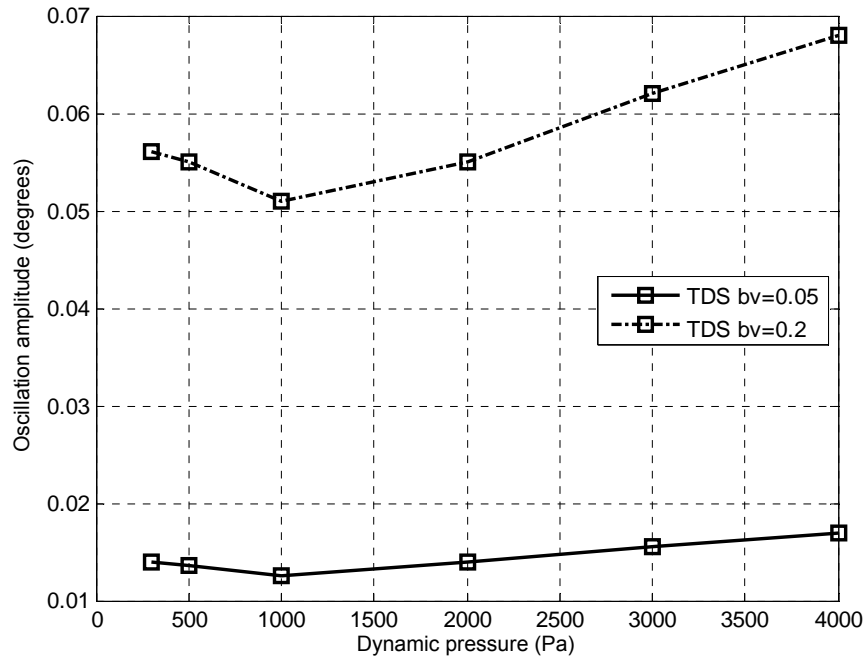
Figure 102. LCO amplitudes of the aeroservoelastic system with respect to dynamic pressure for various backlash values

Table 36. Step response properties of aeroservoelastic system with quantized sensor at two different dynamic pressure conditions

$\bar{q}$ simulation		0 Pa	4,000 Pa
ω_n	Hz	6.03	5.43
$tr_{5\%}$	s	0.074	0.067
ts	s	0.100	0.748
Mp	%	3.0	1.5
e_{ss}	deg	-0.029 ±0.015	-0.034 ±0.013
$\delta_{\alpha\theta}$	deg	1.26	1.97
cr_1	A	1.32	1.82
cr_2	A	0	0.018
cr_3	A	0.421	0.453
cr_4	A	1.06	1.82

6.2.4. Controller Synthesis by Using gq-Method

In Section 6.2.3, it is discussed that the increase in the gain of the weighting function $[W_{Fd}]$ of aerodynamic disturbance forces at 10 Hz in g-method affects the synthesis procedure similar to the input weighting function $[W_{\bar{q}2}]$ of disturbance to dynamic pressure in q-method. Hence in Section 6.2.3, the gain of the $[W_{Fd}]$ function at 10 Hz is kept same as its value at q-method synthesis. In this Section, this parameter is also used as a tuning parameter. The controllers are synthesized both considering the uncertainty of damping via input weighting function $[W_{c2}]$ of damping uncertainty and the uncertainty of dynamic pressure via $[W_{Fd}]$ function.

6.2.4.1. H∞ controller synthesis

The H∞ controller is synthesized by altering the $[W_{Fd}]$ function parameters of the selected H∞ controller of g-method, and the results are given in Appendix D. The selected values of the tuning parameters and the properties of the synthesized controller are given in Table 37.

Table 37. Tuned parameters of H∞ controller

Parameter			Value
$[W_{Fd}]$	g_{Fd_F}	@ 0 Hz	2,800 N
		@ 10 Hz	50 N.m
	g_{Fd_M}	@ 0 Hz	16.8 N
		@ 10 Hz	0.3 N.m
$[W_{c2}]$	δ_c		2 N.m.s/rad
	ω_{c2}		6 Hz
$\bar{q}_{cont}$			AP #1
Order of the reduced controller			13
Infinity norm of the weighted ASE system			0.932

The results of the standard analyses of the aeroservoelastic system with the synthesized controller are given in Table 38, Table 39, and in Figure 103 through Figure 106. As it can be seen from these results, the synthesized controller enlarges the stability limits out of the incompressible flow limits, and fairly satisfies the bandwidth requirement.
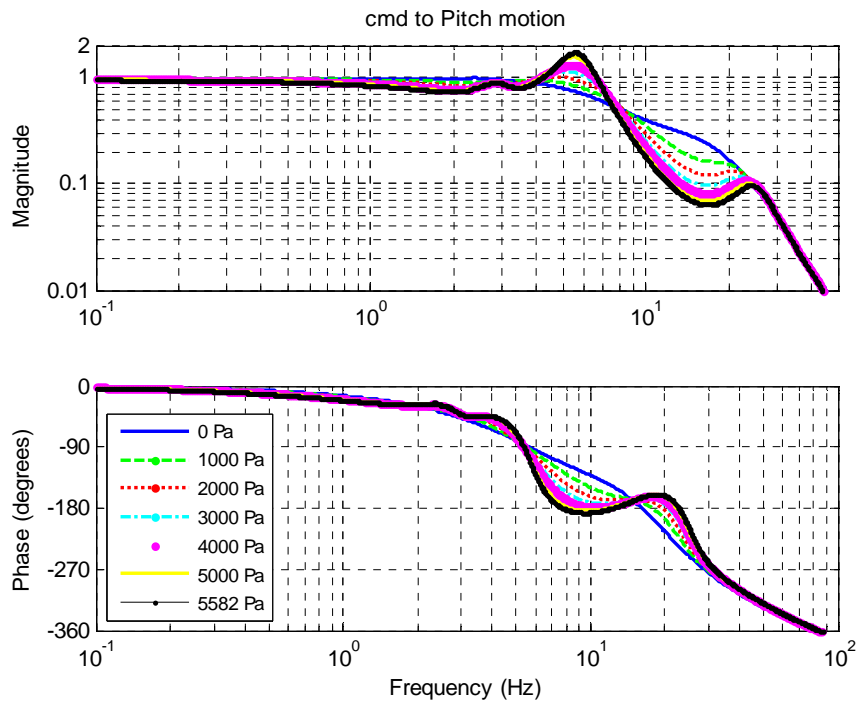
(a) main graphics
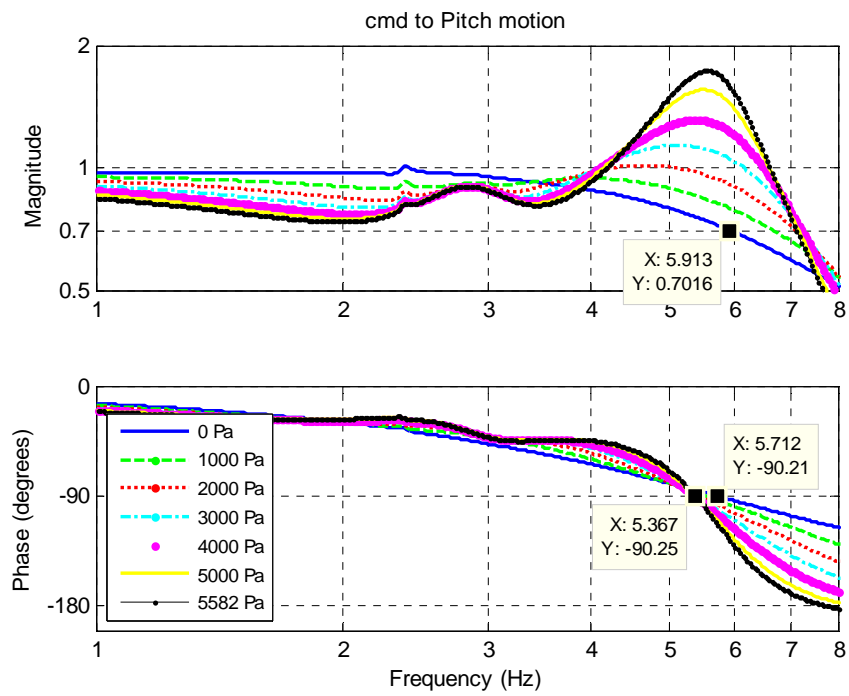
(b) detailed graphics

Figure 103. Frequency response from command input to pitch motion for various values of dynamic pressure
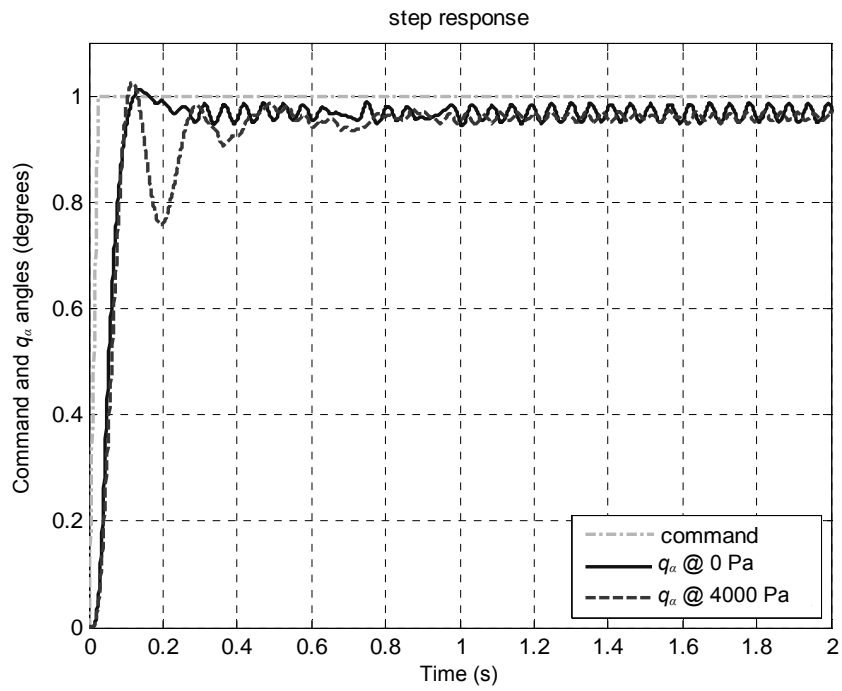
Figure 104. Step response of the aeroservoelastic system
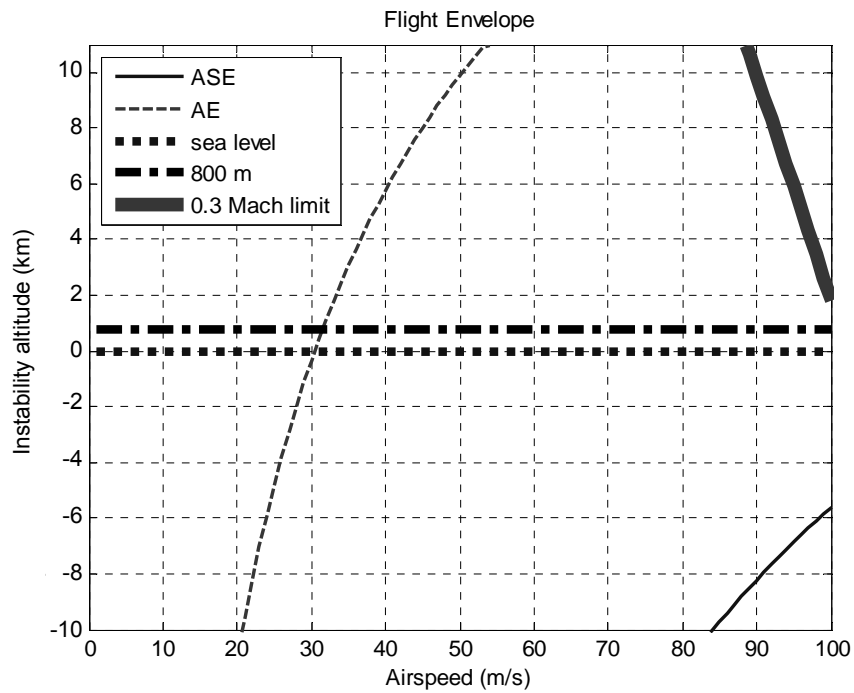
Figure 105. Flutter flight envelope

238

(a) deflection of torsional spring, $\delta_{\alpha\theta}$

(b) q_α
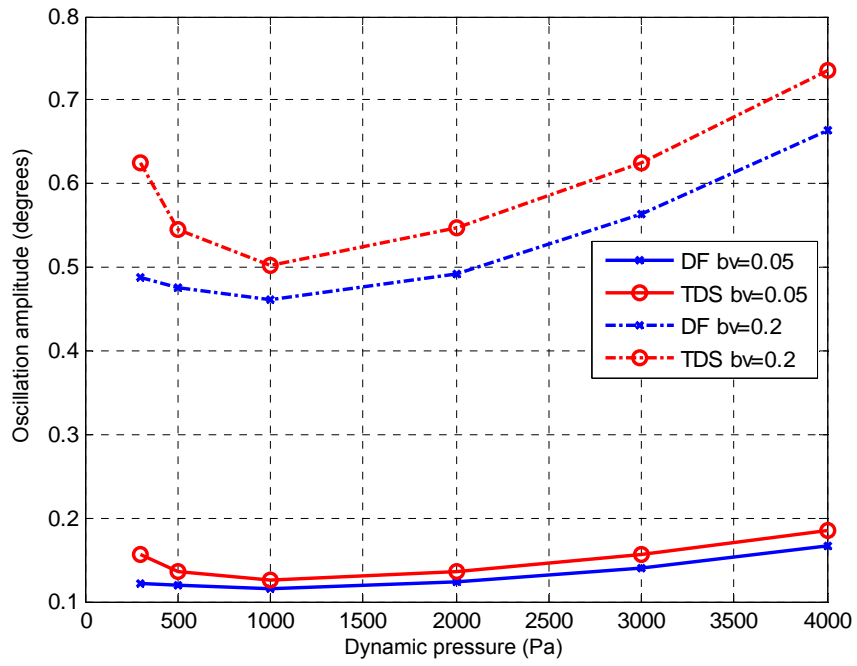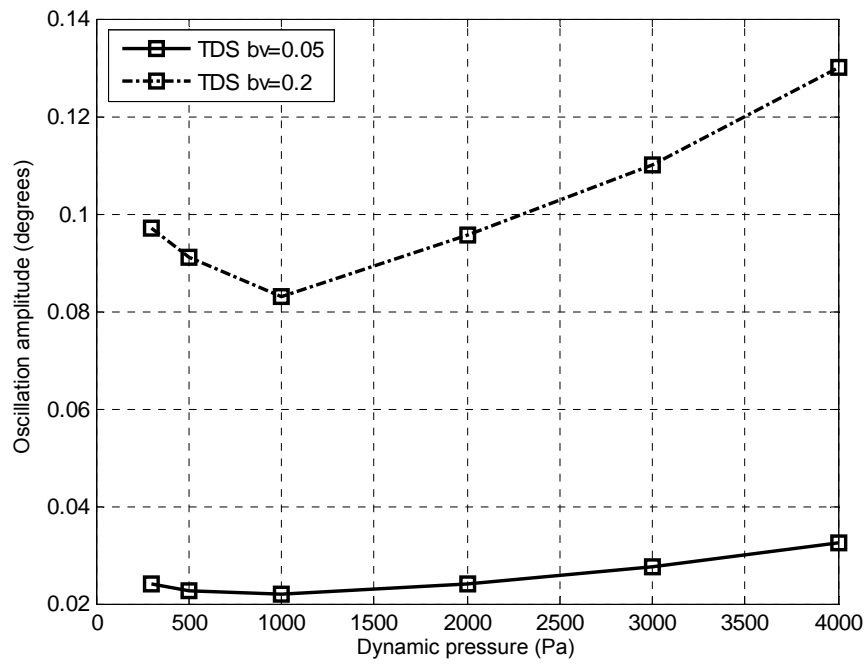
Figure 106. LCO amplitudes of the aeroservoelastic system with respect to dynamic pressure for various backlash values

Table 38. Nominal stability limits

$\bar{q}_{ins_{low}}$	Pa	-988
$\omega_{ins_{low}}$	Hz	2.93
$\bar{q}_{ins}$	Pa	-*
ω_{ins}	Hz	-*

* There is no instability up to 100,000 Pa

Table 39. Step response properties of aeroservoelastic system with quantized sensor at two different dynamic pressure conditions

$\bar{q}$ simulation		0 Pa	4,000 Pa
ω_n	Hz	5.70	5.36
$tr_{5\%}$	s	0.077	0.070
ts	s	-	-
Mp	%	1.2	2.6
e_{ss}	deg	-0.033 ±0.019	-0.038 ±0.016
$\delta_{\alpha\theta}$	deg	1.19	2.13
cr_1	A	0.87	0.92
cr_2	A	0	0.019
cr_3	A	0.270	0.364
cr_4	A	0.57	0.92

6.2.4.2. H$_2$ controller synthesis

The H$_2$ controller is synthesized by improving the synthesized H$_2$ controllers of g-method via modifying the parameters of the $\left[W_{Fd}\right]$ block. The properties of different H$_2$ controllers are presented in Appendix D. The selected values of the tuning parameters and the properties of the synthesized controller are given in Table 40. The results of the standard analyses of the aeroservoelastic system with the selected controller are given in Table 41, Table 42, and in Figure 107 through Figure 110. From

the results it is seen that the selected controller stabilizes the aeroservoelastic system in incompressible region, but it can fairly satisfy the bandwidth requirement.

Table 40. Tuned parameters of H_2 controller

Parameter			Value
$[W_{Fd}]$	g_{Fd_F}	@ 0 Hz	2,800 N
		@ 10 Hz	50 N.m
	g_{Fd_M}	@ 0 Hz	28 N
		@ 10 Hz	0.5 N.m
$[W_{c2}]$	δ_c		2 N.m.s/rad
	ω_{c2}		6 Hz
$\bar{q}_{cont}$			AP #4
Order of the reduced controller			12
H_2 norm of the weighted ASE system			11.297

Table 41. Nominal stability limits

$\bar{q}_{ins_{low}}$	Pa	-851
$\omega_{ins_{low}}$	Hz	13.0
$\bar{q}_{ins}$	Pa	8,467
ω_{ins}	Hz	5.42
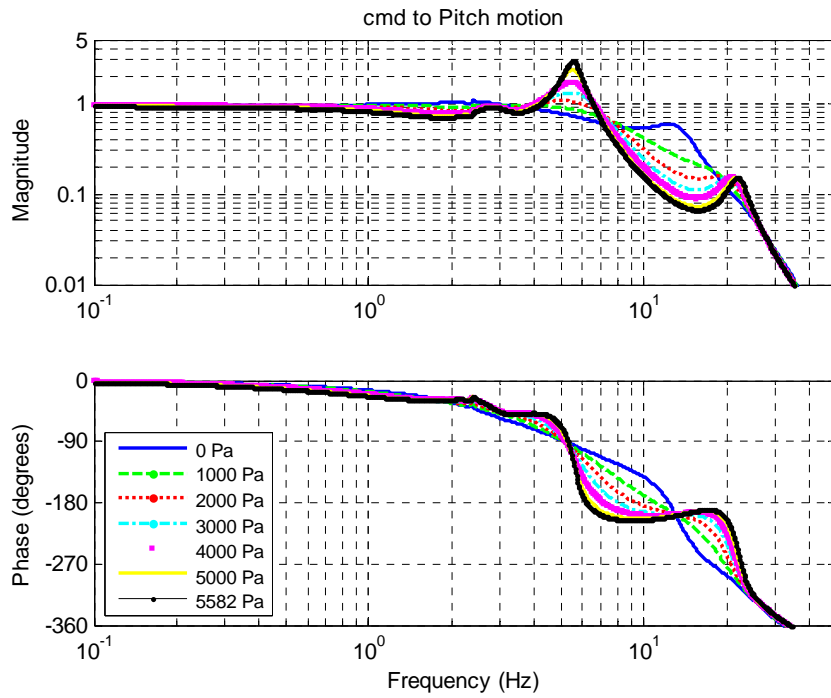
(a) main graphics
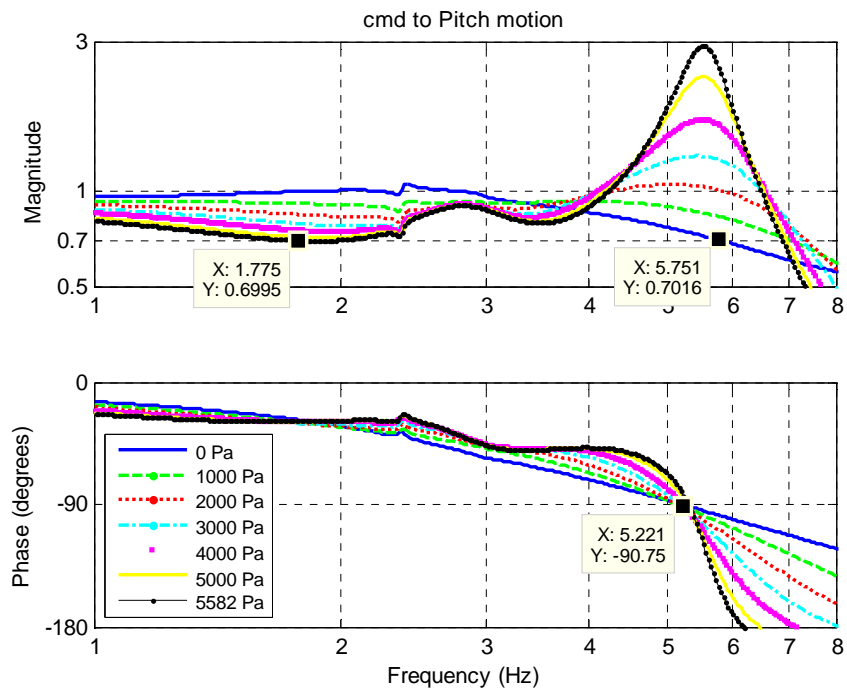
(b) detailed graphics

Figure 107. Frequency response from command input to pitch motion for various values of dynamic pressure
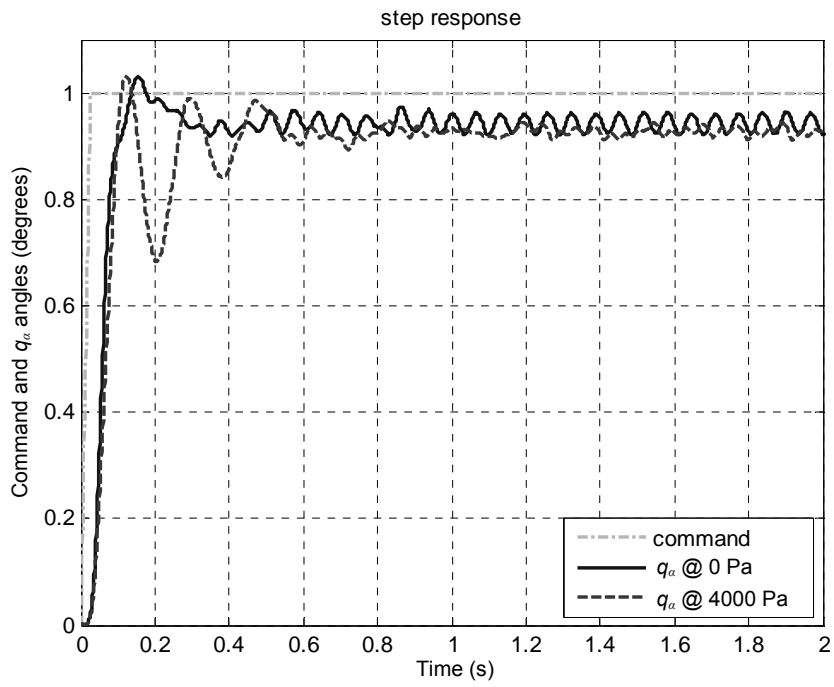
Figure 108. Step response of the aeroservoelastic system
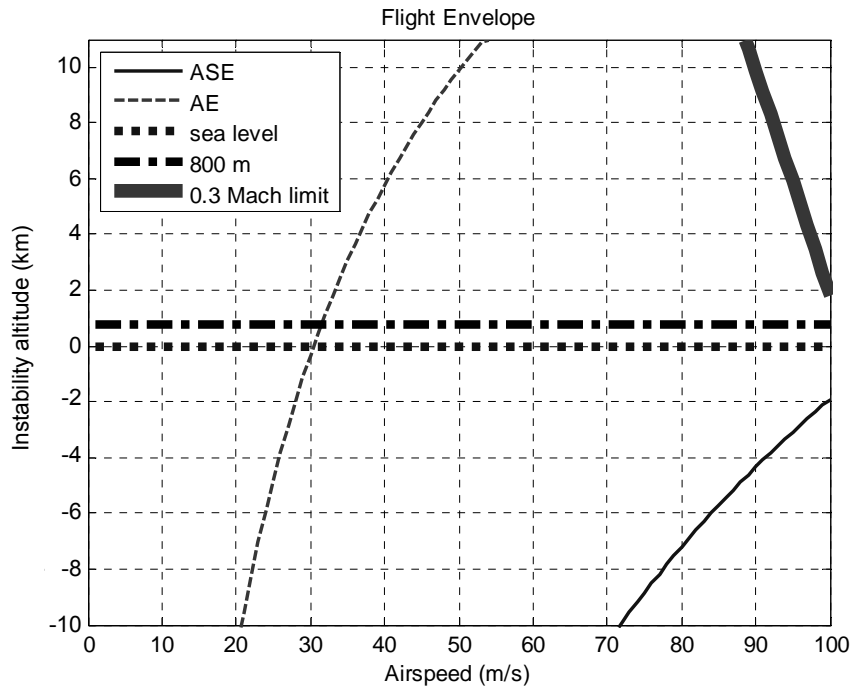
Figure 109. Flutter flight envelope

243

(a) deflection of torsional spring, $\delta_{\alpha\theta}$

(b) q_α
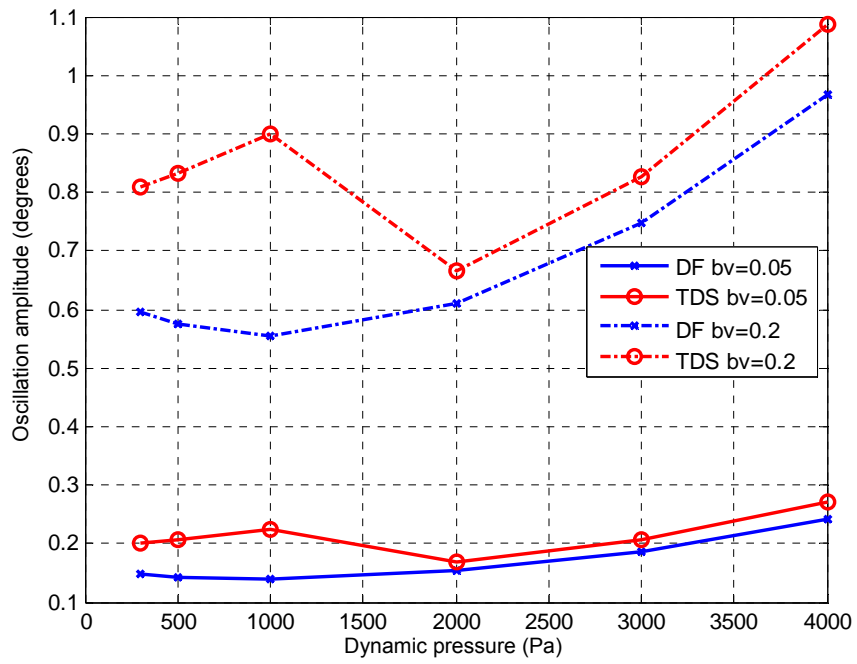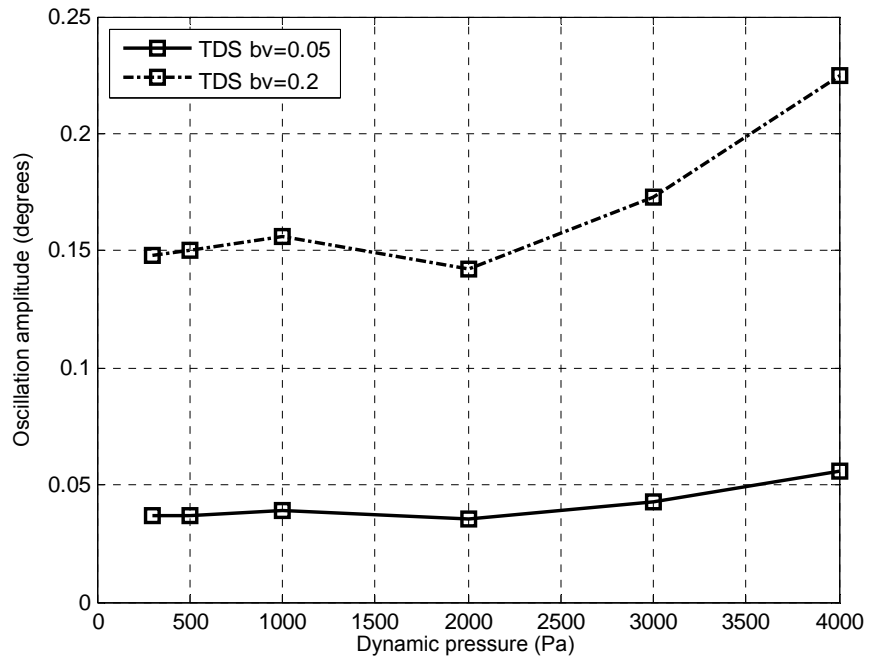
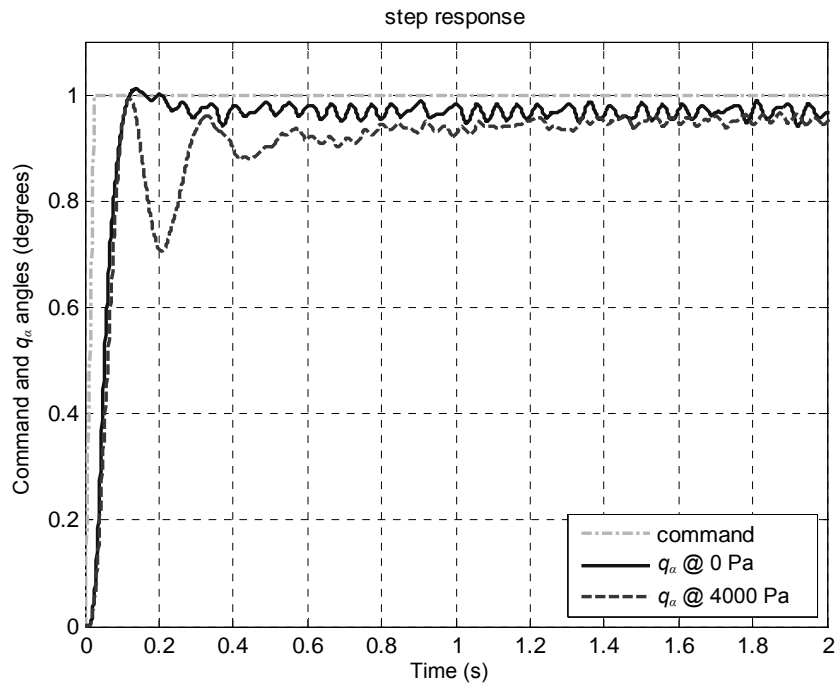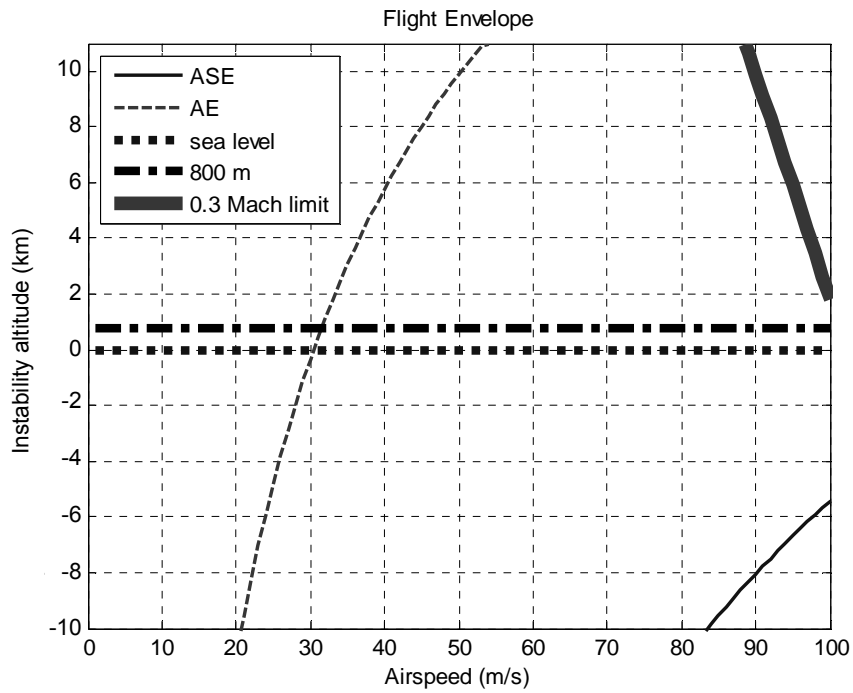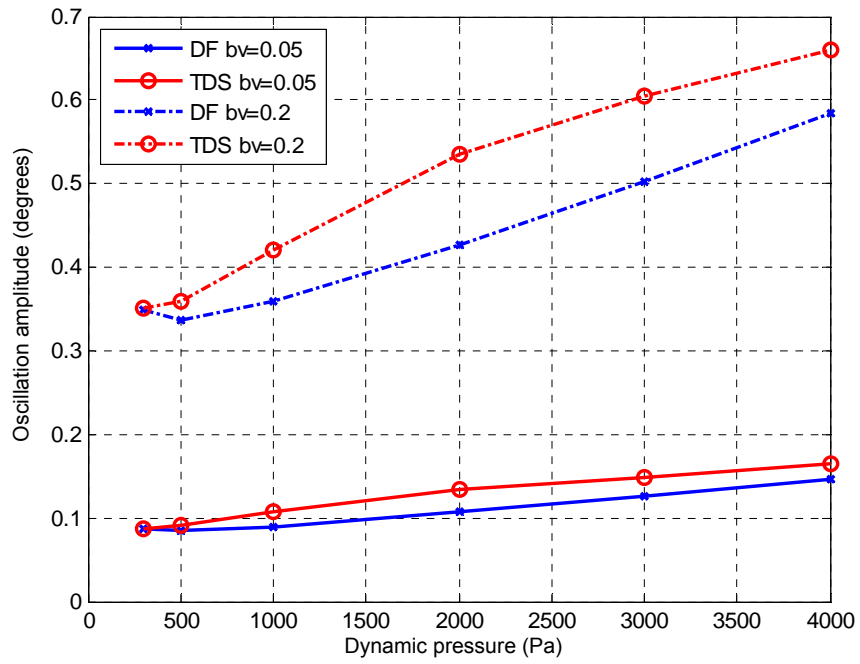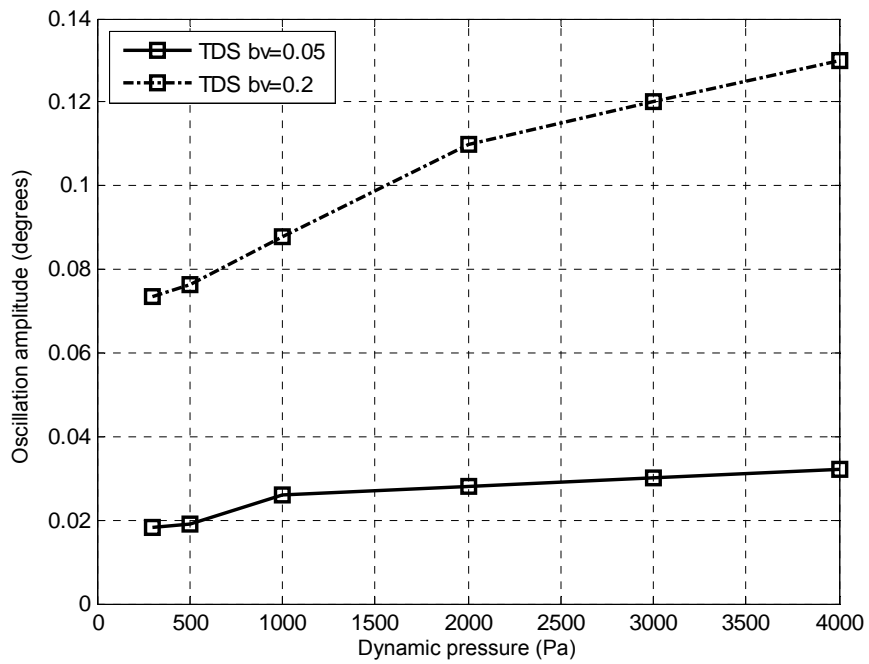**Figure 110.** LCO amplitudes of the aeroservoelastic system with respect to dynamic pressure for various backlash values

244

Table 42. Step response properties of aeroservoelastic system with
quantized sensor at two different dynamic pressure conditions

$\bar{q}$ simulation		0 Pa	4,000 Pa
ω_n	Hz	5.21	5.22
$tr_{5\%}$	s	0.090	0.071
ts	s	-	-
Mp	%	2.9	3.0
e_{ss}	deg	-0.056 ±0.023	-0.072 ±0.017
$\delta_{\alpha\theta}$	deg	1.23	2.17
cr_1	A	0.59	0.59
cr_2	A	0	0.018
cr_3	A	0.139	0.276
cr_4	A	0.30	0.57

6.2.4.3. *μ* controller synthesis

The μ controller is synthesized by altering the parameters of the weighting function $\left[W_{F_d}\right]$ of the aerodynamic disturbance forces. The properties of aeroservoelastic system with various μ controllers are presented in Appendix D. The selected values of the tuning parameters and the properties of the synthesized controller are given in Table 44. The results of the analyses are given in Table 44, Table 45, and in Figure 111 through Figure 114. From the results it can be seen that the synthesized controller enhances the flight envelope out of incompressible flight region. Furthermore, it satisfies the bandwidth requirement within an acceptable tolerance.

Table 43. Tuned parameters of μ controller

Parameter			Value
$[W_{Fd}]$	g_{Fd_F}	@ 0 Hz	2,800 N
		@ 10 Hz	50 N.m
	g_{Fd_M}	@ 0 Hz	16.8 N
		@ 10 Hz	0.3 N.m
$[W_{c2}]$	δ_c		1 N.m.s/rad
	ω_{c2}		6 Hz
$\bar{q}_{cont}$			AP #1
Order of the reduced controller			18
Infinity norm of the weighted ASE system			0.527

Table 44. Nominal stability limits

$\bar{q}_{ins_{low}}$	Pa	-998
$\omega_{ins_{low}}$	Hz	2.94
$\bar{q}_{ins}$	Pa	-*
ω_{ins}	Hz	-*

* There is no instability up to 100,000 Pa

Table 45. Step response properties of aeroservoelastic system with quantized sensor at two different dynamic pressure conditions

$\bar{q}$ simulation		0 Pa	4,000 Pa
ω_n	Hz	5.75	5.76
$tr_{5\%}$	s	0.075	0.062
ts	s	0.100	0.329
Mp	%	2.8	3.8
e_{ss}	deg	-0.027 ±0.014	-0.029 ±0.011
$\delta_{\alpha\theta}$	deg	1.17	2.01
cr_1	A	1.87	2.21
cr_2	A	0	0.018
cr_3	A	0.525	0.541
cr_4	A	1.29	1.75
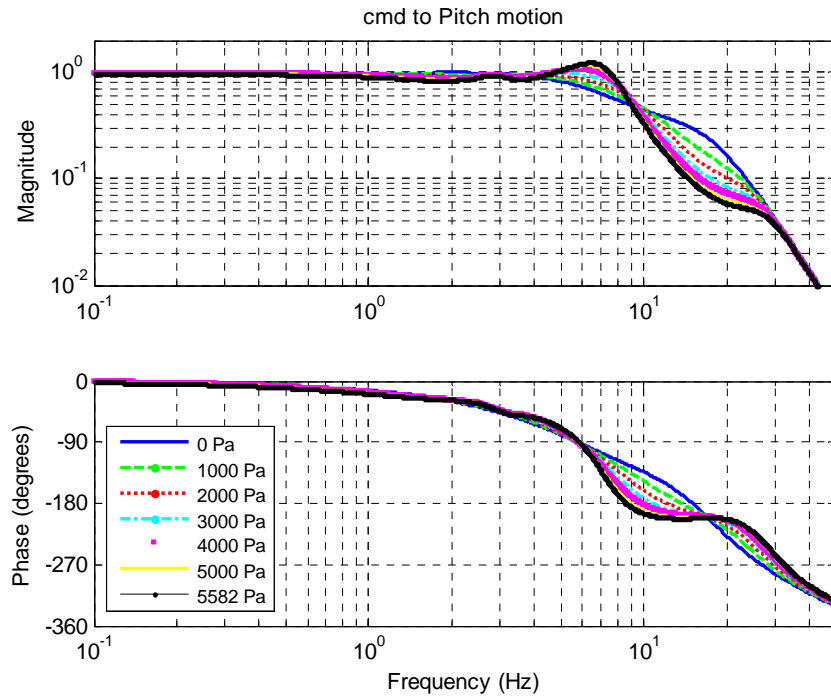
(a) main graphics
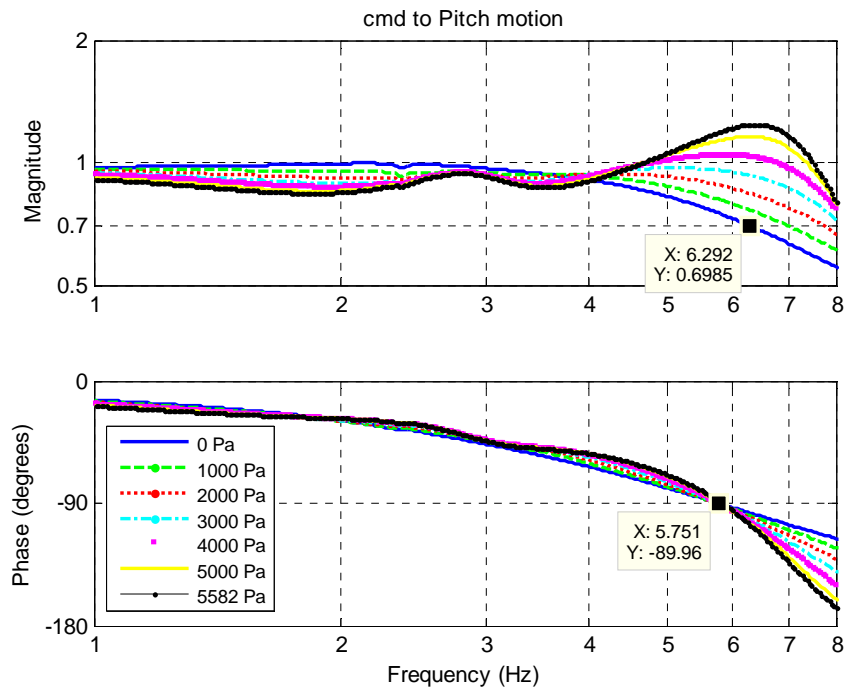
(b) detailed graphics

Figure 111. Frequency response from command input to pitch motion for various values of dynamic pressure
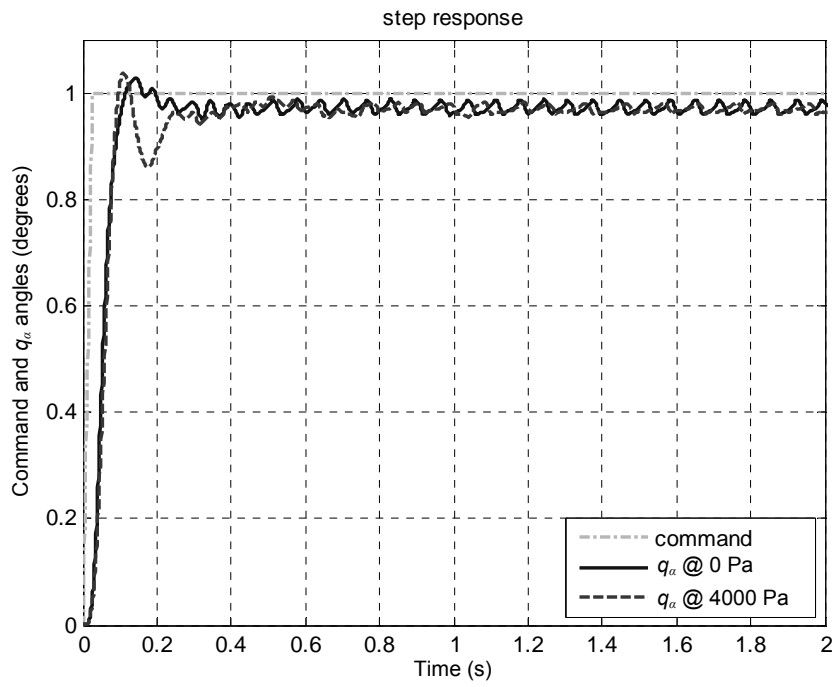
Figure 112. Step response of the aeroservoelastic system
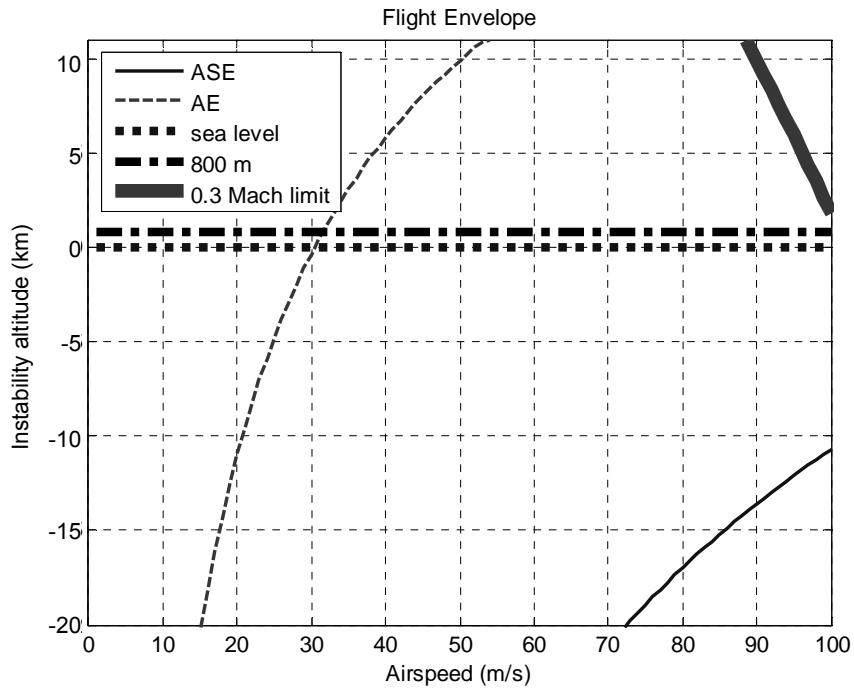
Figure 113. Flutter flight envelope

248

(a) deflection of torsional spring, $\delta_{\alpha\theta}$

(b) q_α
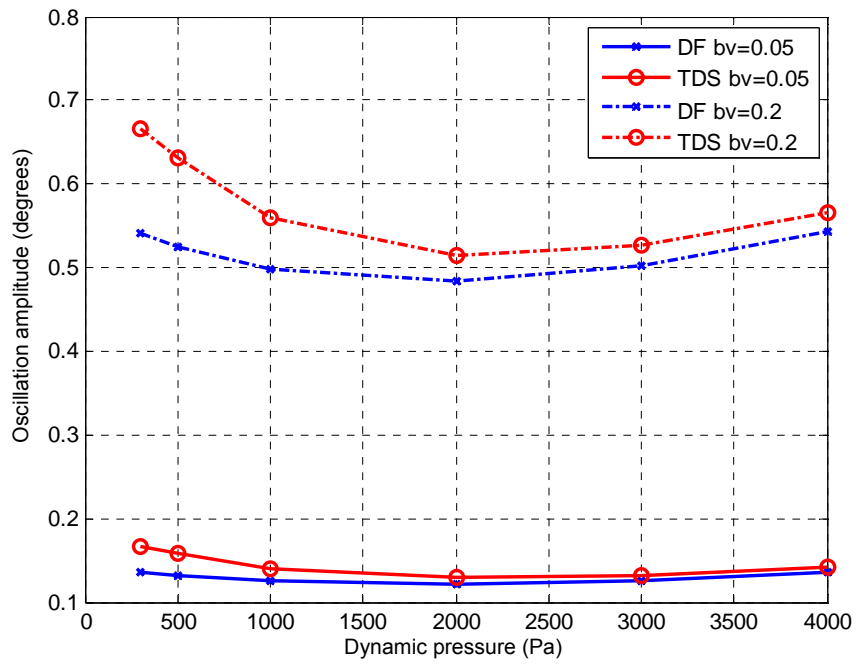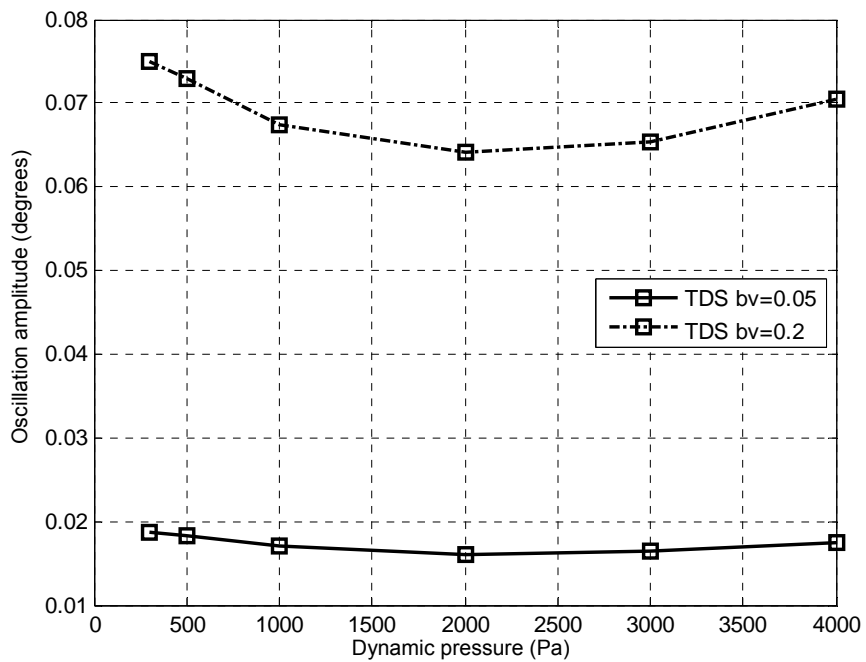
Figure 114. LCO amplitudes of the aeroservoelastic system with respect to dynamic pressure for various backlash values

6.2.5. Controller Synthesis by Using gk-Method

Lind [38] suggested to model system nonlinearities by using uncertainties in a robust controller synthesis. In the study of Lind [38] it is mentioned that, if the possible system differences due to nonlinearity is enclosed by the nominal system with uncertainties, the synthesized controller can take these differentiations into account. However, in the same study it is also mentioned that the dynamics of the nonlinearity cannot be considered by the synthesized controller. In this Section, the suggested method is applied for the backlash at the pitch degree of freedom of the typical section wing. For its implementation, a parametric uncertainty is added to the torsional spring as shown in Figure 115. From the definition of the describing function of a backlash, it is known that the stiffness value varies between zero and the linear stiffness value. However, a controller can not be obtained from synthesis when a 100% uncertainty is defined for the torsional spring. Thus, decreasing the uncertainty level between 5% to 20% percent, various controllers are synthesized. Analyzing the aeroservoelastic systems with these controllers it seen that the inclusion of the stiffness uncertainty, and the increase of the percentage of the stiffness uncertainty, increase the amplitude of the LCO. Moreover a considerable enhancement is seen neither in bandwidth nor in the performance of the system. Hence, it is seen that the suggested solution method do not improve the LCO of this particular ASE system.
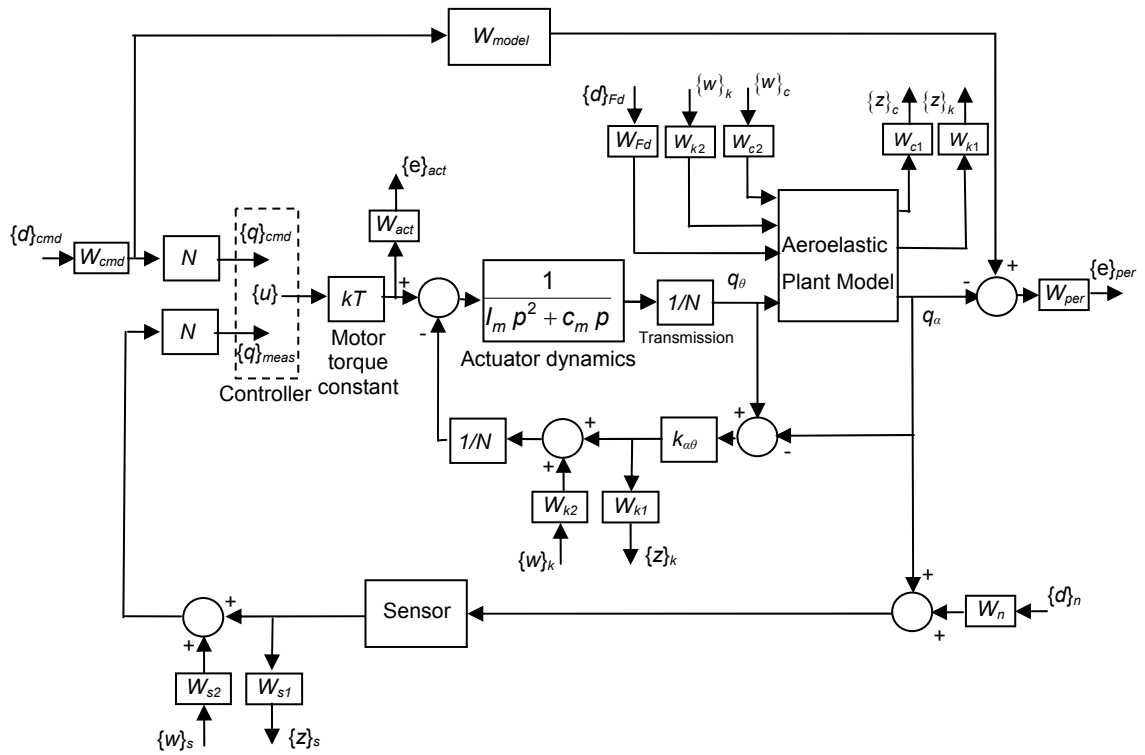
Figure 115. Interconnection structure of aeroelastic plant for gk-method

6.2.6. Comparison of the Controllers

For the subsonic incompressible flow, nine cases are analyzed. These cases are mainly based on two different flutter suppression methods, namely the q- and the g-methods. However, three of the nine implementations are performed by using gq-method, which uses the flutter suppression approach of both the q- and the g-methods and its synthesis procedure is based on the g-method. For the three flutter suppression methods, H_∞, H_2, and μ type controllers are synthesized. During the synthesis procedures the uncertainties, noise levels, and performance requirements except the tuning parameters are fixed, in order to be able to compare the performance of these controllers. The results of the analyses, that is performed for the aeroservoelastic system with the synthesized

controllers, are classified under three categories; linear stability, linear performance, and nonlinear analyses.

For the ease of understanding, the controllers synthesized with a specific flutter suppression method are named with its method name; i.e., q controllers are the controllers synthesized by q-method. Similar naming is applied for the type of controllers; i.e., H_2 type controllers are used as controllers synthesized by H_2 method. Hence, H_2&q controller is the H_2 type controller synthesized by q-method.

The results of the linear stability analyses of the aeroservoelastic system with the synthesized controllers are given in Table 46 and in Figure 116. It can be seen from these results that, all controllers enlarge the flutter flight envelope beyond the incompressible limits of 0.3 Mach above sea level. Analyzing the Figure 116 it can be seen that, considering the controller types; the μ controllers enlarge the flight envelope better than the other controller types and the second best controller type is the H_∞ controller. Considering the flutter suppression methods, except the H_2&g controller, the g and the gq-methods enlarge the flight envelope better than the q-method.

Table 46. Linear stability results

Controller		H_∞&q	H_2&q	μ&q	H_∞&g	H_2&g	μ&g	H_∞&gq	H_2&gq	μ&gq
Order [#]		14	13	20	13	13	18	13	12	18
$\bar{q}_{ins_{low}}$	Pa	-815	-612	-1,036	-995	-1,202	-1,004	-998	-851	-998
$\omega_{ins_{low}}$	Hz	14.4	12.7	2.95	2.88	2.75	2.92	2.93	13.0	2.94
$\bar{q}_{ins}$	Pa	9,359	8,036	9,754	-[*]	-[*]	-[*]	-[*]	8,467	-[*]
ω_{ins}	Hz	6.30	5.61	7.57	-[*]	-[*]	-[*]	-[*]	5.42	-[*]

[#] order of the reduced controller
[*] No instability found up to 100 000 Pa.
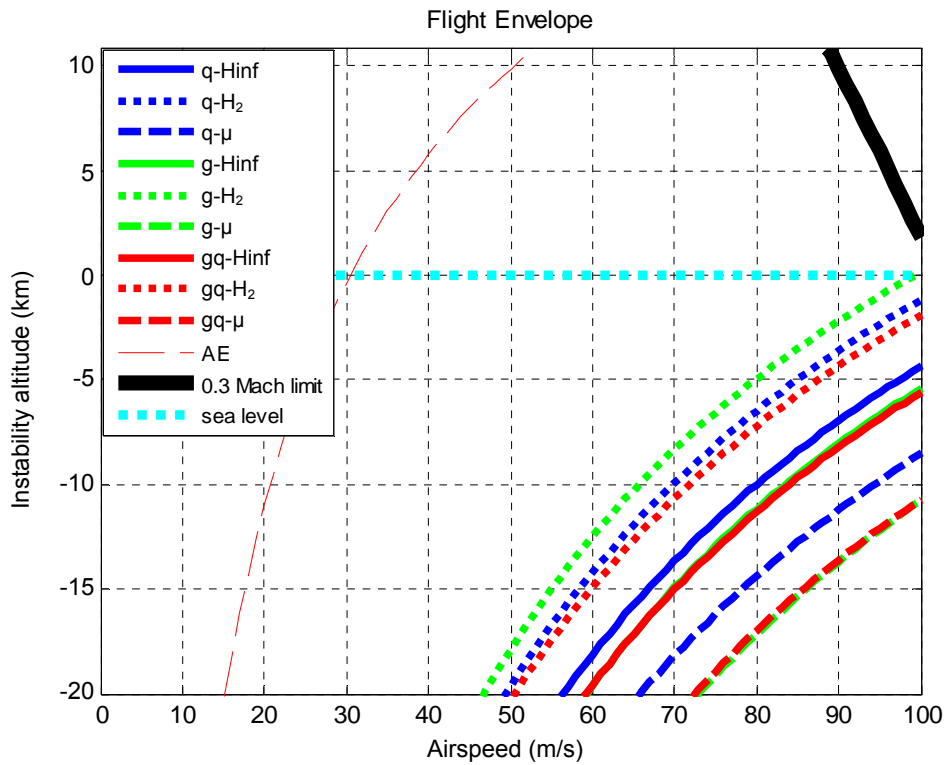
Figure 116. Flutter flight envelopes of the ASE system with various controllers

In Table 47, the linear performance results of analyses executed for the aeroservoelastic system with the synthesized controllers are given. For a second order system, most parameters given in Table 47 are dependent on each other, and can be derived from one other. For larger order systems, such as the aeroservoelastic systems constructed in this study that have orders higher than eighteen, it is worthless to derive those parameters from one another. However, the relations of the parameters in second order system can still provide an insight for a higher order system. Regardless of this, in this study all parameters are gathered and used in the comparisons of the systems. In the following paragraphs these comparisons are performed according to the results presented in Table 47.

Table 47. Linear performance results

	Controller	H∞&q	H₂&q	μ&q	H∞&g	H₂&g	μ&g	H∞&gq	H₂&gq	μ&gq
		Hz								
$\bar{q}$ simulation 0 Pa	ω_n (Hz)	6.00	5.63	5.84	5.83	5.47	6.03	5.70	5.21	5.75
	$tr_{5\%}$ (s)	0.076	0.085	0.072	0.079	0.088	0.074	0.077	0.090	0.075
	ts (s)	0.145	-	0.371	-	-	0.100	-	-	0.100
	Mp (%)	5.7	6.3	4.8	1.1	3.5	3.0	1.2	2.9	2.8
	e_{ss} (deg)	-0.008 ±0.022	-0.032 ±0.023	-0.028 ±0.021	-0.033 ±0.022	-0.055 ±0.029	-0.029 ±0.015	-0.033 ±0.019	-0.056 ±0.023	-0.027 ±0.014
	$\delta_{\alpha\theta}$ (deg)	1.29	1.33	1.23	1.21	1.22	1.26	1.19	1.23	1.17
	cr_1 (A)	0.98	0.66	2.65	0.81	0.56	1.32	0.87	0.59	1.87
	cr_2 (A)	0	0	0	0	0	0	0	0	0
	cr_3 (A)	0.233	0.111	0.774	0.248	0.115	0.421	0.270	0.139	0.525
	cr_4 (A)	0.50	0.25	2.19	0.80	0.29	1.06	0.57	0.30	1.29
$\bar{q}$ simulation 4,000 Pa	ω_n (Hz)	6.03	5.47	6.43	4.97	1.57	5.43	5.36	5.22	5.76
	$tr_{5\%}$ (s)	0.065	0.068	0.056	0.076	0.082	0.067	0.070	0.071	0.062
	ts (s)	1.130	-	-	-	-	0.748	-	-	0.329
	Mp (%)	6.5	5.9	5.6	-	-	1.5	2.6	3.0	3.8
	e_{ss} (deg)	-0.024 ±0.019	-0.055 ±0.019	-0.039 ±0.014	-0.044 ±0.010	-0.076 ±0.014	-0.034 ±0.013	-0.038 ±0.016	-0.072 ±0.017	-0.029 ±0.011
	$\delta_{\alpha\theta}$ (deg)	2.32	2.21	2.11	1.99	1.90	1.97	2.13	2.17	2.01
	cr_1 (A)	0.80	0.58	2.93	0.77	0.49	1.82	0.92	0.59	2.21
	cr_2 (A)	0.019	0.017	0.018	0.019	0.017	0.018	0.019	0.018	0.018
	cr_3 (A)	0.323	0.246	0.896	0.263	0.134	0.453	0.364	0.276	0.541
	cr_4 (A)	0.73	0.45	2.93	0.58	0.43	1.82	0.92	0.57	1.75

Considering the bandwidth requirement it can be seen that;

- q controllers perform better than same type of g or gq controllers.
- q and gq controllers are not affected much from the change of dynamic pressure and perform comparable in the dynamic pressures of 0 Pa and 4,000 Pa. However, a noticeable degradation occurs in the performance of g controllers with the increase of dynamic pressure.
- Among the controller types, μ type controllers perform slightly better than the H_∞ type controllers. H_2 type controllers have the worst performance.

Considering the rise time requirement it can be seen that;

- according to the type of the controller, the controllers are sorted from best to worst as μ, H_∞, and H_2 controllers,
- according to the flutter suppression method the controllers are sorted from best to worst as q, gq, and g controllers.

In the step response analysis performed in time domain, settling time is accepted as the time that the tracking error drops below 5% percent and remains within this error band. However, as it can be seen from the table, most of the controllers cannot decrease the error below 5%. μ type controllers successfully decrease the error below 5% in five out of six cases. Other than μ controllers, only the H_∞&q controller succeeds to force the error within 5% settling band. Among those, the μ&gq controller provides the best settling time.

As expected, the sort formed for flutter suppression methods in the rise time results are reversed for the overshoot performance, and they are sorted from best to worst as g, gq, and q controllers. However, considering

the type of the controllers, contrary to expectations H_∞ type controllers provide the best overshoot performance. H_2 and μ type controllers give comparable results.

Due to the discretization of the sensor of the time domain model, some small amplitude oscillations remain on the controlled degree of freedom of the wing. Hence, steady state error is composed of two merits, the mean error and the oscillation amplitude. Considering the mean error;
- q controllers have the best performance and the g and gq-methods have comparable performances,
- H_2 type controllers have the worst steady state errors. H_∞ and μ type controllers have comparable performances.

Considering the oscillation amplitudes;
- gq and g controllers have a better performance than the q controllers,
- μ controllers have the smallest oscillation amplitudes and H_2 controllers have the worst performance.

μ&gq, μ&g, and H_∞&q controllers have the best performances considering the two merits of the steady state error.

$\delta_{\alpha\theta}$ is the deflection of the torsional spring that transfers the control torques to the typical section wing. Hence, this deflection is related to the resultant stress in the spring, and is important for the strength of the structure. $\delta_{\alpha\theta}$ is derived from the step response analysis performed in time domain, and the maximum deflection of the torsional spring is recorded. Comparing the results it can be seen that, g controllers have the smallest and the q-methods have the largest deflections among the flutter suppression controllers. Considering the controller types, μ type controllers have the best and H_∞ type controllers have the worst deflections. But, the H_2&g controller has the minimum deflections.

For the comparison of the current consumption performances of the controllers, four different data are collected from the step response analysis. These data are; cr_1 is the maximum current drawn, cr_2 is the mean of the current drawn after settling of the motion, cr_3 is the standard deviation of the current drawn after settling of the motion, cr_4 is the maximum current drawn after settling of the motion. From the results it is seen the cr_2 increases with the dynamic pressure, however its value is not large enough for a meaningful comparison of the controllers. The rest of the three data provide sufficient information for the comparison. Although the ratio of these three data slightly varies for the controllers, it is seen that they have a strong dependency. Hence, the results of the comparisons according to all three data are similar. Considering the flutter suppression methods, the g controllers have the smallest and the q controllers have the largest amount of current consumption. Considering the controller types, H_2 controllers have the least current consumption. H_∞ controllers have the second best performance, with an additional current consumption of approximately 0.3 A for cr_1. On the other hand, μ controllers have the worst current consumption values with up to 2.5 A additional current consumption differences for cr_1, which is five times the current consumption of H_2&g controller.

Since there are no solid performance requirements for the aeroservoelastic system, it is hard to derive a conclusion for the best controller. Each method has its own advantages. q controllers stand out with their performances for bandwidth and rise time. g controllers stand out with their performances for current consumption, $\delta_{\alpha\theta}$, and overshoot. On the other hand, gq controllers provide intermediate performances between q and g controllers for all criteria. Considering the controller types, H_2 type controllers stand out with their low current consumption, however they have the worst performance nearly in all other criteria. μ controllers nearly have the best performances in all criteria except their incomparable

current consumption performance. On the other hand, H∞ controllers have comparable performances to *μ* controllers with an acceptable current consumption performance.

The results of the backlash analyses are gathered in Figure 117. In this figure, nonlinear analyses results of the aeroservoelastic system with 0.2° backlash value are presented for various controllers. Considering the $\delta_{\alpha\theta}$ deflection of the torsional spring; g controllers have the best performance and the q controllers have the worst performance. Note that the results are in accordance with the results of steady state oscillations of the system without the backlash. Similarly, for the q_α pitch motion of the fin; q controllers have the worst performances and g and gq controllers have comparable performances. Although there are some irregularities, considering the controller types, in general the *μ* controllers have slightly better performance than the H∞ controllers and the H$_2$ controllers have the worst performance. From the figures it can be seen that among the controllers, *μ*&g controller has the best performance, considering both the $\delta_{\alpha\theta}$ and q_α.
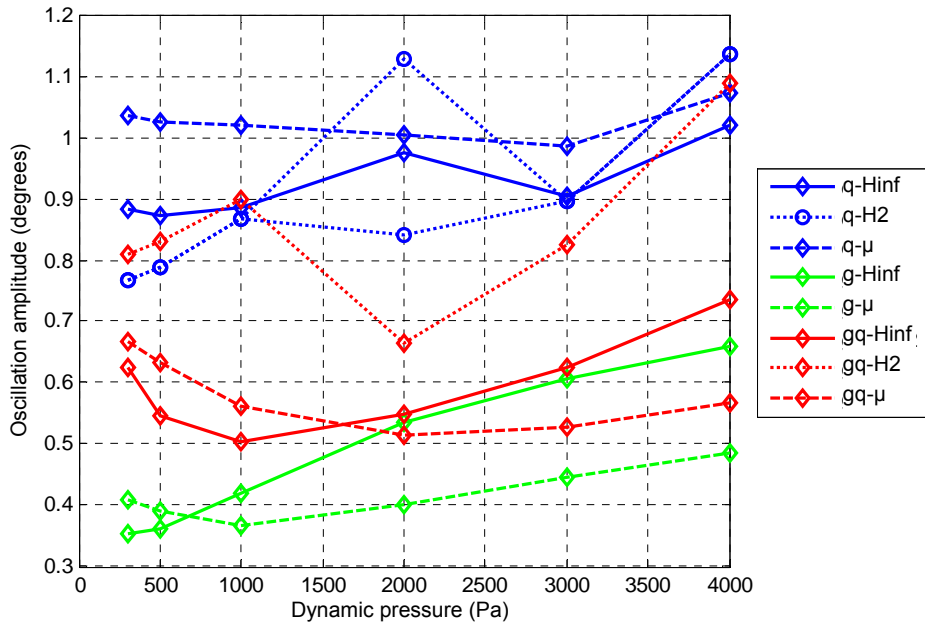
(a) deflection of torsional spring, $\delta_{\alpha\theta}$
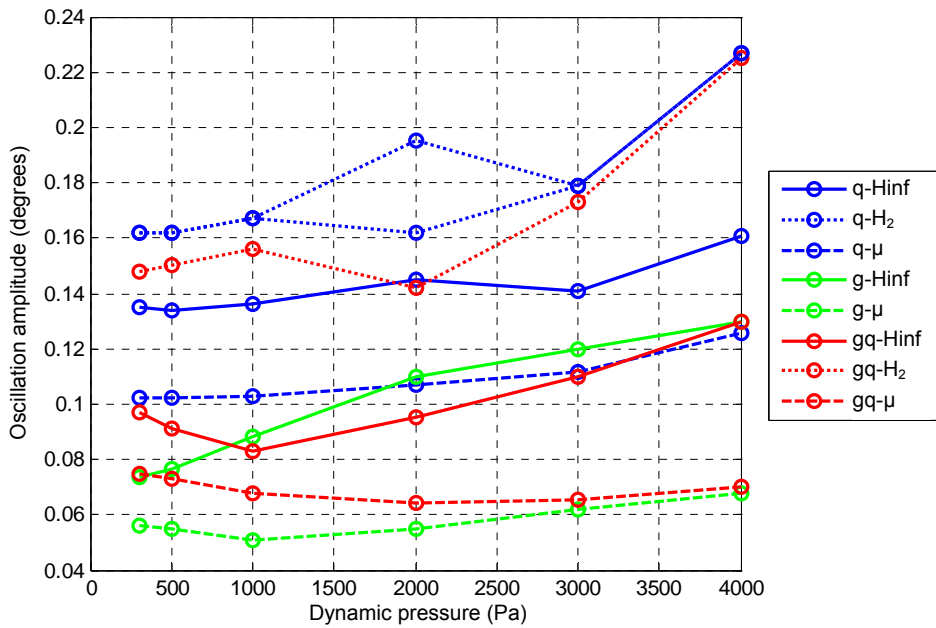
(b) pitch motion of fin, q_{α}

Figure 117. LCO amplitudes of the aeroservoelastic system with respect to dynamic pressure for different controllers (backlash value = 0.2°)

6.3. Unsteady Compressible Subsonic Flow

In this Section, some studies conducted for the unsteady compressible subsonic flow are presented. For this purpose, a proper aeroelastic model is constructed by modifying the spring constants, damping values, position of center of mass, allowable peak torque, and transmission ratio values of the ATD. The parameters of the new model, Model 2, are given in Table 48.

Table 48. Properties of the Model 2

Parameter		unit	Model 2
Elastic axis location	a	-	-0.6
Half chord	b	m	0.15
Span	l	m	0.6
Mass of the wing	m	kg	9.83
Total plunging mass	m_p	kg	28.7
Mass moment of inertia of the wing	I_α	kg.m^2	0.128
Plunge stiffness	k_h	kN/m	15,000
Total torsional stiffness	$k_{\theta\alpha}$	N.m/rad	1,100
Plunge damping	c_h	N.s/m	65.6
Pitch damping	c_α	N.m.s/rad	0.476
Position of center of mass from elastic axis	x_{cg}	m	0.105
Motor torque constant	kT	N.m/A	2.22
Motor continuous stall torque	T_{cs}	N.m	3.53
Allowable peak torque	T_p	N.m	42.36
Mass moment of inertia of motor and transmission calculated at the wing shaft	I_m	kg.m^2	0.000297
Motor and transmission damping	c_m	N.m.s/rad	0.000124
Transmission ratio	N	-	87

The indicial functions of the Model 2 are derived by following the procedure presented in Section 2.5.2. A curve fitting operation is applied to the indicial functions $\phi^T{}_{cM}$, $\phi^T{}_{cq}$, and $\phi^T{}_{cMq}$. The indicial function $\phi^T{}_c$ is directly used since $\phi^T_c = \phi_{c'}$, as given in Equation (2.86). The squared 2-norms of the residuals of the curve fits which defines the quality of curve fitting are given in Table 49. Derived parameters of the indicial functions through curve fitting are given in Table 50 through Table 52. The calculated values of the indicial functions $\phi^T{}_c$, $\phi^T{}_{cM}$, $\phi^T{}_{cq}$, and, $\phi^T{}_{cMq}$ by Equations (2.86) through (2.89) and their curve fits are presented in Figure 118 through Figure 127. From these figures and Table 49 it can be seen that, some of the curve fits, such as $\phi^T{}_{cM}$ at 0.5 Mach, are not as successful as the others. However it should be noted that these curve fits are applied to the indicial functions obtained by Mazeltsky, which are also curve fits. Further improvement can be achieved by increasing the orders of the fitted equations, however this will increase the order of the aeroservoelastic system. Hence, the curve fit results given are used in this study. The derivation of the indicial functions of the fin of ATD and analysis of effect of the indicial function error on the performance of the aeroservoelastic system are left as future studies.

Table 49. The squared 2-norms of the residuals of the curve fits.

	ϕ^{T}_{cM}	ϕ^{T}_{cq}	ϕ^{T}_{cMq}
0.5 Mach	0.2080	0.0478	0.0001
0.6 Mach	0.0024	0.0049	0.0322
0.7 Mach	0.0000	0.0035	0.0056

Table 50. Curve fit results for ϕ^{T}_{cM} at compressible subsonic speeds.

$\phi_{cM}(s) = b_{0cM} + b_{1cM}e^{-\beta_{1cM}s} + b_{2cM}e^{-\beta_{2cM}s} + b_{3cM}e^{-\beta_{3cM}s}$							
M	b_{0cM}	b_{1cM}	β_{1cM}	b_{2cM}	β_{2cM}	$b_{3cM'}$	β_{3cM}
0.5	-0.0578	0.0691	0.282	-0.0575	1.82	-0.415	1.82
0.6	-0.0625	0.0229	0.0626	-0.478	2.22	0.200	8.440
0.7	-0.0700	0.127	0.0675	-0.103	0.0729	-0.227	0.996

Table 51. Curve fit results for ϕ^{T}_{cq} at compressible subsonic speeds.

$\phi_{cq}(s) = b_{0cq} + b_{1cq}e^{-\beta_{1cq}s} + b_{2cq}e^{-\beta_{2cq}s} + b_{3cq}e^{-\beta_{3cq}s}$							
M	b_{0cq}	b_{1cq}	β_{1cq}	b_{2cq}	β_{2cq}	b_{3cq}	β_{3cq}
0.5	0.635	-0.291	0.0949	-0.602	5.06	0.646	7.29
0.6	0.688	-0.235	0.0623	-0.253	0.353	0.125	0.600
0.7	0.770	-0.282	0.0538	-0.332	0.363	0.109	0.612

Table 52. Curve fit results for ϕ^{T}_{cMq} at compressible subsonic speeds.

$\phi_{cMq}(s) = b_{0cMq} + b_{1cMq}e^{-\beta_{1cMq}s} + b_{2cMq}e^{-\beta_{2cMq}s} + b_{3cMq}e^{-\beta_{3cMq}s}$							
M	b_{0cMq}	b_{1cMq}	β_{1cMq}	b_{2cMq}	β_{2cMq}	b_{3cMq}	β_{3cMq}
0.5	-0.104	0.0141	0.0910	-0.136	5.25	-0.0548	1.10
0.6	-0.113	-0.343	1.22	0.662	1.67	-0.404	2.31
0.7	-0.126	0.00700	0.0282	-0.0722	1.05	0.0423	1.07
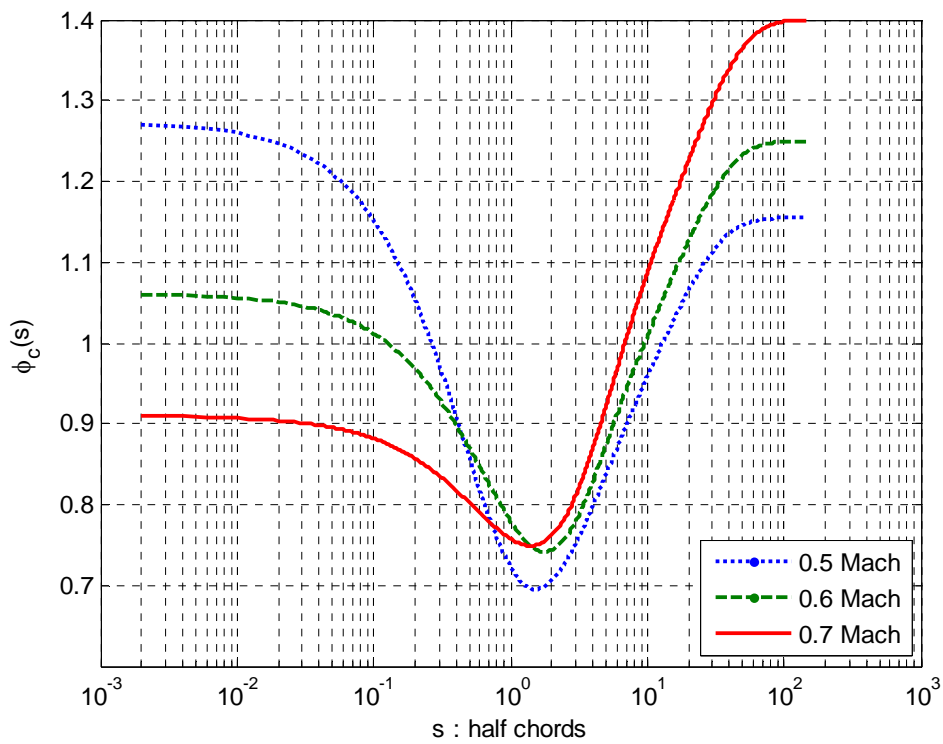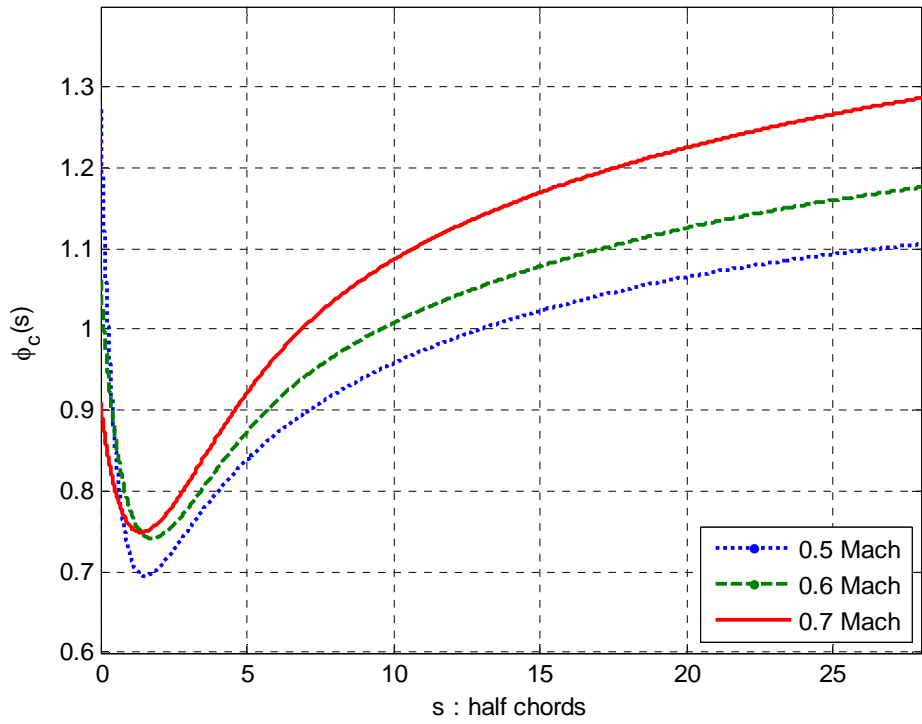
Figure 118. $\phi^T{}_c$ versus s (half chord) at 0.5, 0.6, and 0.7 Mach numbers
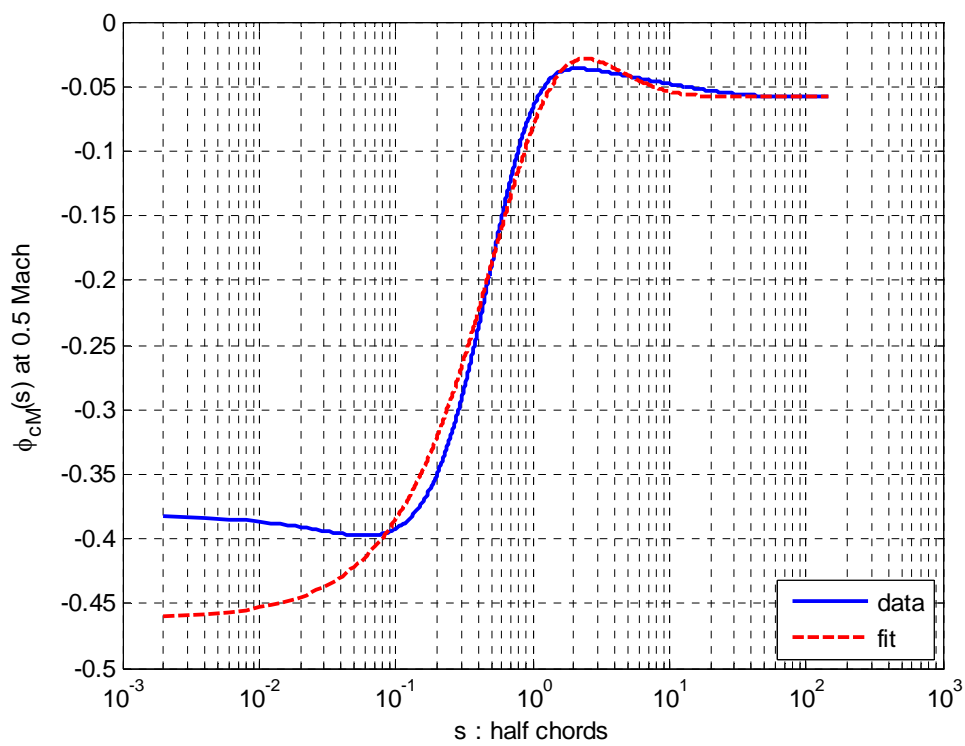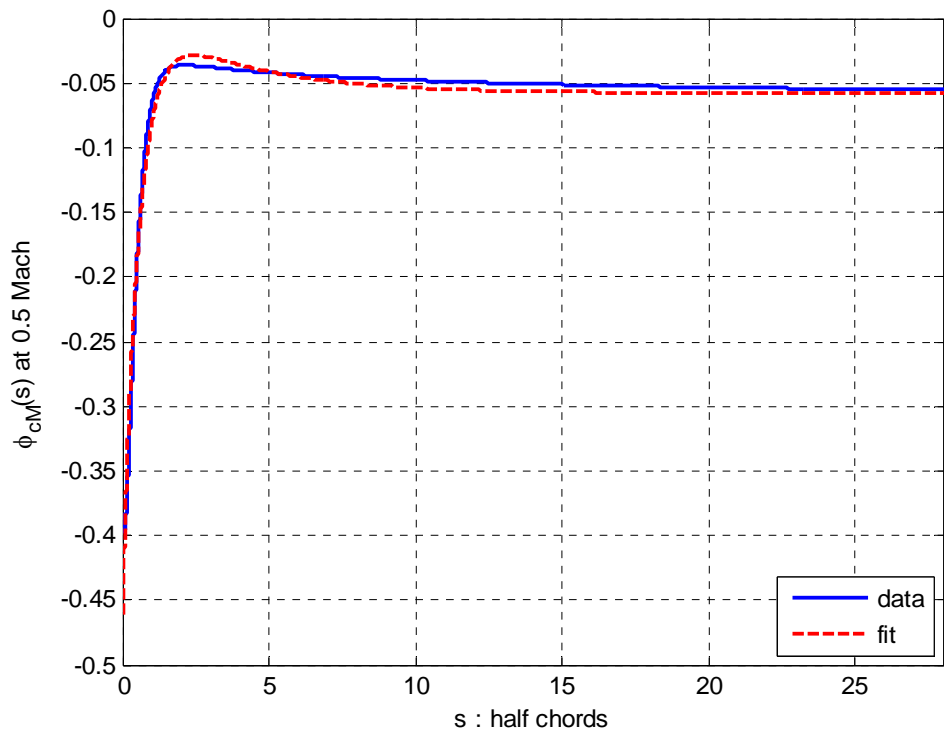
Figure 119. ϕ^T_{cM} versus s (half chord) at 0.5 Mach number
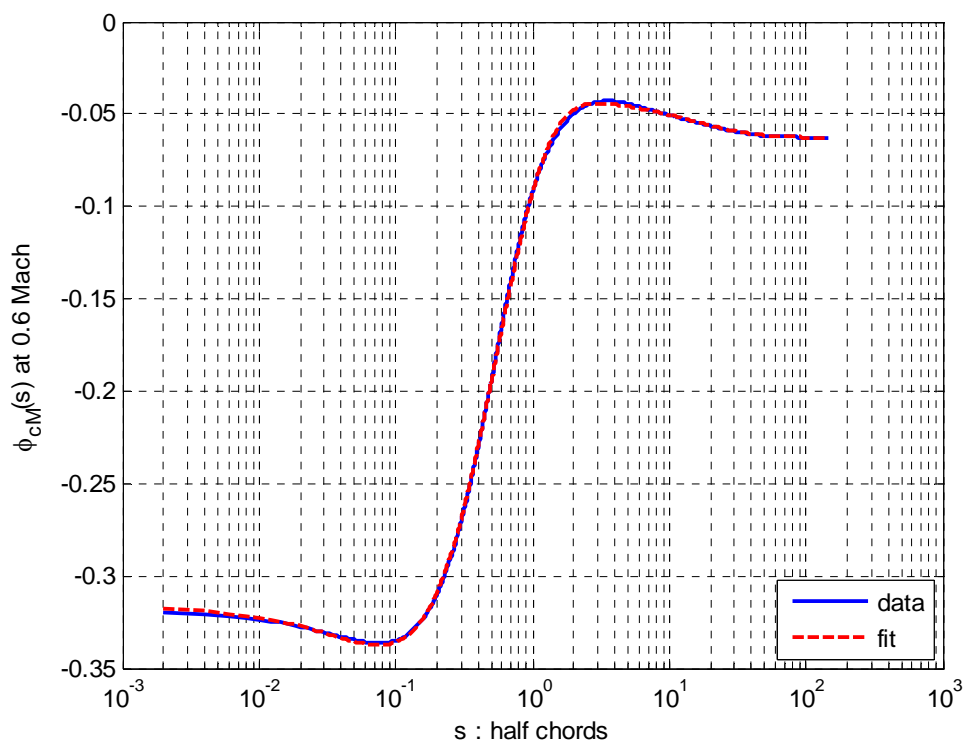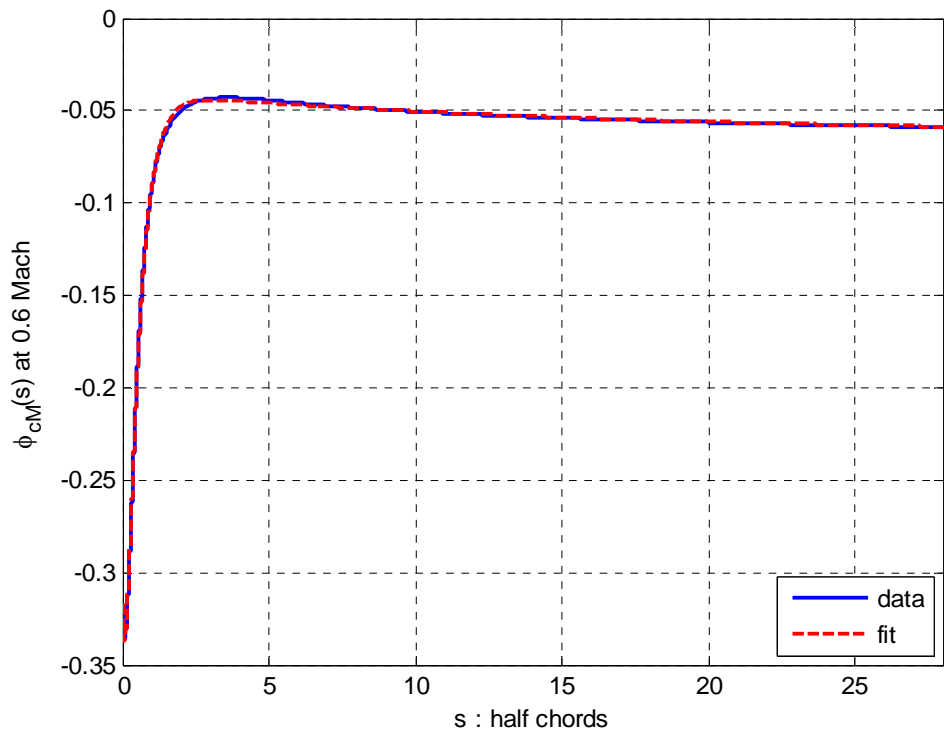
Figure 120. ϕ^T_{cM} versus s (half chord) at 0.6 Mach number
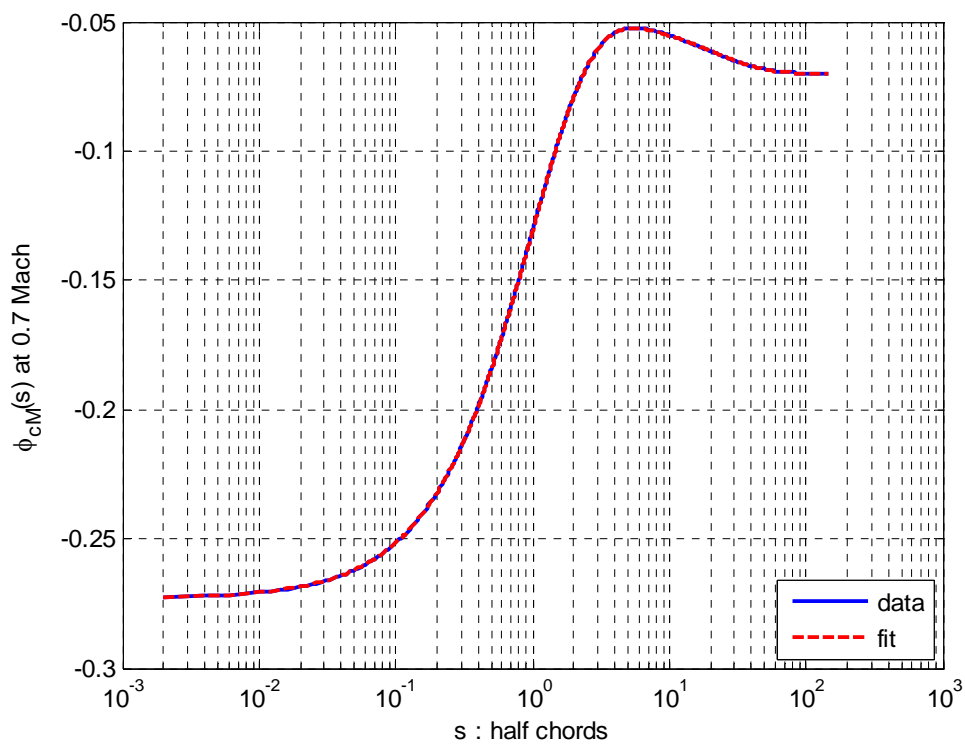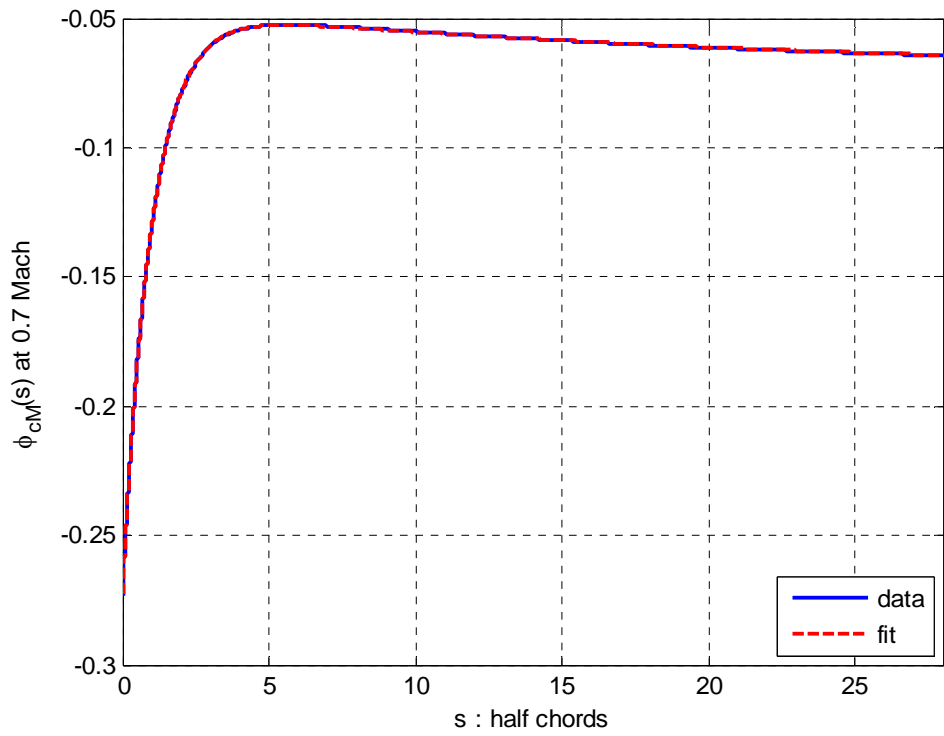
Figure 121. ϕ^T_{cM} versus s (half chord) at 0.7 Mach number

266
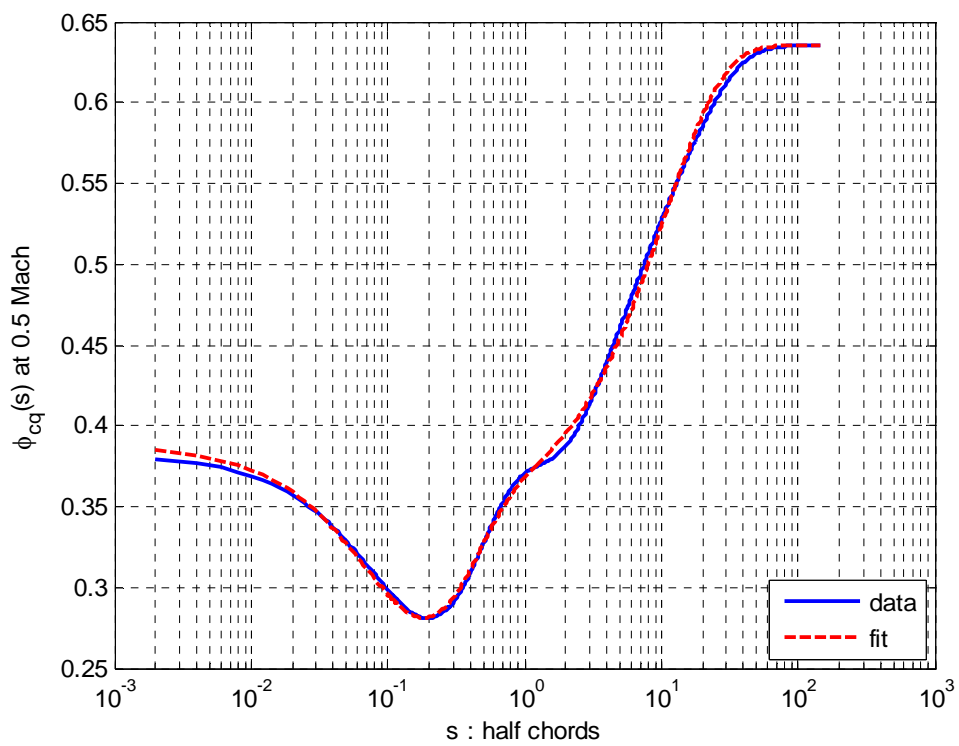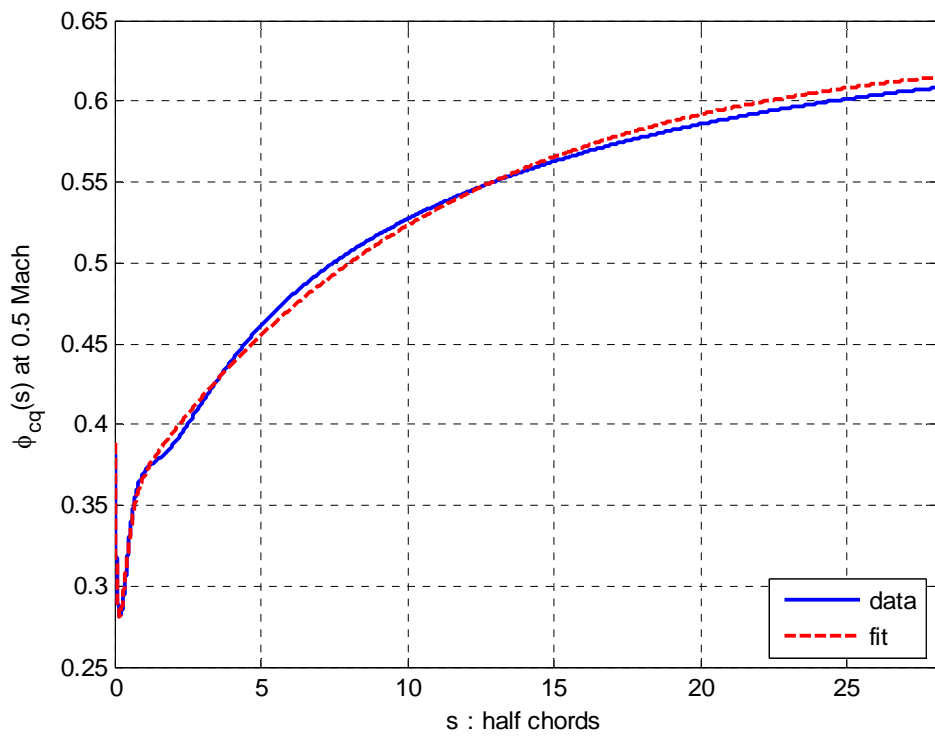
Figure 122. ϕ^{T}_{cq} versus s (half chord) at 0.5 Mach number
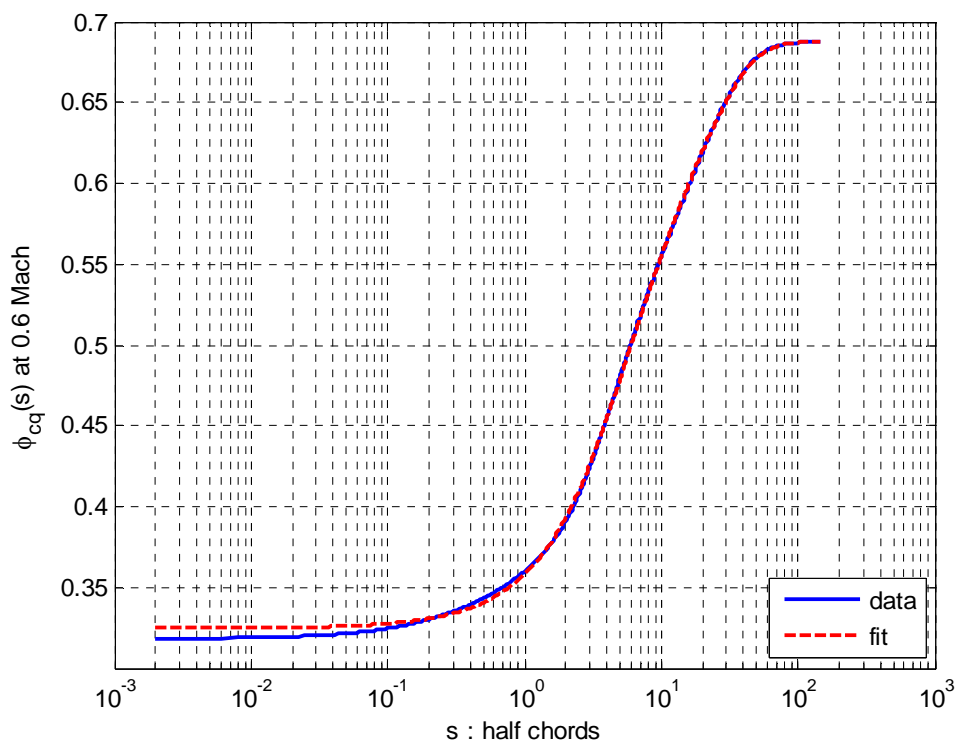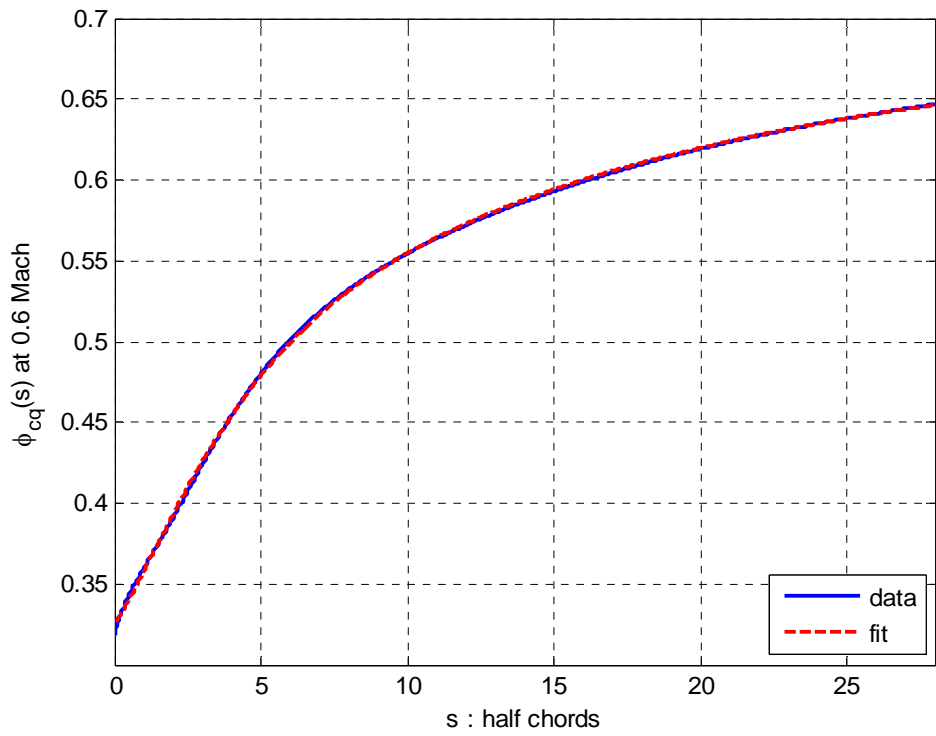
Figure 123. ϕ^T_{cq} versus s (half chord) at 0.6 Mach number
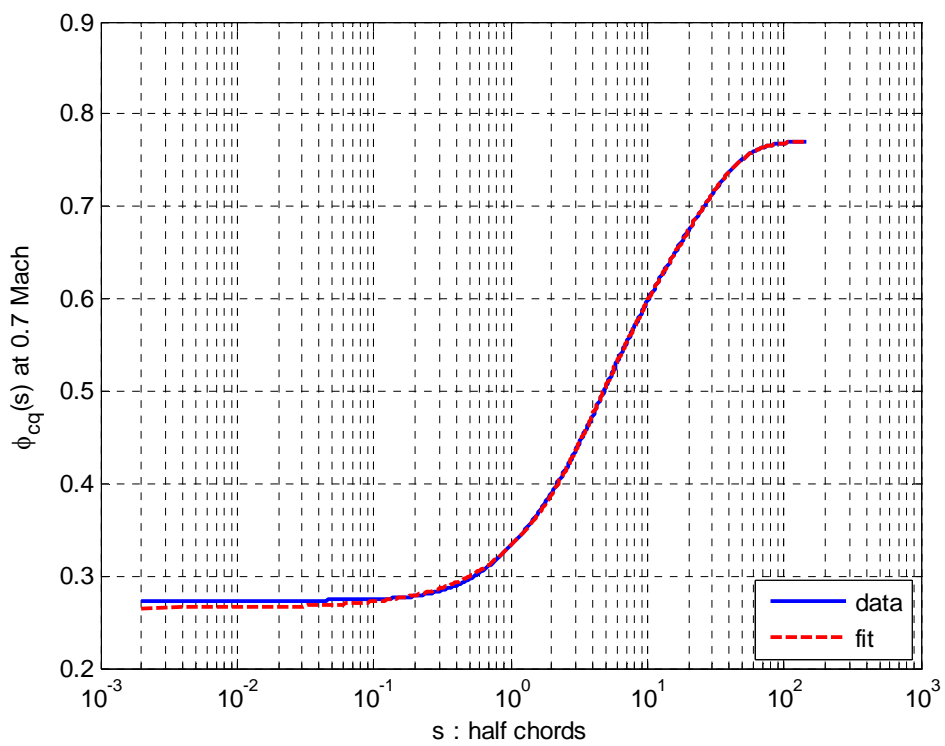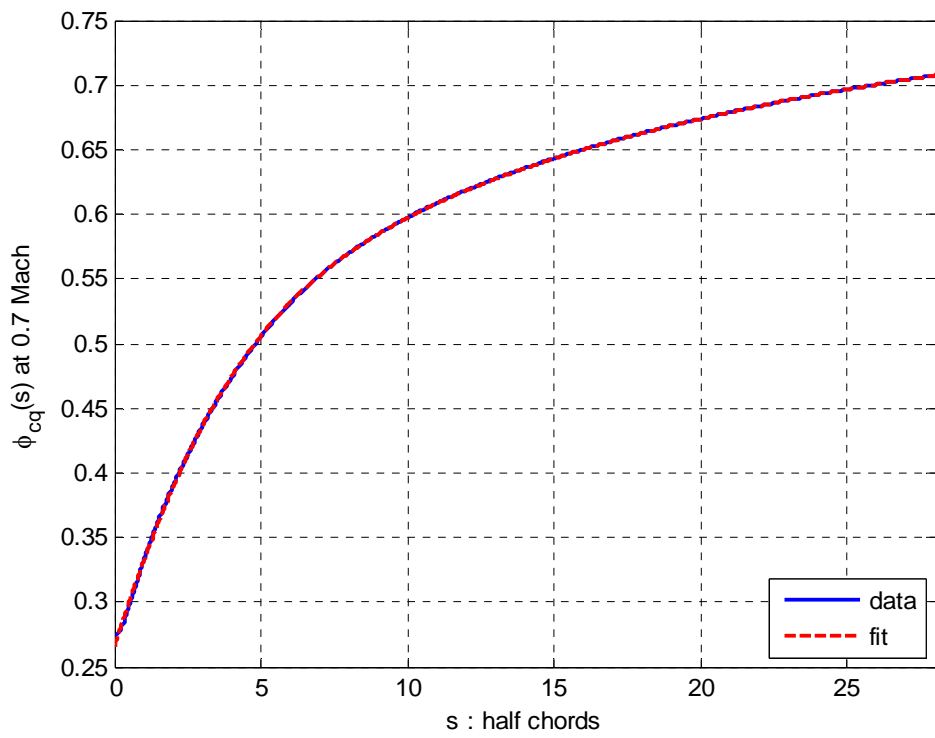
Figure 124. ϕ^T_{cq} versus s (half chord) at 0.7 Mach number
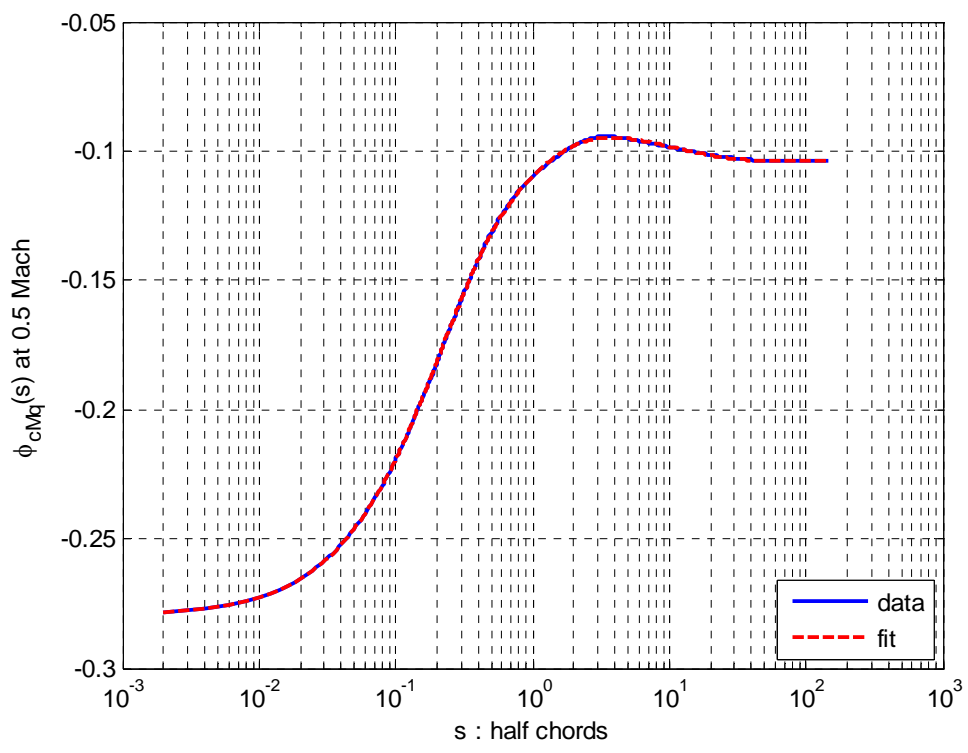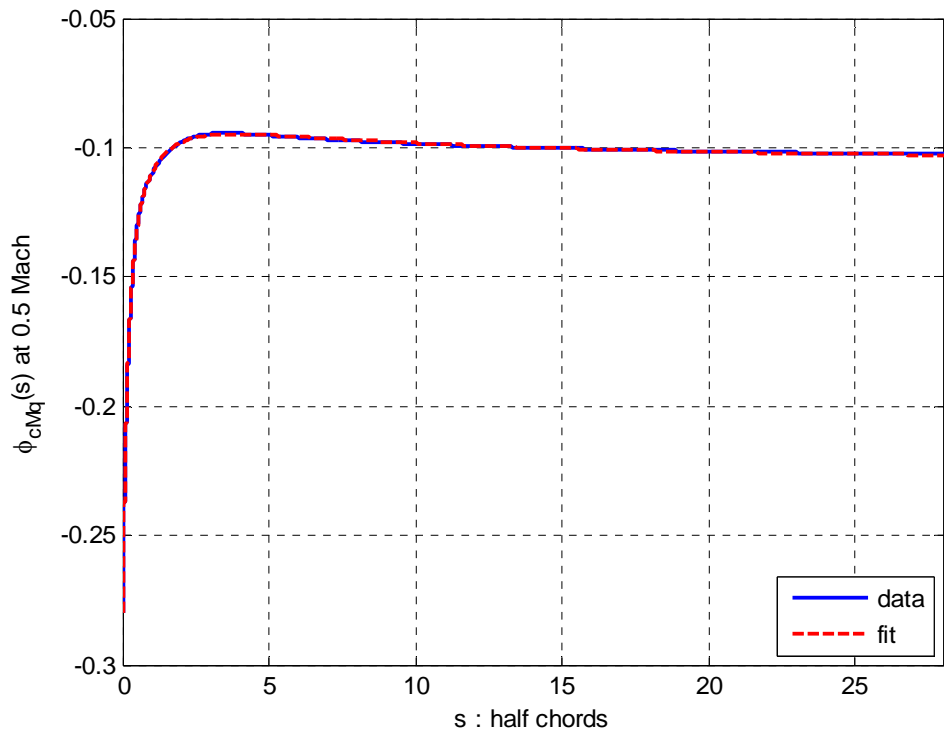
Figure 125. ϕ^T_{cMq} versus s (half chord) at 0.5 Mach number
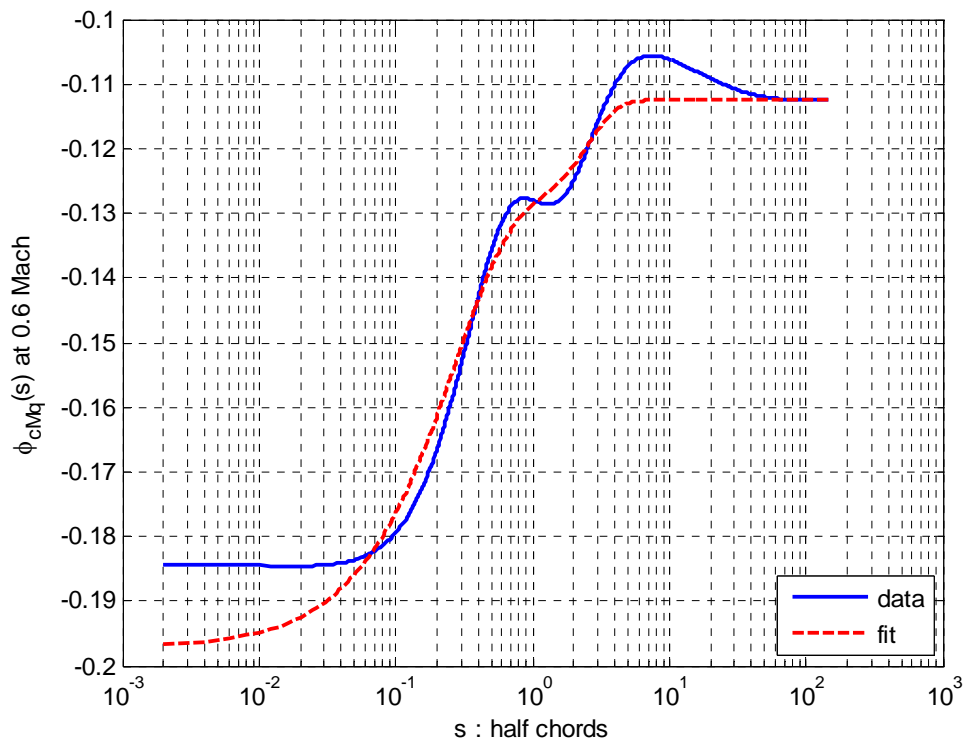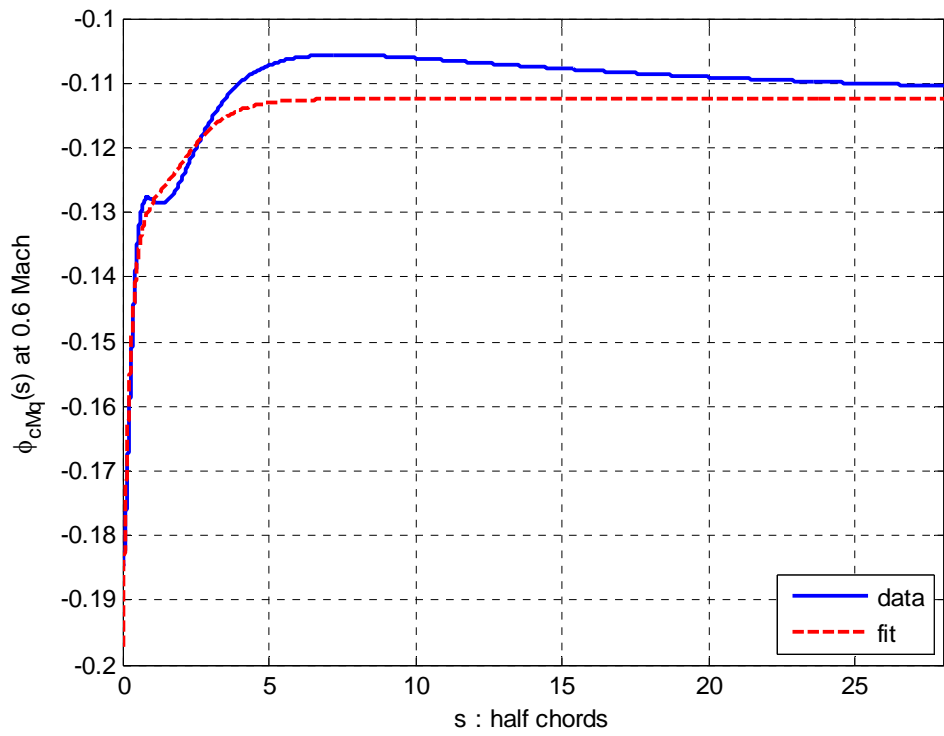
Figure 126. ϕ^T_{cMq} versus s (half chord) at 0.6 Mach number
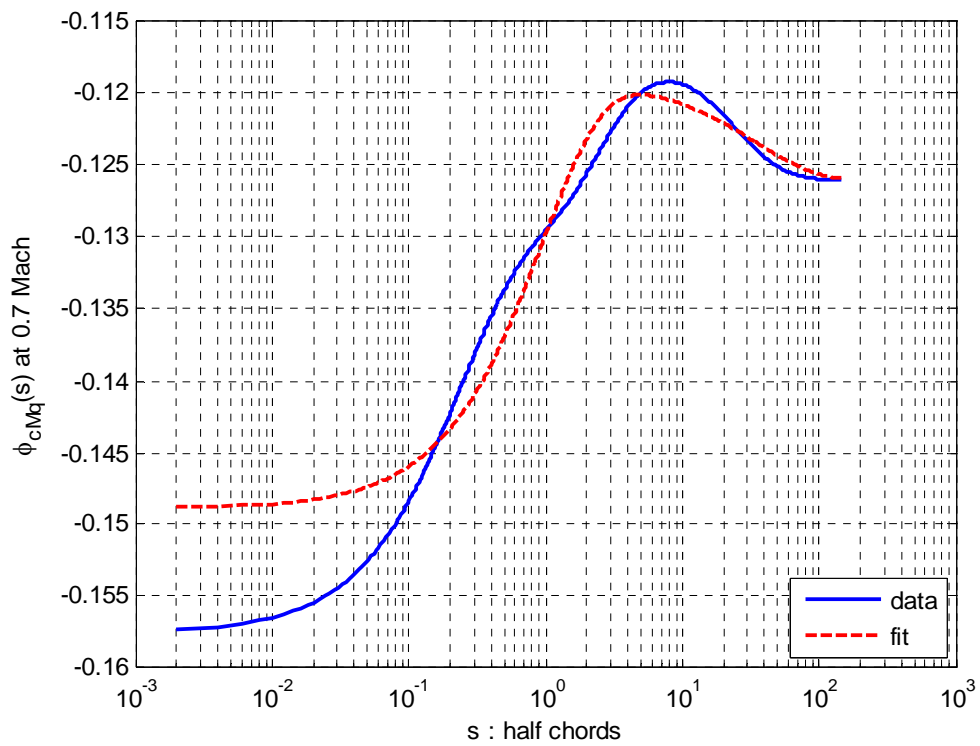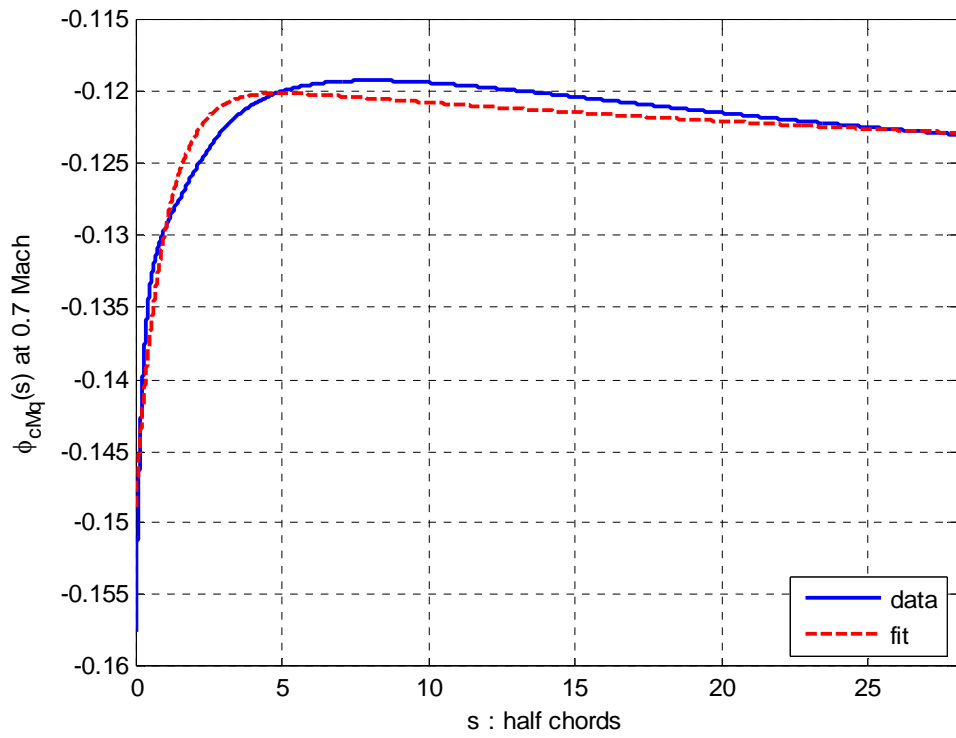
Figure 127. ϕ^{T}_{cMq} versus s (half chord) at 0.7 Mach number

The initial values selected for the altitude and Mach number, and the calculated values of the rest of the dependent aerodynamic parameters are given in Table 53.

Table 53. Initial flow parameters

Altitude	h	m	800
Mach number	M	-	0.5
Airspeed	U_0	m/s	168.6
Air density	ρ	kg/m^3	1.134
Dynamic pressure	$\bar{q}_0$	Pa	16,113

Using the parameters given in Table 48 and Table 53, the aeroelastic model is constructed by using the equations given in Section 2.5.2. Similar to the Section 6.2, various analyses are performed in order to derive the aeroelastic properties of the Model 2.
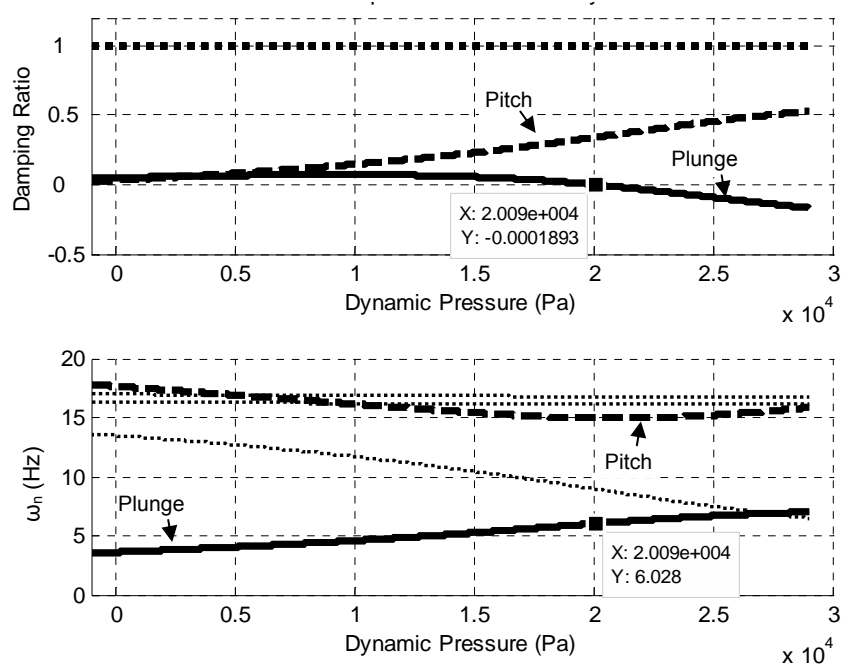
(a) modal properties of aeroelastic system
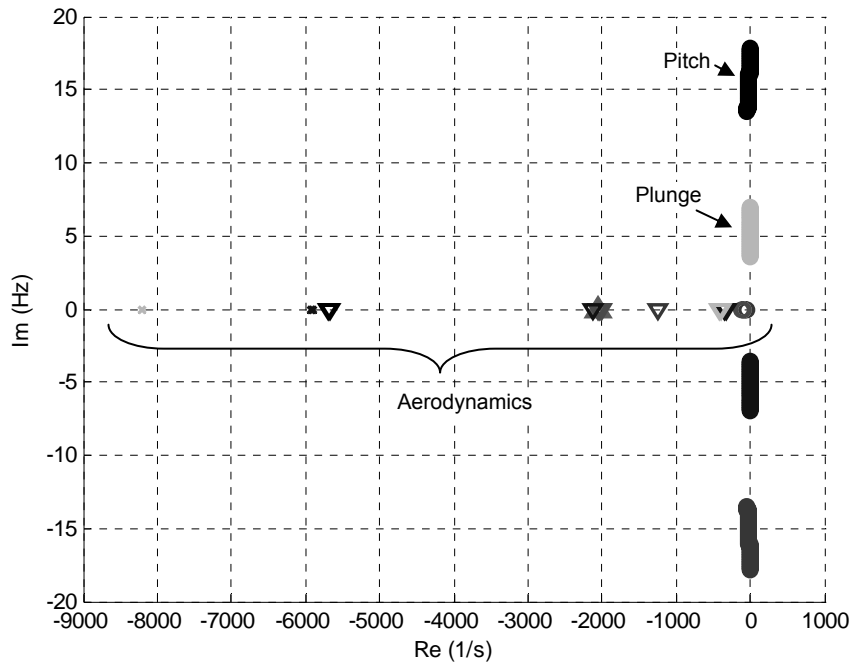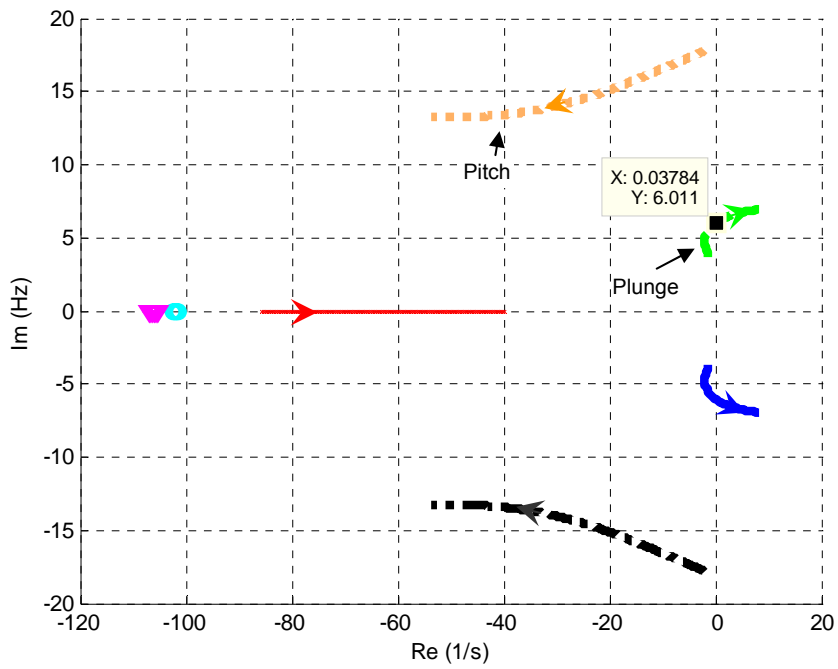
(b) root locus plot

(c) detailed root locus plot

Figure 128. Flutter search results of p-method by varying air density

Performing the μ-method flutter analysis by using the algorithm presented in Section 3.3.1, it is seen that for the aeroelastic Model 2, flutter occurs at $\bar{q}_{flut}$ =20,078 Pa and at ω_{flut} =6.0 Hz. The p-method analysis is also performed and the results are given in Figure 128, which are used for crosschecking. From the figure it can be seen that the damping ratio of the aeroelastic system drops below zero at a dynamic pressure which is slightly below 20,090 Pa, and the frequency of the corresponding pole is 6.03 Hz. Thus, the solutions of the two methods verify each other. It can also be seen from the figures that the aeroelastic system has much more states in compressible flow than incompressible flow due to additional aerodynamic states.

As discussed in Section 3.4.2, due to the aerodynamic match point requirement, the result of the μ-method in compressible flow is not a physical state in the world atmosphere. Hence, the procedure described in Section 3.4.2 is used and the instability match points for the Mach numbers of 0.5, 0.6, and 0.7 are calculated. The results are presented in Table 54. It can be seen that, the use of μ-method without the match point iteration gives worse results in compressible flow than in incompressible flow.

Table 54. Flutter match points of the aeroelastic system

Mach	Dynamic pressure	Frequency	Altitude	Airspeed
	$\bar{q}_{flut}$	ω_{flut}	h_{flut}	U_{flut}
	Pa	Hz	m	m/s
0.5	19,065	5.98	-613	171
0.6	13,574	5.64	5,025	192
0.7	9,429	5.23	9,470	211

6.3.1. Controller Synthesis by Using q-Method

Similar to the incompressible case, the controller synthesis begins with defining the numerical values of the parameters of the reference plant and the uncertainty/performance weightings. The reference plant parameters are given in Table 55. The numerical values of the uncertainty/performance weightings are given in Table 56.

Table 55. Reference plant parameters

ω_{nref}	10 Hz
ζ_{ref}	$1/\sqrt{2}$

Table 56. Numerical values of uncertainty/performance weightings

Uncertainty Name	Gain		Corner Frequency		Scale Parameter	
$[W_{cmd}]$	g_{cmd}	4°	ω_{cmd}	2 Hz	κ_{cmd}	0.01
$[W_n]$	g_{noise}	0.0055°				
$[W_{Fd}]$	g_{Fd_F}	32,000 N	ω_{Fd_F}	0.046 Hz	κ_{Fd_F}	0.001
	g_{Fd_M}	560 N.m	ω_{Fd_M}	0.046 Hz	κ_{Fd_M}	0.001
$[W_{act}]$	g_{act}	0.0236 (N.m)$^{-1}$	ω_{act}	100 Hz	κ_{act}	100
$[W_{per}]$	g_{per}	0.125 deg^{-1}	ω_{per}	50 Hz	κ_{per}	0.01
$[W_{s1}]$	g_{s1}	0.1 deg^{-1}				
$[W_{s2}]$	g_{s2}	0.0055°	ω_{s2}	10 Hz	κ_{s2}	10,000
$[W_{\bar{q}1}]$	$g_{\bar{q}_F 1}$	6.25 N^{-1}				
	$g_{\bar{q}_M 1}$	400 (N.m)$^{-1}$				
$[W_{\bar{q}2}]$	$g_{\bar{q}_F 2}$	1,000 N	$\omega_{\bar{q}_F 2}$	50 Hz	$\kappa_{\bar{q}_F 2}$	0.001
	$g_{\bar{q}_M 2}$	15.6 N.m	$\omega_{\bar{q}_M 2}$	50 Hz	$\kappa_{\bar{q}_M 2}$	0.001

The values given in Table 56 are obtained after numerous iterations during H∞ controller synthesis. With these given values, the norm of the weighted ASE system is obtained below one. During the synthesis steps;

- The gain of the command is decreased to 4° even though initially a greater value is aimed,

- Noise level, g_{noise} term, is decreased, which corresponds to a better measurement system,

- The force and moment values of weighting function $[W_{Fd}]$ of the uncertainty of aerodynamic forces are obtained similar to the incompressible case. The gain values are tuned by considering the steady state error in step response.

- Parameters of the weighting function $[W_{act}]$ of the actuator are kept the same as in incompressible case. However, the peak torque value is increased to the maximum possible value that can be obtained with the servo controller-motor system used in ATD. Moreover, the transmission ratio is increased.

- Performance requirement that is the maximum allowed tracking error is loosen to 0.8°. But, the frequency is increased to 50 Hz, in order to suppress the peaks of the ASE system around 35 to 45 Hz.

- The output weighting function $[W_{s1}]$ of the sensor noise kept same as in the incompressible case. The input weighting function $[W_{s2}]$ of the sensor noise is changed due to modified noise level g_{noise} .

- The output weighting function $[W_{\bar{q}1}]$ of disturbance to dynamic pressure is obtained similar to the incompressible case.

- For the derivation of the input weighting function $[W_{\bar{q}2}]$ of disturbance to dynamic pressure, the disturbance $\bar{q}_{dist}$ to dynamic pressure is modified as 12,500 Pa. The frequency is increased up to 50 Hz, in order to cover the peaks of the ASE system around 35 to 45 Hz.

After the definitions of the reference model and the weighting functions, the interconnection structure system shown in Figure 16 is constructed by using MATLAB$^®$ *sysic* command. The constructed system has 28 states, 7 outputs, and 8 inputs.

Similar to the incompressible case, the controller is synthesized using MATLAB$^®$ *hinfsyn* command. The synthesized controller has 28 states, same as the number of states of the interconnection structure system, $[P]$. Frequency plots of the controller are given in Figure 129. H$_\infty$ norm of the ASE with the synthesized controller is obtained as 0.979. The order reduction of the controller is derived by following the similar procedure used in incompressible flow case, Section 6.2.2.1. The controller of the aeroservoelastic system is selected as the 14th order controller that is reduced by using balanced reduction method (Figure 130). The H$_\infty$ norm of the aeroservoelastic system with the reduced controller is computed between 0.985 and 0.986.

After the controller synthesis, the analysis of the aeroservoelastic system with the synthesized controller is performed. In Table 57, the instability points of the aeroservoelastic system calculated by using μ-method are given. Performing the match point search as described in Section 3.4.2, the instability match points of the aeroservoelastic system are calculated as given in Table 58. It can be seen from these tables that the result of the direct use of μ-method in compressible flow is not sufficient even in the same Mach number which is 0.5.
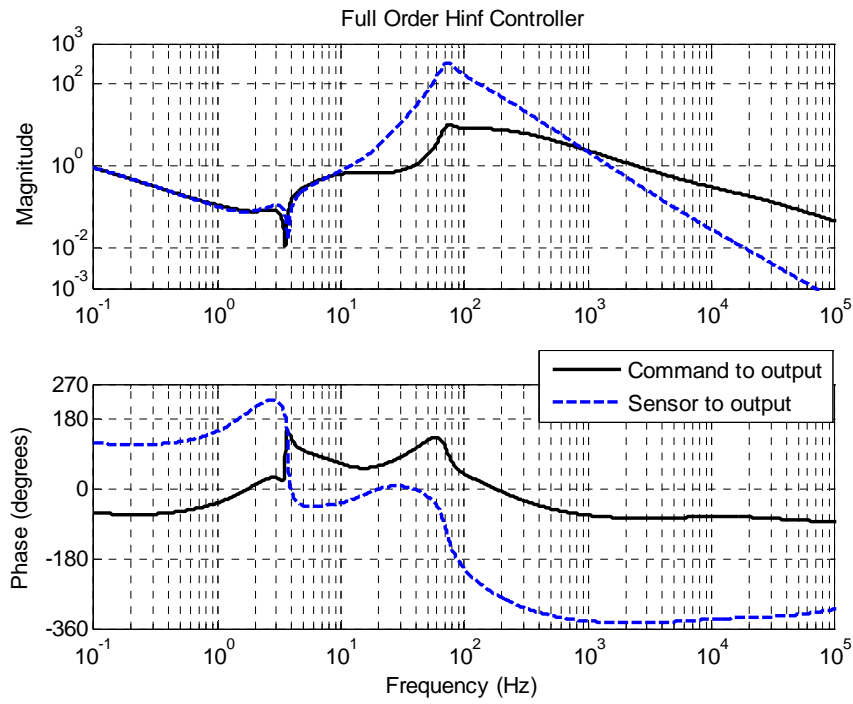
Figure 129. H∞ controller
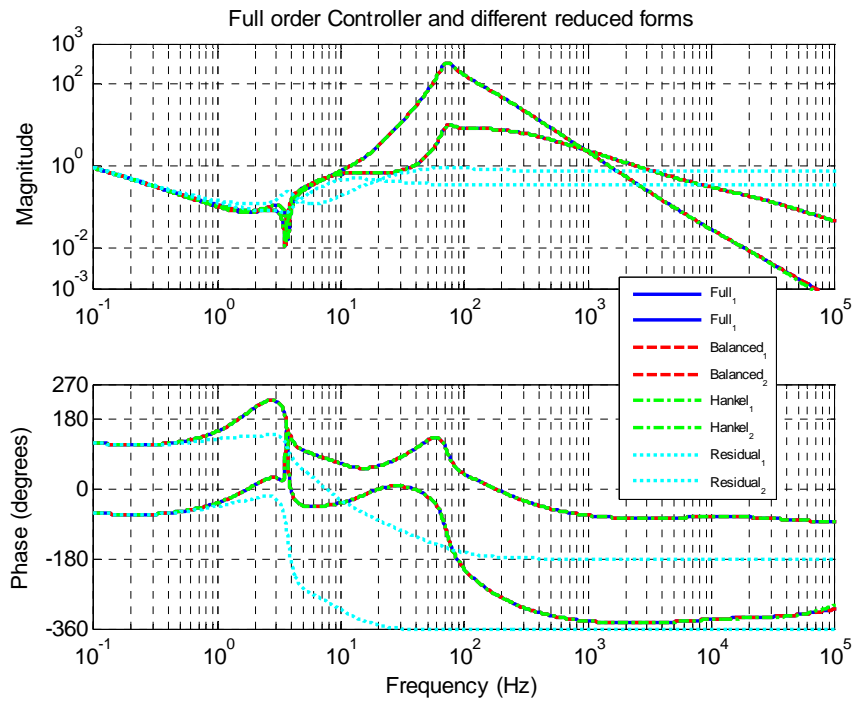
Figure 130. 14th order reduced controllers

Table 57. Nominal stability limits calculated by using μ-analysis

$\bar{q}_{ins_{low}}$	Pa	-10,872
$\omega_{ins_{low}}$	Hz	34.5
$\bar{q}_{ins}$	Pa	79,200
ω_{Ins}	Hz	11.7

Table 58. Instability match points of the aeroservoelastic system

Mach	Dynamic pressure	Frequency	Altitude	Airspeed
	$\bar{q}_{ins}$	ω_{ins}	h_{ins}	U_{ins}
	Pa	Hz	m	m/s
0.5	50,495	12.78	-9,750	188
0.6	38,641	12.79	-3,635	212
0.7	32,161	12.24	655	236

The performance analyses are performed at five different match points, at three different Mach numbers. The results are given in Figure 131 and in Table 59. In the table, first five rows define the simulation parameters, in which first two are sufficient to define the rest of the parameters. The simulations are also performed for 0.6 and 0.7 Mach at 20,000 m altitude, and it is seen that similar results with 0.5 Mach 20,000 m altitude is obtained.

From the step response analyses results, it can be seen that the controller that is synthesized at 0.5 Mach number and 800 m altitude, can satisfy stability and performance to some extend, at 0.6 and 0.7 Mach numbers. At 20,000 m altitude, the bandwidth of the system decreases down to 7.77 Hz, and the settling time increases up to 0.556 s. In higher dynamic pressures the rise time decreases below 0.03 s but the overshoot value increases up to 20%.

Table 59. Step response properties of aeroservoelastic system at various aerodynamic conditions with quantized sensor

	Mach		0.5	0.5	0.6	0.7	0.7
Simulation parameters	Altitude	m	0	20,000	0	5,000	10,000
	$\bar{q}$	Pa	17,232	958	25,534	18,528	9,067
	U	m/s	170	148	204	224	210
	ρ	kg/m^3	1.225	0.088	1.225	0.736	0.413
Simulation results	wn	Hz	9.87	7.77	10.86	10.45	9.95
	$tr_{5\%}$	s	0.043	0.048	0.026	0.028	0.041
	ts	s	0.058	0.556	0.077	0.234	0.268
	Mp	%	1.42	14.9	20.35	16.78	7.66
	e_{ss}	deg	-0.033 ±0.004	-0.026 ±0.005	-0.027 ±0.005	-0.025 ±0.003	-0.027 ±0.005
	$\delta_{\alpha\theta}$	deg	0.75	0.20	1.10	0.95	0.41
	cr_1	A	0.97	1.05	1.01	1.02	1.13
	cr_2	A	0.028	0.004	0.007	0.002	0.005
	cr_3	A	0.272	0.296	0.314	0.218	0.327
	cr_4	A	0.916	0.709	0.893	0.560	0.837
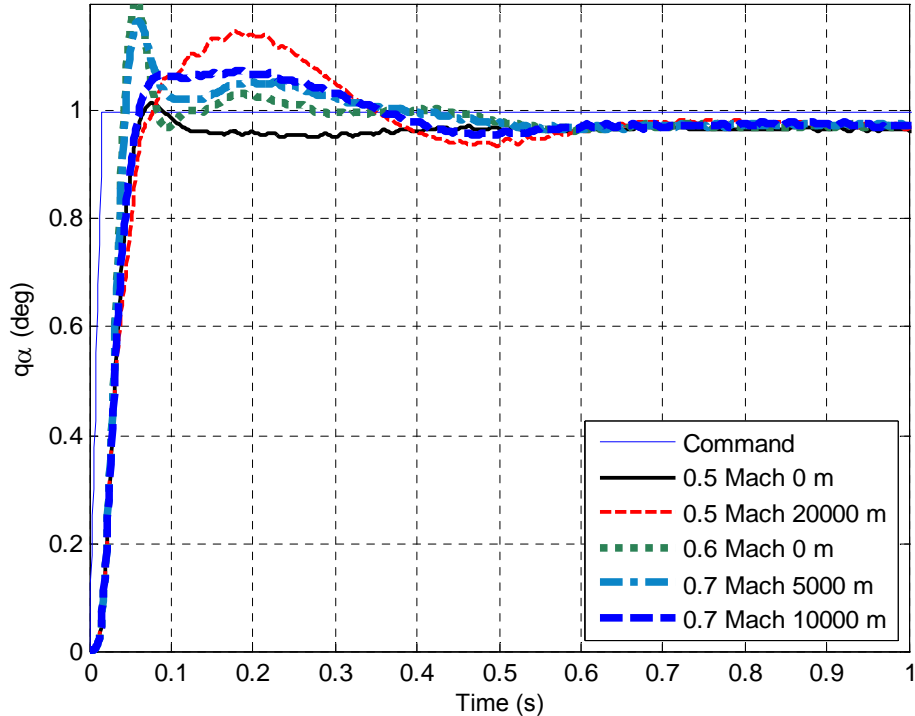
Figure 131. Step response of the ASE system at various match points

In compressible flow, the backlash analyses are performed by varying the altitude and keeping the Mach number fixed and vice versa. The results of these analyses are given in Figure 132. From the results it is seen that, the oscillation amplitudes of the aeroservoelastic system increases with increasing altitude and decreasing Mach number. Note that in both cases the dynamic pressure decreases. It can be also seen that, the oscillation amplitude of $\delta_{\alpha\theta}$, the degree of freedom that the backlash exist, is increased up to two to three times of the backlash value. But, the controller suppressed the oscillation of q_α, the pitch motion of the typical section wing, down to a comparable value to the backlash value.

On the other hand, the analyses are performed for the backlash values of 0.05° and 0.2°. It is seen that the results of these two analyses can be assumed to be linearly dependent to the backlash value.

Through the backlash analysis at 0.5 Mach and 5,000 m, it is seen from the time plots of the analyses results that the system is not converged to a stable value or an LCO event at 40th second. But the oscillations still exist. The time domain analyses results are given in Figure 133 (a), (e), and (i). Deriving the FFT of these time signals, Figure 133 (b), (f), and (j), it is seen that although some dominant peaks exist, the amplitudes at the rest of the frequencies are a lot larger than the FFT plots of the LCO derived in this study.
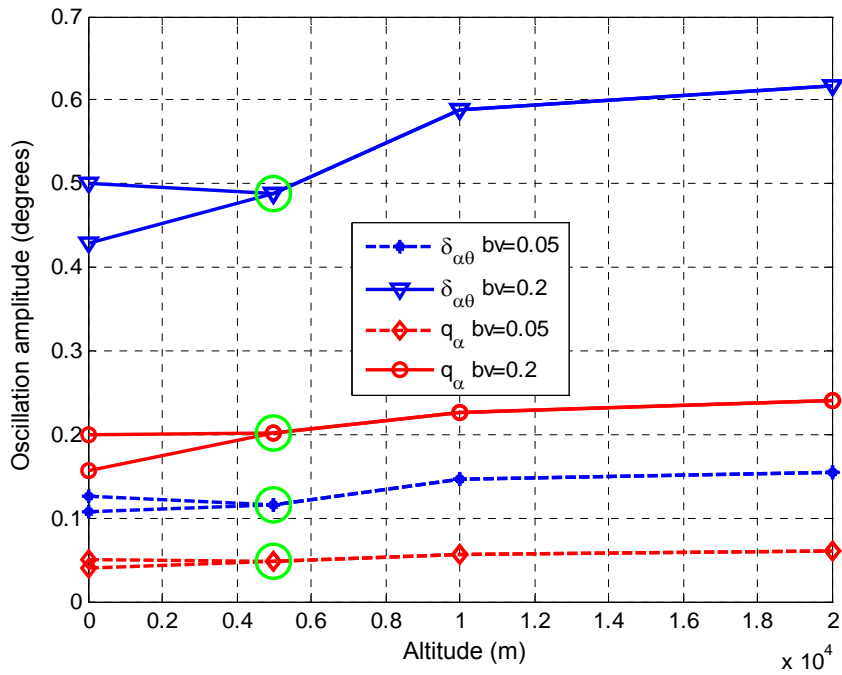
(a) with respect to altitude at 0.5 Mach
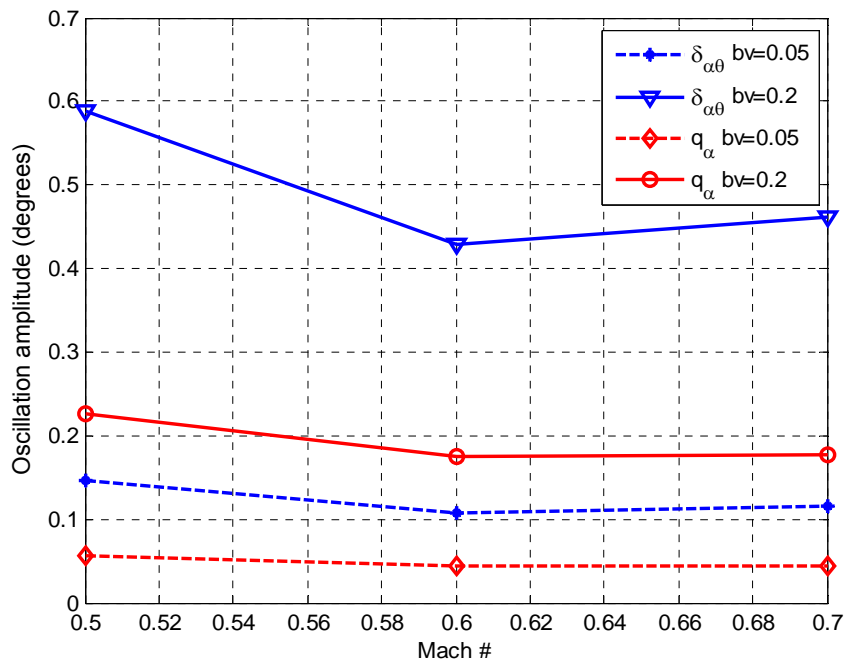
(b) with respect to Mach number at 10,000 m

Figure 132. LCO amplitudes of the aeroservoelastic system for various

backlash values
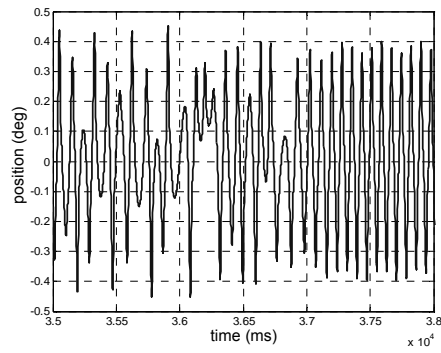
(a) Time plot of $\delta_{\alpha\theta}$
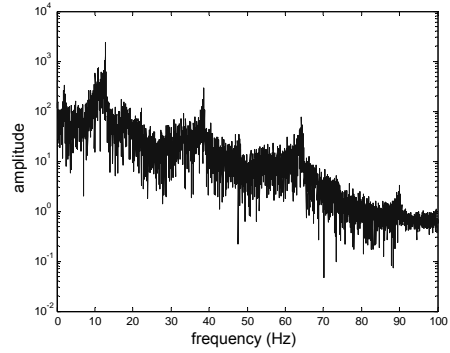
(b) FFT plot of $\delta_{\alpha\theta}$
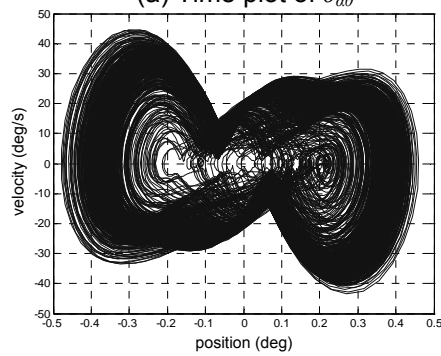
(c) Phase plane plot of $\delta_{\alpha\theta}$
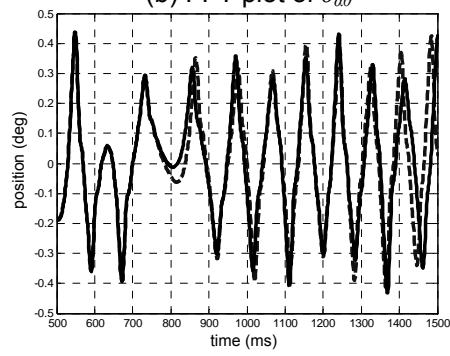
(d) Sensitivity analysis results of $\delta_{\alpha\theta}$

(e) Time plot of q_α

(f) FFT plot of q_α

(g) Phase plane plot of q_α

(h) Sensitivity analysis results of q_α

284
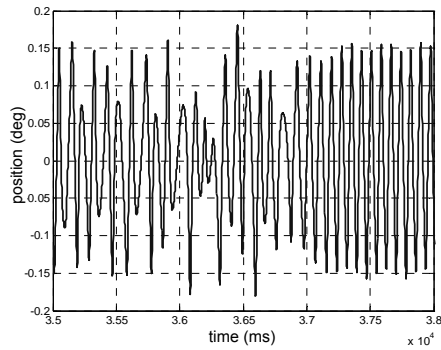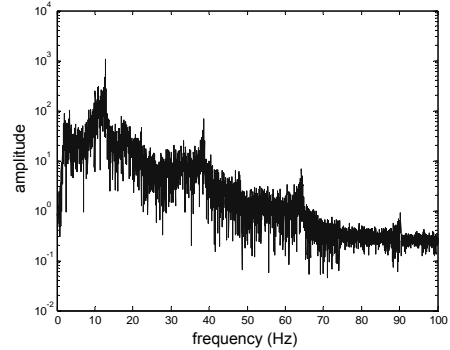
(i) Time plot of q_h

(j) FFT plot of q_h
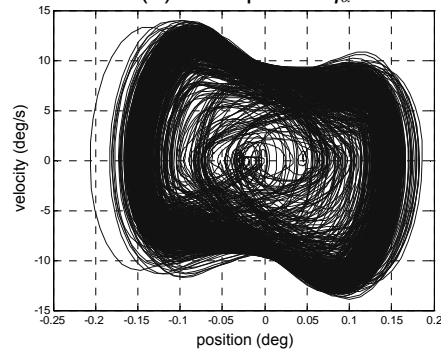
(k) Phase plane plot of q_h
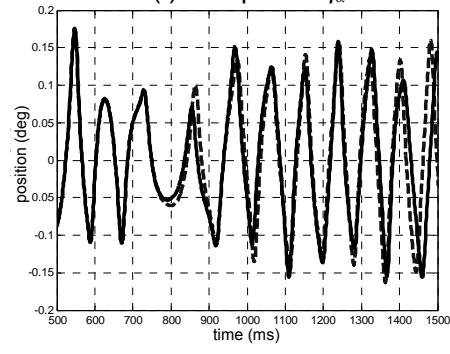
(l) Sensitivity analysis results of q_h
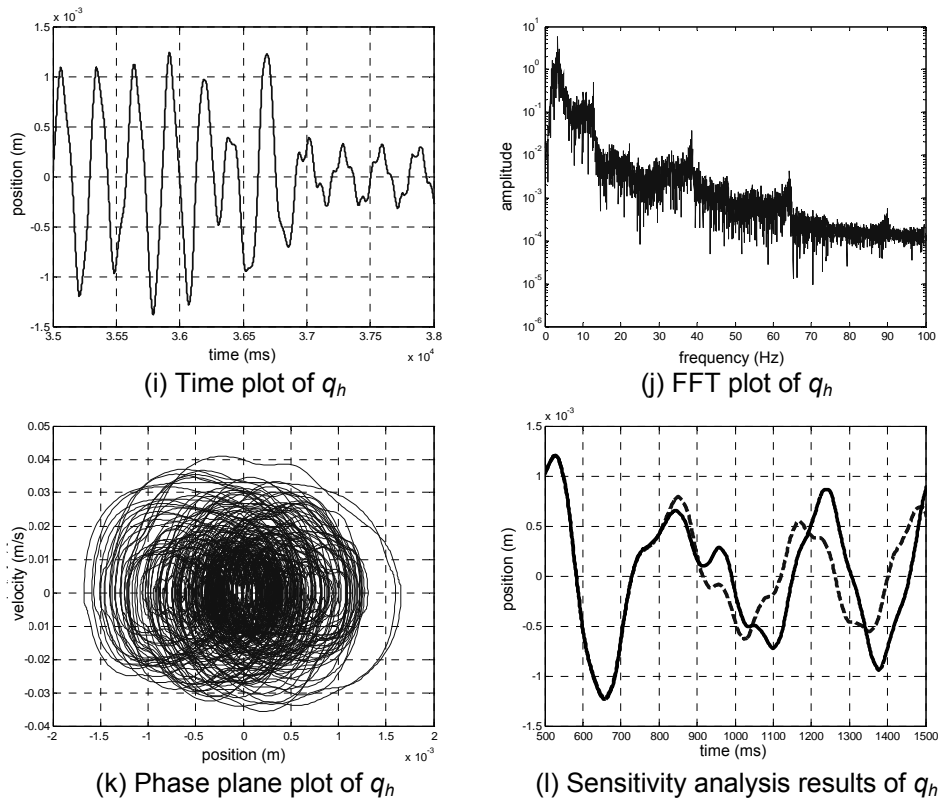
Figure 133. Analysis results of the aeroservoelastic system at 0.5 Mach
and 10,000 m with a 0.2° backlash value

In order to further investigate the system, phase plane plots are
constructed and presented in Figure 133 (c), (g), and (k). As it can be seen
from the figures, the phase plots are not composed of one closed circle as
in an LCO case. By going one step forward a sensitivity analysis is
performed. For this purpose, the amplitude of the aerodynamic force input,
which is used in the backlash analysis as a pulse input, is increased by 1%.
The analysis is performed and the time results of the two analyses are
plotted on top of each other. The results are presented in Figure 133 (d),
(g), and (l). It is seen from the results that after 0.8 s, the results starts to
separate from each other. With this information, it is concluded that the
aeroservoelastic system with the q controller possibly acts chaotically at 0.5
Mach and 10,000 m altitude. These points are encircled in Figure 132.

285

Since a steady state condition is not satisfied, the presented values in Figure 132 are the maximum values of the corresponding signal.

6.3.2. Controller Synthesis by Using g-Method

In the controller synthesis by using g-method, the numerical values of the parameters of the reference plant and the uncertainty/performance weightings are initially taken same as in Table 55 and Table 56. But the weightings functions $\left[W_{\bar{q}1}\right]$ and $\left[W_{\bar{q}2}\right]$ for the output and input of disturbance to dynamic pressure that are specific to q-method are not used in controller synthesis. On the other hand, the output and input weighting functions $\left[W_{c1}\right]$ and $\left[W_{c2}\right]$ of the damping uncertainty of the g-method are included to the controller synthesis. As in the case of incompressible flow, the damping uncertainty is introduced only to the pitch degree of freedom. The gain g_{c1} of the function $\left[W_{c1}\right]$ is the inverse of the expected speed as explained in Section 4.4. The expected speed is calculated by using the bandwidth of the reference model, which is 10 Hz. The amplitude of the oscillation at this frequency is assumed as 1°; hence, the expected speed is calculated as 1.097 rad/s. Therefore, the value of the g_{c1} term is 0.912 s/rad. The gain g_{c2} of the function $\left[W_{c2}\right]$ is calculated by multiplying the expected speed with the δ_c term. The term δ_c is the expected or required damping variation that is used to define the flutter to the controller synthesis algorithm. Hence, the increase of this value enlarges the required flutter envelope to be suppressed by the controller. However, there exists trade of between the flutter boundary, system performance, and the H∞ norm of the ASE system with the synthesized controller. Consequently, after numerous iterations the δ_c term is taken as 6 N.m.s/rad. During the iterations it is seen that the ASE system had sometimes encounters instability around 35 to 45 Hz. Hence, the corner frequency ω_{c2} of the function $\left[W_{c2}\right]$ is taken as 50 Hz in order to cover

these frequencies. On the other hand, the gain value of the performance weighting is tightened back to 0.5°, which decreases the steady state error. The modified an the newly introduced uncertainty/performance weightings are given in Table 60

Table 60. Numerical values of uncertainty/performance weightings

Uncertainty Name	Gain		Corner Frequency		Scale Parameter	
$[W_{per}]$	g_{per}	2 deg^{-1}	ω_{per}	50 Hz	κ_{per}	0.01
$[W_{c1}]$	g_{c1}	0.912 s/rad				
$[W_{c2}]$	g_{c2}	δ_c*1.097 rad/s	ω_{c2}	50 Hz	κ_{c2}	0.01

Similar to the previous cases, after the definition of the reference model and the weighting functions, the interconnection structure system is constructed by using MATLAB® *sysic* command. The constructed system has 27 states, 7 outputs, and 8 inputs. Then, the controller is synthesized using MATLAB® *hinfsyn* command. The controller has 27 states, which is the same as the number of states of the interconnection structure system, [*P*]. Frequency plots of the controller are given in Figure 134. H$_\infty$ norm of the aeroservoelastic system with the synthesized controller is obtained as 0.967. The reduced controller is obtained by using balanced reduction method as 14th order, with H$_\infty$ norm between 0.969 and 0.960, Figure 135.

For the analysis, similar steps are followed as in Section 6.3.1. The results are given in Table 61 through Table 63 and in Figure 136 and Figure 137.
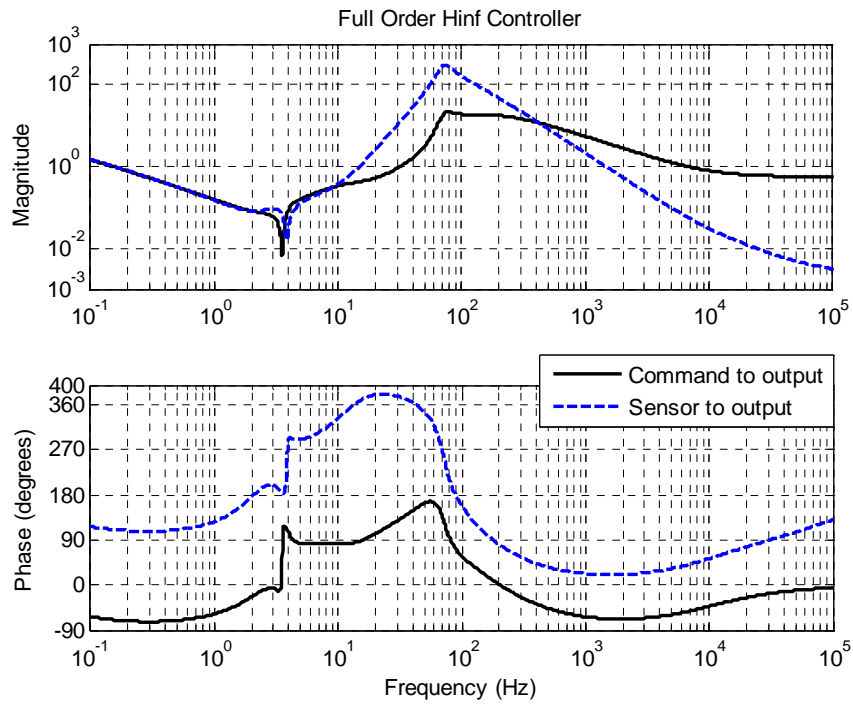
Figure 134. H$_\infty$ controller
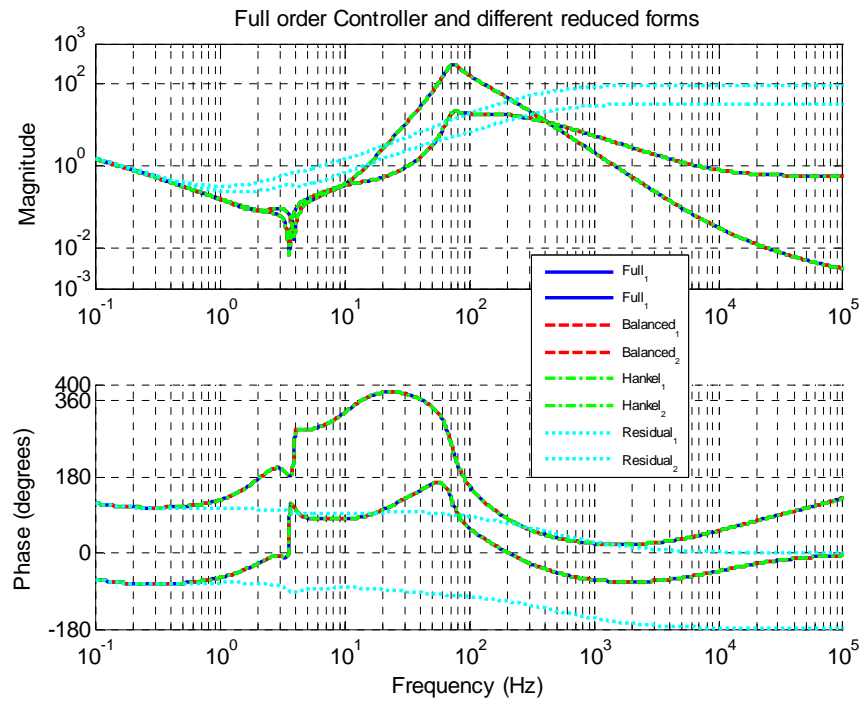
Figure 135. 14th order reduced controllers

Table 61. Nominal stability limits calculated by using μ-analysis

$\bar{q}_{ins_{low}}$	Pa	-13,673
$\omega_{ins_{low}}$	Hz	3.43
$\bar{q}_{ins}$	Pa	55,982
ω_{Ins}	Hz	9.64

Table 62. Instability match points of the aeroservoelastic system

Mach	Dynamic pressure $\bar{q}_{ins}$ Pa	Frequency ω_{ins} Hz	Altitude h_{ins} m	Airspeed U_{ins} m/s
0.5	40,578	9.93	-7,560	184
0.6	30,894	9.92	-1,635	208
0.7	25,112	9.55	2,260	231

Table 63. Step response properties of aeroservoelastic system at various aerodynamic conditions with quantized sensor

	Mach		0.5	0.5	0.6	0.7	0.7
Simulation parameters	Altitude	m	0	20,000	0	5,000	10,000
	$\bar{q}$	Pa	17,232	958	25,534	18,528	9,067
	U	m/s	170	148	204	224	210
	ρ	kg/m^3	1.225	0.088	1.225	0.736	0.413
Simulation results	wn	Hz	9.69	5.49	9.83	9.57	9.22
	$tr_{5\%}$	s	0.047	0.058	0.028	0.028	0.042
	ts	s	0.061	0.456	0.223	0.199	0.192
	Mp	%	0.84	17.6	29.88	25.49	7.95
	e_{ss}	deg	-0.024 ±0.003	-0.020 ±0.003	-0.021 ±0.003	-0.020 ±0.004	-0.021 ±0.004
	$\delta_{\alpha\theta}$	deg	0.73	0.18	1.10	0.97	0.42
	cr_1	A	1.54	1.54	1.54	1.54	1.54
	cr_2	A	0.029	0.003	0.007	0.002	0.005
	cr_3	A	0.252	0.303	0.327	0.245	0.369
	cr_4	A	0.605	0.769	0.843	0.574	0.844
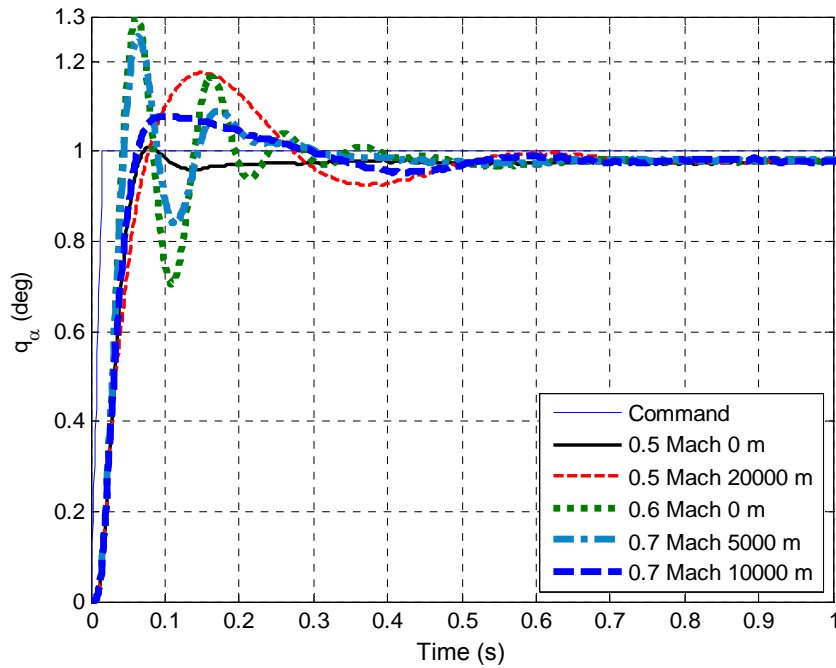
Figure 136. Step response of the ASE system at varios match points

Similar to the q-method, in the g-method it is seen from the step response analyses results that, the controller that is synthesized at 0.5 Mach number and 800 m altitude can satisfy stability and performance to some extend at 0.6 and 0.7 Mach numbers. However some performance degradations occur as the flow conditions varies. At 20,000 m altitude, the bandwidth of the system decreases down to 5.49 Hz, and the settling time increases up to 0.456 s. It is seen from the results that, as the flow conditions vary from the design condition, the overshoot values increase and the worst condition 30% overshoot occurs at the 0.6 Mach and 0 m. This is the case at which the highest dynamic pressure occurs.
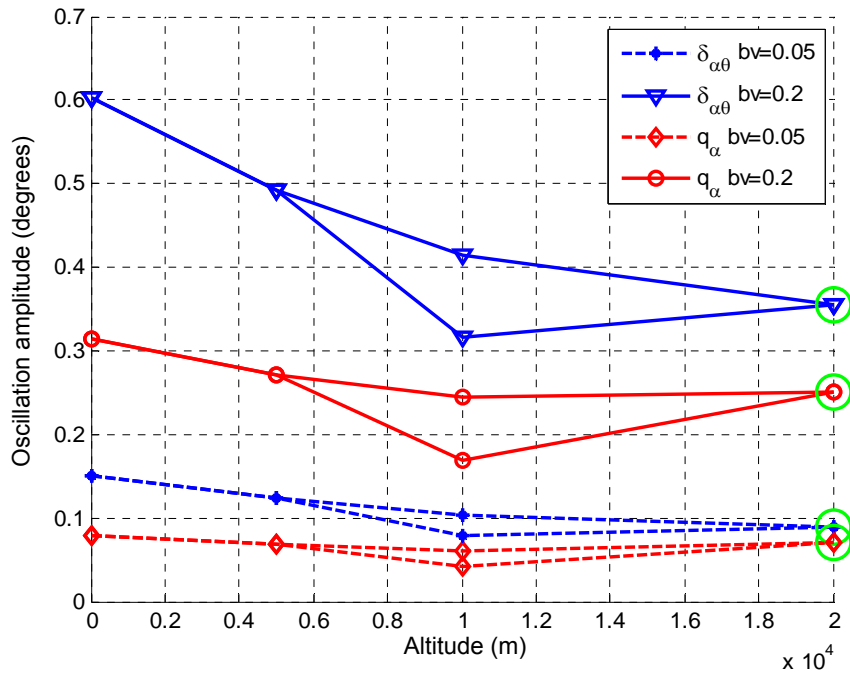
(a) with respect to altitude at 0.5 Mach
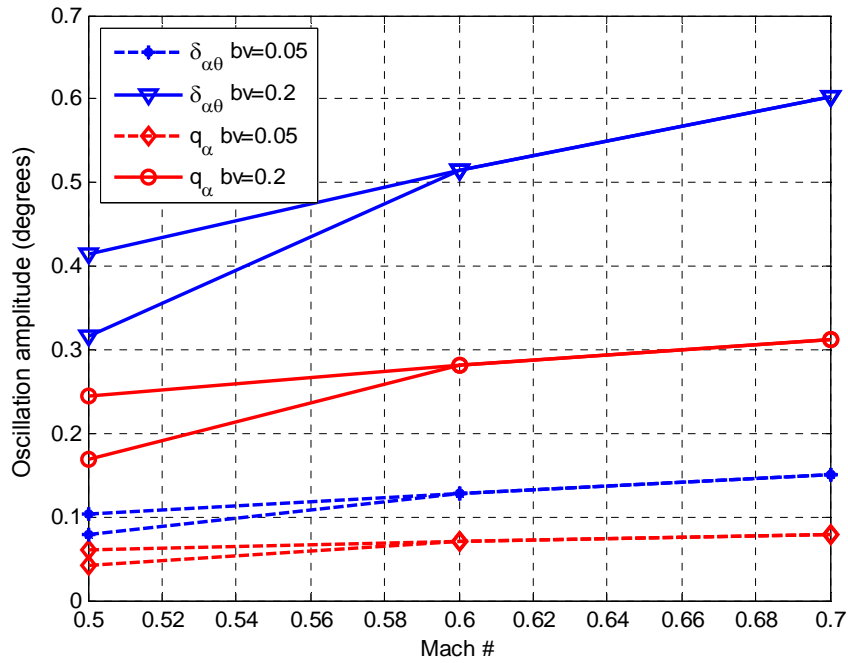
(b) with respect to Mach number at 10,000 m

Figure 137. LCO amplitudes of the aeroservoelastic system for various backlash values

291

The backlash analyses are performed with the same approach to the q-method in compressible flow. The results of these analyses are given in Figure 137. From the results it seen that, the oscillation amplitudes of the aeroservoelastic system increases with the; decreasing altitude and increasing Mach number. Note that in both cases the dynamic pressure increases. It can be also seen that, the oscillation amplitude of $\delta_{\alpha\theta}$, the degree of freedom that the backlash exist, is increases up to two to three times of the backlash value. But, the controller suppressed the oscillation of q_α, the pitch motion of the typical section wing, down to a comparable value to the backlash value.

Similar to the q-method analyses, a linearly dependency to the backlash value is seen from the backlash analyses in g-method.

Through the backlash analysis at 0.5 Mach and 20,000 m, it is seen from the time plots of the analysis results that the system is not converged to a stable value or to an LCO event at 40th second. Hence, similar to the q-method additional analyses are performed and a possible chaos is observed for the aeroservoelastic system with the synthesized g controller at 0.5 Mach and 20,000 m. These points are encircled in Figure 137. Since a steady state condition is not satisfied, the presented values in Figure 137 are the maximum values of the corresponding signal.

6.3.3. Comparison of Controllers

For subsonic compressible flow two case studies are analyzed, regarding two different flutter suppression methods. For both methods, namely q-method and g-method, H$_\infty$ type controllers are synthesized. Similar to the incompressible case the results are classified under three categories; linear stability, linear performance, and nonlinear analyses.

The linear stability results of the aeroservoelastic system with the two controllers and the stability limits of the aeroelastic system are given in Figure 138. As it can be seen from this figure, both controllers enlarge the flutter flight envelope from aeroelastic stability limits. In 0.5 and 0.6 Mach numbers the instability limits are enlarged below sea level. However, among the two controllers the q controller enlarges the envelope better than the g controller for the Model 2 in compressible flow.
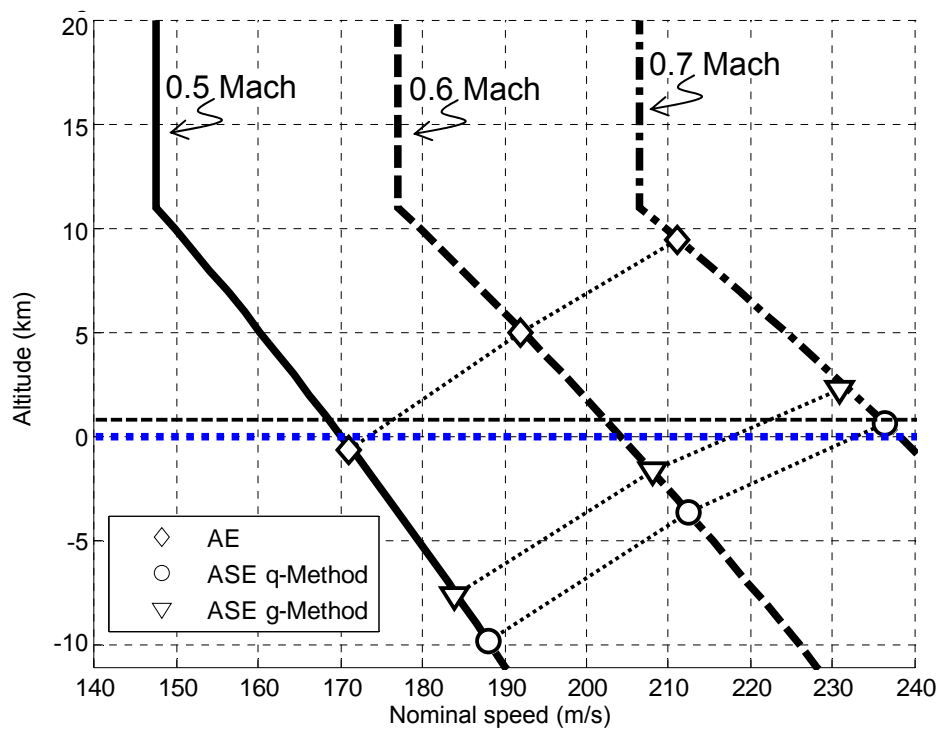
Figure 138. Flutter flight envelope

The performance results of the controllers are given in Table 59, Table 63, Figure 131, and Figure 136. Considering the bandwidth requirement it is seen that the q controller provides a better bandwidth. Moreover, q controller is affected from the flow variation less than the g controller. The rise time performance of the q controller is better than or equal to the g controller in all cases. On the other hand, the settling time

performances of the two controllers are comparable. In three out of five cases, the g controller provides smaller settling times than the q controller. Considering the overshoot, it is seen that the q controller performes better in four out of five cases. However, considering the steady state error the g controller performes better in all cases. The two controllers perform comparably according to deformation of the torsional spring. The q controller consumes less current than the g-method nearly in all cases. As a sum up, considering the bandwidth, rise time, overshoot, and current consumption requirements the q controller performs better than the g controller. The g controller is better for the steady state error and partially in settling time requirements.
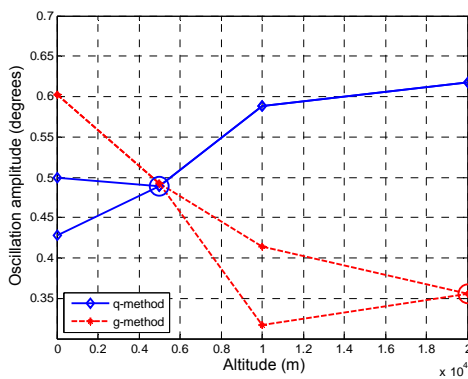
(a) $\delta_{\alpha\theta}$ w.r.t. altitude
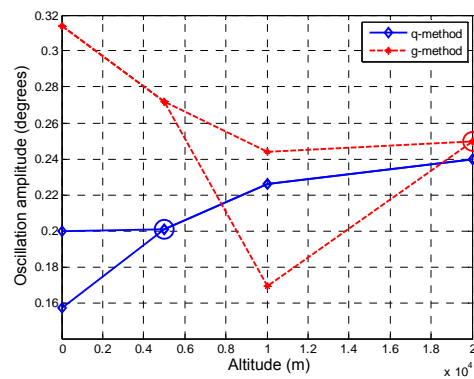
(b) q_α w.r.t. altitude
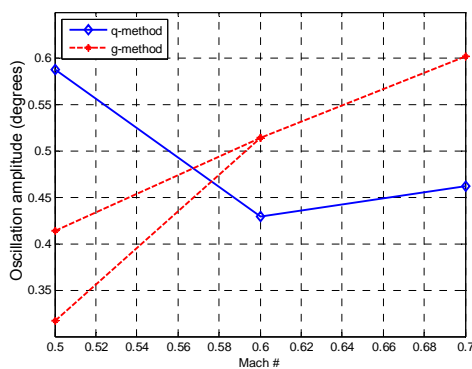
(c) $\delta_{\alpha\theta}$ w.r.t. Mach number
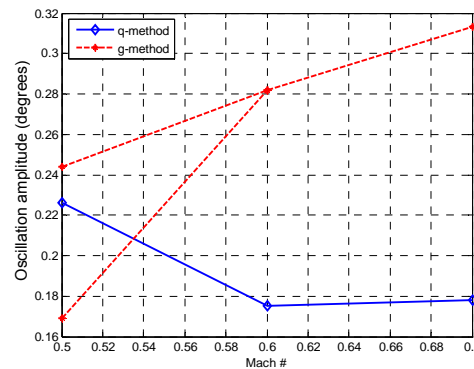
(d) q_α w.r.t. Mach number

Figure 139. LCO amplitudes of the aeroservoelastic with different controllers (backlash value = 0.2°)

Nonlinear analysis results of the aeroservoelastic system with 0.2°
backlash value and two different controllers are presented in Figure 139.
From the figures it can be seen that the controllers are affected differently
from the variation of the flow conditions. The performance of the q
controller enhances as the altitude decreases or the Mach number
increases, which stands for an increase in the dynamic pressure. On the
contrary, the performance of the g controller enhances at the opposite
cases. Considering the deformation of the spring, $\delta_{\alpha\theta}$, that is the degree of
freedom at which the backlash exist; the controllers perform comparably
and the amplitude of the oscillations increases up to two or three times of
the backlash value. However, considering the pitch motion of the typical
section wing, q_α, that is one of the performance merits defined in controller
synthesis and also in the analysis, the q controller performes better nearly
in all cases. This is in contrast with the steady state error results obtained
without the backlash, in which the g controller performes better than the q
controller. In fact, steady state error is the only evident advantage of the g
controller that is seen in performance analyses.

As a conclussion, the controller synthesized by using the q-method
performs better in general than the controller synthesized by using the
g-method for the aeroservoelastic Model 2 in the selected compressible
flow cases.

6.4. Unsteady Compressible Supersonic Flow

In this Section, some case studies conducted for the unsteady
compressible supersonic flow is presented. A proper aeroelastic model is
constructed and two H$_\infty$ type controllers are synthesized by means of q
and g-methods at 1.2 Mach. The conducted aeroservoelastic systems are
assessed according to the stability, performance, and effect of backlash.

The aeroelastic model, Model 3 is constructed by modifying the spring constants and damping values of the Model 2. The parameters of the Model 3 are given in Table 64.

Table 64. Properties of the Model 3

Parameter		unit	Model 3
Elastic axis location	a	-	-0.6
Half chord	b	m	0.15
Span	l	m	0.6
Mass of the wing	m	kg	9.83
Total plunging mass	m_p	kg	28.7
Mass moment of inertia of the wing	I_α	kg.m^2	0.128
Plunge stiffness	k_h	kN/m	30,000
Total torsional stiffness	$k_{\theta\alpha}$	N.m/rad	7,000
Plunge damping	c_h	N.s/m	293.4
Pitch damping	c_α	N.m.s/rad	2.999
Position of center of mass from elastic axis	x_{cg}	m	0.105
Motor torque constant	kT	N.m/A	2.22
Motor continuous stall torque	T_{cs}	N.m	3.53
Allowable peak torque	T_p	N.m	42.36
Mass moment of inertia of motor and transmission calculated at the wing shaft	I_m	kg.m^2	0.000297
Motor and transmission damping	c_m	N.m.s/rad	0.000124
Transmission ratio	N	-	87

The indicial functions of the Model 3 are derived by following the procedure presented in Section 2.5.3. On the contrary to the subsonic case, a curve fitting operation is applied to all indicial functions. Because, for the supersonic case, closed form piecewise equations of the indicial functions are exist. Note that in compressible subsonic flow, the curve fit equations of the indicial functions derived by Mazetsky are exists, and ϕ^T_c is directly used without applying any modification. The squared 2-norms of

296

the residuals of the curve fits which defines the quality of curve fitting are given in Table 65. The derived parameters of the indicial functions through curve fitting are given in Table 66 through Table 69. The calculated values of the indicial functions ϕ^T_c, ϕ^T_{cM}, ϕ^T_{cq}, and, ϕ^T_{cMq} by Equations (2.138) through (2.145) and their curve fits are presented in Figure 140 through Figure 143. It is seen that the curve fit results of supersonic indicial functions especially the ϕ^T_c at 1.2 Mach are worse than the curve fit results of subsonic flow. The reason is the piecewise characteristics of the supersonic indicial function equations, which causes discontinuity at the derivatives of the function.

Table 65. The squared 2-norms of the residuals of the curve fits.

	ϕ^T_c	ϕ^T_{cM}	ϕ^T_{cq}	ϕ^T_{cMq}
1.2 Mach	1.5737	0.0354	0.0084	0.0037
1.5 Mach	0.0507	0.0341	0.0006	0.0064
2.0 Mach	0.0125	0.0082	0.0004	0.0003

Table 66. Curve fit results for ϕ^T_c at compressible supersonic speeds.

$\phi_c(s) = b_{0c} + b_{1c}e^{-\beta_{1c}s} + b_{2c}e^{-\beta_{2c}s} + b_{3c}e^{-\beta_{3c}s}$							
M	b_{0c}	b_{1c}	β_{1c}	b_{2c}	β_{2c}	b_{3c}	β_{3c}
1.2	0.9597	-0.1128	0.1929	-0.3288	0.1929	-0.0523	0.1929
1.5	0.5694	1.0081	0.8686	-0.4914	0.691	-0.6473	0.691
2.0	0.3676	0.2844	0.9788	0.1276	0.4011	-0.4549	0.6301

Table 67. Curve fit results for ϕ^T_{cM} at compressible supersonic speeds.

$\phi_{cM}(s) = b_{0cM} + b_{1cM}e^{-\beta_{1cM}s} + b_{2cM}e^{-\beta_{2cM}s} + b_{3cM}e^{-\beta_{3cM}s}$						
M	b_{0cM}	b_{1cM}	β_{1cM}	b_{2cM}	β_{2cM}	b_{3cM}	β_{3cM}
1.2	-0.2879	0.8945	0.3460	0.2292	1.0868	-0.9982	0.5771
1.5	-0.1708	0.4844	0.6046	0.1534	0.6046	-0.606	0.7407
2.0	-0.1103	0.3547	0.6026	-0.0561	0.3363	-0.289	0.7792

Table 68. Curve fit results for ϕ^T_{cq} at compressible supersonic speeds.

$\phi_{cq}(s) = b_{0cq} + b_{1cq}e^{-\beta_{1cq}s} + b_{2cq}e^{-\beta_{2cq}s} + b_{3cq}e^{-\beta_{3cq}s}$						
M	b_{0cq}	b_{1cq}	β_{1cq}	b_{2cq}	β_{2cq}	b_{3cq}	β_{3cq}
1.2	0.2879	-0.4125	0.7371	-0.0907	0.7371	0.3754	1.0217
1.5	0.1708	-0.3734	0.9802	0.0775	0.5729	0.2544	1.3523
2.0	0.1103	-0.3643	1.214	0.0958	0.857	0.2549	1.4688

Table 69. Curve fit results for ϕ^T_{cMq} at compressible supersonic speeds.

$\phi_{cMq}(s) = b_{0cMq} + b_{1cMq}e^{-\beta_{1cMq}s} + b_{2cMq}e^{-\beta_{2cMq}s} + b_{3cMq}e^{-\beta_{3cMq}s}$						
M	b_{0cMq}	b_{1cMq}	β_{1cMq}	b_{2cMq}	β_{2cMq}	b_{3cMq}	β_{3cMq}
1.2	-0.1664	-0.2422	0.9287	0.0158	0.6658	0.2994	0.6658
1.5	-0.0987	-0.2395	0.3154	0.0008	0.2865	0.2692	0.3411
2.0	-0.0637	-0.3025	1.5809	-0.0095	0.61	0.3191	1.4693

Initial flow parameters are given in Table 70. The aeroelastic model is constructed by using the parameters given in Table 64, Table 70 and the equations given in Section 2.5.2. Similar to the Section 6.3, various analyses are performed in order to derive the aeroelastic properties of Model 3.
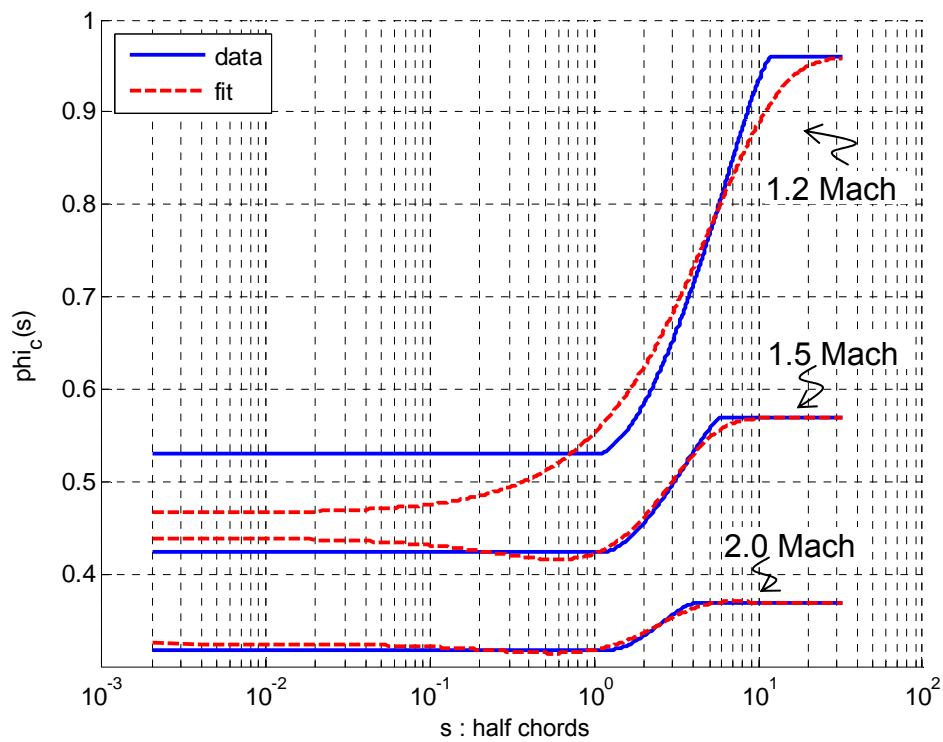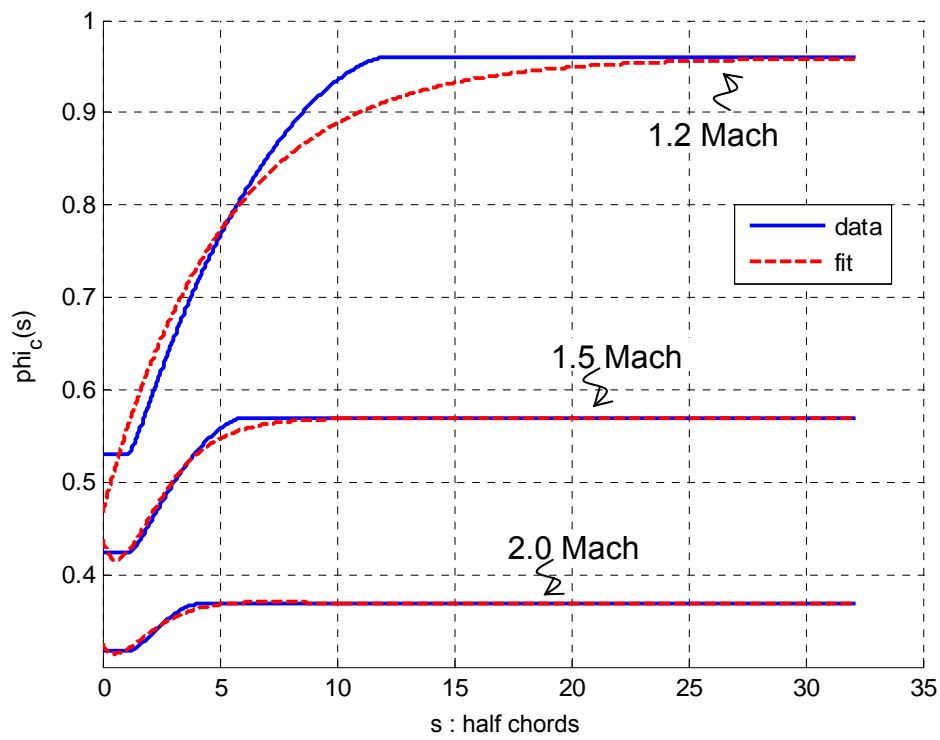
Figure 140. $\phi^T{}_c$ versus s (half chord) at 1.2, 1.5, and 2.0 Mach numbers
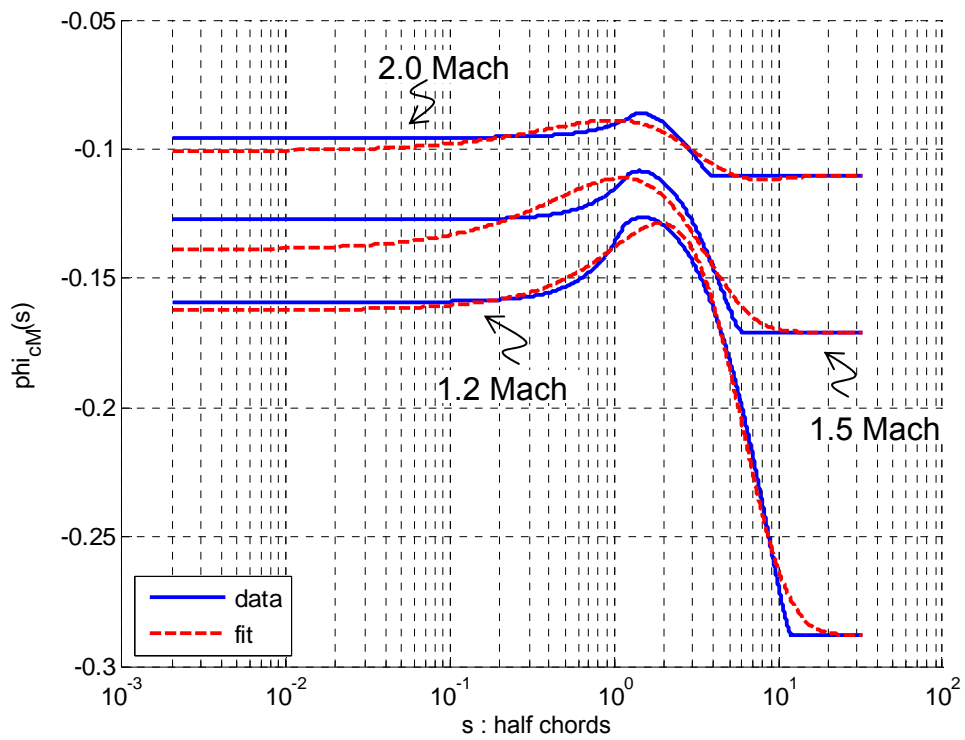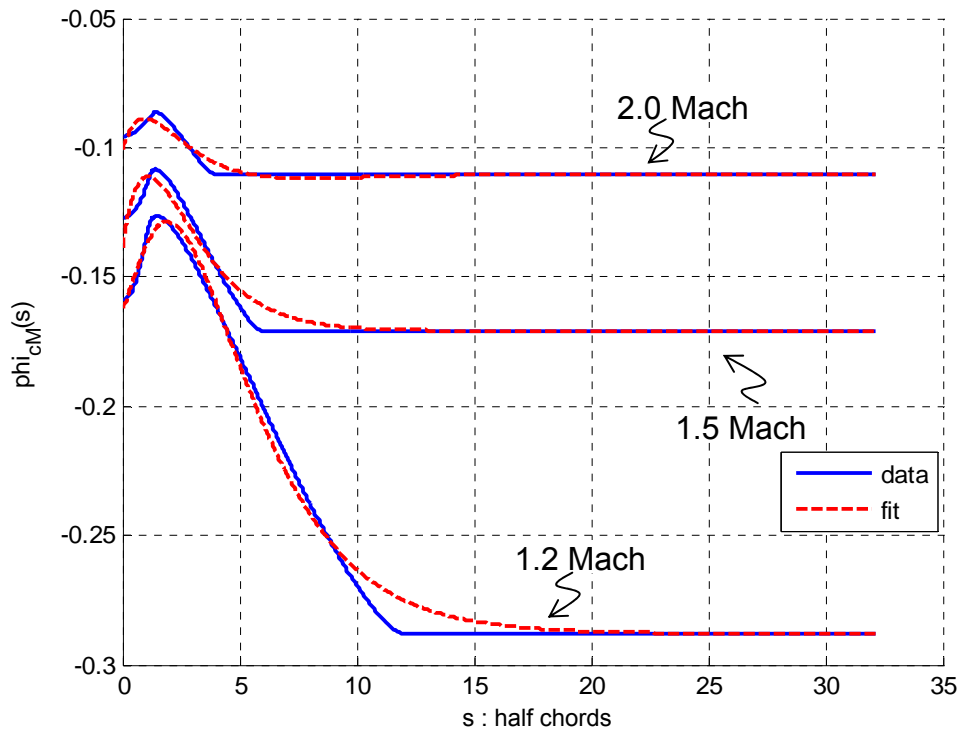
Figure 141. $\phi^T{}_{cM}$ versus s (half chord) 1.2, 1.5, and 2.0 Mach number
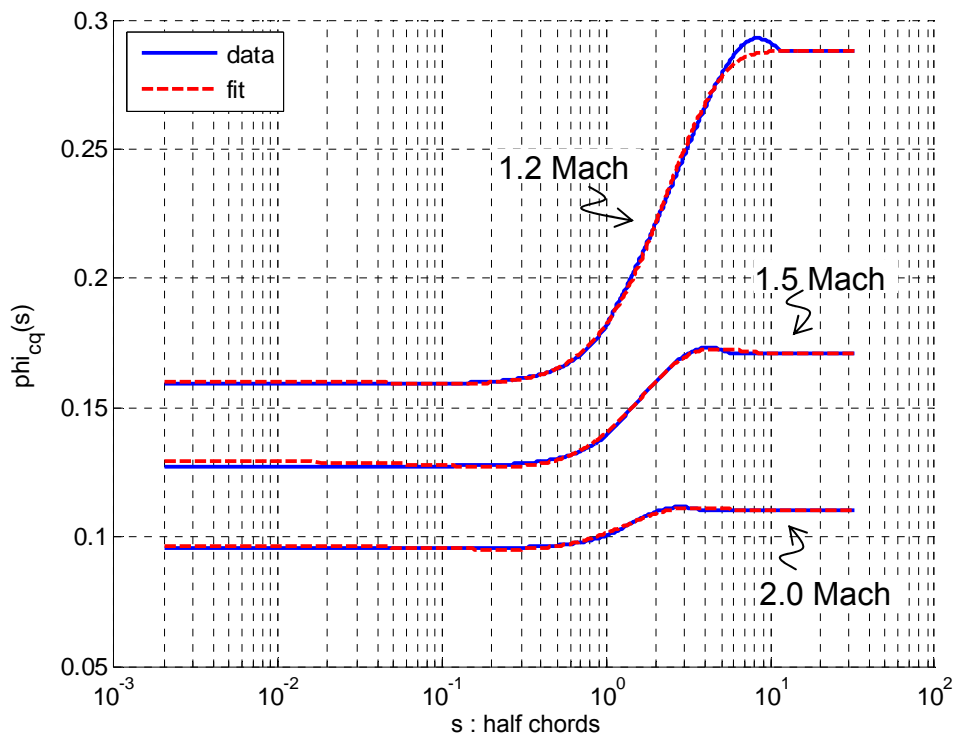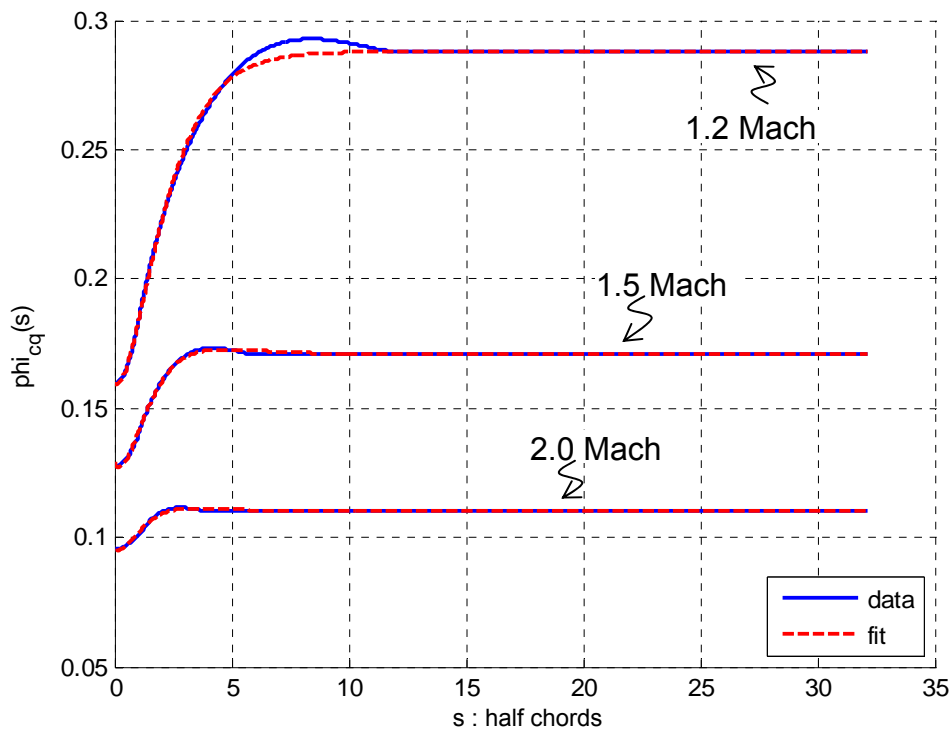
Figure 142. ϕ^T_{cq} versus s (half chord) 1.2, 1.5, and 2.0 Mach number

Figure 143. ϕ^T_{cMq} versus s (half chord) 1.2, 1.5, and 2.0 Mach number

302
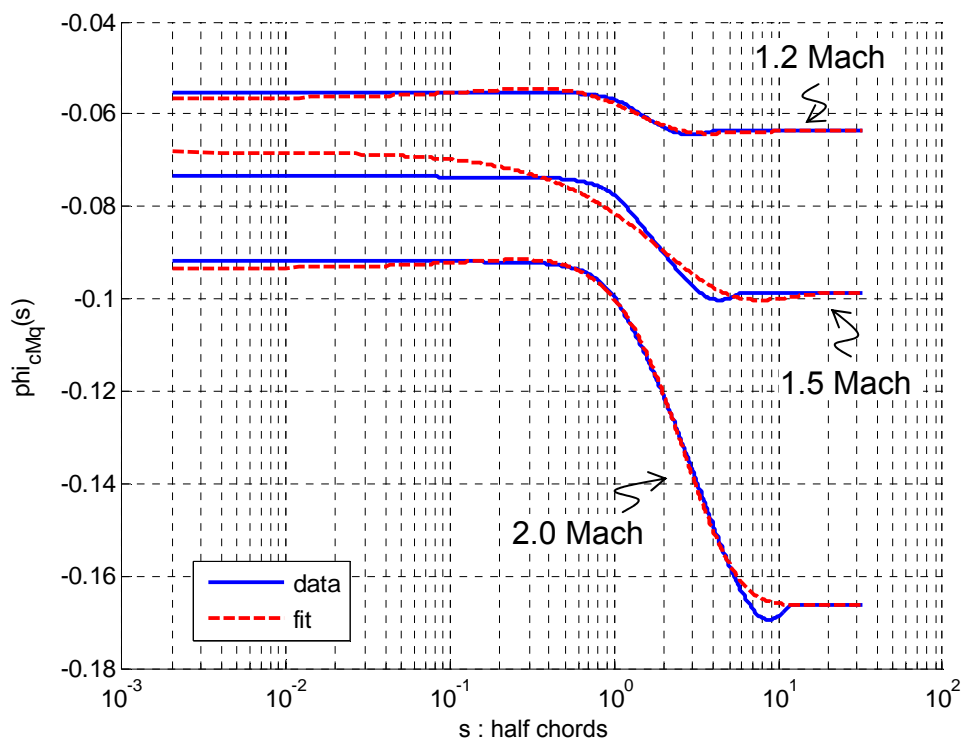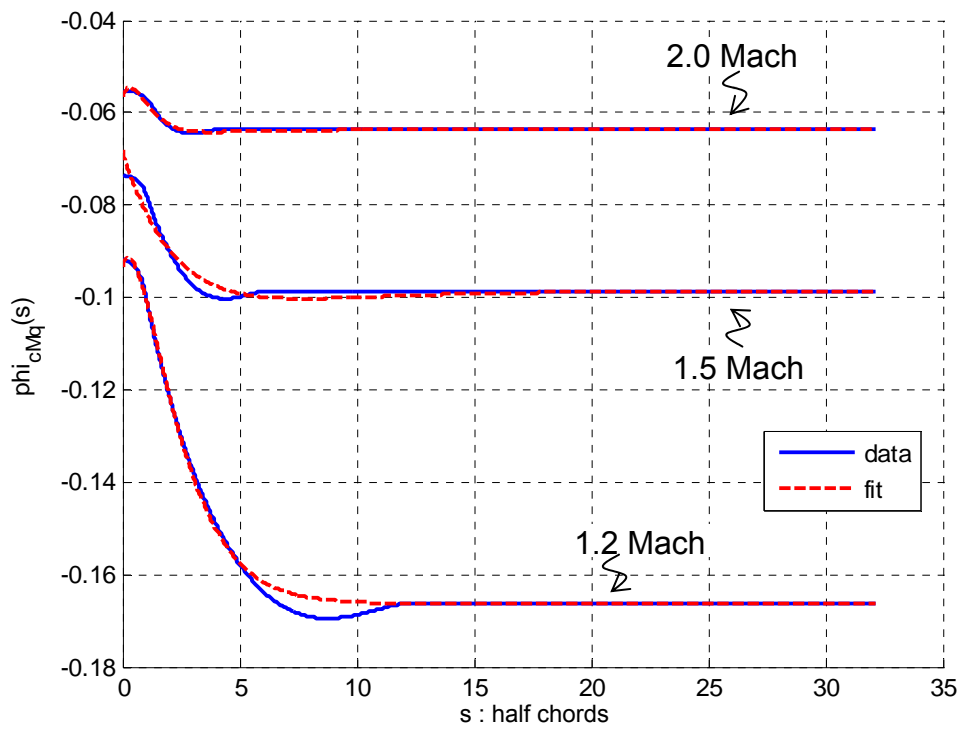
Table 70. Initial flow parameters

Altitude	h	m	0
Mach number	M	-	1.2
Airspeed	U_0	m/s	408.4
Air density	ρ	kg/m^3	1.225
Dynamic pressure	$\bar{q}_0$	Pa	102,130

By performing the flutter analysis by using μ-method it is seen that for the aeroelastic Model 3, flutter occurs at $\bar{q}_{flut}$ =117,411 Pa and at ω_{flut} =58.4 Hz. The p-method analysis is also performed and the results are given in Figure 128, which are used for crosschecking. It can be seen from the figures that the damping ratio of the aeroelastic system drops below 0 slightly above 117,000 Pa, and the frequency of the corresponding pole is 58.37 Hz. Thus, the solutions of the two methods verify each other.
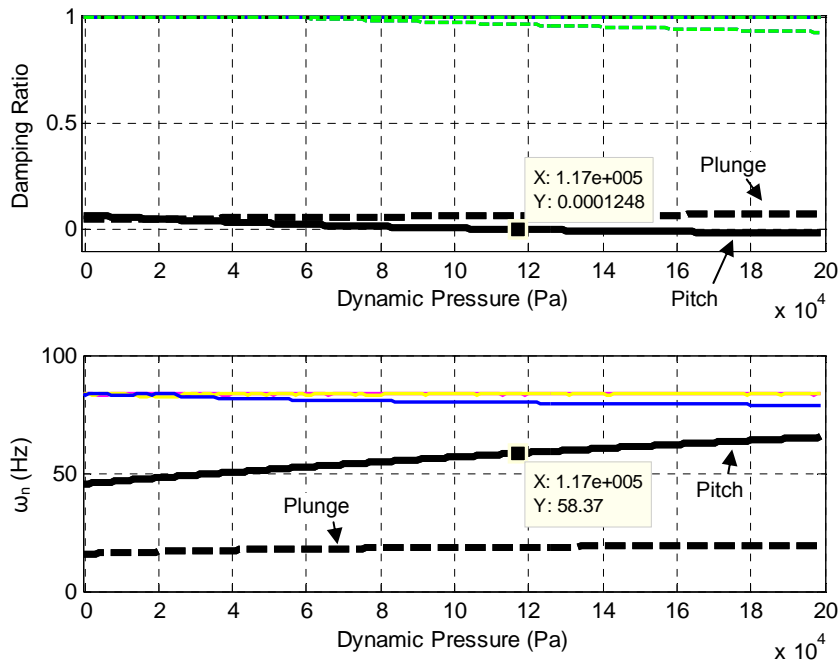
(a) modal properties of aeroelastic system
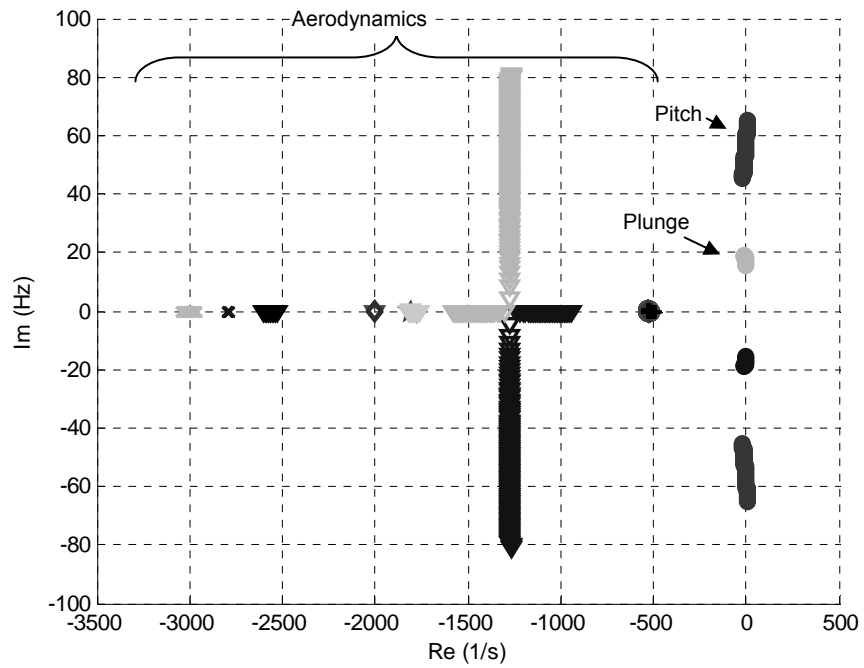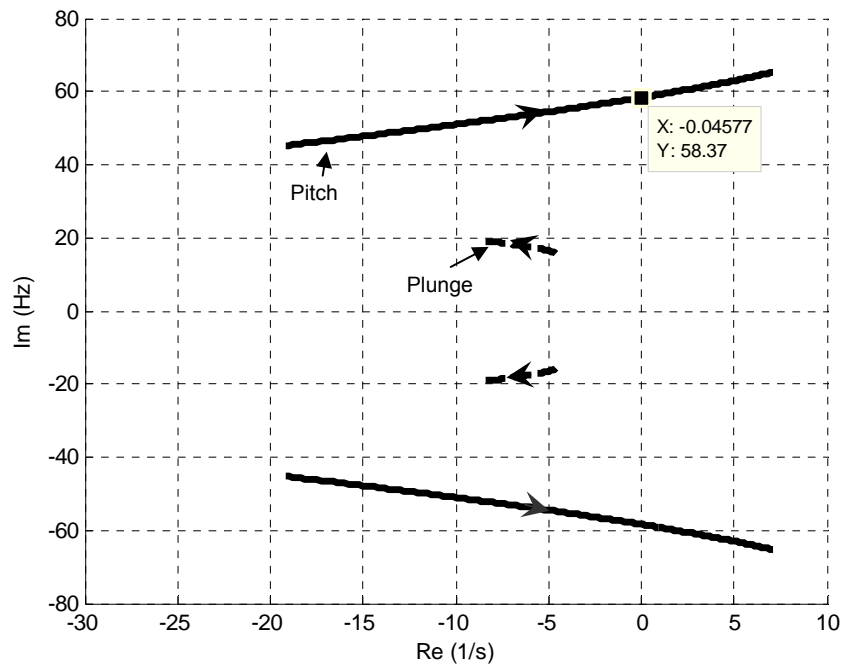
(b) root locus plot

(c) detailed root locus plot

Figure 144. Flutter search results of p-method by varying air density

Instability match points of Model 3 are calculated for various Mach numbers and presented in Table 71.

Table 71. Flutter match points of the aeroelastic system

Mach	Dynamic pressure	Frequency	Altitude	Airspeed
	$\bar{q}_{ins}$	ω_{ins}	h_{ins}	U_{ins}
	Pa	Hz	m	m/s
0.3	140,232	24.9	-35,468	137
0.5	53,730.8	18.6	-10,410	189
0.6	40,152.3	18.0	-3,987.3	213
0.7	30,307.9	17.6	1,139.7	235
1.2	112,679	58.0	-836.54	412
1.5	-	-	-*	-
2.0	-	-	-*	-

* System is stable down to -50,000 m

6.4.1. Controller Synthesis by Using q-Method

Similar to the previous cases, the controller synthesis process begins with determining the numerical values of the parameters of the reference plant and the uncertainty/performance weightings. This controller synthesis is based on the synthesized q controller in Section 6.3.1. The modified uncertainty/performance parameters are given in Table 72. For the rest of the unchanged uncertainty/performance weightings, numerical values given in Table 56 and for the parameters of the reference plant, numerical values given in Table 55 are used.

The values given in Table 72 are obtained after numerous iterations during H_∞ controller synthesis. These values are tuned considering the stability limits obtained by μ-method flutter analysis and H_∞ norm of the aeroservoelastic system. Moreover, a step response analysis is performed

and a fine tuning is conducted according to the step response analysis results. During the synthesis steps;

Table 72. Numerical values of uncertainty/performance weightings

Uncertainty Name	Gain		Corner Frequency		Scale Parameter	
$[W_{Fd}]$	g_{Fd_F}	37,950 N	ω_{Fd_F}	0.1 Hz	κ_{Fd_F}	0.001
	g_{Fd_M}	3,450 N.m	ω_{Fd_M}	0.1 Hz	κ_{Fd_M}	0.001
$[W_{per}]$	g_{per}	1 deg^{-1}	ω_{per}	30 Hz	κ_{per}	0.01
$[W_{\bar{q}1}]$	$g_{\bar{q}_F 1}$	6.67 N^{-1}				
	$g_{\bar{q}_M 1}$	73.5 (N.m)$^{-1}$				
$[W_{\bar{q}2}]$	$g_{\bar{q}_F 2}$	3,750 N	$\omega_{\bar{q}_F 2}$	60 Hz	$\kappa_{\bar{q}_F 2}$	0.001
	$g_{\bar{q}_M 2}$	340 N.m	$\omega_{\bar{q}_M 2}$	60 Hz	$\kappa_{\bar{q}_M 2}$	0.001

- The force and moment values of the weighting function $[W_{Fd}]$ of aerodynamic force uncertainty are obtained similar to the incompressible case. The gain values are tuned by considering the steady state error in step response.

- The performance requirement, the maximum allowed tracking error, is relaxed to 1° and the frequency is decreased to 30 Hz.

- The output weighting $[W_{\bar{q}1}]$ function of the disturbance to dynamic pressure is obtained similar to the incompressible case.

- For the derivation of the input weighting function $[W_{\bar{q}2}]$ of the disturbance to dynamic pressure, the disturbance $\bar{q}_{dist}$ to dynamic pressure is modified as 50,000 Pa. The frequency is increased up to 60 Hz, in order to cover the flutter frequency of the AE system around 58.4 Hz.

- The controller synthesis altitude is selected as 5,000 m.

After the definitions of the reference model and the weighting functions, the interconnection structure system shown in Figure 16 is constructed by using MATLAB® *sysic* command. The constructed system has 28 states, 7 outputs, and 8 inputs.

Similar to the previous cases the controller is synthesized by using MATLAB® *hinfsyn* command. The frequency plot of the full order controller that has 28 states is given in Figure 145. The H_∞ norm of the aeroservoelastic system with the synthesized controller is obtained as 0.991. The reduced controller is derived by using balanced reduction method as 14th order, with H_∞ norm between 0.991 and 0.992, Figure 146.

The analyses of the aeroservoelastic system with the synthesized controller are performed in three parts; namely stability, performance, and backlash analyses. The instability points of the aeroservoelastic system calculated by using μ-method are given in Table 73. According to these results the synthesized controller stabilizes the ASE system below 0 Pa and above 230,000 Pa which constitutes a good envelope considering the design point of 54,450 Pa, which is the dynamic pressure at 1.2 Mach and 5,000 m altitude. Note that 230,000 Pa corresponds to more than 1.8 Mach at sea level. By performing flight envelope search algorithms the instability match points of the aeroservoelastic system are calculated as given in Table 74. The calculations are performed for seven Mach numbers, from 0.3 to 2.0 Mach. It is seen that the controller enlarges the flutter flight envelope below sea level in all these Mach numbers.
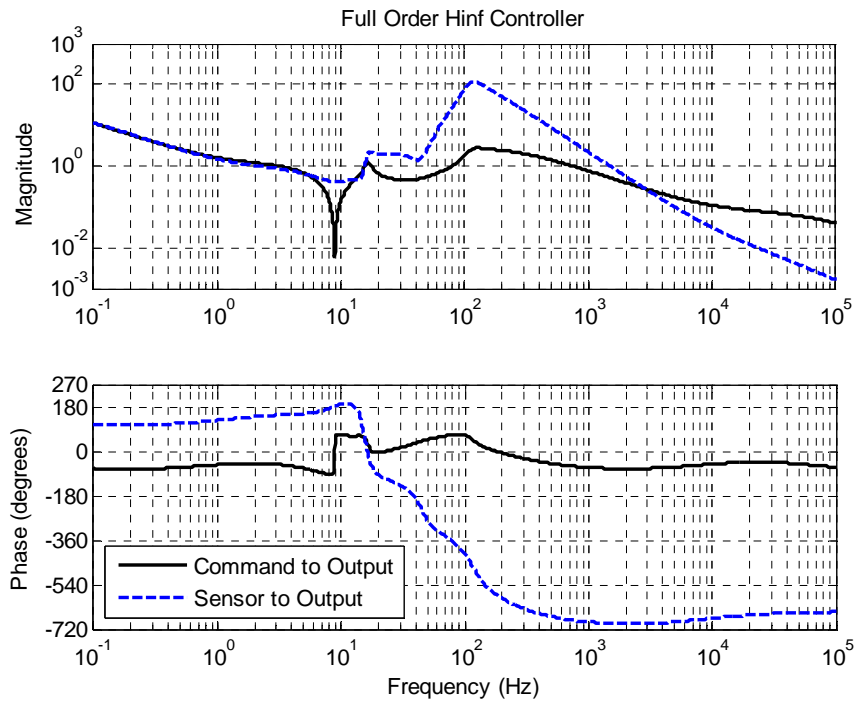
Figure 145. H_∞ controller
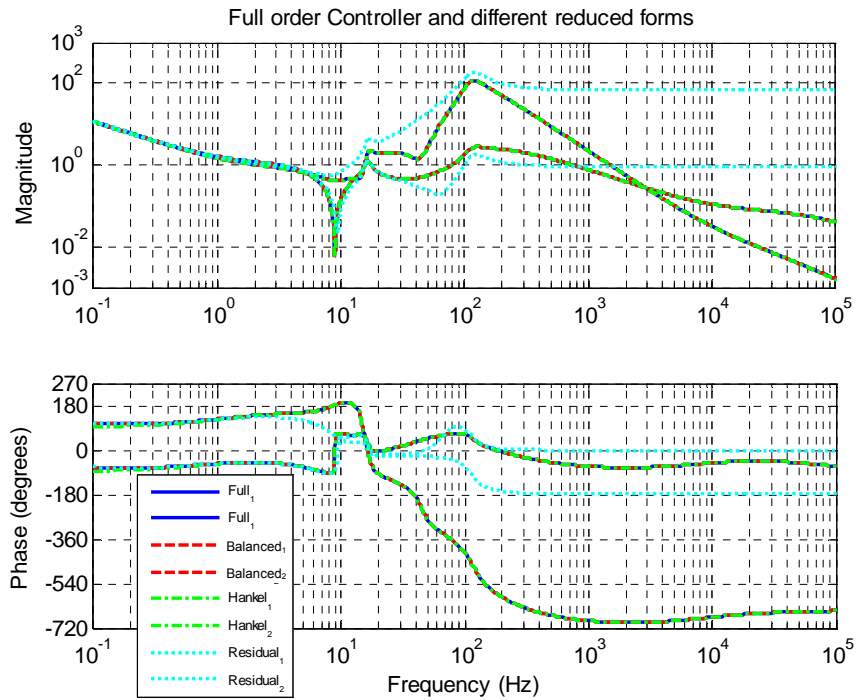
Figure 146. 14th order reduced controllers

Table 73. Nominal stability limits calculated by using μ-analysis

$\overline{q}_{ins_{low}}$	Pa	-33,596
$\omega_{ins_{low}}$	Hz	12.7
$\overline{q}_{ins}$	Pa	236,067
ω_{Ins}	Hz	79.1

Table 74. Instability match points of the aeroservoelastic system

Mach	Dynamic pressure	Frequency	Altitude	Airspeed
	$\overline{q}_{ins}$	ω_{ins}	h_{ins}	U_{ins}
	Pa	Hz	m	m/s
0.3	78,598	31.5	-27,145	130
0.5	59,825	29.3	-11,540	191
0.6	50,964	28.6	-6,229.7	218
0.7	45,584	27.8	-2,347.8	244
1.2	204,028	74.3	-6,237.8	436
1.5	414,906	86.8	-8,837.7	559
2.0	702,384	91.9	-8,344.9	742

The performance analyses are performed at nine different match points, at three supersonic and two subsonic Mach numbers. The results are given in Table 75 and Figure 147. From the step response analyses results, it can be seen that the controller that is synthesized at 1.2 Mach number and 5,000 m altitude can satisfy stability and performance to some extend, up to 2.0 Mach number and down to 0.3 Mach number. At lower altitudes of Mach numbers of 1.2, 1.5, and 2.0; it is seen that bandwidth of the ASE system decreases and its rise time and settling time increase. On the other hand, at higher altitudes or at lower Mach numbers, the overshoot of the ASE system increases up to 37%. These characteristics of the synthesized q controller can be easily seen in Figure 147. Furthermore, it can be seen that the ASE system has similar attitudes at 20,000 m altitude, at all analyzed Mach numbers; 0.3, 1.2, 1.5, and 2.0

Mach. There is also a similar attitude between the results of the analysis performed at 0 m altitude and 1.2, 1.5, and 2.0 Mach numbers. However, it is seen that the ASE system behaves different at 0 m altitude and 0.7 Mach than the other analyses points at 0 m altitude. Interestingly its attitude resembles the results of the analyses performed at 20,000 m altitude.

Table 75. Step response properties of aeroservoelastic system at various aerodynamic conditions with quantized sensor

		Mach	0.3	0.7	1.2	1.2	1.5	1.5	2.0	2.0	2.0
Simulation parameters		Altitude	m	20,000	0	0	20,000	0	20,000	0	5,000	20,000
		q	Pa	344.83	34,754	102,130	5,517.2	159,590	8,620.7	283,710	151,250	15,326
		U	m/s	88.5	238	408	354	510	443	681	641	590
		ρ	kg/m^3	0.088	1.225	1.225	0.088	1.225	0.088	1.225	0.736	0.088
Simulation results		ω_n	Hz	15.0	15.0	6.25	14.8	6.87	14.8	5.83	9.57	14.8
		$tr_{5\%}$	s	0.027	0.023	0.598	0.028	0.582	0.028	0.695	0.049	0.028
		ts	s	0.216	0.210	1.097	0.163	0.705	0.163	1.245	0.063	0.162
		Mp	%	37.48	35.82	0.00	31.98	0.00	32.32	0.00	0.00	31.40
		e_{ss}	deg	-0.028	-0.028	-0.046	-0.029	-0.045	-0.030	-0.047	-0.038	-0.030
		$\delta_{\alpha\theta}$	deg	0.005	0.009	0.003	0.003	0.006	0.012	0.004	0.005	0.003
		cr_1	A	0.06	0.13	1.36	0.10	1.27	0.09	1.45	0.84	0.10
		cr_2	A	0.57	0.65	1.29	0.61	1.20	0.61	1.36	0.90	0.65
		cr_3	A	0.000	0.014	0.860	0.045	0.799	0.043	0.914	0.489	0.050
		cr_4	A	0.132	0.120	0.139	0.120	0.142	0.123	0.153	0.138	0.129

311
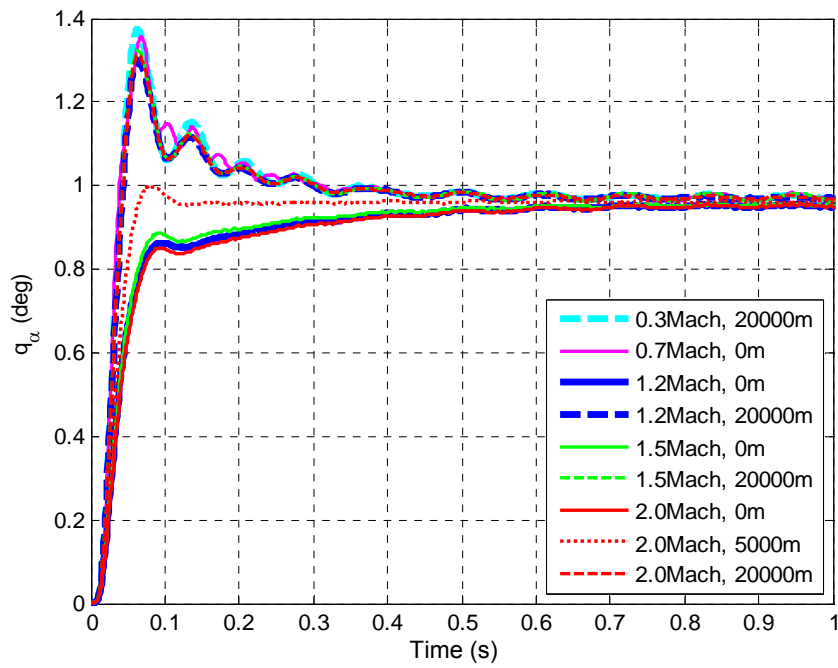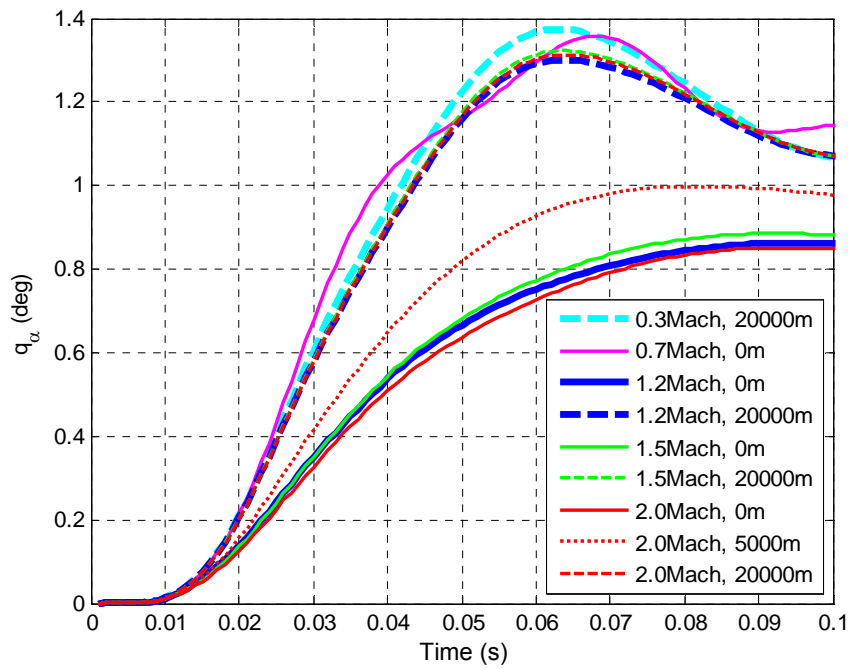
(a) first 1 second

(b) first 0.1 second

Figure 147. Step response of the aeroservoelastic system at varios match points

Some backlash analyses are performed both in frequency and time domain. The effect of backlash is analyzed both varying the altitude and the Mach number. For this purpose first the altitude is fixed at 10,000 m and the analyses are performed at six different Mach numbers from 0.3 to 2.0 Mach. Then, the Mach number is fixed at 1.2, and the altitude is varied from 0 to 20,000 m at four discrete steps. The results of these analyses are presented in Table 76 and Figure 148.

Table 76. LCO analyses results of the aeroservoelastic system

Mach	Altitude	bv	Frequency domain solutions			Time domain solutions					
			$k_{\alpha\theta}$	$\delta_{\alpha\theta}$		$\delta_{\alpha\theta}$		q_α		q_h	
	m	deg	N.m/rad	deg	Hz	deg	Hz	deg	Hz	mm	Hz
0.3	10,000	0.2	4,455.8	0.691	32.6	0.810	33.6	0.980	33.6	0.785	33.6
0.5	10,000	0.2	4,361.7	0.665	32.3	0.758	32.9	0.925	32.9	0.690	32.9
0.7	10,000	0.2	4,322.8	0.655	30.4	0.748	30.9	0.890	30.9	0.314	30.9
1.2	0	0.2	6,496.7	3.54	8.70	2.31	8.53	1.29	8.53	10.4	8.53
1.2	5,000	0.2	6,514.6	3.67	8.76	3.20	8.73	3.50	8.73	16.0	8.73
1.2	10,000	0.2	6,377.1	2.86	8.80	2.37	8.80	5.84	8.80	12.0	8.80
1.2	20,000	0.2	4,886.0	0.835	8.87	0.707	33.5	0.875	33.5	0.628	33.5
1.5	10,000	0.2	6,419.4	3.07	8.81	2.67	8.80	7.26	8.80	139	8.80
2	10,000	0.2	6,477.1	3.41	8.81	3.01	8.79	7.10	8.79	15.7	8.79

It is seen that the frequency domain analyses predict the frequency of the LCO similar to the time domain analyses results with less than 3% error except one case. However, the error in the amplitude of the LCO prediction is mostly between 10% to 20%, and 53% in one case. Nonetheless, the frequency domain method gives an idea about the order of magnitude of the LCO amplitude with a fast computation.
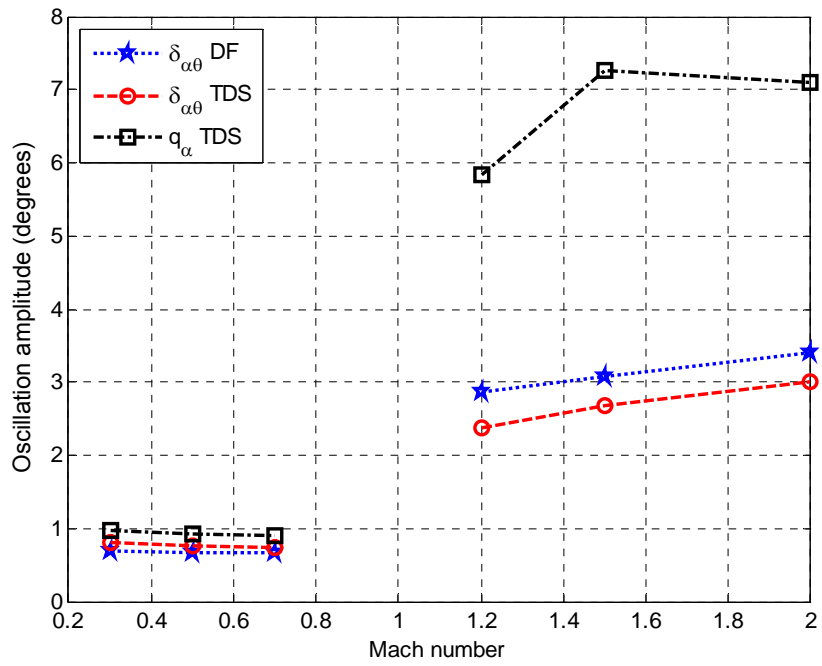
(a) with respect to Mach number at 10,000 m
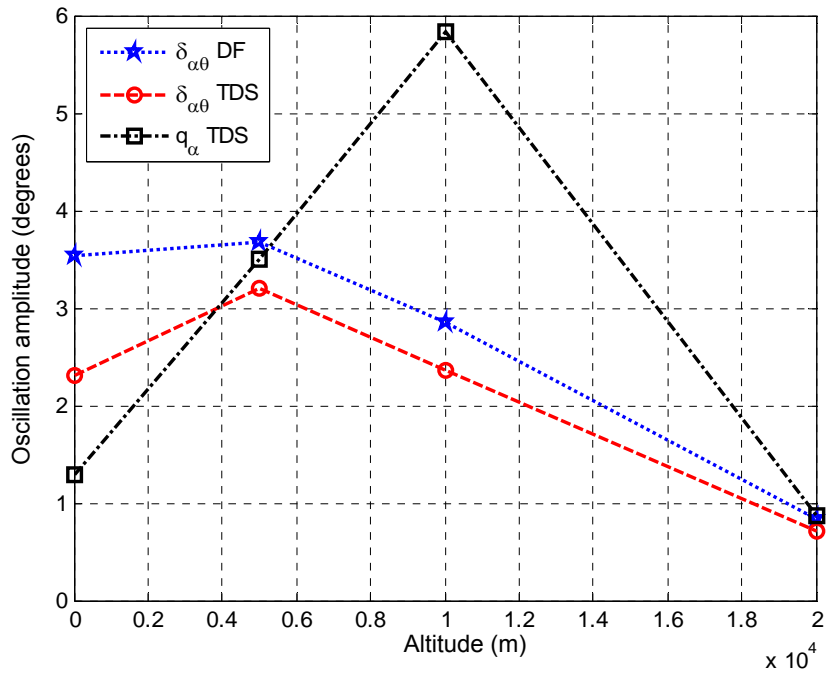
(b) with respect to altitude at 1.2 Mach

Figure 148. LCO amplitudes of the aeroservoelastic system

314

It can be seen from Table 76 that the obtained LCO's obtained are in two groups according to their frequencies. There is an LCO group with frequencies around 8.7 Hz and another group with frequencies around 33 Hz. It is also seen that the LCO's at 8.7 Hz have larger oscillation amplitudes. In all cases a small and a large initial impulse are applied as discussed in Section 6.2.2.1, but the ASE system converged to the same LCO from upper and lower oscillation amplitudes of the pitch motion of the typical section wing, q_α.

The variation of the properties of the LCO with respect to altitude and Mach number can be examined from Figure 148. It is noticeable that the LCO amplitudes are much smaller in subsonic flow than in supersonic flow. The frequencies of the LCO in subsonic flow are around 33 Hz, and those in supersonic flow are around 8.7 Hz. Moreover, LCO amplitudes increase with increasing Mach numbers. The altitude variation displays a complicated picture. With the increasing altitude, $\delta_{\alpha\theta}$ the deformation of the torsional spring first increases up to 5,000 m, then decreases. On the other hand, oscillation amplitude of q_α increases up to 10,000 m with the increasing altitude, and suddenly drops to a level that is comparable with the LCO's at subsonic flow. It is seen that the frequency of LCO changes from 8.7 Hz to 33 Hz when the altitude is increased from 10,000 m to 20,000 m.

Another interesting point is that, q_α is greater than the oscillation amplitude of the deformation of torsional spring $\delta_{\alpha\theta}$ nearly in all cases. Furthermore, the oscillation amplitude of q_α is much larger than the backlash value. Hence, the synthesized controller cannot suppress the amplitude of the LCO, especially the q_α, to a comparable level with the backlash value as in the case studies performed in Section 6.2 and 6.3.
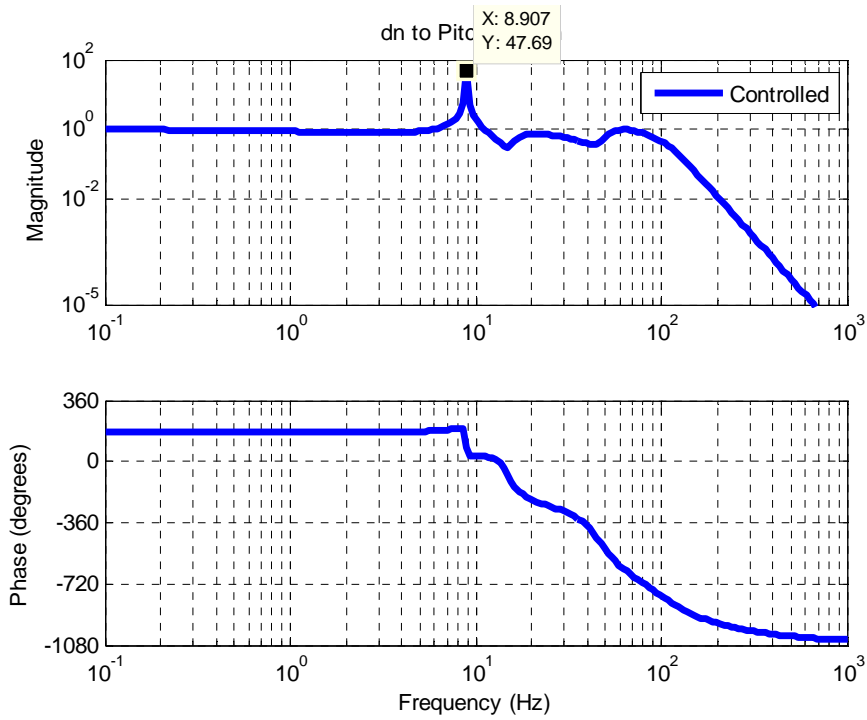
Figure 149. Frequency response from sensor noise input to pitch motion
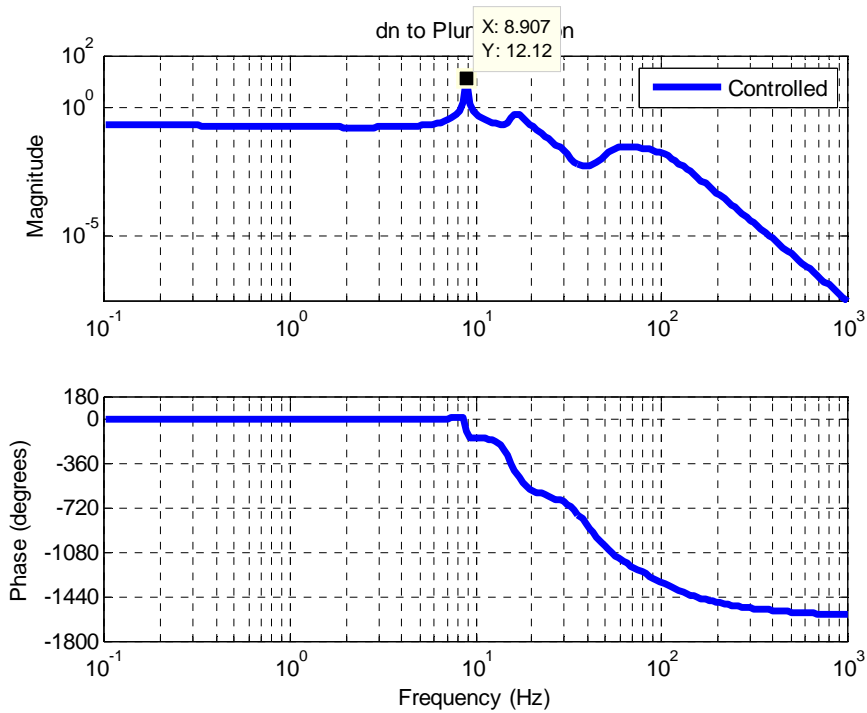
Figure 150. Frequency response from sensor noise input to plunge motion

316
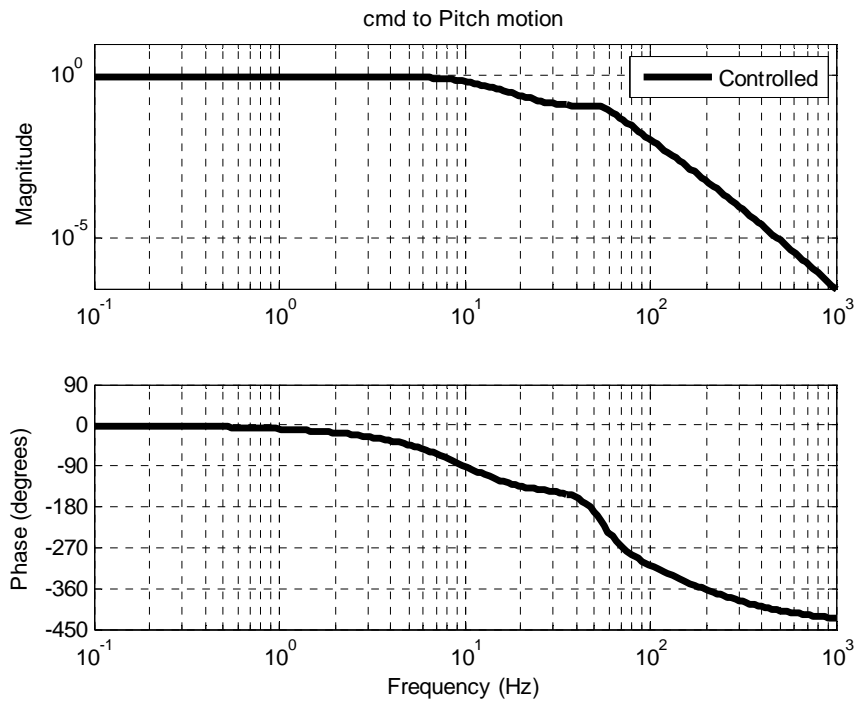
Figure 151. Frequency response from command input to pitch motion
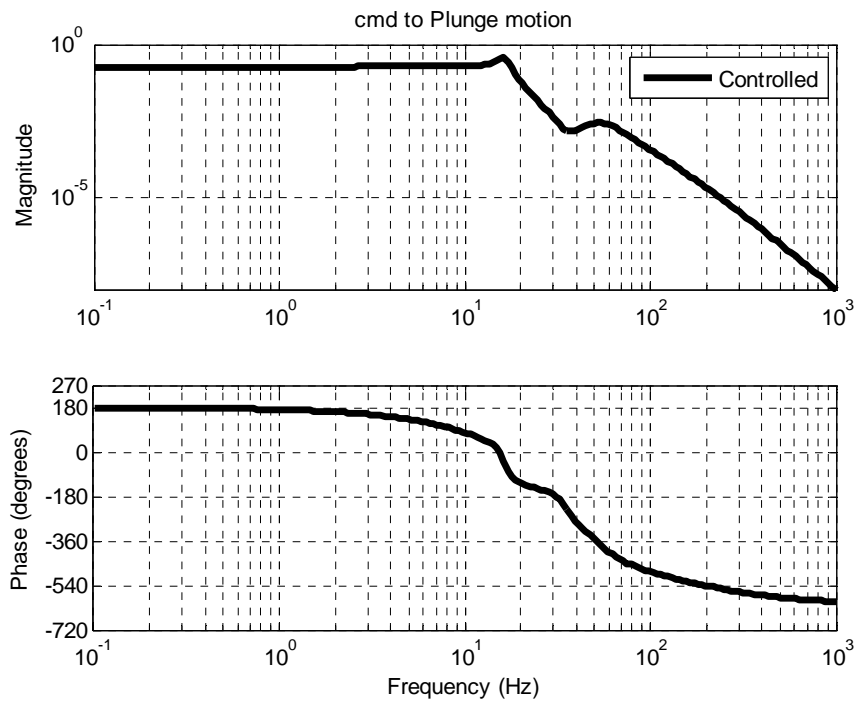
Figure 152. Frequency response from command input to plunge motion

Examining the Bode plot of the synthesized controller given in Figure 145, it is seen that the plot of command to output has a dip slightly below 9 Hz, but this dip is not present in the plot of sensor to output. Note that the frequency is close to the frequency of LCO with large oscillation amplitudes. Examining the Bode plots of the previously implemented controllers that are successful in backlash analyses in Section 6.2 and 6.3, it is seen that both command to output and sensor to output plots have dips at the same time around these low frequencies. Furthermore, the frequency domain analyses of the ASE performed at the nominal dynamic pressure in synthesis step, similar to the Section 6.2.2.1.1, are examined. The command and noise to pitch and plunge graphs are given in Figure 149 through Figure 152. From these figures it is seen that, the command to pitch and plunge plots are normal as expected. However, in noise to pitch and plunge graphs, a peak is observed at 8.9 Hz. Hence, in synthesis step, a clue for the large amplitude oscillations is obtained, but the effect is not seen in step response analyses which uses the aeroservoelastic plant without any backlash. Examining the ASE system it is seen that the mode with the 8.9 Hz frequency belongs to the motor dynamics with the torsional spring.

6.4.2. Controller Synthesis by Using g-Method

In the controller synthesis by using g-method, the numerical values of the parameters of the reference plant and the uncertainty/performance weightings are initially taken same as in Table 55 and Table 56. But the output $\left[W_{\bar{q}1} \right]$ and input $\left[W_{\bar{q}2} \right]$ weighting functions of the disturbance to dynamic pressure, which are specific to q-method are not used in controller synthesis. On the other hand, the output $[W_{c1}]$ and input $[W_{c2}]$ weighting functions of the damping uncertainty of the g-method are included to the controller synthesis. As in the other cases of this study, the

damping uncertainty is introduced only to the pitch degree of freedom. The gain g_{c1} of the function $[W_{c1}]$ is the inverse of the expected speed as explained in Section 4.4. The expected speed is calculated as 1.097 rad/s by using the similar approach in the subsonic compressible case. Therefore, the value of the term g_{c1} is calculated as 0.912 s/rad. With the similar reasoning of the subsonic compressible case, after numerous iterations the δ_c term of the function $[W_{c2}]$ is taken as 10 N.m.s/rad. In order to cover the aeroelastic flutter frequency, the corner frequency ω_{c2} of the function $[W_{c2}]$ is taken as 60 Hz. On the other hand, the gain value of the performance weighting is tightened back to 0.3°, which decreased the steady state error. After numerous iterations the controller is synthesized at the altitude of 10,000 m. The modified and the newly introduced uncertainty/performance weightings are given in Table 77.

Table 77. Numerical values of uncertainty/performance weightings

Uncertainty Name	Gain		Corner Frequency		Scale Parameter	
$[W_{per}]$	g_{per}	3.33 deg^{-1}	ω_{per}	30 Hz	κ_{per}	0.01
$[W_{c1}]$	g_{c1}	0.912 s/rad	-	-	-	-
$[W_{c2}]$	g_{c2}	δ_c*1.097 rad/s	ω_{c2}	60 Hz	κ_{c2}	0.01

Figure 153. H$_\infty$ controller
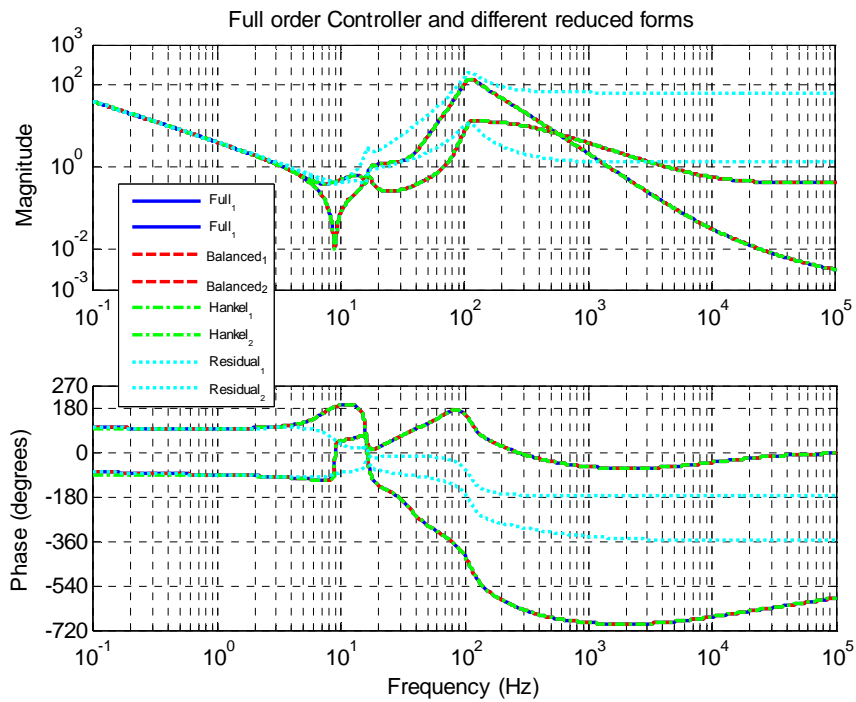
Figure 154. 13$^{\text{th}}$ order reduced controllers

Similar to the previous cases, after the definition of the reference model and the weighting functions, the interconnection structure system is constructed by using MATLAB® *sysic* command. The constructed system has 27 states, 7 outputs, and 8 inputs. The controller is synthesized using MATLAB® *hinfsyn* command. The frequency plots of the controller are given in Figure 134. The H_∞ norm of the aeroservoelastic system with the synthesized controller is obtained as 0.957. The order of the controller is reduced from 27th to 13th order by using various reduction methods. The frequency plots of the full order controller and 13th order controllers reduced by various methods are given in Figure 135. The H_∞ norm of the aeroservoelastic system with the reduced controller by balanced method is computed between 0.969 and 0.970. This value is lower than the norms of the aeroservoelastic system with the controllers reduced by means of other reduction methods. Hence, the controller reduced by balanced method is chosen for the rest of the study.

For the analyses, similar steps are followed as in Section 6.4.1. By performing the μ-method flutter analysis, the instability points of the aeroservoelastic system with the g controller are obtained as presented in Table 78. According to the μ-method flutter analysis, the synthesized controller enlarges the stability limits of the aeroservoelastic system below 0 Pa and above 230,000 Pa, similar to the q&H_∞ controller. By performing the flutter envelope calculation methods, the instability match points of the ASE system with the g controller are attained as given in Table 79. Similar to q controller, the g controller guaranteed the stability above sea level in the analyzed Mach numbers, varying from 0.3 to 2.0 Mach.

The step response analyses are performed at the Mach numbers from 0.3 to 2.0 and in the altitudes from 0 m to 20,000 m. The results are presented in Table 80 and Figure 155. It is seen from the step response analyses that the synthesized g-method controller has an acceptable

performance in the analyzed aerodynamic conditions. The most adverse property of this controller is its bandwidth degradation at the lower altitudes of high Mach numbers. On the other hand, this controller provides a rise time less than 102 ms, a settling time less than 175 ms, an overshoot less than 15%, a steady state error less than 0.01° mean and 0.015° oscillation amplitude, and a torsional spring deformation less than 0.015° in all analyzed conditions. Similar to the ASE system with the q&H∞ controller, the attitudes of this ASE system can be grouped as 0 m altitude and 20,000 m altitude excluding the results of the analysis performed at 0.7 Mach. The ASE system performs a slightly overdamped behavior at 0m altitude, and underdamped behavior at 20,000 m altitude as it can be seen from Figure 155.

Table 78. Nominal stability limits calculated by using μ-analysis

$\bar{q}_{ins_{low}}$	Pa	-16,267
$\omega_{ins_{low}}$	Hz	13.3
$\bar{q}_{ins}$	Pa	238,104
ω_{ins}	Hz	82.6

Table 79. Instability match points of the aeroservoelastic system

Mach	Dynamic pressure	Frequency	Altitude	Airspeed
	$\bar{q}_{ins}$	ω_{ins}	h_{ins}	U_{ins}
	Pa	Hz	m	m/s
0.3	86,943	25.6	-28,531	131
0.5	57,493	22.8	-11,119	190
0.6	47,505	22.3	-5,558.1	217
0.7	39,766	21.8	-1,150.9	241
1.2	186,504	77.9	-5,381.2	432
1.5	302,728	85.8	-5,742.7	543
2.0	459,468	87.4	-4,258.7	713

Table 80. Step response properties of aeroservoelastic system at various aerodynamic conditions with quantized sensor

	Mach	0.3	0.7	1.2	1.2	1.5	1.5	2.0	2.0	2.0
Simulation parameters	Altitude (m)	20,000	0	0	20,000	0	20,000	0	5,000	20,000
	q (Pa)	344.83	34,754	102,130	5,517.2	159,590	8,620.7	283,710	151,250	15,326
	U (m/s)	88.5	238	408	354	510	443	681	641	590
	ρ (kg/m^3)	0.088	1.225	1.225	0.088	1.225	0.088	1.225	0.7361	0.088
Simulation results	ω_n (Hz)	14.85	12.83	5.02	14.56	5.38	14.54	4.92	7.16	14.45
	$tr_{5\%}$ (s)	0.031	0.029	0.096	0.033	0.082	0.033	0.101	0.063	0.035
	ts (s)	0.173	0.157	0.109	0.077	0.095	0.078	0.114	0.074	0.078
	Mp (%)	14.18	10.26	0.00	10.87	0.00	11.18	0.00	1.20	10.71
	e_{ss} (deg)	-0.005	-0.006	-0.009	-0.006	-0.009	-0.005	-0.009	-0.007	-0.005
	$\delta_{\alpha\theta}$ (deg)	0.006	0.012	0.007	0.007	0.007	0.006	0.005	0.008	0.006
	cr_1 (A)	0.05	0.10	1.44	0.08	1.33	0.08	1.53	0.83	0.09
	cr_2 (A)	0.67	0.67	1.33	0.67	1.34	0.67	1.49	1.02	0.67
	cr_3 (A)	0.000	0.015	0.984	0.046	0.829	0.044	0.950	0.505	0.051
	cr_4 (A)	0.148	0.146	0.152	0.145	0.173	0.143	0.154	0.162	0.132
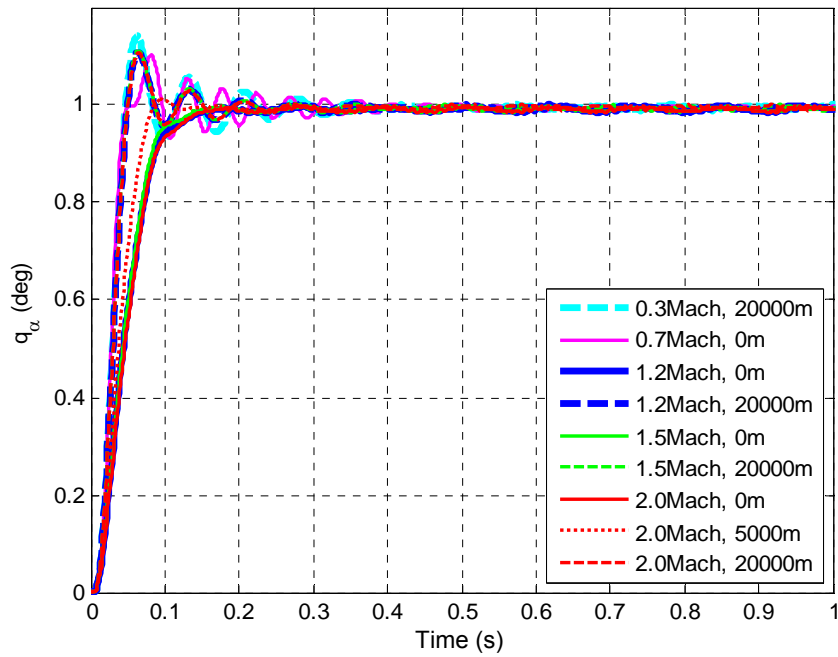
(a) first 1 second
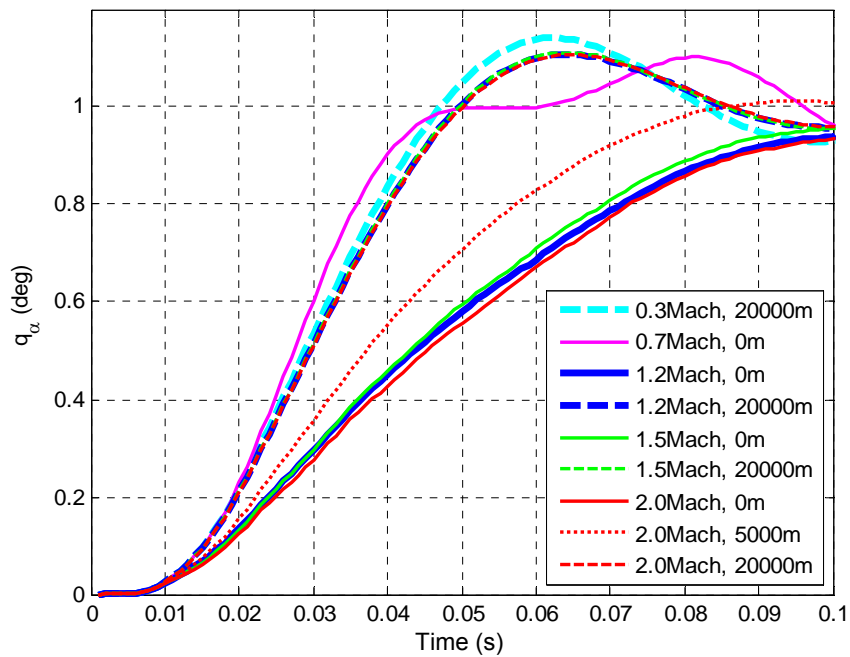
(b) first 0.1 second

Figure 155. Step response of the aeroservoelastic system at varios match points

For the ASE system with g controller, the backlash analyses are performed both in frequency and time domain. The analyses are performed at the similar points used in Section 6.4.1. The results are depicted in Table 81 and Figure 156.

Table 81. LCO analyses results of the aeroservoelastic system

Mach	Altitude	bv	Frequency domain solutions			Time domain solutions					
			$k_{\alpha\theta}$	$\delta_{\alpha\theta}$		$\delta_{\alpha\theta}$		q_α		q_h	
	m	deg	N.m/rad	deg	Hz	deg	Hz	deg	Hz	mm	Hz
0.3	10,000	0.2	3,096.7	0.441	13.0	0.507	10.3	1.56	10.3	0.372	10.3
0.5	10,000	0.2	2,384.6	0.366	13.1	0.483	9.26	2.54	9.26	0.601	9.26
0.7	10,000	0.2	2,111.8	0.343	14.4	0.399	12.7	1.01	12.7	0.798	12.7
1.2	0	0.2	6,477.9	3.41	8.68	3.16	8.66	1.96	8.66	15.6	8.66
1.2	5,000	0.2	6,403.6	2.99	8.72	2.71	8.70	3.22	8.70	13.5	8.70
1.2	10,000	0.2	6,112.9	2.01	8.75	1.77	8.73	4.67	8.73	8.82	8.73
1.2	20,000	0.2	3,284.9	0.465	8.88	0.587	8.83	7.85	8.83	1.52	8.83
1.5	10,000	0.2	6,137.6	2.06	8.76	1.85	8.73	4.97	8.73	9.31	8.73
2.0	10,000	0.2	6,231.4	2.32	8.76	2.09	8.78	4.93	8.78	10.6	8.78

Similar to the Section 6.4.1, it is seen that the frequency domain solutions can be used to predicts the LCO in magnitude of order with a fast computation.

Although it is not evident as in the LCO analyses results of q controller, a grouping can be conducted according to LCO frequency. In supersonic region the LCO frequencies are all around 8.7 Hz, but in subsonic range the LCO frequencies are different than 8.7 Hz although close to it. It can be seen from Figure 156 (a) that the LCO amplitudes at subsonic flow are much less than that of supersonic flow. It can be also seen that the LCO amplitudes increase with increasing Mach numbers in supersonic region. In Figure 156 (b), the variations of the LCO amplitudes with respect to altitude are given. It is seen that with the increasing altitude; $\delta_{\alpha\theta}$ decreases but the q_α increases.
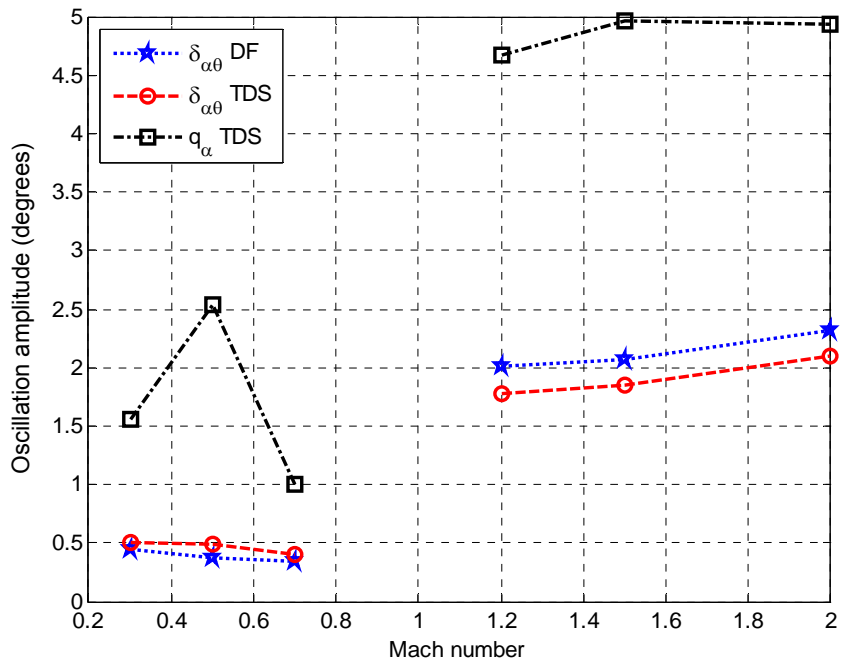
(a) with respect Mach number at 10,000 m
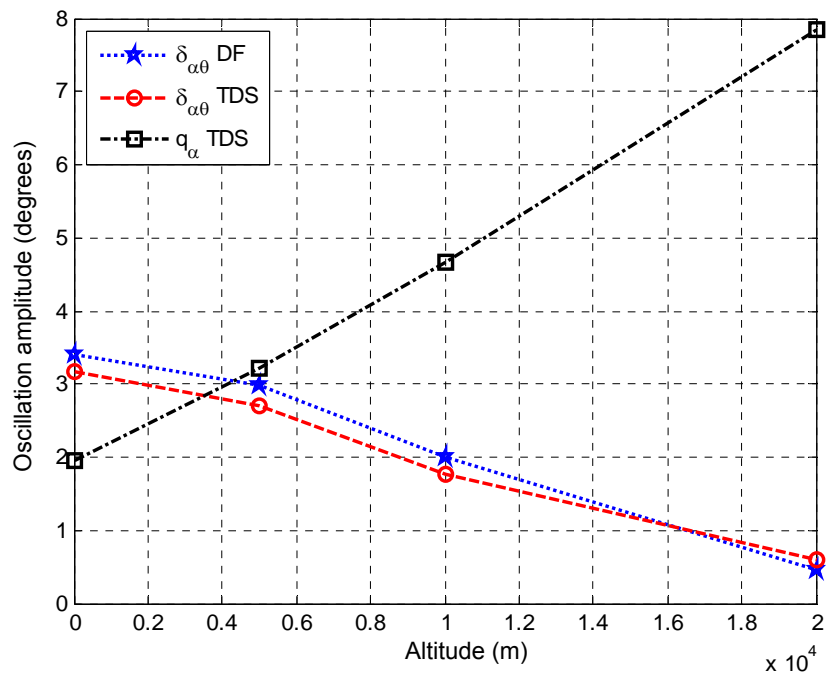
(b) with respect to altitude at 1.2 Mach

Figure 156. LCO amplitudes of the aeroservoelastic system

Similar to the q controller, the g controller is not satisfactory at the suppression of the amplitude of the LCO down to comparable limits to the backlash value as in the case studies performed in subsonic compressible and subsonic incompressible flows. Examining the Bode plot of the controller and the frequency domain analyses of the ASE system performed at the nominal dynamic pressure same problems obtained in q controller are identified.

6.4.3. Comparison of Controllers

Similar to the subsonic compressible flow, two case studies are conducted for the supersonic compressible flow. In the case studies H_∞ type controllers are synthesized by using q and g flutter suppression methods. The results are classified under three categories; linear stability, linear performance, and backlash analyses.
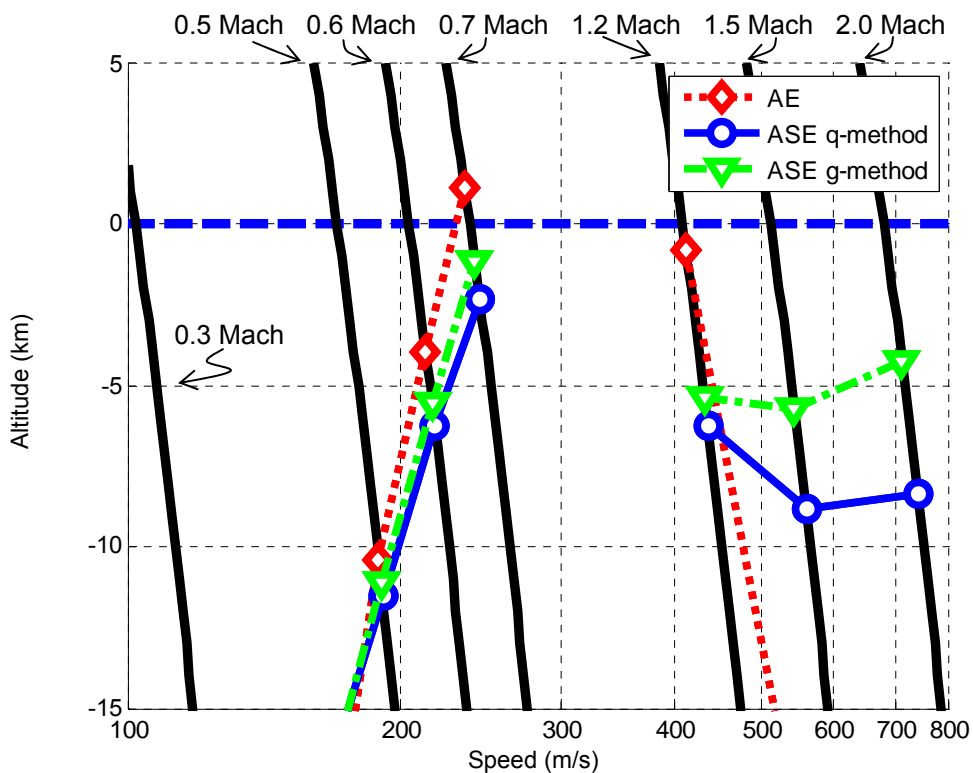
Figure 157. Flutter flight envelope

The linear stability results of the aeroservoelastic system with the two controllers and the stability limits of the aeroelastic system are given in Figure 157. As it can be seen from this figure, both controllers enlarge the flutter flight envelope below sea level in the analyzed Mach numbers. However, among the two controllers the q controller enlarges the envelope better than the g controller for the Model 3.

The performance results of the controllers are given in Table 75 and Table 80. Comparing the two controllers in terms of the bandwidth property, it can be seen from these tables that the q controller has better bandwidth and furthermore its bandwidth is less affected from the flow variation. Considering the rise time, q controller is slightly better in most of the cases, except the 0 m altitude in 1.2, 1.5, and 2.0 Mach numbers. In these specific points, which can be generalized as low altitude high Mach numbers, the q controller becomes overdamped. At these points the rise time increases from 50 ms, the maximum rise time value of the q controller at the other points, to 700 ms. However, although the g controller has slightly worse rise time in most of the cases, its rise time value varies between 29 ms to 101 ms. The g controller also has smaller settling time, overshoot values, and steady state error nearly in all cases. On the other hand, the q controller has smaller oscillations nearly in all cases and consumes less current in all cases.
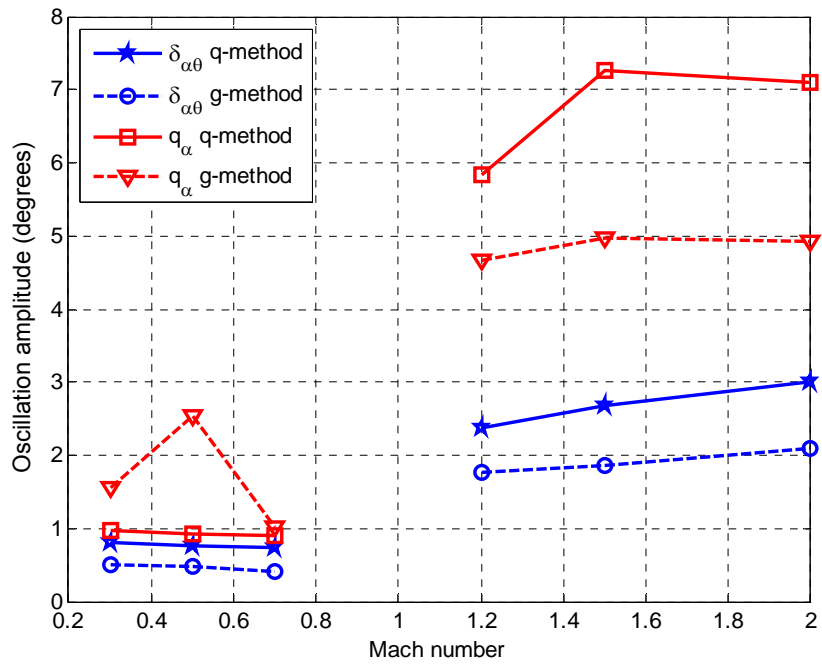
(a) with respect to Mach number at 10,000 m
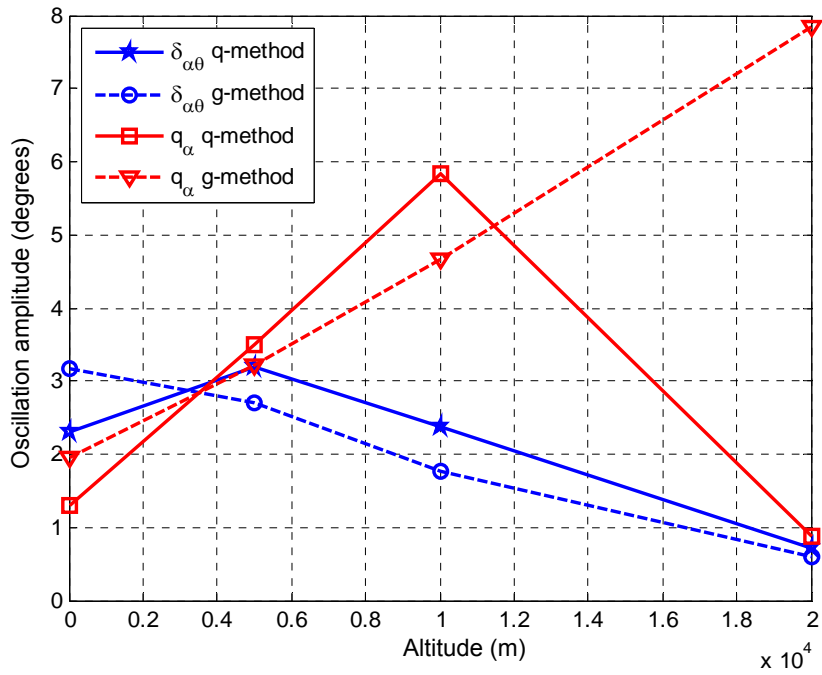
(b) with respect to altitude at 1.2 Mach

Figure 158. LCO amplitudes of the aeroservoelastic system

The detailed discussions on each case study are conducted in the corresponding sections. Focusing on the comparison of the two controllers, it can be stated that the LCO amplitudes of the g controller is less than that of q controller in most of the cases. Moreover, the frequency of the LCO's of ASE system with q controller in subsonic flow are around 33 Hz, where at the same flow conditions the ASE system with g controller has LCO with 9 to 12 Hz frequency. Note that the amplitudes of the LCO's of $\delta_{\alpha\theta}$ of the two controllers are comparable in these conditions. Under these circumstances, it can be also stated that the g controller has an advantage considering the fatigue life.

6.5. Postscript on Chapter 6

In this Chapter, several case studies are presented covering the application of methods either developed or referred to up to Chapter 5. These case studies are grouped in three sections according to the flow regime as subsonic incompressible, subsonic compressible, and supersonic.

In the subsonic incompressible flow regime, nine implementations are compared considering the flutter suppression methods and controller types. A mathematical aeroelastic model is constructed and nine different controllers are synthesized for it. The synthesized controllers are compared considering the stability limits, performances, and effect of backlash. It is seen that considering the stability analysis and the effect of backlash, the g and the gq controllers are better than the q controllers, but the q controllers can still satisfy the stability of the ASE system in the incompressible flow limits above the sea level. The performances of the synthesized controllers are comparable, each have advantages for different performance criteria. Considering the controller types, it is seen that in general the μ controllers have better stability margins and LCO

amplitudes than the other controllers. However, μ controllers consume incomparably large amount of current. Whereas, the H_∞ controllers generally yield the second best solutions considering the stability limits, performance, and the LCO amplitudes with an acceptable amount of current consumption. The H_2 controller only stands out with its low current consumption.

In compressible subsonic flow, a suitable mathematical aeroelastic model is created by modifying the aeroelastic model of incompressible flow. In this flow regime, only H_∞ type controllers are synthesized by means of q and g flutter suppression methods. Similar to the incompressible case, analyses are performed under three groups, namely the stability limits, performance, and the backlash effect. It is seen that, the q controller appears to be the best in all cases for this aeroelastic model.

The mathematical aeroelastic model of supersonic flow is constructed by modifying the aeroelastic model of subsonic compressible flow. Similar to the subsonic compressible flow, H_∞ type controllers are synthesized by means of q and g flutter suppression methods, and analyses are performed under three groups. It is seen that the q controller enlarges the stability limit of the ASE system better than the g controller. However it is seen that the g controller also satisfies the stability at the searched Mach numbers above sea level. On the other hand, in general the g controller yields a smaller amplitude LCO and better performance. Considering the performance criteria, the q controller is better than the g controller only at current consumption.

Since no solid performance requirements are stated for the aeroservoelastic models, a unique selection of the controller cannot be performed. However, it is seen that both controllers have some advantages and disadvantages. Moreover, it is seen that these

advantages may vary according to the properties of the aeroelastic model or flow regime. Nonetheless, it is seen that the proposed q-method is a successful flutter suppression method and its overall performance is comparable to the g-method.

CHAPTER 7

DISCUSSION AND CONCLUSION

7.1. Summary

In this study, different approaches for the controller synthesis and analysis of aeroelastic control surfaces of missiles are implemented. The missile control surface is considered as a fin type, fully movable aerodynamic surface that has no adjacent lifting surfaces, which is usually the case. The fin is also used on some aircraft as a horizontal stabilizer or canard, which enlarges the application area of this study. Mathematical models of the aeroelastic system are derived with the typical section wing and the thin airfoil theories for the structural and aerodynamic parts of the problem, respectively. The aeroelastic model is derived for various flow conditions, which provides a large domain to verify the control synthesis and analysis approaches. In the derivation of the aeroelastic matrices for the unsteady flow regions, Theodorsen's function and indicial functions are used. In the literature, derivation of Theodorsen's function for the state space equation of aeroelastic systems already exists in the works of Chang [52] and Lind [38]. However, their method was restricted to the selection of different number of lag terms for different indicial functions. A proper format for the selection of different number of lag terms was provided by Edwards [57], but the equations given were only for incompressible flow and their derivations were not provided either. From

the aerodynamic point of view, the following contribution is made in this study:

- The step by step derivations of state space equations of indicial functions are accomplished by using Roger's rational function approximation method for the aeroelastic fin model.

Various flutter search methods are briefly examined. Among them the μ-method is selected as the main search method. This method has a robust flutter search capability in addition to the nominal flutter search. The equations of the aeroelastic fin model are modified for the μ-method as required. In order to crosscheck the results, the p-method is selected as the secondary method. Some additional algorithms are given in order to implement the μ flutter analysis method to the compressible flow. Thus, the μ-method can be used to assess the instability match points of the aeroelastic and aeroservoelastic systems.

The mathematical model of the aeroservoelastic system is derived. In order to perform flutter analysis via μ-method, the required modification process for the mathematical model of the aeroservoelastic system is accomplished. Two different controller synthesis procedures are provided. The following contributions are made regarding aeroservoelasticity:

- The q-method is established for the synthesis of a controller for a CAS, considering some performance specifications and also taking flutter suppression into account.
- A flutter suppression method available in the literature (g-method) for airplane wings is adapted and implemented to fins (missile control surfaces).

In order to analyze the effect of backlash on the aeroservoelastic system, the backlash is modeled in the time domain. A Simulink® model of the aeroservoelastic system including the backlash model is constructed for time domain analysis. In the frequency domain, the backlash is modeled by means of sinusoidal input describing functions. The solution method used in the search for limit cycle oscillations is given.

Several implementations of the given procedures are performed on a set of case studies. For this purpose three distinct aeroelastic models are constructed, each encountering flutter in different flow regimes; namely, incompressible subsonic, compressible subsonic, and compressible supersonic. The incompressible subsonic model is constructed in accordance with the ATD, a wind tunnel test setup developed for aeroservoelastic studies, with slight modifications. The analyses of the aeroelastic systems are performed. Three different flutter suppression methods are used, q, g, and gq, which is a mixture of the q and g methods. Using each of the three different controller synthesis procedures of flutter suppression, namely q, g, and gq-methods, three different types of controllers, H_2, H_∞, and μ, are synthesized. The flutter margins, performances, and LCO's of the aeroservoelastic systems with these controllers are analyzed. Comparisons of the results are presented. In order to analyze the performance of the q and g flutter suppression methods, the case studies are extended to the compressible subsonic and compressible supersonic flow regions. In these flow regimes, H_∞ type controllers are synthesized by means of q and g flutter suppression methods. Similar to the incompressible subsonic flow regime, stability limits, performances, and LCO's of the ASE systems are analyzed in order to compare the synthesized controllers. The following contributions are made in the case studies section:

- Development of a controller synthesis procedure that directly uses the disturbance to dynamic pressure for flutter suppression,
- Synthesis and comparison of H_2, H_∞, and μ controllers for control actuation systems with fully movable control surfaces by using the developed controller design procedure,
- Limit cycle analysis of the q-method and g-method controllers for the fin with backlash type of nonlinearity.

In addition to the contributions listed above, the following studies are performed in this thesis:
- Implementation of a flutter suppression method used in the controller synthesis originally presented by Vipperman et al. [26] for airplane wings, to a control actuation system with fully movable control surfaces.
- Comparison of the two different flutter suppression methods.
- Comparison of H_2 and robust controllers in terms of flutter suppression performance on the aeroservoelastic system with fin.
- Implementation of the method suggested by Lind [38], which is a robust controller synthesis approach that considers system nonlinearities, to the fin with backlash type nonlinearity.
- Implementation of the aeroelastic and aeroservoelastic analyses by using p and μ-methods.
- Performance analyses of the aeroservoelastic systems.
- Analyses of the effect of the backlash type of nonlinearity on the aeroelastic systems.
- Analyses of the effect of the backlash type of nonlinearity on the performance of the aeroservoelastic system with the controller mentioned above.

7.2. Discussion and Conclusions

The typical section wing that is used in the structural modeling part of aeroelastic system is a simple but a valid model. It was used by many aeroelastic pioneers. But it has restrictions, such that the lifting surfaces should have a large aspect ratio, small sweep, and smoothly varying cross sectional characteristics across span. More complicated wings can be structurally modeled with different methods such as finite element method (by finite number of normal coordinates), Rayleigh–Ritz method (finite number of assumed mode shapes), or lumped mass (rigid segments) method. For the aerodynamics, it is also possible to use nonlinear aerodynamics obtained through CFD analysis. In practice, CFD was used in two ways; either a direct time domain flutter search can be performed or the generalized aerodynamic force matrix can be derived. Both usages, primarily the first one, are time consuming methods. These methods can be advantageous when analyzing a finished product. However, their utilization in synthesis steps of the aeroelastic system will not be effective. In this study, the lift and moment equations calculated with potential flow theory are used. This theory was widely used in flutter analysis, such that the commercial programs such as NASTRAN FLDS, UAI/ASTROS use simplified potential flow theories for unsteady aerodynamics in aeroelastic analysis. The main purpose of this study is to establish a method for the synthesis of a controller for a CAS, considering some performance specifications and also taking flutter suppression into account. Hence, using the lift and moment equations obtained by potential flow theory and the typical section wing model is considered to be adequate for this study.

Among the flutter search methods, μ-method is selected as the primary flutter search method in this study. This method is one of the recently developed methods; furthermore it can be extended to robust flutter search. In this study, both μ and p-methods are used for the

computation of instabilities. It is seen that the results of the both methods are in agreement. Among these methods, the p-method performs a brute force approach, but provides larger information. In the p-method, the frequencies and the damping values of all modes of the system, and their variations with the dynamic pressure are derived. This information can be used to trace the effect of controller tuning. However, the accuracy of the p-method is limited by the minimum interval between the search points. Hence, increasing the accuracy results in an increased computation time. The p-method also requires some post-processing work to derive the solution from the results. It is better to use the p-method, in order to get an idea about the system rather than specifically obtaining the instability point. On the other hand, the μ-method directly calculates the dynamic pressure of instability and the frequency and damping value of the corresponding mode of the system, but does not provide any additional information about the system. Nevertheless, the μ-method is a much faster and accurate calculation method. Furthermore, the μ-method is appropriate for the instability match point calculations, which is an indispensable compressible flow analyses. In this study, the μ-method is adapted to the instability match point search by using a bisection search algorithm.

As already mentioned, flutter is an instability that occurs due to the interaction of inertial, elastic and aerodynamic forces. Assuming that the inertial and the elastic properties of the structure are unchanged, the aerodynamics is left as the only varying parameter. This is the main assumption in the μ flutter search method. In this study, it is aimed to convert this search algorithm to a controller synthesis method. In the literature, the direct use of the μ-method for synthesis purposes does not exist. With this method, it is possible to directly set the stability margin that is required from the aeroservoelastic system. For the purpose of comparison, an alternative flutter suppression method available in the

literature is used. The alternative method is adapted from the study of Vipperman et al. [26], in which an airplane wing was used and a parametric uncertainty was added to the first mode of the system to account for the variation of the real part of a complex-conjugate pole pair. In this study, the method presented by Vipperman is applied to the fin (missile control surface), and the parametric uncertainty is added to the damping parameter of the pitch degree of freedom of the fin.

Three different types of controllers are synthesized, namely H_2, H_∞, and μ, in MATLAB® by using the flutter suppression methods. In the synthesis of H_∞ controllers it is seen that the selection of upper and lower values of the γ limits, which is the search limit parameters of the MATLAB®'s *hinfsyn* command, affects the optimization algorithm used for the synthesis. The synthesis algorithm can sometimes converges to local minima. It is specifically advised to vary the limits of γ and re-run the synthesis algorithm if the γ norm of the system is slightly above one.

Through the case studies it is seen that:

- The established q-method successfully suppresses the onset of flutter. Furthermore, a satisfactory performance is obtained from the aeroservoelastic system by using the q-method controller. It is seen that the tough part of this method is to determine the values of the additional states due to perturbation to dynamic pressure $\{z\}_{\bar{q}}$ and the values of perturbation to dynamic pressure $\{w\}_{\bar{q}}$. These are the input and output vectors of the aeroservoelastic plant to the dynamic pressure uncertainty port. After these parameters and the rest of the uncertainty and performance parameters are set, two free parameters remain for the tuning of the synthesized controller. These two parameters are the dynamic pressure $\bar{q}_{cont}$ at which the

controller is synthesized and the disturbance to dynamic pressure $\bar{q}_{dist}$. It is seen that, these parameters affect the stability and performance of the system. The increase of $\bar{q}_{cont}$ increases the upper limit of the flutter flight envelope, however it reduces the lower limit. Hence, a tuning is required for the selection of $\bar{q}_{cont}$. The second tuning parameter is the dynamic pressure of disturbance, which is used as the primary object for the flutter suppression. During the case studies it is seen that, increasing $\bar{q}_{dist}$ increases the stability margin from both upper and lower limits as expected. However, after a limit value of $\bar{q}_{dist}$, the γ norm of the controller exceeds one, thus a proper controller cannot be obtained. In H∞ type controller synthesis it is seen that the upper limit of $\bar{q}_{dist}$ is well below the obtained nominal stability margin of the ASE system, which is due to the conservative property of the H∞ controller.

- The g-method is successfully implemented to the fin, and effective flutter suppression controllers are synthesized. The key point of this method is the derivation of the values of perturbation to damping $\{w\}_c$ and the values of additional states due to perturbation to damping $\{z\}_c$, which corresponds to the velocity states of the pitch degree of freedom. After the uncertainty and the performance parameters of the system are set, the performance of the controller is tuned by means of the damping uncertainty, which is a parameter of $\{w\}_c$.

- The method suggested by Lind [38] is implemented to a fin in order to improve the LCO suppression property of the controller. Lind suggested using the uncertainties in robust controller synthesis in order to deal with the nonlinearities. This implementation is

performed on the g-method. Considering the sinusoidal input describing function for backlash it can be assumed that the effective stiffness value in a backlash varies from zero to a linear stiffness value. This corresponds to an additive stiffness uncertainty with a magnitude equal to the linear stiffness value. However, an uncertainty equal to 100% of linear stiffness value overwhelms the system and the γ norm of the synthesized controller exceeds one. This means the resultant controller do not guarantee robust stability and performance. Hence, in order to decrease the γ value below one, the stiffness uncertainty is decreased. Solutions are obtained for the uncertainties that are equal to the 5%-20% of the linear stiffness value. From these analyses it is seen that the inclusion of the stiffness uncertainty, and the increase of the stiffness uncertainty percentage, increases the amplitude of the LCO. Furthermore, a considerable enhancement can be seen neither in bandwidth nor in the performance of the system. Hence, it is seen that the suggested method did not improve the LCO suppression property of the synthesized g controller for this specific ASE system.

- Thirteen distinct case studies are performed considering the flutter suppression methods, controller types and flow regimes. It is seen that the established q-method and the other methods, g and gq, have comparable success, and their relative merits vary according to aerodynamic systems. All of the flutter suppression methods successfully enlarge the stability envelope of the ASE system. They perform comparably in the step response analyses and in terms of bandwidth in frequency response. Among the q and g-methods; the q-method is better in subsonic compressible flow, the g-method is better in supersonic flow, and in incompressible subsonic flow one or the other performs better depending on the various criteria

considered. Similar to the step response performance comparison, the flutter suppression methods' performances in LCO suppression are also comparable. In each flow region a distinct aeroelastic model is used, which is one of the driving effect in their performance variation at different flow regions. Through this study it is seen that the established q-method is a successful flutter suppression method and its overall performance is comparable to the g-method.

- Through the case studies, the successes of the different types of controllers are also compared. It is seen that the H_2 controller is the least current consuming controller. However, its flutter suppression capability, step response, and LCO suppression performance are the worst. The μ controller is the best controller considering the flutter suppression, step response, and LCO suppression; but it has an incomparably large current consumption. Moreover, the order of the synthesized μ controllers are nearly one and a half times that of the H_2 controllers. On the other hand, it is observed that the H_∞ controllers yield comparable results with μ controllers considering the flutter suppression, step response, and LCO suppression in general. The current consumption of H_∞ controllers is at a comparable level to H_2 controllers, but not as good as H_2 controllers. Moreover, the order of the H_∞ controller is only one or two states greater than the H_2 controller.

- During the nonlinear analysis performed in incompressible subsonic flow it is seen that; no LCO is obtained in the analyzed aeroelastic system below a certain dynamic pressure value. With the increase of dynamic pressure the aeroelastic system becomes a system with two stability conditions. One solution is the steady solution at zero degree and the other is an LCO. Further increasing the dynamic

pressure the steady solution vanishes and then flutter occurs for the aeroelastic system. In contrast to the aeroelastic system, for the aeroservoelastic system an LCO is obtained in all of the searched dynamic pressures, up to the dynamic pressure of flutter. However, the motion in pitch degree of freedom of the fin is much less in the aeroservoelastic system than in the aeroelastic system.

- The nonlinear analyses are also performed in the frequency domain by means of quasi-linearization. The backlash is modeled via its sinusoidal input describing function. It is seen that nearly in all cases the frequency domain analyses only predict the LCO with one order of magnitude accuracy. However, the frequency domain solutions give a fast solution, and the behavior of the LCO, its amplitude and frequency, with varying conditions can be predicted.

- In the case studies in the supersonic region, LCO analyses are performed in incompressible subsonic, compressible subsonic, and supersonic regions, for the same model. It is seen that the LCO amplitudes dramatically increases in the supersonic region for the model analyzed. The amplitude of the oscillations continues to increase with increasing Mach number in the supersonic region. It is also seen in the case studies of subsonic flow regions that there is nearly a linear relation between the amplitude of the LCO and the backlash value. Thus, the importance of backlash value increases in the supersonic region for this ASE model.

During the very last period of the thesis study, an opportunity is available for an experimental flutter suppression demonstration. An Aeroservoelastic Test Setup is developed in TÜBİTAK-SAGE in the scope of a M.Sc. thesis conducted by Utku ÜNAL in the Mechanical Engineering Department of METU [17]. This model is tested in the Ankara Wind

Tunnel. From the tests it is seen that, ATD encounters first LCO at 48 m/s airspeed and then flutter at 60.5 m/s airspeed. After these tests, a small demonstration is performed for flutter suppression. For this purpose an H∞ controller is synthesized using the proposed controller synthesis method, the q-method. However, the synthesis is performed with the limited knowledge about the ATD. The detailed system identification was not performed before demonstration. Furthermore, during the aeroelastic tests it was seen that the ATD has more friction and damping than the originally expected values. However, the synthesis is performed according to design specifications of the ATD. In the demonstrations, the synthesized controller successfully suppressed the system up to 70 m/s, which is the practical speed limit of the wind tunnel.

In most of the studies in the literature, the synthesized controllers are analyzed considering the stability limits, performances, or LCO. In this study, a complete analysis, considering the stability limits, performance and LCO, is performed for the aeroservoelastic systems with the synthesized controllers. This brings a special value to this study.

7.3. Recommendations for Future Work

In this study, methods for synthesis of flutter suppression controllers and their analysis are developed or applied. The ATD which was constructed in the scope of a master thesis was available during the very last period of the PhD schedule. But due to the schedule of the ART, only a demonstrative experiment could be performed. Hence, some systematic tests of the given flutter suppression algorithms are recommended as the primary future work.

Secondly, adaptation of the present controller synthesis algorithms for flutter suppression to a finite element aeroelastic model is

recommended. This will enlarge the practical implementation domain of the given algorithms.

In this study, the aerodynamic indicial functions are modeled via rational function approximations and third order functions are used for the indicial functions. In finite element aeroelastic models in the literature similar rational function approximations were also used. The orders of these functions are restricted in order to minimize the order of the synthesized controller. Thus, a necessary future work would involve analyzing the effect of the aerodynamic modeling errors on the performance of the controller synthesized by using the established flutter suppression method.

From the controller synthesis point of view, controller syntheses with H_∞ method with gain scheduling and mixed H_2/H_∞ methods are recommended. H_∞ method with gain scheduling will divide the domain in which the dynamic pressure changes. Thus the conservatism of the H_∞ method will be decreased and better performances can be obtained. On the other hand the mixed H_2/H_∞ methods may overcome the conservatism of the H_∞ method by defining less restrictive noise and performance constraints via the advantage of the H_2 controller.

REFERENCES

[1]   Fung, Y. C., "An Introduction to the Theory Aeroelasticity", Dover, 1969.

[2]   Bisplinghoff, R. L., Ashley, H., Halfman, R. L., "Aeroelasticity", Dover, 1996.

[3]   Bisplinghoff, R. L., Ashley, H., "Principles of Aeroelasticity", Dover, 1962.

[4]   Garric, I. E., "Perspectives in Aeroelasticity", Israel Journal of Technology, Vol. 10, No. 1-2, 1972, pp 1-22.

[5]   Garric, I. E., "Aeroelasticity – Frontiers and Beyond", Journal of Aircraft, Vol. 9, No. 9, 1976, pp 641-657.

[6]   Garric, I. E., Reed W. H., "Historical Development of Aircraft Flutter", Journal of Aircraft, Vol. 18, No. 11, 1981, pp 897-912.

[7]   Felt, L. R., Huttsell, L. J., Noll, T. E., Cooley, D. E., "Aeroservoelastic Encounters", Journal of Aircraft, Vol. 16, No. 7, 1979, pp 471-483.

[8]   Tanrıkulu, Ö., "Aeroelastodynamic Stability Analysis of Rocket Control Surfaces at Low Subsonic Speeds", Internal Report GU 92/02, TÜBİTAK-SAGE, 1992.

[9]   Tanrıkulu, Ö., "Structural Dynamics of Guided Missiles", Internal Report GU 92/03, TÜBİTAK-SAGE, 1992.

[10]   Kuran, B., "Aeroelastic Analysis of Tail Fins", Internal Report 22119 DB 94/1, TÜBİTAK-SAGE, 1994.

[11]   Kuran, B., Önen, C., Özgüven, H. N., "Effects of Aeroelasticity on the Stability of Unguided Missiles" CEAS International Forum on Aeroelasticity and Structural Dynamics, Rome, Italy, 1997.

[12]   Durak, B., "Basık Dairesel Silindirik Kabukların Aeroelastik Analizi", M.Sc. Thesis, ITU, Aeronautical Engineering Department, February, 1998.

[13]   Yıldız, E. N., "Aeroelastic Analysis of Nonlinear Control Surfaces", M.Sc. Thesis, METU, Mechanical Engineering Department, December, 2000.

[14]   Sever, İ. A., "Nonlinear Body Bending Aeroelasticity of Kinetic Energy Projectiles", M.Sc. Thesis, METU, Mechanical Engineering Department, December, 1999.

[15]   Pehlivanoğlu, G., "Effects of Transverse Flexibility on Unguided and Guided Missiles", M.Sc. Thesis, METU, Aeronautical Engineering Department, September 1999.

[16]   Akmeşe, A., Cömert, M. D., Platin, B. E., "Aeroservoelastic Analysis of Missile Control Surfaces Via Robust Control Methods," Proceedings of 16th IFAC Symposium on Automatic Control in Aerospace, Edited by Alexander Nebylov, Vol. 2, St.Petersburg, Russia, 2004, pp 159-163.

[17] Ünal, U., "Design, Construction, and Performance Testing of an Aeroservoelastic Test Apparatus to be Used in AWT (Ankara Wind Tunnel)", M.Sc. Thesis, METU, Mechanical Engineering Department, December, 2005.

[18] Tanrıkulu, Ö., "Aeroservoelastomechanics of Typical Section", Internal Report 22126 SI 94/9, TÜBİTAK-SAGE, 1994.

[19] Horikawa, H., Dowell, E. H., "An Elementary Explanation of the Flutter Mechanism with Active Feedback Controls", Journal of Aircraft, Vol. 16, No. 4, 1979, pp 225-231.

[20] Roger, K. L., Hodges, G. E., Felt, L., "Active Flutter Suppression – a Flight Test Demonstration", Journal of Aircraft, Vol. 12, No. 6, 1975, pp 551-556.

[21] Poyneer, R. E., "Design and Evaluation of a Multi-Surface Control System for the CCV B-52", Journal of Aircraft, Vol. 12, No. 3, 1975, pp 135-138.

[22] Edwards, J. W., Breakwell, J. V., Bryson, A. E., "Active Flutter Control Using Generalized Unsteady Aerodynamic Theory", Journal of Guidance and Control, Vol. 1, No. 1, 1978, pp 32-40.

[23] Mahesh, J. K., Stone, C. R., Garrad, W. L., Dunn, H. J., "Control Law Synthesis for Flutter Suppression Using Linear Quadratic Gaussian Theory", Journal of Guidance and Control, Vol. 4, No. 4, 1981, pp 415-422.

[24] Ohta, H., Fujimori, A., Nikiforuk, P. N., Gupta, M. M., "Active Flutter Suppression for Two-Dimensional Airfoils", Journal of Guidance, Vol. 12, No. 2, 1989, pp 188-194.

[25] Block, J. J., Strganac, T. W., "Applied Active Control for a Nonlinear Aeroelastic Structure", Journal of Guidance, Control, and Dynamics, Vol. 21, No. 6, 1998, pp 838-845.

[26] Vipperman, J. S., Barker, J. M., Clark, R. L., Balas, G. J., "Comparison of μ- and H2 Synthesis Controllers on an Experimental Typical Section", Journal of Guidance, Control, and Dynamics, Vol. 22, No. 2, 1999, pp 278-285.

[27] Waszak, M. R., "Robust Multivariable Flutter Suppression for the Benchmark Active Control Technology (BACT) Wind Tunnel Model", 11th Symposium on Structural Dynamics and Control, Blacksburg, Virginia, USA, May, 1997.

[28] Gade, P. V. N., "Performance Enhancement and Stability Robustness of Wing/Store Flutter Suppression System", Ph.D. Dissertation, Virginia Polytechnic Institute and State University, Department of Engineering Science and Mechanics, February, 1998.

[29] Kim, S. H., Lee, I., "Aeroelastic Analysis of a Flexible Airfoil with a Freeplay Non-linearity", Journal of Sound and vibration, Vol. 193, No. 4, 1996, pp 832-846.

[30] Yehezkely, E., Karpel, M., "Nonlinear Flutter Analysis of Missile with Pneumatic Fin Actuators", Journal of Guidance and Control, Vol. 19, No. 3, 1996, pp 644-670.

[31] Laurenson, R. M., Trn, R. M., "Flutter Analysis of Missile Control Surfaces Containing Structural Nonlinearities", AIAA Journal, Vol. 18, No. 10, 1980, pp 1245-1251.

[32] Ko, J., Strganac, T. W., Kurdila, A. J., "Stability and Control of a Structurally Nonlinear Aeroelastic System", Journal of Guidance, Control, and Dynamics, Vol. 21, No. 5, 1998, pp 718-725.

[33] Tang, D., Dowell, E. H., Virgin, L. N., "Limit Cycle Behavior of an Airfoil with a Control Surface", Journal of Fluid and Structures, Vol. 12, 1998, pp 839-858.

[34] Tang, D., Conner, M. D., Dowell, E. H., "Reduced Order Aerodynamic Model and Its Application to a Nonlinear Aeroelastic System", Journal of Aircraft, Vol. 35, No. 2, 1998, pp 332-338.

[35] Lee, I., Kim, S. H., "Aeroelastic Analysis of a Flexible Control Surface with a Structural Nonlinearity", Journal of Aircraft, Vol. 32, No. 4, 1995, pp 868-874.

[36] Price, S. J., Lee, B. H. K., Alighanbari, H., "Postinstability behaviour of a Two-Dimensional Airfoil with a Structural Nonlinearity", Journal of Aircraft, Vol. 31, No. 6, 1994, pp 1395-1401.

[37] Brase, L. O., Eversman, W., "Application of Transient Aerodynamics to the Structurally Nonlinear Flutter Problem", Journal of Aircraft, Vol. 25,No. 11, 1988, pp 1060-1068.

[38] Lind, R., Brenner, M., "Robust Aeroservoelastic Stability Analysis", Springer-Verlag, 1999.

[39] Liebst, B. S., "Accelerometer Placement in Active Flutter Suppression Systems", Journal of Guidance, Vol. 10, No. 5, 1987, pp 441-446.

[40] Leishman, J. G., Nguyen, K. Q., "State-Space Representation of Unsteady Airfoil Behavior", AIAA Journal, Vol. 28, No. 5, 1990, pp 836-844.

[41] Conner, M. D., Virgin, L. N., Dowell, E. H., "Accurate Numerical Integration of State Space Models for Aeroelastic Systems with Free Play", AIAA Journal, Vol. 34, No. 10, 1996, pp 2202-2205.

[42] Özbay, H., Bachmann, G. R., "H2/H∞ Controller for a Two-Dimensional Thin Airfoil Flutter Suppression", Journal of Guidance, Control, and Dynamics, Vol. 17, No. 4, 1994, pp 722-728.

[43] Nissim, E., "Comparative Study Between Two Different Active Flutter Suppression Systems", Journal of Aircraft, Vol. 15, No. 12, 1978, pp 843-848.

[44] Hoadley, S. T., Karpel, M., "Application of Aeroservoelastic Modeling Using Minimum-State Unsteady Aerodynamic Approximations", Journal of Guidance, Vol. 14, No. 6, 1991, pp 1267-1276.

[45] Lind, R., Brenner, M. J., "Robust Flutter Margin Analysis That Incorporates Flight Data", NASA/TP-1998-206543, 1998.

[46] Lind, R., Brenner, M. J., "Robust Flutter Margin of an F/A-18 Aircraft From Aeroelastic Flight Data", Journal of Guidance, Control and Dynamics, Vol. 20, No. 3, 1997, pp 597-604.

[47] Lind, R., Brenner, M. J., "Incorporating Flight Data into a Robust Aeroelastic Model", Journal of Aircraft, Vol. 35, No. 3, 1998, pp 470-477.

[48] Newsom, J. R., "Designing Active Control Laws in a Computational Aeroelasticity Environment", PhD Dissertation, Virginia Polytechnic Institute and State University, April, 2002.

[49] Rodden, W. P., Johnson, E. H., "MSC/NASTRAN Aeroelastic Analysis", MSC User's Guide, V68, 1994.

351

[50] Anderson, J. D. Jr., "Fundamentals of Aerodynamics", Mc Graw Hill, 1991.

[51] Theodorsen, T., "General Theory of Aerodynamic Instability and the Mechanism of Flutter", NACA Report No. 496, 1935.

[52] Nam, C., Kim, Y., Aeroservoelastic Analysis of the Airfoil, http://ctas.east.asu.edu/chnam/ASE_Book/Chap3.pdf, 2001, (last visited on December 20, 2005).

[53] Mazelsky, B., "Determination of Indicial Lift and Moment of a Two-dimensional Pitching Airfoil at Subsonic Mach Numbers from Oscillatory Coefficients with Numerical Calculations for a Mach Number of 0.7", N.A.C.A. T.N. 2613, 1952.

[54] Mazelsky, B., Drischler, J. A., "Numerical Determination of Indicial Lift and Moment Functions for a Two-dimensional Sinking and Pitching Airfoil at Mach Numbers 0.5 and 0.6", N.A.C.A. T.N. 2739, 1952.

[55] Dowell, E. H., Crawley, E. F., Curtiss Jr, H. C., Peters, D. A., Scanlan, R. H., Sisto, F., "A Modern Course in Aeroelasticity", 3rd Ed., Kluwer, 1995.

[56] Rodden, W. P., Johnson, E. H., "Aeroelastic Analysis, User's Guide", MSC/NASTRAN, V68, 1994.

[57] Edwards, J. W., Ashley, H., Breakwell, J. V., "Unsteady Aerodynamic Modeling for Arbitrary Motions", AIAA Journal, Vol. 17, April, 1979.

[58] Civil Air Regulations Amendment 4b-16 [Reg. Docket No. 1797], "Airplane Airworthiness; Transport Categories Flutter, Deformation, and

Vibration Requirements", United States of America Federal Aviations Agency, Washington, D.C.

[59] Military Specification MIL-A-8870C(AS) "Airplane Strength and Rigidity Vibration, Flutter, and Divergence", Department of Defence of United States of America, May 1987.

[60] Military Specification MIL-M-8856B, "Missiles, Guided Structural Integrity General Specifications for", Department of Defence of United States of America, October 1990.

[61] "FLDS 120, MSC.Flightloads and MSC.Aeroelasticity Course Notes", December 2001.

[62] Balas, G. J., Doyle, J. C., Glover, K., Packard, A., Smith, R., "μ-Analysis and Synthesis Toolbox, For Use with MATLAB®, User's Guide", The MathWorks, Version 4, January 2001.

[63] Shampine, L. F., Reichelt, M. W., "The MATLAB ODE Suite", SIAM Journal on Scientific Computing, Vol. 18, No. 1, 1997, pp 1-22.

[64] Slotine, J. J. E., Li, W., "Applied Nonlinear Control", Prentice Hall, 1991.

[65] Ogata, K., "Modern Control Engineering", Prentice Hall, 1990.

[66] Gelb, A., Vander Velde, W. E., "Multiple-input Describing Functions and Nonlinear System Design", McGraw-Hill, 1968.

APPENDIX A

ROBUST CONTROLLER SYNTHESIS

In Figure A 1 the general frame work for robust controller synthesis and analysis are given. The interconnected systems can be rearranged to fit this general framework.
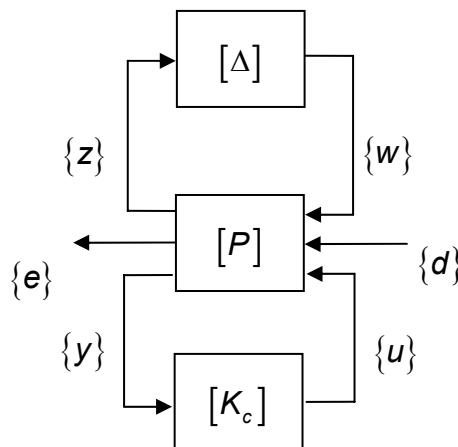
Figure A 1. General Framework

In Figure A 1; $\{d\}$ is the exogenous input vector containing the commands and the input noise, $\{e\}$ is the vector of outputs or errors, $\{z\}$ is the weighted perturbation output vector, $\{w\}$ denotes the perturbation input vector, $\{y\}$ is the measured output vector, and $\{u\}$ is the vector of controller inputs. The uncertainty may be modeled in two ways, either as

an external input or as a perturbation to the nominal model. The performance of the system is measured in terms of the behavior of the outputs or errors.

The assumptions that characterize the uncertainty, performance, and nominal models determine the analysis techniques that must be used. The models are assumed to be finite dimensional linear time invariant (FDLTI) systems. The uncertain inputs are assumed to be either filtered white noise, weighted power, or weighted $\mathcal{L}_p$ signal. The performance is measured as weighted output variances, or as power or as weighted output $\mathcal{L}_p$ norms. The perturbations are assumed to be themselves FDLTI systems that are norm bounded as input-output operators. Various combinations of these assumptions form the basis for all the standard linear system analysis tools.

Since the nominal model is an FDLTI system, the interconnection system has the following form

$$[P(p)] = \begin{bmatrix} [P_{11}(p)] & [P_{12}(p)] & [P_{13}(p)] \\ [P_{21}(p)] & [P_{22}(p)] & [P_{23}(p)] \\ [P_{31}(p)] & [P_{32}(p)] & [P_{33}(p)] \end{bmatrix} \tag{A.1}$$

The closed loop system from the exogenous inputs to the output can be written by using LFT on the perturbation and controller as

$$\begin{aligned} \{e\} &= F_u \left(F_l \left([P], [K_c] \right) \right), [\Delta] \right) \{d\} \\ &= F_l \left(F_u \left([P], [\Delta] \right), [K_c] \right) \{d\} \end{aligned} \tag{A.2}$$

For the analysis methods, the controller can be viewed just as another system component. Thus the controller can be included into the

interconnection structure by using LFT as given in Equation (A.3). The analysis framework is given in Figure A 2.

$$[N(p)] = F_l\left([P(p)],[K_c(p)]\right) = \begin{bmatrix} [N_{11}(p)] & [N_{12}(p)] \\ [N_{21}(p)] & [N_{22}(p)] \end{bmatrix} \tag{A.3}$$
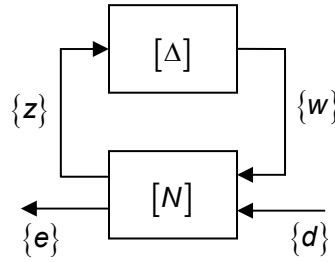
Figure A 2. Analysis Framework

The analysis can be performed by deriving a norm of the transfer matrix $[N]$ as given in Equation (A.4). Detailed explanation of μ analysis is given in Section 3.3.2.3.

$$\left\|[N]\right\|_i \ , \ (i : 2, \infty, \text{ or } \mu) \tag{A.4}$$

According to the problem type $[N]$ and the input and output ports can be selected as follows:

- nominal performance $\left([\Delta] = 0\right)$: $[N] = [N_{22}]$, $\{z\}$ and $\{w\}$ neglected,

- robust stability : $[N] = [N_{11}]$, $\{e\}$ and $\{d\}$ neglected,

- robust performance : $[N] = \begin{bmatrix} [N_{11}] & [N_{12}] \\ [N_{21}] & [N_{22}] \end{bmatrix}$.

For the synthesis methods, the general framework can be modified into the synthesis framework by using LFT, Figure A 3. The transfer matrix

from $\{d\}$ to $\{e\}$ is given in Equation (A.5). The H_2, H_∞, and μ controller synthesis problems are to find the controller that minimizes the corresponding norm of the transfer matrix from $\{d\}$ to $\{e\}$, as given in Equation (A.6).
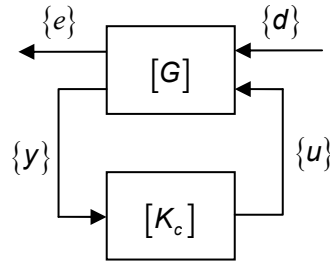
Figure A 3. Synthesis Framework

$$\{e\} = F_I\left([G],[K_c]\right)\{d\} = \left[[G_{11}] + [G_{12}][K_c]\left([I] - [G_{22}][K_c]\right)^{-1}[G_{21}]\right]\{d\} \quad \text{(A.5)}$$

$$\min_{[K_c]} \left\| F_I\left([G],[K_c]\right) \right\|_i , \; (i : 2, \infty, \text{ or } \mu) \quad \text{(A.6)}$$

where

$$[G] = \begin{bmatrix} [G_{11}] & [G_{12}] \\ [G_{21}] & [G_{22}] \end{bmatrix} \quad \text{(A.7)}$$

According to the problem type $[G]$ can be selected as follows

- nominal performance only $\left([\Delta] = 0\right)$: $\quad [G] = \begin{bmatrix} [P_{22}] & [P_{23}] \\ [P_{32}] & [P_{33}] \end{bmatrix}$,

- robust stability only : $\quad [G] = \begin{bmatrix} [P_{11}] & [P_{13}] \\ [P_{31}] & [P_{33}] \end{bmatrix}$,

357

- robust performance :

$$[G] = [P] = \begin{bmatrix} \begin{bmatrix} [P_{11}] & [P_{12}] \\ [P_{21}] & [P_{22}] \end{bmatrix} & \begin{bmatrix} [P_{13}] \\ [P_{23}] \end{bmatrix} \\ \begin{bmatrix} [P_{31}] & [P_{32}] \end{bmatrix} & [P_{33}] \end{bmatrix}.$$

APPENDIX B

STATE SPACE AEROELASTIC SYSTEM MATRICES FOR μ-METHOD ANALYSIS

B.1. Unsteady Subsonic Incompressible Flow

In unsteady subsonic incompressible flow, the parameterization over dynamic pressure can be performed similar to the steady subsonic incompressible case as given in Section 3.3.1. However, in the unsteady subsonic aerodynamic equation the acceleration term depends on the dynamic pressure as given in Equation (2.44). Thus, perturbation of the dynamic pressure effects the acceleration term and the output $\{z\}_{\bar{q}}$ of the state space aeroelastic system equation for the perturbation, depend on the acceleration states. Since the acceleration states are the outputs of the aeroelastic system equation, the acceleration states are replaced with its symbolic solution obtained from Equation (2.66). Thus the state space equation of the aeroelastic system, which is parameterized over the dynamic pressure in unsteady subsonic flow becomes as

$$\left\{ \frac{\{\dot{\xi}\}}{\{z\}_{\bar{q}}} \right\} = \left[\begin{array}{c:c} [A_{AE}] & [B] \\ \hdashline \left[[C_{11}] \quad [C_{12}] \quad [D_{Ac}] \right] & [D] \end{array} \right] \left\{ \frac{\{\xi\}}{\{w\}_{\bar{q}}} \right\} \tag{B.1}$$

where $[A_{AE}]$ is given in Equation (2.69), $\{\xi\}$ is given in Equation (2.67) and

$$[B] = \begin{bmatrix} [0_{2x2}] \\ ([M]-[A_1]\bar{q})^{-1} \\ [0_{2x2}] \end{bmatrix} \tag{B.2}$$

$$[C_{11}] = [A_1]([M]-[A_1]\bar{q})^{-1}([A_4]\bar{q}-[K]) + [A_4] \tag{B.3}$$

$$[C_{12}] = [A_1]([M]-[A_1]\bar{q})^{-1}(([A_2]+[A_3])\bar{q}-[C]) + ([A_2]+[A_3]) \tag{B.4}$$

$$[D] = \left[[A_1]([M]-[A_1]\bar{q})^{-1} \right] \tag{B.5}$$

B.2. Unsteady Compressible Flow

The parameterization over dynamic pressure for unsteady compressible flow is still more similar to the steady subsonic incompressible case, which is given in Section 3.3.1. In compressible flow, $\{z\}_{\bar{q}}$ depends on the aerodynamic states through not only the matrices $[A_1]$ and $[A_2]$, but also the through the aerodynamic coefficient matrices $[D_{Ac}]$, $[D_{Acq}]$, $[D_{AcM}]$, and $[D_{AcMq}]$ introduced in Section 2.5.2. Thus, the parameterized state space equation of the aeroelastic system for unsteady compressible flow, over the dynamic pressure becomes as

$$\left\{ \begin{array}{c} \{\dot{\xi}\} \\ \{z\}_{\bar{q}} \end{array} \right\} = \left[\begin{array}{c|c} [A_{AE}] & [B_{AE}] \\ \hline \left[[A_1] \quad [A_2] \quad [D_{Ac}] \quad [D_{Acq}] \quad [D_{AcM}] \quad [D_{AcMq}] \right] & [0_{2x2}] \end{array} \right] \left\{ \begin{array}{c} \{\xi\} \\ \{w\}_{\bar{q}} \end{array} \right\} \tag{B.6}$$

where $[A_{AE}]$ is given in Equation (2.136), $[B_{AE}]$ is given in Equation (2.137), $\{\xi\}$ is given in Equation (2.134), and the structural and

aerodynamic coefficient matrices are given in Equation (2.127) through (2.132).

Equation (B.6) is both applicable to unsteady subsonic and supersonic compressible flow, since the state space equation format of both flow regimes are identical.

APPENDIX C

DESCRIBING FUNCTION METHOD

Describing function method is used to derive approximate linear models of nonlinear systems. The method is based on the frequency response method. Hence it assumes the input to the system is harmonically oscillating. There are also additional conditions that the system should satisfy, in order to apply the describing function method:

" 1. There is only a single nonlinear component

2. The nonlinear component is time-invariant

3. Corresponding to a sinusoidal input x=sin(ωt), only the fundamental component $y_1(t)$ in the output $y(t)$ has to be considered

4. The nonlinearity is odd" [64]

Assume a nonlinear system, y that satisfies the above conditions, and a sinusoidal input as

$$x = A\sin(\omega t) = Ae^{i\omega t} \tag{C.1}$$

For a single valued nonlinearity such as backlash the output of the system will be harmonically, but usually non-sinusoidal. Hence the output can be expended by using Fourier series as given in Equation (C.2).

$$y(t) = \sum_{i=1}^{\infty} a_i(A,\omega)\sin(i\omega t) + \sum_{i=0}^{\infty} b_i(A,\omega)\sin(i\omega t)$$

(C.2)

where

$$a_i = \frac{1}{\pi}\int_{-\pi}^{\pi} y(t)\,\sin(i\omega t)\,d(\omega t)$$

$$b_0 = \frac{1}{\pi}\int_{-\pi}^{\pi} y(t)\,d(\omega t)$$

(C.3)

$$b_i = \frac{1}{\pi}\int_{-\pi}^{\pi} y(t)\,\cos(i\omega t)\,d(\omega t)$$

Due to the third and the fourth conditions in the previous page, Equation (C.2) can be simplified as given below.

$$y(t) \approx a_1(A,\omega)\sin(\omega t) + b_1(A,\omega)\cos(\omega t) = \left[a_1(A,\omega) + ib_1(A,\omega)\right]e^{i\omega t} \quad (C.4)$$

Similar to frequency response function, the describing function is the complex fundamental harmonic gain of the nonlinearity. Describing function denoted by $\upsilon(A,\omega)$ is

$$\upsilon(A,\omega) = \frac{\left[a_1(A,\omega) + ib_1(A,\omega)\right]}{A} = \frac{M(A,\omega)}{A}e^{i\phi(A,\omega)}$$

(C.5)

where

$$M(A,\omega) = \sqrt{a_1(A,\omega)^2 + b_1(A,\omega)^2}$$

(C.6)

$$\phi(A,\omega) = a\tan\left(\frac{b_1(A,\omega)}{a_1(A,\omega)}\right) \qquad\qquad (C.7)$$

From Equation (C.5) it can be seen that the describing function is function of input coefficients. Hence for a defined input, describing function will become a linear function. This linearization is named as the quasi-linearization, since the input still affects the output. Nonlinearities that depend on single argument are called memoryless. For all memoryless nonlinearities, describing functions are real and independent of input frequency ω. The derivation of the general case of describing function can be find in reference [66].

Piecewise linear functions are single valued nonlinearities. Backlash, saturation, ideal relay, and preload type of nonlinearities are the special cases of this nonlinearity. It is also called gain-changing nonlinearity. In Figure C 1 the graphical representation of the piecewise-linear function is given. In this figure k_1 and k_2 correspond to the slopes of the function at two different region.
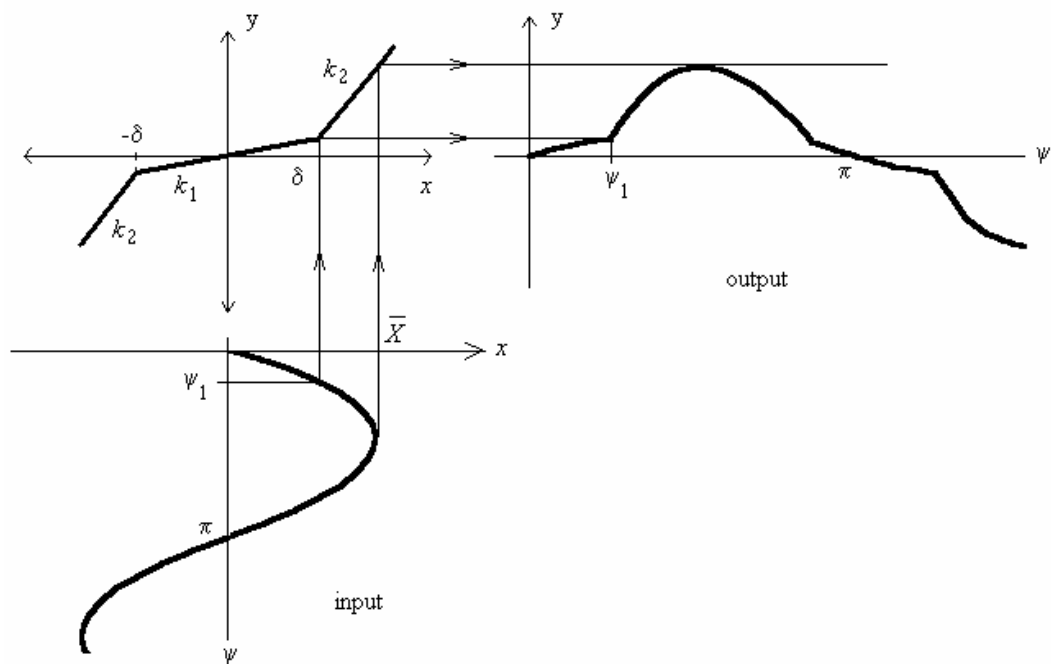
Figure C 1. Input-output relation for piecewise-linear functions [13].

The mathematical representation of the piecewise linear function is

$$y(t) = \begin{cases} k_1 A\sin(\omega t) & ,0 \le \omega t \le \gamma \\ (k_1 - k_2)\delta + k_2 A\sin(\omega t) & ,\gamma \le \omega t \le \pi/2 \end{cases}$$ (C.8)

where

$$\gamma = a\sin\left(\frac{\delta}{A}\right)$$ (C.9)

Using equations (C.8) and (C.9), a_1 given in Equation (C.3) can be calculated as

$$a_1 = \frac{4}{\pi} \int_0^{\pi/2} y(t)\,\sin(\omega t)\,d(\omega t)$$

$$= \begin{cases} \dfrac{4}{\pi} \int_0^{\gamma} k_1 A \sin(\omega t)\,\sin(\omega t)\,d(\omega t) & ,0 \le \omega t \le \gamma \\[4mm] \dfrac{4}{\pi} \int_0^{\gamma} k_1 A \sin(\omega t)\,\sin(\omega t)\,d(\omega t) \\[2mm] \quad + \dfrac{4}{\pi} \int_{\gamma}^{\pi/2} \{(k_1 - k_2)\delta + k_2 A \sin(\omega t)\}\,\sin(\omega t)\,d(\omega t) & ,\gamma \le \omega t \le \pi/2 \end{cases}$$

$$= \begin{cases} k_1 A & ,0 \le \omega t \le \gamma \\[4mm] \dfrac{2(k_1 - k_2)A}{\pi}\left(\arcsin\left(\dfrac{\delta}{A}\right) + \dfrac{\delta}{A}\sqrt{1-\left(\dfrac{\delta}{A}\right)^2} \right) + k_2 A & ,\gamma \le \omega t \le \pi/2 \end{cases} \qquad (C.10)$$

Since these nonlinearities are single valued, $b_1 = 0$. Hence, the describing function can be derived substituting Equation (C.10) into (C.5) as

$$v(A) = \frac{a_1}{A} = \begin{cases} k_1 & ,A \le \delta \\[4mm] \dfrac{2(k_1 - k_2)}{\pi}\left(\arcsin\left(\dfrac{\delta}{A}\right) + \dfrac{\delta}{A}\sqrt{1-\left(\dfrac{\delta}{A}\right)^2} \right) + k_2 & ,A \ge \delta \end{cases} \qquad (C.11)$$

Describing function of the backlash type of nonlinearity can be obtained by setting k_2 to zero.

366

RESULTS OF THE ANALYSES OF THE AEROSERVOELASTIC SYSTEMS WITH VARIOUS CONTROLLERS

D.1. q-Method H$_\infty$ Controllers

Table 82. Parameters and stability analysis results of various q-method H$_\infty$ controllers

Case #	Synthesis parameters					Controller properties				Stability analysis results				
	Controller # *	$\bar{q}_{dist}$	$\omega_{\bar{q}2}$	[W_{Fd}] scale		Controller type & order	norm			robust	nominal			
				@1Hz	@10Hz		H$_2$	H$_\infty$	μ	$\bar{q}_{inst}$	$\bar{q}_{inst\_low}$	ω_{inst_low}	$\bar{q}_{inst}$	ω_{inst}
		Pa	Hz							Pa	Pa	Hz	Pa	Hz
1	3	1,500	10	1/5	50	H$_\infty$ / 14	-	0.769	0.768	1,625	-815	14.4	9,359	6.3
2‡	3	1,500	20	1/5	50	H$_\infty$ / 14	-	1.088	1.083	1,790	-998	15.3	14,455	6.2
3‡	3	1,500	18	1/5	50	H$_\infty$ / 14	-	1.039	1.035	1,744	-951	-951.8	15,201	6.3
4‡	3	1,500	16	1/5	50	H$_\infty$ / 14	-	0.982	0.979	1,720	-910	15.0	11,962	6.3
5‡	3	1,500	14	1/5	50	H$_\infty$ / 14	-	0.916	0.914	1,669	-876	14.9	10,966	6.3
6‡	3	1,500	12	1/5	50	H$_\infty$ / 14	-	0.840	0.839	1,660	-850	14.7	10,071	6.3
7	3	1,500	8	1/5	50	H$_\infty$ / 14	-	0.769	0.754	1,508	-693	13.8	8,244	6.1
8‡	3	2,000	10	1/5	50	H$_\infty$ / 14	-	0.954	0.946	1,588	-794	14.8	9,530	6.4
9‡	2	1,500	10	1/5	50	H$_\infty$ / 14	-	0.833	0.826	1,381	-865	14.3	8,526	6.2
10	4	1,500	10	1/5	50	H$_\infty$ / 14	-	0.769	0.766	1,826	-641	14.4	10,078	6.2

* Equivalent $\bar{q}_{cont}$ is given in Table 20.

‡ The stabilizing controller has poles at right hand side plane

Table 83. Time domain analysis results of various q-method H∞ controllers

Case #	q simulation	ω_n	e_{ss} mean	e_{ss} oscillation	$tr_{5\%}$	ts	Mp	$\delta_{\alpha\theta}$	Current C_{mean_steady}	C_{max_step}	C_{std_steady}	C_{max_steady}
	Pa	Hz	deg	deg	s	s	%	deg	A	A	A	A
1	0	6.00	-0.008	-0.022	0.076	0.145	5.68	1.29	0.000	0.98	0.233	0.50
	4,000	6.03	-0.024	0.019	0.065	1.130	6.45	2.32	0.019	0.80	0.323	0.73
2	0	5.98	-0.017	0.037	0.076	-	4.72	1.26	0.000	1.13	0.333	1.11
	4,000	5.90	-0.033	0.021	0.062	-	3.83	2.20	0.016	1.09	0.440	1.05
3	0	5.98	-0.016	0.039	0.076	-	4.87	1.27	0.000	1.11	0.323	1.09
	4,000	5.94	-0.031	0.019	0.062	-	4.29	2.33	0.018	1.11	0.408	0.98
4	0	5.95	-0.014	0.040	0.078	-	5.14	1.27	0.000	1.04	0.318	1.00
	4,000	5.95	-0.036	0.017	0.063	-	4.66	2.14	0.018	1.13	0.384	1.05
5	0	6.00	-0.023	0.031	0.078	-	5.18	1.28	0.000	0.92	0.279	0.64
	4,000	5.98	-0.033	0.019	0.063	-	5.13	2.14		1.02	0.357	1.02
6	0	5.90	-0.014	0.022	0.076	0.140	5.12	1.28	0.000	0.97	0.231	0.44
	4,000	6.02	-0.028	0.016	0.065	1.710	5.59	2.12	0.018	0.90	0.373	0.84
7	0	5.90	-0.008	0.024	0.077	0.160	6.40	1.36	0.000	0.90	0.196	0.65
	4,000	5.94	-0.025	0.022	0.063	1.420	7.30	2.28	0.016	0.79	0.338	0.78
8	0	5.94	-0.016	0.041	0.075	-	5.10	1.30	0.000	1.07	0.291	1.07
	4,000	6.06	-0.034	0.019	0.063	-	5.98	2.12	0.017	1.04	0.393	0.95
9	0	6.00	-0.014	0.023	0.075	0.100	4.48	1.32	0.000	0.93	0.231	0.70
	4,000	6.00	-0.029	0.019	0.063	2.435	6.95	2.27	0.018	0.84	0.348	0.82
10	0	5.78	-0.005	0.042	0.078	0.150	7.58	1.33	0.000	0.99	0.242	0.71
	4,000	5.98	-0.022	0.019	0.063	1.190	5.94	2.23	0.018	0.80	0.293	0.75

D.2. q-Method H$_2$ Controllers

Table 84. Parameters and stability analysis results of various q-method H$_2$ controllers

Case #	Controller #*	$\bar{q}_{dist}$	$\omega_{\bar{q}2}$	$[W_{Fd}]$ scale @1Hz	@10Hz	Controller type & order	H$_2$	H$_\infty$	μ	$\bar{q}_{inst\_low}$	ω_{inst_low}	$\bar{q}_{inst}$	ω_{Inst}
		Pa	*Hz*							*Pa*	*Hz*	*Pa*	*Hz*
1	1	1,500	10	1/5	50	H$_2$ / 13	8.065	1.562	1.310	-827	12.7	7,353	5.6
2	3	1,500	10	1/5	50	H$_2$ / 13	7.858	1.455	1.281	-612	12.7	8,036	5.6
3	3	2,000	10	1/5	50	H$_2$ / 13	9.394	1.764	1.506	-635	13.1	8,681	5.7
4	3	1,000	10	1/5	50	H$_2$ / 13	6.251	1.137	1.037	-594	12.2	7,141	5.5
5	3	1,500	15	1/5	50	H$_2$ / 13	9.636	1.796	1.552	-698	13.2	10,292	5.6
6	4	1,500	10	1/5	50	H$_2$ / 13	7.715	1.398	1.261	-453	12.7	8,577	5.6
7	3	1,500	10	1	100	H$_2$ / 13	10.333	1.927	1.656	-571	13.3	7,211	5.9

* Equivalent $\bar{q}_{cont}$ is given in Table 20.

Table 85. Time domain analysis results of various q-method H_2 controllers

Case #	q simulation	ω_n	e_{ss} mean	e_{ss} oscillation	$tr_{5\%}$	ts	Mp	$\delta_{\alpha\theta}$	Current c_{mean_steady}	c_{max_step}	c_{std_steady}	c_{max_steady}
	Pa	Hz	deg	deg	s	s	%	deg	A	A	A	A
1	0	5.63	-0.034	0.024	0.074	-	2.38	1.29	0.000	0.65	0.121	0.24
1	4,000	5.47	-0.057	0.018	0.067	-	5.99	2.22	0.018	0.57	0.229	0.48
2	0	5.63	-0.032	0.023	0.085	-	6.28	1.33	0.000	0.66	0.111	0.25
2	4,000	5.47	-0.055	0.019	0.068	-	5.87	2.21	0.017	0.58	0.246	0.45
3	0	5.67	-0.031	0.023	0.084	-	6.15	1.33	0.000	0.66	0.137	0.40
3	4,000	5.47	-0.058	0.020	0.067	-	5.71	2.22	0.018	0.58	0.236	0.50
4	0	5.73	-0.033	0.022	0.086	-	6.14	1.32	0.000	0.65	0.087	0.17
4	4,000	5.40	-0.051	0.017	0.068	-	5.68	2.15	0.017	0.58	0.197	0.40
5	0	5.68	-0.031	0.022	0.083	-	5.76	1.33	0.000	0.66	0.137	0.30
5	4,000	5.43	-0.060	0.018	0.066	-	4.44	2.18	0.019	0.57	0.255	0.54
6	0	5.73	-0.030	0.023	0.090	-	10.01	1.35	0.000	0.69	0.120	0.27
6	4,000	5.47	-0.054	0.018	0.066	-	5.68	2.10	0.019	0.59	0.237	0.43
7	0	5.62	-0.034	0.026	0.083	-	5.57	1.33	0.000	0.67	0.135	0.30
7	4,000	5.73	-0.047	0.017	0.065	-	8.12	2.37	0.018	0.63	0.262	0.59

D.3. q-Method *μ* Controllers

Table 86. Parameters and stability analysis results of various q-method *μ* controllers

Case #	Controller # *	$\bar{q}_{dist}$	$\omega_{\bar{q}2}$	$[W_{Fd}]$ scale @1Hz	$[W_{Fd}]$ scale @10Hz	Controller type & order	H_2	H_∞	μ	robust $\bar{q}_{inst}$	$\bar{q}_{inst\_low}$	ω_{inst_low}	$\bar{q}_{inst}$	ω_{inst}
		Pa	Hz							Pa	Pa	Hz	Pa	Hz
1	5	5,000	10	1/5	50	μ / 20		4.168	0.991	-569	-603	14.3	6,222	6.3
2‡	5	6,000	10	1/5	50	μ / 19		4.627	1.115	-637	-670	14.4	6,378	6.3
3‡	5	4,000	10	1/5	50	μ / 20			0.885	-500	-533	14.1	5,958	6.4
4	5	5,000	10	1	100	μ / 21		2.607	1.199	-634	-673	15.5	8,502	6.7
5	5	3,000	10	1/5	50	μ / 19		2.477	0.760	-454	-486	13.8	6,025	6.3
6	5	3,000	10	1	100	μ / 22			0.833	-588	-629	15.9	8,561	7.0
7	3	3,000	10	1/5	50	μ / 18			0.840	-811	-842	13.7	5,050	6.3
8	3	3,000	10	1	100	μ / 20			1.007	-902	-939	15.4	7,586	6.7
9	3	2,500	10	2	100	μ / 20			0.979	-1,359	-1,036	3.0	9,754	7.6
10	3	2,500	10	2	100	μ / 21			0.953	-1,360	-1,036	3.0	9,744	7.6
11	3	2,500	10	2	125	μ / 21			1.011	-1,290	-1,032	3.0	9,648	7.5

* Equivalent $\bar{q}_{cont}$ is given in Table 20.

‡ The stabilizing controller has poles at right hand side plane

Table 87. Time domain analysis results of various q-method *µ* controllers

Case #	q simulation	ω_n	e_{ss} mean	e_{ss} oscillation	$tr_{5\%}$	ts	Mp	$\delta_{\alpha\theta}$	c_{mean_steady}	c_{max_step}	c_{std_steady}	c_{max_steady}
	Pa	Hz	deg	deg	s	s	%	deg	A	A	A	A
1	0	5.33	-0.046	0.018	0.086	-	7.05	1.32	0.000	0.99	0.260	0.67
	4,000	6.11	-0.057	0.018	0.063	-	6.27	2.47	0.016	0.98	0.331	0.98
2	0	5.33	-0.045	0.018	0.086	-	5.33	1.29	0.000	0.76	0.281	0.74
	4,000	6.05	-0.057	0.016	0.064	-	4.78	2.32	0.017	0.87	0.364	0.87
3	0	5.36	-0.037	0.038	0.086	-	8.03	1.35	0.000	0.88	0.270	0.80
	4,000	6.18	-0.050	0.019	0.062	-	7.20	2.35	0.019	0.92	0.333	0.76
4	0	5.54	-0.043	0.038	0.083	-	5.64	1.32	0.000	1.48	0.384	1.48
	4,000	6.13	-0.047	0.017	0.061	-	4.73	2.19	0.016	1.43	0.528	1.22
5	0	5.43	-0.037	0.022	0.087	-	9.46	1.38	0.000	0.78	0.164	0.36
	4,000	6.13	-0.045	0.018	0.062	-	8.11	2.36	0.018	0.75	0.302	0.72
6	0	5.73	-0.030	0.025	0.079	-	7.46	1.39	0.000	1.55	0.431	1.48
	4,000	6.32	-0.037	0.019	0.058	-	6.46	2.10	0.019	1.47	0.525	1.42
7	0	5.73	-0.036	0.022	0.082	-	4.13	1.29	0.000	0.72	0.204	0.44
	4,000	6.19	-0.045	0.021	0.064	-	10.52	2.46	0.018	0.93	0.299	0.68
8	0	5.62	-0.033	0.021	0.078	-	3.73	1.30	0.000	1.02	0.273	0.56
	4,000	6.22	-0.040	0.017	0.060	-	7.35	2.35	0.018	1.22	0.527	1.13
9	0	5.84	-0.028	0.021	0.072	0.371	4.78	1.23	0.000	2.65	0.774	2.19
	4,000	6.43	-0.039	0.014	0.056	-	5.63	2.11	0.018	2.93	0.896	2.93
10	0	5.84	-0.028	0.021	0.072	0.371	4.78	1.23	0.000	2.65	0.774	2.19
	4,000	6.43	-0.039	0.014	0.056	-	5.63	2.11	0.018	2.93	0.896	2.93
11	0	5.81	-0.030	0.020	0.075	5.512	3.86	1.25	0.000	2.51	0.754	2.47
	4,000	6.38	-0.038	0.015	0.057	-	5.82	1.94	0.019	2.47	0.822	2.26

D.4. g and gq-Method H∞ Controllers

Table 88. Parameters and stability analysis results of various g-method H∞ controllers

Case #	Controller #*	δ_c	ω_{c2}	$[W_{Fd}]$ scale		Controller type & order	norm			robust	nominal			
				@ 0Hz	@10Hz		H_2	H_∞	μ	$\bar{q}_{inst}$	$\bar{q}_{inst\_low}$	ω_{inst_low}	$\bar{q}_{inst}$	ω_{Inst}
		N.m.s/rad	Hz							Pa	Pa	Hz	Pa	Hz
1	1	2	6	1/5	50	H∞ / 13		0.810	0.767	2,256	-995	2.9	F	F
2	3	2	6	1/5	50	H∞ / 13		0.789	0.752	2,576	-997	2.9	F	F
3	5	2	6	1/5	50	H∞ / 13		0.754	0.723	3,129	-1,007	2.9	F	F
4	1	3	6	1/5	50	H∞ / 14		0.954	0.947	2,388	-959	2.9	F	F
5	1	1	6	1/5	50	H∞ / 13		0.640	0.625	2,010	-1022	2.9	F	F
6	1	2	6	1/5	100	H∞ / 13		0.800	0.754	2,304	-970	2.9	F	F
7	1	2	6	3/5	100	H∞ / 13		0.932	0.907	1,310	-988	2.9	F	F

* Equivalent $\bar{q}_{cont}$ is given in Table 20.

F There is no instability in the incompressible region

Table 89. Time domain analysis results of various g-method H∞ controllers

Case #	q simulation	ω_n	e_{ss} mean	e_{ss} oscillation	$tr_{5\%}$	ts	Mp	$\delta_{\alpha\theta}$	Current c_{mean_steady}	Current c_{max_step}	Current c_{std_steady}	Current c_{max_steady}
	Pa	Hz	deg	deg	s	s	%	deg	A	A	A	A
1	0	5.83	-0.033	0.022	0.079	-	1.07	1.21	0.000	0.81	0.248	0.80
	4,000	4.97	-0.045	0.009	0.076	-	-	1.99	0.019	0.77	0.263	0.58
2	0	5.71	-0.032	0.023	0.079	-	2.62	1.26	0.000	0.78	0.256	0.75
	4,000	5.03	-0.044	0.010	0.075	-	-	2.02	0.018	0.72	0.245	0.55
3	0	5.43	-0.032	0.023	0.081	-	5.46	1.32	0.000	0.85	0.234	0.59
	4,000	5.12	-0.041	0.009	0.075	-	-	2.00	0.017	0.66	0.256	0.56
4	0	5.70	-0.033	0.022	0.077	-	1.24	1.17	0.000	1.01	0.296	0.99
	4,000	4.98	-0.050	0.014	0.076	-	-	1.97	0.016	0.95	0.404	0.93
5	0	5.81	-0.033	0.021	0.081	-	0.61	1.38	0.000	0.96	0.181	0.58
	4,000	1.80	-0.047	0.009	0.076	-	-	2.11	0.018	0.81	0.193	0.40
6	0	5.84	-0.032	0.022	0.079	-	1.10	1.22	0.000	0.79	0.250	0.78
	4,000	4.92	-0.038	0.016	0.077	-	-	1.91	0.017	0.08	0.295	0.76
7	0	5.70	-0.033	0.019	0.077	-	1.21	1.19	0.000	0.87	0.270	0.57
	4,000	5.36	0.038	0.016	0.070	-	2.56	2.13	0.019	0.92	0.364	0.92

D.5. g and gq-Method H$_2$ Controllers

Table 90. Parameters and stability analysis results of various g-method H$_2$ controllers

Case #	Controller # *	δ_c	ω_{c2}	$[W_{Fd}]$ scale @ 0Hz	@10Hz	Controller type & order	H$_2$	H$_\infty$	μ	$\bar{q}_{inst\_low}$	ω_{inst_low}	$\bar{q}_{inst}$	ω_{Inst}
		N.m.s/rad	*Hz*							*Pa*	*Hz*	*Pa*	*Hz*
1	1	2	6	1/5	50	H$_2$ / 13	7.966	1.335	1.312	-1,149	2.8	F	F
2	1	1	6	1/5	50	H$_2$ / 13	5.946	1.028	1.009	-1,204	2.8	F	F
3	3	2	6	1/5	50	H$_2$ / 13	7.778	1.307	1.283	-1,182	2.8	F	F
4	3	2	6	2	100	H$_2$ / 14	16.840	2.632	2.629	-983	2.9	8,422	5.8
5	4	2	6	1/5	50	H$_2$ / 13	7.648	1.288	1.263	-1,202	2.7	F	F
6	4	2	6	2/5	50	H$_2$ / 13	8.506	1.412	1.397	-1,050	12.2	F	F
7	4	2	6	1/5	100	H$_2$ / 13	7.491	1.266	1.239	-1,103	2.7	F	F
8	4	2	6	1	100	H$_2$ / 12	11.297	1.823	1.821	-851	13.0	8,467	5.4

* Equivalent $\bar{q}_{cont}$ is given in Table 20.

F There is no instability in the incompressible region

Table 91. Time domain analysis results of various g-method H_2 controllers

Case #	q simulation	ω_n	e_{ss} mean	e_{ss} oscillation	$tr_{5\%}$	ts	Mp	$\delta_{\alpha\theta}$	Current c_{max_step}	Current c_{mean_steady}	Current c_{std_steady}	Current c_{max_steady}
	Pa	Hz	deg	deg	s	s	%	deg	A	A	A	A
1	0	5.24	0.055	0.025	0.078	-	-	1.16	0.000	0.54	0.138	0.37
	4,000	1.25	-0.080	0.016	0.085	-	-	1.89	0.017	0.48	0.176	0.45
2	0	5.24	-0.055	0.026	0.077	-	-	1.16	0.000	0.54	0.095	0.26
	4,000	1.05	-0.074	0.012	0.084	-	5.40	1.95	0.017	0.49	0.117	0.30
3	0	5.38	-0.055	0.022	0.082	-	1.24	1.20	0.000	0.56	0.107	0.27
	4,000	1.45	-0.077	0.015	0.081	-	-	1.89	0.017	0.49	0.148	0.45
4	0	5.12	-0.058	0.024	0.084	-	0.97	1.20	0.000	0.66	0.202	0.41
	4,000	5.43	-0.081	0.020	0.068	-	4.38	2.34	0.015	0.76	0.372	0.76
5	0	5.47	-0.055	0.029	0.088	-	3.51	1.22	0.000	0.56	0.115	0.29
	4,000	1.57	-0.076	0.014	0.082	-	-	1.90	0.017	0.49	0.134	0.43
6	0	5.38	-0.056	0.020	0.091	-	3.31	1.22	0.000	0.56	0.102	0.19
	4,000	1.70	-0.078	0.017	0.076	-	-	2.02	0.016	0.49	0.175	0.48
7	0	5.47	-0.053	0.024	0.086	-	3.72	1.22	0.000	0.56	0.118	0.33
	4,000	1.56	-0.069	0.010	0.086	-	-	1.93	0.017	0.49	0.141	0.40
8	0	5.21	-0.056	0.023	0.090	-	2.94	1.23	0.000	0.59	0.139	0.30
	4,000	5.22	-0.072	0.017	0.071	-	3.00	2.17	0.018	0.59	0.276	0.57

D.6. g and gq-Method *µ* Controllers

Table 92. Parameters and stability analysis results of various g-method *µ* controllers

Case #	Controller # *	\multicolumn{4}{c}{Synthesis parameters}				\multicolumn{4}{c}{Controller properties}			\multicolumn{5}{c}{Stability analysis results}				
		δ_c	ω_{c2}	\multicolumn{2}{c}{$[W_{Fd}]$ scale}	Controller type & order	\multicolumn{3}{c}{norm}	robust	\multicolumn{4}{c}{nominal}			
				@ 0Hz	@10Hz		H_2	H_∞	μ	$\bar{q}_{inst}$	$\bar{q}_{inst\_low}$	ω_{inst_low}	$\bar{q}_{inst}$	ω_{Inst}
		N.m.s/rad	Hz							Pa	Pa	Hz	Pa	Hz
1	1	2	6	1/5	100	µ / 18		12.044	0.568	3,145	-1,028	2.9	ꟳ	ꟳ
2	1	1	6	3/5	100	µ / 18		30.692	0.527	2,486	-998	2.9	ꟳ	ꟳ
3	1	2	6	1/5	50	µ / 16		15.529	0.570	3,093	-1,015	2.9	ꟳ	ꟳ
4	1	1	6	1/5	50	µ / 18			0.428	2,663	-1,004	2.9	ꟳ	ꟳ
5	4	1	6	3/5	100	µ / 17		37.297	0.474		-986	2.9	ꟳ	ꟳ

* Equivalent $\bar{q}_{cont}$ is given in Table 20.

ꟳ There is no instability in the incompressible region

Table 93. Time domain analysis results of various g-method *µ* controllers

Case #	q simulation	ω_n	\multicolumn{2}{c}{e_{ss}}	$tr_{5\%}$	ts	Mp	$\delta_{\alpha\theta}$	\multicolumn{4}{c}{Current}			
			mean	oscillation					c_{max_step}	c_{mean_steady}	c_{std_steady}	c_{max_steady}
	Pa	Hz	deg	deg	s	s	%	deg	A	A	A	A
1	0	6.14	-0.034	0.017	0.074	-	1.64	1.24	0.000	2.18	0.721	1.83
	4,000	5.43	-0.040	0.008	0.072	1.423	-	2.11	0.018	2.18	0.799	1.64
2	0	5.75	-0.027	0.014	0.075	0.100	2.75	1.17	0.000	1.87	0.525	1.29
	4,000	5.76	-0.029	0.011	0.062	0.329	3.83	2.01	0.018	2.21	0.541	1.75
3	0	5.95	-0.033	0.016	0.076	-	2.61	1.20	0.000	2.39	0.713	2.39
	4,000	5.40	-0.043	0.008	0.069	-	-	2.01	0.015	2.27	0.671	1.31
4	0	6.03	-0.029	0.015	0.074	0.100	2.95	1.26	0.000	1.32	0.421	1.06
	4,000	5.43	-0.034	0.013	0.067	0.748	1.45	1.97	0.018	1.82	0.453	1.82
5	0	5.78	-0.026	0.015	0.075	0.101	3.50	1.21	0.000	1.89	0.501	1.27
	4,000	5.76	-0.029	0.011	0.062	0.349	3.17	2.00	0.018	2.19	0.542	1.61

CURRICULUM VITAE

PERSONAL INFORMATION

Surname, Name: Akmeşe, Alper
Nationality: Turkish (TC)
Date and Place of Birth: 20 April 1974 , Erzincan
Marital Status: Married
Phone: +90 312 442 79 04
Fax: +90 312 590 91 48
Email: aakmese@gmail.com

EDUCATION

Degree	Institution	Year of Graduation
MS	METU Mechanical Engineering	2000
BS	METU Mechanical Engineering	1997
High School	Gazi Anadolu High School, Ankara	1993

WORK EXPERIENCE

Year	Place	Enrollment
2002- Present	TÜBİTAK SAGE	Senior Research Engineer
2000- 2002	TÜBİTAK SAGE	Research Engineer
1997-1999	METU Department of Mechanical Engineering	Research Assistant
1996 August	MAKVASAN	Intern Engineering Student
1995 August	Nurol Machinery and Industry Inc.	Intern Engineering Student

FOREIGN LANGUAGES

Fluent English,

PUBLICATIONS

1. Söylemez, E., Akmeşe, A., " Uzaysal Dört-Çubuk Mekanizmaları İçin Freudenstein Denklemi", 9. Ulusal Makina Teorisi Sempozyumu Bildiri Kitabı, Eylül 1999, s.1-13.

2. Akmeşe, A., "Two Degrees of Freedom Adjustable Mechanism Design", Master Thesis, METU, 2000.

3. Akmeşe, A., Cömert, M.D., Platin, B.E., "Aeroservoelastic Analysis of Missile Control Surfaces Via Robust Control Methods", Proceedings of 16th IFAC Symposium on Automatic Control in Aerospace, June 14-18, 2004, St.Petersburg, Russia.

HOBBIES

Guitar, Scuba, Basketball, Motorcycling